

Hemanta Hazarika · Motoki Kazama
Wei F. Lee *Editors*

Geotechnical Hazards from Large Earthquakes and Heavy Rainfalls

Geotechnical Hazards from Large Earthquakes and Heavy Rainfalls

Hemanta Hazarika · Motoki Kazama
Wei F. Lee
Editors

Geotechnical Hazards from Large Earthquakes and Heavy Rainfalls



Springer

Editors

Hemanta Hazarika
Kyushu University
Fukuoka
Japan

Wei F. Lee
Taoyuan County Government
Taoyuan
Taiwan

Motoki Kazama
Tohoku University
Sendai
Japan

ISBN 978-4-431-56203-0
DOI 10.1007/978-4-431-56205-4

ISBN 978-4-431-56205-4 (eBook)

Library of Congress Control Number: 2016943863

© Springer Japan 2017

This work is subject to copyright. All rights are reserved by the Publisher, whether the whole or part of the material is concerned, specifically the rights of translation, reprinting, reuse of illustrations, recitation, broadcasting, reproduction on microfilms or in any other physical way, and transmission or information storage and retrieval, electronic adaptation, computer software, or by similar or dissimilar methodology now known or hereafter developed.

The use of general descriptive names, registered names, trademarks, service marks, etc. in this publication does not imply, even in the absence of a specific statement, that such names are exempt from the relevant protective laws and regulations and therefore free for general use.

The publisher, the authors and the editors are safe to assume that the advice and information in this book are believed to be true and accurate at the date of publication. Neither the publisher nor the authors or the editors give a warranty, express or implied, with respect to the material contained herein or for any errors or omissions that may have been made.

Printed on acid-free paper

This Springer imprint is published by Springer Nature
The registered company is Springer Japan KK

Photographs



Photo 1 Participants of the workshop



Photo 2 Professor M. Kazama (*left*) and Prof. K. Ishihara (*right*) delivering the opening address



Photo 3 Professor A. Wakai (*left*) and Prof. T.S. Ueng (*right*) delivering the keynote lectures



Photo 4 During the session



Photo 5 Students and young researcher interaction session



Photo 6 Professor I. Towhata (*left*), Prof. Y.S. Fang (*right*) and Prof. H. Hazarika (*below*) delivering the closing remarks



Photo 7 Workshop dinner party at Moji Port, Kita Kyushu



Photo 8 Delegates of the technical tour (in front of Sakanishi check dam, Kumamoto)

Preface

Geotechnical Hazards from Large Earthquakes and Heavy Rainfalls is a compilation of peer-reviewed papers presented in the sixth Japan–Taiwan Joint International Workshop on Geotechnical Hazards from Large Earthquakes and Heavy Rainfalls. The workshop was held under the auspices of the Asian Technical Committee No. 3 on Geotechnology for Natural Hazards (ATC3) of the International Society for Soil Mechanics and Geotechnical Engineering (ISSMGE). It was co-organized by the Japanese Geotechnical Society (JGS) and the Taiwanese Geotechnical Society (TGS).

ATC3 was established in 1993 under the leadership of its founding chairman, Prof. K. Ishihara, Professor Emeritus of the University of Tokyo, Japan, to deal with the geotechnical aspects concerning earthquake-triggered and rainfall-induced natural hazards in the Asian region. Since its inception, ATC3 has always been very active in organizing academic events and research activities between Japan and Taiwan. Towards this end, five workshops were successfully held between 2004 and 2012 both in Japan and Taiwan. The aim of this sixth workshop was to exchange information related to geotechnical natural hazards and establish a joint research framework for future collaboration between Japan and Taiwan as well as other Asian countries.

The workshop was financially supported by Kita-Kyushu City, the Kita-Kyushu City Convention Association, and the Japanese Geotechnical Society. The editors are very grateful to these three organizations for their encouragement and support of the workshop and the publication of this book.

The book focuses on geotechnical and natural hazards-related issues in the Asian region such as earthquakes, tsunami, and rainfall-induced debris flows, slope failures, landslides, and so on. It contains the latest information and mitigation technology on earthquake and rainfall-induced geotechnical natural hazards. The volume comprises 57 contributions including three keynote and special lectures that were delivered during the workshop by distinguished scholars and experts in this field. All the manuscripts were thoroughly reviewed by at least two reviewers

selected from an international panel of experts in order to check for the relevance to the theme as well as the quality of technical contents and presentation.

The publication of this volume has been possible through the sustained efforts of the staff of the Geotechnical Engineering Research Group of the Department of Civil Engineering, Kyushu University. The editors express their sincere thanks to all the members. Special thanks go to Mr. Babloo Chaudhary, a Ph.D. student in the Geotechnical Engineering Research Group of Kyushu University, for his tireless efforts and dedication, which were instrumental in the timely publication of the book. The editors also would like to express their sincere gratitude to all the reviewers for their time and effort to review the manuscripts.

Geotechnical Hazards from Large Earthquakes and Heavy Rainfalls provides a wealth of knowledge and information, and helps disseminate the latest information and technology in the field of geotechnical natural hazards. The book is aimed at researchers, designers, consultants, government officials, academicians, and students working in those fields. The editors hope that in the years to come, the developments, the state of the art, the knowledge, and findings that have been compiled in this book will contribute towards the development of a new chapter in disaster prevention and mitigation of geotechnical structures not only in the Asian region, but also in the other regions of the world.

Fukuoka, Japan

Sendai, Japan

Taoyuan, Taiwan

Hemanta Hazarika

Motoki Kazama

Wei F. Lee

Acknowledgments

Financial Support

The chairpersons of the International Workshop on Geotechnical Hazards from Large Earthquakes and Heavy Rainfalls and the editors of this book gratefully acknowledge the financial support provided by Kita-Kyushu City, the Kita-Kyushu City Convention Association, and the Japanese Geotechnical Society.

Panel of Reviewers

The manuscript for each chapter included in this book was carefully reviewed for the quality and clarity of technical contents and presentation by at least two members of a review panel consisting of the following international experts. The editors wish to express their sincere gratitude to all the reviewers for their valuable time and contributions.

- A. Abdullah, Malaysia
- N.P. Bhandary, Japan
- B. Chaudhary, India
- T.C. Chen, Taiwan
- J.J. Dong, Taiwan
- L. Ge, Taiwan
- T. Hara, Japan
- K. Harada, Japan
- H. Hazarika, Japan
- T. Kiyota, Japan

W.F. Lee, Taiwan
B.S. Lin, Taiwan
S.S. Lin, Taiwan
W. Lin, Japan
M. Wada, Japan
T. Ohsumi, Japan
M. Okamura, Japan
R.P. Orense, New Zealand
S. Suttisak, Thailand
H. Toyota, Japan
A. Wakai, Japan
G. Wang, Japan
H. Yi, China

Organization

Advisory Committee

Chairpersons:

Prof. M. Kazama (Tohoku University, Japan)

Prof. S.S. Lin (National Taiwan Ocean University, Taiwan)

Members:

Prof. D.T. Bergado (Asian Institute of Technology, Thailand)

Prof. C.H. Chen (National Taiwan University, Taiwan)

Prof. J.W. Chen (National Cheng Kung University, Taiwan)

Prof. Y.S. Fang (National Chao Tung University, Taiwan)

Prof. K. Ishihara (Chuo University, Japan)

Prof. T. Kokusho (Chuo University, Japan)

Prof. T. Kyoya (Tohoku University, Japan)

Prof. H.J. Liao (National Taiwan University of Science and Technology, Taiwan)

Prof. H.D. Lin (National Taiwan University of Science and Technology, Taiwan)

Prof. M.L. Lin (Taiwan National University, Taiwan)

Prof. H. Nagase (Kyushu Institute of Technology, Japan)

Prof. I. Towhata (University of Tokyo, Japan)

Prof. L.M. Wang (Earthquake Administration of Gansu Province, China)

Prof. S. Yasuda (Tokyo Denki University, Japan)

Prof. N. Yasufuku (Kyushu University, Japan)

Prof. K. Yasuhara (Ibaraki University, Japan)

Prof. N. Yoshida (Tohoku Gakuin University, Japan)

Organizing Committee

Chairpersons:

Prof. H. Hazarika (Kyushu University, Japan)
Dr. W.F. Lee (Taiwan Geotechnical Society, Taiwan)

Members:

Dr. N.P. Bhandary (Ehime University, Japan)
Prof. G. Chen (Kyushu University, Japan)
Prof. T.C. Chen (National Ping Tung University of Science and Technology, Taiwan)
Dr. S.Y. Chi (Sinotech GERC Research Center, Taiwan)
Prof. J.J. Dong (National Central University, Taiwan)
Dr. Z. Furukawa (Kyushu University, Japan)
Dr. T. Hara (Kochi University, Japan)
Dr. K. Harada (Fudo Tetra Corporation, Japan)
Dr. A. Hirooka (Kyushu Institute of Technology, Japan)
Dr. R. Ishikura (Kyushu University, Japan)
Prof. C.J. Jeng (Huafan University, Taiwan)
Dr. K. Kasama (Kyushu University, Japan)
Dr. T. Kiyota (University of Tokyo, Japan)
Prof. Y. Mitani (Kyushu University, Japan)
Dr. T. Mori (Tohoku University, Japan)
Dr. H. Nakazawa (Fukken Corporation, Japan)
Prof. M. Okamura (Ehime University, Japan)
Dr. H. Takahashi (Port and Airport Research Institute, Japan)
Prof. Y. Tsukamoto (Tokyo University of Science, Japan)
Dr. H. Toyota (Nagaoka University of Technology, Japan)
Dr. M. Wada (Kiso Jiban Consultant, Japan)
Prof. A. Wakai (Gunma University, Japan)
Prof. C.C. Wang (Cheng Shou University, Taiwan)
Dr. G. Wang (Kyoto University, Japan)
Dr. L. Wang (Chuo Kaihatsu Corporation, Japan)
Prof. T.T. Wang (National Taipei University of Technology, Taiwan)
Dr. M. Yoshimine (Tokyo Metropolitan University, Japan)

Secretariat:

Mr. Babloo Chaudhary (Kyushu University, Japan)

Contents

Part I Keytopics on Earthquake and Rainfall Induced Geohazards

| | |
|---|----|
| Initial Trigger for Slope Failures in Volcanic Ash Layer of Hillside Surface in Izu-Oshima Island in Japan Due to a Typhoon Rainfall in 2013 | 3 |
| Akihiko Wakai and Satoshi Goto | |
| A Case Study on Silty Sand Liquefaction | 17 |
| Wei F. Lee and Luois Y.N. Ge | |
| Bearing Capacity of Breakwater Mound Under Tsunami-Induced Seepage Flow | 27 |
| H. Takahashi, S. Sassa, Y. Morikawa and D. Takano | |

Part II Earthquake Induced Liquefaction and Countermeasures

| | |
|--|----|
| Verification of Improvement Effectiveness by Compaction Methods During the 2011 off the Pacific Coast of Tohoku Earthquake | 39 |
| Kenji Harada, Jun Ohbayashi and Yuichi Taguchi | |
| Development of Rational Soil Liquefaction Countermeasure Consisting of Lattice-Shaped Soil Improvement by Jet Grouting for Existing Housing Estates | 49 |
| Takahiro Yamauchi, Hiroaki Tezuka and Yoshimichi Tsukamoto | |
| Uplift Mechanism of Rectangular Tunnel in Liquefied Soils | 61 |
| Chung-Jung Lee, Yue-Chen Wei, Wen-Ya Chuang, Wen-Yi Hung, Wen-Lung Wu and Tai-Yuan Ho | |
| Seismic Response of Geosynthetic Reinforced Earth Embankment on Different Soil Foundation | 75 |
| Wen-Yi Hung and Chung-Jung Lee | |

| | |
|--|-----|
| Development of a New In-place Cement-Mixing Method by High-Pressure Injection | 87 |
| Hiroaki Tezuka, Takahiro Yamauchi and Fumio Tatsuoka | |
| Use of Swedish Weight Sounding Tests for Detecting Liquefiable Backfills Reclaimed in Iron Sand Mining Pits in Asahi City of Chiba in Japan | 101 |
| Yoshimichi Tsukamoto, Shohei Kawabe and Shigeru Kanemitsu | |
| GIS-Based Study on Liquefaction-Induced Soil Subsidence in the Urayasu Area Due to the 2011 off the Pacific Coast of Tohoku Earthquake | 111 |
| Rama Mohan Pokhrel and Takashi Kiyota | |
| Effects of Non-plastic Fines on Undrained Cyclic Behavior of Loose Sand | 121 |
| Yolanda Alberto-Hernandez and Ikuo Towhata | |
| An Investigation on the Liquefaction-Induced Sloped Ground Failure During the 1964 Niigata Earthquake | 133 |
| Gabriele Chiaro, Junichi Koseki and Takashi Kiyota | |
| Laboratory Experiments on Seepage in Liquefied Sand | 145 |
| Tzou-Shin Ueng and Zih-Fang Wang | |
| Effects of Cyclic Triaxial Loading Rates on Liquefaction Behavior of Fine-Grained Soils | 155 |
| Ya-Han Hsu, Louis Ge and Meng-Heng Chiang | |
| Effect of Gravel Content on Saturated Hydraulic Conductivity in Sand | 163 |
| Tsung-Yuan Wang, Li-Ling Lin and Yi-Zhi Tsai | |
| Effects of Overconsolidation, Cement Stabilisation, and Unsaturation on the Liquefaction Resistance of Urayasu Sand | 171 |
| Shotaro Hagiwara, Yoshimichi Tsukamoto and Shohei Kawabe | |
| Part III Landslides, Slope Failures and Debris Flows | |
| Loessial Landslides Induced by the Minxian-Zhangxian Ms6.6 Earthquake of China in 2013 | 183 |
| L.M. Wang, Q. Wang, Z.J. Wu and A.L. Che | |
| Numerical Simulation of Run-Out Behavior of Earthquake-Induced Landslides | 193 |
| Meei-Ling Lin and Ching-Ya Huang | |

| | |
|---|-----|
| The Geometric Characteristics and Initiation Mechanisms of the Earthquake-Triggered Daguangbao Landslide | 203 |
| J.J. Dong, C.C. Tsao, C.M. Yang, W.J. Wu, C.T. Lee, M.L. Lin, W.F. Zhang, X.J. Pei, G.H. Wang and R.Q. Huang | |
| Centrifuge Modeling of Relationships Between Earthquake Intensities and Scales of Post-quake Triggering Rainfall and Landslide | 215 |
| M.H. Wu, J.P. Wang and J.C. Yeh | |
| Time-Prediction Method of the Onset of a Rainfall-Induced Landslide Based on the Monitoring of Surface Displacement and Groundwater Level in the Slope | 223 |
| Katsuo Sasahara | |
| Typhoon Rainfall Induces Slope Creep, Groundwater Variation, and Slope Movement. | 235 |
| C.J. Jeng, C.Y. Yang and J.H. Lin | |
| Topographic Characteristic of the Rainfall-Inducing Landslide in Slate Stratum—Case of Ai-Liao Catchment, South Taiwan. | 249 |
| Tien-Chien Chen, Ping-Yuan Jhang and Huei-Jing Ciou | |
| Site Investigation and In Situ Testing on Shallow Landslide Scars of Natural Slopes Covered by Volcanic Ash and Pumice Fall | 259 |
| Kentaro Yamamoto, Yukiyoshi Teramoto, Mizuki Hira and Katsuhisa Nagakawa | |
| Overhaul the Anchored Slopes in Taiwan | 269 |
| Hung-Jiun Liao and Shih-Hao Cheng | |
| A Study by Field Measurement and Numerical Simulation About Rainfall Seepage Mechanism in Case of Torrential Rainfall | 281 |
| Toru Danjo, Tomofumi Koyama, Hideki Nakamura, Yuto Tsuruzawa and Naoki Fukuyama | |
| Numerical Simulation for the Earthquake-Induced Deformation of a Residential Land Slope Reinforced with Landslide Prevention Piles | 291 |
| Taisuke Watanabe, Akihiko Wakai, Takayuki Fukazu, Ryo Obuchi, Tomohiro Mori and Shingo Sato | |
| Centrifuge Model Test on Slope Reinforcement by Rock Bolt with Facing Plate | 301 |
| Shion Nakamoto and Jiro Takemura | |
| Numerical Simulation of Post-Entrainment Debris Flow at Alluvial Fan Using FLO-2D Model | 311 |
| Zheng Han, Guangqi Chen, Yange Li, Linrong Xu and Fusong Fan | |

| | |
|--|-----|
| Photomicrograph Investigation of Rock Thin Sections Taken from Landslides Scree by the Eastern Honshu Earthquake, 2008 | 323 |
| Tsuneo Ohsumi | |
| An Extension to Weiler–Atherton Clipping Algorithm for the Face-to-Face Contact in Three-Dimensional Discrete Element Method | 333 |
| H. Zhang, G. Chen, S.G. Liu, P.D. Jing and Z. Han | |
| Application of Three-Dimensional Discontinuous Deformation Analysis to Simulate Characteristics of Planar Translational Slope Failure | 339 |
| P.D. Jing, G. Chen, H. Zhang and W. Wang | |
| Part IV Evaluation and Mitigation of Geohazards | |
| Hazard Mapping for Earthquake-Induced Geo-disaster Chain | 349 |
| Guangqi Chen, Yanan Fan and Yange Li | |
| Monitoring Techniques for Sediment Disaster in Mountant Area | 363 |
| Lin Bing Shyan, Lien Hei Pan, Liu Yi Chen, Li Cheng Yang and Chen Ping Sen | |
| Seismic Performance of Piles from EQWEAP and Monte Carlo Simulation Analyses | 375 |
| D.W. Chang, Y.H. Lin, C.H. Liu, S.C. Chu and H.C. Chao | |
| The Overflow Model Experiment Using the Waterway for Examining the Countermeasure Effect Against the Tsunami-Induced Tide Embankment Scouring | 385 |
| Tomohiro Mori, Hiroaki Kabuki, Motoki Kazama, Peter K. Hutaapea, Jongkwan Kim, Ryuji Sakamoto and Koujiro Takao | |
| Analysis of a Coastal Structure Damaged Due to Compound Effect of Earthquake and Tsunami | 399 |
| H. Hazarika, T. Hara, K. Kuribayashi, S. Kuroda, T. Nishi, H. Furuichi, K. Takezawa and T. Ohsumi | |
| An Example of the Restoration Method of Levees Damaged by the Great East Japan Earthquake. | 411 |
| Tohru Yanagihata, Osamu Nakayama, Yasushi Sasaki, Ryosuke Uzuoka and Tetsuya Nakamura | |
| Remediation of a Failed Slope Located at Fault Fracture Zone. | 421 |
| San-Shyan Lin, Jen-Cheng Liao, Sheng-Der Yang and Li-Yuan Huang | |

| | |
|--|-----|
| Case Study of Using the Low-Pressure Grouting Method to Uplift a Tilted Building | 431 |
| C.J. Kuo, Y.K. Lin, S.C. Shieh and C.H. Chen | |
| A Study on the Bio-treatment Technique of Ground Improvement with Urease Microorganisms Which Live in Japan | 441 |
| Seiji Kano, Takeo Moriwaki and Kyohei Ochi | |
| Behavior of Breakwater Foundation Reinforced with Steel Sheet Piles Under Seismic Loading | 449 |
| Babloo Chaudhary, Hemanta Hazarika, Naoya Monji, Kengo Nishimura, Ryohei Ishikura and Kiyonobu Kasama | |
| Shaking Table Model Tests on Mitigation of Liquefaction-Induced Distortion of Shallow Foundation | 463 |
| Rouzbeh Rasouli, Ikuo Towhata and Hadrien Rattez | |
| Study on the Effect of Union Basement on Decreasing Destruction During Liquefaction | 479 |
| G. Liu, R. Ishikura, N. Yasufuku, K. Kasama and N. Matsuo | |
| Part V Piles and Retaining Walls | |
| Analysis of the Lateral Force on Stabilizing Piles in $c\text{-}\phi$ Soil | 491 |
| Yi He, Hemanta Hazarika, Noriyuki Yasufuku and Ryohei Ishikura | |
| Application of Close-Range Photogrammetry for Post-Failure Reconnaissance of a Retaining Wall | 503 |
| Yung-Yen Ko, Jen-Yu Han and Jun-Yun Chou | |
| Seismic Response of a Newly Developed Geocell-Reinforced Soil Retaining Wall Backfilled with Gravel by Shaking Table Model Test | 513 |
| Han Xinye, Mera Tomoharu, Katagiri Toshihiko and Kiyota Takashi | |
| Ultimate Lateral Resistance of Piles in Soils Based on Active Pile Length | 525 |
| Mary Roxanne Aglipay, Kazuo Konagai, Takashi Kiyota and Hiroyuki Kyokawa | |
| Effect of Backfill Reinforcement on Retaining Wall Under Dynamic Loading | 535 |
| Babloo Chaudhary, Hemanta Hazarika and A. Murali Krishan | |
| Numerical Study on the Seismic Response of Waterfront Retaining Wall Reinforced with Cushion | 545 |
| Amizatulhani Abdullah, Hemanta Hazarika, Noriyuki Yasufuku and Ryohei Ishikura | |

| | |
|---|-----|
| Factors Controlling the Behavior of Piled Foundations Due to Cyclic Lateral Loading. | 555 |
| Mahmoud F. Awad-Allah, Noriyuki Yasufuku and A.H. Abdel-Rahman | |
| Centrifugal Model Loading Tests on Reinforced Soil Retaining Wall with Groundwater Permeation. | 569 |
| Makoto Kobayashi, Kinya Miura and Takeharu Konami | |
| Horizontal Pressure on a Non-yielding Wall Due to Flexible and Rigid Strip Loading | 585 |
| Yung-Show Fang, Chia-Pei Lin and Cheng Liu | |
| Part VI Other Related Topics | |
| Matric Suction and Shear Modulus of Unsaturated Compacted Lateritic Soil Subjected to Drying and Wetting | 599 |
| Horn-Da Lin, Cheng-Chun Wang and Johnson H.S. Kung | |
| A Constant-Head Well Permeameter Measurement of Saturated Hydraulic Conductivity in the Vadose Zone and the Capabilities of Carbon Dioxide Injection | 609 |
| Makoto Nishigaki and Sten-Magnus Mostek | |
| Remediation of Volcanic Ash Soil in Related to Soil Erodibility Against the Heavy Rainfall | 619 |
| Rina Devnita, Ridha Hudaya, Rija Sudirja, Ade Setiawan, Mega F. Rosana and Hemanta Hazarika | |
| Structural Pattern's Effects on the Tensile Properties of Hexagonal Wire Meshes (12 cm × 15 cm). | 629 |
| Chiwan Hsieh, Zhi-Yao Cai and In-Wei Liu | |

About the Editors



Hemanta Hazarika is Professor in the Department of Civil Engineering, Kyushu University, Fukuoka, Japan.

He obtained his Bachelor of Technology (B.Tech.) degree in Civil Engineering from the Indian Institute of Technology (IIT), Madras, India, in 1990 and his Master's and Ph.D. degrees in Geotechnical Engineering from Nagoya University, Japan, in 1993 and 1996, respectively. Before moving to his present position, he worked as a practicing engineer for a few years and spent several years teaching and conducting research in academia as well as with public sector research institutes in Japan.

Professor Hazarika's research activities include soil-structure interaction, stability of soil structures during earthquakes and tsunami, ground improvement, application of recycled waste and lightweight materials in construction, stability of cut slopes, and landslides and protection against them.

He has published and presented more than 180 technical papers in various international journals and conferences and symposia. He has authored two books on soil mechanics. One is *Soil Mechanics Fundamentals* (CRC Press), which is in English, and the other is in Japanese. The second edition of his book titled *Soil Mechanics Fundamentals and Applications* was published in March 2015.

Professor Hazarika is also credited with serving as the editor of two books in his research areas: one is related to earthquake hazards and mitigations and the other is on waste tire recycling.

Currently he is the chairman of the technical committee on Integrated Approach to Risk Management of Geodisasters and Climate Change Adaptation of the Japanese Geotechnical Society. He is also serving at present as the secretary of two Asian technical committees of the International Society of Soil Mechanics and Geotechnical Engineering (ISSMGE). One is Geotechnology for Natural Hazards (ATC3), and the other is Mitigation and Adaptation to Climate Change-Induced Geodisasters (ATC1). He was also secretary of the ISSMGE technical committee

No. 4 (then TC4) on Geotechnical Earthquake Engineering and Associated Problems.

Professor Hazarika has also been serving as an expert for the Japan International Cooperation Agency (JICA) of the Government of Japan on various projects related to Asian countries and ASEAN.



Motoki Kazama is Professor in the Department of Civil and Environmental Engineering, Graduate School of Engineering, Tohoku University, Sendai, Japan.

He graduated from the Civil Engineering Department of Tohoku University in 1981 and was a research engineer of the Port and Harbor Research Institute, Ministry of Transport, from 1981 to 1994. During that period, he was a member of the Structural Division and engaged in research on the earthquake-proof design of port and harbor structures such as a gravity-type quay wall, improved ground foundation structures, and so on. He obtained the Doctorate in Engineering from Tohoku University in 1993.

Professor Kazama moved to Tohoku University in 1994, where he supervised the Geotechnical Engineering Laboratory. After moving there, his main research activities have been concerned with soil dynamics. Those include dynamic soil-structure interaction, seismic response analysis of soft soil ground, dynamic property of soils, and the deformation property of soils subjected to cyclic loading. He received a research achievement prize from the Japan Society of Civil Engineering for a series of his research achievements in 2010.

The 2011 earthquake off the Pacific Coast of Tohoku caused serious damage. Sendai City, where Tokoku University is located, is a major city in the affected area. As a civil engineer, Prof. Kazama has contributed to the restoration work following the Great East Japan Disaster.

Currently he is the Vice President of the Japanese Geotechnical Society and is the Chairman of the Asian technical committee of the International Society of Soil Mechanics and Geotechnical Engineering (ISSMGE) on Geotechnology for Natural Hazards.



Dr. Wei F. Lee received his Ph.D. from the Department of Civil Engineering of the University of Washington in 2000. He is currently the deputy general manager of both the Ground Master Construction Company and the MICE Engineering Consulting Company, one of the most prominent geotechnical engineering turnkey joint ventures in Taiwan. Before Dr. Lee joined the Ground Master Group, he was a counselor and task force executive of the Taoyuan Aerotropolis Project of the Taoyuan County Government, Taiwan. Prior to joining the Taoyuan County Government, he was Research Professor at the National Taiwan University of Science and Technology, NTUST.

Dr. Lee has served as a board member of the Taiwan Geotechnical Society for more than 12 years. He is also a member of several technical and board-level committees of the International Society of Soil Mechanics and Geotechnical Engineering (ISSMGE). He has published more than 170 conference and journal papers; he is also a member of the editorial advisory panel of the Institution of Civil Engineers (ICE) journal *Forensic Engineering* and an editorial reviewing member of the ASCE *Journal of Performance of Constructed Facilities* and other international journals. In addition, he has been involved in organizing several international conferences and workshops, including the ATC3 Japan–Taiwan Joint Symposium on Geotechnical Hazards.

Dr. Lee is one of the pioneer researchers in Taiwan in geotechnical earthquake engineering, forensic geotechnical engineering, and maintenance engineering of geotechnical structures. During his professional career, he has been the principal investigator or project manager of more than 200 research and engineering projects, including subway constructions, seismic design and mitigation of foundations, transportation infrastructure management systems, and performance monitoring for bridges against aging and multi-hazards.

Part I

**Keytopics on Earthquake and Rainfall
Induced Geohazards**

Initial Trigger for Slope Failures in Volcanic Ash Layer of Hillside Surface in Izu-Oshima Island in Japan Due to a Typhoon Rainfall in 2013

Akihiko Wakai and Satoshi Goto

Abstract In the year 2013, the typhoon Wipha passed through the neighbourhood of the Izu-Oshima Island from 15 to 16 October 2013, and on the early morning of 16 October, a large number of slope failures occurred at various sites in the island. The largest one occurred at a caldera external slope located in the western part of the island near Motomachi Town. In this study, the initial trigger for such huge failures in the upstream slope, as the beginning of this serious mud flood disaster, has been discussed in mechanical point of view. According to the results obtained from the experimental and analytical examinations including the centrifuge model tests, it can be concluded that the increase of the pore water pressure in the thin ash-fall deposits layer with high permeability has promoted the decrease of the effective confining pressure in the layer, and it caused the surface failures in the hillside slopes.

Keywords Izu-Oshima Island • Slope failure • Ash-fall deposit • Rainfall • Pore water pressure • Centrifuge test

1 Introduction

Izu-Oshima Island is a volcanic island, of area of 91 km², off the south of the Tokyo metropolitan area, 100 km away from the centre of Tokyo. Most of the hillside surface of the Mt. Mihara, located at the centre of the island, is covered with volcanic ashes due to frequent volcanic eruptions of the mountain. In the year 2013, the typhoon Wipha (called as the typhoon No. 26 in Japan) passed through the neighbourhood of the island from 15 to 16 October 2013, and the total amount of the precipitation around the suffered area was quite large quantities as more than

A. Wakai (✉)
Gunma University, 1-5-1, Tenjin, Kiryu, Gunma 376-8515, Japan
e-mail: wakai@gunma-u.ac.jp

S. Goto
University of Yamanashi, Kofu, Japan



Fig. 1 General overlook view of the mud flood in Izu-Oshima Island caused by Typhoon Wipha in 2013

800 mm. On the early morning of 16 October, a large number of slope failures occurred at various sites in the island. The largest one occurred at a caldera external slope located in the western part of the island near Motomachi Town (Fig. 1). The mud flood brought from the debris and water washed away the downstream villages. The width of the slope collapse was approximately 500 m–1 km, and the mud flood flowed out into the sea, where the runout distance was estimated as more than 2 km. It was reported that approximately 40 people in the damaged district have been sacrificed due to the flood event.

2 Failure Mechanisms

One of the important issues in here is how such a large-scale slope failure occurred in this case. By comparing other small failures to the largest one, it can be found that only the largest one is enormously bigger than others. In geomorphological point of view, the clear difference in their size seems to be affected by the difference in degree of development of valleys. It may be also related to such a fact that the past lava flow events at other slopes are much older than the ones near Motomachi Town. Only in this area, the lava flows have frequently flowed down in recent years and left such a flat topography without deep valleys; here the newest event occurred in 1986. Such a topography might make individual slope failure linked each other,

providing a unified and huge slope failure. In this study, the initial trigger for such huge failures in the upstream slope near Motomachi Town, as the beginning of this serious mud flood disaster, will be discussed in mechanical point of view. Because the failure mechanisms seem to be strongly related to the bedding structures of the slope, it is very important to investigate the mechanical characteristics of the materials corresponding to each volcanic ash layer. The relationships between the slope stability and the increase of the pore water pressure in the thin volcanic ash layer with high permeability are clarified by the experimental and analytical examinations with use of the actual soil samples.

2.1 *Soil Samples and Observed Physical Properties*

Immediately after the disaster, so many small holes of local scouring along the thin high-permeability layers were observed at the exposed scarps (Fig. 2). They are the traces that the confined groundwater flushed the covered soil out at the time of slope failure. The soil around the holes was felt to be extremely soft by touching with fingers. The remained terraces have been formed just beneath the row of the holes and it produced stepped terrains in the slope (Fig. 3). The depth of the rows of the holes were approximately 1 m in many cases, while they remained at plural depths in some cases. Such a shallow depth of the rows of holes especially in the



Fig. 2 Many small holes of local scouring along thin ash-fall deposit layer



Fig. 3 Residual local terrains at collapsed slope. **a** Remained terrace beneath holes. **b** Stepped terrains due to collapse of upper layers

upper-end slopes implies that the initial trigger for such a serious slope disaster can be reduced to simple shallow failures in the slopes discussed in this paper later. Also, the dynamic cone penetration tests were carried out along the slope surface at one of the upper-end slopes. Figure 4 shows the penetration resistance for depth at each point in the slope. The stiffer layer can be seen around 1 m depth, which may be related to the above-mentioned shallow failure mechanisms.

In typical cases in the hillside, the thin and grey high-permeability layers with holes are sandwiched by the brown layers with relatively lower permeability. The

Fig. 4 Penetration resistance for depth at each point in the slope

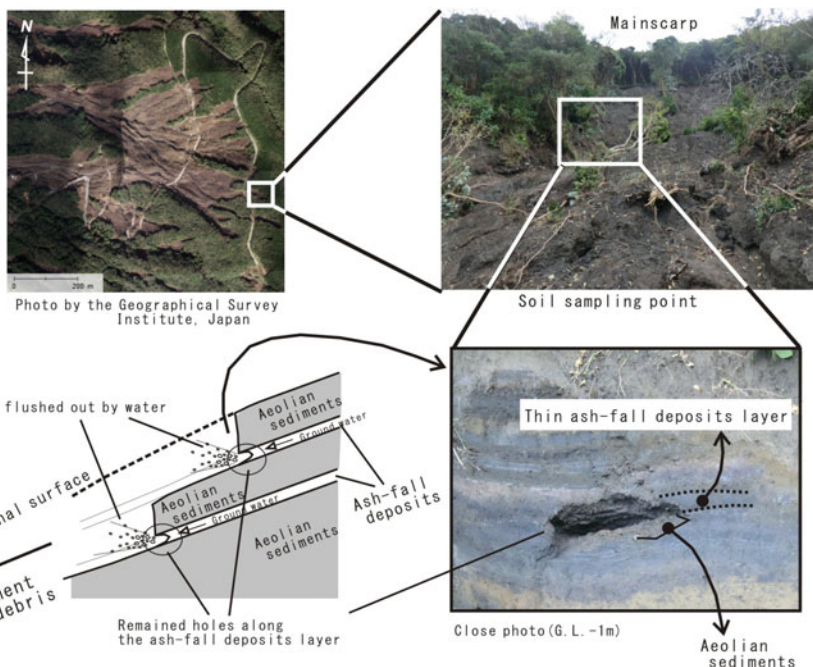
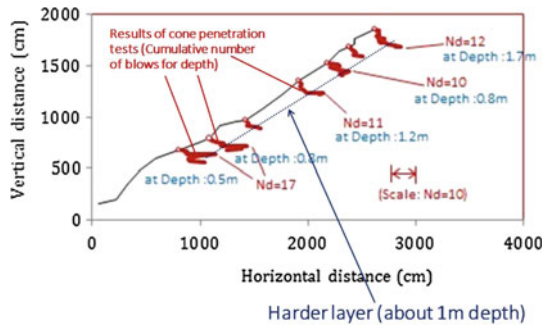


Fig. 5 Details of sampling of two types of soils in hillside slope; ash-fall deposit and aeolian dust layers

former and latter layers are produced from ash-fall deposit and aeolian dust, respectively. According to Koyama and Hayakawa (1996), 24 tephra layers, which overlie the slope outside the caldera, show that 24 eruptions occurred since the formation of the caldera about 1500 years ago. Here, the thin ash-fall layer with holes can be referred to as the tephra of "Y1.0" in 1777 A.D., as suggested in their study. It was the eruption with ash and scoria falls. The soil samples of these two types of materials, i.e. ash-fall deposit and aeolian dust, were obtained at the slope locating in the upper stream end of Oganazawa stream running through Motomachi Town, as shown in Fig. 5.

As seen in the measured particle size distributions of each sample in Fig. 6, both of them are classified as sand containing fines. The fine fraction contents of the ash-fall deposit and the aeolian dust are approximately 20 and 40 %, respectively, that seems the main cause of their difference in the permeability. The in situ properties as well as other physical properties are summarized in Table 1. Here, the ash-fall deposit is so loose that the in situ dry bulk density is smaller than the minimum dry density observed in laboratory. Such a loose state can be formed in a long-term bulking due to confined groundwater flows in intermittent rainfall events and/or chemical changes in the layer. Figure 7 is the relationship between the minimum dry density observed in laboratory and the water content including in situ state. The minimum dry density extremely decreases with a slight water content, in other words, a slight suction can produce such a very loose state even if it is quite few. It implies that the saturation of such loose sand during rainfall can promote increasing the volume contraction and the excess pore pressure in the layer.

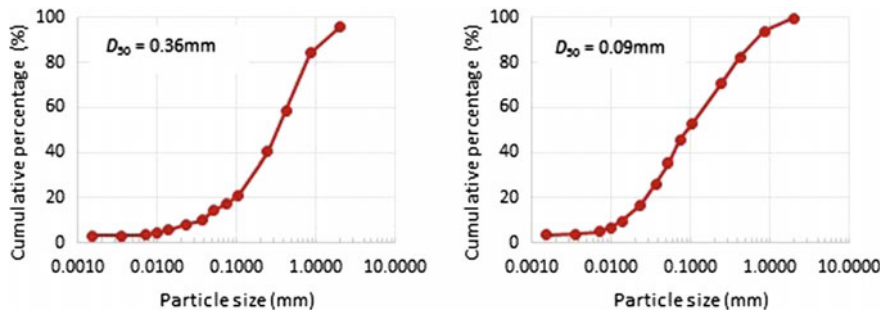


Fig. 6 Measured particle size distributions of two types of soils

Table 1 Physical properties of the volcanic ash soils sampled at the hillside slope in Izu-Oshima Island

| | | | Ash-fall deposit | Aeolian dust |
|-----------------------|---------------|-------------------|------------------|--------------|
| Wet bulk density | ρ_t | g/cm ³ | 1.44 | Unmeasured |
| Dry bulk density | ρ_d | g/cm ³ | 1.24 | Unmeasured |
| Water content | w | % | 16.6 | 29.1 |
| Void ratio | e | | 1.25 | Unmeasured |
| Relative density | D_r | % | -11.5 | Unmeasured |
| Maximum dry density | ρ_{dmax} | g/cm ³ | 1.78 | 1.29 |
| Minimum dry density | ρ_{dmin} | g/cm ³ | 1.28 | 0.96 |
| Soil particle density | ρ_s | g/cm ³ | 2.79 | 2.81 |
| Liquid limit | w_L | % | 23.5 | 30.5 |
| Plastic limit | w_p | % | 23.5 | 22.2 |

Fig. 7 Relationships between minimum dry density observed in laboratory and water content for ash-fall deposit

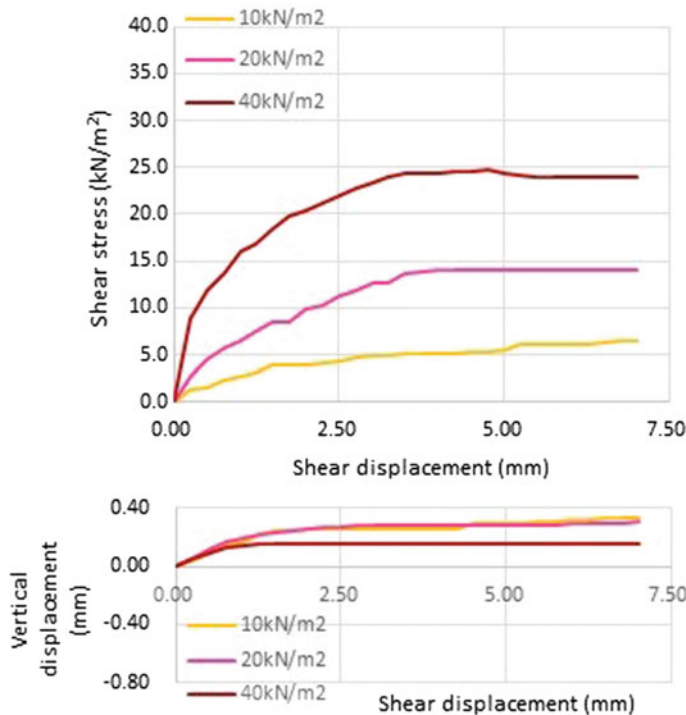
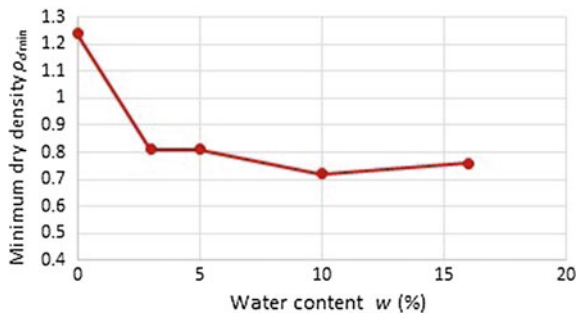


Fig. 8 Results of direct shear tests for ash-fall deposits under drained conditions with use of dried specimens

2.2 Slope Stability Analysis

The results of the direct shear tests for the ash-fall deposits under drained conditions with use of the dried and remoulded specimens were shown in Fig. 8. Here, the dry bulk density of the specimens was 1.52 g/cm^3 , which has been controlled as loosely

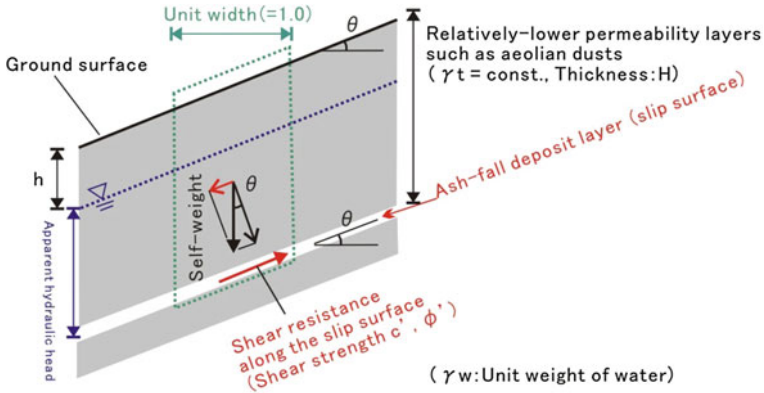


Fig. 9 Semi-infinite slope model assumed in calculation of in situ stress state

as possible (even if it was denser than the in situ conditions). The observed effective shear strength parameters c' and ϕ' are 0 and 32.5° , respectively.

Figure 9 is the semi-infinite slope model assumed in the calculation of in situ stress state, in which the failure along the thin ash-fall layer occurs. The thickness and the wet unit weight of the upper aeolian dust layer are H and γ_t . The total factor of safety F_s , in the case where the ground inclination and the thickness of unsaturated layer above the groundwater level are θ and h , is calculated as

$$F_s = \frac{c' + \{\gamma_t H - \gamma_w (H - h)\} \cos^2 \theta \tan \phi'}{\gamma_t H \sin \theta \cos \theta} \quad (1)$$

Based on the typical conditions in the field, H , γ_t and θ are assumed to be 1.0 m, 18.0 kN/m^3 and 30° , respectively. As a result of calculation by Eq. (1), the critical value of h corresponding to $F_s = 1.0$ is calculated as 0.79 m, which means that the slope failure can occur during a heavy rainfall providing such a hydraulic head.

3 Centrifuge Modelling for Initial Trigger of Slope Failures

The mechanical behaviours of the hillside slope subjected to groundwater loading were simulated by the centrifuge apparatus at Gunma University (Fig. 10) using imitation soil materials. In order to replicate the gravity-induced stresses of a prototype structure in a geometrically $1/N$ reduced model, it is necessary to test the model in a gravitational field N times larger than that of prototype structure. A reduced-scale slope with the inclination of 30° shown in Fig. 11 was prepared in the model box, of the dimensions of $300 \text{ mm} \times 400 \text{ mm} \times 120 \text{ mm}$ in depth, by



Fig. 10 Centrifuge apparatus at Gunma University

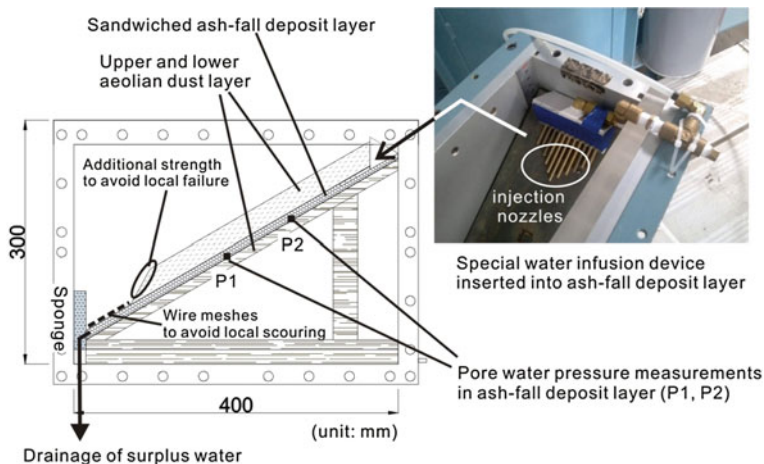
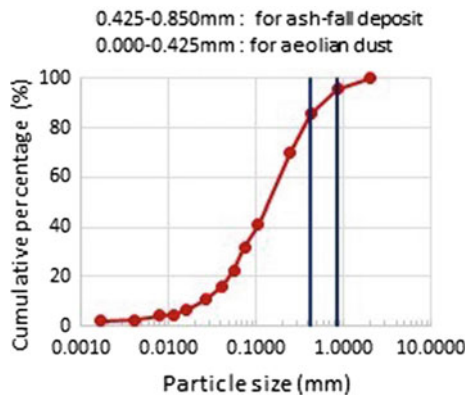


Fig. 11 Reduced-scale slope in centrifuge model box with pore pressure measurements

hand tamping. The geological structure in the model slope was simplified as composed of only three layers, such as the upper aeolian dust, the middle ash-fall deposit and the lower aeolian dust layers. The thickness of the upper aeolian dust layer and the middle ash-fall deposit layers in the model are 30 and 10 mm, respectively. The test was conducted at 30 G and their thickness in the prototype scale became 0.90 and 0.30 m, respectively. The bottom of the lower aeolian dust layer was fixed on the rough board, which promotes layered failures in the thin ash-fall deposit layer on the lower aeolian dust layer.

Fig. 12 Two kinds of imitation soils in place of real soil samples for ash-fall deposit and aeolian dust



Because of the lack of pure samples of ash-fall deposit and aeolian dust, we have decided to use two kinds of imitation soils in place of real soils. The imitation soils were made from the debris sands, which passed a sieve of 2 mm, sampled at the mud flood sediments of Izu-Oshima disaster. Then, the coarser and finer ingredients of the sand as shown in Fig. 12 were used as the imitation soils for the ash-fall deposit and the aeolian dust, respectively. The difference in permeability of two kinds of soils was expected to be brought by their particle size differences.

Based on the results of the direct shear tests for these imitation ash-fall deposits under drained conditions with use of the dried and remoulded specimens (the dry bulk density was 1.18 g/cm³), the effective shear strength parameters c' and ϕ' of the sand were measured as 0 and 36.2°, respectively. The wet density of the upper aeolian dust layer was 1.44 g/cm³. In these conditions, using Eq. (1), the critical pore water pressure at the ash-fall deposit layer corresponding to total slope failure is obtained as 2.5 kPa approximately. This value can be compared with the observed value of the pore water pressure during the centrifuge test as discussed in later.

In the centrifuge test, after applying the centrifuge gravity, the ground water was injected into the thin ash-fall deposit layer forcibly from the rear of the model slope by a special infusion device shown in Fig. 11. The tips of the injection nozzles were inserted into the sandwiched ash-fall deposit layer. The effect of infiltration of the rainwater from the ground surface was ignored in here. The time histories of the observed pore water pressure in the slope for the elapsed time from starting the groundwater injection were shown in Fig. 13. The positions of each pore water pressure measurement (P1, P2) are shown in Fig. 11. As seen in the time histories, the water pressure rose in stages, in response to the increase of the flow-rate level. It was suggested that the excessive increase of the pore water pressure in the ash-fall deposit layer caused a whole collapse of the model slope in the end.

The photos of the slope surface at each moment (at Time: (a) and (b) in Fig. 13) are shown in Fig. 14. They are the looking-down views where the left direction of the photos correspond to the descending direction of the slope. When the water pressure at the lower point P1 reached 3 kPa, the one at the upper point P2 reached about 2 kPa, and a few cracks in the surface gradually were found to have progressed. The blocks of the aeolian dust layer, separated along the cracks, have slid on the failed ash-fall deposit layer, and the failure area continued gradually spreading to the upper part. It was found that the value of the observed water pressure almost accords with the critical water pressure estimated in the previous chapter as 2.5 kPa. Figure 15 is a photo of the damaged model slope which was taken after the experiment, where a peeled surface accompanying a few gullies has been exposed. It is almost the same circumstances observed after the disaster in Izu-Oshima as shown in Fig. 16. Accordingly, the slope failure mechanisms simulated in the centrifuge tests are appeared to be consistent with the actual phenomena precisely.

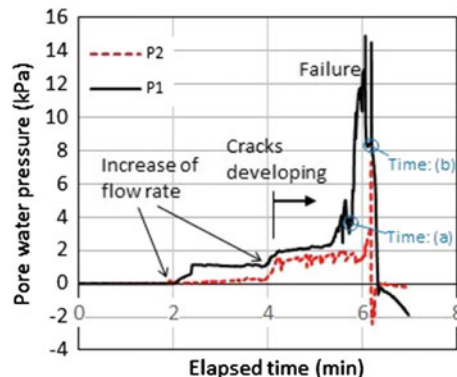


Fig. 13 Time histories of observed pore water pressure during groundwater loading

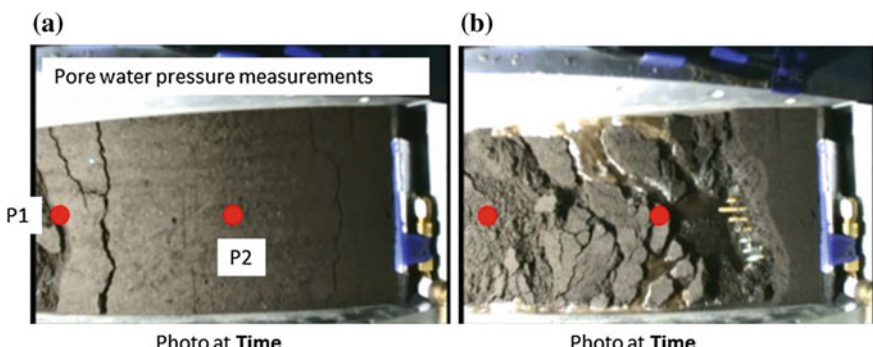


Fig. 14 Photos of model slope surface at each moment (see Fig. 13)



Fig. 15 Photo of damaged model slope after centrifuge test



Fig. 16 Actual slope surface observed after disaster

4 Conclusions

According to the results obtained from the experimental and analytical examinations including the centrifuge model tests, it can be concluded that the increase of the pore water pressure in the thin ash-fall deposits layer with high permeability has promoted the decrease of the effective confining pressure in the layer, and it caused the surface failures in the hillside slopes. After that, the sliding debris has swept the surface soils on the downstream slopes and it might help expanding the collapse area. Based on the above discussions on the mechanisms of such surface failures, more effective countermeasures and risk assessment procedures for similar types of slope disasters can be developed in the future. Because a large number of volcanic ash slopes possessing similar mechanical characteristics to the hillside area of Mt. Mihara in Izu-Oshima exist in Japan, any future studies on this issues would be highly appreciated.

Again, the essential conclusions obtained in this study is as follows:

1. In geomorphological point of view, it was found that, only in the area in the upper stream end of Oganazawa stream running through Motomachi Town, there exists a flat topography without deep valleys that might make individual slope failure linked each other, providing a unified and huge slope failure.
2. The initial trigger for such huge failures in the upstream slope near Motomachi Town, as the beginning of this serious mud flood disaster, has been discussed in mechanical point of view. Because the failure mechanisms were found to be strongly related to the bedding structures of the slope, it is very important to investigate the mechanical characteristics of the materials corresponding to each volcanic ash layer.
3. Immediately after the disaster, so many small holes of local scouring along the thin high-permeability layers were observed at the exposed scarps. They are the traces that the confined groundwater flushed the covered soil out at the time of slope failure. The soil around the holes was felt to be extremely soft by touching with fingers. The depth of the rows of the holes was approximately 1 m in many cases, while they remained at plural depths in some cases. Such a shallow depth of the rows especially in the upper-end slopes implies that the initial trigger for such a serious slope disaster can be reduced to simple shallow failures in the slopes.
4. In typical cases in the hillside, the thin and grey high-permeability layers with holes (i.e. ash-fall deposit) were sandwiched by the brown layers with relatively lower permeability (i.e. aeolian dust). The fine fraction contents of the ash-fall deposit and the aeolian dust are approximately 20 and 40 %, respectively, that seems the main cause of their difference in the permeability. Both of them are classified as sand containing fines.
5. The ash-fall deposit was so loose that the in situ dry bulk density was smaller than the minimum dry density observed in laboratory. Such a loose state might be formed in a long-term bulking due to confined groundwater flows in intermittent rainfall events and/or chemical changes in the layer.

6. As obtained in the observed results, the minimum dry density of the ash-fall deposit extremely decreases with a slight water content, in other words, a slight suction can produce such a very loose state even if it is quite few. It implies that the saturation of such loose sand during rainfall can promote increasing the volume contraction and the excess pore pressure in the layer. Such a mechanism might be related to this disaster.
7. Based on the simple slope stability analysis with an assumption of semi-infinite slope model, using the strength parameters observed in the direct shear tests, the critical value of hydraulic head corresponding to $F_s = 1.0$ is calculated as 0.21 m above the ash-fall deposit layer.
8. The mechanical behaviours of the hillside slope subjected to groundwater loading were simulated by the centrifuge apparatus at Gunma University. As a result, the slope failure mechanisms simulated in the centrifuge tests were shown to be consistent with the actual phenomena precisely. For an example, the value of the observed water pressure almost accords with the critical water pressure which was theoretically estimated.
9. Based on the above discussions on the mechanisms of such surface failures, more effective countermeasures and/or risk assessment procedures for similar types of slope disasters during heavy rainfall can be developed in the future.

Acknowledgments A part of the present study was conducted as a member of the Izu-Oshima Island Typhoon No. 26 Disaster Joint Survey Group of the JSCE, JGS, JSEG and JLS. And the other part of this study was conducted as “A Comprehensive Study on Landslide Disaster in Izu-Oshima Island at Typhoon No. 26 in 2014 (IKuo Towhata Leader)” with support from the Grant-in-Aid for Special Purposes, The Ministry of Education, Culture, Sports, Science and Technology, Japan. We would like to express sincere thanks to them. In addition, we greatly appreciate the assistances of Mr. Masaki Honmyo, Mr. Hirotaka Yokouchi and Mr. Keisuke Sumida, in performing the centrifuge model tests; and of Mr. Takayuki Fukazu and Ms. Hiromi Kameyama, in performing the field investigations; and also, of Tomoyuki Shinozaki, in performing the laboratory soil tests. All of them are the students in the geotechnical engineering laboratory, Gunma University.

References

Izu-Oshima Island Typhoon No. 26 Disaster Joint Survey Group of the JSCE, JGS, JSEG and JLS (2014) Reconnaissance Report on Heavy Rain Disaster in Izu-Oshima Island due to Typhoon No. 26, Oct 2013, Japan (in Japanese)

Koyama M, Hayakawa Y (1996) Syn- and post-caldera eruptive history of Izu-Oshima Volcano based on tephra and loess stratigraphy. *J Geogr* 105:133–162 (in Japanese with English abstract)

A Case Study on Silty Sand Liquefaction

Wei F. Lee and Luois Y.N. Ge

Abstract Silty sand liquefaction has been of great interest of research in geotechnical earthquake engineering. This article presents preliminary results of a case study on nonplastic silty sand liquefaction. Influence factors such as fines contents and disturbance effects on dynamic properties of silty sand are carefully discussed in this paper.

Keywords Silty sand · Dynamic properties · Soil liquefaction · Fines contents · Sampling disturbance

1 Introduction

Nonplastic silty sand liquefaction has been of great research interests in geotechnical earthquake engineering. During the 1999 Chi-Chi earthquake, serious soil liquefaction damages were observed in central Taiwan including Wu Feng, Nan Tou, and Yuen Lin areas. Christchurch and its vicinity of New Zealand have also suffered from severe liquefaction damages during series of earthquakes from 2010 to 2011. Moreover, Tokyo bay area and Chiba perfect was suffered from serious soil liquefaction damages during the 2011 Great East Japan earthquake. For these destructive earthquakes, post-earthquake reconnaissance indicated that most soil liquefactions were taken place in silty sand deposits with high fines content. Preliminary reconnaissance also concludes that majority liquefaction occurred in the reclaimed silty sand deposits (Fig. 1; Lee et al. 2012).

However, it has been difficult to retrieve undisturbed samples of silty sand. Influences of fine contents, void ratio as well as sampling disturbance on liquefaction potential of silty sand containing nonplastic fines were not well studied in

W.F. Lee (✉)

MICE Engineering Ltd. Co., No. 11, Sec. 1 DunHua S. Road, Taipei, Taiwan
e-mail: wflee0206@gmail.com

L.Y.N. Ge

Department of Civil Engineering, National Taiwan University, Taipei, Taiwan

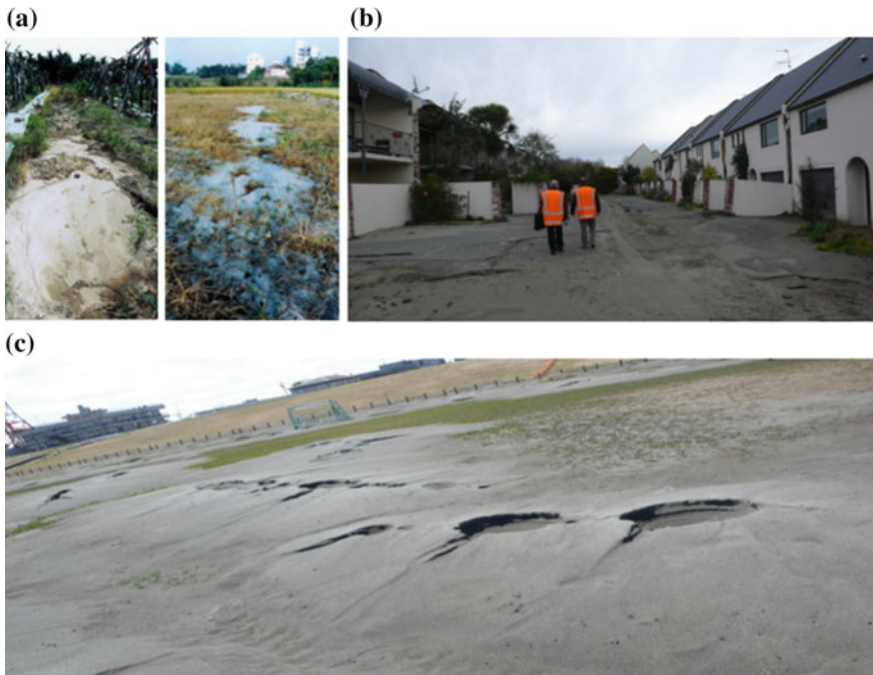


Fig. 1 Non-plastic silty sand liquefaction observed in **a** 1999 Taiwan Chi-Chi earthquake, **b** 2010–2011 New Zealand Christchurch earthquakes, and **c** 2011 Japan Tohoku earthquake

the past. A study site, Hsin Hwa, was selected as the study site, and it was suffered from soil liquefaction during the 2010 Jia Shan Earthquake in Taiwan. Dynamic triaxial tests were carried out on the undisturbed specimens obtained suing gel-push sampler (Lee et al. 2015) and remolded ones to examine the influences of sampling disturbance, fines contents, and void ratios on the dynamic behavior and liquefaction potential of nonplastic silty sand. Details and progress of such a research are presented as follows.

2 Hsin Hwa Liquefaction

Hsin Hwa is located in Tainan City, Taiwan (Fig. 2). This site was selected because massive soil liquefaction was observed during an earthquake of magnitude of 6.4 occurred in 2010. A peak ground acceleration about 385 gal was recorded during this earthquake. Total four boreholes were drilled, where gel-push sampling (Lee et al. 2015) was conducted in three boreholes, and conventional Shelby tube sampling was performed in the fourth one for the purpose of comparison. The soil profile including the SPT-N values of the test site is given in Fig. 3. As depicted in

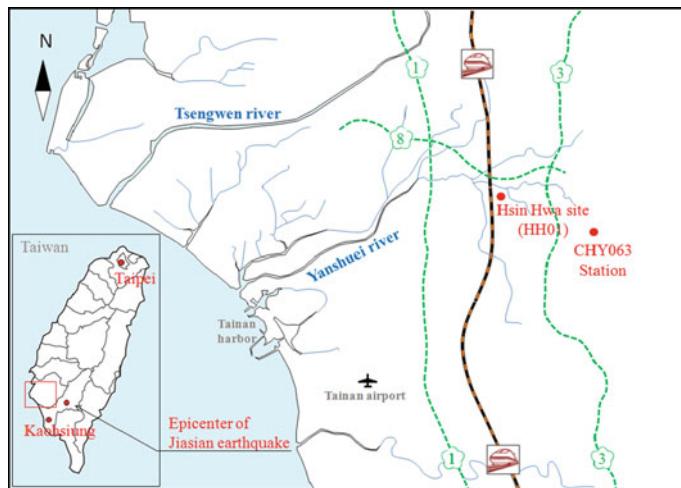


Fig. 2 Geographical location of Jia Sian earthquake

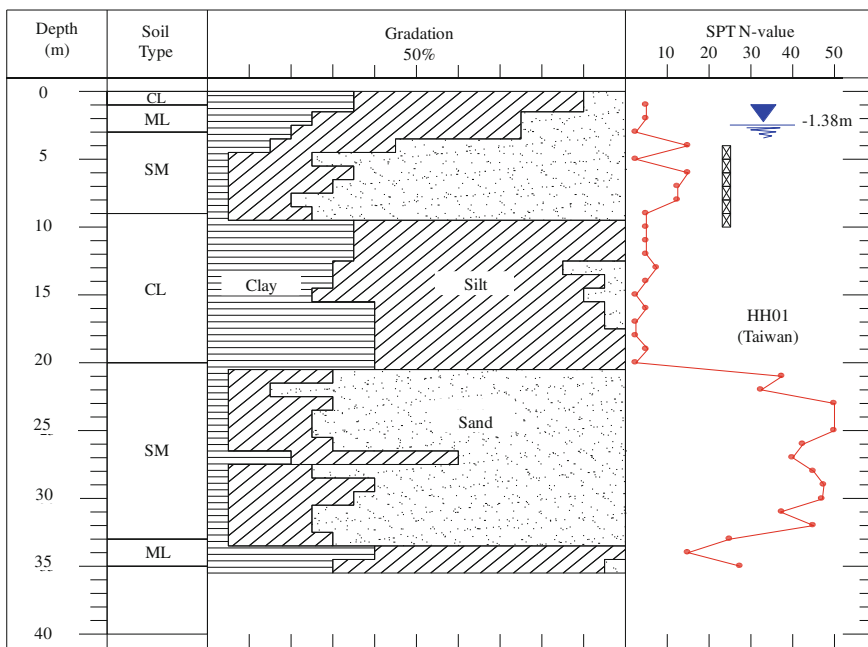


Fig. 3 Summarized soil profile at Hsin Hwa study site

the figure, a silty sand layer, which is located between 2 and 10 m below the ground surface, contains high fines content ranging from 10 % to more than 50 %.

3 Dynamic Properties of Silty Sand

Testing results of two representative specimen groups, categorized by fines contents near 10 and 28 %, respectively, were selected for comparative illustration. Each group contains undisturbed specimens and remolded specimens prepared under similar void ratios and confining pressure control for comparison. The remolded specimens were prepared using wet-damping methodology to effectively control the void ratio; and the undisturbed specimens were prepared from the gel-push sampler with minor trimming. Figure 4 shows the axial strain and pore water pressure excitation histories of two selected groups. The failure pattern of undisturbed specimens was similar to plastic deformation when the excess pore water pressure increased slowly and incrementally. For remolded specimens, the excess pore water pressure increased quickly, and brittle failure has occurred under the same testing condition. Figure 5 shows the strain–stress behaviors of tested specimens. The undisturbed specimen has stronger cyclic resistance and possesses a larger yielding strain than the remolded specimen with a similar density and deviator stress. For specimens with similar fines contents, the remolded ones appear to soften-up (yield) quickly while the undisturbed specimens still exert plastic behavior. For undisturbed specimens with different fines contents, specimens with 28 % fines deform less than those with 10 %, indicating that fines content plays an important role in stabilizing the micro structure of nonplastic silty sand. However, for remolded specimens, specimen with less fines content appears to yield much less than those with higher fines content.

Figure 6 summarizes the test results of post-liquefaction volumetric strains, where the post-liquefaction volume change was measured from the dissipation of excess pore water after liquefaction was identified in each cyclic triaxial test. As shown in the figure, remolded specimens clearly possess larger volumetric strains than undisturbed ones. Post-liquefaction volumetric strains of remolded specimens would be as high as 8–10 %, whereas those of undisturbed specimens remain between 2 and 5 %.

4 Discussion on Engineering Practice

4.1 Cyclic Stress Ratio

Figure 7 summarizes the relationships between the cyclic stress ratio (CSR) and the number of load cycles (N_c) at liquefaction of all tests conducted. As illustrated in

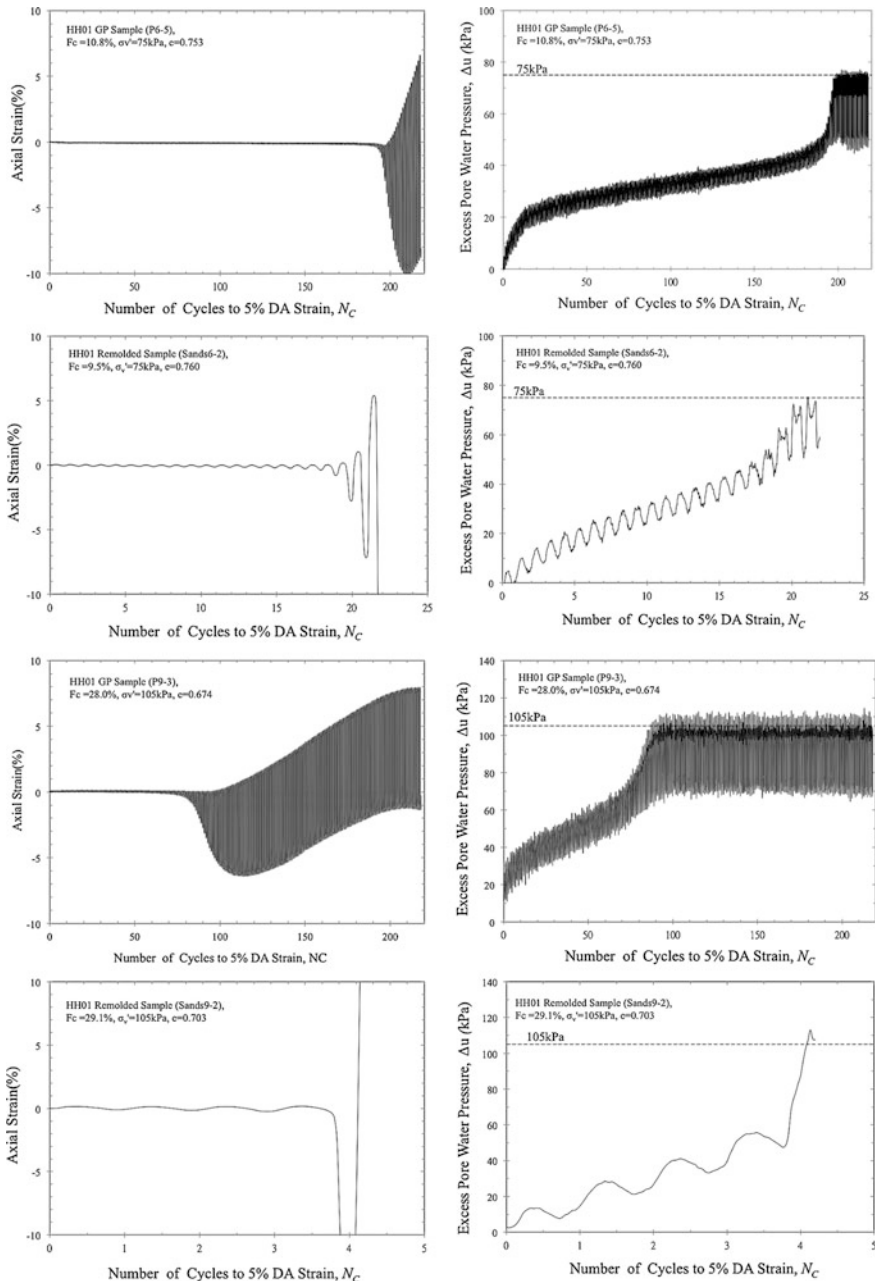


Fig. 4 Axial strain and excess pore water pressure histories of cyclic triaxial tests

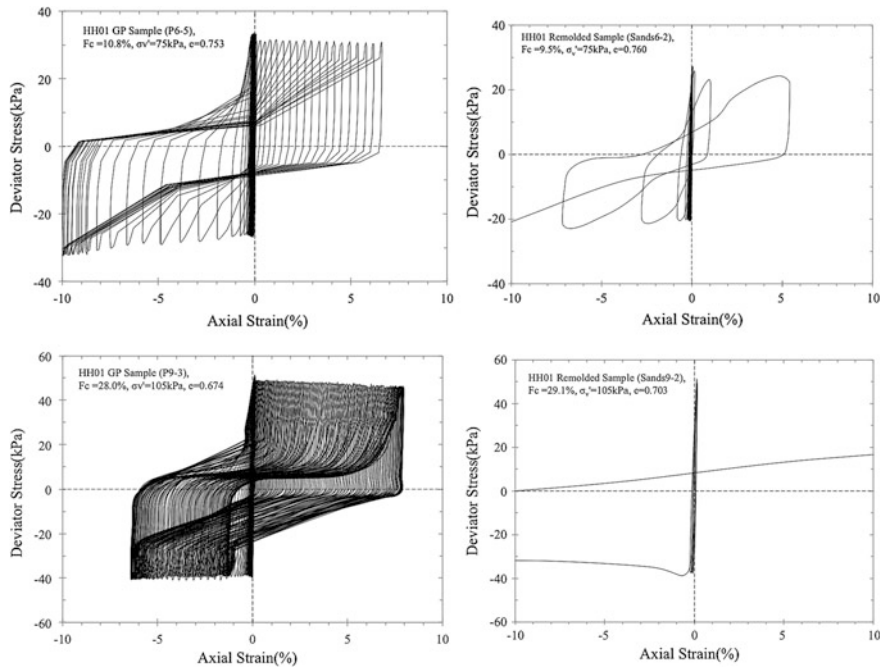
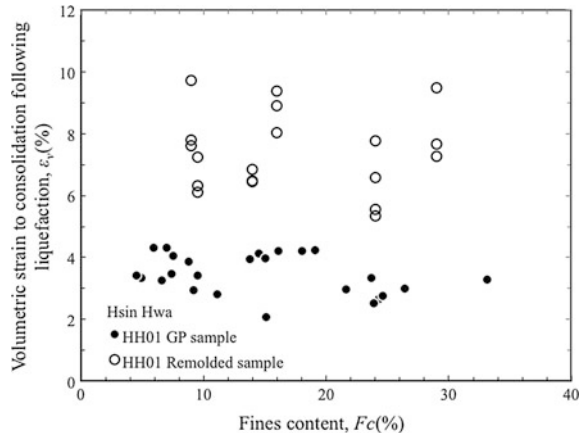


Fig. 5 Strain–stress behaviors of cyclic triaxial tests

Fig. 6 Test results of post-liquefaction volumetric strains according to various fines contents



the figure, undisturbed specimens have higher cyclic strengths than those of remolded specimens with the same fines contents and similar void ratios. It indicates that sampling disturbance could definitely influence the soil liquefaction resistance of nonplastic silty sand. Under the same void ratio condition, specimens with higher fines contents tend to have lower cyclic strengths. Under the similar

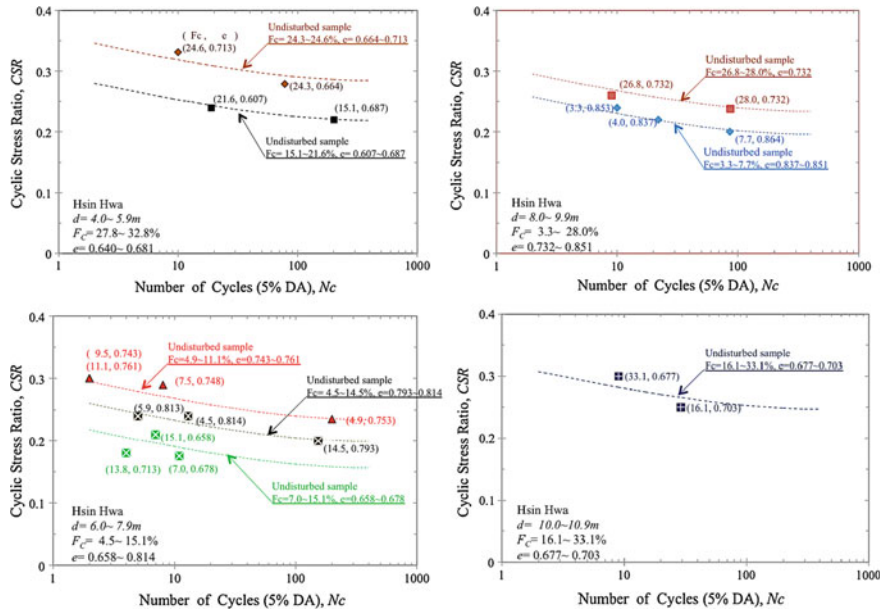
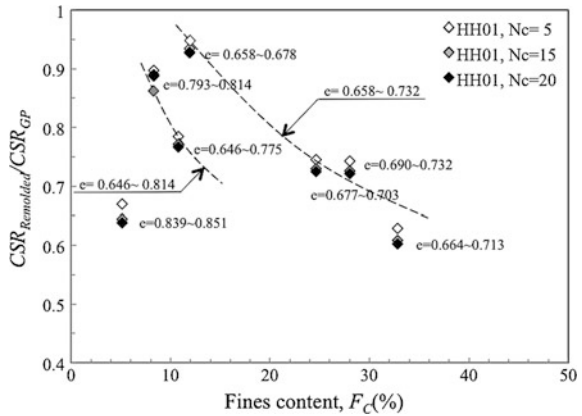


Fig. 7 Summary of results of conducted cyclic triaxial tests

Fig. 8 Influence of sampling disturbance to dynamic properties of nonplastic silty sand with various fines contents



fines content condition, specimens with higher void ratios tend to have lower cyclic strength. This behavior becomes more noticeable for the remolded specimens.

4.2 Influence of Fines Content and Void Ratio

Figure 8 shows the influence of sampling disturbance to dynamic properties of nonplastic silty sand with various fines contents. In the figure, the vertical axis is the

ratio of CSRs between remolded specimens and undisturbed specimens at the 5th, 15th, 20th load cycle (Nc). As shown in the figure, the more fines content the nonplastic silty sand has, more reduction in cyclic strength are observed. When the fines content of soil specimens was 30 %, there was a 40 % reduction in its cyclic strength.

4.3 Examination of Present Liquefaction Evaluation Method

The liquefaction potential evaluation of Hsin Hwa site is shown in Fig. 9, with a vertical axis showing depth, and horizontal axes of fines content, plastic index (PI), SPT-N value, and the liquefaction resistance ratio under the Richter magnitude (Mr) equal to 6.4, respectively. In the figure, red triangles and green circles show the analysis results using the NJRA and Seed's methods, respectively. Blue \times indicates the results of the cyclic triaxial tests on undisturbed specimens. Both NJRA and Seed's methods would estimate the liquefaction resistance of plastic soil layer accurately. However, it seems to overestimate the liquefaction resistance in nonplastic silty sand layer, especially when fines content was higher. Hence, the present liquefaction evaluation methods in a nonplastic silty sand layer are probably inadequately applicable.

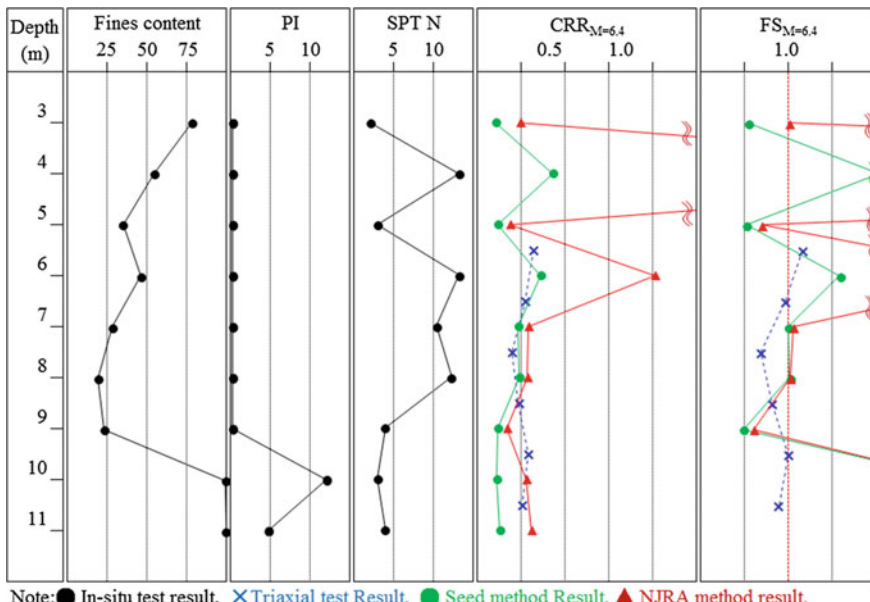


Fig. 9 Comparison of different liquefaction potential evaluations of nonplastic silty sand

5 Conclusions

Results of laboratory tests indicate that higher the void ratio and fines content of the nonplastic silty sand would have a larger cyclic strength reduction when disturbed. This phenomenon is considered to be very important in understanding time sequence of silty sand liquefaction. Void ratio (or relative density) would have deterministic effect on the silty sand liquefaction potential, so as the post-liquefaction volumetric strain. Results of tests on remolded specimens also show higher the fines contents, lower the liquefaction resistance. However, results of tests also imply no general trends of liquefaction resistance for intact specimens with difference fines contents. It is suggested that more efforts are needed to understand the combining effects of fines content, particle packing, aging, and sedimentation history, etc.

References

Lee WF, Ishihara K, Chen CC (2012) Liquefaction of silty sand—preliminary studies from Taiwan, New Zealand, and Japan earthquakes. In: Proceedings of the international symposium on engineering lessons learned from the 2011 great east Japan earthquake, pp 747–758

Lee WF, Chen CC, Chang MM, Ge LYN (2015) A case study on silty sand liquefaction—2010 Hsin Hwa liquefaction in Taiwan. In: Perspectives on earthquake geotechnical engineering. Springer International Publishing, pp 391–414

Bearing Capacity of Breakwater Mound Under Tsunami-Induced Seepage Flow

H. Takahashi, S. Sassa, Y. Morikawa and D. Takano

Abstract Water level difference induced by tsunami generates seepage flow in a mound of caisson-type breakwaters. It has been pointed out that the seepage force weakens a bearing capacity of a mound. The present paper describes bearing capacity properties of a mound under seepage flow, by using centrifuge model tests and finite element method analyses. Two types of model tests were conducted in the study: horizontal load tests and combined tests with horizontal load and seepage flow. According to the model tests, seepage force resulted in decrease of a bearing capacity. In addition, it was confirmed that finite element method analyses could simulate the model tests, and the suitable hypothetical adhesion was shown to simulate the effect of seepage force.

Keywords Bearing capacity · Breakwater · Seepage · Centrifuge · Finite element analysis

1 Introduction

Water level difference induced by tsunami generates long-duration seepage flow and force in a mound of caisson-type breakwaters. It has been pointed out that the seepage force weakens a bearing capacity of a mound. The present paper describes bearing capacity properties of a mound under seepage, by using centrifuge model tests and numerical analyses. Two types of model tests were conducted: horizontal load tests and combined tests with horizontal load and seepage flow. The former ones were to investigate the bearing capacity of a mound without seepage force, and the latter ones were to assess the reduction of bearing capacity of a mound under seepage force. That part of the experiment was written based on Takahashi et al. (2014). The bearing capacity of a mound under seepage was also examined by

H. Takahashi (✉) · S. Sassa · Y. Morikawa · D. Takano
Port and Airport Research Institute, Yokosuka, Japan
e-mail: takahashi-h@pari.go.jp

numerical analyses by the finite element method. The numerical analyses clarified the effects of seepage in more detail.

2 Procedure of Centrifuge Model Test

The beam-type centrifuge machine owned by the Port and Airport Research Institute was used for the model tests (Kitazume and Miyajima 1995). It includes a large square platform measuring $1.6 \times 1.6 \text{ m}^2$, which can hold a large specimen container. A centrifugal acceleration was set to 50g. The centrifuge can be used to simulate the behaviour of a ground of length 60 m by setting the centrifugal acceleration to 50g. Figures 1 and 2 show schematic views of a horizontal load test and a combined test with horizontal load and seepage. A mound and a base layer were made by a one-to-one mixture of crushed stone and Sohma silica sand (cat. 2) (see Fig. 3). The crushed stone has an average particle size of 5 mm and weight of 0.17g, corresponding to 21.3 kg under a centrifugal acceleration of 50g. The average particle size and weight of Sohma silica sand were 2 mm and 0.013g, corresponding to 1.6 kg. The rock ground was made by light tapping, and its dry unit weight was 16.5 kN/m^3 .

Reduction of the bearing capacity may occur as a result of two factors, namely, decrease in the confining pressure owing to an uplift force acting on a caisson, and the seepage force acting on the rubble mound. The former is not a difficult problem and can be easily taken into account in breakwater design, whereas the latter is more difficult and its effect is yet to be clarified. The present study was therefore aimed at examining the effect of the latter problem.

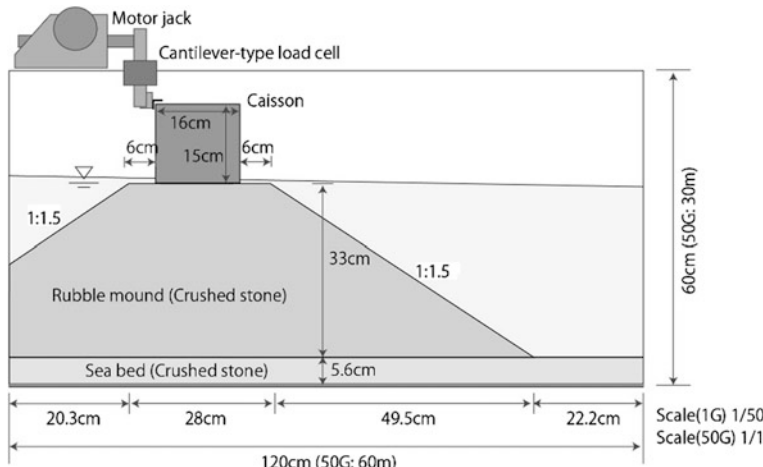


Fig. 1 Schematic view of horizontal load test

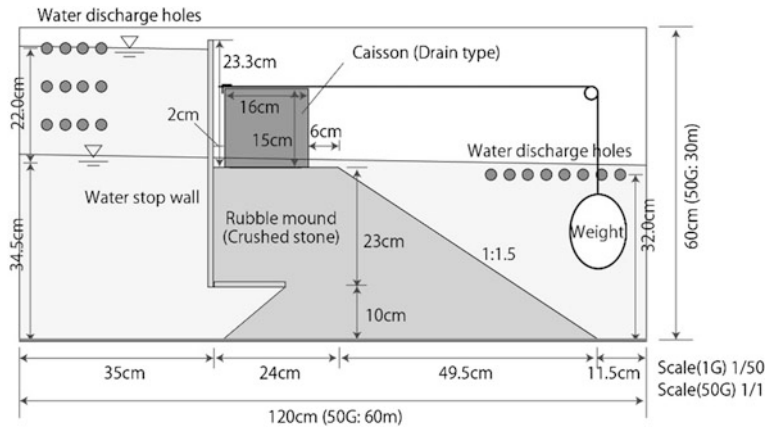


Fig. 2 Schematic view of combined tests with horizontal load and seepage

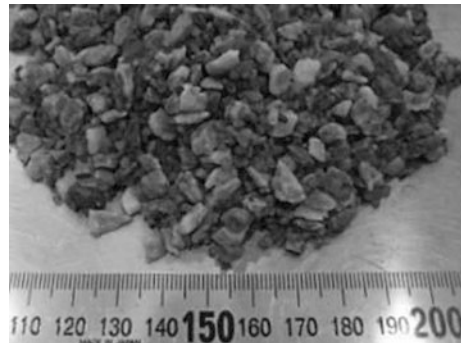


Fig. 3 Crushed stone used for mound

In the combined tests with horizontal load and seepage, the seepage was generated after loading a caisson with weights using a pulley and wire as shown in Fig. 2. A series of test were conducted by changing the horizontal load from the weight. The seepage test profile also had a water stop wall that caused seepage from the bottom. The wall created no water level difference between both sides of a caisson and could eliminate the uplift force acting on a caisson. A dam-break method was adopted, wherein water held in a water supply tank was suddenly released. It is known that the dam-break method cannot be easily used to control either the flow volume and/or the water level. However, in the present model tests, the water level could be controlled by discharging excess water through holes created in the back wall. The water pressure difference was 115 kN/m^2 .

3 Model Test Results

3.1 Results of Horizontal Loading Tests

Figure 4 shows the relationship between load and displacement in the prototype scale. Displacement was measured from 50 mm below the top of the caisson. The load and displacement were measured using a cantilever-type load cell and a displacement gauge, respectively. Because a mound represented relaxation behaviour, the caisson was loaded with alternating loads and rests. The load and displacement resulted in a non-linear relationship, indicating plastic deformation behaviour of the mound. The relationship after a displacement of 0.6 m almost became linear, and the starting point of a straight line was considered to be the beginning of the ground's limit state. The horizontal load at this point was 861 kN/m. In the seepage test mentioned below, seepage was generated under horizontal loads less than that load. In addition, it was confirmed that the effects of mound failure dominated the effects of sliding and over-turning of a caisson, which theoretically occurred at loads of 1039 and 924 kN/m, respectively.

Figure 5 shows the vectors demonstrating displacement and its direction, which were given by the Digital Image Correlation (DIC) method. The figure shows the vectors until the caisson displacement of 1.5 m. In the figure, a laterally deformed area occurred under the caisson's corner, and this forced the slope top to move

Fig. 4 Relationship between load and displacement of horizontal loading test

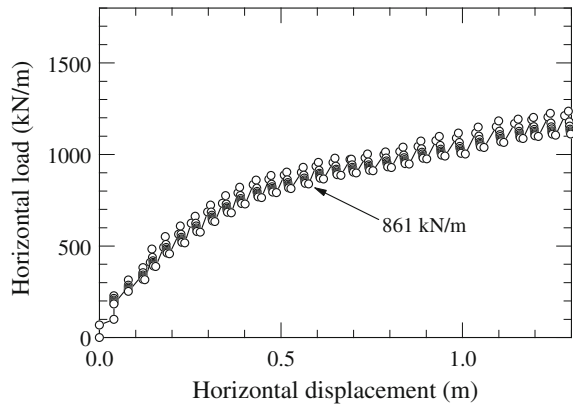
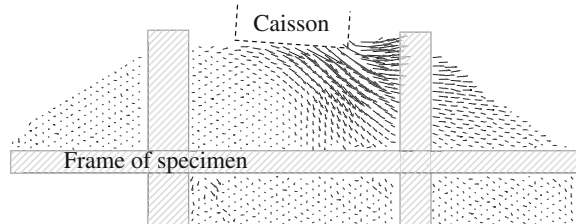


Fig. 5 Displacement vectors of horizontal loading test



forward. The behaviour observed here is a typical failure mode by inclined loading, and higher shear strength under the caisson and a counter weight for the slope top can increase the bearing capacity for loading.

3.2 Excess Pore Water Pressure Distribution

Excess pore water pressure was measured at different points right after the water level difference became steady. In another test case, the excess pore water pressure under the water stop wall was low, a situation in which the hydraulic gradient, i , in the mound would remain low. The present test case increased the amount of supply water for the mound by widening the outlet under the water stop wall, and did not use large crushed stones in front of the wall. These changes were introduced to allow a significant amount of water to percolate into the mound. Figure 6 shows the excess pore water pressure. It can be found that the water pressure under the wall was not reduced from 115 kN/m^2 and i around the slope top reached 0.4.

3.3 Reduction of Bearing Capacity

Figure 7 shows the results of cases where seepage synchronized with horizontal loading as well as the result of the horizontal loading tests shown in Fig. 4. Filled and open circles represent displacements before and after the seepage. As shown in the figure, all caissons were displaced by the seepage force. The case with a horizontal load of 663 kN/m resulted in devastating ground failure and the caisson fell from the slope top. The movements of the caissons indicate the reduction in bearing capacity caused by seepage. The horizontal loads of the cases where the caissons were collapsed or not were 548 and 663 kN/m . Compared with the load at the beginning of the limit state of 861 kN/m , those loads were found to be 64 and 77 %, down 23–36 %.

Fig. 6 Distributions of excess pore water pressure

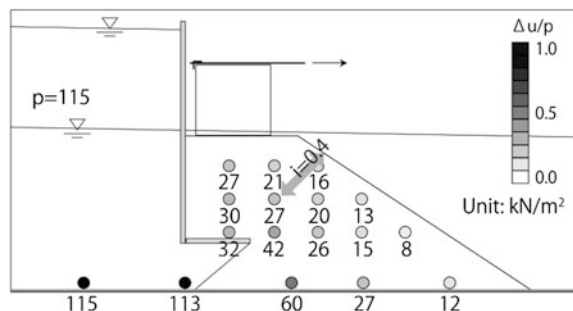
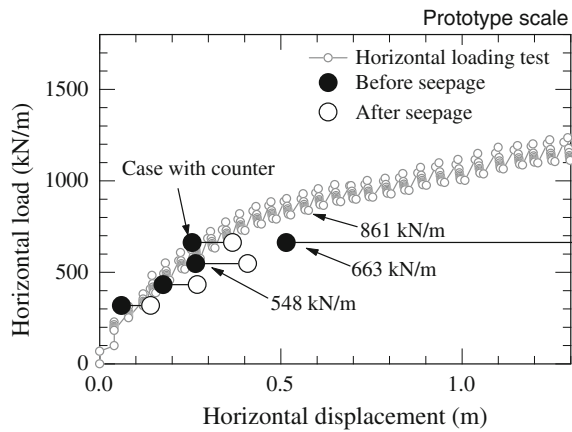


Fig. 7 Relationship between load and displacement of combined tests



The successive pictures capturing the moment of the mound failure and the displacement vectors calculated by the DIC method are shown in Figs. 8 and 9. In Fig. 8, it was first confirmed in model tests that the force of seepage itself was able to break down a mound under an inclined load. The deformation behaviour shown in Fig. 9 was quite similar to that of Fig. 5, taken in the horizontal loading test, and this shows that the mounds collapsed in the same mechanism. These experimental results meant that bearing capacity was reduced with seepage.

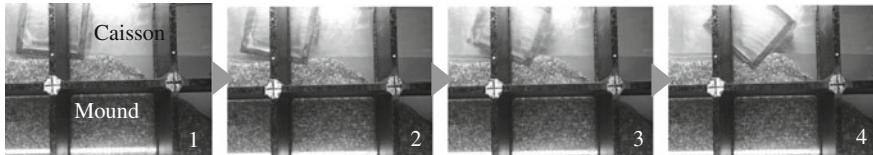


Fig. 8 Successive pictures of mound failure

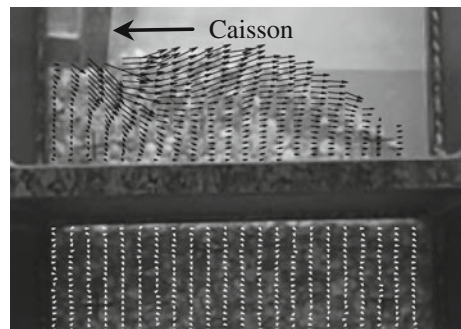


Fig. 9 Displacement vectors of combined tests

4 Numerical Analyses

4.1 Conditions of Numerical Analyses

To examine more detailed characteristic of bearing capacity under seepage, numerical analyses using the finite element method, FEM, were also carried out. The FEM code ‘GeoFem’ was used in this study, which has been developed by the Port and Airport Research Institute (Kobayashi 1988). Figure 10 shows the element mesh for the calculations, which were reproducing the tested model. An elasto-plastic model complying with the Mohr-Coulomb criterion and an elastic model were utilized as models for the mound and other components, respectively. Design standards in Japan (OCDI 2009) prescribe that the hypothetical adhesion of 20 kN/m^2 should be taken into account because Kobayashi et al. (1987) showed the applicability of circular slip analysis with the hypothetical adhesion to the simulation of devastated grounds in some sites. However, seepage force could decrease the confining pressure of a mound, and the large hypothetical adhesion would lead to overestimation of a mound’s shear strength. Therefore, calculations decreasing adhesion were also conducted. With regard to loading method, the nodal point of the caisson was horizontally loaded with or without seepage force, with the loading stopped when the mound collapsed.

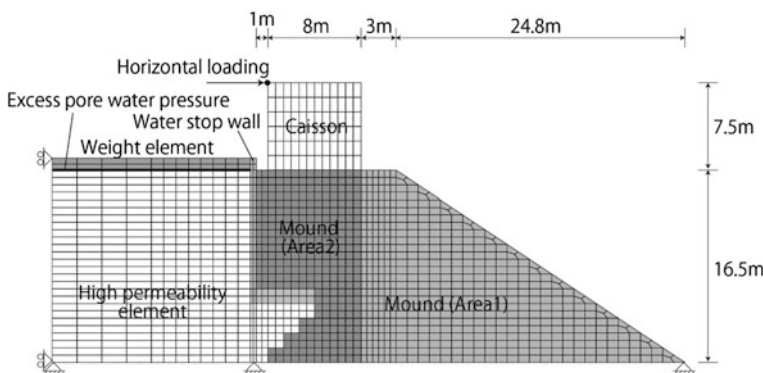


Fig. 10 Finite element mesh for simulation

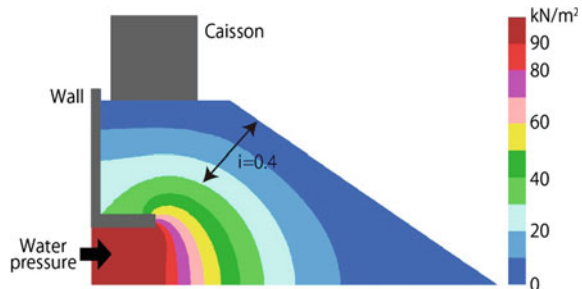
4.2 Results of Numerical Analyses

Figure 11 shows the excess pore water pressure, as calculated. The distributions of excess pore water pressure were similar between the calculation and the model test. The hydraulic gradient, i , around the slope top was approximately 0.4, which is similar to i in the model test (see Fig. 6). In addition, the calculated deformation behaviours were almost the same as those in the model test. The laterally deformed area occurred under the caisson corner, which forced the slope top to move forward. The numerical analyses using FEM further confirmed that the fundamental deformation and failure behaviour observed in the model tests can be simulated.

As mentioned above, the design standards in Japan (OCDI 2009) account for hypothetical adhesion. This is because the shear strength of a mound increases non-linearly with increased confining pressure, as shown in Fig. 12a. Shear strength using hypothetical adhesion can represent this non-linear increasing trend within a certain confining pressure. However, the confining pressure of a mound is reduced by the seepage force; in particular, the pressure of the mound at the front of the caisson decreases. Therefore, the hypothetical adhesion should be also decreased, as indicated by Line (1) to Line (2) in Fig. 12a. Figure 12b shows the friction angles, ϕ_0 , based on the triaxial tests conducted by Kobayashi et al. (1987) and Mizukami and Kobayashi (1991). Additionally, the figure indicates that the hypothetical adhesion of 20 kN/m^2 overestimates the shear strength under low confining pressure.

In the present study, the friction angle in the mound (Area 1) shown in Fig. 10 was fixed to 40° , and the hypothetical adhesion was changed. The shear strength of only one section of the mound was changed to account for the high hypothetical adhesion in the mound (Area 2), in which the confining pressure was high even under seepage. For example, the minimum stresses, σ_{\min} , at the bottom and front of the caisson were 124 and 7 kN/m^2 in 1 m depth, respectively.

Fig. 11 Distribution of excess pore water pressure



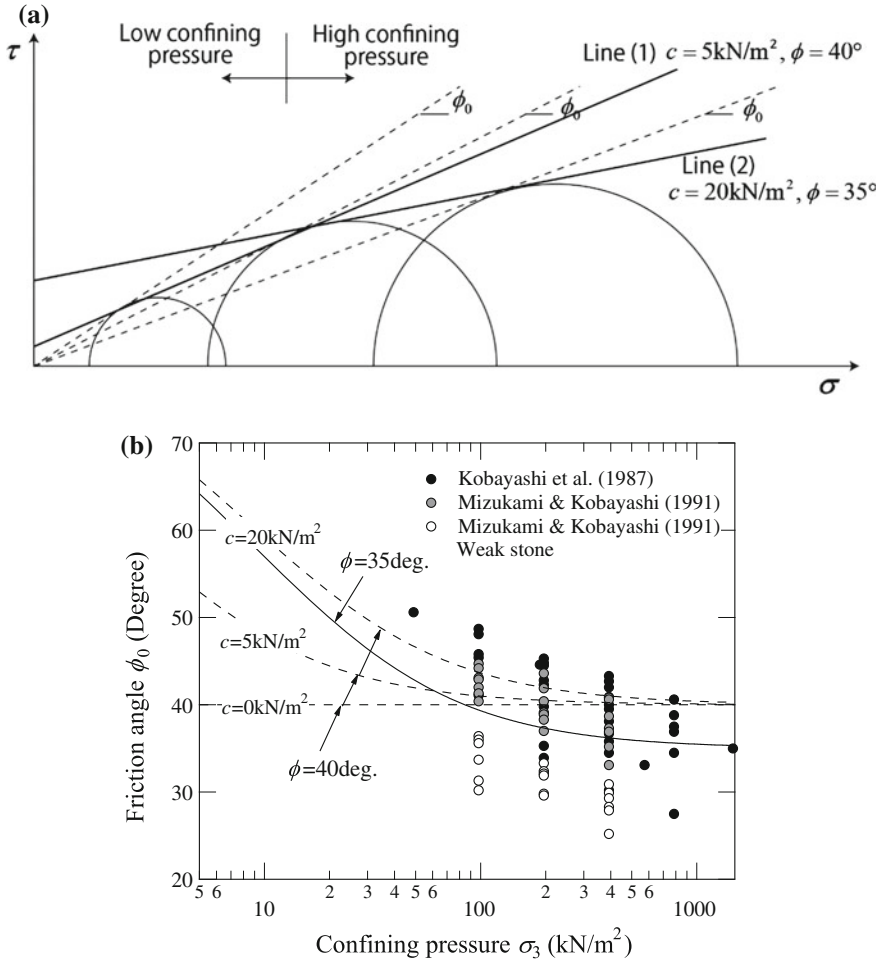


Fig. 12 Relationship between ϕ_0 and confining pressure σ_3 (based on Kobayashi et al. 1987; Mizukami and Kobayashi 1991), **a** definition of ϕ_0 , **b** ϕ_0 and σ_3

Figure 13a shows the horizontal loads at the failure point versus hypothetical adhesion. Less hypothetical adhesion resulted in a smaller failure load independent of the seepage force. The results indicate that the seepage reduced the failure load and that the rate of reduction was large with lower hypothetical adhesion. Figure 13b shows the rates of the failure load versus hypothetical adhesion. The reduction rate rapidly decreased when the hypothetical adhesion approached 0 kN/m 2 . Considering the reduction rate of 64–77 % in the model test, the hypothetical adhesion of approximately 5 kN/m 2 would be suitable to simulate the model test.

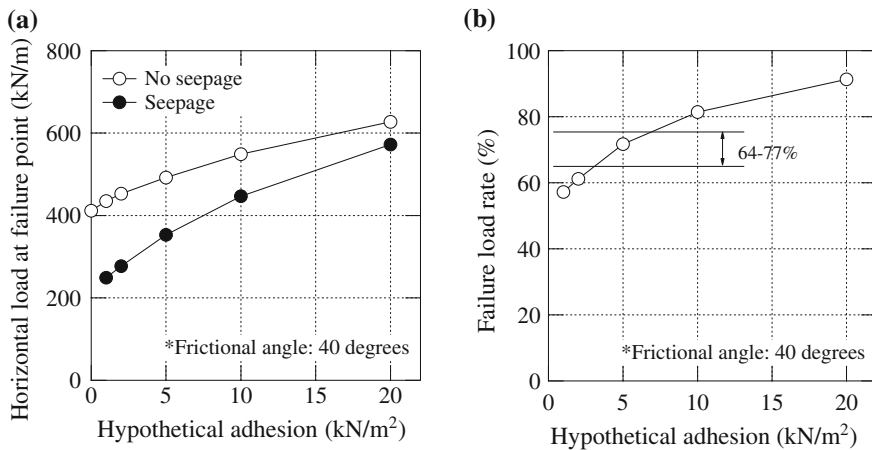


Fig. 13 Failure load and its rate, **a** failure load, **b** failure load rate due to seepage

5 Conclusions

The bearing capacity of a mound with and without seepage was examined by the centrifuge model tests and numerical analyses. It was observed that the actual seepage force could break down the mound under a load. It had been confirmed by the model tests that the seepage force reduced the bearing capacity of the mound. The numerical analyses simulating the model test indicated that the seepage force reduced the bearing capacity. Additionally, it was found that the hypothetical adhesion of 20 kN/m² prescribed in the design standards should be decreased appropriately. However, supplementary studies and discussions are required to determine suitable adhesion.

References

Kitazume M, Miyajima S (1995) Development of PHRI Mark II geotechnical centrifuge, vol 812. Technical Note of the Port and Harbour Research Institute, pp 1–35

Kobayashi M (1988) Stability analysis of geotechnical structures by adaptive finite element procedure, vol 27(2). Report of the Port and Harbour Research Institute, pp 3–22

Kobayashi M, Terashi M, Takahashi K (1987) Bearing capacity of a rubble mound supporting a gravity structure, vol 26(5). Report of the Port and Harbour Research Institute, pp 215–252

Mizukami J, Kobayashi M (1991) Strength characteristics of rubble by large scale triaxial compression test, vol 699. Technical note of Port and Harbour Research Institute, pp 1–23

OCDI—Overseas Coastal Area Development Institute of Japan (2009) Technical standards and commentaries for port and harbour facilities in Japan. OCDI 600–601

Takahashi H, Sassa S, Morikawa Y, Takano D, Maruyama K (2014) Stability of caisson-type breakwater foundation under tsunami-induced seepage. *Soils Found* 54(4):789–805

Part II

Earthquake Induced Liquefaction and

Countermeasures

Verification of Improvement Effectiveness by Compaction Methods During the 2011 off the Pacific Coast of Tohoku Earthquake

Kenji Harada, Jun Ohbayashi and Yuichi Taguchi

Abstract The 2011 off the Pacific Coast of Tohoku Earthquake caused severe liquefaction of reclaimed lands in the Tokyo Bay area. Prior to the earthquake, many ground improvement works have been implemented in reclaimed lands along Tokyo Bay and no damage was observed at any of the improved sites. The main purpose of ground improvement in this area was liquefaction prevention and most of the countermeasures implemented were compaction (densification) methods, such as vibratory and non-vibratory sand compaction pile (SCP) method. This paper presents the conditions of the area after the 2011 earthquake by comparing the performance of unimproved and SCP-improved areas in terms of the distribution of the normalized N -values, fines contents, and the corrected N -values based on pre- (unimproved ground) and post-(SCP-improved ground) boring logs along Tokyo Bay. In addition, the relationship between the corrected SPT N -values in the improved grounds and the shear stress ratio estimated using the maximum surface acceleration obtained from recorded motions near the site was analyzed.

Keywords Compaction-improved ground • Normalized N -value • Corrected N -value • Shear stress ratio

1 Introduction

In Japan, the main countermeasures against liquefaction are the compaction methods, such as vibratory and non-vibratory sand compaction pile (SCP) method. Many case histories verifying the improvement effectiveness have been reported following past large-scale earthquakes and there has been no report of major disruption to structures erected on compacted grounds. Especially, even with the intense shaking induced by the 1995 Hyogo-ken Nambu Earthquake (Great Hanshin-Awaji Earthquake), compaction-improved grounds suffered very little

K. Harada (✉) · J. Ohbayashi · Y. Taguchi
Fudo Tetra Corporation, Tokyo 103-0016, Japan
e-mail: kenji.harada@fudotetra.co.jp

damage due to liquefaction (Yasuda et al. 1996), thus confirming in a qualitative way the effectiveness of compaction-type ground improvement techniques. The 2011 off the Pacific Coastal of Tohoku Earthquake (The Great East Japan Earthquake) with long shaking duration caused severe liquefaction in the reclaimed lands along Tokyo Bay area, although located 350 km away from the epicenter. However, the reclaimed lands that have been improved by vibratory and non-vibratory SCP methods did not liquefy (Yasuda et al. 2012).

In this paper, photos of the conditions differentiating the performance of improved and unimproved sites are shown, as well as the verification of improvement effectiveness after the earthquake by analyzing the boring data and the results of investigation. Furthermore, the relationship between stress ratio and SPT N -value is analyzed using these data.

2 Case Histories Verifying the Improvement Effectiveness by Compaction Method

It was confirmed that no damage was observed at any of the improved sites during the 2011 off the Pacific Coast of Tohoku Earthquake. Figure 1a–c indicates the conditions adjacent to the boundary between the improved and unimproved area as well as the plan figure/cross section of the sand piles. At every site, there were no damages caused by liquefaction, such as the occurrence of sand boils and settlement. However, settlement occurred mainly outside the improved area. Figure 1d indicates the condition of non-vibratory SCP implementation just after the earthquake. Water was ejected from the unimproved area of the site (according to the site supervisor, about 1 h after the earthquake) but there was no ground deformation observed on the improved area.

3 Investigation of Improvement Effectiveness

3.1 Investigated Area and Data Obtained

The investigated areas are the sites improved by compaction methods, such as vibratory and non-vibratory SCP, along Tokyo Bay (Tokyo and Chiba). A total of 27 sites were investigated, and these consist of 14 sites in Tokyo and 13 sites in Chiba. There was no trace of liquefaction observed in all sites. Table 1 summarizes the number of boring logs before/after improvement, with a total of 203 logs used, including 77 logs before improvement and 126 logs after improvement. The boring data was divided into either reclaimed or alluvial layer based on various references and sources (JGS 2010; BPHTMG 2001; Urayasu City 2012).

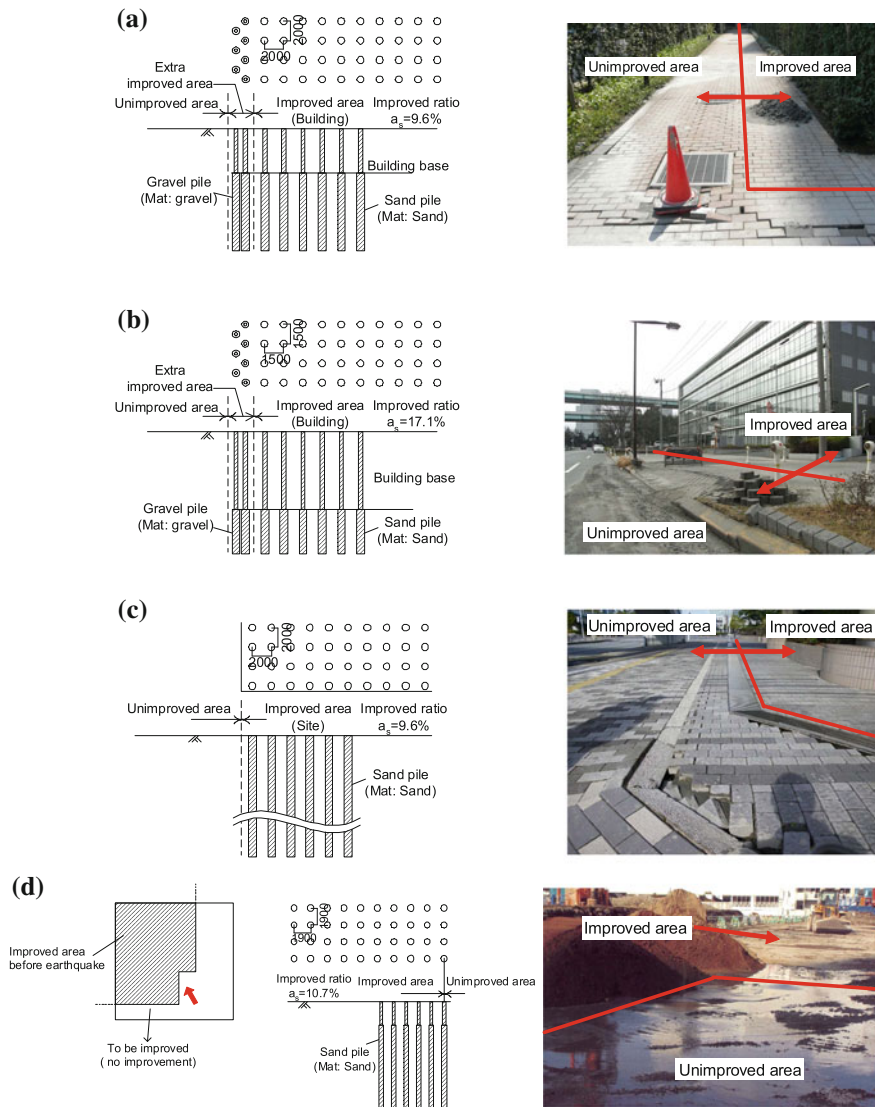


Fig. 1 Conditions of improved areas immediately after the earthquake (Harada et al. 2013), **a** building (Chiba), **b** building (Tokyo), **c** building (Chiba), **d** during implementation

3.2 Investigation Procedure

The following items were formulated based on the pre/post boring logs and other data obtained from the SCP-improved sites along Tokyo Bay for the purpose of understanding the characteristics of the improved/unimproved grounds. The N -values of improved ground were obtained at points in-between the piles.

Table 1 Summary of data used

| Region | Site number | Before improvement | | After improvement | | Total |
|--------|-------------|--------------------|--------------------------------|-------------------|--------------------------------|-------|
| | | Boring log | SPT N-value Reclaimed layer | Boring log | SPT N-value Reclaimed layer | |
| Tokyo | 14 | 22 | 94 164 | 78 | 183 451 | 100 |
| | | | 258 | | 634 | 277 |
| Chiba | 13 | 55 | 207 599 | 48 | 106 414 | 892 |
| | | | 806 | | 520 | 313 |
| Total | 27 | 77 | 301 763 | 126 | 289 865 | 1326 |
| | | | 1064 | | 1154 | 203 |
| | | | | | | 590 |
| | | | | | | 1628 |
| | | | | | | 2218 |

1. Distributions of fines content, F_c , at each reclaimed and alluvial layer
2. Distributions of normalized SPT N -values, N_1 , before/after improvement at each reclaimed and alluvial layer

The normalized N -value is obtained from Eq. (1) (JRA 1996)

$$N_1 = \frac{1.7N}{\sigma'_v/98 + 0.7} \quad (1)$$

where σ'_v : effective overburden pressure (kN/m^2)

3. Relations between N_1 before/after improvement and F_c at each reclaimed and alluvial layer
4. Distributions of corrected N -values, N_a , before/after improvement at each reclaimed and alluvial layer

After the data whose $F_c > 50\%$ are excluded, the N_a -values of the remaining data points are calculated using Eq. (2) (JRA 1996)

$$N_a = c_1 \cdot N_1 + c_2$$

$$c_1 = \begin{cases} 0 & 0 \leq F_c < 10 \\ 10 & 10 \leq F_c < 60 \\ 60 & 60 \leq F_c \end{cases} \quad (2)$$

$$c_2 = \begin{cases} 0 & 0 \leq F_c < 10 \\ (F_c - 10)/18 & 10 \leq F_c \end{cases}$$

where c_1 , c_2 : coefficients of corrected N -value.

Based on the analyses of these data, the relationship between the maximum shear stress ratio, L , and the corrected N -values of the improved sites, where no damage was observed, was compared with the relation obtained for natural deposits (JRA 1996) in order to examine the improvement effectiveness. To calculate L , the following equation is used:

Equation (3)

$$L = \frac{\tau_{\max}}{\sigma'_v} = (1 - 0.015Z) \frac{\alpha_{\max}}{g} \cdot \frac{\sigma_v}{\sigma'_v} \quad (3)$$

where

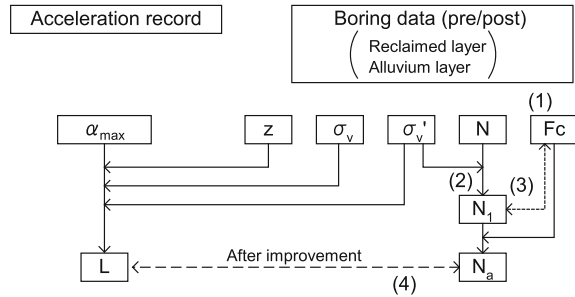
τ_{\max} maximum cyclic shear stress (kN/m^2)

α_{\max} maximum surface acceleration (gal)

g acceleration due to gravity ($=980$ gal)

σ_v overburden pressure (kN/m^2)

z depth (m)

Fig. 2 Study flow

α_{\max} was obtained from record motions of the observation point near the site (NIED 2011). Figure 2 shows the procedure of the study and the relationship among the used soil parameters.

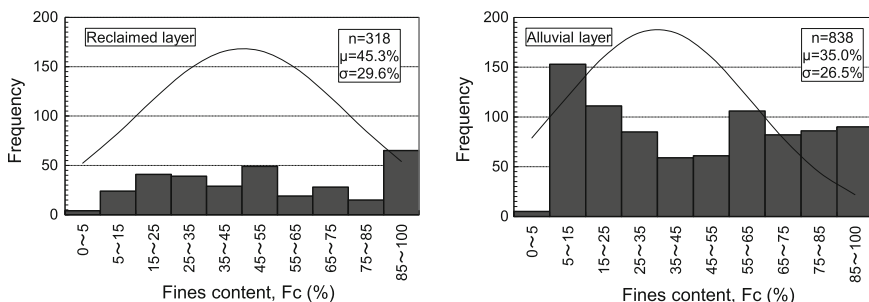
3.3 Results

1. Distributions of fines content, F_c , for each layer

Figure 3 shows the histograms of the fines content, F_c , for reclaimed and alluvial layers. Though the plots are both scattered, the average fines content of reclaimed layer is about 45 %, which is 10 % greater than that of alluvial layer. The symbols n , μ , σ are number of data, average, and standard deviator of the data, respectively.

2. Distributions of normalized SPT N -values, N_1 , before/after improvement

Figure 4 illustrates the histograms of the normalized N -values, N_1 , of improved and unimproved grounds for each layer. Though they are also scattered, the average normalized N -value of both layers before improvement is around 10. On the other hand, that after improvement is 21, indicating an increase in N -value of 14.

**Fig. 3** Distributions of fines content

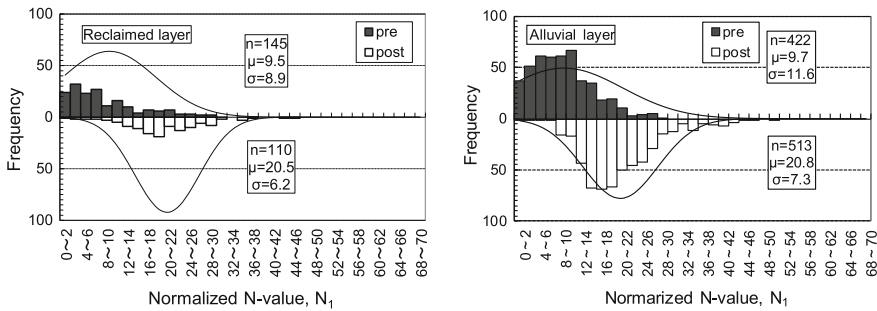


Fig. 4 Distributions of normalized N -values

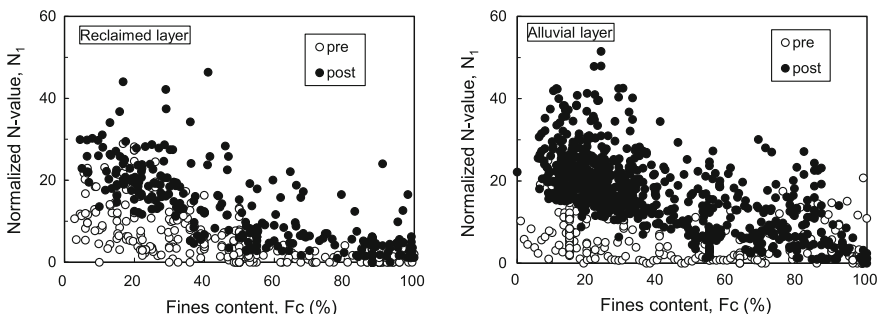


Fig. 5 Relationships between fines content and normalized N -values

3. Relations between N_1 before/after improvement and F_c

Figure 5 shows the relationship between the normalized N -values and fines content for each layer. The normalized N -values show a trend wherein the higher the fines contents, the smaller are the N -values, both in terms of the normalized value and the increased amount due to the improvement.

4. Distributions of corrected SPT N -values, N_a , before/after improvement at each reclaimed and alluvial layer

The histograms of the corrected N -values of improved and unimproved grounds for each layer are shown in Fig. 6. Because liquefaction did not occur at the improved grounds, the lower limit of N_a -value is around 15, according to the figure.

Figure 7 shows the relationship between the maximum shear stress ratio and corrected N -values in the improved grounds where liquefaction did not occur. It can be argued that the liquefaction resistance curve of the improved grounds is best represented by the dashed curve, which is on the left side of the curve proposed by JRA (1996). Thus, it is inferred that the liquefaction resistance of the improved ground is higher than that of the natural ground, even though both grounds have the same N -values. Harada et al. (2013) pointed out that this is due to the increase in

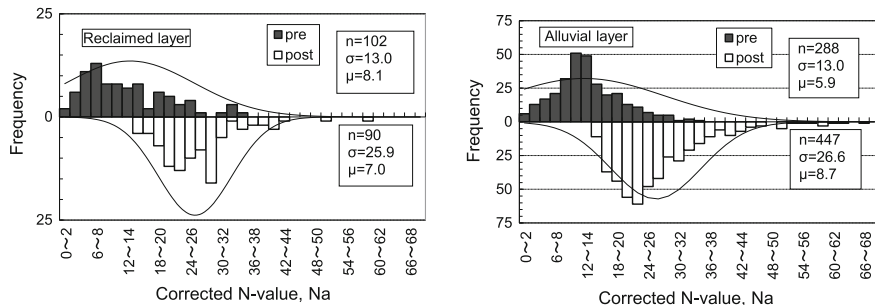
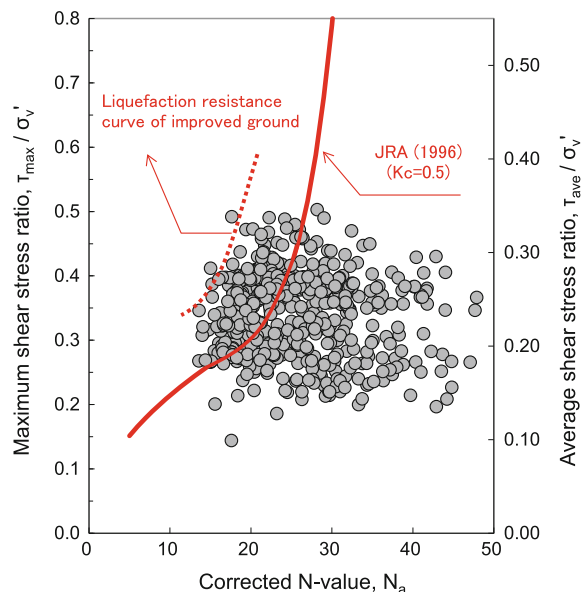


Fig. 6 Distributions of corrected N -values

Fig. 7 Relationships between shear stress ratio and corrected N -values



lateral stress ratio K_c ($=\sigma'_h / \sigma'_v$, where σ'_h : effective lateral stress), induced by the installation of sand piles and the effect of composite ground consisting of the compacted sand piles and the ground surrounding them.

4 Summary

This paper discussed the conditions of the improved/unimproved grounds during the 2011 off the Pacific Coast of Tohoku Earthquake and compared the distributions of the normalized N -values, fines contents and the corrected N -values based on the

pre- (unimproved ground) and post-(SCP-improved ground) boring logs along Tokyo Bay. In addition, the relationship between the corrected SPT N -values in the improved grounds and the cyclic shear stress ratio were analyzed. Based on the results of the investigation and analyses, the compaction methods were also found to be very effective in this earthquake which was characterized by long shaking duration. It was also noted that the liquefaction resistance of the SCP-improved ground is higher than that of the natural ground, even though both have the same SPT N -values.

References

Bureau of Port and Harbor, Tokyo Metropolitan Government, BPHTMG (2001) Geotechnical conditions in Tokyo Port—New Edition (in Japanese)

Harada K, Ohbayashi J, Matsumoto J, Yoshitomi H, Yasuda S, Orense R (2013) Verification of effectiveness of liquefaction countermeasures during past large scale earthquakes in Japan. In: Orense RP et al (eds) Proceedings of the New Zealand—Japan workshop on soil liquefaction during recent large-scale earthquakes. Taylor & Francis Group, pp 181–192

Japanese Geotechnical Society, JGS (2010) Geotechnical conditions in the Kanto Region, Kanto branch of the Japanese Geotechnical Society, 132 p (in Japanese)

Japan Road Association, JRA (1996) Specifications for highway bridges (in Japanese)

National Research Institute for Earth Science and Disaster Prevention, NIED (2011) K-NET WWW Service, Japan (<http://www.k-net.bosai.go.jp/>)

Urayasu City (2012). In: 1st meeting data compiled by the technical committee on measures against liquefaction (in Japanese)

Yasuda S, Ishihara K, Harada K, Shinkawa N (1996) Effect of soil improvement on ground subsidence due to liquefaction. Special Issue Soils Found 99–107

Yasuda S, Harada K, Ishikawa K, Kanemaru Y (2012) Characteristics of the liquefaction in Tokyo Bay area by the 2011 Great East Japan Earthquake. Soils Found 52(5):793–810

Development of Rational Soil Liquefaction Countermeasure Consisting of Lattice-Shaped Soil Improvement by Jet Grouting for Existing Housing Estates

Takahiro Yamauchi, Hiroaki Tezuka and Yoshimichi Tsukamoto

Abstract The lattice-shaped soil improvement by means of jet grouting is one of the promising methods for soil liquefaction countermeasures. In order to develop a more effective construction method for residential houses, a series of centrifuge model tests and numerical analyses are conducted to see if there would be any more rational shapes of underground soil improvement structures to counter against soil liquefaction. It is found that the ordinary lattice walls with a surface cover would be more effective. The field verification tests are also conducted to examine if the micro machine developed in the present study can be practically used in residential areas.

Keywords Soil liquefaction countermeasure · Jet grouting · Centrifuge test · Numerical analysis · Field test

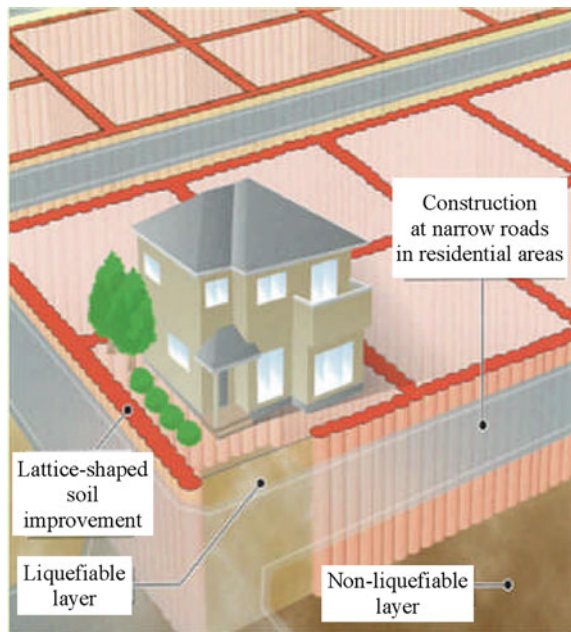
1 Introduction

Following the 2011 Great East Japan Earthquake, soil liquefaction was observed over wide areas including Tokyo and other eight prefectures and 80 municipalities. Lots of residential houses, roads, revetments, and other infrastructures were greatly damaged in Urayasu city and other reclaimed areas along Tokyo Bay. In order to control the recurrence of disasters in the areas heavily affected by soil liquefaction, some projects were initiated in November 2011, by the Ministry of Land, Infrastructure, Transport and Tourism (MLIT). They are aimed at preventing

T. Yamauchi (✉) · H. Tezuka
Maeda Corporation, 2-10-2, Fujimi, Chiyoda City,
Tokyo 102-8151, Japan
e-mail: yamauchi.tak@jcity.maeda.co.jp

Y. Tsukamoto
Department of Civil Engineering, Tokyo University of Science,
2641, Yamazaki, Noda, Chiba 278-8510, Japan
e-mail: ytsoil@rs.noda.tus.ac.jp

Fig. 1 Lattice-shaped underground soil improvement structures



damages due to soil liquefaction in future earthquakes around these areas under the subsidies of Great East Japan Earthquake reconstruction. The municipalities having suffered from soil liquefaction then started to establish study committees, and have been conducting discussions on how damages due to soil liquefaction can be prevented especially by combining soil liquefaction countermeasures for roads and other public facilities with private housing sites. This approach is herein called “integrated control measures.”

One of the promising integrated control measures at present is the construction of lattice-shaped underground soil improvement structures, that stabilizes soils using cement, (Yoshida et al. 1990, 1991; JCMA 2009; Tezuka et al. 2013a, b), is shown in Fig. 1. This construction method, however, stabilizes soils using the conventional deep mixing method, which is the mechanical agitation and jet grouting method. Constructions near boundaries of existing houses require machinery much smaller than conventionally adopted. In addition, at least part of costs of construction works involved in such integrated control measures needs to be paid by owners of houses. It is therefore highly required to reduce construction costs in order to achieve agreements among residents, which is essential for implementing the projects.

With all the above background in mind, the present study is aimed at proposing a more economical and more effective construction method of lattice-shaped underground soil improvement structures, to serve as an integrated soil liquefaction control measure. The development of this construction method needs to overcome the following problems of cost reduction, development of small machinery to work

in narrow space, and ability to produce improved soil structures with thin walls as well as arbitrary shapes in large diameter.

The present study was started as one of the projects funded under the MLIT construction technology research and development subsidy system in 2011. In what follows, the application and verification of lattice-shaped soil improvement technology for preventing soil liquefaction are examined, where more effective shapes of improved soil structures are examined in numerical analyses as well as centrifuge model tests, and field tests are also conducted to see if this construction method would work well in a model residential setup.

2 Outline of Micro-Jet Grouting Method

The micro-jet grouting method is one of the multi-jet methods, which is downsized to fit into existing housing sites. The multi-jet method itself is a jet grouting method, which is characterized by its ability to produce soil improvement structures with arbitrary shapes and large diameter. This method enables formations of underground soil improvement structures of arbitrary shapes, ranging from walls, fans to lattices, as shown in Figs. 2 and 3. Any underground soil improvement structures can be constructed by combining the shapes of walls, fans, and lattices. This method is therefore expected to provide basis for highly effective soil liquefaction

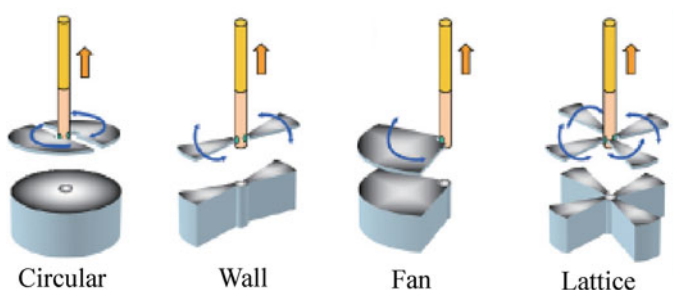


Fig. 2 Soil improvement with arbitrary shapes



Fig. 3 Confirmation of shapes of soil improvement in field tests

Table 1 Specifications for micro machine

| | |
|------------------------------------|------------------------|
| Rod diameter (mm) | 73 |
| Rod length (m) | 1.0, 1.5 |
| Maximum jet flow rate and pressure | 200 l/min and 30 MPa |
| Flow rate of compressed air | 5 Nm ³ /min |
| Mass of leader and spindle | 400 kg |

control measures at housing sites. The multi-jet method has already been used for 34 sites and was found as a highly reliable method.

During the development of a micro-jet method, a micro machine was developed, which can be used at narrow existing housing sites with a width of 1 m and an overhead clearance of approximately 2 m, to cope with construction at boundaries of existing housing sites. The specifications for this machine are listed in Table 1.

3 Proposing Rational Shapes of Soil Improvement in Centrifuge Model Tests

Several shapes of underground soil improvement structures are examined to find the most effective one to prevent soil liquefaction damages, as shown in Fig. 4. These shapes are among the good candidates from the results of preliminary model shaking table tests in a 1-G gravitational field. A series of centrifugal model tests are conducted in the present study in an 80-G gravitational field. The pore water pressure ground surface settlement are measured during the model tests. The test series are listed in Fig. 5. In case-4 of the “lattice with surface cover,” the bottom end of the lattice structure is fully embedded in the bedrock. In case-5 of the “floating lattice with surface cover,” the underground structure in the section of an adjacent public facility is embedded in the bedrock. In the section of the housing

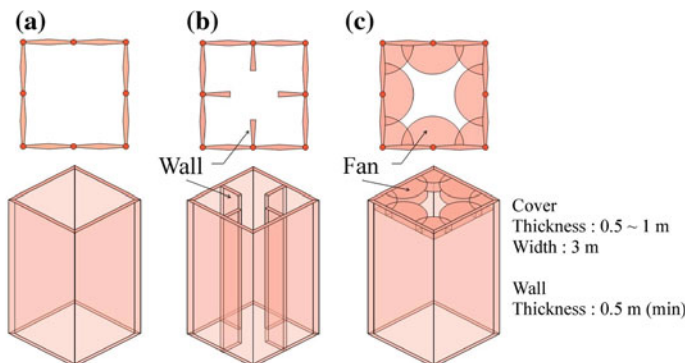
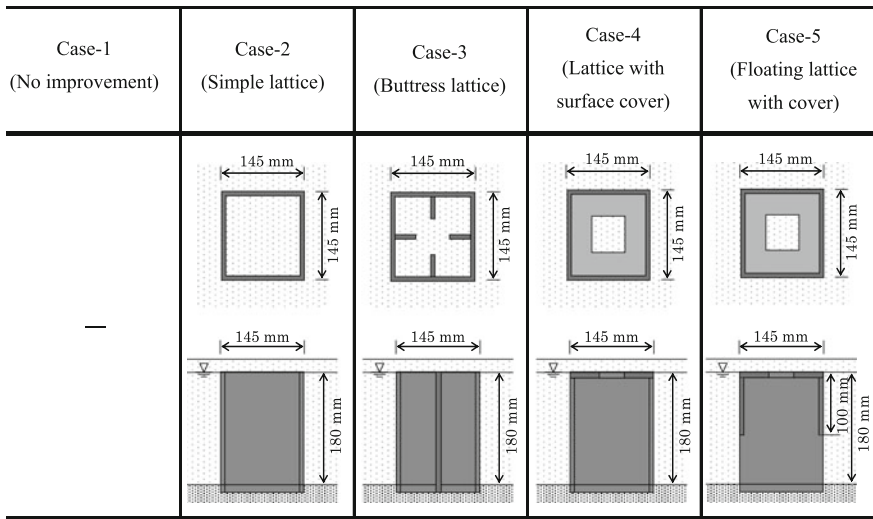
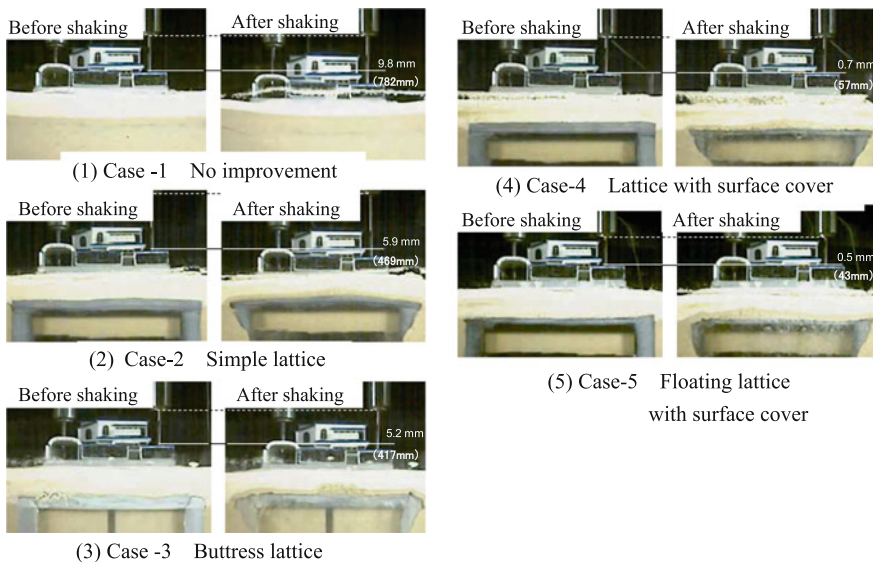


Fig. 4 Shapes of soil improvement examined. **a** Simple lattice, **b** buttress lattice, **c** lattice with surface cover

**Fig. 5** Test series in centrifuge model tests**Fig. 6** Settlements of model houses after shaking

site, the underground structure is floated to cover part of the liquefiable layer in the vertical direction. The front and rear sides of the structure model are embedded in the bedrock. The ground surface settlements observed at the end of model tests are shown in Fig. 6. The soil improvement is found to be least effective in the “simple lattice” shape followed by the “buttress lattice” and “lattice with surface cover.”

4 Verifying Rational Shapes of Soil Improvement in 3D Effective Stress Numerical Analyses

An analytical study is carried out to verify if the rational shapes of soil improvement identified in the above centrifuge model tests would really work well. To examine such 3D shapes of soil improvement, the numerical code of FLIP3D with three-dimensional effective stress analysis is used. FLIP has been prevalent as a general code for two-dimensional effective stress analysis. Figure 7 shows an analysis model used for three-dimensional effective stress analysis (FLIP3D), which assumes the models produced in the centrifuge model tests. Table 2 lists material parameters.

The settlements of model houses observed in the centrifuge model tests and the numerical analyses are compared with each other in the five cases, (no improvement, simple lattice, buttress lattice, lattice with surface cover, and floating lattice with surface cover), as shown in Fig. 8. It is found that the settlements of model houses are reproduced highly accurately. To see any reasons why the settlements are in good agreement, comparisons are made on the excess pore water pressure ratios observed in the simple lattice and the lattice with surface cover, as shown in Fig. 9. The lattice with surface cover effectively reduces excess pore water pressures near the ground surface inside the lattice square. The results of comparisons of deformation characteristics of the underground structures are shown in Fig. 10. The lattice with surface cover effectively controls the deformation of the structures near the ground surface. It seems therefore that the shear deformation near the ground surface inside the lattice square is controlled and that the increase in the pore water pressures near the ground surface is also controlled.

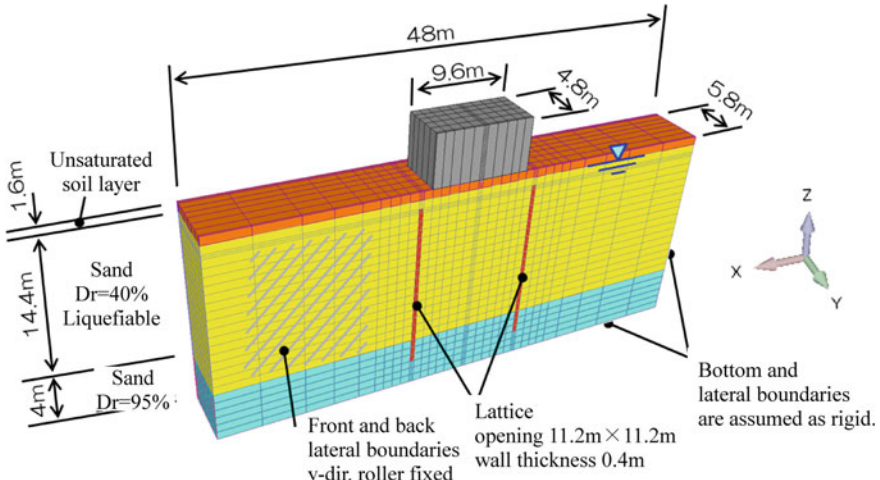
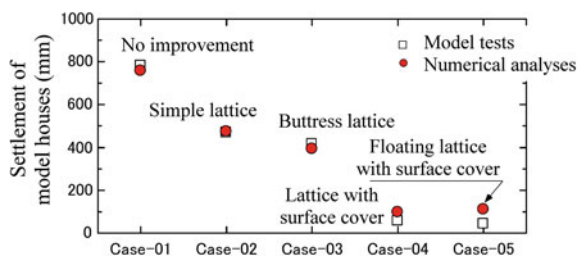
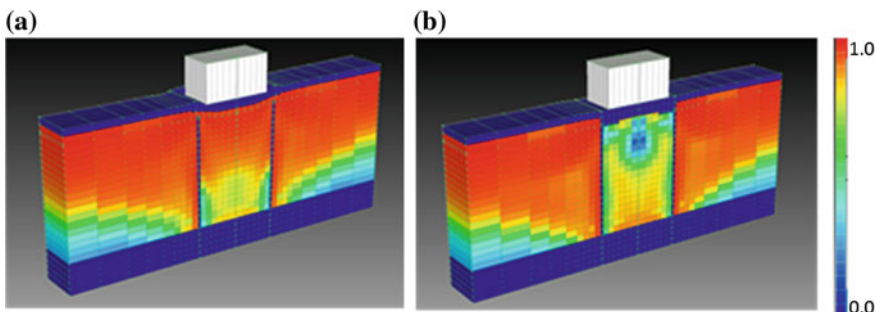


Fig. 7 Analysis model and material parameters

Table 2 Parameters assumed in the numerical analyses

| | Unsaturated layer | Liquefiable layer | Basement layer |
|------------------------------|-------------------|-------------------|----------------|
| ρ_l (t/m ³) | 1.91 | | |
| G_{\max} (MPa) | 52.29 | | 126.22 |
| v | 0.33 | | |
| c (kPa) | 0 | | |
| ϕ (°) | 38.30 | | 41.20 |
| F_c (%) | 10.0 | | |
| h_{\max} | 0.24 | | |
| ϕ_{PT} (°) | | 28.0 | |
| W_1 | | 6.057 | |
| P_1 | | 0.500 | |
| P_2 | | 1.025 | |
| C_1 | | 1.600 | |
| S_1 | | 0.005 | |

**Fig. 8** Settlements of model houses in the centrifuge model tests and numerical analyses**Fig. 9** Comparisons of excess pore water pressure ratios. **a** Simple lattice, **b** lattice with surface cover

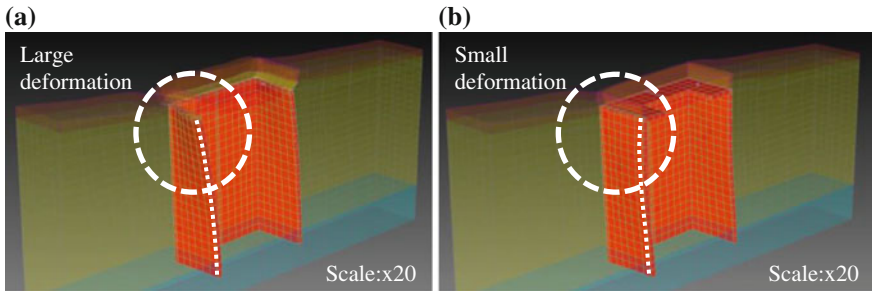


Fig. 10 Comparisons of deformation characteristics of underground structures. **a** Simple lattice, **b** lattice with surface cover

5 Field Verifications of Construction Procedure and Machinery

Field verification tests are conducted on the underground soil improvement structures of simple lattice and of lattice with surface cover, which are among the cases mentioned above. The field tests are aimed at checking construction procedures and machinery under the conditions of narrow space with a mat foundation assuming an existing house, and then at checking the influences on surrounding areas and the quality and effectiveness of soil improvement. The field verification tests are conducted at a site designated by Urayasu city government in 2012.

Figure 11 shows the location where the verification test is conducted. The groundwater level is at GL -1.4 m. The surface layer is composed of a silt formation from GL -2.8 to -4.2 m, underlain by reclaimed fill mainly composed of fine sand with an N -value of approximately 5 down to GL -9.5 m. The reclaimed fill overlies an alluvial formation mainly composed of fine sand with an N -value of approximately 15 down to GL -11.8 m and an alluvial silt formation below GL -11.8 m. This field test site was liquefied during the 2011 Great East Japan Earthquake.

Figure 12 shows the plan and cross-sectional views of underground structures in the field tests. The bottoms of the underground soil improvement structures are embedded to the non-liquefiable formation for both cases of lattice with surface cover (case 1) and simple lattice (case 2). In order to verify the effects on existing housing sites, a $10\text{ m} \times 10\text{ m}$ reinforced concrete slab with a thickness of 20 cm is installed at a ground surface to simulate a mat foundation, as shown in Fig. 13. The tests on the construction procedure and machinery are also shown in Fig. 13. A model house and a wall simulating the exterior are installed with a spacing of 1 m and construction is carried out in narrow space. The standard cycles of construction work per borehole are conducted and it is found that one underground structure could be developed in a day.

The underground structures produced in the field tests are partly excavated to check the quality and shapes, as shown in Fig. 14. The surface cover of case 1 has a

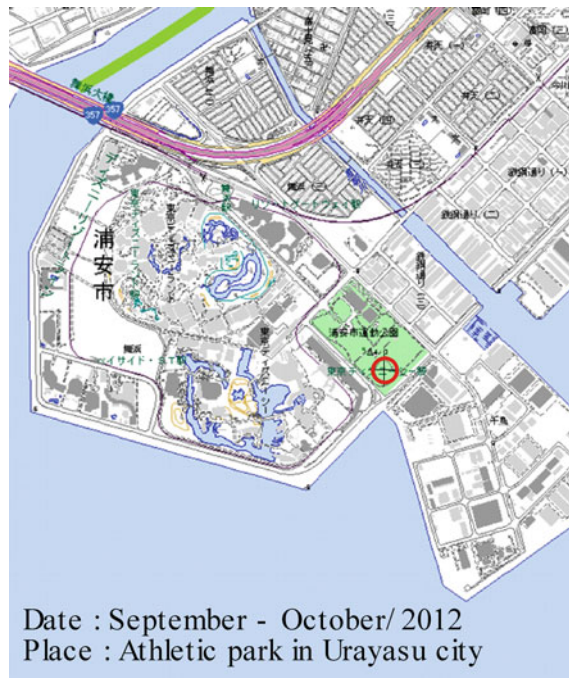


Fig. 11 Location of field tests in Urayasu city

Fig. 12 Plan and cross-sectional views of field tests. **a** Plan view, **b** cross section

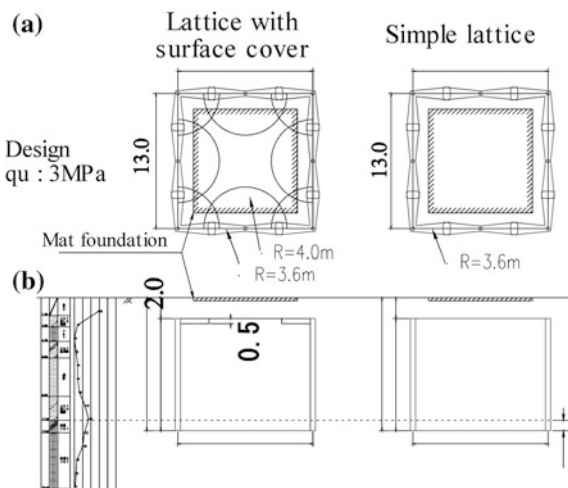




Fig. 13 Model mat foundation of an existing house and micro machine

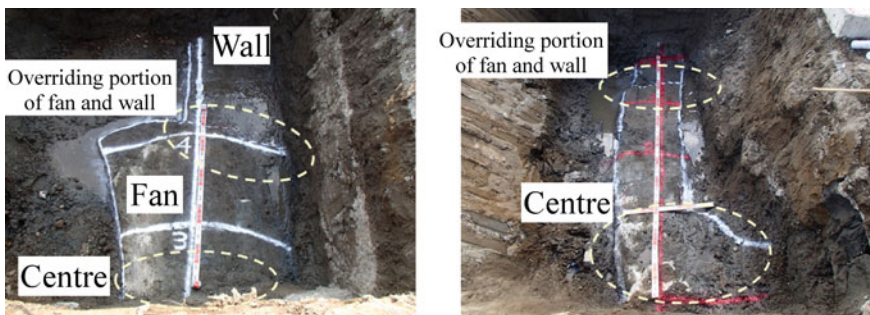


Fig. 14 Checking quality of soil improvement

radius of improvement of 4.2 m, which is larger than the design value of 4 m. The underground structure is expanded at an angle of 30° to explicitly show the distance of jetting. In case 2, the minimum wall thickness is 65 cm, which is larger than the design value of 50 cm. A block of the structure is excavated as a sample for unconfined compression test and indirect tensile test, and both of the unconfined compressive strength and tensile strength exceed the design levels of 3 and 0.33 MPa, respectively.

6 Conclusions

The present study was aimed at developing a more effective construction method for soil liquefaction countermeasures for residential houses together with adjacent roads and other public facilities. The soil improvement structures with lattice walls and surface cover were found to provide a more effective shape, based on the centrifuge model tests and numerical analyses. It was found that the volume of soil improvement could be reduced to 7–10 % by using the shapes proposed in the present study, while the volume of improvement could be reduced to approximately 50 % when conventional lattice-shaped soil improvement by jet grouting is adopted. Therefore, cost can be reduced greatly.

From the results of the field verification tests conducted in a simulated model house using a micro machine, it was shown that the proposed method is highly practicable. The method is applicable not only to soil liquefaction control projects, but also to soil liquefaction control in narrow space for social infrastructure systems and industrial facilities. The micro machine has been designed to satisfy the construction specifications equivalent to those of conventional machines. The reliability of the total quality of the micro machine will be improved by conducting trial construction.

References

Japan Construction Mechanization Association (2009) Multi-jet method (arbitrary-shape, large-diameter jet grouting using high-pressure jets). Construction Technology Certification Report, (in Japanese)

Tezuka H, Yamauchi T, Yasui T (2013a) Development of new high pressure injection mixing methods. *Geotech Eng J* 8(2):179–195, JGS, (in Japanese)

Tezuka H, Yamauchi T, Kawanishi A (2013b) Development of quality management for high pressure injection mixing methods. *Geotech Eng J* 8(2):251–263, JGS, (in Japanese)

Yoshida H, Kubo H, Jimbo T, Sakakibara M (1990) Development of large-diameter soil stabilization method (part 1) effects of pressure and flow during water jet cutting. In: Proceedings of 25th annual conference on geotechnical engineering, 1917–1918, JGS, (in Japanese)

Yoshida H, Asano R, Jimbo T, Sakakibara M (1991) Development of large-diameter soil stabilization method (part 2) effects of the rate of nozzle movement and the number of cycles during water jet cutting. In: Proceedings of 26th annual conference on geotechnical engineering, 1923–1924, JGS, (in Japanese)

Uplift Mechanism of Rectangular Tunnel in Liquefied Soils

Chung-Jung Lee, Yue-Chen Wei, Wen-Ya Chuang, Wen-Yi Hung,
Wen-Lung Wu and Tai-Yuan Ho

Abstract Underground structures located in liquefiable soil deposits are susceptible to floating during earthquakes. These damage cases have been observed in huge earthquake events. A series of centrifuge tunnel model shaking table tests was conducted to investigate the uplift behaviour of rectangular tunnel embedded in liquefiable soils. The test results show that the buried depth of tunnel, the input amplitude of base acceleration and the number of loading cycles all influence the magnitude of tunnel uplift displacement. The higher hydraulic gradient between the soil beneath the tunnel bottom and the surrounding soil became obvious and the surrounding soil squeezing into the tunnel bottom is the major cause of tunnel uplifting. According to the analysis of model test results, the following conclusions are addressed: (1) Magnitude of tunnel uplift is significantly influenced by the viscosity of pore fluid used in the tests (less permeability of soil) and the embedded depth of tunnel. The tunnel would experience the less uplift if the tunnel is embedded in the deeper depth and in the less viscous pore fluid (higher permeability of soil). (2) Once the tunnel begins floating the liquefied sand will squeeze into the tunnel bottom due to high seepage forces from the outside of tunnel and the deeper soils below the tunnel towards the bottom of tunnel. (3) Once the safety factor against uplift (FS) calculated with the proposed method is less than 1 the tunnel would start floating and FS back to 1 the tunnel would stop floating during shaking.

Keywords Uplift mechanism of tunnel · Liquefaction · Centrifuge shaking table test

C.-J. Lee (✉) · Y.-C. Wei · W.-Y. Chuang · W.-Y. Hung
Department of Civil Engineering, National Central University,
Jhongli, Taoyuan, Taiwan
e-mail: cjeeciv@ncu.edu.tw

W.-L. Wu · T.-Y. Ho
CECI Engineering Consultants, Inc., Taipei, Taiwan

1 Introduction

Loose saturated sands are susceptible to generating larger excess pore water pressures during earthquakes, leading to a loss in the sand stiffness and strength. Investigations into damage sites after earthquakes reveal that soil liquefaction is one of the major factors that contribute to severe damage to buildings, oil tanks, bridges, tunnels, embankments, buried pipelines and marine structures (Abdoun et al. 2005; Lee 2005). Underground structures located in liquefiable soil deposits are susceptible to floating up during earthquakes and have been observed in recent major earthquake events (Tobita et al. 2010, 2012; Chian and Madabhushi 2010, 2012).

In Taipei city, an underground conduit was constructed between the Banchia railway station and the Taipei railway station to make way for both the Taiwan railway and the Taiwan high-speed railway systems, thereby, reducing the interference of these systems with road traffic. This tunnel was constructed using a cut-and-cover method. Two parallel slurry walls 36 m in depth and 1 m thick were built first, and the parallel walls with a bracing system were used to support the surrounding soils during soil excavation to a 17 m deep. Finally, the tunnel was constructed. The completed tunnel was enclosed by two parallel walls. Because parts of this tunnel route passed through liquefiable soils, the possibility of tunnel uplift and lateral displacement as a result of lateral spreading and/or liquefaction during larger earthquakes raised concerns after an upgrade of the design peak ground acceleration (PGA). As a result, it became necessary to re-evaluate the seismic behaviour of the liquefiable sand between the parallel walls, as well as the protective effects of the two parallel walls against uplift of tunnel and lateral spreading. In this paper, the uplift mechanism of rectangular tunnel during earthquake-induced liquefaction is major concern.

In situ investigations of liquefaction phenomena are difficult because earthquakes occur infrequently and unpredictably. Small-scale physical modelling provides an alternative to geotechnical earthquake engineering and has been used to gain insights into failure mechanisms. Geotechnical modelling requires the reproduction of the strength and stiffness associated with soil behaviour. Soil behaviour strongly depends on stress levels and stress histories. Centrifuge modelling enables complex scenarios to be reproduced at small scales and at low costs. The use of a soil with a soil density ρ both in a prototype and in a centrifuge model subjected to an inertial acceleration field of N times the earth's gravity yields a vertical stress at a depth h_m (the subscript m denotes the centrifuge model) that is identical to that of the corresponding prototype at a depth h_p (the subscript p denotes the prototype), where $h_p = Nh_m$. The model: prototype scale factor for linear dimensions is 1: N . This relationship is the scaling law of the centrifuge modelling; that is, the stress and pressure similarities are achieved at homologous points. The scaling relationships were applied to a prototype subjected to base shaking (the amplitude of the base acceleration, a_p , and the frequency, f_p) in the earth's gravity (1g), such that the corresponding $1/N$ centrifuge model was tested at an acceleration of Ng and subjected to base shaking (where the amplitude of acceleration is $a_m = Na_p$ and the

frequency is $f_m = Nf_p$). The scale factors that retained the stress and pressure similarities of the linear dimensions and base acceleration, a , of the centrifuge model and the prototype were $1:N$ and $1:N^{-1}$, respectively. A series of centrifuge tunnel model shaking table tests at an acceleration of $80g$ was conducted to investigate the uplift mechanism of rectangular tunnel embedded at different depths in liquefiable soils.

2 Centrifuge Modelling

2.1 Testing Equipment, Tested Sand, and Preparation of Sand Beds

This study was conducted in the Centrifuge at the National Central University (NCU), Taiwan. The NCU Centrifuge has a nominal radius of 3 m and has a 1-D servo-hydraulically controlled shaker integrated into a swing basket (Lee et al. 2012). The shaker has a maximum nominal shaking force of 53.4 kN with a maximum table displacement of ± 6.4 mm and operates up to an acceleration of $80g$. The nominal operating frequency range of shaking is 0–250 Hz. The table-payload mounting area is 1000 mm \times 546 mm \times 500 mm. Fine quartz sand was used to prepare the sand beds. The characteristics of the fine quartz sand used are summarized in Table 1. A laminar container (711 mm (L) \times 356 mm (W) \times 353 mm (H)) was used to contain the sand deposits. The quartz sand was pluviated with a regular path into the container from a hopper at a fixed falling height and at a constant flow rate to prepare fairly uniform sand beds with a relative density of 55 %. The internal friction angle of tested sand bed was about 35.7° . The air pluviation process was interrupted as required for embedding the model tunnel, the accelerometers and pore water pressure transducers (PPTs) at specified elevations and locations. The prepared sand deposit was saturated with water or viscous fluid (kinematic viscosity ≈ 40 cSt) by a vacuum method.

2.2 Design and Fabrication of Model Tunnel

The prototype dimensions of the cross section of the rectangular rail tunnel are $9.15\text{ m} \times 18\text{ m}$ ($h_p \times b_p$). The model tunnel was tested at an acceleration of $80g$,

Table 1 Characteristics of fine quartz sand

| | G_s | D_{50} (mm) | D_{10} (mm) | ^a ρ_{\max} (g/cm 3) | ^a ρ_{\min} (g/cm 3) |
|-------------|-------|---------------|---------------|---|---|
| Quartz sand | 2.65 | 0.193 | 0.147 | 1.66 | 1.44 |

^aThe maximum and minimum densities of the sand were measured in the dry state, according to the method (JSF T 161-1990) specified by the Japanese Geotechnical Society

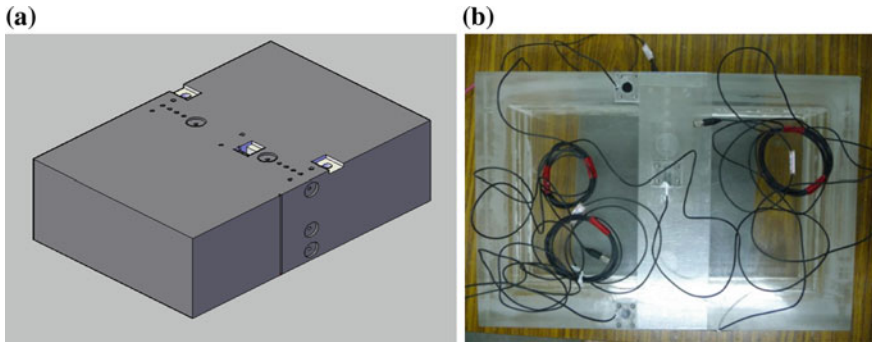


Fig. 1 Model tunnel: **a** 3-D model tunnel image; **b** model tunnel with instrumented transduces inside

therefore, the dimensions of model tunnel are scaled to 1/80 in length and are $0.114\text{ m} \times 0.225\text{ m}$ ($h_m \times b_m$) per the centrifuge scaling law. Here h , b are the tunnel height and tunnel width, respectively. The suffixes $_m$ and $_p$ represent the dimension in model scale and in prototype scale. The unit weight of model tunnel including the transducers (accelerometers, pore water pressure transduces, and earth pressure cells) instrumented and embedded inside the model tunnel is 9.02 kN/m^3 and is nearly the same as the unit weight of in situ concrete tunnel including the railway and the other facilities (8.85 kN/m^3). The model tunnel was made of acrylic as shown in Fig. 1. The surface on the model tunnel was roughed with sand paper. The earth pressure cells, pore water pressure transducers, and accelerometer were instrumented on the 4-side surfaces to monitor the seismic responses of model tunnel subjected to the base shaking.

2.3 Testing Set-up and Testing Conditions

Figure 2a–c show the soil profiles and the instrumentation layouts used in the models. The dimensions in Fig. 2a–c are in centimeters, and the prototype dimensions in parentheses are in meters. Table 2 is the list of test number and testing conditions used in the study. Pore water pressure transducers (PPT#), earth pressure cells (EPC#), and accelerometers (A#) were instrumented in and around the model tunnel to monitor the changes of excess pore water pressure, the earth pressures and the accelerations on the surfaces and inside of model tunnel. Two vertical arrays of accelerometer and of pore water pressure transducer was also instrumented at the middle and right-hand side of the tunnel model in the sand deposit to capture the seismic response as clear as possible. All the accelerometers, EPCs, PPTs and LVDTs were mounted in an effort to measure the following seismic responses of model: (1) Tunnel uplift displacement; (2) Ground surface

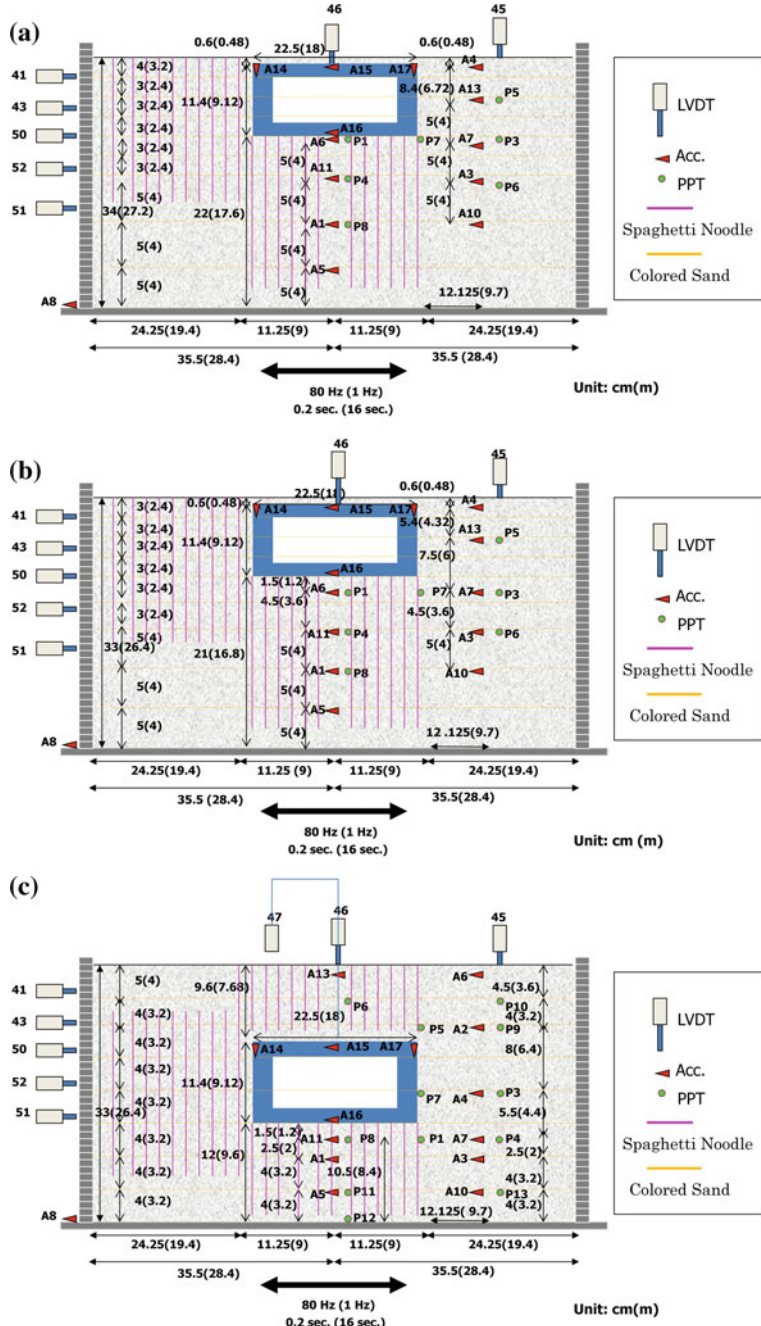


Fig. 2 Testing set-up: **a** Tunnel-1; **b** Tunnel-2; **c** Tunnel-3

Table 2 Test number and testing conditions (all dimensions in prototype)

| Test no. | Pore fluid | Embedment depth (m) | Depth of sand deposit (m) | γ_{sat} (kN/m ³) | γ_{tunnel} (kN/m ³) | Max. shaking magnitude (g) | Shaking frequency (Hz) | Shaking elapsed time (s) |
|----------|------------------|---------------------|---------------------------|--|---|----------------------------|------------------------|--------------------------|
| Tunnel-1 | MCE ^a | 0.48 | 27.2 | 19.17 | 9.02 | S1:0.13 | 1 | 16 |
| | | | | | | S2:0.23 | | |
| Tunnel-2 | Water | 0.48 | 26.4 | 19.04 | 9.02 | S1:0.13 | 1 | 16 |
| | | | | | | S2:0.23 | | |
| Tunnel-3 | Water | 7.68 | 26.4 | 19.04 | 9.02 | S1:0.25 | 1 | 16 |

^aMCE Methocel cellulose ether solution (viscous fluid, kinematic viscosity $\cong 40$ cSt)

settlements and lateral movements of the rectangular container rings; (3) The seismic responses of the tunnel at the centre of the container and aside the tunnel during shaking; (4) To capture excess pore water dissipation in the far field during the shaking and at the post shaking stage; (5) Several PTTs were also installed beneath the tunnel or at the right-hand side wall of the tunnel to record the pore pressure generation and dissipation around the tunnel; (6) A horizontal PPT array was installed at the bottom of tunnel to capture the pore pressure changes underlying the tunnel, which is the most important thing observed in this study; (7) EPCs were installed on the surfaces of the model tunnel used to measure the earth pressures acting around the tunnel; (8) Several rows of spaghetti were inserted into the sand deposit to investigate the movements of soil near to the model tunnel after tunnel floating.

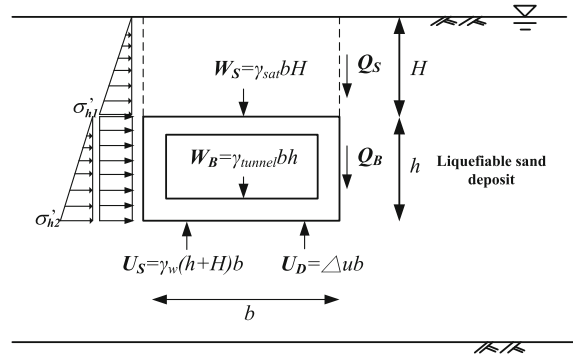
3 Test Results and Interpretations

Based on the equilibrium of vertical forces acting on a embedded tunnel the safety factor (FS) can be used to evaluate the uplifting of tunnel caused by soil liquefaction (Koseki et al. 1997). The vertical equilibrium in the triggering condition of uplift as shown in Fig. 3 is expressed as:

$$W_s + W_B + Q_s + Q_B = U_s + U_D \quad (1)$$

where $W_s = \gamma_{\text{sat}}bh$ = the total overburden weight of soil above the tunnel; $W_B = \gamma_{\text{tunnel}}bh$ = the weight of tunnel; $Q_s = H\sigma_{v1}K_o \tan \phi$ = the friction resistance of soil above the tunnel; $Q_B = h(\sigma'_{v1} + \sigma'_{v2})K_o \tan \delta$ = the friction resistance of soil along the two side walls of tunnel; $U_s = \gamma_w(h + H)b$ = static pore water pressure at the elevation of tunnel bottom; $U_D = \Delta ub$ = excess pore water pressure at the elevation of tunnel bottom; σ'_{v1} and σ'_{v2} are the effective vertical stresses at the tunnel top and bottom. The safety factor against tunnel uplift can be derived as follows

Fig. 3 Vertical forces on an embedded tunnel during uplifting caused by soil liquefaction



$$FS = \frac{W_s + W_B + Q_s + Q_B}{U_s + U_D} \quad (2)$$

Koseki et al. (1997) examined the relationship between the FS and uplift displacement of box-type structures and concluded that the uplift continues when the FS is less than or almost equal to 1. Equation 2 can be used to evaluate the triggering condition of uplift.

The liquefaction and post-liquefaction behaviours of sand deposits are basically governed by the generation and dissipation of excess pore water pressure. The excess pore water pressure ratio is defined as the measured excess pore water pressure, Δu , divided by the corresponding effective overburden pressure, σ'_v :

$$r_u = \frac{\Delta u}{\sigma'_v} \quad (3)$$

Tunnel-1 and Tunnel-2 are shallowly embedded (0.48 m) in the sand deposit which is saturated with MCE solution (Tunnel-1) and water (Tunnel-2), respectively. Use of viscous pore fluid to replace the water in the sand bed can retard the excess pore water pressure dissipation to simulate the shallow tunnel embedded in the sand deposit having lower permeability (Tunnel-1). Figures 4 and 5 display the time histories of uplift displacement, excess pore water pressure measured at P5 (far away from the tunnel) and acceleration measured at A8 for Tunnel-1 and Tunnel-2 in the S1 event, respectively. The uplift displacement continuously developed even after shaking in Tunnel-1 because of the excess pore water pressure keeping higher. Figure 6a, b displays the time histories of uplift displacement for Tunnel-1 and Tunnel-2 in the S1 and S2 events. The shallow tunnel embedded in the lower permeability deposit would experience the larger uplift displacement. Figure 7 displays the time histories of uplift displacement versus excess pore water pressure for Tunnel-3 ($a_{max} = 0.25g$) and the instrumentation positions and the transducer numbers. Figure 8 displays the time histories of uplift displacement measured at Tunnel-1, Tunnel-2, and Tunnel-3 for comparison. The deeper tunnel (embedded

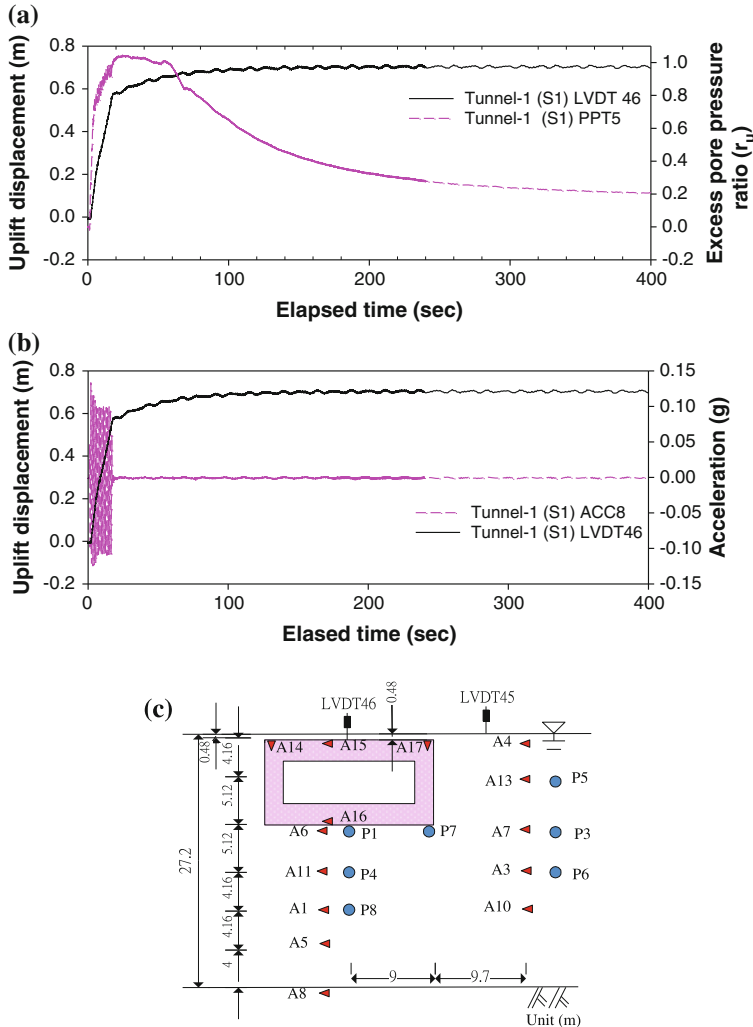


Fig. 4 Time histories of uplift displacement versus excess pore water pressure and acceleration for Tunnel-1 (S1): **a** uplift displacement versus ratio of excess pore water pressure; **b** uplift displacement versus Acceleration; **c** instrumentation positions and transducer number

depth = 7.68 m) experienced the less uplift displacement. Figures 9 and 10 display the developed excess pore water pressures measured at the same elevations but at different positions for Tunnel-1 and Tunnel-3. The installed positions of pore water pressure transducers are shown in Figs. 4c and 7. Figure 11 displays the failure mechanism of tunnel after floating. In Tunnel-1 (shallow tunnel) the measured excess pore water pressure at the position far away from the centre of embedded tunnel is much higher than those measured at the position near to or at the centre of

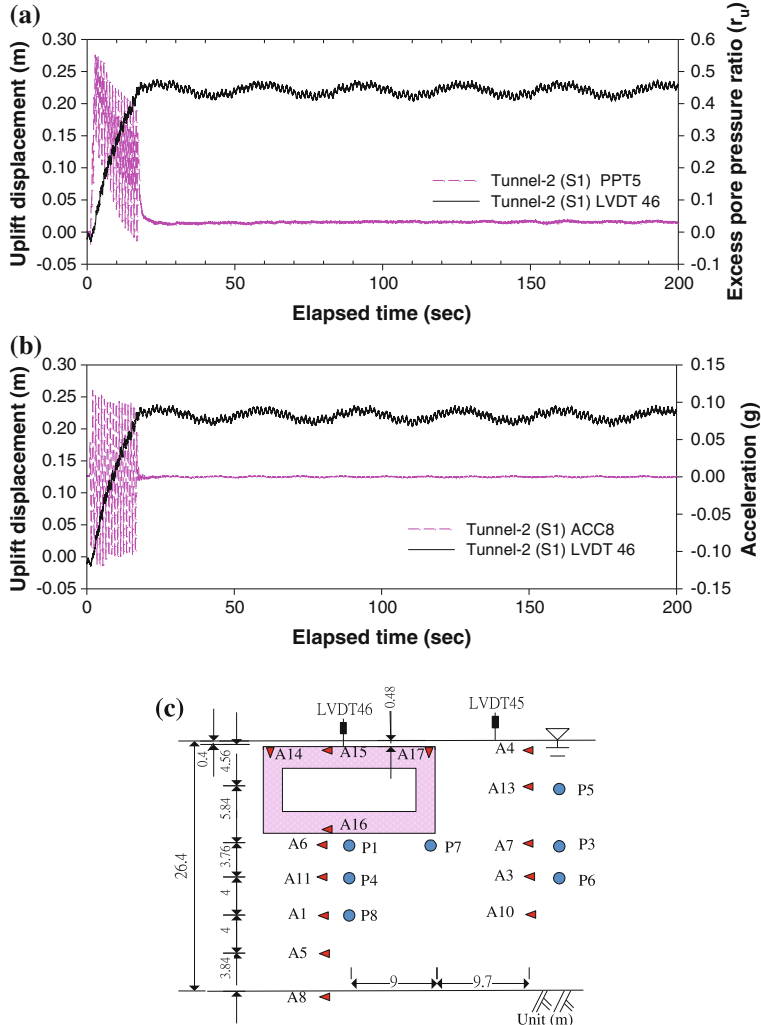


Fig. 5 Time histories of uplift displacement versus excess pore water pressure and acceleration for Tunnel-2 (S1): **a** uplift displacement versus ratio of excess pore water pressure; **b** uplift displacement versus Acceleration; **c** instrumentation positions and transducer number

tunnel. Larger hydraulic gradients cause the water from the free field flowing to the tunnel bottom. The surrounding soil would squeeze into the tunnel bottom. By contrast in Tunnel-3 the less difference of the magnitude of excess pore water pressures measured at the same elevation below the tunnel bottom are observed. Therefore, the less surrounding sand squeezed into the tunnel bottom and the less uplifting of tunnel is expected. Use of Eq. 2 and measured the excess pore water pressures can calculate the factor of safety as shown in Fig. 12 during and after

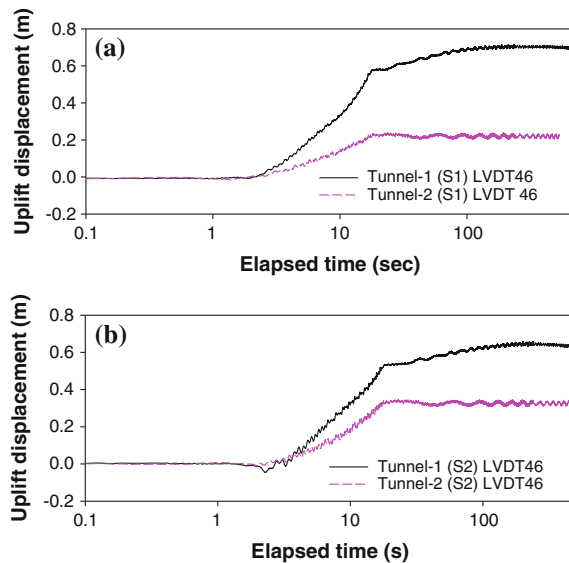


Fig. 6 Time histories of uplift displacement for Tunnel-1 and Tunnel-2 in the event 1 and event 2: **a** event 1 ($a_{\max} = 0.13g$); **b** event 2 ($a_{\max} = 0.23g$)

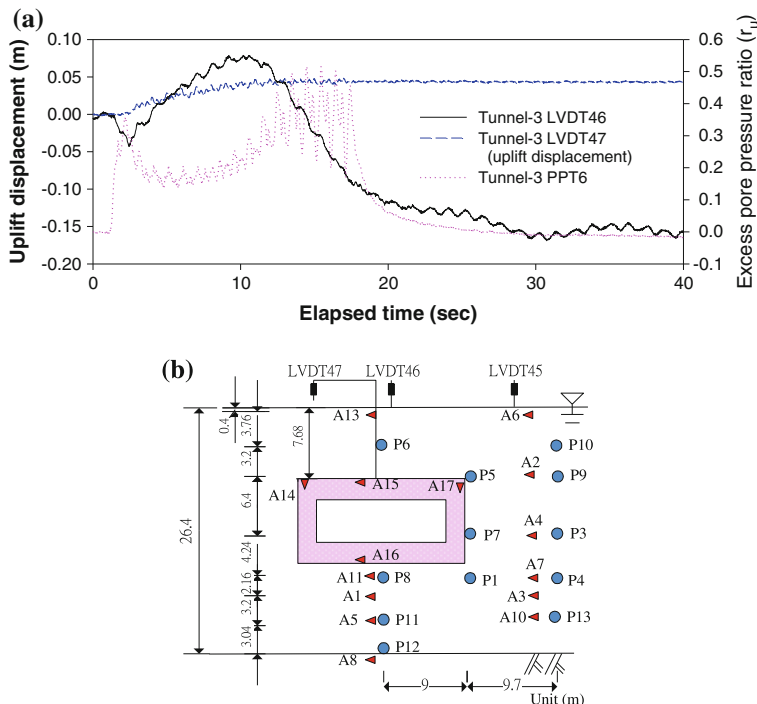


Fig. 7 Time histories of uplift displacement versus excess pore water pressure for Tunnel-3 ($a_{\max} = 0.25g$)

Fig. 8 Time histories of uplift displacement for Tunnel-1 (S2, $a_{\max} = 0.23g$), Tunnel-2 (S2, $a_{\max} = 0.23g$) and Tunnel-3 (S3, $a_{\max} = 0.25g$)

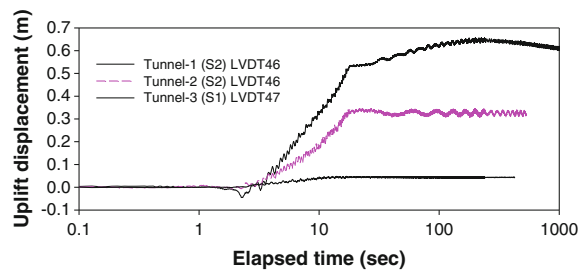


Fig. 9 Time histories of excess pore water pressure at different positions for Tunnel-1 (S2) ($a_{\max} = 0.23g$)

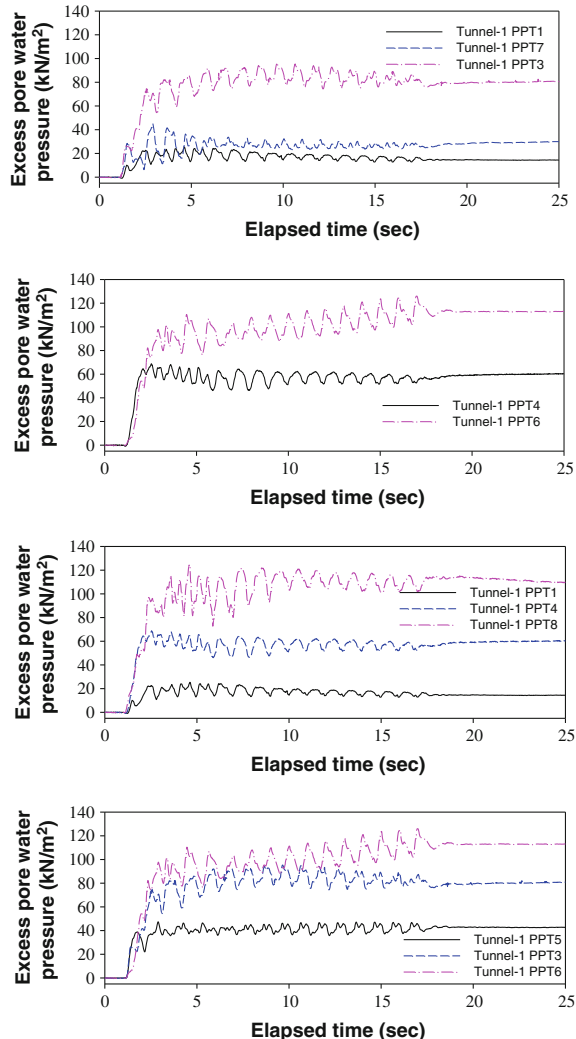
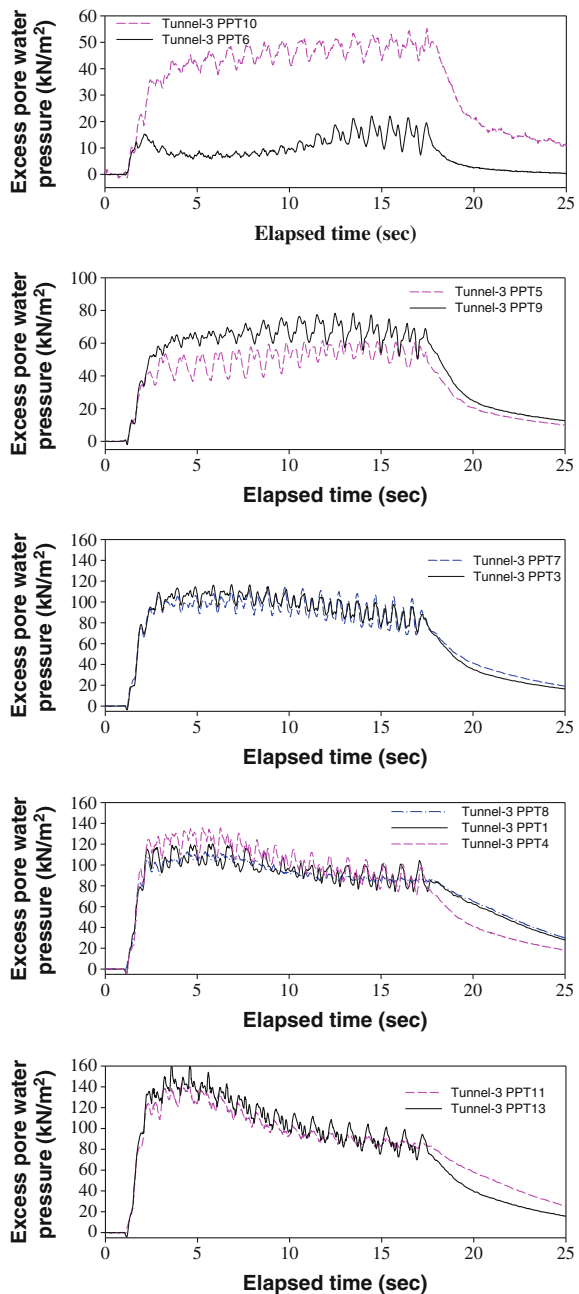


Fig. 10 Time histories of excess pore water pressure at different positions for Tunnel-3 ($a_{\max} = 0.25g$)



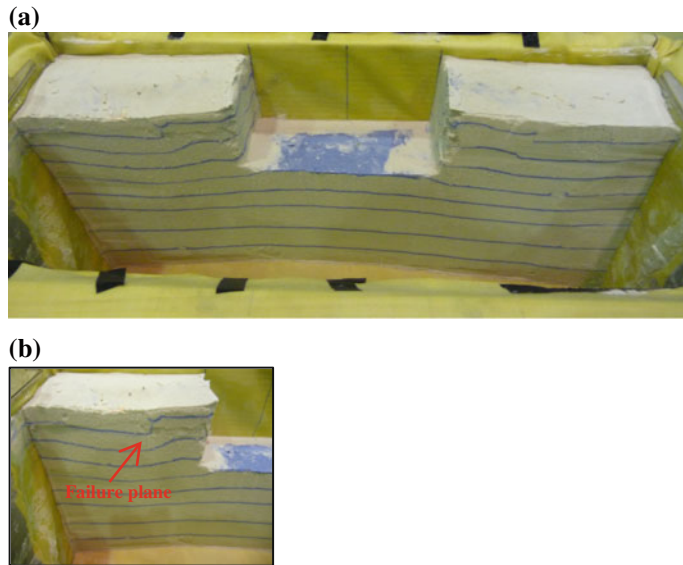


Fig. 11 The failure mechanism of uplifting for Tunnel-1 after testing: **a** fullview; **b** near view

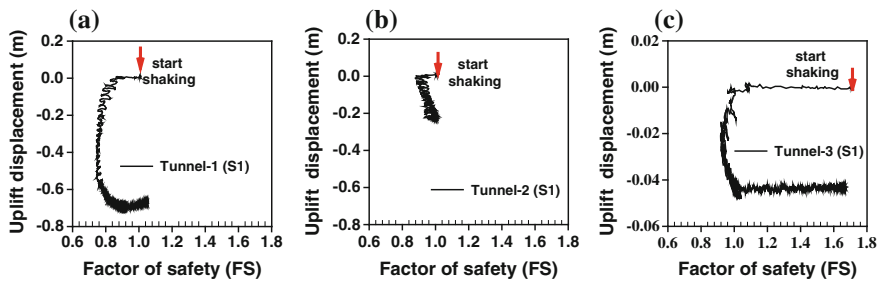


Fig. 12 Magnitude of tunnel uplifting displacement versus Factor of safety during and after shaking: **a** Tunnel-1 (S1); **b** Tunnel-2 (S2); **c** Tunnel-3 (S1)

shaking for Tunnel-1, Tunnel-2, and Tunnel-3. Once the safety factor against uplift (FS) calculated with the proposed method is less than 1 the tunnel would start floating, and after the FS returning to 1 the tunnel stops floating.

4 Summary and Conclusions

According to the model test results, the following conclusions are addressed: (1) The magnitude of tunnel uplift is significantly influenced by the viscosity of pore fluid used and the embedded depth of tunnel. Use of viscous pore fluid would reduce the

rate of excess pore water pressure generation and dissipation and prolong the elapsed time of liquefaction. Therefore, the tunnel embedded in the deeper depth and in the less viscous pore fluid would experience the less magnitude of tunnel uplift during and after shaking. (2) The higher hydraulic gradient between the soil beneath the tunnel bottom and the surrounding soil in the free field became very obvious. The surrounding soil squeezing into the tunnel bottom induced by the higher hydraulic gradient is one of the major causes of tunnel uplifting. (3) The larger magnitude and the longer duration of the base shaking subjected to the liquefiable sand deposit, the larger magnitude of tunnel uplift occurred. (4) Once the safety factor against uplift (FS) calculated with the proposed method is less than 1 the tunnel would start floating during shaking, and after the FS returning to 1 the tunnel stops floating.

References

Abdoun T, Dobry R, Zimmie TF, Zeghal M (2005) Centrifuge research of countermeasures to protect pile foundations against liquefaction-induced lateral spreading. *J Earthquake Eng* 9 (1):105–125

Chian SC, Madabhushi SPG (2010) Influence of fluid viscosity on the response of buried structures in earthquakes. In: 7th international conference of physical modelling in geotechnics, pp 111–115

Chian SC, Madabhushi SPG (2012) Effect of buried depth and diameter on uplift of underground structures in liquefied soils. *Soil Dyn Earthq Eng* 41:181–190

Koseki J, Matsuo O, Koga Y (1997) Uplift behavior of underground structures caused by liquefaction of surrounding soil during earthquake. *Soils Found* 37(1):97–108

Lee CJ (2005) Centrifuge modeling of the behavior of Caisson-type quay walls during earthquake. *Soil Dyn Earthq Eng* 25(2):117–131

Lee CJ, Wei YC, Kou YC (2012) Boundary effects of a laminar container in centrifuge shaking table tests. *Soil Dyn Earthq Eng* 34(1):37–51

Tobita T, Kan GC, Iai S (2010) Uplift behavior of buried structures under strong shaking. In: 7th international conference of physical modeling in geotechnics, pp 1439–1444

Tobita T, Kan G-C, Iai S (2012) Estimation of liquefaction-induced manhole uplift displacements and trench-backfill settlements. *J Geotech Geoenvironmental Eng ASCE* 138(4):491–499

Seismic Response of Geosynthetic Reinforced Earth Embankment on Different Soil Foundation

Wen-Yi Hung and Chung-Jung Lee

Abstract The reinforced earth embankment has a brilliant performance on the resistance to seismic loadings, but the additional settlement of reinforced earth embankment would result from the liquefaction of sandy foundation. Therefore, three centrifuge shaking table tests were performed to study the seismic behaviour of reinforced earth embedment on liquefiable and non-liquefiable sand deposits. From the test results, it was observed that the liquefaction would not occur easily under the GRE embankment. But the deep soil layer away from the GRE embankment would liquefy and the shear wave could not propagate up to the soil completely. The largest settlement occurred at the centre of GRE embankment. After 1 Hz seismic event, the maximum settlements normalized by the embankment height were about 0.11, 2.78, and 25.18 % for the dry, water-saturated non-liquefied and liquefied models, respectively.

Keywords Centrifuge shaking table test · Reinforced earth embankment · Seismic response

1 General Introductions

The major advantage of reinforced soil structures, as compared with the reinforced concrete structures, is their flexibility and capability to absorb deformation due to poor foundation. In addition, the observations made after Ji-Ji earthquake of Taiwan or Hanshin-Awaji earthquake of Japan showed that most of the reinforced soil structures in the field survived without serious damages. The excellent performance of reinforced earth structures on the resistance of seismic loadings was proved by

W.-Y. Hung (✉) · C.-J. Lee

Department of Civil Engineering, National Central University,
Jhongli, Taoyuan, Taiwan R.O.C.
e-mail: wyhung@ncu.edu.tw

C.-J. Lee
e-mail: cjleeciv@cc.ncu.edu.tw

the past studies (Nova-Roessig and Sitar 2006; Liu et al. 2011). The reinforced earth embankment has a brilliant performance on the resistance to seismic loading, but the additional settlement of reinforced earth embankment will result from the liquefaction of sand foundation. Therefore, three centrifuge shaking table tests were performed in the Centrifuge Modelling Laboratory at National Central University (NCU) to study the seismic behaviour of reinforced earth embedment on liquefiable and non-liquefiable sand deposits.

2 Test Materials and Model Preparation

2.1 *Sand and Reinforcement Materials*

In order to avoid the particle effect for the centrifuge model, fine quartz sand with mean particle size of 0.19 mm was selected to build the model. Its specific gravity is 2.65 with the maximum and the minimum dry unit weight of 16.6 and 13.8 kN/m³, respectively. The friction angle at about 40 % relative density is 35°. According to the Unified Soil Classification System, the sand is classified to poorly graded sand (SP). The scaling factor of reinforcement strength is N , which means that the reinforcement strength used in the centrifuge model should be reduced N times smaller than that used in prototype when the model is tested in Ng acceleration field. Therefore, a very weak geosynthetic material with tensile strengths of 1.25 kN/m was selected to simulate the prototype reinforcement material with strength of 100.0 kN/m in 80 g acceleration field.

2.2 *Model Preparation and Test Procedure*

In this study, three geosynthetic reinforced earth (GRE) embankment models were prepared with wrapped face, 100 % coverage rate of reinforcement material and sandy backfill. The purpose of this study was to investigate the seismic behaviour of GRE embankment. In the design of GRE embankment models, it must be ensured that (1) the external instabilities including sliding and overturning do not occur. (2) The internal instability of pullout and breakage failures do not occur.

Three models were labelled as GREE_D, GREE_W and GREE_VF, where D, W and VF mean that the foundation soils are dry, saturated by water and saturated by viscous fluid, respectively. The GRE embankment model has 10 layers with a total height of 100 mm and located on a 200 mm-thick foundation. The reinforcement length is 0.7 times height and the overlap length is 0.4 time of reinforcement length. The widths at the top and bottom of embankment are 100 and 200 mm, respectively. The face slope is about 63° with inclination of 1:0.5 (vertical:horizontal, V:H). In 80 g acceleration field, the models simulate the GRE embankment with 8 m-high

with the reinforcement spacing of 0.8 m. The model profile and the configuration of sensors for models GREE_D, GREE_W, and GREE_VF are shown in Fig. 1a, b, respectively. Figure 2a is the top views of completed GRE embankment model after removing the lateral supports and Fig. 2b shows the one side of wrapped face with ten layers.

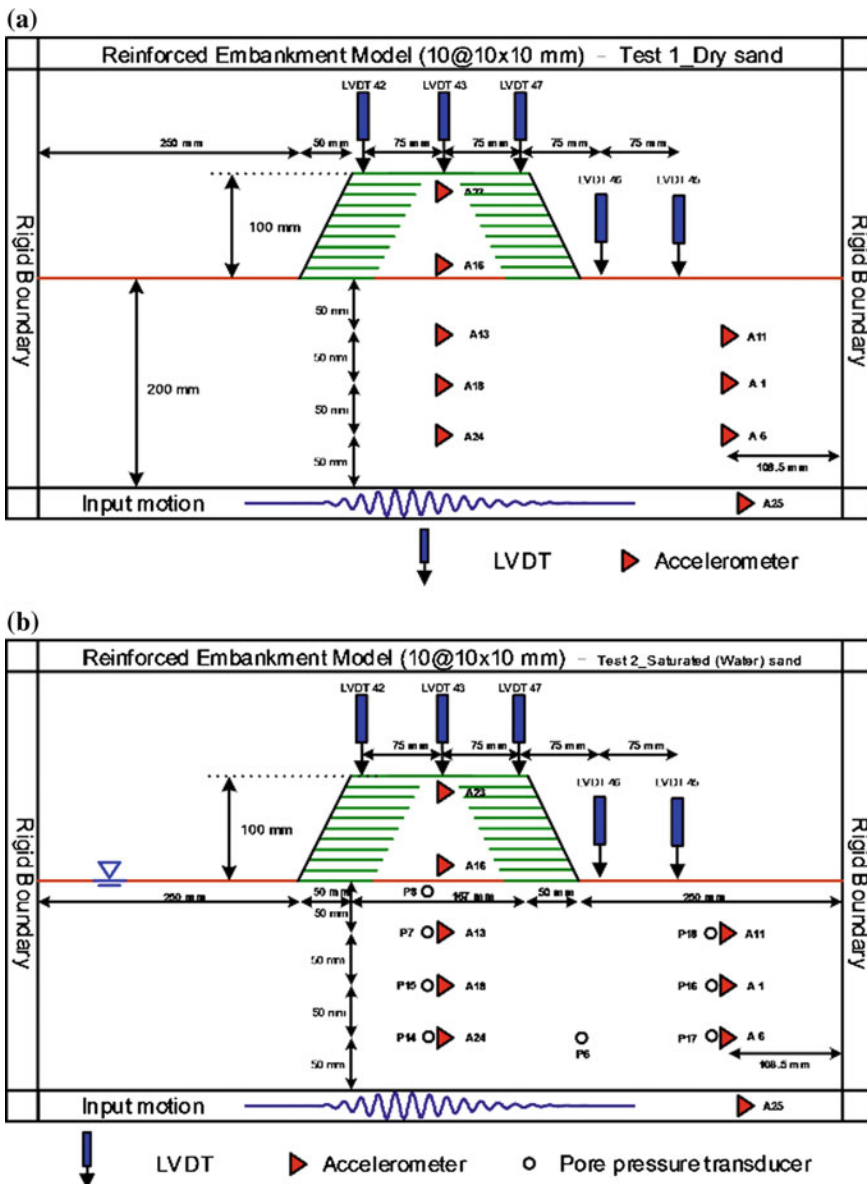


Fig. 1 Arrangement of GRE embankment models in model scale **a** model GREE_D; **b** models GREE_W and GREE_VF

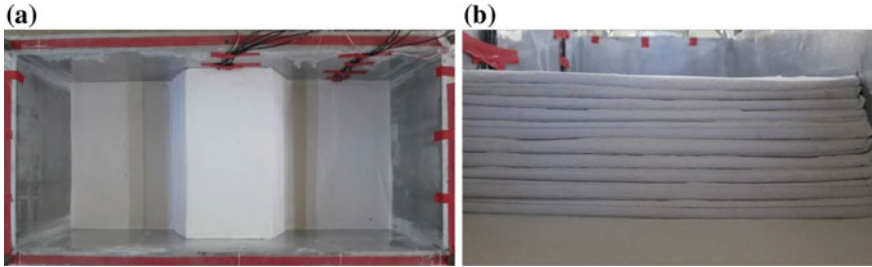


Fig. 2 The completed GRE embankment model after removing away the hard Styrofoam boards **a** top view; **b** one side of slope face

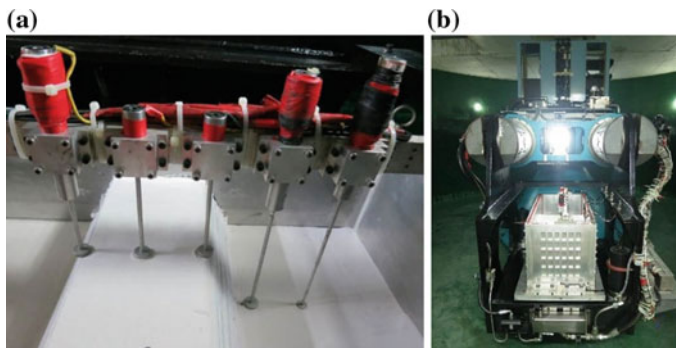


Fig. 3 Model preparation **a** the installation of LVDTs; **b** setup of tested model

Accelerometers and linear variable differential transformers (LVDTs) were installed as shown in Fig. 3a. For models GREE_W and GREE_VF, water pressure transducers were installed near by the accelerometers to monitor the generation and dissipation of excite water pressure during and after shaking. The completed model shown in Fig. 3b was accelerated step by step to 80 g, and the increment of acceleration in each step is 10 g. The model was maintained and lasted for 3 min at each step to ensure the consolidation of sand model at the current overburden pressure. At 80 g, the model was then excited with a series of one-dimensional seismic events. Firstly, a 1 Hz single sine wave was applied to detect the initial properties of GRE embankment and foundation soil, including the shear wave velocity and natural frequency. Then, 15 cycles sinusoidal waves with frequency of 1 and 3 Hz were input to the models to study the seismic response of GRE embankment and foundation soil. Finally, the model was detected again by single sine wave and white noise. The seismic events for each test were shown in Table 1.

Table 1 The seismic events for each test

| Seismic events | GREE_D | GREE_W | GREE_VF |
|----------------|-------------------------|-------------------------|------------------------|
| s1 | 1 Hz 1 cycle, 0.008 g | 1 Hz, 1 cycle, 0.004 g | 1 Hz 1 cycle, 0.013 g |
| | 1 Hz 1 cycle, 0.003 g | 1 Hz, 1 cycle, 0.007 g | |
| s2 | 1 Hz, 15 cycles, 0.15 g | 1 Hz, 15 cycles, 0.09 g | 1 Hz, 15 cycles, 0.3 g |
| | | 1 Hz, 15 cycles, 0.15 g | |
| | | 1 Hz, 15 cycles, 0.19 g | |
| | | 1 Hz, 15 cycles, 0.23 g | |
| s3 | 3 Hz, 15 cycles, 0.08 g | 3 Hz, 15 cycles, 0.05 g | 3 Hz, 15 cycles, 0.2 g |
| | | 3 Hz, 15cycles, 0.07 g | |
| | | 3 Hz, 15cycles, 0.11 g | |
| | | 3 Hz, 15cycles, 0.14 g | |
| s4 | 1 Hz 1 cycle, 0.003 g | 1 Hz 1 cycle, 0.007 g | 1 Hz 1 cycle, 0.014 g |
| s5 | White noise | White noise | White noise |

3 Test Results and Analysis

3.1 Fundamental Properties of Models by Small Shaking

It was found from the past studies that the arrangement of reinforcement material affects the stability of GRE structure. The natural frequency of GRE embankment is significantly related to its height. Thus, the profiles of three GRE embankment models in this study are the same. The small shaking events, s1 and s4, were used to detect the natural frequencies and shear wave velocities of GRE embankment and foundation soil before and after the main shaking events (Lee et al. 2014). As shown in Table 2, the shear wave velocity of GRE embankment is calculated from the accelerometers A16 and A23, and that of soil layer at free field is calculated from the accelerometers A25 and A11. It can be seen that the shear wave velocity of soil layer increases with the increasing surface loading.

Table 2 Shear wave velocities of the GRE embankment and the foundation

| Test No. | GRE embankment (m/s) | Soil layer under embankment (m/s) | Soil layer of free field (m/s) |
|----------|----------------------|-----------------------------------|--------------------------------|
| GREE_D | 233.3 | 187.5 | 166.7 |
| GREE_W | 175.0 | 166.7 | 136.4 |
| GREE_VF | 175.0 | 200.0 | 166.7 |

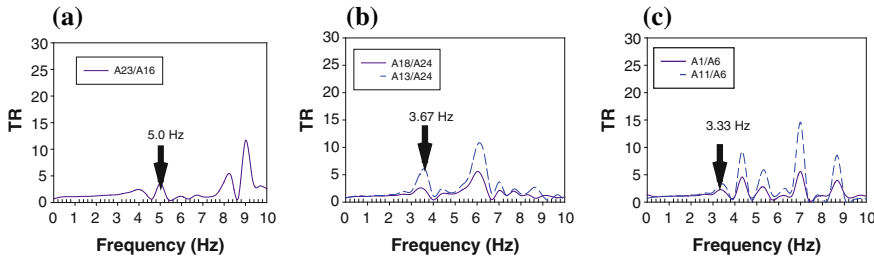


Fig. 4 The transfer functions of seismic event s1 for the model GREE_VF at **a** GRE embankment; **b** soil layer under GRE embankment; **c** soil layer of free field

The shear velocity can be used to briefly predict the natural frequency of the soil deposit by the formula of $4H/V_s$, where H is the thickness of soil layer. On the other hand, the Fast Fourier Transform (FFT) was also used to transfer the time history of acceleration to the frequency domain. Then, the Fourier spectrums of accelerometer A23 divided by that of A16 was the transfer function (TR) of GRE embankment as shown in Fig. 4a. It shows the amplification of acceleration at different frequencies. The frequency at the first peak of transfer function, 5.0 Hz, is the natural frequency of GRE embankment for model GREE_VF. By the same way, the natural frequencies of soil layers under GRE embankment and of free field are 3.67 and 3.33 Hz, respectively, obtained from the accelerometer arrays of A13-A18-A24 and A11-A1-A6 as shown in Fig. 4b, c. Table 3 summarizes the natural frequencies calculated from the theoretical formula and obtained from the transfer functions of small shaking events of s1 and s4. The theoretical value is closed to the result of s1 event. The natural frequency of soil layer with surface loading is larger than that of soil layer of free field. For the three models, the dry, water-saturated and viscous fluid-saturated sandy foundations have the same natural frequency before main shakings. After the main shaking events, the natural frequency of the system increases with the increasing relative density of soil model.

Table 3 Natural frequencies of the GRE embankment and the foundation

| Test no. | | A23/A16 (Hz) | A13/A25 (Hz) | A11/A25 (Hz) |
|----------|------------------------|--------------|--------------|--------------|
| GREE_D | Theoretical value (s1) | – | 2.93 | 2.6 |
| | Natural frequency (s1) | 6.15 | 3.46 | 2.69 |
| | Natural frequency (s4) | 7.3 | 3.67 | 3.3 |
| GREE_W | Theoretical value (s1) | – | 2.6 | 2.13 |
| | Natural frequency (s1) | 5.4 | 3.4 | 2.6 |
| | Natural frequency (s4) | 5.8 | 3.8 | 3.4 |
| GREE_VF | Theoretical value (s1) | – | 3.13 | 2.6 |
| | Natural frequency (s1) | 5 | 3.67 | 3.33 |
| | Natural frequency (s4) | 5.3 | 4.17 | 3.5 |

3.2 Pore Water Pressure Time History

Figure 5 shows the excess pore water pressure time history of seismic event s2 and s3 for model GREE_W. During the main shaking, the excess pore water pressure generated and dissipated at the same time. The quantity of dissipation is much more than that of generation leading to that the excess pore water pressure did not accumulate. Therefore, the soil layer would not liquefy if the water pressure can be driven out as soon as possible. On the other hand, the generated excess water pressure under the GRE embankment was smaller than that of free field, and the effective overburden pressure of the soil layer under the GRE embankment was much greater than that of free field. Thus, liquefaction was not easy to occur under the GRE embankment.

As for the model GREE_VF, Fig. 6 show the excitation and dissipation time histories of excess pore pressure. Figure 7 shows the excess pore pressure time history and the effective overburden pressure at the same depth within the first 30 s of records, where the effective overburden pressure was calculated according to the original depth as shown in Fig. 4. It was clearly observed from the s2 event that the excess pore pressure would increase and be greater than the effective overburden

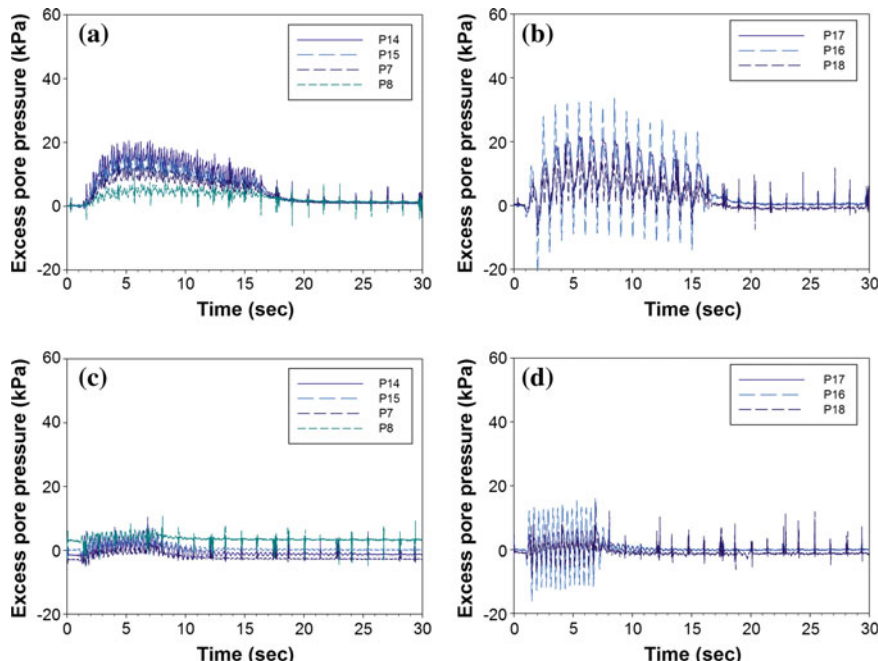


Fig. 5 Excess pore water pressure time history of model GREE_W measured from soil layer **a** under the GRE embankment at seismic event s2; **b** of free field at seismic event s2; **c** under the GRE embankment at seismic event s3; **d** of free field at seismic event s3

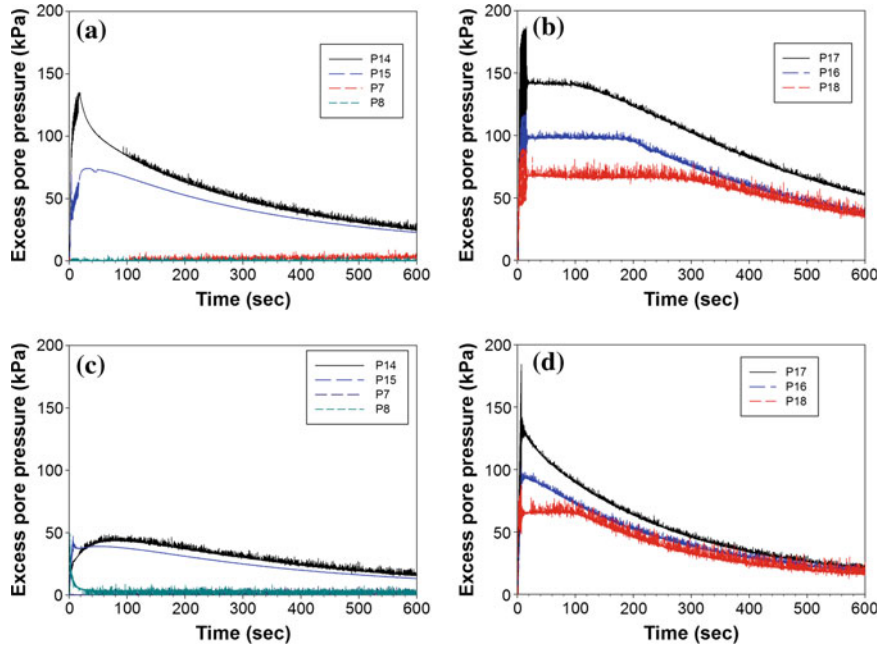


Fig. 6 Excess pore water pressure time history of model GREE_VF measured from soil layer **a** under the GRE embankment at seismic event s2; **b** of free field at seismic event s2; **c** under the GRE embankment at seismic event s3; **d** of free field at seismic event s3

pressure within three cycles if the soil layer liquefy. The blue dot line and the red solid line are the pore pressure time histories of the soils in free field and under GRE embankment, respectively. The difference between these two lines would decrease with increasing depth of soil deposit. From the figures, the soil of free field liquefied but that under the GRE embankment did not. As combined the acceleration time histories, it can be seen that the acceleration amplifications are smaller than 1, meaning that the soil below the accelerometer A14 might liquefy first and then the shear wave could not propagate up to the soil completely.

3.3 Deformations of GRE Embankment

For the model GREE_W, the GRE embankment settled and the tension cracks occurred at the end of embedded reinforcement layers during the increasing artificial acceleration field by NCU centrifuge. Figure 8 shows the development of tension cracks on the top of embankment. The width and the depth of cracks were

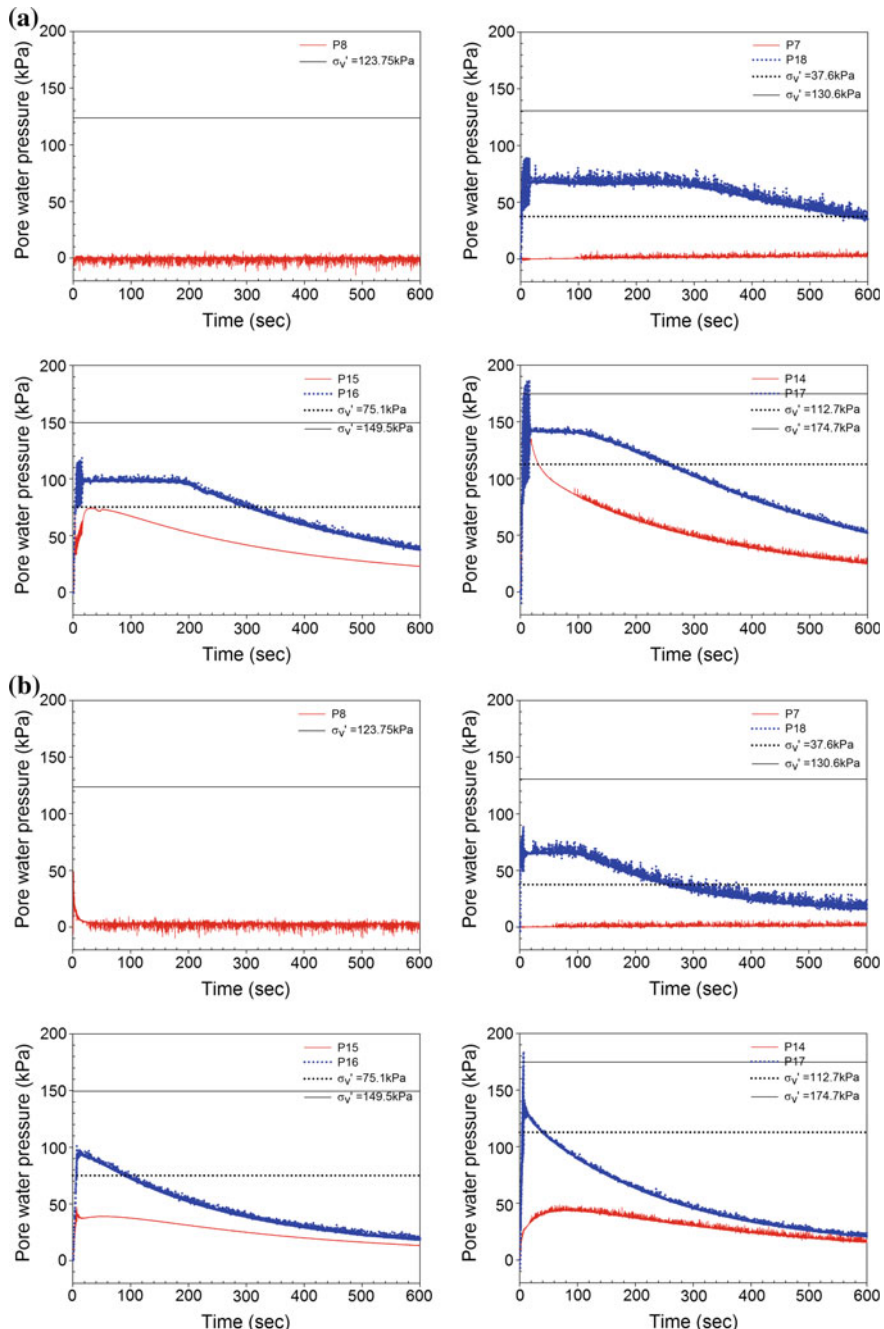


Fig. 7 Excess pore pressure time history of model GREE_VF measured at different depths of foundation soil **a** seismic event s2; **b** seismic event s3

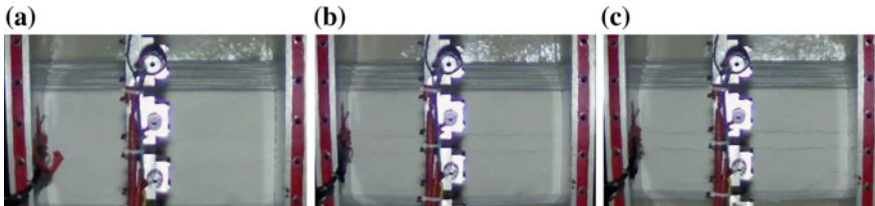


Fig. 8 The development of tension cracks on the top of embankment for model GREE_W during the increasing acceleration field **a** 10 g; **b** 40 g; **c** 80 g

Table 4 The maximum settlement after main shakings

| Seismic events | Settlement (m) | | | | |
|----------------|----------------|---------|---------|---------|--------|
| | LVDT 45 | LVDT 42 | LVDT 43 | LVDT 47 | LVDT 4 |
| GREE_D s2 | 0.001 | 0.009 | 0.004 | 0.000 | 0.000 |
| GREE_D s3 | 0.001 | 0.007 | 0.004 | 0.000 | 0.000 |
| GREE_W s2-4 | 0.127 | 0.222 | 0.110 | 0.045 | 0.049 |
| GREE_W s3-4 | 0.075 | 0.126 | 0.059 | 0.008 | 0.011 |
| GREE_VF s2 | 2.014 | 1.616 | 0.778 | -0.082 | 1.376 |
| GREE_VF s3 | 0.285 | 0.198 | 0.028 | 0.208 | 0.249 |

increasing with the larger artificial acceleration from 10 to 80 g. During the main shakings, five LVDTs were used to measure the settlements. LVDT 45, LVDT 42, and LVDT 43 were installed on the top of GRE embankment from left to right, respectively. LVDT 47 and LVDT 46 were setup at the front ground surface, the former located at near the toe of embankment and the latter was on the free field. Table 4 summarizes the measurements of each seismic event in prototype scale. Generally, the largest settlement occurred at the centre of GRE embankment. The settlements of model GREE_D were the smallest and those of model GREE_VF were the largest because of soil liquefaction. The maximum settlements normalized by the embankment height for the models of GREE_D, GREE_W, and GREE_VF after s2 event were about 0.11, 2.78 and 25.18 %, respectively. On the other hand, those for the three models after s3 event were about 0.09, 1.58 and 3.56 %, respectively.

It can be observed that the tension cracks occurred on the top of GRE embankment after shaking. Figure 9 shows the locations of tension cracks and the settlements on the top of GRE embankment for models GREE_D, GREE_W, and GREE_VF. After the main shaking events, the foundation settled and the reinforced earth zone moved outward leading to the significant tension cracks that happened at the end of reinforcement materials. As for the settlements of ground surface, they were much smaller than those of embankment. It should be mentioned that the

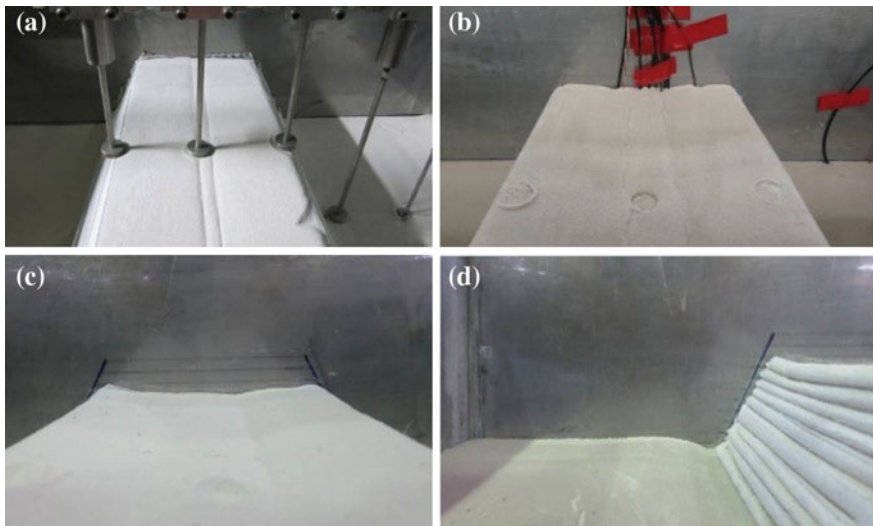


Fig. 9 Tension cracks and deformations of models **a** GREE_D; **b** GREE_W; **c** GREE_VF; **d** settlement of GRE embankment and heaving up of foundation for model GREE_VF

ground surface near the toe heaved up about 0.082 m as shown in Fig. 9d, resulting in the large settlement of GRE embankment after soil liquefaction.

4 Conclusions

Three centrifuge shaking table tests were performed to study the seismic behaviour of GRE embedment on liquefiable and non-liquefiable sand deposits. From the test results, it can be found that the liquefaction was not easy to occur under the GRE embankment, but the deep soil layer away from the GRE embankment would liquefy and the shear wave could not propagate up to the soil completely. Generally, the largest settlement occurred at the centre of GRE embankment. The maximum settlements normalized by the embankment height for the dry (GREE_D), water-saturated non-liquefied (GREE_W) and liquefied (GREE_VF) models after 1 Hz seismic event were about 0.11, 2.78 and 25.18 %, respectively.

Acknowledgments The authors would like to express their gratitude for the financial and technical supports from the National Science Council (NSC 101-2221-E-492-027 and NSC 102-2221-E-008-116). These supports make this study and the future researches possible.

References

Lee CJ, Hung WY, Tsai CH, Chen T, Tu YC, Huang CC (2014) Shear wave velocity measurements and soil–pile system identifications in dynamic centrifuge tests. *Bull Earthq Eng* 12:717–734

Liu H, Wang X, Song E (2011) Reinforcement load and deformation mode of geosynthetic-reinforced soil walls subject to seismic loading during service life. *Geotext Geomembr* 29 (1):1–16

Nova-Roessig L, Sitar N (2006) Centrifuge model studies of the seismic response of reinforced soil slope. *J Geotech Geoenviron Eng* 132(3):388–400

Development of a New In-place Cement-Mixing Method by High-Pressure Injection

Hiroaki Tezuka, Takahiro Yamauchi and Fumio Tatsuoka

Abstract Jet grouting technology is examined and developed as one of soil liquefaction countermeasure methods. The examination of the mechanism of jetting is performed to increase the diameter of stabilized soil columns and also to produce arbitrary shapes of improved soil structures. The in situ performance verification are also performed to verify arbitrary shapes and large diameters of stabilized soil columns, mechanical properties of stabilized soil columns, and real-time construction management.

Keywords Soil liquefaction countermeasure · Jet grouting · Mechanism of jetting · Real-time construction management

1 Introduction

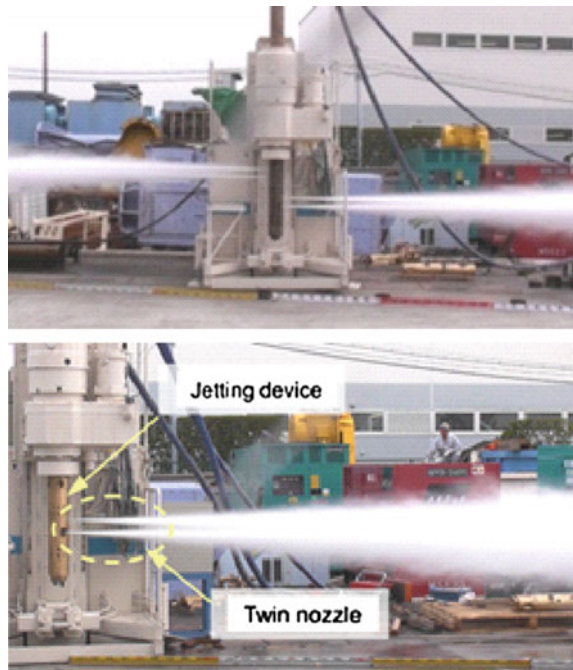
The jet grouting method has been developed to produce mainly cylindrical cement-mixed soil columns by jetting a mixture of cement paste and air into the ground at high pressure and mixing-in-place it with existing soil. Various types of jet grouting using high-pressure jets have been widely used in practice typically to construct temporary earth retaining walls and diaphragm walls in excavation work and to protect launching and arriving shafts for shield tunneling.

H. Tezuka (✉) · T. Yamauchi
Maeda Corporation, 2-10-2, Fujimi, Chiyoda, Tokyo 102-8151, Japan
e-mail: teduka.h@jcity.maeda.co.jp

F. Tatsuoka
Department of Civil Engineering, Tokyo University of Science,
2641, Yamazaki, Noda, Chiba 278-8510, Japan
e-mail: tatsuoka@rs.noda.tus.ac.jp

Soil liquefaction induced by the off the Pacific Coast of Tohoku Earthquake that occurred on March 11, 2011 over a wide area centering around the coastal reclaimed areas caused serious damage to numerous structures, resulting in exorbitant time and cost required for restoration. Needs for stabilizing soils have, therefore, been increasing as a means of preventing soil liquefaction to reinforce existing structures. Against the above background, the soil stabilization technology is required to increase the diameter of stabilized soil columns and to enable the development of stabilized soil columns of an arbitrary shape such as wall, fan or lattice while reducing cost and construction period. The authors developed the multi-jet method as a new variation of jet grouting method using high-pressure jets. This paper presents the results of examination of the mechanism of jetting performed to increase the diameter of stabilized soil columns. This paper also presents the results of in situ performance verification performed to verify (i) arbitrary shapes and large diameters of stabilized soil columns; (ii) mechanical properties of stabilized soil columns; and (iii) real-time construction management. Figure 1 shows water, instead of cement paste, jetted in the air using the multi-jet method.

Fig. 1 Multi-jet method



2 Discussions on Jetting Mechanism Realizing a Large Diameter

2.1 Discussions on an Optimum Pipe Structure

2.1.1 Outline of High-Pressure Water Jetting Tests in the Air

In field full-scale practice, a high-pressure hose from a high-pressure pump is connected to the head of a vertical rod. Cement slurry jetted horizontally from an outlet connected to the top of the rod in the ground is monitored. In ordinary methods, the direction of the jet is changed in the rod from vertical to horizontal using an elbow. Then, turbulent flow occurs in the manner depending on the shape of the elbow. Due to this phenomenon, cement is mixed with soil in a smaller area. To increase the area of cement-mixed soil as much as possible, the structure of the piping is required to minimize the possibility of occurrence of turbulent flow. To examine the above, a series of aerial water jetting tests were then conducted.

Figure 2 outlines these tests. Three types of piping, elbow, bent, and straight were developed, as shown in Fig. 3. Water was jetted in the air and time histories of jet load were obtained by measuring jet pressure with a load cell at a distance of 1.6 m from the nozzle. In case 3, the piping was of a basic structure exhibiting a straight line with no elbows or bents and jets were in a nearly ideal condition. In cases 1 and 2, the outer diameter was set to be less than the rod diameter used in the multi-jet method ($\phi 142$ mm). The test conditions for the aerial jetting tests are listed in Table 1. In all cases, a nozzle was used with a minimum loss of energy based on Shavlovsky (1972).



Fig. 2 Aerial water jetting

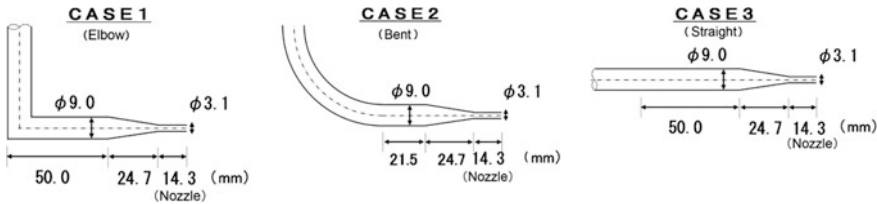


Fig. 3 Piping used in aerial jetting tests

Table 1 Specifications for aerial jetting

| Test case | Amount of injection (l/min) | Injection pressure ^a (MPa) |
|-----------|-----------------------------|---------------------------------------|
| 1 | 222 | 37 |
| 2 | | 35 |
| 3 | | 35 |

^aThe injection pressure was controlled keeping constant the amount of injection

2.1.2 Test Results and Discussions

Jet loads were measured using a load cell, as shown in Fig. 4. In case 1 with an elbow, jet tended to diffuse (Fig. 2), and loads varied greatly and the mean load was small. In case 2 with a bent, on the other hand, jet converged well (Fig. 2), and loads varied little and the mean load was higher. The jet performance was similar to that in case 3, where jets were in a nearly ideal state. It was thus confirmed that jetting performance is improved drastically by adopting a bent instead of an elbow.

2.2 Optimum Amount of Air and Effectiveness of Twin Nozzles

2.2.1 High-Pressure Water Jetting Tests in a Large Water Tank

Shavlovsky (1972) and Technical handbook on grouting (1997) describe that attenuation of water jet by distance is improved by applying air jet along water jet. Underwater water jetting tests were conducted in a large water tank with transparent side walls of acrylic plates to observe jet performance (Fig. 5). By examining the optimum amount of air jet, the effectiveness of twin nozzles was confirmed. The test conditions are listed in Table 2. The amount of compressed air was varied at different steps and air was jetted along water jet. Jet loads were measured using a load cell.

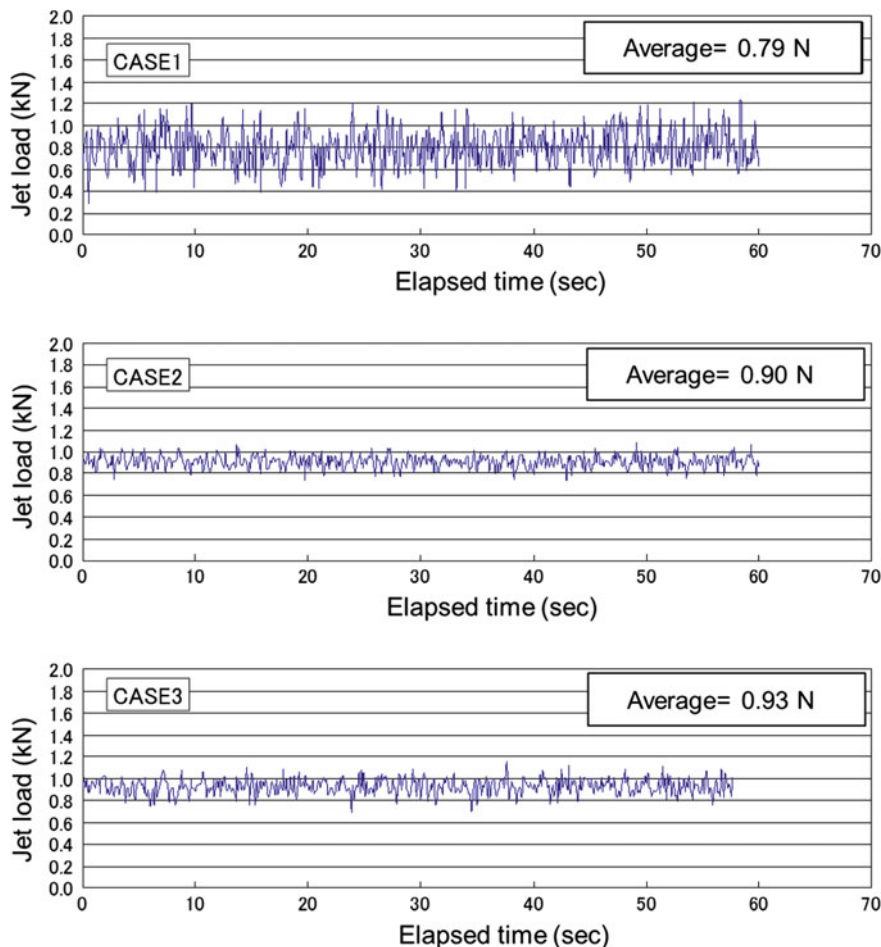


Fig. 4 Time histories of jet load during aerial jetting

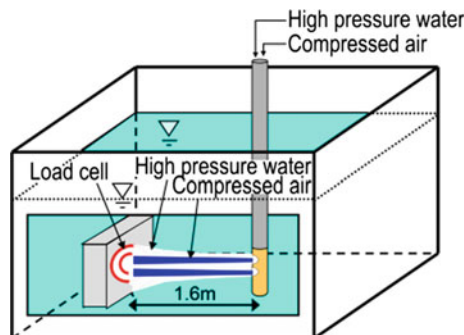


Fig. 5 Underwater jetting test in a large water tank

Table 2 Specifications for underwater jetting tests

| Test case | Amount of injection (l/min) | Injection pressure (MPa) | | Amount of air (Nm ³ /min) | Air pressure (MPa) |
|-----------|-----------------------------|--------------------------|--------|--------------------------------------|--------------------|
| No. 1 | 121 (single nozzle) | 35–40 | 0–10.0 | 0–10.0 | 1.03 |
| No. 2 | 222 (single nozzle) | | | | |
| No. 3 | 222 (twin nozzle) | | | | |

2.2.2 Test Results and Discussions

Test conditions in case 3 are shown in Fig. 6. When only high-pressure water was applied, it traveled over a distance of approximately 1.0 m. Rapid attenuation of energy was confirmed. When only compressed air was applied, it traveled approximately 0.5 m. When both high-pressure water and compressed air were applied, the distance of travel increased drastically to approximately 2.9 m.

Compressed air was varied in three cases and loads were measured using a load cell. Figure 7 shows the relationship between the load measured by the load cell and the amount of compressed air. Figure 8 shows the relationship between the ratio of the load measured by load cell to the load where no compressive air was applied, and the amount of compressed air. As compressed air increased, jet load increased. The maximum jet loads were shown at a compressed air amount of 4.0 through 9.0 Nm³/min. The amount of compressed air at which jet load was at the maximum level was larger as water jet increased.

The total amount of jet was 222 l/min both in Figs. 7 and 8. A comparison was made in cases where one and two nozzles were used for discharge. The maximum jet load and the above ratio were greater when two nozzles were used. It was thus

Fig. 6 Travel distance of jets at different states (case 3)

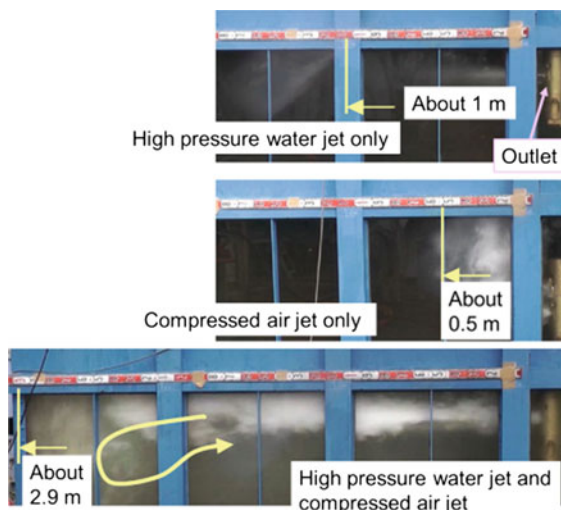


Fig. 7 Relationship between jet load and the amount of compressed air

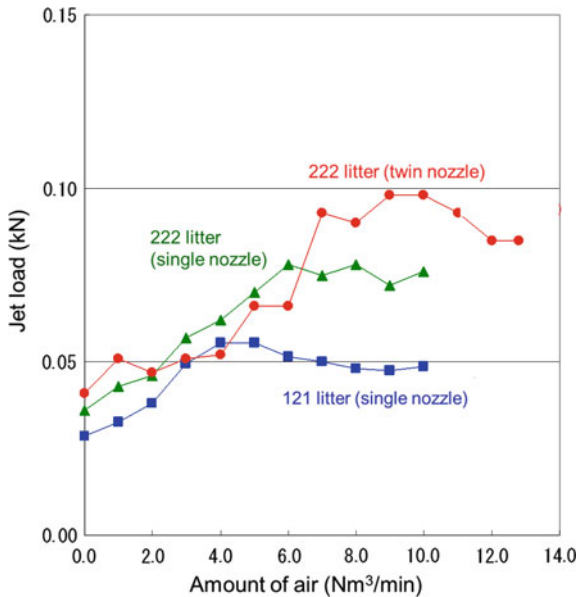
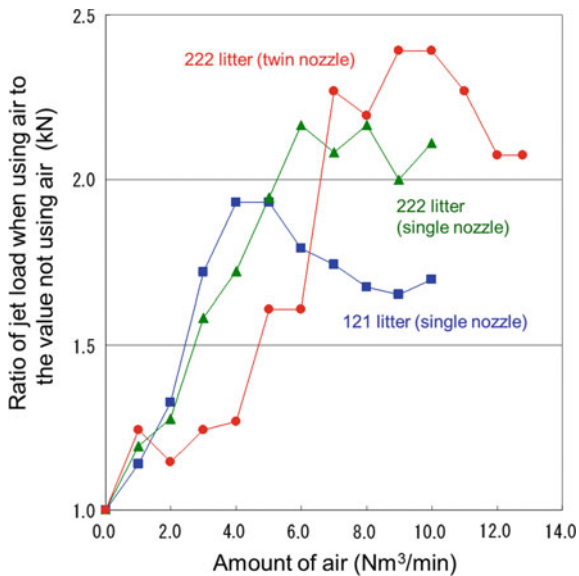


Fig. 8 Normalized relationship between jet load and the amount of compressed air



verified that adopting twin nozzles, twin nozzles was rational for ensuring high efficiency of ground cutting.

3 In Situ Performance Verification Tests

3.1 *Stabilized Soil Columns of an Arbitrary Shape*

Conventional jet grouting methods can produce only cylindrical stabilized soil columns by rotating the dedicated rod in one direction. On the other hand, the multi-jet method can produce stabilized soil columns of an arbitrary shape by controlling the oscillation of the dedicated rod highly accurately in units of 0.1° , as illustrated in Fig. 9. To this end, the dedicated rod has numerous holes to inject cement paste in multiple directions at a high pressure. As a result, this method can produce stabilized soil columns of an arbitrary shape, e.g., wall, fan, or lattice (Fig. 10).

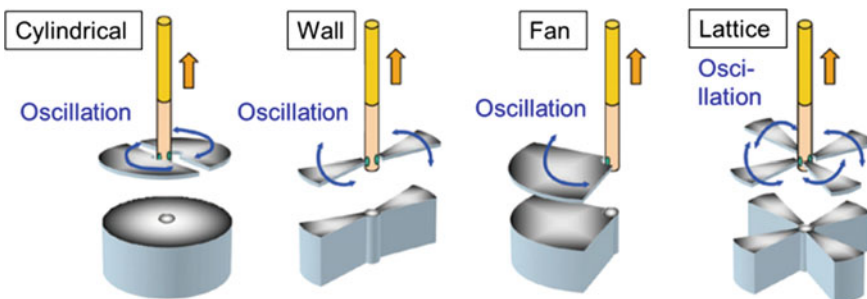
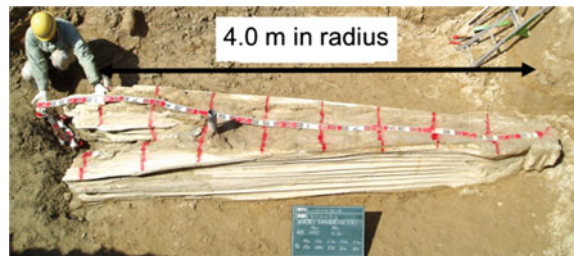


Fig. 9 Schematic views of stabilized soil columns produced in different shapes



Fig. 10 Views of excavated stabilized soil column in in situ performance verification tests

Fig. 11 Typical large-diameter stabilize soil column (radius: 4.0 m)



It was confirmed that large stabilized soil columns with a maximum radius of 4.0 m can be produced by the multi-jet method (Fig. 11), compared to a maximum radius of approximately 5.0 m by conventional stabilized soil columns.

3.2 Controlling the Size of Stabilized Soil Columns

According to the existing literatures (Shavlovsky 1972; Technical handbook on grouting 1997; Yoshida et al. 1990, 1991), the diameter of stabilized soil columns is determined by the energy of jetting E . The diameter of stabilized soil column confirmed by excavating columns in the performance verification tests can be expressed as a function of Q and T , where Q is the flow of jet (l/min) and T is the duration of jetting (min/m) on a 360° scale. An empirical equation to determine the energy of jetting for a specified diameter of stabilized soil column was derived achieving the highest correlation between the diameter and E (Eq. 1) (JCMA 2009).

$$E = Q \times T^{0.3}, \quad (1)$$

In order to take into account the effects of the type and conditions of soil on the relationship between the diameter of stabilized soil column and the energy of jetting E , soils were classified into three classes based on the boundary value of SPT N values for each soil type (Table 3). Figure 12 shows the relationship between the radius of stabilized soil column and the energy of jetting for each soil classification. As a result, it was verified that stabilized soil columns of an arbitrary radius up to 4.0 m could be produced by adjusting the energy of jetting E controlling the flow of jet Q and the duration of jetting T .

Table 3 Soil classifications based on N values

| Soil type | Class 1 | Class 2 | Class 3 |
|---------------|----------|----------------|-----------------|
| Sandy soil | $N < 50$ | $50 < N < 100$ | $100 < N < 150$ |
| Clayey soil | $N < 3$ | $3 < N < 5$ | $5 < N < 7$ |
| Gravelly sand | — | $N < 50$ | $50 < N < 100$ |

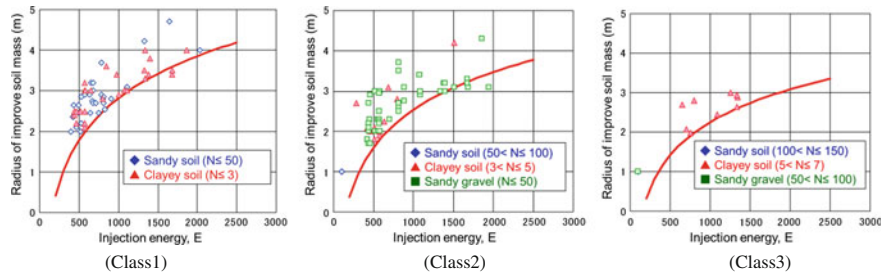


Fig. 12 Relationships between the energy of jetting and the radius of stabilized soil column

3.3 Real-Time Construction Management

3.3.1 Development of a Dedicated Management System

In order to obtain the specified finished shape and quality of stabilized soil columns by the multi-jet method, holes should be drilled and columns should be developed satisfying control standard values in terms of lifting rate of the rod, angle of oscillation, rate of rotation, flow of stabilizers, jet pressure, and amount of air. To this end, a dedicated management system was developed capable of displaying and controlling real time the above control parameters during hole drilling and column development.

3.3.2 Confirmation of the Diameter of Stabilized Soil Column Right After Stabilization Work

In order to visually inspect the size and shape of stabilized soil column right at the end of production procedure when the stabilized soil has not yet been strongly hardened, a video cone with a built-in small camera and an outlet to discharge phenolphthalein solution was developed (Fig. 13).

A video cone was inserted for a given design travel distance right at the periphery of produced stabilized soil column using a cone penetration device (Fig. 14). Then, phenolphthalein solution was discharged at a designated depth. A stabilized soil column, if any, would turn red in reaction of cement to phenolphthalein.

3.3.3 Sampling of Unhardened Stabilized Soil at the End of Stabilizing Procedure

A sampling cone was developed to retrieve unhardened stabilized soil at the end of stabilizing procedure (Fig. 15). Stabilized soil can be retrieved from any depth as

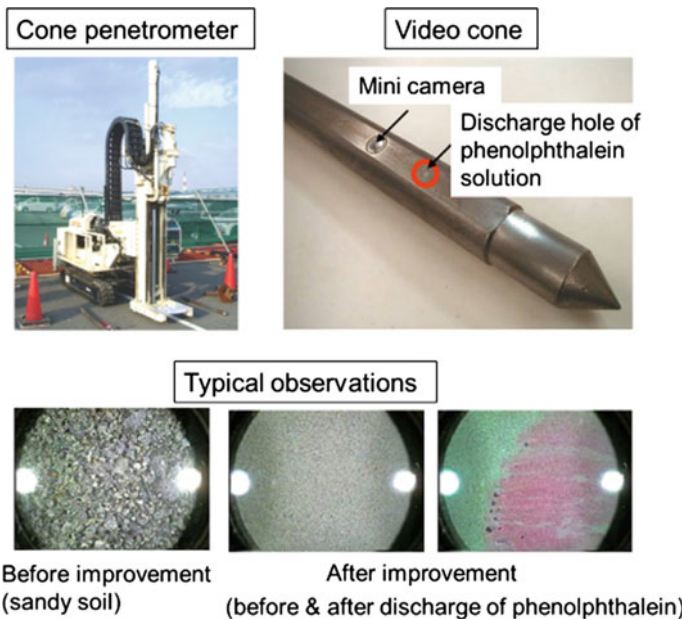


Fig. 13 Outline of video cone and typical views

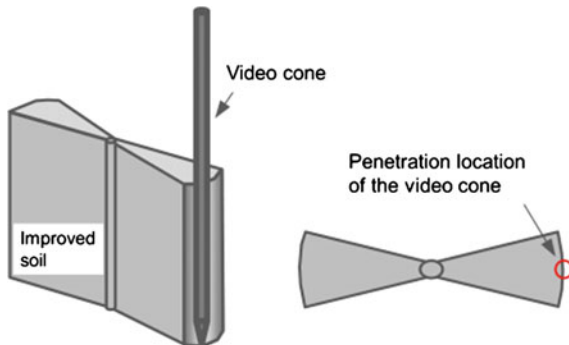


Fig. 14 Location of a video cone inserted in the field

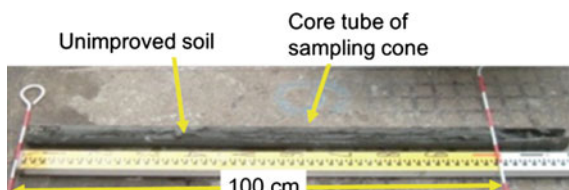


Fig. 15 Sampling cone and typical sampled stabilized soil

long as it has not yet been strongly hardened. The sampled stabilized soil is used for predicting its strength at a curing time of 28 days by using the hydrochloric acid dissolution heat method (JCMA 2009), while referring to an empirical relationship between the strength and the curing time.

3.4 Correlations Between Unconfined Compressive Strength and Elastic Wave Velocity of Stabilized Soil

The relationships between the elastic shear wave velocity V_s by ultrasonic pulse tests and the unconfined compressive strength q_u of specimens prepared in the laboratory and undisturbed core sample retrieved from the field were obtained. Figure 16 shows the relationship for all data. Although there is a certain correlation between V_s and q_u , the scatter is relatively large. The data was therefore classified according to whether the specimen was obtained in the field or produced in laboratory and to the soil type. Figure 17 shows the V_s - q_u relations of clayey and sandy soils and sandy gravel for the specimens produced in the laboratory and the undisturbed core samples retrieved in the field, respectively. The correlations in the classified relations presented in Fig. 17 are noticeably better than the one in Fig. 16. It is particularly the case with the data of the specimen produced in the laboratory (Fig. 17), which due likely to relatively high homogeneity of the specimens. The correlation with the core samples from the field, (Fig. 17) is lower regardless of the site and soil type due likely to an inevitable scatter in the soil properties in the field.

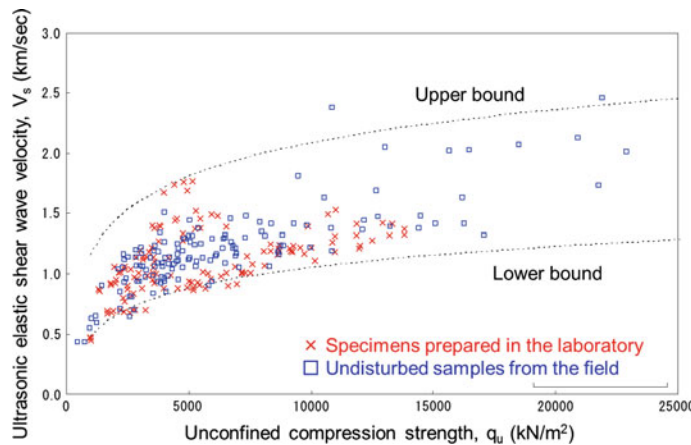


Fig. 16 V_s (ultrasonic pulse test) versus q_u relation (all data)

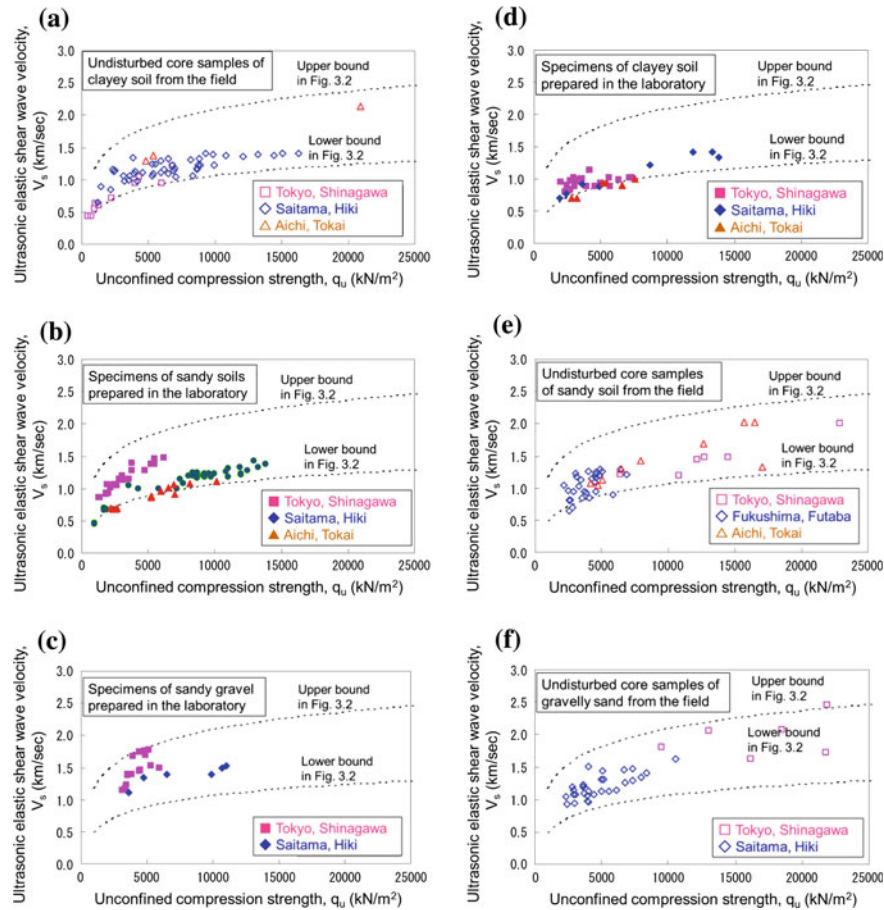


Fig. 17 V_s (ultrasonic pulse test) versus q_u relations (specimens produced in the laboratory and undisturbed core samples from the field). **a** Laboratory mixed sample of clay, **d** filled core sample of clay. **b** Laboratory mixed sample of sand, **e** filled core sample of clay. **c** Laboratory mixed sample of gravel, **f** filled core sample of clay

4 Conclusions

The multi-jet method was developed and has been used in regular construction work particularly to mitigate the damage to existing structure by soil liquefaction since June 2007. This method is characterized by its unique capability of producing stabilized soil columns having an arbitrary shape (not only solid cylindrical shape that can be produced by the conventional jet grouting methods) and a large size (up to a radius of 4 m). These features make this method more cost effective in many applications. This method was used at 36 sites as of June 2014 mainly for seismic damage mitigation. The research on this method is being performed to make this soil stabilization method more rational and reliable.

References

Japan Construction Mechanization Association (2009) Multi-jet method (arbitrary-shape, large-diameter jet grouting using high-pressure jets). Construction technology certification report (in Japanese)

Shavlovsky DS (1972) Proceedings of the 1st international symposium. Jet Cutting Technology, BHRA

Technical handbook on grouting (1997) Editorial committee on the latest technical handbook on grouting, pp 695–722

Tezuka H, Yamauchi T, Yasui T (2013a) Development of new high pressure injection mixing methods. *Geotech Eng J* 8(2):179–195, JGS (in Japanese)

Tezuka H, Yamauchi T, Kawanishi A (2013b) Development of quality management for high pressure injection mixing methods. *Geotech Eng J* 8(2):251–263, JGS (in Japanese)

Yoshida H, Kubo H, Jimbo T, Sakakibara M (1990) Development of large-diameter soil stabilization method (Part 1): effects of pressure and flow during water jet cutting. In: Proceedings of 25th annual conference on geotechnical engineering, pp 1917–1918, JGS (in Japanese)

Yoshida H, Asano R, Jimbo T, Sakakibara M (1991) Development of large-diameter soil stabilization method (Part 2): effects of the rate of nozzle movement and the number of cycles during water jet cutting. In: Proceedings of 26th annual conference on geotechnical engineering, pp 1923–1924, JGS (in Japanese)

Use of Swedish Weight Sounding Tests for Detecting Liquefiable Backfills Reclaimed in Iron Sand Mining Pits in Asahi City of Chiba in Japan

Yoshimichi Tsukamoto, Shohei Kawabe and Shigeru Kanemitsu

Abstract Following the 2011 Great East Japan Earthquake and its aftershocks, soil liquefaction and associated phenomena have been observed in various regions on Kanto plain, including Asahi city in Chiba Prefecture, where hundreds of private houses were damaged due to ground failures mainly associated with subsurface soil liquefaction. In the present study, a series of Swedish weight sounding (SWS) tests were carried out at a dozen of sites in Asahi city. It was found that soil liquefaction occurred mainly at areas corresponding to the soil deposits filled back into iron sand mining pits, which had been extensively carried out during the period starting in 1910s and mainly from 1950s to 1970s. The Swedish penetration resistance was found relatively low in the reclaimed deposits and to increase rapidly when it touched upon the underlying natural deposits at the bottom of the reclaimed deposits. With a help of such typical depth-wise profiles, the depth of reclamation is estimated at each location in Asahi city. The soil liquefaction triggering is then discussed with a help of factors of safety against soil liquefaction estimated from SWS test results.

Keywords Swedish weight sounding test · Soil liquefaction · 2011 Great East Japan Earthquake

Y. Tsukamoto (✉) · S. Kanemitsu
Department of Civil Engineering, Tokyo University of Science,
2641, Yamazaki, Noda, Chiba 278-8510, Japan
e-mail: ytsoil@rs.noda.tus.ac.jp

S. Kawabe
National Agriculture and Food Research Organization,
Tsukuba, Ibaraki 305-8609, Japan
e-mail: skawabe@affrc.go.jp

1 Introduction

Following the 2011 Great East Japan Earthquake and its aftershocks, soil liquefaction and associated phenomena have been observed in various regions on Kanto plain, including some areas located along the lower stream of Tonegawa river, (Kanemitsu et al. 2013; Kawabe et al. 2012; Tsukamoto et al. 2012a, b, c). In Asahi city of Chiba Prefecture as shown in Fig. 1, hundreds of private houses were damaged due to ground failures mainly associated with subsurface soil liquefaction. It is typical to see in Fig. 1 that Asahi city consists of lowlands and uplands, and such collapses of residential houses were distributed around lowland areas close to the boundary of lowlands and uplands as well as some areas in the midst of lowlands. It is known that some of the areas in Asahi city had been designated for iron sand mining. Iron sand mining had started in 1910s and had been extensively carried out during the period from 1950s to 1970s around this area in Chiba, where soils had been excavated from designated mining pits, iron sands had been retrieved, and the remaining surplus soils had been filled back into the original mining pits.

In the present study, a series of Swedish weight sounding (SWS) tests were carried out at a dozen of sites in Asahi city to examine whether soil liquefaction should have in fact occurred at the areas corresponding to the soil deposits which had been filled back into iron sand mining pits.

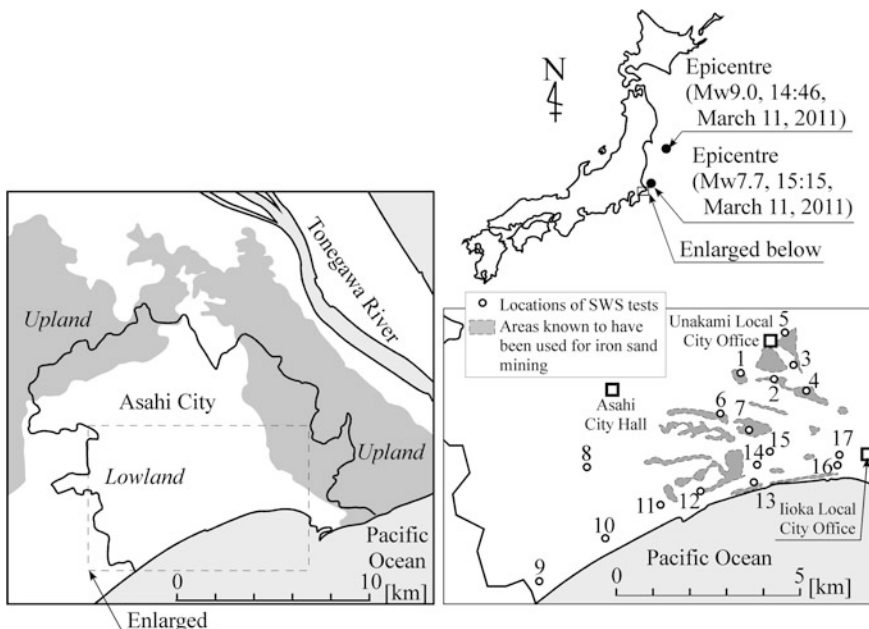


Fig. 1 Location

2 Swedish Weight Sounding Tests

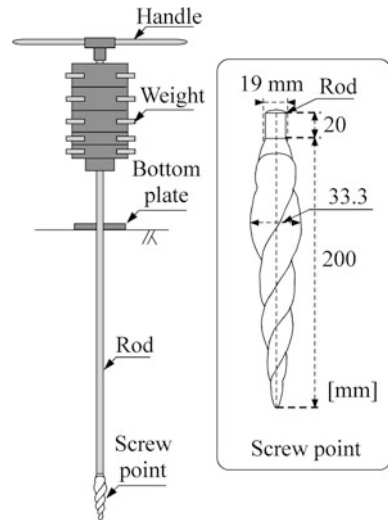
SWS tests were conducted at 17 sites on May 10–12 and May 18 and 19, 2013, as summarized in Table 1. The locations of SWS tests are shown in Fig. 1. In Fig. 1, the areas that have been used for iron sand mining are also shown, which can be traced from the history of old Iioka town. Since the current Asahi city was formed from old Asahi, Unakami, Iioka, and Higata towns, and the appropriate books for history of the other towns are not available, the areas used for iron sand mining in the other old towns are not known and not traced herein.

SWS tests are frequently used for earthquake reconnaissance. The testing equipment is portable as shown in Fig. 2. The testing procedure is robust and the interpretation of test results is described by Tsukamoto et al. (2004). The testing procedure basically consists of two phases, static penetration, and rotational penetration. In the phase of static penetration, the depth of static penetration is measured and the total weight is denoted as W_{sw} (kN). When static penetration is

Table 1 Summary of SWS test results

| District | Location no. | Results of interview to local residents | Average of SPT N -values converted from SWS penetration resistance (range of depth) (m) | Depth estimated as bottom of backfill (m) |
|----------|--------------|---|---|---|
| A | 1 | – | 11.1 (0–5.4) | 5.5 |
| | 2 | Backfill of iron sand mining pit | 8.5 (0–5.1) | 5 |
| | 3 | Backfill of iron sand mining pit | 5.1 (0–6.4) | 6.5 |
| | 4 | – | 9.5 (0–5.4) | 5.5 |
| | 5 | – | 7.1 (0–7.1) | 7 |
| B | 6 | – | 7.0 (0–4.1) | 4 |
| | 7 | – | 11.3 (0–4.9) | 5 |
| C | 8 | – | 3.5 (0–2.1) | – |
| D | 9 | – | 11.4 (0–3.4) | 3.5 |
| E | 10 | – | 13.6 (0–4.9) | 5 |
| F | 11 | – | 5.1 (0–4.1) | 4 |
| | 12 | Backfill of iron sand mining pit | 12.0 (0–3.1) | 3 |
| G | 13 | – | 5.9 (0–4.9) | 5 |
| | 14 | – | 5.9 (0–4.6) | 4.5 |
| | 15 | – | 11.1 (0–4.4) | 4.5 |
| H | 16 | – | 5.2 (0–3.0) | 3.5 |
| | 17 | – | 7.4 (0–3.6) | 3.5 |

Fig. 2 Swedish weight sounding test



ceased, the rotational penetration is performed. The number of half a turn necessary to penetrate the rod through 25 cm is denoted as N_a , which is converted to the number of half a turn per meter, N_{sw} (ht/m). SWS tests are found excellent in detecting thin weak soil layers, though it is not possible to determine precisely a depth of a groundwater level and types of soils underneath a ground surface. In the present study, the depth of a groundwater level was estimated by observing the boundary of wet and dry portions of the rods during extraction of the penetrated rods.

3 Estimating Depths of Reclamation

From the interview to local residents, it was confirmed that the locations of No. 2, 3 and 12 in fact correspond to the reclaimed deposits which had been filled back into iron sand mining pits. The results of SWS tests conducted at these three locations are shown in Figs. 3, 4 and 5. The values of W_{sw} and N_{sw} can be converted to SPT N -values by using the following empirical equation proposed by Tsukamoto et al. (2004),

$$N = \frac{\sqrt{e_{\max} - e_{\min}}}{10} (N_{sw} + 40 W_{sw}), \quad (1)$$

where W_{sw} ranges from 0 to 1 in kN under static penetration, and takes a value of 1 under rotational penetration. Herein, from the geotechnical data locally available,

Fig. 3 Plots of W_{sw} and N_{sw} and converted SPT N -value against depth (Location No. 2)

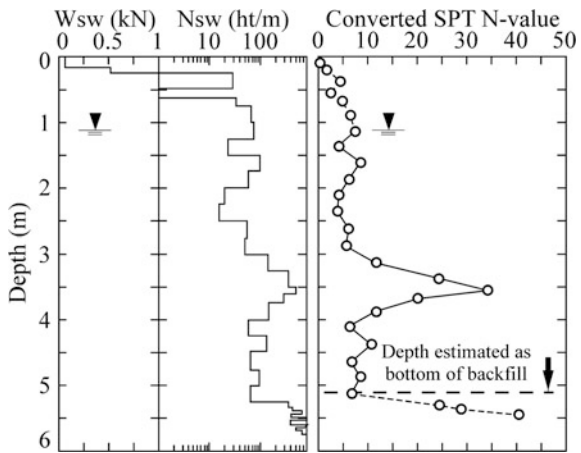
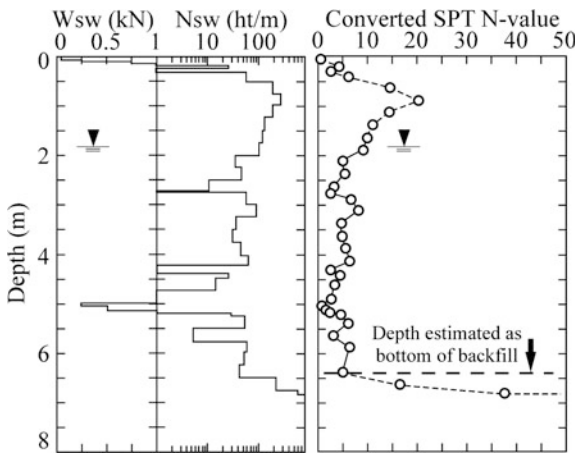


Fig. 4 Plots of W_{sw} and N_{sw} and converted SPT N -value against depth (Location No. 3)



the soil materials used for reclamation into iron sand mining pits typically have a fines content of less than $F_c = 5\%$, a mean particle diameter of $D_{50} = 0.2$ mm, and a soil particle density of around $\rho_s = 3$ g/cm³ due to its significant content of iron. The value of $e_{max} - e_{min}$ is therefore assumed to be 0.4 in the present study. The depth-wise profiles of SPT N -values thus converted at the locations of No. 2, 3 and 12 are also shown in Figs. 3, 4 and 5. It is found in all of the test results at these three locations that the converted SPT N -values are relatively low in the reclaimed deposits and begin to increase rapidly when touching upon the underlying natural deposits at the bottom of the reclaimed deposits. With a help of such typical depth-wise profiles, the depth of reclamation can be determined at each location, as shown in Figs. 3, 4 and 5. It is therefore worthwhile to examine whether such

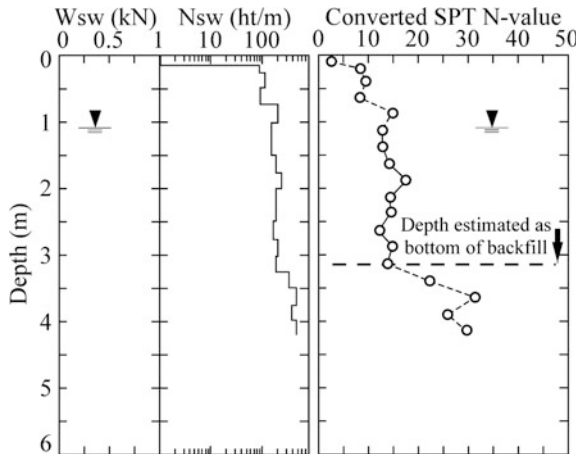


Fig. 5 Plots of W_{sw} and N_{sw} and converted SPT N -value against depth (Location No. 12)

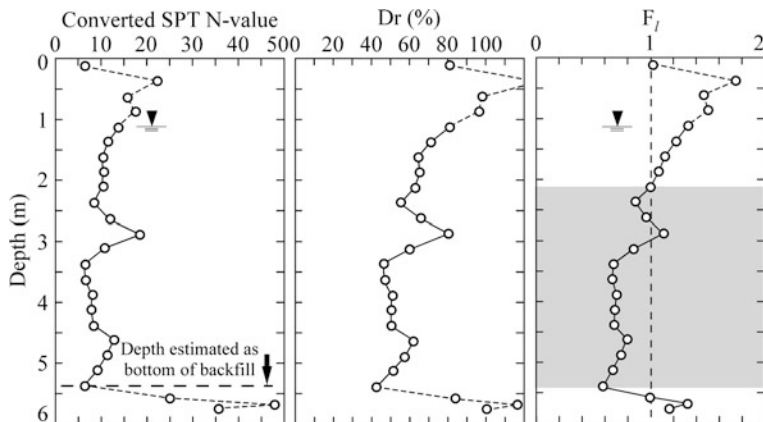


Fig. 6 Plots of converted SPT N -value, relative density Dr and factor of safety against liquefaction F_l against depth (Location No. 1)

typical depth-wise profiles can be obtained at other locations, and the depths of reclamation can also be estimated. The plots of converted SPT N -values against depth at the locations of No. 1, 6, 10, 13, and 16 are shown in Figs. 6, 7, 8, 9 and 10. These depth-wise profiles of converted SPT N -values would suggest that all of the locations except for No. 8 correspond to the reclaimed deposits filled back into iron sand mining pits and the depths of reclamation can be estimated accordingly, as summarized in Table 1.

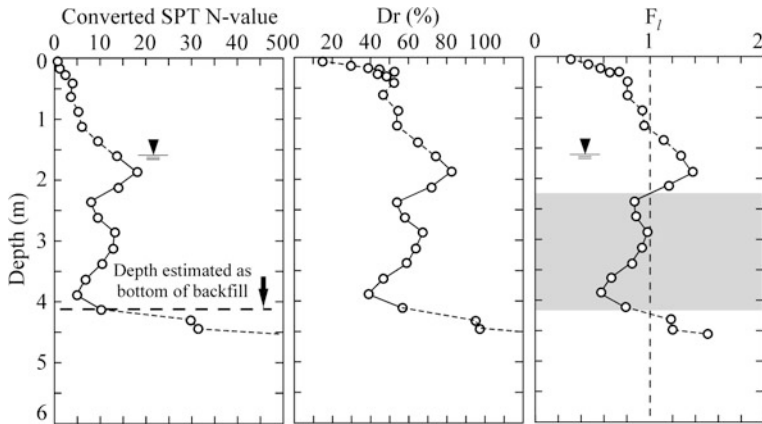


Fig. 7 Plots of converted SPT N -value, relative density D_r and factor of safety against liquefaction F_l against depth (Location No. 6)

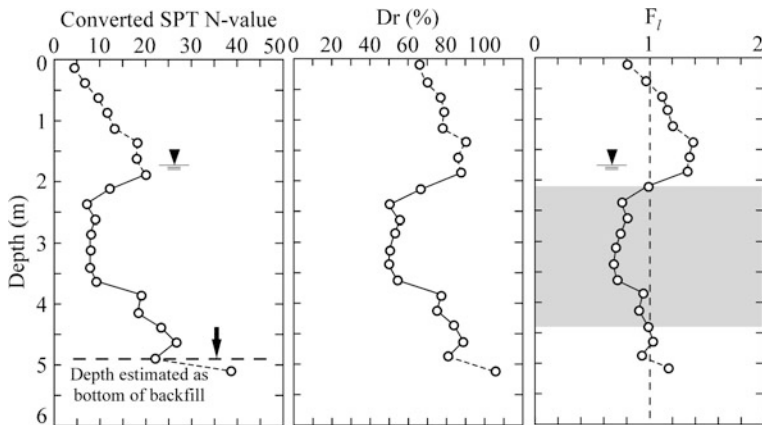


Fig. 8 Plots of converted SPT N -value, relative density D_r and factor of safety against liquefaction F_l against depth (Location No. 10)

4 Evaluating Soil Liquefaction Triggering

It is then important to examine the soil liquefaction triggering can also be evaluated based on the observed field data of SWS tests. Herein, the relative density D_r can be estimated from the values of W_{sw} and N_{sw} by using the following empirical equation proposed by Tsukamoto et al. (2004),

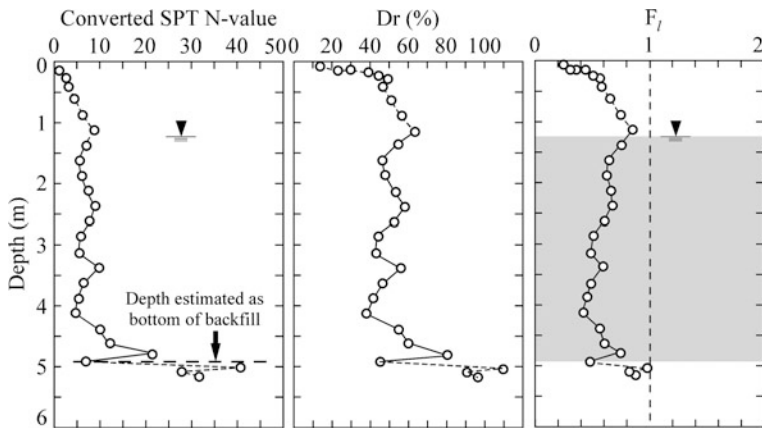


Fig. 9 Plots of converted SPT N -value, relative density D_r and factor of safety against liquefaction F_l against depth (Location No. 13)

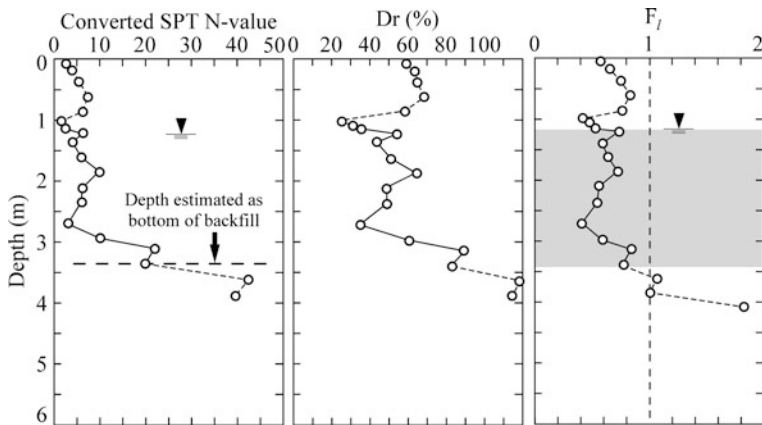


Fig. 10 Plots of converted SPT N -value, relative density D_r and factor of safety against liquefaction F_l against depth (Location No. 16)

$$D_r = \sqrt{\frac{(N_{sw} + 40 W_{sw}) (e_{max} - e_{min})^{2.2}}{90}} \sqrt{\frac{98}{\sigma'_v}} \quad (2)$$

Since the depth-wise profiles of SPT N -values are estimated and the mean particle diameter of $D_{50} = 0.2$ mm is available, the empirical formulae proposed by Tatsuoka et al. (1980) can be used for evaluating the liquefaction resistance of soil, which is then converted into the maximum shear strength ratio of soil, $\tau_{max,l}/\sigma'_v$, as employed in the usual practice, (Ishihara 1996). Herein, in order to take into account the effects of long-lasting shaking of the main shock measuring $M = 9$ as well as its

Table 2 Summary of local seismograph data

| District | Location no. | Location of local seismograph closest | Maximum ground surface accelerations observed |
|----------|------------------|---------------------------------------|---|
| A | 1, 2, 3, 4 and 5 | Unakami local city office | 147 gal (Main shock, EW) 159 gal (Main shock, NS) <i>206 gal (Aftershock, EW)</i> 174 gal (Aftershock, NS) |
| B | 6 and 7 | | |
| C | 8 | Asahi city hall | 153 gal (Main shock, EW) 157 gal (Main shock, NS) 204 gal (Aftershock, EW) <i>221 gal (Aftershock, NS)</i> |
| D | 9 | | |
| E | 10 | | |
| F | 11 | | |
| | 12 | | |
| G | 13, 14 and 15 | Iioka local city office | 206 gal (Main shock, EW) 203 gal (Main shock, NS) 211 gal (Aftershock, EW) <i>265 gal (Aftershock, NS)</i> |
| H | 16 and 17 | | |

aftershock observed about 30 min after the main shock, as shown in Fig. 1, it would be appropriate to introduce the earthquake magnitude scaling factor (MSF) to obtain the reasonable value of maximum shear strength ratio of soil, (Idriss and Boulanger 2008). In the present study, the value of MSF = 0.7 is assumed and the corresponding maximum shear strength ratio of soil is determined by multiplying with MSF = 0.7. From the records of the ground surface accelerations obtained in Asahi city as summarized in Table 2, the seismograph station closest to each location can be determined, and the corresponding maximum ground surface acceleration of either North–South or East–West component observed during either the main shock or aftershock can be determined, which are denoted in italic in Table 2. It is known that those stations have not experienced soil liquefaction during the earthquakes concerned. The depth-wise profile of the maximum shear stress ratio, τ_{\max}/σ'_v , can then be estimated, (Ishihara 1996). Since the factor of safety against liquefaction is defined as $F_l = (\tau_{\max,l}/\sigma'_v)/(\tau_{\max}/\sigma'_v)$, the depth-wise profile of factors of safety against liquefaction F_l can eventually be obtained.

The depth-wise profiles of the relative density D_r and factor of safety against liquefaction F_l thus estimated are shown in Figs. 6, 7, 8, 9 and 10. It is found that the deposits reclaimed into iron sand mining pits would have been responsible for soil liquefaction triggering.

5 Conclusions

From the results of SWS tests carried out at 17 sites in Asahi city, soil liquefaction was found to occur mainly at areas corresponding to deposits reclaimed in iron sand mining pits, which had been extensively carried out during the period starting in 1910s and mainly from 1950s to 1970s. From the depth-wise profiles of SPT N -

values converted from Swedish penetration resistance, the depth of reclamation at each location was estimated. From the depth-wise profiles of factors of safety against liquefaction, the deposits reclaimed in iron sand mining pits were responsible for soil liquefaction triggering.

Acknowledgments The authors are grateful to the continuous supports from Professors K. Ishihara and A. Onoue. Thanks are also extended to Mr. M. Namikawa of Asahi city and Mr. F. Kudo of Pacific Consultants for their cooperation in conducting SWS tests in Asahi city. The information on the history of old Iioka town and the seismograph data was obtained with a help of Mr. M. Namikawa and Mr. F. Kudo. The SWS tests described in the present study were conducted with a help of students of Tokyo university of Science, S. Hagiwara, N. Fuki, S. Onitsuka, Y. Takekawa and E. Matsuyama. The authors are grateful to their cooperation.

References

Idriss IM, Boulanger RW (2008) Soil liquefaction during earthquakes. Earthquake Engineering Research Institute, USA

Ishihara K (1996) Soil behaviour in earthquake geotechnics., The Oxford engineering science seriesClarendon Press, Oxford

Kanemitsu S, Tsukamoto Y, Kawabe S (2013) Liquefaction-induced ground deformation observed at Gohno-ike pond in Kamisu city during 2011 Great East Japan Earthquake. In: 10th international conference on Urban Earthquake Engineering, 1–2 Mar 2013, Tokyo Institute of Technology, Tokyo, Japan, Paper ID 20-415, pp 455–458

Kawabe S, Tsukamoto Y, Kokusho T, Takahashi R (2012) Soil liquefaction observed at Katori City located along the lower stream of Tonegawa River during 2011 Great East Japan Earthquake. In: Proceedings of international symposium on engineering lessons learned from the Giant Earthquake, One Year after the 2011 Great East Japan Earthquake, 1–4 Mar 2012, Kenchiku-kaikan, Tokyo, Japan, CD

Tatsuoka F, Iwasaki T, Tokida K et al (1980) Standard penetration tests and soil liquefaction potential evaluation. *Soils Found* 20(4):95–111

Tsukamoto Y, Ishihara K, Sawada S (2004) Correlation between penetration resistance of Swedish weight sounding tests and SPT blow counts in sandy soils. *Soils Found* 44(3):13–24

Tsukamoto Y, Kawabe S, Kokusho T, Araki K (2012a) Soil liquefaction observed at areas located along the lower stream of Tonegawa River during 2011 Great East Japan Earthquake. In: Proceedings of international symposium on engineering lessons learned from the Giant Earthquake, One Year after the 2011 Great East Japan Earthquake, 1–4 Mar 2012, Kenchiku-kaikan, Tokyo, Japan, CD

Tsukamoto Y, Kawabe S, Kokusho T, Araki K (2012b) Observed performance and estimated soil profiles of reclaimed and natural deposits at Kamisu City during 2011 Great East Japan Earthquake. In: Joint conference proceedings, 9th international conference on Urban Earthquake Engineering/ 4th Asia Conference on Earthquake Engineering 6–8 Mar 2012, Tokyo Institute of Technology, Tokyo, Japan, Paper ID 02-285, pp 143–146

Tsukamoto Y, Kawabe S, Kokusho T (2012c) Soil liquefaction observed at the lower stream of Tonegawa river during the 2011 off the Pacific Coast of Tohoku Earthquake. *Soils and Foundations*, vol 52, Issue 5, Special Issue on Geotechnical Aspects of the 2011 off the Pacific Coast of Tohoku Earthquake, pp 987–999

GIS-Based Study on Liquefaction-Induced Soil Subsidence in the Urayasu Area Due to the 2011 off the Pacific Coast of Tohoku Earthquake

Rama Mohan Pokhrel and Takashi Kiyota

Abstract Soil liquefaction is one of the geotechnical-related effects of earthquakes especially in cities built on young alluvial deposits and reclaimed land. Geotechnical problems associated with liquefaction in these areas include ground subsidence. Therefore, a detailed study on the occurrence and extent of ground subsidence after severe liquefaction following an earthquake is essential in such an area. Urayasu City in the Tokyo Bay area, Japan was selected as the study area. This area is a young reclaimed land where severe liquefaction occurred following the 2011 off the Pacific Coast of Tohoku Earthquake ($M = 9.0$). Twenty-three borehole locations were selected for the study of liquefaction potential and a geostatistical method of interpolation was applied to attain a spatial variation of liquefaction potential within the area. The ground subsidence was estimated by using airborne Light Detection and Ranging (LiDAR) images before (2006) and after (2011) the earthquake, giving the spatial distribution of soil subsidence. The liquefaction potential and ground subsidence were determined using a P_L distribution map and ground subsidence map, respectively. By studying these maps, the relationship between liquefaction potential and ground subsidence was developed. The relationship shows that high ground subsidence is observed in the area with high liquefaction potential.

Keywords Liquefaction • Soil subsidence • Urayasu • Reclaimed land • GIS

R.M. Pokhrel (✉) · T. Kiyota
Institute of Industrial Science, The University of Tokyo,
4-6-1, Komaba, Meguro-ku, Tokyo 153-8505, Japan
e-mail: pokhrelmohan@gmail.com

T. Kiyota
e-mail: kiyota@iis.u-tokyo.ac.jp

1 Introduction

Soil liquefaction is one of the most serious geotechnical issues related to earthquakes that may induce severe ground subsidence, especially in the young alluvial deposit or reclaimed land. For example, Urayasu City in Chiba Prefecture, Japan, which is geologically composed of newly reclaimed land, suffered severe liquefaction at the time of the 2011 off the Pacific Coast of Tohoku Earthquake ($M = 9.0$). The reclamations in Urayasu City area were completed between 1966 and 1985 (Yasuda et al. 2012). Soil dredged from the bottom of the sea was filled to approximately sea level height in the reclamation area and the filled surface was covered with hill sand from the Boso Peninsula (Yasuda et al. 2012). Therefore, the soil in the Urayasu reclaimed land area is prone to liquefaction. The 2011 earthquake caused tilting of houses, buckling of roads and lifelines cut-off, which were associated with ground subsidence. Extensive sand boiling was observed in this area (Fig. 1), in which the amount of ground subsidence seems directly associated with the amount of boiled sand. In this paper, a detailed study is presented for evaluating the potential and severity of liquefaction-induced ground subsidence. In particular, the variation of ground subsidence with liquefaction potential is studied for the case of Urayasu city. To do so, 23 boreholes (Urayasu City 2012) shown in Fig. 2, were selected and a geostatistical method of interpolation was applied to attain a map spatial variation of liquefaction potential within the area. A kriging method of interpolation in a Geographic Information System (GIS) platform was used to evaluate the spatial distribution of liquefaction potential in the area. This



Fig. 1 Boiled sand during off the Pacific Coast of Tohoku earthquake March 2011 in the Urayasu area

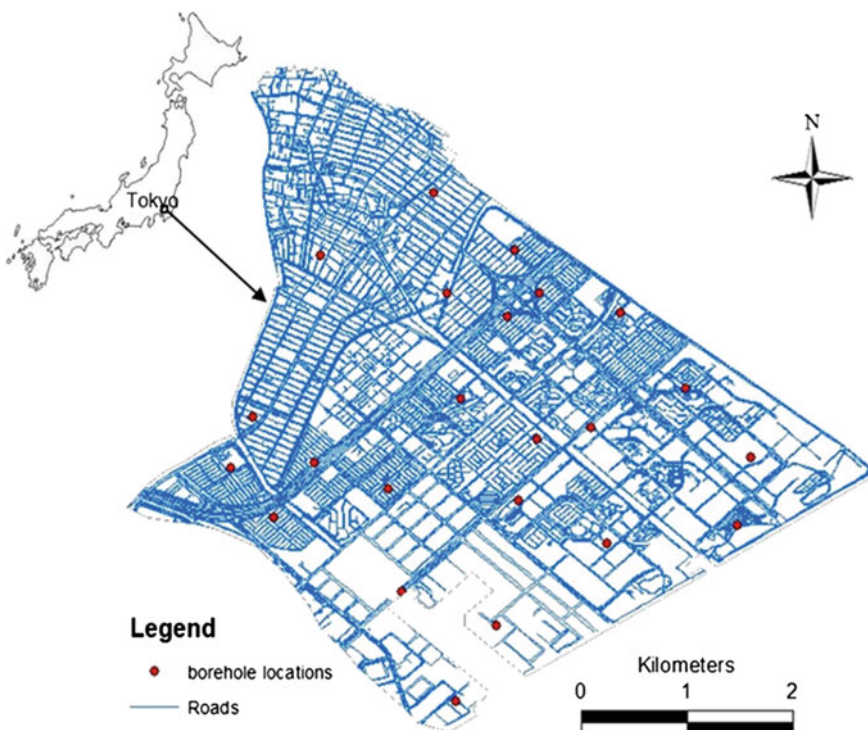


Fig. 2 Location of study area with borehole points used in this study (Urayasu City 2012)

method gives the liquefaction potential value at each point. Similarly, ground subsidence was estimated by using airborne Light Detection and Ranging (LiDAR) images before and after the earthquake (Konagai et al. 2013). This map gives the spatial distribution of soil subsidence. By studying these maps, the relationship between liquefaction potential and ground subsidence was investigated.

2 Liquefaction Potential Distribution Map

Data from 23 boreholes (Fig. 2) were used for this study. Firstly, the liquefaction potential at each borehole location was quantified by introducing the liquefaction potential index (P_L) (Iwasaki et al. 1978, 1982). Second, the liquefaction potential for the whole area was estimated by interpolating P_L values obtained for the 23 boreholes. The kriging method of interpolation considers both the distance and the degree of variation among known data points and estimates values in unknown areas (Pokhrel et al. 2012, 2013). In kriging, the first step is to examine the data in order to identify the spatial structure, which is often represented by the empirical

semivariogram (Isaaks and Srivastava 1989). In this technique, optimal, unbiased estimates of regionalized variables are made at unsampled locations using the structural properties of the semivariogram and the initial set of data values (David 1977).

A semivariogram is a relationship graph between semivariance and the distance between all the pairs of available data points, as schematically illustrated in Fig. 3. The experimental semivariance for liquefaction potential is calculated using Eq. (1).

$$\gamma(h) = \frac{1}{2N(h)} \sum_{i=1}^{N(h)} (P_L(i) - P_L(i, h))^2 \quad (1)$$

where $\gamma(h)$ is the estimated value of the semivariance for a distance of h ; $N(h)$ is the number of paired data points at a distance of h ; and $(P_L(i) - P_L(i, h))$ is the difference in P_L of i th paired locations whose distance is h .

The experimental variogram was developed based on the liquefaction potential values evaluated from the data of each sampled borehole. It gives the degree of relationship between points on the surface. This empirical variogram was fitted to the theoretical variogram function to model the spatial autocorrelation curve, as shown in Fig. 3. It quantifies a basic principle: things that are closer together are more alike than things that are farther apart. Thus, pairs of locations that are closer together (far left of the x -axis of the semivariogram curve) should have lower values on the y -axis of the semivariogram curve. As pairs of locations become farther apart (moving to the right on the x -axis of the semivariogram curve), they should become more dissimilar and have a higher squared difference (and move up on the y -axis of the semivariogram curve).

The next step in the kriging method is to compute the weights from the model variogram. These weights are used as inputs in Eq. (2) to evaluate the liquefaction potential at any location in the study area.

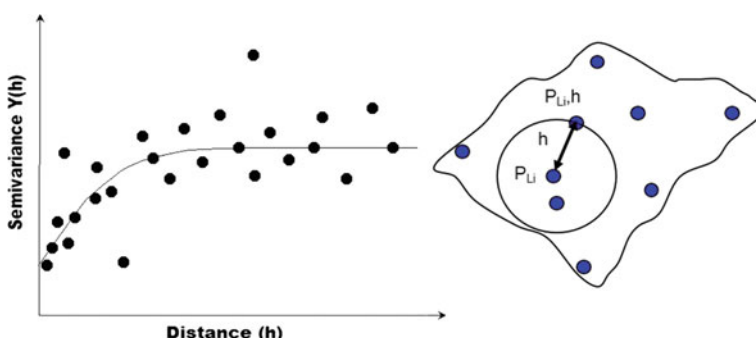


Fig. 3 Kriging variogram curve

$$P_L(x, y) = \sum_{i=1}^n \lambda_i(x_i, y_i) P_L(i) \quad (2)$$

where $P_L(x, y)$ is P_L at (x, y) estimated by interpolation; $P_L(i)$ is the evaluated P_L value at the i th location; $\lambda_i(x_i, y_i)$ is the weight for $P_L(i)$ used to estimate $P_L(x, y)$; and n is the number of locations used for the kriging interpolation.

In kriging, weights are based not only on the distance between the measured points and the prediction location but also on the overall spatial relationships (the model variogram, Fig. 3) among the measured values surrounding the prediction location. The principle of kriging interpolation is to make unbiased estimates of $P_L(x, y)$. For this condition, $\sum_{i=1}^n \lambda_i(x_i, y_i) = 1$. By using the above-explained methodology the spatial variation of P_L for the Urayasu area is prepared and shown in Fig. 7.

3 Ground Subsidence Map and Detection of Soil Subsidence Value

As mentioned previously, this study focused on the relationship between P_L and ground subsidence in the reclaimed area. Konagai et al. (2013) obtained elevation data (subsidence map) for Urayasu city by analysing LiDAR images before (2006) and after (2011) the off the Pacific Coast of Tohoku Earthquake. The same map is used in this study as a ground subsidence map. A LiDAR system is capable of rapid and accurate collection of topographic and elevation data. The high-resolution Digital Surface Models (DSM) were displayed as raster graphic images of pixels containing information of their elevations. The spatial resolution of the data taken by the LiDAR survey was 0.792 points per square metre for the 2006 survey and 4.089 points per square metre for the 2011 survey (Konagai et al. 2013). The elevation value taken at each point from the Digital Surface Model (DSM) data of 2011 was subtracted from the elevation value from 2006 at each of the corresponding points.

Figure 4 represents a characteristic soil subsidence map obtained in the Urayasu city area (Konagai et al. 2013). The colour intensity represents the amount of change in elevation. The intensity increases from light blue to dark blue representing the increase in the amount of lowering (subsidence) and from light yellow to dark yellow representing the increase in upliftment (heave) of the surface. In this analysis the maximum possible change in elevation due to liquefaction is considered as 70 cm; therefore; 70 cm is a threshold value for the map. The value having change in elevation greater than 70 cm is plotted as no value in the map (plotted as a white colour). To estimate ground subsidence at a specific point, the required area was zoomed out as an area X in Fig. 4. A line was drawn (A–B) representing a length of 55 m. A profile (Fig. 5) along line A–B shows the change in elevation at each point along the line. In Fig. 5, it is observed that the maximum subsidence

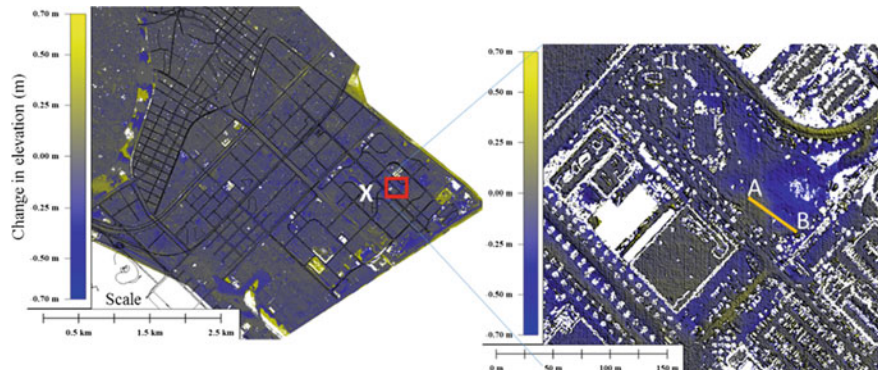


Fig. 4 Ground subsidence map of Urayasu area (Konagai et al. 2013)

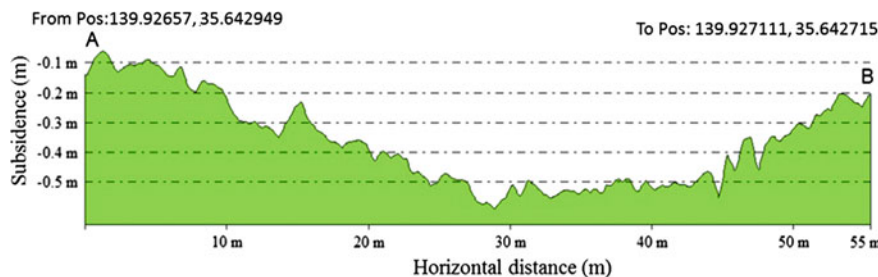


Fig. 5 Ground subsidence along *line A-B* shown in Fig. 4

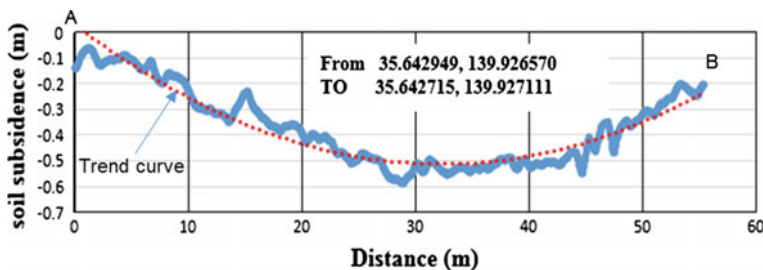


Fig. 6 Ground subsidence and trend *curve* along A-B

value is about 60 cm and the minimum subsidence value is 5 cm. However, it is difficult to accurately evaluate the maximum subsidence value in such types of curves. Therefore, to identify the nature of subsidence in a particular section a trend line was drawn, as shown in Fig. 6. The maximum subsidence point on that trend curve is then taken as the maximum subsidence value of this particular section.

From Fig. 6, it can be concluded that the maximum subsidence value of the section is 50 cm.

In order to minimise the effects of temporary obstacles like cars, buses, trees and some new buildings, etc., the minimum length for the section line should be 50 m or more. To avoid possible error in the measurement of ground subsidence in this study due to large temporary structures, values were taken in the open space area.

4 Discussion and Results

The spatial variation of liquefaction potential map, prepared as described in Sect. 2, is shown in Fig. 7. In this figure it is seen that most of the area falls on the high liquefaction potential zone. The old area with natural and alluvial deposit has low or no liquefaction. In the real field also there was no liquefaction observed in the

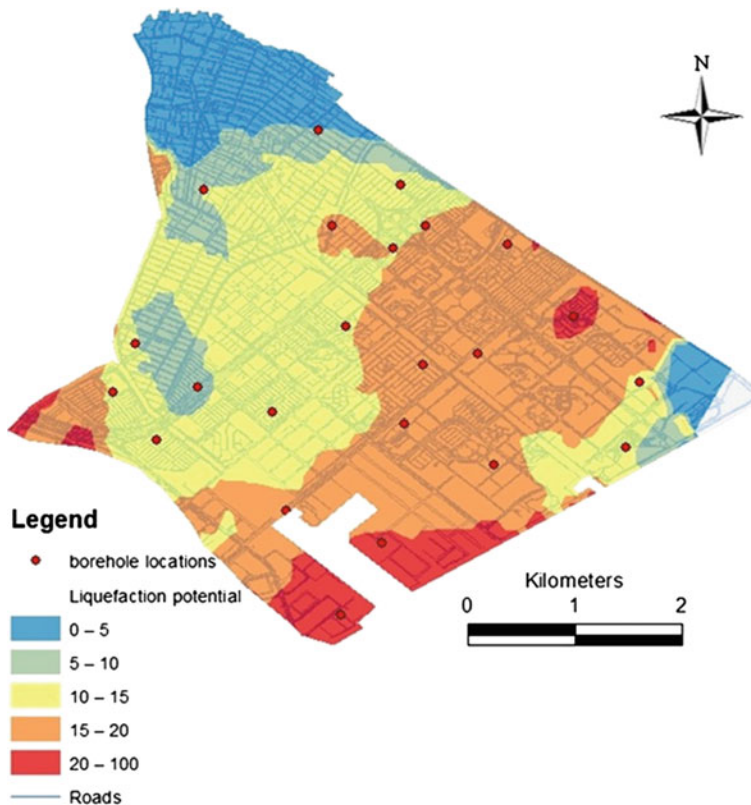


Fig. 7 Spatial variation of liquefaction potential map prepared by using 23 boreholes available in Urayasu area

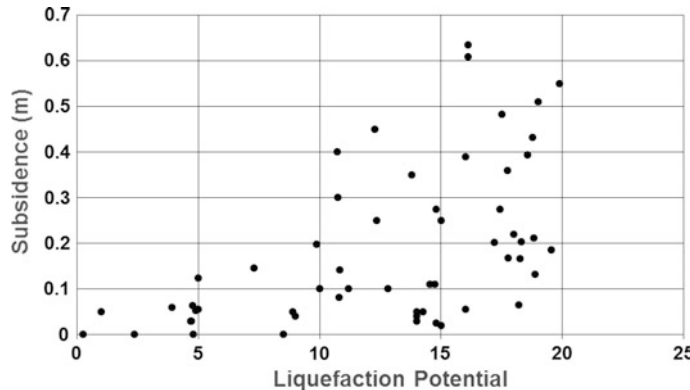


Fig. 8 The relationship between liquefaction potential and ground subsidence for Urayasu area

natural soil. Figure 7 is used to determine the liquefaction potential value for a particular point. The corresponding ground subsidence value is determined by using the methodology described in Sect. 3. The subsidence data are also taken from all the borehole points shown in Fig. 2. There is a direct relationship between liquefaction potential and ground subsidence is shown in Fig. 8. The greater the liquefaction potential, the greater the ground subsidence.

5 Conclusions

Following the 2011 off the Pacific Coast of Tohoku Earthquake, most of the reclaimed area of Urayasu city faced severe liquefaction. The common problems associated with liquefaction are sand boiling, tilting of structures, uplift of light underground structures, lifeline cut-off, etc. Among these problems, ground subsidence was observed as the main problem. The spatial distribution of liquefaction potential was prepared by using the geostatistical method over 23 boreholes and was compared with ground subsidence extracted from DSM by Konagai et al. (2013). The result shows there is positive relationship between liquefaction potential and ground subsidence. Those areas which have high liquefaction potential have higher ground subsidence. The old natural deposits area with very low liquefaction potential did not have any ground subsidence.

Acknowledgments The authors are grateful to the Japan Society for the Promotion of Science (JSPS) for the JSPS postdoctoral fellowship supporting this research. The borehole data and relevant experimental data were provided by the Technical Committee on measures against liquefaction (chaired by Prof. Ishihara) organised by Urayasu city.

References

David M (1977) Geostatistical ore reserve estimation. Elsevier, Amsterdam

Isaaks EH, Srivastava RM (1989) An introduction to applied geostatistics. Oxford University Press, Oxford, p 561

Iwasaki T, Tatsuoka F, Tokida K, Yasuda S (1978) A practical method for assessing soil liquefaction potential based on case studies at various sites in Japan. In: Proceedings 2nd international conference on Microzonation, San Francisco, vol 2, pp 885–896

Iwasaki T, Tokida K, Tatsuoka F, Watanabe S, Yasuda S, Sato H (1982) Microzonation for soil liquefaction potential using simplified methods. In: Proceedings of 3rd international earthquake Microzonation conference, Seattle, pp 1319–1330

Konagai K, Kiyota T, Suyama S, Asakura T, Shibuya K, Eto C (2013) Maps of soil subsidence for Tokyo bay shore areas liquefied in the March 11th, 2011 off the pacific Coast of Tohoku Earthquake. *Soil Dyn Earthq Eng* 53:240–253

Pokhrel RM, Kuwano J, Tachibana S (2012) Geostatistical analysis for spatial evaluation of liquefaction potential in Saitama City. *Lowland Technol Int* 14(1):45–51

Pokhrel RM, Kuwano J, Tachibana S (2013) A kriging method of interpolation used to map liquefaction potential over alluvial ground. *Eng Geol* 152:26–37

Urayasu City (2012) Data compiled by the Technical Committee on measures against Liquefaction. <http://www.city.urayasu.chiba.jp/menu11324.html> (in Japanese)

Yasuda S, Harada K, Ishikawa K, Kanemaru Y (2012) Characteristics of liquefaction in Tokyo Bay area by the 2011 Great East Japan Earthquake. *Soils Found* 52(5):793–810

Effects of Non-plastic Fines on Undrained Cyclic Behavior of Loose Sand

Yolanda Alberto-Hernandez and Ikuo Towhata

Abstract Currently the occurrence of liquefaction in silty sand (e.g., 1999 Chi-chi Earthquake, repeated liquefaction in Christchurch in 2010 and 2011, and the March 2011 Earthquake in East Japan) has increased the importance of understanding the effect of non-plastic fines on cyclic behavior of sand. The study on their influence has been carried out by several investigators through both field and laboratory tests, obtaining different outcomes that depend on the parameter of comparison. In laboratory testing, void ratio, relative density or sand skeleton void ratio are commonly used for comparing, however, for different fines contents, these values cannot be kept constant at the same time and are no longer representative of particle contact after 30 % of fines. The authors carried out a series of torsion shear tests and a comprehensive review of previous studies and their results is presented and explained in this work, considering a micromechanical interpretation to omit the use of void ratio and relative density. In this regard, a different approach was used by comparing compaction energy during sample preparation which intends to simulate natural conditions. Sand retrieved from Tokyo Bay area after the liquefaction events of March 2011, was used to conduct monotonic and cyclic tests in a hollow shear torsional apparatus with fines varying from 0 to 80 %. Differences observed in stress-strain curves, effective stress paths and excess pore pressure distribution, are shown. Moreover, liquefaction curves and relevant conclusions regarding the effect of fines content are provided. It was found that the liquefaction resistance and other mechanical properties are basically deteriorated by adding more non-plastic fines, although a certain fluctuation occurs. Finally, these results are used to conciliate different conclusions presented in past literatures.

Keywords Liquefaction • Torsional shear tests • Sand with fines

Y. Alberto-Hernandez (✉) · I. Towhata
University of Tokyo, 7-3-1 Hongo, Bunkyo-ku, Tokyo 113-8656, Japan
e-mail: yalb@geot.t.u-tokyo.ac.jp

1 Introduction

To date several researchers have undertaken the study of silty sand undergoing undrained loading. This problem has gained importance due to the recent events of liquefaction in Taiwan, New Zealand, or Japan that have caused a large number of casualties and economic loss. Laboratory testing has been performed keeping a parameter constant during cyclic or monotonic loading while changing the fines content. Usually, the parameter kept constant is a density index as void ratio, relative density or sand skeleton void ratio, which considers that the volume occupied by fines is part of the sand matrix voids. Results obtained from this research are contradictory sometimes even for the same study, especially if the range of fines content tested exceeds 30 %.

On the other hand, most previsions for evaluating liquefaction risk are simplified methods that were developed on the basis of field tests and data from liquefied sites (e.g., Tokimatsu and Yoshimi 1983; JRA 1996; Youd and Idris 1997). Therefore, it is necessary that conclusions of the effect of non-plastic fines on liquefaction resistance can be related to field parameters, as the SPT N-value. In this regard, the experimental program conducted on this test was based on keeping the compaction energy constant during sample reconstitution as a mean to represent natural conditions and connect the obtained results to field conditions.

2 Overview of Non-plastic Fines Behavior

Table 1 shows a brief compilation of the most recent research conducted on the influence of fines content on the liquefaction of sands just to notice that depending on the parameter of comparison, conclusions may differ. Overall, it can be noted that the selection of void ration as the parameter comparison causes that as fines content (FC) increases, cyclic resistance ratio (CRR) decreases. When relative density is the parameter of comparison, as fines content increases, cyclic resistance ratio increases. If tests are compared at the same sand skeleton void ratio, as fines content grows, cyclic resistance ratio decreases. Other parameters are also used for comparison, as the equivalent granular void ratio, e^* (Thevanayagam 2000), that introduces a measure of the fraction of fines which actively take part in the force chain. When comparing tests at the same equivalent void ratio, cyclic resistance ratio is found to be independent of fines.

The impossibility to keep all parameters constant at the same time causes the differences between tests conducted at the same void ratio or same relative density. For instance, Fig. 1 shows the minimum and maximum void ratios for Tokyo Bay sand measured with the Japanese Geotechnical Society standards, which has some restraints that will be explained later. Both curves, e_{\max} and e_{\min} , show a v-shape having their minimum values around 30 and 40 %, respectively. This minimum value, as explained by Lade et al. (1998), is achieved when the voids in the sand

Table 1 Previous studies on fines content and liquefaction

| Researcher example | Material | Fines content, F.C. (%) | Parameter kept constant | Conclusion |
|---------------------------|---|-------------------------|---|---|
| Amini and Qi (2000) | Ottawa sand 20–30 and non-plastic fines | 10–50 | Void ratio, e | As FC increases, CRR decreases |
| Polito and Martin (2001) | Yatesville sand and fines | 0–20 | Sand skeleton void ratio, e_s | As FC increases, CRR increases |
| Bouckovalas et al. (2003) | Different sands and silt | 0–30 | Void ratio | As FC increases, CRR decreases but for low confining stress, as FC increases, CRR increases |
| Carraro et al. (2003) | Ottawa sand and ground silica fines | 0–15 | Relative density, D_r | As FC increases, CRR increases |
| Huang et al. (2004) | Mai Liao sand and fines | 0, 15, 30, 50 | Void ratio, e | As FC increases, CRR decreases |
| Rahman and Lo (2008) | Sidney sand and Majura fines | 0–20 | Equivalent granular void ratio, e^* | CRR is independent of FC |
| Chang and Hong (2008) | Silica sand and kaolinite | 0–35 | Void ratio, e | As FC increases, CRR decreases |
| Bayat et al. (2012) | Sand with kaolinite and bentonite | 0–30 | Void ratio, e | As FC increases CRR decreases for $FC > FC_{thr}$ the opposite is observed |
| Missoum et al. (2012) | Silty sand from Chlef, Algeria | 0–40 | Equivalent void ratio, e^* (Thevanayagam 2002) | As FC increases, CRR decreases |

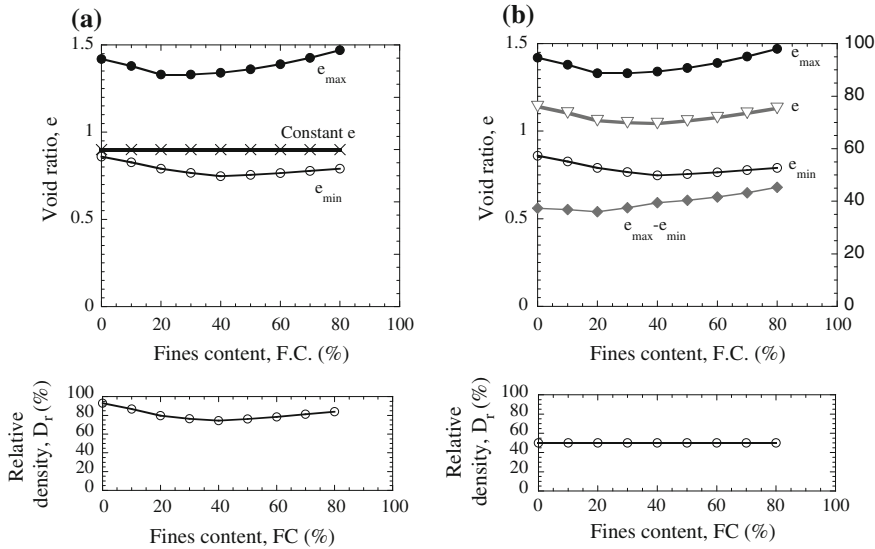


Fig. 1 **a** Relative density variation with fines content when void ratio is kept constant and **b** void ratio variation with fines content when relative density is kept constant

matrix are completely filled with fine particles, this point is known as the threshold fines content, F_{thr} , and is usually between 25 and 35 %. With the addition of fines, the sand matrix fragility increases until reaching F_{thr} . This point is the more unstable in the mix of sand with fines and after it, fragility of soil decreases and soil becomes stronger (Thevanayagam et al. 2002).

In Fig. 1a, void ratio is kept constant and the variation in relative density can be observed in the bottom figure. As fines content approaches F_{thr} , relative density decreases, therefore tests conducted in this range will find a reduction in cyclic resistance ratio. Figure 1b shows the value of relative density kept constant (bottom) and the variation of void ratio with fines content. In this case, the concept of void ratio range ($e_{\max} - e_{\min}$) needs to be introduced. As studied by Panayiotopoulos (1989), the most important factors in the packing of sands are the concepts of minimum and maximum void ratios; the difference between these parameters is defined as void ratio range by Cubrinovski and Ishihara (1999) and it was found to be inversely proportional to the normalized penetration resistance, N_1 , if relative density is kept constant. It can be understood then that when void ratio range reduces, liquefaction resistance increases.

In Fig. 2, the concepts of sand skeleton void ratio and equivalent void ratio are explained. These parameters are intended to reduce the influence of fines content on the analysis of liquefaction.

When these parameters are used for comparison some researchers have found that cyclic resistance ratio remains constant with fines contents, while others observed an increase in cyclic resistance ratio. Polito and Martin (2001) conducted

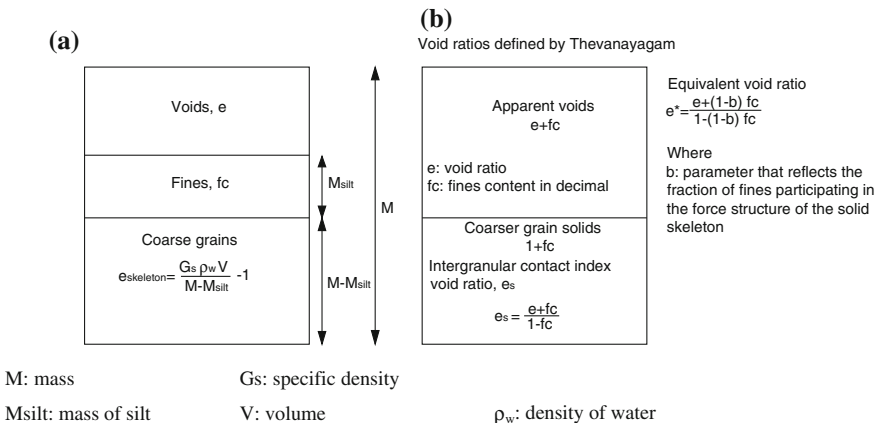


Fig. 2 Definition of **a** sand skeleton void ratio and **b** equivalent void ratio

cyclic shear tests on Monterey sand and Yatesville sand, comparing sand skeleton void ratio for different fines contents. They found that for Monterey sand cyclic resistance ratio did not change significantly with fines, while for Yatesville sand cyclic resistance ratio increased. The difference between these sands is the decrease in void ratio when keeping constant the sand skeleton void ratio, Whereas for Monterey sand, void ratio decreases parallel to minimum and maximum void ratio, keeping relative density constant, for Yatesville sand, void ratio drops faster than the lines of minimum and maximum void ratio causing an increase in relative density.

Another important factor to notice in the experiments shown in Table 1 is the range of fines content used; this exhibits one disadvantage of the parameters used for comparison. Void ratio, relative density, sand skeleton void ratio, and even equivalent void ratio are not suitable indexes of particle contact for fines contents greater than 30 %. Since both fines and sand are contributing to the force structure of the solid skeleton, after the threshold fines content is not possible to keep using e , D_r , e_s or e^* .

3 Experimental Procedure

Seeking to understand the influence of fines content on the liquefaction resistance of sands, torsional shear tests were conducted on sand retrieved from Tokyo Bay after the liquefaction events of 2011. Samples were formed by air pluviation keeping the height of fall constant with the purpose of comparing samples at the same level of compaction energy. This approach looks to eliminate the dependence on density parameters that can produce misleading conclusions.

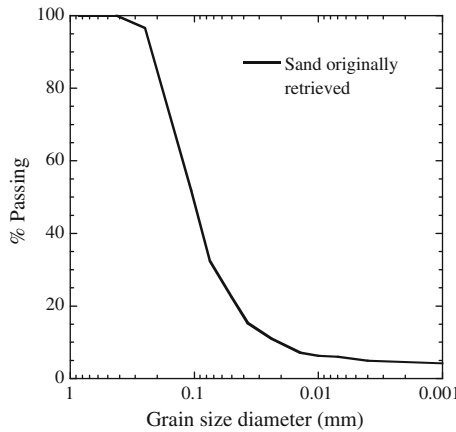


Fig. 3 Grain size distribution of sand retrieved from Tokyo Bay

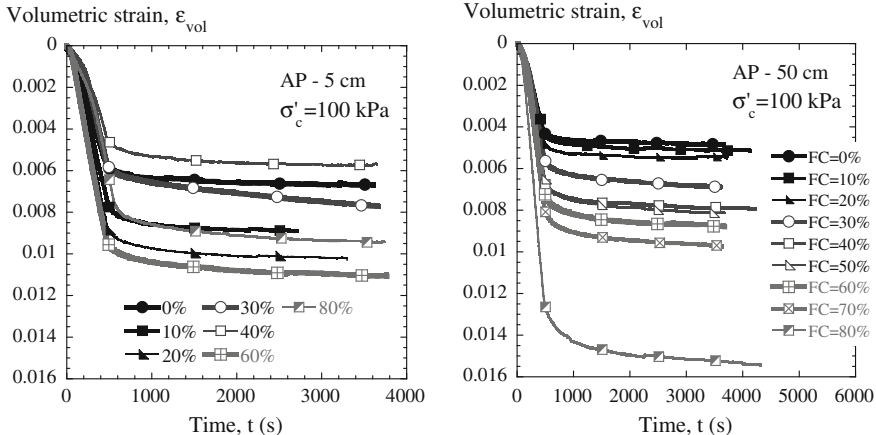


Fig. 4 Volumetric strain during consolidation for AP-5 and AP-50 cm

Figure 3 shows the grain size distribution of the sand as it was found on the ground. Once in the laboratory, sand was sieved to separate the fines ($<0.074 \text{ mm}$) from the sand. Fines were found to be non-plastic. Sand was washed and air-dried to mix it with silt for the desired fines content.

A hollow cylinder torsional device was used to conduct the experiments. Samples were prepared using a funnel and keeping a height of fall of 5 and 50 cm. Saturation was conducted using a double vacuum procedure similar to that used by Ampadu and Tatsuoka (1993). For samples with large amount of fines, the period under vacuum was extended and the volume of de-aired water percolated was increased to three times the volume of the sample.

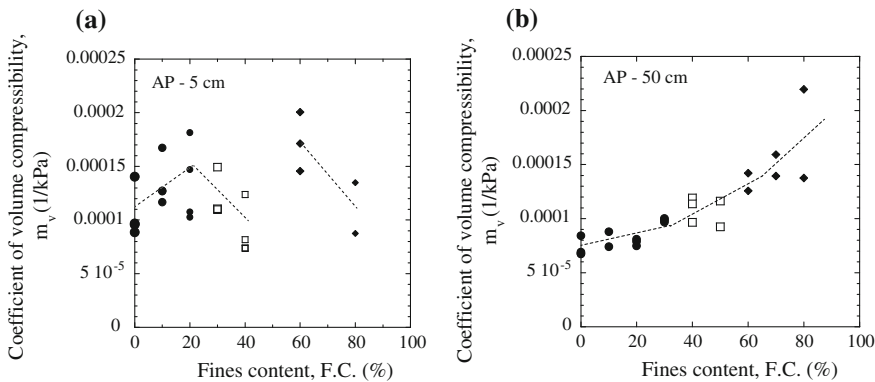


Fig. 5 Variation of coefficient of volume compressibility with fines content samples formed by **a** AP-5 and **b** AP-50 cm. Dashed lines show the trend of m_v

When samples achieved satisfactory values of saturation (Skempton's $B > 0.97$) they were consolidated to an effective confining stress of 100 kPa. Figure 4 shows some examples of the volumetric strain measured during consolidation for samples prepared by air pluviation with a height of fall of 5 cm (AP-5 cm) and 50 cm (AP-50 cm). The AP-5 cm curves show that 40 and 0 % exhibit less volumetric strain during consolidation, while 20 and 60 % had larger deformation. In the AP-50 cm figure, it is observed that volumetric strain increases with fines content.

During consolidation, the coefficient of volume compressibility was computed as the ratio of the increment in pressure over the volumetric strain measured during primary consolidation: $m_v = \frac{\Delta P}{\varepsilon_{vol}}$.

Figure 5 depicts the variation of the coefficient of volume compressibility with fines for samples prepared by AP-5 (left) and 50 cm (right). In the points computed for AP-5 cm (Fig. 5a), it is observed that from 0 to 20 %, m_v grows with fines; then there is a reduction from 20 to 40 %. From 60 to 80 % there is again a decrease in m_v , although the values are larger than those in the previous fines contents. In the samples formed by AP-50 cm (Fig. 5b), m_v increases with fines content in overall. Yet, a closer look shows that from 40 to 50 % there is a diminution in the values of m_v . The dashed lines in both figures exhibit the trend of m_v in different ranges of fines content.

The importance of obtaining this value comes from its relation to SPT N -value. Stroud and Butler (1975) found an inverse relation between the coefficient of volume compressibility and SPT N -value as:

$$N = \frac{1}{f_2 m_v}$$

f_2 : parameter dependent of plasticity index.

Using m_v , it is expected to establish a relation between the tests conducted in laboratory and the results found in the field. After consolidation, monotonic and cyclic loading was applied to study the undrained behavior of this sand.

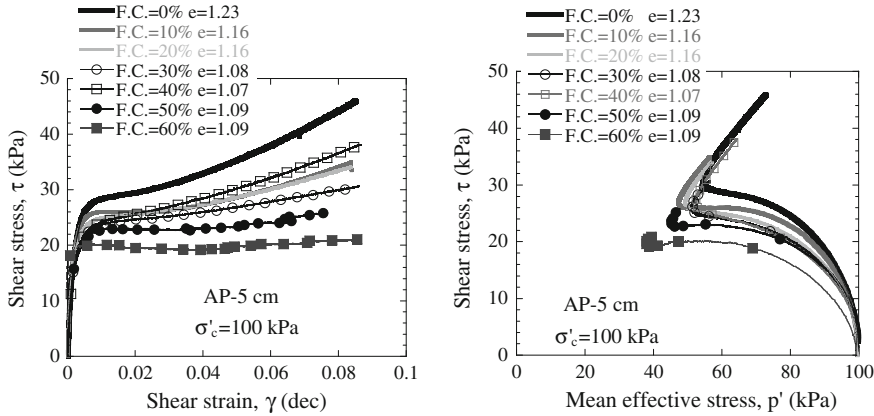


Fig. 6 Stress-strain curves and effective stress paths during monotonic undrained loading for AP-5 cm

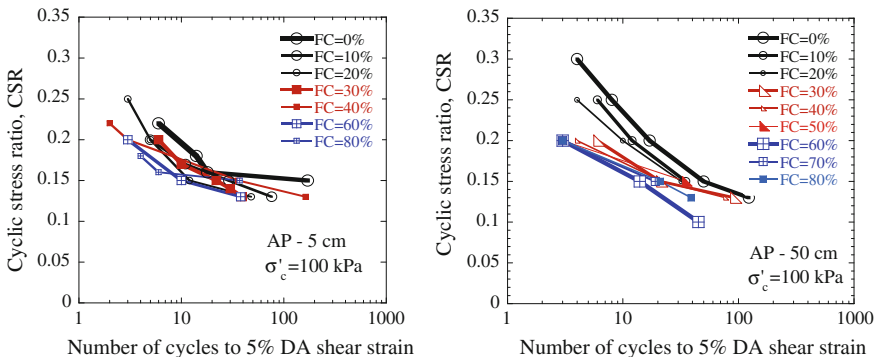


Fig. 7 Liquefaction curves for AP-5 and AP-50 cm. Colors represent different groups of behavior identified

Results of monotonic loading applied on samples made by AP-5 cm are shown in Fig. 6 in fines content from 0 to 60 %. It is observed that from 0 to 20 there is a decrease in the maximum shear strength, while a small increase is observed from 30 to 40 %. Curves of 50 and 60 % show a decrease in effective stress that does not recover and an increment in shear strain for a constant shear stress.

Details on the stress-strain curves and stress paths from cyclic loading can be found in Alberto and Towhata (2013). Liquefaction curves are presented in Fig. 7. Three groups of behaviors are identified and distinguished with different colors in the graphs, from 0 to 20 % (black) there is a decrease in liquefaction resistance, and then cyclic resistance grows from 30 to 50 % (red). Finally, from 60 to 80 % (blue) there is a slight increase in the cyclic resistance ratio.

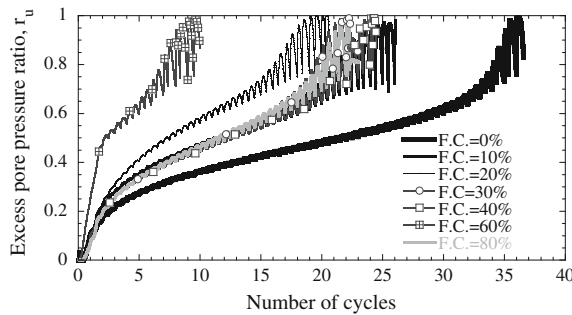


Fig. 8 Excess pore pressure ratio for different fines content at $m_v = 1.22 \times 10^{-4}$ (1/kPa)

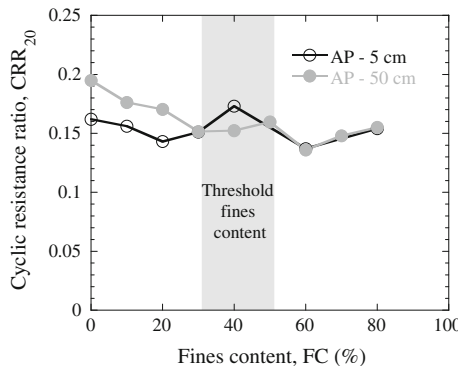


Fig. 9 CRR and FC

Some samples were compared at the same value of $m_v = 1.22 \times 10^{-4}$ (1/kPa) to observe the behavior of excess pore pressure ratio during cyclic loading. The curves from 0 to 80 % for a cyclic stress ratio $CSR = 0.15$, can be seen in Fig. 8. Clean sand ($FC = 0\%$) shows more resistance than silty sand, since it requires more cycles of loading to reach $r_u = 1$. From 0 to 20 % the number of cycles decreases. Samples with 30 and 40 % of fines exhibit more cycles than 20 % but a similar number to 80 %. The $FC = 60\%$ sample liquefies at 10 cycles being the less resistant.

Figure 9 shows the variation of cyclic resistance ratio with fines content for AP-5 and 50 cm. Conclusions from monotonic and cyclic loading of samples compared at the same compaction energy divide the soil response in three different groups: (a) for $FC < FC_{thr}$, liquefaction resistance decreases, therefore clean sand is stronger than silty sand, (b) for $FC > FC_{thr}$ liquefaction resistance increases, (c) for large fines content, cyclic resistance ratio grows slightly but the overall values of CRR are lower than in the previous groups.

4 Conclusions

Using the constant energy approach for comparison, there is a clearer understanding of the actual influence of fines on the liquefaction resistance. The reason of this behavior is the arrangement of particles: below FC_{thr} , fines reduce the contact between sand grains, when $FC \approx FC_{thr}$ both sand and fines contribute to the force chain and when $FC \gg FC_{thr}$, resistance increases as the contacts fine-to-fine augmentation. Considering this perspective, results obtained by previous researchers can also be understood. Moreover, the use of the coefficient of volume compressibility, clarifies the influence of the fines on the liquefaction resistance of sand.

References

Alberto Y, Towhata I (2013) Torsional shear test for determining the influence of fines content on the cyclic behavior of Urayasu sand. In: 48th Japanese Geotechnical Society, annual conference, Toyama, June 2013, p 2

Amini F, Qi GZ (2000) Liquefaction testing of stratified silty sands. *J Geotech Geoenviron Eng* 126(3):208–217

Ampadu SK, Tatsuoka F (1993) Effect of setting method on the behaviour of clays in triaxial compression from saturation to undrained shear. *Soils Found* 33(2):14–34

Bayat M, Bayat E, Aminpour H, Salarpour A (2012) Shear strength and pore-water pressure characteristics of sandy soil mixed with plastic fine. *Arab J Geosci*

Bouckovalas GD, Andrianopoulos KI, Papadimitriou AG (2003) A critical state interpretation for the cyclic liquefaction resistance of silty sands. *Soil Dyn Earthq Eng* 23(2):115–125

Carraro J, Bandini P, Salgado R (2003) Liquefaction resistance of clean and nonplastic silty sands based on cone penetration resistance. *J Geotech Geoenviron Eng* 129(11):965–976

Chang W, Hong M (2008) Effects of clay content on liquefaction characteristics of gap-graded clayey sands. *Soils Found* 48(1):101–114

Cubrinovski M, Ishihara K (1999) Empirical correlation between SPT N-value and relative density for sandy soils. *Soils Found* 39(5):61–71

Huang Y-T, Huang A-B, Kuo Y-C, Tsai M-D (2004) A laboratory study on the undrained strength of a silty sand from Central Western Taiwan. *Soil Dyn Earthq Eng* 24(9–10):733–743

Lade P, Liggio C, Yamamoto J (1998) Effects of non-plastic fines on minimum and maximum void ratios of sand. *ASTM Geotech Test J* 21(4):336–347

Missoum H, Belkhadir M, Bendani K, Maliki M (2012) Laboratory investigation into the effects of silty fines on liquefaction susceptibility of Chlef (Algeria) sandy soils. *Geotech Geol Eng*

Panayiotopoulos K (1989) Packing of sands—A review. *Soil Tillage Res* 13:101–121

Polito C, Martin JR (2001) Effects of nonplastic fines on the liquefaction resistance of sands. *J Geotech Geoenviron Eng* 127(5):408–415

Rahman MM, Lo SR (2008) The prediction of equivalent granular steady state line of loose sand with fines. *Geomech Geoeng* 3(3):179–190

Stroud MA, Butler FG (1975) The standard penetration test and the engineering properties of glacial materials. In: Proceedings of the symposium on engineering properties of glacial materials, p 14

Thevanayagam S (2000) Liquefaction potential and undrained fragility of silty soils. In: Proceedings of the 12th world conference on earthquake engineering, pp 1–8

Thevanayagam S, Shethan T, Mohan S, Liang J (2002) Undrained fragility of clean sands, silty sands, and sandy silts. *J Geotech Geoenviron Eng* 128(10):849–859

Tokimatsu K, Yoshimi Y (1983) Empirical correlation of soil liquefaction based on SPT N-value and fines content. *Soils Found* 23(4):56–74

Youd T, Idris I (1997) Summary report: proceedings of the NCEER workshop on evaluation of liquefaction resistance of soils. National Center for Earthquake Engineering Research. Technical report NCEER-97-0022

An Investigation on the Liquefaction-Induced Sloped Ground Failure During the 1964 Niigata Earthquake

Gabriele Chiaro, Junichi Koseki and Takashi Kiyota

Abstract Liquefaction of sloped ground is a major natural phenomenon of geotechnical significance associated with damage during earthquakes, which is not fully understood yet. To address this issue, this paper presents a simplified semi-empirical procedure for predicting earthquake-induced sloped ground failure, namely liquefaction and shear failure. It consists of a framework where cyclic stress ratio (CSR), static stress ratio (SSR) and undrained shear strength (USS) are formulated considering simple shear conditions, which closely simulate the field stress during earthquakes. The occurrence or nonoccurrence of ground failure is assessed by means of a plot η_{\max} ($=[\text{SSR} + \text{CSR}]/\text{USS}$) versus η_{\min} ($=[\text{SSR} - \text{CSR}]/\text{USS}$), where a liquefaction zone, a shear failure zone and a safe zone (i.e., no-liquefaction and no-failure) are defined. By the proposed simplified procedure, the liquefaction-induced failure of a very gentle sloped ground that occurred in Ebigase (Japan) during the 1964 Niigata Earthquake ($M_w = 7.5$ and $a_{\max} = 0.16g$) is evaluated for various soil elements, located at different depths beneath sloped ground level. Predictions are well in accordance with field observations confirming that under such earthquake and sloped ground conditions, severe liquefaction could happen only within the intermediate loose sandy soil layer, approximately at a depth in-between 3.5 and 6.5 m below the ground surface.

Keywords Liquefaction • Slope failure • Sloped ground • Prediction • 1964 Niigata Earthquake

G. Chiaro (✉)

Department of Civil and Natural Resources Engineering, University of Canterbury,
Private Bag 4800, Christchurch 8140, New Zealand
e-mail: gabriele.chiaro@canterbury.ac.nz

J. Koseki

Department of Civil Engineering, University of Tokyo, 7-3-1 Hongo,
Bunkyo-ku, Tokyo 113-8656, Japan

T. Kiyota

Institute of Industrial Science, University of Tokyo, 4-6-1 Komaba,
Meguro-ku, Tokyo 153-8505, Japan

1 Introduction

Following most of the seismic events with a moment magnitude $M_w > 6.5\text{--}7$, which usually produce also large ground acceleration ($a_{\max} > 0.15g$), the extensive damage to infrastructures, buildings, and lifeline facilities have been associated with the occurrence of lateral spreading and/or flow sliding (i.e., ground failure) in liquefied gentle sloped ground.

Prediction of ground failure involving earthquake-induced liquefaction of sloped sandy deposits is a major challenge in geomechanics due to the great number of factors that need to be considered such as initial static shear stress, cyclic shear stress, density state, loading conditions, etc. Yet, such prediction is crucial for researchers and practicing engineers to understand comprehensively the triggering conditions and consequences of liquefaction and to develop effective countermeasures against liquefaction. Existing practical methods for evaluating the liquefaction potential of soils on a site, such as the simplified procedure by Seed and Idriss (1971), are traditionally based on results of field investigations (e.g., SPT and CPT tests), which summarize the mechanical properties of soil based on empirical formulation defining seismic event and on consideration based on past experiences. However, they do not directly consider the sloped ground conditions. Instead, an empirical coefficient K_α (Idriss and Boulanger 2002) is used to reflect the sloped ground state. Nevertheless, there may be debates about the adequacy of such empirical coefficient especially if evaluated in the laboratory using triaxial conditions rather than simple shear one (Chiaro et al. 2014).

Aimed at investigating the role which static shear stress (i.e., sloped ground conditions) plays on the liquefaction behavior and large deformation properties of saturated sand, Chiaro et al. (2012, 2013a) performed a series of undrained cyclic torsional simple shear tests on loose fully saturated Toyoura sand specimens ($D_r = 44\text{--}50\%$) under various combinations of static and cyclic shear stresses. From the study of failure mechanisms, three types of failure (i.e., cyclic liquefaction, rapid flow liquefaction, and shear failure) were identified based on the difference in effective stress paths and the modes of development of shear strain during both monotonic and cyclic undrained loadings. The study confirmed that to achieve full liquefaction state, the reversal of shear stress during cyclic loading is essential. Alternatively, when the shear stress is not reversed, large shear deformation may bring sand to failure although liquefaction does not take place. Following these findings, in order to establish a framework to directly compare field and laboratory liquefaction behaviors of sand, Chiaro and Koseki (2012, 2013) presented a simplified semi-empirical procedure for predicting earthquake-induced sloped ground failure, namely liquefaction and shear failure.

In this paper, the proposed simplified procedure is described in detail and its performance is assessed for the case of liquefaction-induced failure of a very gentle sloped ground occurred in Ebigase during the 1964 Niigata Earthquake ($M_w = 7.5$ and $a_{\max} = 0.16g$) as described in details by Hamada et al. (1994).

2 A Simplified Semi-empirical Procedure for Earthquake-Induced Sloped Ground Failure

The proposed simplified semi-empirical procedure for predicting earthquake-induced sloped ground failure consists of a framework where cyclic stress ratio (CSR), static stress ratio (SSR), and undrained shear strength (USS) are formulated considering simple shear conditions (i.e., actual stress conditions in the ground during earthquakes).

2.1 Cyclic Stress Ratio

As well acknowledged, the earthquake-induced CSR at a depth z below the ground (Fig. 1) can be evaluated in accordance with the simplified procedure proposed by Seed and Idriss (1971), by converting the typical irregular earthquake record to an equivalent series of uniform stress cycles (Seed et al. 1975):

$$\text{CSR}_{7.5} = \frac{\tau_{\text{cyclic}}}{\sigma'_v} = 0.65 \frac{a_{\text{max}} \sigma_v}{a_g \sigma'_v} r_d \quad (1)$$

where a_{max} (g) is the peak ground (horizontal) acceleration; a_g is the gravity acceleration (=1g), σ_v and σ'_v are the total and effective vertical stress components, respectively. The stress reduction coefficient (r_d) is to account for the flexibility of the soil column and it is a unit less factor.

In order to evaluate the liquefaction hazard at a site, both the a_{max} (local ground response) and the effective number of cycles (earthquake severity) are needed. The

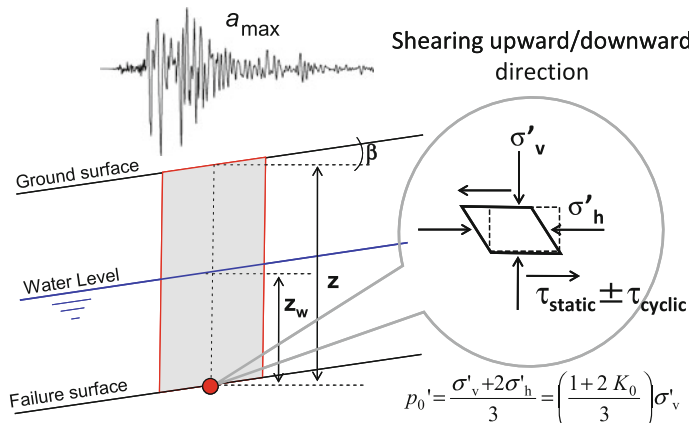


Fig. 1 Stress conditions acting on a soil element beneath sloped ground during an earthquake (Chiaro and Koseki 2013)

magnitude scaling factor (MSF) can then be used to correct the analysis for earthquake magnitudes other than 7.5 (Youd and Idriss 2001; Idriss and Boulanger 2004; etc.), provided that such an earthquake induces 15 equivalent stress cycles of uniform amplitude. Accordingly, the concept of effective peak ground acceleration ($a_{7.5}$) was introduced by Chiaro and Koseki (2013)

$$a_{7.5} = a_{\max} / \text{MSF} \quad (2)$$

where, in this study, MSF is defined in accordance to Idriss and Boulanger (2008)

$$\text{MSF} = [6.9 \exp(-M_w/4) - 0.058] \leq 1.8 \quad (3)$$

in which M_w is the moment magnitude. $a_{7.5}$ represents a critical input parameter for calculating $\text{CSR}_{7.5}$, and thus assessing and comparing the extent of liquefaction induced by earthquakes with different magnitudes and ground accelerations. Typical variation of MSF and $a_{7.5}$ with M_w are shown in Fig. 2.

By adjusting the Seed-Idriss procedure for calculating CRS to the case of simple shear conditions while using the concept of $a_{7.5}$, Eq. (1) can be rewritten as follows:

$$\text{CSR}_{7.5} = \frac{\tau_{\text{cyclic}}}{p_0} = \frac{0.65(a_{7.5}/a_g)r_d}{[(1+2K_0)/3][1-0.5(z_w/z)]} \quad (4)$$

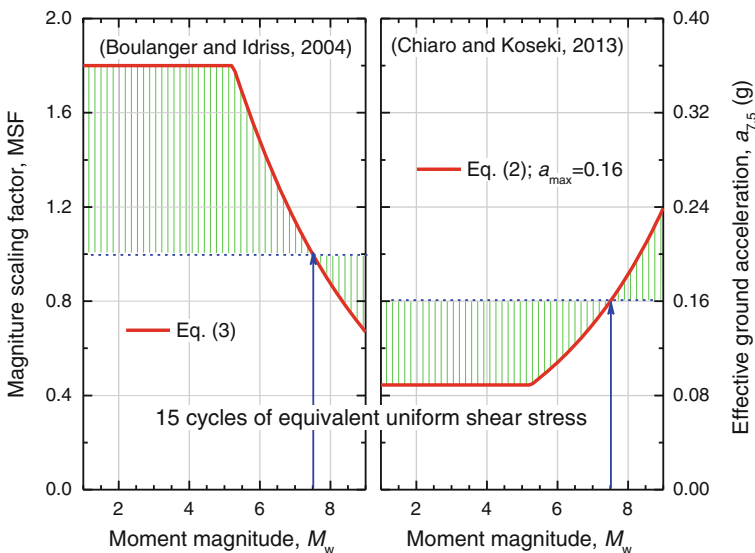


Fig. 2 Variation of MSF and $a_{7.5}$ with the moment magnitude

where, in this study, r_d is defined in accordance to Iwasaki et al. (1978)

$$r_d = (1 - 0.015 z) \quad (5)$$

In the above, K_0 is the coefficient of earth pressure at rest; z is the depth underneath the ground surface and z_w that beneath the water table, respectively. Note that, values of the unit weight of soils below and above the ground water table have been assumed to derive CSR.

2.2 Static Stress Ratio

Assuming the infinite slope state and the simple shear conditions, the SSR induced by gravity on a soil element of sloped ground, at a depth z underneath the ground surface and a depth z_w beneath the water table, can be calculated as follows (Chiari 2010):

$$\text{SSR} = \frac{\tau_{\text{static}}}{p'_0} = \frac{\tan \beta}{[(1 + 2K_0)/3][1 - 0.5(z_w/z)]} = \frac{i/100}{[(1 + 2K_0)/3][1 - 0.5(z_w/z)]} \quad (6)$$

where i is the gradient of slope (%).

2.3 Undrained Shear Strength

On the basis of results of monotonic undrained torsional simple shear tests on Toyoura sand (Chiari et al. 2012, 2013a) as well as simulation results using a newly developed model for liquefiable sand (Chiari et al. 2013b), it is found that USS significantly depends on relative density state as well as the SSR applied on a soil element. Accordingly, an empirical formulation for USS is suggested in this study

$$\text{USS} = 0.1015 + 0.0046 D_r + 0.180 \text{ SSR} \quad (7)$$

2.4 Practical Graphical Method

Once the stress conditions and soil strength are known, two important factors namely normalized minimum (η_{\min}) and maximum (η_{\max}) shear stress states can be defined:

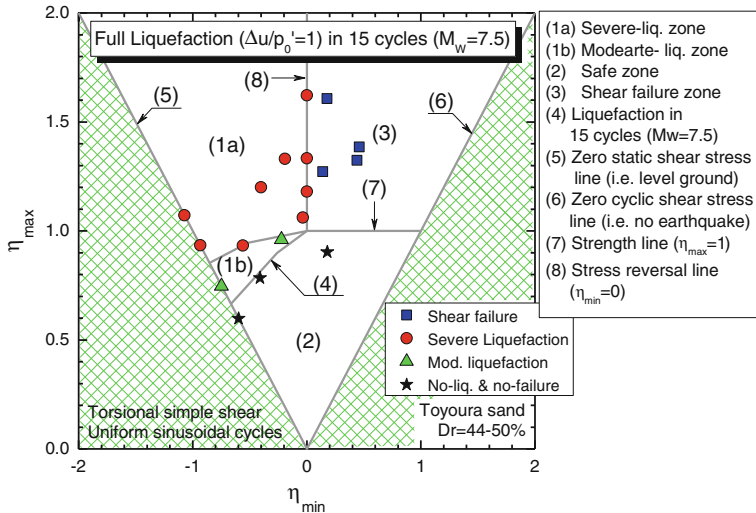


Fig. 3 Soil liquefaction/failure modes based on the proposed simplified procedure (experimental data from Chiaro et al. 2012, 2013a; Kiyota et al. 2008; Arangelovski and Towhata 2004)

$$\eta_{\min} = \frac{\text{SSR} - \text{CSR}_{7.5}}{\text{USS}} \quad (8)$$

$$\eta_{\max} = \frac{\text{SSR} + \text{CSR}_{7.5}}{\text{USS}} \quad (9)$$

Finally, the occurrence or not of ground failure can be assessed by means of the graphical method shown in Fig. 3. It consists of a plot η_{\min} versus η_{\max} , where a liquefaction zone (severe and moderate), a shear failure zone and a safe zone (i.e., no-liquefaction and no-failure) are clearly defined.

3 Liquefaction-Induced Failure of Gentle Sloped Ground in Ebigase During the 1964 Niigata Earthquake

On June 1964, a 7.5 moment magnitude (M_w) earthquake hit Niigata City (Japan) and its neighboring area. Hamada et al. (1994) reported that the peak ground acceleration (a_{\max}) in those areas was approximately 0.16g. Due to the severity of seismic shaking and particular soil conditions, a large area suffered liquefaction, which caused severe damage to buildings, infrastructures, and lifeline facilities as well as casualties. Large permanent horizontal displacement, subsidence and rising zones, a number of ground fissures and various sand boiling, observed in the

Ebigase area (Niigata City), were the evidence that the very gentle slope of a natural levee was extensively damaged by liquefaction. The estimated liquefied soils had a thickness (H) of 4–7 m, while the maximum horizontal displacement (D) measured at the ground surface was over 8 m. Thereby, extremely large shear strains ($\gamma = D/H$) of 90–200 % were triggered by liquefaction.

4 Back-Calculation of Stress State and Soil Strength in the Sloped Ground in Ebigase

As described by Hamada et al. (1994), a post-seismic field survey revealed that the soil consisted mostly of sand from a sand dune (Ts), alluvial sandy soils (As-1 and As-2) and alluvial clayey soils (Ac). A typically soil profile is shown in Fig. 4. The alluvial sandy soil layer (As-1) was very loose to loose since its N-SPT values were typically below 10. Alternatively, denser sand was found in the layer As-2, since N-SPT gradually increased up to 30. The water table was very shallow and was located at approximately 2 m below the ground surface. The liquefied layer was located within the As-1 and As-2 layers.

In this study, the (CSR)_{7.5}, SSR, USS were evaluated for various soil elements, located at different depths beneath sloped ground level, as shown in Fig. 4. Soil elements labeled L-1 through L-6 are those within the liquefied sandy layer, while N-1 and N-2 are those within the underlying non-liquefied sandy layer. The stress state and soil strength values estimated using the proposed simplified procedure are listed in Table 1 for completeness.

Fig. 4 Soil column examined (Ts: dune sand; As-1 and As-2 alluvial sandy soils; and Ac: alluvial clayey soil) (adapted from Hamada et al. 1994)

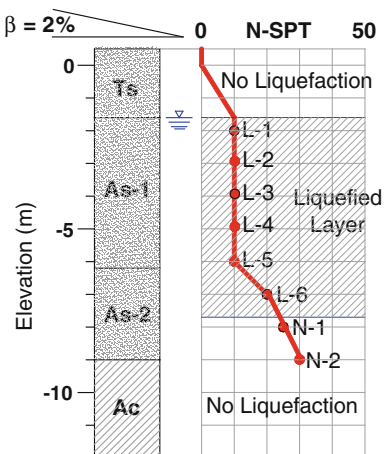


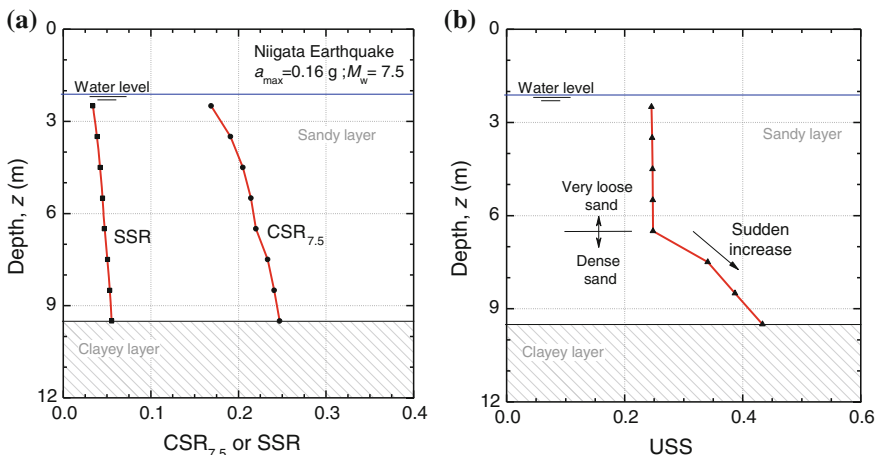
Table 1 Stress conditions and soil strength in the sloped ground in Ebigase

| Case | z (m) | z_w (m) | N-SPT | D_r (%) | $CSR_{7.5}$ | SSR | USS | η_{\max} | η_{\min} | Liquefaction behavior | |
|------|---------|-----------|-------|-----------|-------------|-------|-------|---------------|---------------|-----------------------|------------|
| | | | | | | | | | | Hamada et al. (1994) | This study |
| L-1 | 2.5 | 0.4 | 10 | 30 | 0.169 | 0.034 | 0.246 | 0.824 | -0.550 | Yes | Yes |
| L-2 | 3.5 | 1.4 | 10 | 30 | 0.191 | 0.039 | 0.246 | 0.932 | -0.618 | Yes | Yes |
| L-3 | 4.5 | 2.4 | 10 | 30 | 0.205 | 0.042 | 0.247 | 1.001 | -0.659 | Yes | Yes |
| L-4 | 5.5 | 3.4 | 10 | 30 | 0.214 | 0.045 | 0.248 | 1.046 | -0.684 | Yes | Yes |
| L-5 | 6.5 | 4.4 | 10 | 30 | 0.220 | 0.047 | 0.248 | 1.077 | -0.698 | Yes | Yes |
| L-6 | 7.5 | 5.4 | 20 | 50 | 0.233 | 0.051 | 0.341 | 0.834 | -0.537 | Yes | Yes |
| N-1 | 8.5 | 6.4 | 25 | 60 | 0.241 | 0.053 | 0.387 | 0.759 | -0.485 | No | No |
| N-2 | 9.5 | 7.4 | 30 | 70 | 0.247 | 0.055 | 0.433 | 0.698 | -0.442 | No | No |

4.1 Evaluation of CSR , SSR , and USS

Figure 5a shows the variation of $CSR_{7.5}$ and SSR along the depth (z). It appears that SSR increases gradually with z , from 0.034 up to 0.055. Alternatively, $CSR_{7.5}$ increases with z by following a non-linear trend. The minimum $CSR_{7.5}$ is approximately 0.17, while the maximum $CSR_{7.5}$ value is approximately 0.25. It should be noted that both the $CSR_{7.5}$ and SSR values change with D_r through the coefficient of earth pressure at rest (Jaky 1944; $K_0 = 1 - \sin \phi'$; where ϕ' is the friction angle). In this study, it is assumed that $\phi' = 28 + 0.14 D_r$ (Schmertmann 1978).

For simplicity, in this study, the Niigata sand USS was estimated based on Eq. (7) obtained for Toyoura sand, although some difference may be found in reality. Figure 5b shows the variation of USS beside z . It can be seen that at a depth

**Fig. 5** Variation of a) CSR and SSR ; and b) USS with depth

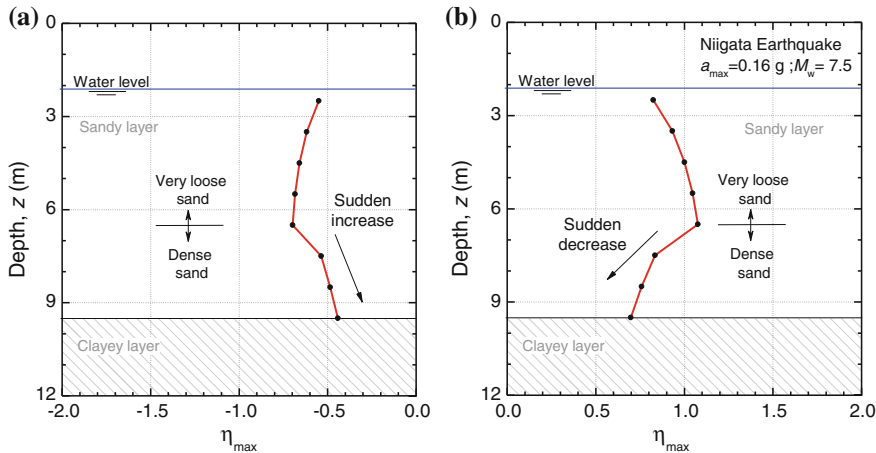


Fig. 6 Variation of **a** minimum and **b** maximum normalized shear stresses with depth

of about 6 m, USS increases markedly due to an increase in sand density from 0.246 for loose sand ($D_r = 30\%$) up to 0.433 for ($D_r = 70\%$).

4.2 Evaluation of η_{\min} and η_{\max}

In Fig. 6, variations along z are reported for both the normalized minimum (η_{\min}) and maximum (η_{\max}) shear stresses. It can be observed that, η_{\min} initially decreases up to a depth of 6 m and then suddenly increases as a consequence of the significant increase in soil density. In contrast, η_{\max} first increases up to a depth of 6 m and then suddenly decreases according to the substantial increase in soil density. It is worth mentioning that due to the slope conditions, the stress state is non-symmetrical (i.e., $\eta_{\min} \neq \eta_{\max}$).

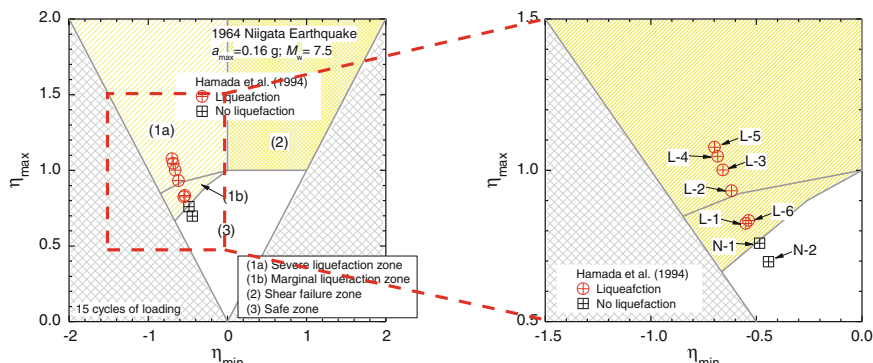


Fig. 7 Comparison between observed and predicted failure behaviors of a very gentle slope in Ebigase during the 1964 Niigata Earthquake

For this reason, compared to level ground conditions, where $\eta_{\min} = \eta_{\max}$, much more severe liquefaction can be expected (Chiaro and Koseki 2013).

5 Prediction of Liquefaction Behavior for Sloped Ground

Figure 7 shows the predictions of liquefaction behavior obtained by using the proposed simplified procedure for the case of a very gentle slope in Ebigase during the 1964 Niigata Earthquake ($M_w = 7.5$ and $a_{\max} = 0.16g$). One can see that under such severe seismic conditions, severe liquefaction could happen only within the intermediate loose sandy soil layer, approximately at a depth in-between 3.5 and 6.5 m below the ground surface (soil elements L-2 through L-5). Marginal liquefaction can be expected for soil elements L-1 (just below the water table) and L-6 ($D_r = 50\%$). On the other hand, for the denser soil elements N-1 and N-2 liquefaction could not be triggered by the earthquake. These predictions are well in accordance with the failure behavior observed in the field (Hamada et al. 1994).

6 Conclusions

Prediction of ground failure involving earthquake-induced liquefaction of sloped sandy deposits is essential for understanding comprehensively the triggers and consequences of liquefaction. In this paper, an attempt was made to identify the key factors that govern failure of sandy sloped ground during earthquakes and a semi-empirical simplified procedure to assess whenever liquefaction or shear failure may occur within a saturated sandy sloped deposit was presented.

Using the proposed method, the liquefaction-induced failure of a very gentle sloped ground that occurred in Ebigase (Japan) during the 1964 Niigata Earthquake ($M_w = 7.5$ and $a_{\max} = 0.16g$) was carefully evaluated. Similar to field observation, predictions confirmed that given the sloped ground conditions, under such strong earthquake, severe liquefaction could happen only within the intermediate loose sandy soil layer, approximately at a depth in-between 3.5 and 6.5 m below the ground surface. On the other hand, for the denser soil elements, liquefaction could not be triggered by the earthquake.

Despite the number of approximations that can be made in this kind of study (with regards to determination of soil densities, cyclic and static stress ratios, and undrained strength in the field), the proposed simplified procedure provides a useful framework for assessing liquefaction and shear failure of sloped ground in many practical proposes. Whenever greater accuracy is justified, the method can be readily supplemented by test data on particular soils or by ground response analysis to provide evaluations that are more definitive.

References

Arangelovski G, Towhata I (2004) Accumulated deformation of sand with initial shear stress and effective stress state lying near failure conditions. *Soils Found* 44(6):1–16

Chiari G (2010) Deformation properties of sand with initial static shear in undrained cyclic torsional shear tests and their modelling. Ph.D. thesis, University of Tokyo

Chiari G, Koseki J (2012) Liquefaction and failure mechanisms of sandy sloped ground during earthquakes: a comparison between laboratory and field observations. In: Proceedings of AEES conference, Gold Coast, Australia, CD-ROM, pp 1–7

Chiari G, Koseki J (2013) Prediction of earthquake-induced liquefaction for level and gently sloped ground. In: Proceedings of 19th NZGS geotechnical symposium, Queenstown, New Zealand, pp 61–68

Chiari G, Koseki J, Sato T (2012) Effects of initial static shear on liquefaction and large deformation properties of loose saturated Toyoura sand in undrained cyclic torsional shear tests. *Soils Found* 52(3):498–510

Chiari G, Kiyota T, Koseki J (2013a) Strain localization characteristics of loose saturated Toyoura sand in undrained cyclic torsional shear tests with initial static shear. *Soils Found* 53(1):23–34

Chiari G, Koseki J, De Silva LIN (2013b) A density- and stress dependent elasto-plastic model for sands subjected to monotonic torsional shear loading. *Geotech Eng J SEAGS* 44(2):18–26

Chiari G, Kiyota T, Koseki J (2014) Large-strain behavior of liquefiable sandy sloped ground evaluated by undrained cyclic torsional shear tests. In: international symposium geohazards, Katmandu, Nepal, pp 51–61

Hamada M, O'Rourke TD, Yoshida N (1994) Liquefaction-induced large ground displacement. In: Performance of ground soil during earthquake 13th ICSMFE, pp 93–108

Idriss IM, Boulanger RW (2002) Estimating K_a for use in evaluating cyclic resistance of sloping ground. In: Proceedings of 8th US-Japan workshop earthquake resistant design of lifeline facilities and countermeasures against liquefaction, Tokyo, Japan, pp 449–468

Idriss IM, Boulanger RW (2004) Semi-empirical procedure for evaluating liquefaction potential during earthquakes. In: Proceedings of 11th international conference on soil dynamics and earthquake engineering and 3rd international conferences on earthquake geotechnical engineering, Berkeley, CA, pp 32–56

Idriss IM, Boulanger RW (2008) Soil liquefaction during earthquakes. Earthquake Engineering Research Institute (EERI)

Iwasaki T, Tatsuoka F, Tokida K, Yasuda S (1978) A practical method for assessing soil liquefaction potential base on case studies at various sites in Japan. In: Proceedings of 2nd international conference on microzonation safer construction—research and application, San Francisco, CA, vol 2, pp 885–896

Jaky J (1944) The coefficient of earth pressure at rest. *J Soc Hungarian Arch Eng* 355–358

Kiyota T, Sato T, Koseki J, Abadimaran M (2008) Behavior of liquefied sands under extremely large strain levels in cyclic torsional shear tests. *Soils Found* 48(5):727–739

Schmertmann JH (1978) Use of SPT to measure dynamic soil properties?—Yes, but...! Dynamic geotechnical testing ASTM, SPT 654, Philadelphia, PA

Seed HB, Idriss IM (1971) Simplified procedure for evaluating soil liquefaction potential. *J Soil Mech Found Div ASCE* 97(SM9):1249–1273

Seed HB, Idriss IM, Makdisi F, Banerjee N (1975) Representation of irregular stress time histories by equivalent uniform stress series in liquefaction analyses. Report No. EERC 75-29, University of California, Berkeley

Youd TL, Idriss IM (2001) Liquefaction resistance of soils: summary report from the 1996 NCEER and 1998 NCEER/NSF workshops on evaluation of liquefaction resistance of soils. *J Geotech Geoenv Eng ASCE* 127(4):297–313

Laboratory Experiments on Seepage in Liquefied Sand

Tzou-Shin Ueng and Zih-Fang Wang

Abstract For understanding and modelling the behavior of saturated sand before, during, and after liquefaction, such as drainage, pore pressure build-up and dissipation, and settlement, the permeability of liquefied sand is one of the important soil properties. Previous researches on evaluating the changes of permeability of liquefied sand during and after liquefaction were proposed based on the assumption of drainage flow through the liquefied sand or the application of solidification and consolidation theory. However, these considerations of the water flow and the movements of soil particles did not truly represent the conditions within the soil during and after liquefaction, and the results were not well verified. In this study, a new experimental approach was proposed by combining the simple seepage test and the liquefaction test to evaluate the water flow within the saturated Vietnam silica sand before, during, and after liquefaction. The permeability of the sand was calculated directly from the hydraulic gradient which drove the water flow through the specimen. Results showed that the critical state of the specimen for sand boiling can be predicted well by using the Terzaghi's theoretical equation. The permeability of liquefied sand during liquefaction was about four times the initial value, while it reduced to 0.9 times the initial value after full dissipation of the excess pore pressures.

Keywords Saturated sand · Sand boiling · Liquefaction · Permeability · Hydraulic gradient · Settlement

1 Introduction

There are two situations when the pore water pressure in sand reaches its overburden stress resulting in a state that the sand loses grain contacts and its shear strength. One is sand boiling. Terzaghi and Peck (1967) observed that the soil

T.-S. Ueng (✉) · Z.-F. Wang
National Taiwan University, Taipei, Taiwan
e-mail: ueng@ntu.edu.tw

particles begin to be lifted into suspension when the seepage force equals the initial effective stress in soil. He expressed the critical hydraulic gradient i_{cr} as the buoyant unit weight of soil γ' divided by the unit weight of water γ_w , i.e., $i_{cr} = \gamma'/\gamma_w$. Skempton and Brogan (1994) conducted a series of piping tests and found that the critical hydraulic gradient of internally stable soil is consistent with Terzaghi's theoretical value. Wang (2012) compared the prediction methods of critical hydraulic gradient proposed by Terzaghi and Peck (1967), Wu (1980), Liu (1992), and Zhou et al. (2010) and concluded that Terzaghi's theoretical equation can predict well for the critical hydraulic gradient for internally stable soils.

The other situation is soil liquefaction during earthquake. The damage to structures may be attributed concurrently to the seismic loading and the post-liquefaction behavior of the liquefied ground. According to Ueng (2006) and Ueng et al. (2010), test results from large scale 1 g shaking table tests performed at National Center for Research on Earthquake Engineering (NCREE) indicated that for a homogeneous soil stratum subjected to seismic loading, the shallower soil is more susceptible to liquefaction than the deeper soil. Besides, it was found that significant settlements were induced only when liquefaction occurred, while the measured settlements were very small when there was no liquefaction.

Ishihara (1994) summarized the results of various predictions for VELACS model 1 and concluded that the post-liquefaction behavior of liquefied sands is significantly affected by the soil permeability. Centrifuge tests were conducted using resistivity measurement by Arulanandan and Sybico (1992) to characterize the soil structure during and after liquefaction. By applying the Kozeny–Carman equation to the test results, it was concluded that the coefficient of permeability of the specimen was increased 6–7 times its initial value during liquefaction as the pore shape factor and tortuosity decreased. It was further indicated that the predicted settlement using the initial permeability of the specimen would be underestimated. A modified consolidation theory proposed by Scott (1986) showed the relation between solidification velocity and permeability of saturated sands. Kim et al. (2009) combined Scott's theory with their centrifuge test results and developed a nonlinear solidification model. It was found that the solidification velocity increased with the increase of particle size and relative density of the specimens. Wang et al. (2013) combined the test results of 1-g shaking table tests with the nonlinear solidification model and consolidation theory, and concluded that the post-liquefaction behavior can be predicted well by considering the changes of permeability after liquefaction.

Previous researches on soil liquefaction have found that the behavior of liquefiable soils is partly governed by the soil permeability and its changes during and after seismic loading. However, evaluating on the changes of permeability of liquefied sand during and after liquefaction based on the assumption of drainage flow through the liquefied sand or the application of solidification and consolidation theory did not truly represent the conditions within the soil during and after liquefaction. For this reason, a new experimental approach was proposed in this study by combining seepage and liquefaction tests to directly evaluate the changes of

permeability of saturated sand during liquefaction. A basic mechanism of soil responses and water flow during liquefaction was then discussed based on these test results.

2 Experiment Program

Fine Vietnam silica sand was used for the saturated sand specimens of $D_r = 40.7\%$. The physical properties of the sand are shown in Table 1. The experimental system shown in Fig. 1 includes the permeameter containing a sand specimen of 100 mm in diameter and 500 mm in length, a constant head water supply system, and a data acquisition system for continuous measurements of water pressure and flow velocity during the tests. Four pressure transducers, P1, P2, P3, and P4 were installed on the wall of the permeameter. The test program summarized in Table 2 includes: (1) simple seepage-induced failure (sand boiling) test; (2) liquefaction test without seepage; and (3) liquefaction test with seepage. The temperature of water was controlled at 20 °C throughout the tests. For simple seepage-induced failure test, the sand specimen was subjected to stepwise increased upward flow from the bottom until sand boiling occurred. Each step of flow increase was applied after both the measured flow and the water pressures reached the stable values. For liquefaction test with seepage, a small upward flow was applied prior to the application of vibration to the sand specimen, and maintained at a constant value throughout the liquefaction test. Liquefaction of the sand was induced by applying a series of shocks manually using a rubber hammer. The frequency and duration of the shocks was about 4.5 Hz and 6 s, respectively. The vibration amplitude was conditioned to induce a liquefied zone down to a depth between P2 and P3. The excess pore pressures, the flow velocity and the surface settlements were recorded during the tests. Therefore, the changes of water pressures and the seepage situations could be observed during the process of soil liquefaction. Each of the above mentioned tests should be conducted at least twice for ensuring the repeatability of the test results.

3 Test Results

For the analysis of the test results, the zones of the specimen between P1 and P2, P2 and P3, and P3 and P4 are defined as zone 1, zone 2, and zone 3, respectively. The thickness of zone 1, zone 2, and zone 3 are 100, 150, and 150 mm, respectively. In

Table 1 Physical properties of fine Vietnam silica sand

| Color | Particle shape | G_s | D_{10} (mm) | D_{60} (mm) | C_u | e_{\max} | e_{\min} |
|-------|----------------|-------|---------------|---------------|-------|------------|------------|
| White | Sub-angular | 2.65 | 0.22 | 0.34 | 1.545 | 0.906 | 0.631 |

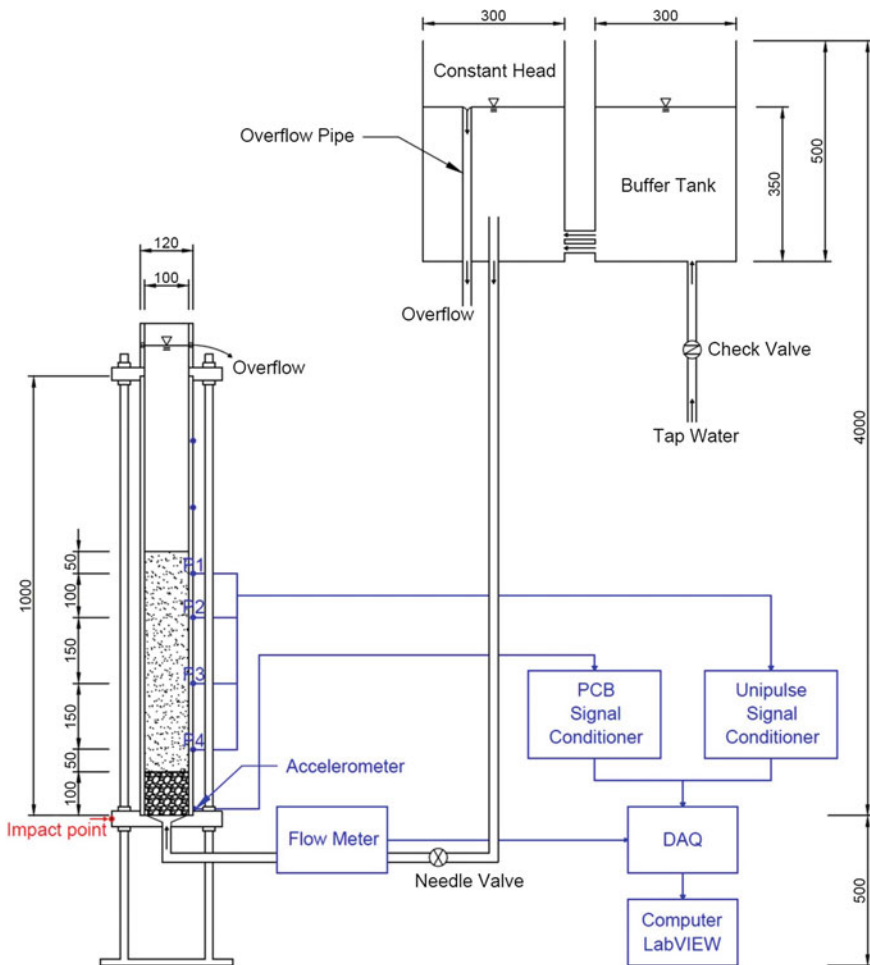


Fig. 1 Schematic diagram of the experiment system (length in mm)

Table 2 Summary of test program

| Test no. | Test series | Initial flow velocity, v_i (10^{-2} cm/s) |
|----------|--|--|
| S | Simple seepage-induced failure (sand boiling) test | — |
| L | Liquefaction test without seepage | 0 |
| LS1 | Liquefaction test with seepage | ≈ 2.2 |
| LS2 | Liquefaction test with seepage | ≈ 1.0 |

in this study, the pore water pressure changes were recorded by the four pressure transducers throughout the tests. The excess pore pressures exceeding the initial hydrostatic pressures at the locations of the four pressure transducers were expressed in terms of the height of water in mm. When the excess pore pressures at the locations of P1, P2, P3, and P4 are different, the excess pore pressure head gradient is defined as

$$i_{ej} = \frac{h_{e(j+1)} - h_{ej}}{H_j}, \quad (j = 1, 2, 3) \quad (1)$$

where i_{ej} is the excess pore pressure head gradient in zone j , h_{ej} is the excess pore pressure head at pressure transducer P_j , and H_j is the thickness of zone j . In test S, i_{ej} is equal to hydraulic gradient i , which induces the upward water flow. However, in test L and LS, the i_{ej} generated by vibrations with or without water flow may not necessarily be the driving source of the water flow. Further discussions will be given in the later sections.

3.1 Simple Seepage-Induced Failure Test

The Terzaghi's theoretical critical hydraulic gradient of the specimen, $i_{cr,t}$ is 0.92. Figure 2 shows the relation between the measured flow velocity, v of water flow through the sand specimen and the corresponding hydraulic gradient, i in test S. A linear relation between the flow velocity and the hydraulic gradient before the sand specimen reaches its critical condition was observed. The coefficients of permeability of the sand specimen in zone 1, zone 2, and zone 3 were about 6.0×10^{-2} cm/s. The starting point of the deviation from the linear relation was defined as the critical state of the specimen. The critical hydraulic gradient in the three zones ranged from 0.91 to 0.94 with an average critical hydraulic gradient i_{cr,m_avg} of about 0.92, which is almost equal to the $i_{cr,r}$. The specimen began to expand once it exceeded the critical state. Thereafter, a further increase in the flow velocity caused a sudden drop of the hydraulic gradient. The peak hydraulic gradient for the failure of the specimen corresponds to the starting point of the hydraulic gradient drop with increasing flow velocity. The average peak hydraulic gradient of the three zones, i_{peak_avg} is about 1.14, which is about 1.2 times the $i_{cr,t}$. Thereafter, the hydraulic gradient disproportionately decreased with increasing flow velocity, and significant expansion of the specimen was observed.

3.2 Liquefaction Tests

The time histories of the excess pore pressures measured by the four pressure transducers in test L is shown in Fig. 3. It was observed that for a homogeneous

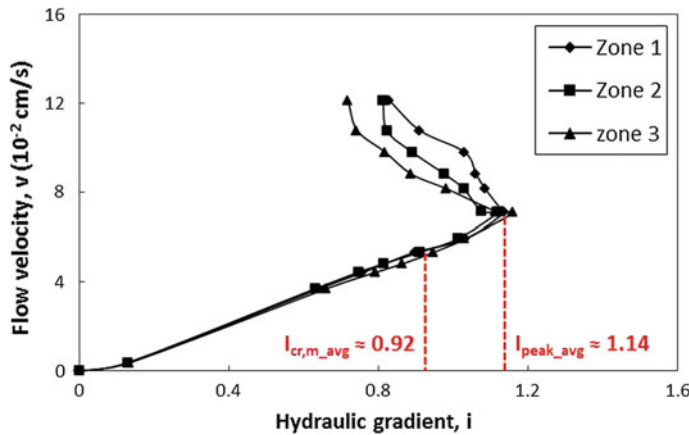


Fig. 2 Flow velocity versus hydraulic gradient in test S

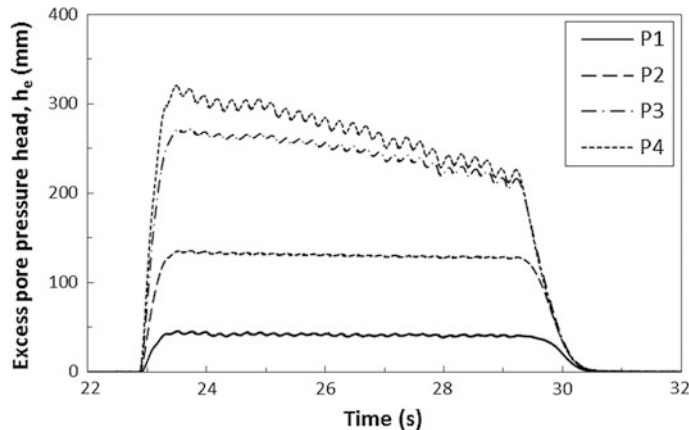


Fig. 3 Time histories of the excess pore pressures in test L

sand column, the soil at shallower depth is more susceptible to liquefaction than the deeper soil. In such case, the pressure transducers P1 and P2 recorded the response of the liquefied zone of the sand specimen, while the pressure transducers P3 and P4 recorded the response of the non-liquefied zone of the sand specimen throughout the tests. The excess pore pressures measured by P1 and P2 in the liquefied zone maintained about the same value equal to the initial effective stress corresponding to the depth of P1 and P2 during liquefaction. The excess pore pressure head gradient in zone 1 during liquefaction i_{el} calculated by Eq. (1) is about 0.92. On the other hand, the excess pore pressures measured in the non-liquefied zone began to decrease about the time when the shallower layer liquefied. It was inferred that the dissipation of the excess pore pressure in the non-liquefied zone during vibration

may be affected by the changes of permeability in the liquefied zone. Thereafter, fast dissipations of the excess pore pressures measured in both liquefied and non-liquefied zone were observed when the vibration stopped.

In test LS1, an upward flow velocity of about 1.0×10^{-2} cm/s was applied during the liquefaction tests. The time histories of the excess pore pressures in both liquefied and non-liquefied zone had the same trend with that observed in test L. The excess pore pressure head gradient in zone 1 during liquefaction i_{el} calculated by Eq. (1) is about 0.96.

In test LS2, an upward flow velocity of about 2.2×10^{-2} cm/s was applied during the liquefaction tests. The time histories of the excess pore pressures measured in the liquefied zone had the same trend with that observed in the test series L. The excess pore pressure head gradient in zone 1 during liquefaction i_{el} calculated by Eq. (1) is about 1.00.

In addition, the recorded changes of the locations of the colored sands and the surface of the sand specimen showed that the settlement of the sand specimen in the liquefaction tests occurred at the beginning of vibration, continued during the process of vibration, and ceased about the time when vibration stopped. Significant settlement was induced only when liquefaction occurred, while almost no settlement was observed in the non-liquefied zone after liquefaction tests. The liquefied zones in test L, LS1, and LS2 had settlement S_l of about 3, 2.5, and 2 mm, respectively. The S_l decreased with the increasing upward flow velocity probably because the upward flow may hinder the sand particles from sedimentation after liquefaction. The initial flow velocity v_i , the flow velocity during liquefaction v_l , and other results of test L, LS1, and LS2 are summarized in Table 3, some of the results will be discussed in the later section.

Table 3 Results of the liquefaction tests

| Test no. | v_i (10^{-2} cm/s) | v_l (10^{-2} cm/s) | i_i | i_{el} | i_l | k_i (10^{-2} cm/s) | k_l/k_i | k_{end}/k_i | S_l (mm) |
|----------|-------------------------|-------------------------|-------|----------|-------|-------------------------|-----------|---------------|------------|
| L-1 | 0 | 0 | 0 | 0.917 | — | — | — | — | 3.0 |
| L-2 | 0 | 0 | 0 | 0.915 | — | — | — | — | 3.0 |
| L-3 | 0 | 0 | 0 | 0.918 | — | — | — | — | — |
| L_avg | 0 | 0 | 0 | 0.917 | — | — | — | — | 3.0 |
| LS1-1 | 0.980 | 0.945 | 0.168 | 0.955 | 0.039 | 5.818 | 4.214 | 0.912 | 2.5 |
| LS1-2 | 0.972 | 0.929 | 0.160 | 0.952 | 0.035 | 6.093 | 4.356 | 0.907 | 2.5 |
| LS1-3 | 0.965 | 0.915 | 0.185 | 0.957 | 0.041 | 5.215 | 4.284 | 0.941 | — |
| LS1-4 | 0.959 | 0.981 | 0.177 | 0.955 | 0.039 | 5.418 | 4.667 | 0.840 | — |
| LS1_avg | 0.969 | 0.942 | 0.172 | 0.955 | 0.038 | 5.636 | 4.378 | 0.900 | 2.5 |
| LS2-1 | 2.139 | 2.076 | 0.362 | 1.002 | 0.085 | 5.913 | 4.118 | 0.878 | 2.0 |
| LS2-2 | 2.297 | 2.142 | 0.339 | 0.997 | 0.080 | 6.777 | 3.938 | 0.934 | 2.0 |
| LS2_avg | 2.218 | 2.109 | 0.350 | 1.000 | 0.083 | 6.345 | 4.022 | 0.908 | 2.0 |

4 Permeability of Liquefied Sand

According to the results of the liquefaction tests, it was found that the i_{el} increased with the increasing upward flow velocity. In this study, an effective hydraulic gradient in zone 1 during liquefaction i_l is defined as the net source that drives the upward water flow through the liquefied zone during liquefaction. The i_l can be expressed as

$$i_l = i_{el_LS} - i_{el_L} \quad (2)$$

where i_{el_L} and i_{el_LS} are the excess pore pressure head gradients in zone 1 during liquefaction in tests L and LS, respectively. Under the assumption of the applicability of Darcy's law, the coefficient of permeability of the liquefied sand during liquefaction k_l can be calculated from the measured flow velocity during liquefaction v_l divided by the effective hydraulic gradient in zone 1 during liquefaction i_l , i.e., $k_l = v_l/i_l$.

Figure 4 shows a linear relation between the i_{el} and v_l obtained in all of the liquefaction tests. The k_l can then be calculated by combining Eq. (2) and Darcy's law or directly obtained from the inverse slope of the linear relation in Fig. 4. In addition, the coefficients of permeability of the sand specimen before vibration k_i and after excess pore pressure dissipation k_{end} were obtained by the constant head permeability tests. It was found that the k_l obtained in the liquefaction tests with different water flow velocities were all about 4 times the initial values, i.e., $k_l/k_i \approx 4$. This also verified that the applied upward water flow in this study did not affect the changes in the permeability of the sand specimen during liquefaction. Due to the significant increase of the permeability of the sand, a smaller hydraulic gradient is required to cause the same upward water flow through the liquefied sand during liquefaction. Therefore, the i_l was only about one fourth of the initial hydraulic gradient i_i . On the other hand, the coefficients of permeability after full dissipation of the excess pore pressure in the test series LS were about 0.9 times the initial values, i.e., $k_{end}/k_i \approx 0.9$. This can be attributed to the decrease in the void ratio of the sand specimen after full dissipation of the excess pore pressure. The changes of the coefficient of permeability of the sand for all of the liquefaction tests are summarized in Table 3.

The mechanism of the increase in the permeability of the liquefied sand during liquefaction can be interpreted by applying Kozeny–Carman equation for the permeability of saturated porous media (Kozeny 1927; Carman 1956)

$$k = \left(\frac{1}{k_0 T^2} \right) \left(\frac{\gamma_p}{\mu} \right) \frac{1}{S_0^2} \left(\frac{e^3}{1+e} \right) \quad (3)$$

where k is the coefficient of permeability of the porous media, k_0 is the pore shape factor, T is the tortuosity factor, γ_p is the unit weight of the flowing fluid, μ is the viscosity of the flowing fluid, S_0 is the wetted surface area per unit volume of

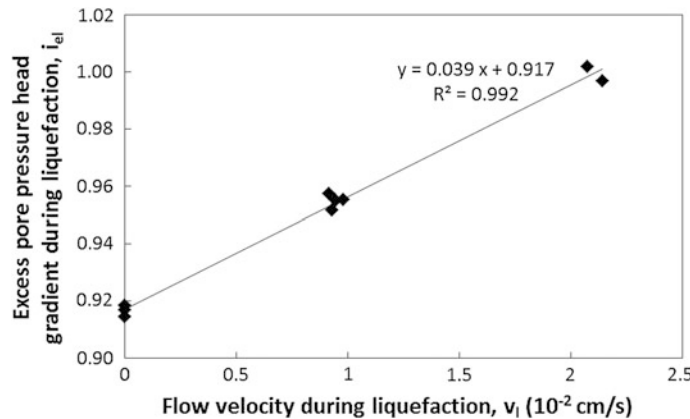


Fig. 4 Excess pore pressure gradient versus flow velocity within liquefied sand

particles, e is the void ratio of the porous media. A simplified representation of the tortuosity factor T can be expressed as the mean length of the flow path of the fluid through the porous media L divided by the distance between the ends of the porous media C , i.e., $T = L/C$. Figure 5 shows the schematic diagram of water flow through the sand at initial and liquefied states. At the initial state of the sand specimen, the sand particles are contact with each other. The water flow cannot pass through the contact point in the sand specimen. Thus, the flow path of the water through the sand specimen L is much longer than the length of the sand specimen C . During liquefaction of the sand, the sand particles lose their contacts resulting in shorter path for water to flow through the liquefied sand. The water can more directly flow through the sand specimen without bypassing the grain contacts. Therefore, the coefficient of permeability of the sand specimen during liquefaction increases as the tortuosity of the sand specimen decreases; while it is assumed that the change in the void ratio of the liquefied sand during liquefaction was negligible.

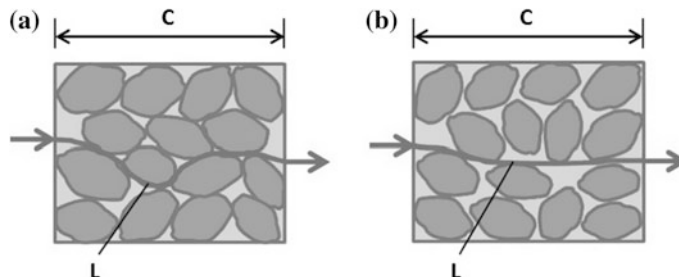


Fig. 5 Schematic diagram of water flow through sand specimen at different states. **a** initial stage, **b** liquefied stage

5 Conclusions

In this study, a new experimental approach was proposed by combining the simple seepage test with the liquefaction test to directly evaluate the variation of permeability of saturated sand before, during and after liquefaction. Test results of simple seepage-induced failure tests showed that the critical state of the specimen for sand boiling can be predicted well by using the Terzaghi's theoretical equation. As for liquefaction tests, the permeability of the liquefied sand was found to be about four times the initial value during liquefaction and it reduced to about 0.9 of the initial value after full dissipation of the excess pore pressure and complete settlement of the sand specimen. The sand particles lose their contacts at liquefaction, which create an easier path for water to flow through the liquefied sand. The coefficient of permeability of the sand specimen increases as the tortuosity of the sand specimen decreases during liquefaction. In addition, it was found that significant settlements were induced only when liquefaction occurred, while almost no settlement were observed in the non-liquefied zone of the sand specimen after liquefaction tests.

References

Arulanandan K, Sybico Jr J (1992) Post-liquefaction settlement of sands. In: Proceeding of the Wroth memorial symposium. Oxford University, England pp 94–110

Carman PC (1956) Flow of gases through porous media. Academic, New York

Ishihara K (1994) Review of the predictions for model 1 in the VELACS program. In: Arulanandan K, Scott RF (eds) Verification of numerical procedures for the analysis of soil liquefaction problems. Balkema A. A., Rotterdam, pp 1353–1368

Kim SR, Hwang JI, Ko HY, Kim MM (2009) Development of dissipation model of excess pore pressure in liquefied sandy ground. *J Geotech Geoenviron Eng ASCE* 135(4):544–554

Kozeny J (1927) Ueber kapillare Leitung des Wassers im Boden. Wien, Akad. Wiss., vol 136, Part 2a, p 271

Liu J (1992) Seepage stability and seepage control of soil. Water Resources and Electric Power Press, Beijing (in Chinese)

Scott RF (1986) Solidification and consolidation of a liquefied sand column. *Soils Found* 26 (4):23–31

Skempton AW, Brogan JM (1994) Experiments on piping in sandy gravels. *Geotechnique* 44 (3):449–460

Terzaghi K, Peck RB (1967) Soil mechanics in engineering practice, 2nd edn. Wiley, New York, pp 60–62

Ueng TS (2006) Inference of behavior of saturated sandy soils during earthquakes from laboratory experiments. *J GeoEng* 1(1):1–9

Ueng TS, Wu CW, Cheng HW, Chen CH (2010) Settlement of saturated clean sand deposits in shaking table tests. *Soil Dyn Earthq Eng* 30(1):50–60

Wang JY (2012) Experimental study on seepage failure of uniform and gap-graded soils. M.S. thesis, National Taiwan University of Science and Technology, Taiwan

Wang B, Zen K, Chen GQ, Zhang YB, Kasama K (2013) Excess pore pressure dissipation and solidification after liquefaction of saturated sand deposits. *Soil Dynam Earthq Eng* 49:157–164

Wu LJ (1980) Calculation of critical hydraulic gradient for piping in cohesionless soils. *Hydro-Sci Eng* 4:90–95 (in Chinese)

Zhou J, Bai YF, Yao ZX (2010) A mathematical model for determination of the critical hydraulic gradient in soil piping. *GeoEnviron Eng Geotech*, pp 239–244

Effects of Cyclic Triaxial Loading Rates on Liquefaction Behavior of Fine-Grained Soils

Ya-Han Hsu, Louis Ge and Meng-Heng Chiang

Abstract Low-plasticity silt has been found susceptible to liquefaction in recent earthquake reconnaissance. As silt is less permeable than sand, a different excess pore water pressure dissipation mechanism could take place. This may have an effect on the cyclic strength at different loading rates, although the influence on loading rate is neglected in general. According to the ASTM testing standard, a typical loading rate for cyclic triaxial tests should be set between 2 and 0.1 Hz. However, it is evident from the test results in this study that various loading rates lead to different cyclic resistance curves. In this paper, we present a series of dynamic cyclic triaxial tests on reconstituted silt specimens with silica silt and the Tieliku silt which is in situ silt under various loading rates. It is concluded that the low-plasticity silt may be rate-dependent in cyclic triaxial testing.

Keywords Liquefaction · Cyclic triaxial tests · Low-plasticity silt · Loading rate

1 Introduction

Research of soil liquefaction has been carried out extensively on clean sand and silty sand for decades, which leads to the development of liquefaction potential assessments (e.g., Seed and Idriss 1982; Andrew and Martin 2000). It is well accepted in practice that soil is not liquefiable when its fine contents that pass the US #200 sieve exceed a certain amount. However, from recent earthquake including 1994 Northridge earthquake and 1999 Chi-Chi earthquake, low-plasticity silts were found liquefied (Bray and Sancio 2006). These low-plasticity silts are

Y.-H. Hsu · L. Ge (✉) · M.-H. Chiang
Department of Civil Engineering, National Taiwan University,
No. 1, Section 4, Roosevelt Road, Taipei 10617, Taiwan
e-mail: louisge@ntu.edu.tw

Y.-H. Hsu
e-mail: r02521101@ntu.edu.tw

classified as not susceptible for liquefaction based on the current criteria, indicating a further study is needed to understand their liquefaction behaviors.

Fines passing the US #200 sieve consist of silt and clay. Due to their plasticity, it is believed that they have different impact and contribution to liquefaction. The liquefaction behaviors of low-plasticity silts have been examined in recent years (e.g., Bray and Sancio 2006); however, the role of soil plasticity in liquefaction does not have a consistent explanation yet. In those studies, cyclic triaxial tests are often conducted in laboratory. The loading rate during cyclic shearing is considered having a minimum influence on its cyclic resistance for sandy specimens. This may not be true for relatively less permeable silt and low-plastic silt specimens, and a further study is desired. In this study, a series of cyclic triaxial tests were carried out on two types of fine-grained soil, namely silica silts and Tieliku silts, to examine the impact of loading rates on their cyclic strength.

2 Literature Review

The liquefaction behavior of saturated sands was found insignificantly different under very low cyclic stress loading rate (Peacock and Seed 1968; Lee and Fitton 1969). It was also found that the loading rates ranging from 1/60 to 1/3 Hz do not influence the liquefaction behavior of saturated sands (Wong et al. 1975). Similar findings were also obtained by Yoshimi and Oh-oka (1975) that undrained shear strengths did not change much under loading rates between 1/6 and 4 Hz. Ohara et al. (1985) indicated that liquefaction resistance of sand is not influenced by loading rates ranging from 1 to 5 Hz. On the other hand, the coefficient of permeability and the cyclic loading rates have impact on liquefaction resistance under partially drained conditions (Umehara et al. 1985). With the discussion above, the effect of cyclic stress loading rates on less permeable low-plasticity silty specimens remains unclear.

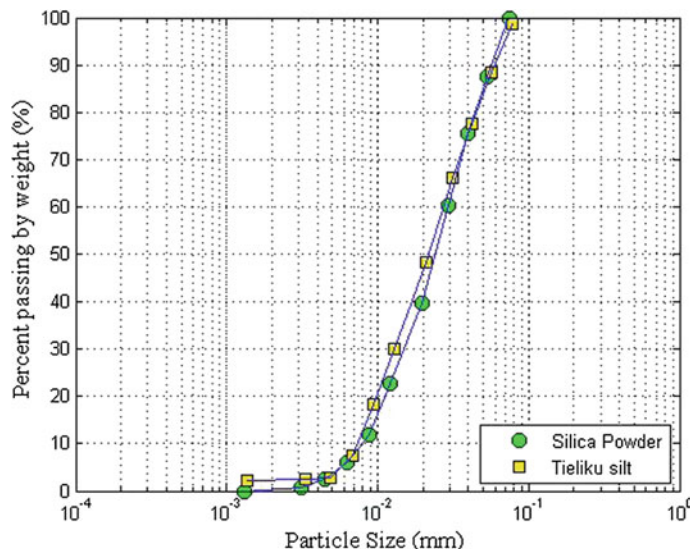
3 Experimental Program

Two groups of tests were performed in this research. The first part was the physical properties of silica silt and Tieliku silt including hydrometer analysis, specific gravity, maximum and minimum void ratio, liquid and plastic limits of Atterberg limits test. The test results are shown in Table 1 and Fig. 1, respectively. It is noted that silica silt is classified as low-plastic silt (ML) while the Tieliku silt is low-plastic clay (CL) in Unified Soil Classification System (USCS).

The second part of the tests was the cyclic triaxial tests with reconstituted soil specimens. The initial void ratio of each specimen was kept as 0.86. Also, each test

Table 1 Physical properties of silica silt and Tieliku silt

| Soil type | Specific gravity (G_s) | Maximum void ratio (e_{\max}) | Minimum void ratio (e_{\min}) | Liquid limit (LL) | Plastic limit (PL) | Plastic index (PI) | USCS classification |
|--------------|----------------------------|-----------------------------------|-----------------------------------|-------------------|--------------------|--------------------|---------------------|
| Silica silt | 2.65 | 1.65 | 0.51 | 26 | NP | NP | ML |
| Tieliku silt | 2.70 | 1.48 | 0.77 | 29 | 21 | 8 | CL |

**Fig. 1** Particle-size distribution curves for silica silt and Tieliku silt**Table 2** Triaxial permeability test results

| Specimen | Plasticity index (PI) | Permeability (cm/s) |
|--------------|-----------------------|-----------------------|
| Silica silt | NP | 1.55×10^{-3} |
| Tieliku silt | 8 | 4.07×10^{-4} |

was conducted with an effective confining pressure of 80 kPa. The cyclic shear loading rates for silica silt specimens included 1, 0.2, 0.1, and 0.01 Hz, respectively. Likewise, the loading rates for Tieliku specimens were 1, 0.1, and 0.01 Hz. The permeability of three types of specimens from triaxial permeability tests are shown in Table 2.

4 Test Results

4.1 Effect of Loading Rates to Cyclic Strength of Silica Silt

The coefficient of permeability of silica silt specimen measured through the triaxial permeability test was 1.55×10^{-3} cm/s, which is about the same as the one of typical sandy soils. Table 3 shows the number of load cycles of triaxial cyclic tests at different loading rates for the silica silt. The corresponding data points shown in Fig. 2 lead to a single liquefaction resistance curve. This indicates that the loading rates do not have significant influence on the cyclic strength of silica silt specimens.

Table 3 Cyclic triaxial test results for silica silt specimens

| Loading rate (Hz) | Test number | Cyclic stress R ratio | Number of load cycles to reach zero effective stress |
|-------------------|-------------|-------------------------|--|
| 1 | QPS11 | 0.136 | 10.2 |
| 1 | QPS12 | 0.132 | 13.1 |
| 1 | QPS13 | 0.116 | 22.1 |
| 1 | QPS14 | 0.087 | 40.1 |
| 0.2 | QPS15 | 0.138 | 11.1 |
| 0.1 | QPS16 | 0.135 | 13.0 |
| 0.1 | QPS17 | 0.149 | 5.1 |
| 0.01 | QPS18 | 0.145 | 6.0 |

Note Each specimen controlled the initial void ratio of 0.86, and the effective confining pressure of 80 kPa

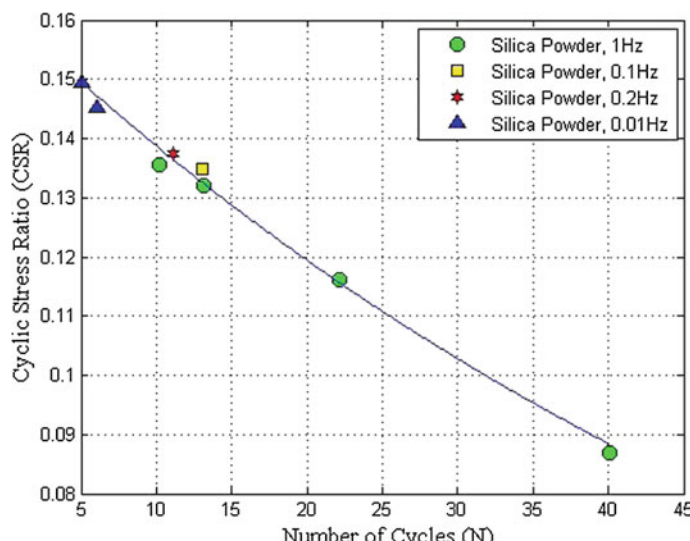


Fig. 2 Relationship between cyclic stress ratio and number of load cycles for silica silt specimen at various loading rates

4.2 Effect of Loading Rates to Cyclic Strength of Tieliku Silt

Table 4 summarizes the cyclic triaxial test results on Tieliku silt specimens with a PI of 8. As shown in Fig. 3, it indicates that the loading rates have a major influence on the cyclic strength of Tieliku silt. At the same cyclic stress ratio, the higher loading rate was applied, the stronger the specimen exhibited. There was a trend that with the increasing of the loading rate, the cyclic strength is getting higher as shown in Fig. 4.

Table 4 Cyclic triaxial test results for Tieliku silt specimens

| Loading rate (Hz) | Test number | Cyclic stress R ratio | Number of load cycles to reach zero effective stress |
|-------------------|-------------|-------------------------|--|
| 1 | TLKC25F | 0.173 | 57.3 |
| 1 | TLKC25G | 0.149 | 142.3 |
| 0.1 | TLKC25A | 0.198 | 12.7 |
| 0.1 | TLKC25B | 0.193 | 15.2 |
| 0.1 | TLKC25C | 0.175 | 22.2 |
| 0.1 | TLKC25D | 0.172 | 31.2 |
| 0.1 | TLKC25E | 0.168 | 24.3 |
| 0.01 | TLKC25F | 0.173 | 21.1 |

Note Each specimen controlled the initial void ratio of 0.86, and the effective confining pressure of 80 kPa

Fig. 3 Relationship between cyclic stress ratio and number of load cycles for Tieliku silt specimen at various loading rates

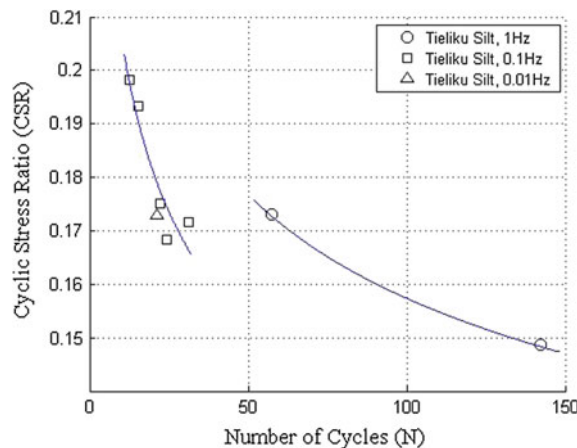
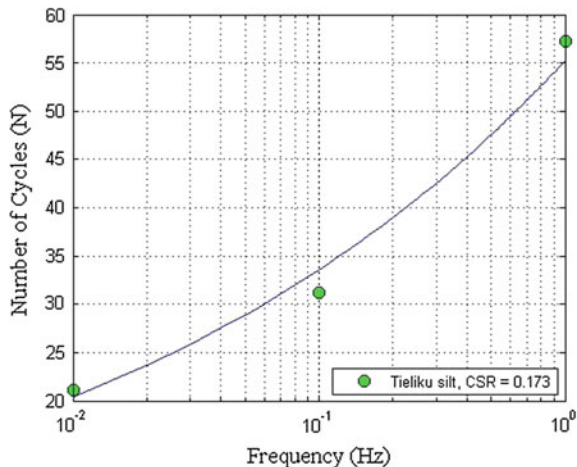


Fig. 4 Relationship between number of load cycles and loading rates for Tieliku silt specimen



5 Discussion and Conclusion

From the test results of this study, there was only a single liquefaction resistance curve of silica silt at various loading rates. It indicated that the loading rates do not have significant influence on the cyclic strength of silica silt. In contrast to silica silt, the liquefaction resistance curves of Tieliku silt will be dominated by loading rates. This result indicates that the loading rates have a major influence on the cyclic strength of Tieliku silt.

The coefficient of permeability is likely to be a primary factor to exhibit different trends of test results at various loading rates. The coefficient of permeability of silica silt specimen is about the same as the one of typical sandy soils. That is to say, silica silt is a permeable soil, so the influence of loading rate on its cyclic strength is insignificant. The Tieliku silt is different from silica silt. The coefficient of permeability of Tieliku silt is about one-fourth of silica silt, which makes that the loading rate has significant impact.

It is concluded that the loading rates have a minimum effect on the cyclic strength of permeable silica silt, while the loading rates have a significant influence on the cyclic strength of less permeable Tieliku silt. Moreover, the cyclic shear strength of the Tieliku silt is proportional to the loading rates.

References

Andrew DCA, Martin GR (2000) Criteria for liquefaction of silty soils. In: Proceedings of 12th world conference on earthquake engineering, No. 0312
 Bray JD, Sancio RB (2006) Assessment of the liquefaction susceptibility of fine-grained soils. J Geotech Geoenvir Eng 132(9):1165–1177

Lee KL, Fitton JA (1969) Factors affecting the cyclic loading strength of soils. In: *Vibration effects of earthquakes on soils and foundations*, ASTM STP450, American Society for Testing and Materials, pp 71–95

O-hara S, Kotsubo S, Yamamoto T (1985) Pore pressure developed in saturated sand subjected to cyclic shear stress under partial-drainage conditions. *Soils Found* 25(2):45–56

Peacock WH, Seed HB (1968) Sand liquefaction under cyclic loading simple shear conditions. *J Soil Mech Found Div* 94(3):689–708

Seed HB, Idriss IM (1982) Ground motions and soil liquefaction during earthquakes. In: *Engineering monograph on earthquake criteria, structural design, and strong motion records*. EERI

Umeshara Y, Zen K, Hamada K (1985) Evaluation of soil liquefaction potentials in partially drained conditions. *Soils Found* 25(2):57–72

Wong RT, Seed HB, Chan CK (1975) Cyclic loading liquefaction of gravelly soils. *J Geotech Eng* 101(6):571–583

Yoshimi Y, Oh-oka H (1975) Influence of degree of shear stress reversal on the liquefaction potential of saturated sands. *Soils Found* 15(3):27–40

Effect of Gravel Content on Saturated Hydraulic Conductivity in Sand

Tsung-Yuan Wang, Li-Ling Lin and Yi-Zhi Tsai

Abstract The influence of the gravel content of gravelly soils on their hydraulic conductivity was studied. The experiment samples with volume percentage of gravel from 0 to 50 % were tested using constant head tests to measure the saturated hydraulic conductivity. Generally, the saturated hydraulic conductivity is positively correlated to the volume percentage of gravel. Moreover, the ratio of macroporosity to total porosity is increased with increasing gravel content. That is, the saturated hydraulic conductivity of gravelly soils is positively correlated to the ratio of macroporosity to total porosity.

Keywords Volume percentage of gravel content · Macroporosity · The ratio of macroporosity to total porosity f^* · Debris flow · Porosity

1 Introduction

The occurrences of debris flows were common during the rainy season in Taiwan. Great efforts were devoted to reduce the risk of debris flows. Soil hydraulic conductivity is one of the critical factors of the value of hydraulic conductivity. The texture of soils influent is permeable or not (Klute and Dirksen 1986). For impermeable soils, the runoff will easily increase. Contrary, the pore pressure will easily develop if the soils are permeable and the debris could become unstable.

If the rain is hard to infiltrate to soil, it would become runoff and takes the rock and soil away on soil surface. However, if the rain infiltrates easily, the soil mass becomes heavy and leads to collapse.

T.-Y. Wang (✉) · L.-L. Lin · Y.-Z. Tsai

Department of Soil and Water Conservation, National Chung Hsing University,
402, Taichung, Taiwan, ROC

e-mail: ha5408740@gmail.com

The heterogeneous soil included rocks, roots, insects, and so on. That would influence the value of hydraulic conductivity. However, the laboratory experiment is hard to reappear field situation. Therefore, this research is focused on how the gravel content influences the saturated hydraulic conductivity.

2 Materials and Methods

2.1 Experiment Design

The studied soils were sampled from Happen Nature Reserve and it crosses the Wulai Township and Yuanshan Township, Taipei Taiwan. The sand properties are shown in Table 1.

The diameter of gravel used in this research was between 3.175 and 3.35 mm and the density of gravel was 2.83 g/cm³. In order to figure out the relationship between the volume percentage of gravel and saturated hydraulic conductivity, we used several volume percentage of gravel about 0, 5, 15, 30, 40, 50 % and used gravel density and soil column volume to calculate the weight of gravel the experiment need.

And the soil bulk density was 1.45 g/cm³. We restricted soil bulk density at 1.45 g/cm³ in order to make sure that the total soil column bulk density was only influenced by the gravel we added.

The texture of column we used was Acrylic and its height is 3 cm, with a diameter 4.865 cm and the volume 55.77 cm³.

In order to pack the gravel into soil column homogeneously, we speared out the sand soil on a plate and put the gravel on the surface randomly. Also, we used small spoon to sprinkle the soil and gravel into the column and compacted with thin layers (Oliviera et al. 1996).

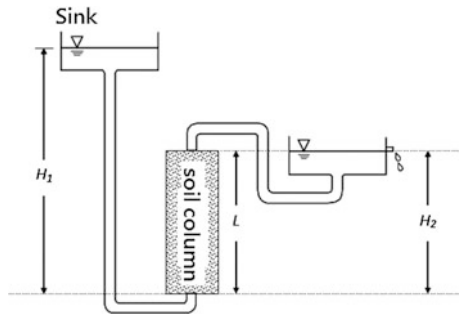
The constant head measurement system design showed in Fig. 1 (Tsai 2011). To ensure the soil column fully saturated, we raised the hydraulic head three times and waited about an hour to wash out the air in the pores.

According to communicating tube rule and Darcy's Law, we measured the water volume that flowed out from the soil column in unit time, and calculated saturated hydraulic conductivity of columns by Darcy law.

Table 1 The properties of soil and added gravel

| Soil sample | Sand (%) | Silt (%) | Clay (%) | Soil texture | Particle density (g/cm ³) | Gravel diameter (mm) |
|-----------------------|----------|----------|----------|--------------|---------------------------------------|----------------------|
| Happen nature reserve | 89.23 | 6.57 | 4.20 | Sand | 2.74 | 3.175–3.35 |

Fig. 1 Constant head measurement tests for measuring the soil hydraulic conductivity



2.2 Calculation of Saturated Hydraulic Conductivity, Total Porosity, Macroporosity, the Ratio of Macroporosity to Total Porosity

2.2.1 Saturated Hydraulic Conductivity

The hydraulic conductivity can be calculated based on Darcys Law (Darcy 1856) as follows:

$$K_s = \frac{Q \times L}{\Delta H \times A} \quad (1)$$

where K_s (cm/h) is saturated hydraulic conductivity. Q (cm³/h) is flow rate, L (cm) is the length of soil column, A is cross-sectional area of soil column, ΔH (cm) is hydraulic head difference. And flow rate Q is given by (2)

$$Q = V/t \quad (2)$$

where V is flow volume (cm³), t is flow time(h). We can get saturated hydraulic conductivity value by measuring the volume of flow and calculated by (2).

2.2.2 Total Porosity, Macroporosity, and the Ratio of Macroporosity to Total Porosity

The decreasing total porosity was not the main factor of decreasing saturated hydraulic conductivity but the influence of macroporosity was much important (Wann 1968).

Although total porosity was not the main influence of saturated hydraulic conductivity, it affected the moisture content of saturated soil (Hillel 1980, Wann 1987). In addition, macroporosity is a part of total porosity. Hence total porosity is an important factor.

Macroporosity is the ratio of the volume of macropores to the total volume, where macropores mean the volume of pores inside the soil column which are unable to keep the water under the influence of gravity. The formula is written as

$$f_{\text{ma}} = \left(\frac{W_{1/3\text{bar}}}{\rho_w} \right) / V_t = \frac{V_{\text{ma}}}{V_t} \quad (3)$$

where f_{ma} (cm^3/cm^3) is macroporosity, $W_{1/3\text{bar}}$ (g) is the water weight that the column drained under the pressure at 1/3 bar, ρ_w (g/cm^3) is water density, V_{ma} (cm^3) is the volume of macropores.

By pressure plate drainage experiment (Lin and Dong 1996), put the saturated column into pressure pot and keep the pressure under 1/3 bar and wait about 2–3 days. After three days, weigh the column. $W_{1/3\text{bar}}$ is saturated column weight minus the column weight under 1/3 bar And we can get macroporosity value by formula (3).

The ratio of macroporosity to total porosity f^* is macroporosity divided by total porosity and is given by formula (4)

$$f^* = \frac{f_{\text{ma}}}{f} \times 100 \% \quad (4)$$

3 Results and Discussion

3.1 The Relationship Between Volume Percentage of Gravel and Macroporosity

The bulk densities, porosities, and permeability of the soil columns with different gravel content are showed in Table 2. Because the gravels replace the sand soil, the weight of column increased. Therefore the bulk density increased.

The gravel is a low-level weathered structure. There are no pores in gravels. So the total porosity decreased when the gravels pack into the column (Table 2).

Table 2 Gravel contents and its porosities

| Volume percentage of gravel (%) | Bulk density (g/cm^3) | Total porosity f (%) | Macroporosity f_{ma} (%) | The ratio of macroporosity to total porosity f^* (%) | The saturated hydraulic conductivity (cm/h) |
|---------------------------------|---|------------------------|-----------------------------------|--|---|
| 0 | 1.45 | 39.65 | 21.93 | 55.31 | 43.52 |
| 5 | 1.52 | 38.46 | 24.64 | 64.07 | 33.12 |
| 15 | 1.66 | 32.16 | 19.90 | 61.87 | 46.75 |
| 30 | 1.86 | 30.52 | 19.81 | 64.90 | 51.17 |
| 40 | 2.00 | 28.74 | 20.48 | 71.26 | 91.20 |
| 50 | 2.14 | 29.79 | 22.16 | 74.39 | 120.37 |

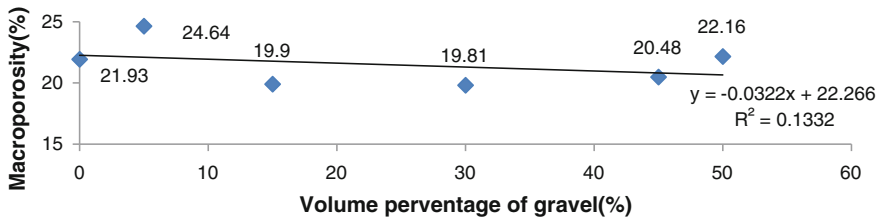


Fig. 2 The relationship between macroporosity and volume percentage of gravel

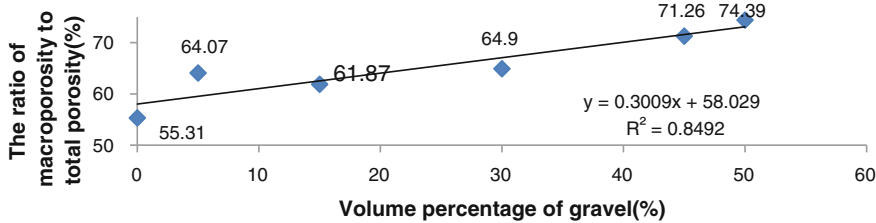


Fig. 3 The relationship between the volume percentage of gravel and the ratio of macroporosity to total porosity

The macroporosity is kept in a constant value about 20 %, shown in Fig. 2. We speculated that the diameter of gravel this research used (3.175–3.35 mm) is close to the boundary between the sand and gravel (2 mm), and we packed the column homogeneously, that causes the sand filled into the macropores. In the other hand, when the gravel is added, macropores will increase. That the reason why macroporosity does not increase.

Figure 3 showed that with the increasing gravel content, the ratio of the macroporosity to the total porosity f^* is increased. It indicated that although the total pores decreased with the gravels added, the macropores still increased slightly. Therefore the macroporosity has a constant value (Fig. 2).

3.2 The Relationship Between Saturated Hydraulic Conductivity, Macroporosity, and Gravel Content

From Figs. 3 and 4, we can observe that the f^* and saturated hydraulic conductivity is positively correlated with volume percentage of gravel. That is, the saturated hydraulic conductivity of the tested samples is increased with increasing f^* . It also indicated that the increased macropores lead to the increase in saturated hydraulic conductivity, as shown in Fig. 5.

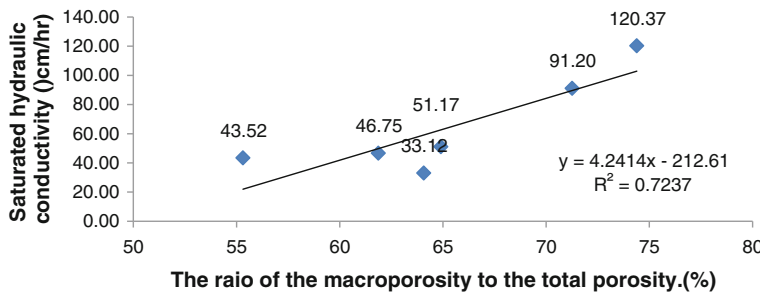


Fig. 4 The relationship between saturated hydraulic conductivity and the ratio of macroporosity to total porosity

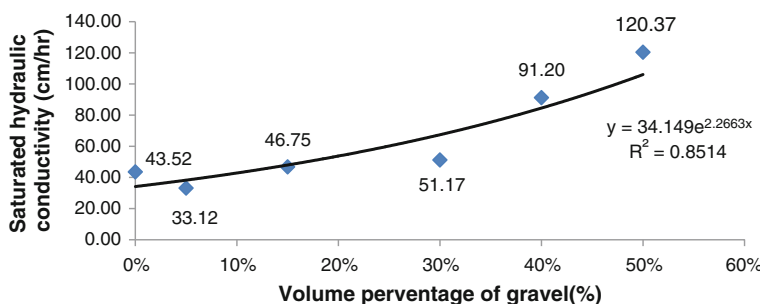


Fig. 5 The relationship between volume percentage of gravel and saturated hydraulic conductivity

4 Conclusion

Soil contains gravel will affect saturated hydraulic conductivity, and it is positively correlated with the volume percentage of gravel, meaning that with the higher percentage of gravel, saturated hydraulic conductivity is an increasing trend.

When the soil mixed with the gravel, the bulk density increased, the total porosity decreased, but f^* increased. It means that the increasing volume percentage of gravel comes with the f^* increased.

Therefore, the volume percentage of gravel increased leading to f^* increased, and the saturated hydraulic conductivity increased too.

References

Darcy H (1856) Les Fontaines Publique de la ville de Dijon. Dalmont, Paris
 Hillel D (1980) Fundamentals of soil physics (Hsin-Sen Wan Trans (1987)). Academic Press, New York

Klute A, Dirksen C (1986) Hydraulic conductivity and diffusivity: laboratory methods. In: Klute A (ed) Methods of soil analysis. Part 1. Monograph 9. American Society of Agronomy, Madison, WI

Lin L-L, Dong X-P (1996) Soil physic experiment handbook. Department of Soil and Water Conservation, National Chung Hsing University, Taiwan, ROC (in Chinese)

Oliviera IB, Demond AH, Salehzadeh A (1996) Packing of sands for the production of homogeneous porous media. *Soil Sci Soc Am J* 60:49–53

Tsai Y-Z (2011) Practice of special topics in soil science lecture. Department of Soil and Water Conservation, National Chung Hsing University, Taiwan, ROC (in Chinese)

Wann SS (1968) Soil water and its movement. *J Soil Water Conserv* 1(1):19–25 (in Chinese)

Wann SS (1987) Principle of soil physic. Taiwan, National Translation and Compilation Center (in Chinese) (Hillel D (1980) Fundamentals of soil physics)

Effects of Overconsolidation, Cement Stabilisation, and Unsaturation on the Liquefaction Resistance of Urayasu Sand

Shotaro Hagiwara, Yoshimichi Tsukamoto and Shohei Kawabe

Abstract Following the 2011 Great East Japan Earthquake and its aftershocks, soil liquefaction and associated phenomena have been widely observed at reclaimed lands along Tokyo bay. Enormous amounts of sand boils were erupted in the city of Urayasu. It is known that the fines content of reclaimed liquefiable soils in Urayasu city varies significantly from 10 to 40–50 %. In the present study, the soil sample erupted as sand boils was retrieved from the city of Urayasu, and multiple series of saturated undrained cyclic triaxial tests are conducted to obtain the liquefaction resistance of fines-containing sand and clean sand without fines. The physical effects of overconsolidation as well as the chemical effects of loosely mixed cement stabilisation are especially examined. In addition, a series of unsaturated undrained cyclic triaxial tests are conducted to obtain the cyclic resistance of fines-containing sand as well as clean sand without fines. The effects of fines on the cyclic resistance of unsaturated Urayasu sand are examined. The effects of overconsolidation, loosely mixed cement stabilisation and unsaturation on the liquefaction resistance of Urayasu sand are then compared and discussed in detail.

Keywords Liquefaction resistance • Urayasu sand • Overconsolidation • Cement stabilisation

S. Hagiwara · Y. Tsukamoto (✉)

Department of Civil Engineering, Tokyo University of Science,
2641, Yamazaki, Noda, Chiba 278-8510, Japan
e-mail: ytsoil@rs.noda.tus.ac.jp

S. Kawabe

National Agriculture and Food Research Organization, Tsukuba
Ibaraki 305-8609, Japan
e-mail: skawabe@affrc.go.jp

1 Introduction

Following the 2011 Great East Japan Earthquake and its aftershocks, soil liquefaction and associated phenomena have been widely observed at reclaimed lands along Tokyo bay (Yasuda et al. 2012). Enormous amounts of sand boils were erupted in the city of Urayasu in Chiba. It is known that the fines content of reclaimed liquefiable soils in Urayasu city varies significantly from 10 to 40–50 %. There can be several methods to improve the susceptibility of soils to liquefaction. One method is certainly to physically increase the liquefaction resistance of soils by densification. Another method is to chemically improve it by cement stabilisation. There can be another method to improve it by making soils unsaturated. Such physical effects can be achieved in laboratory triaxial tests by overconsolidating triaxial specimens during consolidation, while chemical effects can be achieved by loosely mixing soil samples with cement.

In the present study, the soil sample erupted as sand boils in the city of Urayasu was retrieved, and a series of overconsolidated triaxial soil specimens as well as loosely cemented triaxial soil specimens are prepared. Multiple series of saturated undrained cyclic triaxial tests are then conducted to obtain the liquefaction resistance of Urayasu sand. In addition, another series of unsaturated undrained cyclic triaxial tests are conducted to examine the cyclic resistance of fines-containing Urayasu sand as well as clean sand without fines. The effects of fines on the cyclic resistance of unsaturated Urayasu sand are then examined.

2 Soil Samples and Liquefaction Resistance

Two soil samples of Urayasu sand are prepared. One sample is a silty sand containing fines of $F_c = 40.1\%$. The other sample is clean sand prepared by excluding fines, and therefore contains no fines. The physical properties and grain size distributions of the two soil samples thus prepared are shown in Table 1 and Fig. 1. For the silty sand sample with a fines content of $F_c = 40.1\%$, the soil specimens with relative densities of $D_r = 80$ and 60 % are prepared by the method of wet tamping. For the clean sand sample with $F_c = 0\%$, the soil specimens with a relative density of $D_r = 80\%$ are also prepared by the method of wet tamping. A series of saturated and isotropically consolidated undrained cyclic triaxial tests are then conducted.

The test results for the silty sand and clean sand specimens are shown in Figs. 2 and 3, in the plots of effective stress path, $p'-q$, and deviator stress q –axial strain ε_a .

Table 1 Physical properties of Urayasu sand

| | | |
|---|------|------|
| Fines content F_c (%) | 40.1 | 0 |
| Specific gravity, ρ_s (g/cm ³) | 2.71 | 2.70 |
| Maximum void ratio e_{\max} | 1.45 | 1.46 |
| Minimum void ratio e_{\min} | 0.85 | 0.89 |

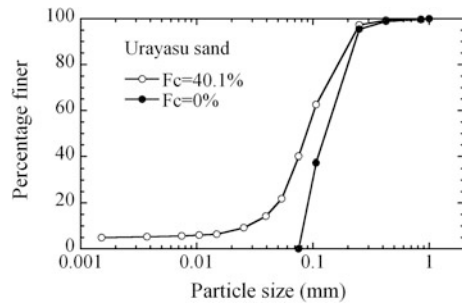


Fig. 1 Grain size distributions of Urayasu sand

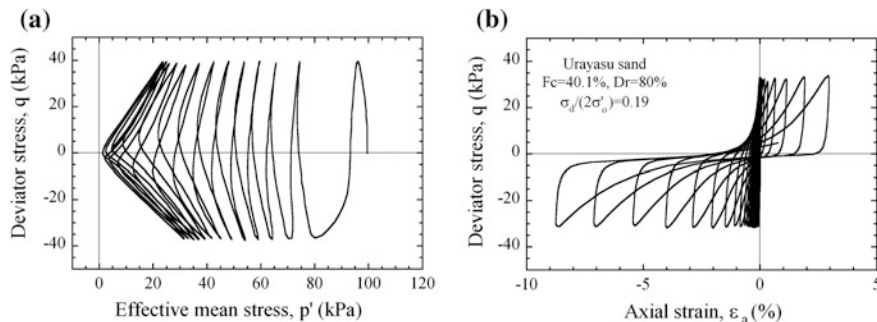


Fig. 2 Results of undrained cyclic triaxial test, (Urayasu sand, $F_c = 40.1\%$, $D_r = 80\%$), **a** effective stress path $p'-q$, **b** deviator stress q -axial strain ε_a

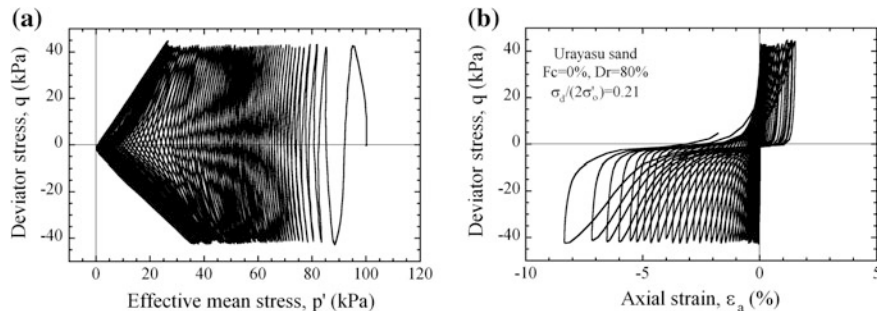
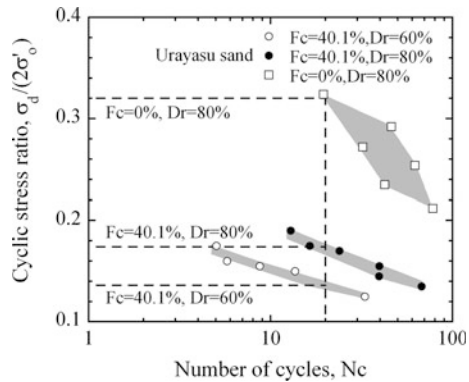


Fig. 3 Results of undrained cyclic triaxial test, (Urayasu sand, $F_c = 0\%$, $D_r = 80\%$), **a** effective stress path $p'-q$, **b** deviator stress q -axial strain ε_a

It is found in the results of silty sand that the excess pore pressure tends to develop more progressively than clean sand. It is also found for silty sand that after achieving the phase of cyclic mobility, the axial strain tends to develop towards extension as well as compression. On the other hand, for clean sand, the

Fig. 4 Plots of cyclic stress ratio $\sigma_d/(2\sigma'_o)$ against number of cycles N_c , (Urayasu sand)

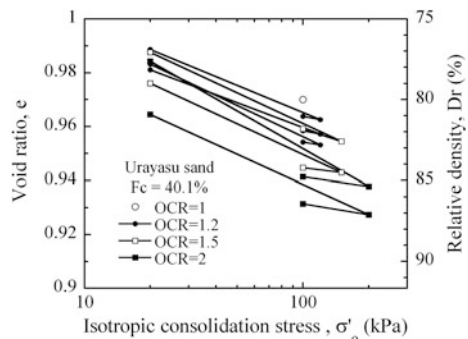


development of axial strain towards compression tends to be suppressed and it tends to develop towards extension only. The plots of cyclic stress ratio, $\sigma_d/(2\sigma'_o)$, against number of cycles N_c necessary to cause the double amplitude axial strain of $DA\epsilon_a = 5\%$ are summarised in Fig. 4. It is typical to see that the liquefaction resistance for laboratory constituted clean sand is greater than that for silty sand.

3 Physical Effects of Overconsolidation

In order to achieve different degrees of overconsolidation in laboratory triaxial soil specimens, different consolidation stress histories are applied as shown in Fig. 5. The soil sample used herein is a silty sand with $F_c = 40.1\%$. All the soil specimens are first isotropically consolidated to $\sigma'_o = 100$ kPa, with the relative density of $D_r = 80\text{--}85\%$. For the soil specimens denoted with $OCR = 1.2$, all round isotropic consolidation stress σ'_o is increased up to 120 kPa, and then reduced down to 100 kPa. For the soil specimens denoted with $OCR = 1.5$ and 2, all round isotropic

Fig. 5 Plots of void ratio against isotropic consolidation stress σ'_o during overconsolidation, (Urayasu sand, $F_c = 40.1\%$)



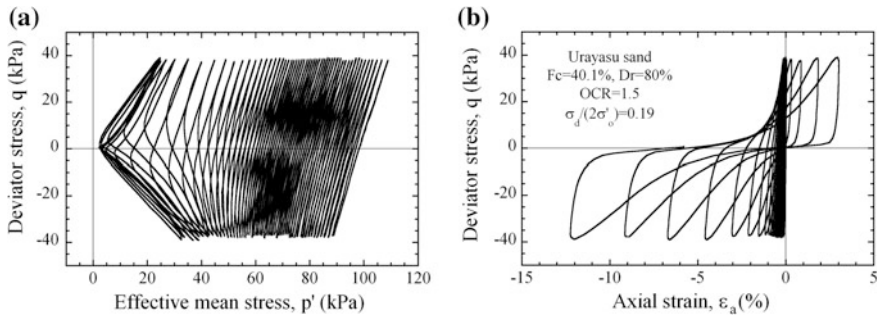
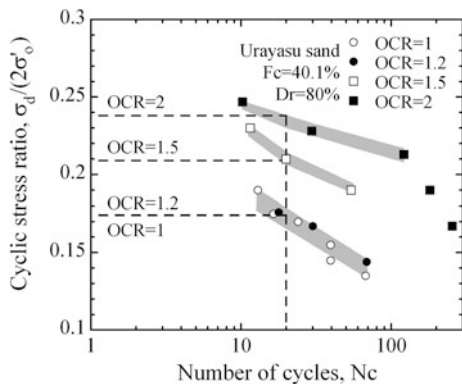


Fig. 6 Results of undrained cyclic triaxial test, (Urayasu sand, $F_c = 40.1\%$, $D_r = 80\%$, $OCR = 1.5$), **a** effective stress path p' - q , **b** deviator stress q -axial strain ϵ_a

consolidation stress σ'_o is increased up to 150, and 200 kPa, respectively, and then reduced down to 100 kPa. It is therefore appropriate to point out that the effects of overconsolidation adopted in the present study apparently includes the rearrangement of soil particles within soil fabric structures, as well as the changes in the void ratio during all round isotropic overconsolidation stress history.

The test results for the soil specimens with $OCR = 1.5$ are shown in Fig. 6. It is found that the development of excess pore pressure in the overconsolidated silty sand tends to be suppressed compared with the normally consolidated silty sand shown in Fig. 2. It is also found that it is after achieving the phase of cyclic mobility that the axial strain tends to develop towards extension as well as compression. The plots of cyclic stress ratio, $\sigma_d/(2\sigma'_o)$, against number of cycles N_c necessary to cause the double amplitude axial strain of $DA\epsilon_a = 5\%$ are summarised in Fig. 7. It is seen that the liquefaction resistance tends to increase after the value of OCR becomes larger than 1.5.

Fig. 7 Plots of cyclic stress ratio $\sigma_d/(2\sigma'_o)$ against number of cycles N_c , (overconsolidated Urayasu sand)



4 Chemical Effects of Loose Cement Stabilisation

Two series of loosely cemented silty sand are prepared in the present study. The soil sample used herein is also a silty sand with $F_c = 40.1\%$. The cement agent used is the ultra microfine cement having an average particle size of 1 micron. The ratios of water to cement content, w/c , are controlled, and the soil specimens with the relative density of $D_r = 80\%$ and values of $w/c = 1170\%$ and 2340% are prepared and left for a period of one month for underwater curing.

The test results for the soil specimens with $w/c = 1170\%$ are shown in Fig. 8. It is found that the development of excess pore pressure in the loosely cemented silty sand tends to be less suppressed compared with the overconsolidated silty sand shown in Fig. 6. The plots of cyclic stress ratio, $\sigma_d/(2\sigma'_0)$, against number of cycles N_c necessary to cause the double amplitude axial strain of $DA\epsilon_a = 5\%$ are summarised in Fig. 9. It is seen that the loosest cement stabilisation with $w/c = 2340\%$

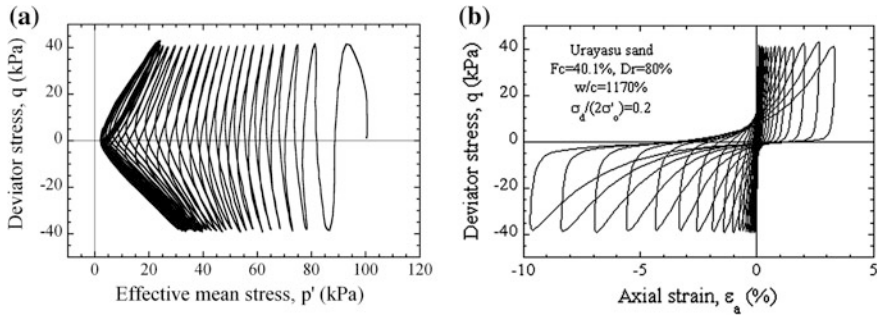
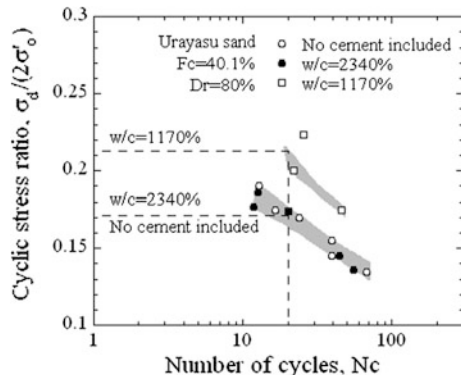


Fig. 8 Results of isotropically consolidated undrained cyclic triaxial test, (Urayasu sand, $F_c = 40.1\%$, $D_r = 80\%$, $w/c = 1170\%$), **a** effective stress path p' - q , **b** deviator stress q -axial strain ϵ_a

Fig. 9 Plots of cyclic stress ratio $\sigma_d/(2\sigma'_0)$ against number of cycles N_c , (loosely cemented Urayasu sand)



does not improve the liquefaction resistance, and it is when the value of w/c becomes 1170 % that the liquefaction resistance clearly increases.

5 Effects of Unsaturation

Another series of unsaturated cyclic triaxial tests are conducted. The two soil samples of silty sand and clean sand are used. The triaxial apparatus specially equipped for testing unsaturated soil specimens is used, which can control and monitor the pore air pressure through glass fibre papers, and also the pore water pressure through a ceramic disk. The soil specimens are prepared by the method of wet tamping and isotropically consolidated to 50 kPa. During the process of consolidation, the pore air pressure is left under ambient pressure, and the negative pore water pressure is gradually introduced into the soil specimens. The soil specimens with $D_r = 60\%$ and $S_r = 70\%$ are eventually prepared. Cyclic triaxial tests are then conducted with pore water and pore air valves closed. Herein, the remotely controlled solenoid valve is introduced for a pore air valve and placed close to the

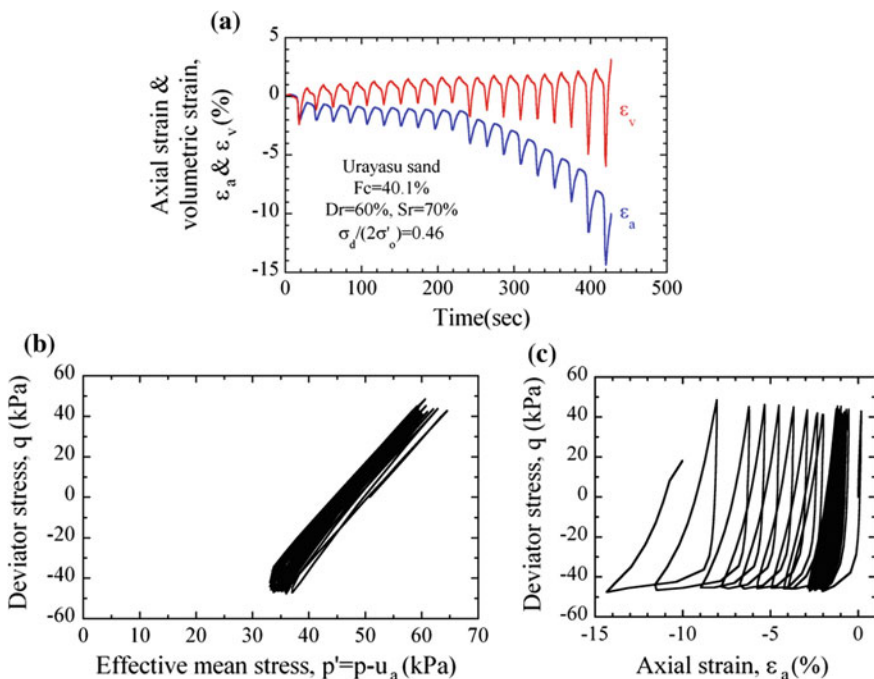


Fig. 10 Results of undrained cyclic triaxial test, (Urayasu sand, $F_c = 40.1\%$, $D_r = 60\%$, $S_r = 70\%$), **a** axial strain and volumetric strain ε_a & ε_v against time, **b** effective stress path $p'-q$, **c** deviator stress q -axial strain ε_a

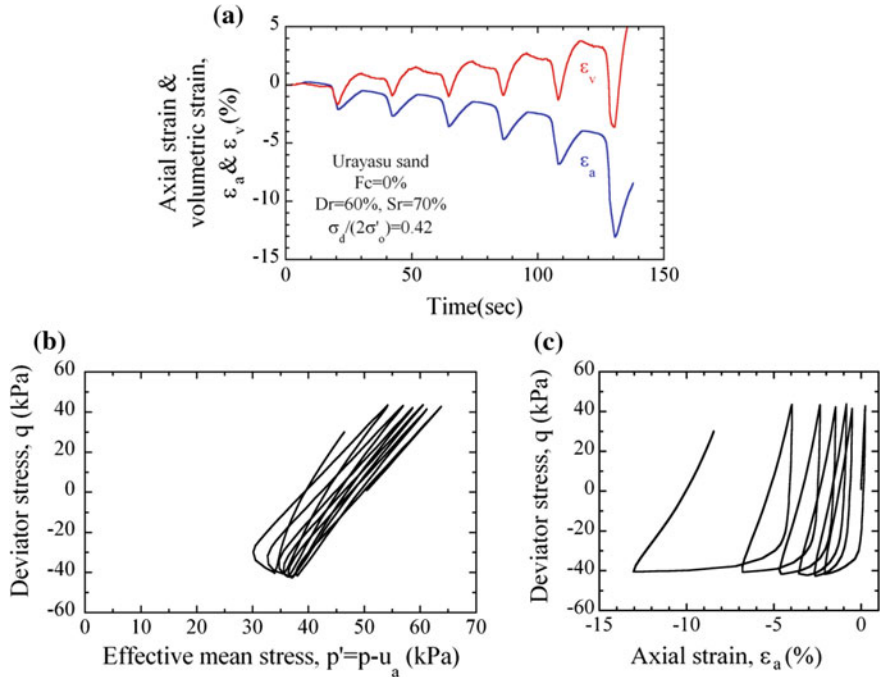


Fig. 11 Results of undrained cyclic triaxial test, (Urayasu sand, $F_c = 0\%$, $D_r = 60\%$, $S_r = 70\%$), **a** axial strain and volumetric strain ε_a & ε_v against time, **b** effective stress path p' – q , **c** deviator stress q –axial strain ε_a

top of soil specimens to reduce the effects of compressibility of air contained in the pore air tube.

The test results for silty sand and clean sand are shown in Figs. 10 and 11. It is found for clean sand that the volumetric strain tends to develop towards compression, which then contributes to the development of excess pore air pressure u_a , leading to the reduction in the effective mean stress $p' = p - u_a$, where p is the mean stress, $p = (\sigma_a + 2\sigma_h)/3$. Therefore, the effective stress path for clean sand easily touches upon the failure envelope, so develops more progressively the axial strain.

6 Comparisons of Improved Liquefaction Resistance

The effects of overconsolidation, loosely mixed cement stabilisation and unsaturation on the liquefaction (cyclic) resistance of Urayasu silty sand are compared as shown in Fig. 12, in the plots of liquefaction resistance against the values of OCR, c/w and S_r , respectively. Herein, the liquefaction resistance for saturated sands as well as the cyclic resistance for unsaturated sands, $\sigma_{d,l}/(2\sigma'_0)$, are determined as the

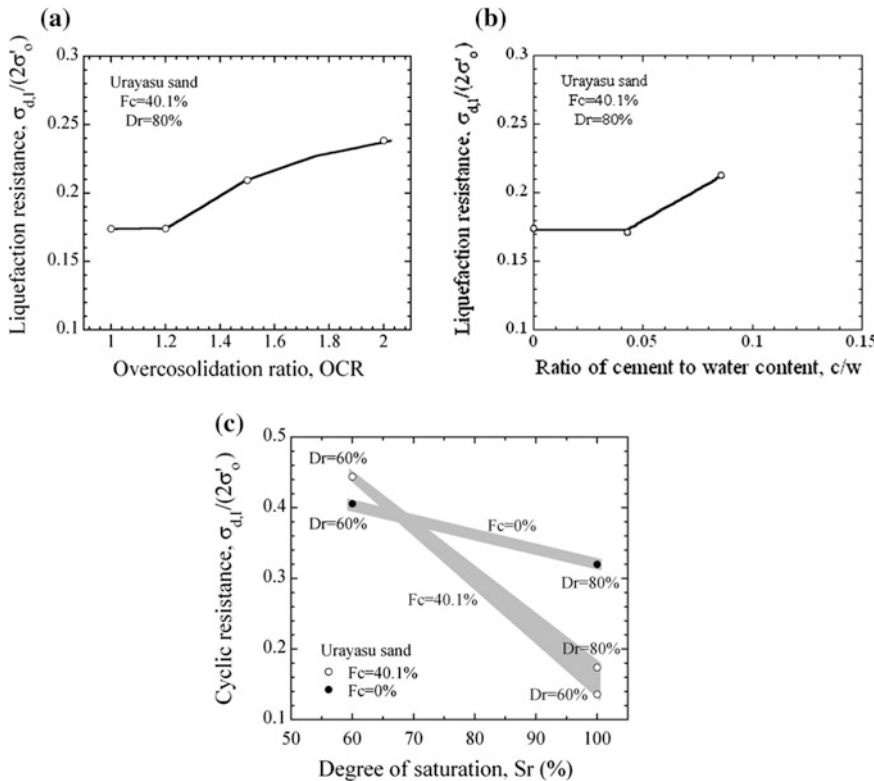


Fig. 12 Plots of liquefaction resistance $\sigma_{d,l}/(2\sigma'_o)$ against **a** overconsolidation OCR, **b** ratio of cement to water content c/w , **c** degree of saturation S_r

cyclic stress ratio, $\sigma_d/(2\sigma'_o)$, necessary to cause the double amplitude axial strain of $DA\epsilon_a = 5\%$ at the number of cycles equal to $N_c = 20$. In the ranges of values of OCR, c/w and S_r adopted in the present study, the cyclic resistance increases significantly for unsaturated Urayasu silty sand.

7 Conclusions

The effects of overconsolidation, loosely mixed cement stabilisation and unsaturation on the liquefaction resistance of Urayasu silty sand were examined based on the results of laboratory triaxial tests. Those physical and chemical effects are found to improve the liquefaction resistance substantially, though the effects of unsaturation significantly increase the cyclic resistance.

Acknowledgments The laboratory triaxial tests described in the present study were conducted with a help of students of Tokyo university of Science, Y. Takekawa and E. Matsuyama. The authors are grateful to their cooperation.

Reference

Yasuda S, Harada K, Ishikawa K, Kanemaru Y (2012) Characteristics of liquefaction in Tokyo Bay area by the 2011 Great East Japan earthquake. *Soils Found* 52(5):793–810

Part III
Landslides, Slope Failures
and Debris Flows

Loessial Landslides Induced by the Minxian–Zhangxian Ms6.6 Earthquake of China in 2013

L.M. Wang, Q. Wang, Z.J. Wu and A.L. Che

Abstract The characteristics of the loessial landslides induced by the Minxian–Zhangxian 6.6 earthquake, Gansu province, China in 2013 were studied based on field investigation, laboratory tests and analysis. The influence of heavy rainfall before the earthquake on seismic safety of loessial slopes was analyzed. The mechanism of a large scale of loessial landslide in Yongguang village triggered by liquefaction during the shaking, which killed 12 people, was revealed. Moreover, the method of evaluating the maximum sliding distance of loessial slopes under the effect of earthquakes was provided based on the data on 86 loessial landslides induced by earthquakes. Furthermore, the strategy of preventing and mitigating disasters caused by seismic loessial landslides was proposed.

Keywords Loess · Landslide · Earthquake · Rainfall · Mechanism · Sliding distance evaluation

1 Introduction

A strong earthquake with a magnitude of Ms6.6 occurred in the boundary between Minxian county and Zhangxian county in Gansu province, China on July 22, 2013, which caused 95 people dead, 2414 people injured and an economic loss of more

L.M. Wang (✉) · Q. Wang · Z.J. Wu
Earthquake Administration of Gansu Province, No. 450,
Donggangxi Road, Lanzhou 730000, China
e-mail: wanglm@gssb.gov.cn

L.M. Wang · Q. Wang · Z.J. Wu
Lanzhou Institute of Seismology, China Earthquake Administration,
No. 450, Donggangxi Road, Lanzhou 730000, China

A.L. Che
Shanghai Jiaotong University, No. 800, Dongchuan Road,
Shanghai 200030, China
e-mail: alche@sjtu.edu.cn

than US\$5 billion. The earthquake-affected area is located in the junction of the Loess Plateau, Qinghai–Tibet Plateau and Qinling Mountains. Totally there were at least 2330 landslides triggered by the earthquake, of which more than 600 landslides and collapses occurred in loessial deposit. These landslides buried villages, blocked roads and damaged power supply and communication cables (Wang and Wu 2013; Xu et al. 2013).

Loess is a special porous soil with weak cohesion. It widely distributed in north China, especially in the Loess Plateau of China, where loess deposited in different periods during the quaternary (Q1, Q2, Q3, and Q4) with a thickness ranging from tens of meters to more than 500 m, and strong earthquakes occur frequently. Loessial landslides are one of major geotechnical disasters in the Loess Plateau of China. They are mainly caused by rainfall and earthquake, which caused more than 1 million people death and inestimable economic loss (Wang et al. 2003).

In this paper, the distribution and characteristics of the earthquake-induced landslides were introduced. The large-scale loessial landslide in Yongguang village was investigated. Dynamic triaxial liquefaction tests on the loess samples taken from the Yongguang village were performed. Based on the test results and field investigation, the mechanism of the loessial landslide in Yongguang village was analyzed. Meanwhile, a method of evaluating the maximum sliding distance of loessial slopes under the effect of earthquakes was provided. Furthermore, a strategy for preventing and mitigating disasters caused by seismic loessial landslides was proposed.

2 Field Investigation, Laboratory Tests, and Analysis

2.1 *Field Investigation of the Loessial Landslides*

The intensity in the meizoseismal zone of the earthquake is VIII degree in a shape of oval along the seismic fault with the long axis of 40 km and short axis of 21 km. For VII degree intensity zone, the long axis is 87 km and short axis 59 km. The area with seismic intensity of VI–VIII is 16,432 km², which is mainly located in a loessial mountainous region of southwestern Loess Plateau with an elevation of 2207–3340 m. Disastrous landslides have developed in loessial deposit, including soil sliding, collapse and mudflow. The dense area of landslides, 30 km long and 8 km wide, is located in zones of VIII and VII seismic intensity along the seismic fault (Fig. 1). Most of the landslides were triggered by PGA of 0.12–0.2 g in the area with the elevation of 2400–2600 m and a slope angle of 10°–20°. Loessial landslides and disasters caused by landslides is shown in Fig. 2.

A large-scale mudflow with a volume of 420,000 m³ was induced in liquefied loessial deposit of Q₃ during the earthquake, which killed 12 people in Yongguang village, Minxian County. The mudflow, which was 100 m wide and 30 m thick slid

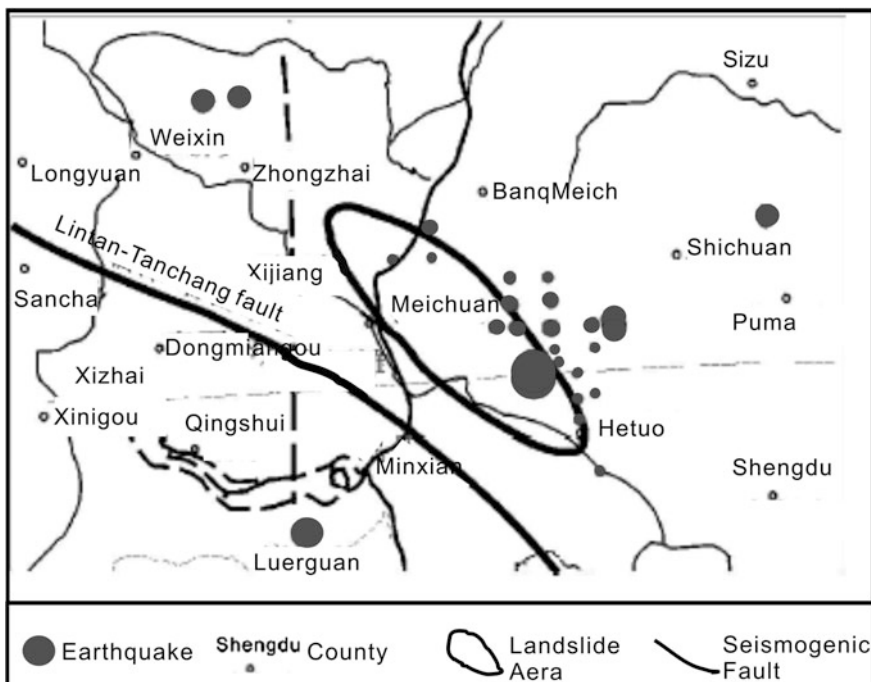


Fig. 1 Distribution of landslides induced by the Minxian–Zhangxian 6.6 earthquake



Fig. 2 Loessial landslides and destroyed houses by landslides during the Minxian–Zhangxian 6.6 earthquake

for 1 km long along a valley with an average slope of 18° shown in Fig. 3. A spring was found in the back edge of landslide, which had almost saturated the slope soil due to persistent rainfall before the earthquake. Liquefaction developed in loess deposit with high water content during the earthquake. Liquefied loessial deposit flowed easily along a valley under the effect of shaking and gravity.

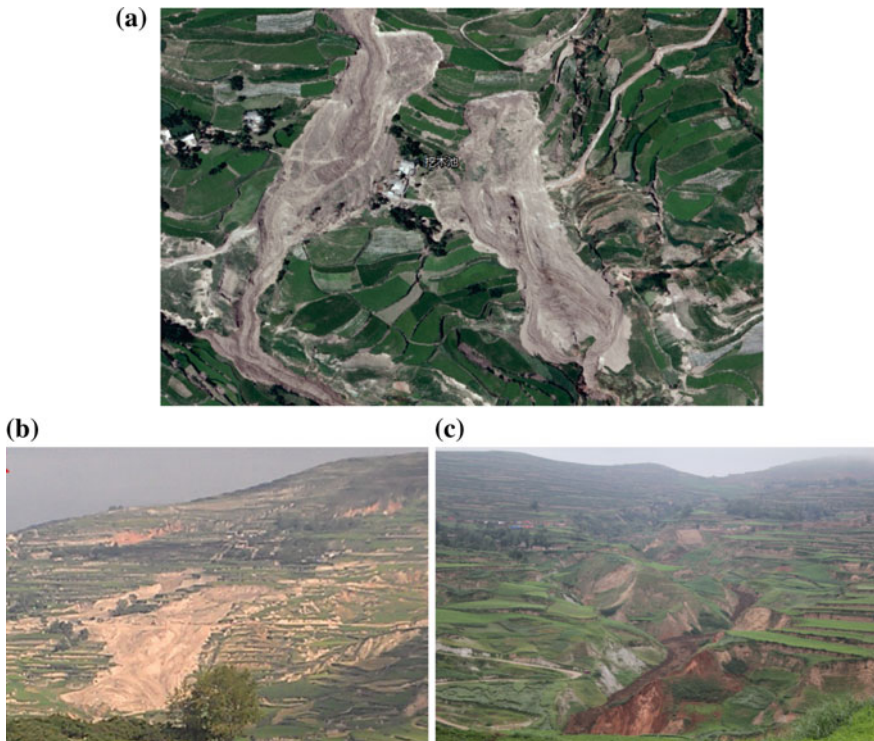


Fig. 3 The landslide in Yongguang village, Minxian County. **a** The aerial image. **b** The main body. **c** Mudflow

2.2 *Laboratory Test*

2.2.1 Samples and Apparatus

The loess samples were taken from different sites within the loessial landslide in Yongguang village. All of the samples are Malan loess formed in Quaternary period (Q₃). The physical parameters are shown in Table 1.

A hollow cyclic apparatus typed WF-12440 was used to perform the dynamic triaxial test on the loessial specimens.

Table 1 Parameters of loess samples

| Sample | ρ (g/cm ³) | ρ_d (g/cm ³) | ω (%) | e |
|--------|-----------------------------|-------------------------------|--------------|-------|
| YG-2 | 2.01 | 1.61 | 24.53 | 0.683 |

2.2.2 Test Methods (Li 1990)

The test methods followed the Chinese code “Specification of soil test (SL237-1999).” The loessial specimens are cylindrical in shape with 50 mm diameter and 100 mm height. The back pressure method was used to saturate the specimens, which may saturate loessial specimens with a saturation degree of more than 90 % with the residual strain less than 1 %. The saturation specimens were consolidated isotropically under consolidation stress of 138 kPa, which simulates the overburden pressure. After finishing the consolidation, the dynamic loading of equivalent sinusoidal wave with 1 Hz frequency was applied on the specimens.

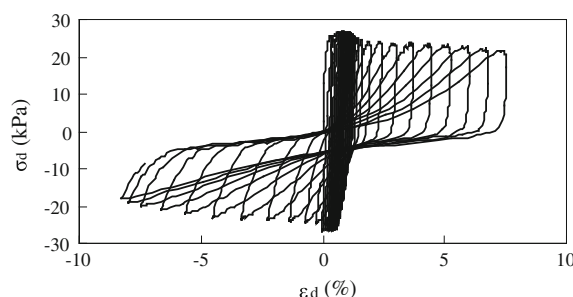
Based on the previous study carried by the authors, two standards of loess liquefaction failure were proposed: if the pore water pressure ratio $U_d/\sigma_0 \geq 0.7$, or $U_d/\sigma_0 \geq 0.2$ and the axial strain $\varepsilon_d \geq 3\%$, the saturated loess may liquefy (Wang et al. 2000, 2011). In this paper, we adopted the second standard because the pore pressure ratio of 0.7 cannot be easily achieved for saturated loess.

2.2.3 Test Results

Dynamic triaxial test results are shown in Figs. 4 and 5. Figure 4 is the relationship between the dynamic stress and the dynamic strain of the loess. As seen in the figure, the dynamic strain ε_d and the area of hysteresis loop increase with the increase of cyclic number. The liquefaction process of the loess developed in three stages which are viscoelastic-plastic, viscous-plastic and plastic. In addition, attenuation of the dynamic stress occurred in viscous-plastic and plastic stage. These phenomena indicate that the saturated loess was sticky when the seismic loading action ended.

Pore water pressure and dynamic strain are the most important indexes to determine the onset of soil liquefaction (Wang et al. 2012). When it comes to liquefaction of sandy soil, pore pressure which comes up to the level of effective confining pressure proves that liquefaction occurs. At this point, the dynamic strain of the sandy soil increase rapidly and the liquefied damage occurred, as shown in Fig. 5a. However, a number of studies have suggested that pore water pressure of

Fig. 4 The relationship between the dynamic stress and the dynamic strain of the loess



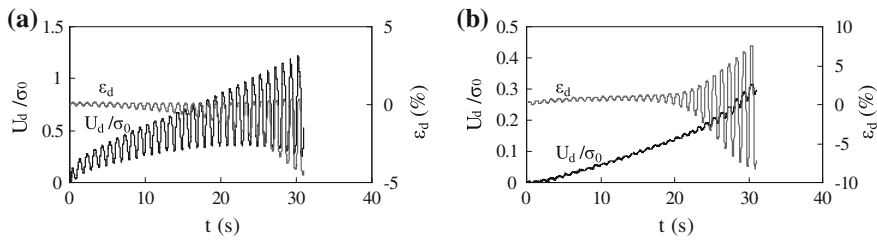


Fig. 5 The development of pore pressure in sandy specimens (Tianshui) and the loess specimen (Yongguang). **a** Sandy specimens. **b** Loess specimen

structural loess cannot reach the effective confining pressure due to the dissipation effect caused by dissolution of the water-resisting and cementing material of small or medium-sized closed pore. The pore water pressure in structural loess is just as much as 0.2–0.7 times of the ordinary sand. The development of pore pressure in the test is shown in Fig. 5b, in which the pore pressure also increases with the increase in cyclic times. However, It rises slowly in the beginning and then shows accelerated growth with increase of cyclic times. The pore pressure ratio reaches 0.22 when the dynamic strain of the sample reaches to 3 %, at which the specimen was failure. The test result shown that loess deposit was partly liquefied under the effect of the Mixian–Zhangxian 6.6 earthquake.

2.3 Mechanism of the Landslides

2.3.1 The Coupling Effect of Rainfall and Earthquake

The climate in the earthquake-affected region is cold and damp with an annual rainfall of 596.5 mm. Before the earthquake, it had been raining for several days and there was a rainfall of 6.6 mm in the evening just before the earthquake (Fig. 6). Water content in loessial deposit increased to 24.53 %, which is higher

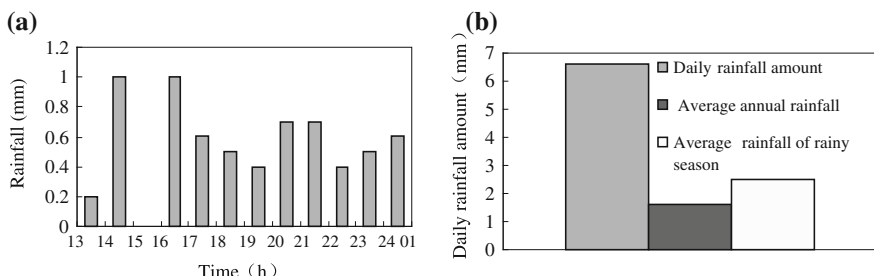


Fig. 6 Rainfall in the day before earthquake and the mean data of rainfall (from Dingxi Weather Bureau). **a** Rainfall in July 21st and July 22nd, 2013. **b** The mean data

than its plastic limit and less than its liquid limit, which could make the shear strength of loess to decrease by 50 % and the stability of slopes to become worse dramatically based on the author's study (Wang et al. 2003). The back analysis shown that the slope produced a large horizontal displacement under the effect of the earthquake, the maximum displacement of 80 cm occurred at the top and the foot of the slope. It was the coupling effect of rainfall and earthquake that caused so many landslides.

2.3.2 The Influence of Liquefaction

Since 1989, many field surveys and laboratory test results show that loess with high water content could be able to produce the phenomenon of liquefaction under the impact of dynamic load (Ishihara et al. 1990; She et al. 2002; Hu and Han 2009; Deng et al. 2012). As mentioned, it has been raining for several days in the region before the earthquake. Soil deposit became saturated after the continuous light rainfalls. Under the effect of the earthquake, excess pore water pressure developed, and then the effective pressure reduced with increase of excess pore pressure. When the ratio of pore pressure reached 0.2, the residual strain of the loess reached 3 %, the loess liquefied. Some of the micropores were destroyed and the particles of the soil were rearranged. Meanwhile, the stability of slopes was dramatically weakened due to the decrease of effective stress of the soil. Consequently, the loessial slope lost its stability and the liquefied soil mass flowed down for about 1 km along the valley.

3 Evaluation of the Maximum Sliding Distance

Evaluation of the maximum sliding distance of seismic loessial landslide could ascertain the endangered scope and put forward suggestion for the prevention. We found that the factors such as seismic intensity, relative altitude, slope angle, unit weight, internal cohesion and internal friction angle have an predominate influence on the safety factor of the loessial slopes based on field geological survey, measuring, in situ and laboratory tests (Wang et al. 2003). In this study, fuzzy information model (Griffiths and Lane 1999) was used by the authors for calculating sliding distance of seismic loessial landslides. Based on 93 seismic loessial landslides caused by the Tianshui South M8.0 earthquake in 1654, the Tong Wei M7.5 earthquake in 1718, the Haiyuan M8.5 earthquake in 1920 and the Gulang M8.0 earthquake in 1927, China, fuzzy information matrix was developed. The slope angle, the relative altitude and the seismic intensity was taken as the arguments for evaluating the maximum sliding distance of loessial seismic landslide. The key

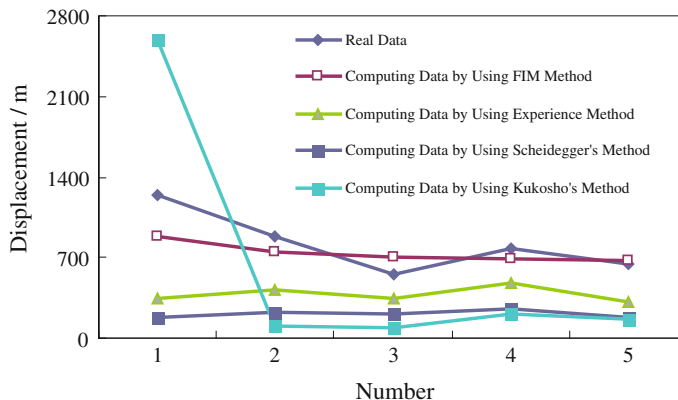


Fig. 7 Results of evaluation of the maximum sliding distance by using different methods

steps of the calculation are information distribution, information diffusion, information integration and error verification.

By comparing with other methods such as experience method, Scheidegger's method and Kukosho's method, the sliding distance evaluated by Fuzzy information model method (FIM) is more coincident with the cases of seismic loessial landslides (Makdisi and Seed 1978; Carro 2003; Kokusho 2009), as shown in Fig. 7.

4 Strategy of Preventing and Mitigating Seismic Landslides Disasters

Loessial landslides are one of major disasters in the Loess Plateau of China. The strategy of preventing and mitigating disasters caused by the landslides proposed by the authors has been adopted in Specification for Seismic Design of Building in Gansu province issued in 2012. In this code, microzonation map of seismic loessial landslides for Lanzhou City, Tianshui City and Qingyang City with two exceedance probabilities of 10 and 2 % in 50 years were compiled for land use planning and major projects planning. Figure 8 shows the microzonation map of loessial landslides for Tianshui City, the landslide hazard are divided into three levels as stable, relatively stable and unstable. The relatively stable and unstable slopes are strongly suggested to be reinforced to be safe for an engineering project. For all slopes, a building should be 5 times of slope height away from the top edge of a slope and 1.5–2.5 times of slope height away from the foot of a slope according to the provincial specification.

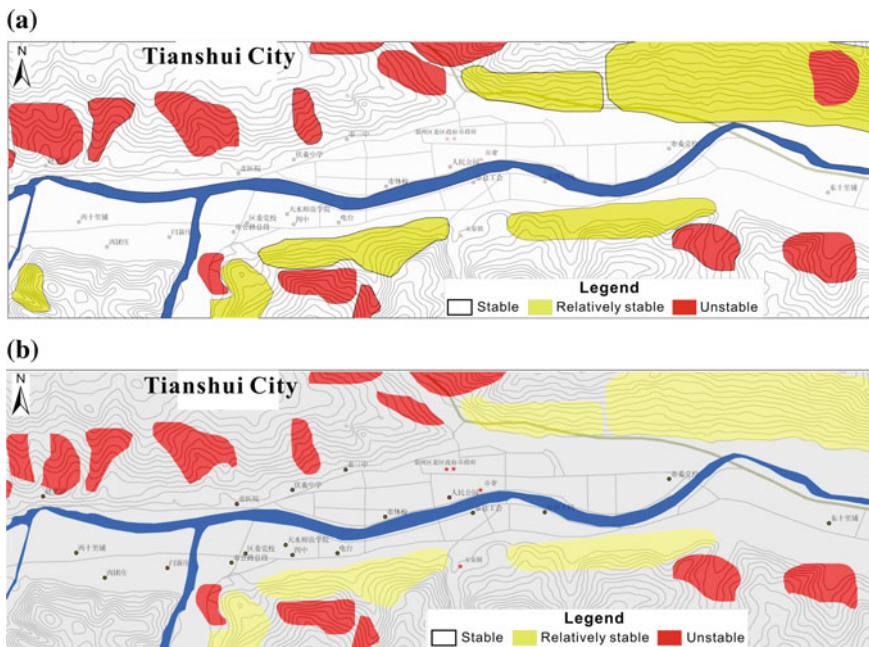


Fig. 8 Microzonation map of seismic loessial landslides for Tianshui City (Committee of experts on Architectural Technology of Gansu province, China 2011). **a** Exceedance probabilities of 2 % in 50 years. **b** Exceedance probabilities of 10 % in 50 years

5 Conclusions

1. So many Disastrous landslides developed in loessial deposit, including soil sliding, collapse and mudflow were induced by the coupling effects of rainfall and the Minxian–Zhangxian 6.6 earthquake. The dense area of landslides, 30 km long and 8 km wide, is located in zones of VIII and VII seismic intensity along the seismic fault.
2. Loess liquefaction triggered the large scale of mudflow in Yongguang village, which flowed down for a long distance of 1 km along the valley much more than that of unliquefied sliding loess mass.
3. Sliding distance evaluated by fuzzy information model method is more coincident with cases of seismic loessial landslides without liquefaction in the Loess Plateau, which may be used for evaluating the influencing area of seismic unsaturated loessial landslides.
4. Microzonation map of seismic loessial landslides for middle and large cities with two exceedance probabilities of 10 and 2 % in 50 years may be used to land use planing and major projects planing for preventing and mitigating the disasters caused by the landslides.

References

Carro M (2003) The application of predictive modeling techniques to landslides induced by earthquakes: the case study of the 26 September 1997 Umbria–Marche earthquake (Italy). *Eng Geol* 69:139–159

Committee of Experts on Architectural Technology of Gansu province, China. (2011). Specification of seismic design of buildings in Gansu Province (DB62/T25-3055-2011)

Deng LS, Fan W, He LP (2012) Liquefaction Property of Seismic Loess under Stochastic Load. *Chin J Rock Mech Eng* 31(6):1274–1280

Griffiths DV, Lane PA (1999) Slope stability analysis by finite element. *Geotechnique* 49(3):387–403

Hu W, Han JG (2009) Laboratory testing study of dynamic properties of saturated loess for effect of its internal structure. *J Eng Geol* 17(5):648–655

Ishihara K, Okusa S, Oyagi N et al (1990) Liquefaction-induced flow slide in the collapsible loess deposit in soviet Tajik. *Soils Found* 30(4):73–89

Kokusho T (2009) Travel distance of failed slopes during 2004 Chuetsu earthquake and its evaluation in terms of energy. *Soil Dyn Earthquake Eng* 29:1158–1169

Li SL (1990) Principles and methods of dynamic triaxial test. Geological Publishing House in China

Makdisi FI, Seed HB (1978) Simplified procedure for estimating dam and embankment earthquake-induced deformations. *J Geotech Eng* 104(7):849–867

She YX, Liu HL, Gao YF (2002) Study on liquefaction mechanism and pore water pressure mode of saturated original loess. *Rock Soil Mech* 23(4):395–399

Wang LM, Wu ZJ (2013) Earthquake damage characteristics of the Minxian–Zhangxian Ms6.6 earthquake and its lessons, China earthquake. *Eng J* 35(3):401–412

Wang LM, Liu HM, Li L et al (2000) Laboratory study on the mechanism and behaviors of saturated loess liquefaction. *Chin J Geotechn Eng* 22(1):89–94

Wang LM, Shi YC, Liu X et al (2003) Loess dynamics. Seismological Press of China

Wang J, Wang LM, Wang P et al (2011) Study on liquefaction characters of saturated loess in different regions. *Hydrogeol Eng Geol* 38(5):54–56

Wang Q, Wang LM, Yuan ZX et al (2012) A study of loess liquefaction induced by the Wenchuan Ms8. 0 earthquake in Tianshuan, Qingshui County, Gansu Province. *Hydrogeol Eng Geol* 39 (2):116–120

Xu SH, Wu ZJ, Sun JJ et al (2013) Study of the characteristics and inducing mechanism of typical earthquake landslides of the Minxian–Zhangxian Ms6.6 earthquake. *China Earthq Eng J* 35 (3):471–476

Numerical Simulation of Run-Out Behavior of Earthquake-Induced Landslides

Meei-Ling Lin and Ching-Ya Huang

Abstract In order to mitigate the landslide hazard induced by the earthquake, the evaluation of the possible affected area is required. Typically, the landslide affected area involved both the sliding area and the run-out distance of the sliding mass. To understand the run-out behavior of the earthquake-induced landslide, a two-stage numerical model was developed in this study to simulate the sliding behavior of the sliding body, and to estimate the potentially affected area. A commercially available program FLAC was used, and the field cases induced by the Chi-Chi Earthquake were used for the study.

Keywords Earthquake · Landslide · Run-out distance · Numerical model

1 Introduction

To mitigate the landslide hazard induced by the earthquake requires evaluation of the damages in the landslide affected area. Typically, the landslide affected area involved both the sliding area and the run-out distance of the sliding mass. Typically when the images obtained from remote sensing or field investigation were conducted, it was difficult to delineate the run-out area from the over-all affected area (Crosta et al. 2006, Finlay et al. 1999). However, to estimate the run-out distance of the earthquake-induced landslide is of vital importance to provide delineation information of potential affected area in landslide vulnerable area (McAdoo et al. 2000). In order to understand the run-out behavior of the earthquake-induced landslide, a two-stage numerical model was developed in this study to simulate the sliding behavior of the landslide mass. The model was calibrated using the laboratory small-scale shaking table slope model test (Wang and Lin 2007), and then applied to the field cases in the May River Basin to evaluate the run-out distance of landslides induced by the Chi-Chi Earthquake (Lin and Kao 2005).

M.-L. Lin (✉) · C.-Y. Huang

Department of Civil Engineering, National Taiwan University, Taipei, Taiwan
e-mail: linml@ntu.edu.tw

2 Construction of Numerical Model

A two-stage model was constructed using the commercially available finite difference program: FLAC (ITASCA 2000). During the first stage, the potential sliding surface was evaluated with the assigned ground motion record, and the initiation time of the sliding behavior was identified based on the maximum shear stress developed in the slope. For the second stage, a sliding block concept was adopted. The potential sliding surface determined from the first stage analysis is assigned as a sliding surface, and the potential sliding mass would start to slide down-slope after the slide being initiated. The sliding mass deforms and slides along the potential surface, then stops when energy is depleted.

2.1 Determination of Sliding Surface and Initiation Time

In order to construct the numerical model, a commercially available finite difference program “FLAC” was used (Agliardi et al. 2001, Bruckl et al. 2006). The material behavior was assumed to be elastic–plastic and the Drucker–Prager failure criterion was adopted. The slope model was constructed with the side boundaries and base boundary at sufficient distances in order to avoid the reflected energy, and thus the fixed boundary can be applied reasonably (Chen and Lee 2003). An illustration of the numerical model and mesh was shown in Fig. 1 for simulation of the small-scale shaking table model slope. After applying the gravity force, the acceleration time record was introduced to the fixed boundary to simulate the earthquake. To determine the potential sliding surface, the variation of the shear stresses inside the slope mass were observed through the whole vibration process. The time record when the maximum shear stress occurs in the slope was found and the distribution of the shear stress in the slope was observed. The shear strain of the slope was obtained to determine the yielding condition, and the potential sliding surface can be determined from the shear strain distribution as illustrated in Fig. 2, and thus the initiation time pin-pointed accordingly.

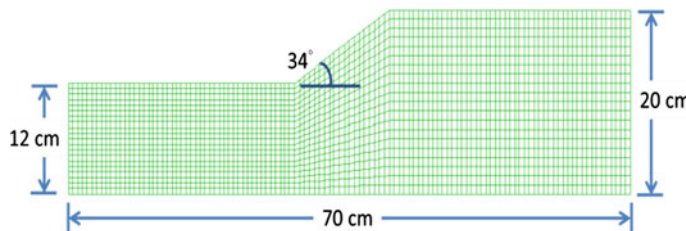


Fig. 1 The numerical model and mesh for small-scale shaking table model slope with fixed boundary

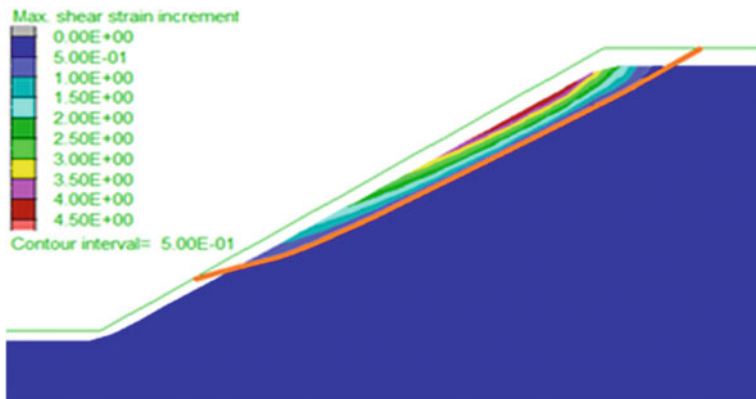
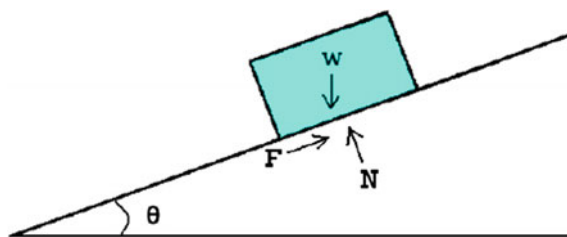


Fig. 2 Distribution of the shear strain in slope corresponding to the observed maximum shear stress and determined potential sliding surface

2.2 *Simulation of Sliding Behavior*

To construct the sliding simulation model, the sliding block concept was adopted as illustrated in Fig. 3. With the potential sliding surface and sliding initiation time determined from the first stage, the slope mass sitting above the potential sliding surface was assumed to start siding along the surface during the vibration time history after the initiation time. However, both the sliding material on the sliding surface and the remaining slope body were considered as deformable continuum. In order to conduct the simulation, the slope model is re-meshed as illustrated in Fig. 4, and the acceleration time record after the initiation time is introduced to the boundary. The mass sitting above the sliding surface starts to deform and slides down along the sliding surface until the energy is depleted. Thus, the deformations of the slope and sliding mass along with the run-out distance of the sliding mass can be determined accordingly.

Fig. 3 Illustration of a sliding block model



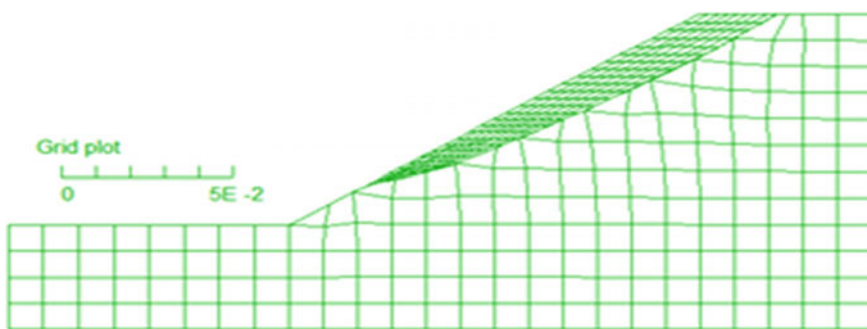


Fig. 4 The slope model and mesh for simulation of sliding behavior

3 Calibration Using Small-Scale Shaking Table Slope Model Test

The numerical model was verified and property of the sliding surface was calibrated using the results of the small-scale shaking table model test conducted by Lin (2007). The slope model test with a slope angle of 34° and slope height of 8 cm was used. The material used for the model slope is Vietnam quartz sand with density of 1590 kg/m^3 and friction angle of 35° . The Young's Modulus of the material is 1.29 MPa and a Poisson's ratio of 0.3 is used. Illustration of the numerical model is as shown in Fig. 1, and results of the calculated time history of shear stress of Grid Number (68, 19) are shown in Fig. 5. From Fig. 5, the occurrence time of the maximum shear stress could be pin-pointed, and the distribution of the corresponding shear strain in the slope was as plotted in Fig. 2. From the distribution of the shear strain, the potential sliding surface was determined and adopted for the second stage analysis and the model was re-meshed as illustrated in Fig. 4 and the acceleration time record after the initiation time was applied to the boundary. As the sliding occurred along the sliding surface, the material properties of the sliding surface would gradually decrease as the strain accumulated, thus a reduction

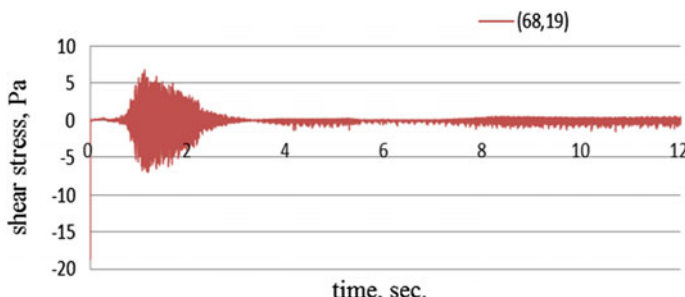


Fig. 5 Time record of shear stress at Grid Number (68, 19) for the slope model in Fig. 1

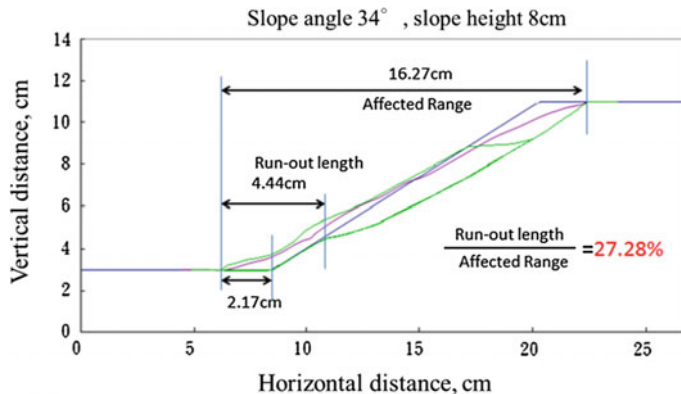


Fig. 6 Comparisons of numerical simulation and shaking table testing results

factor was applied to the slope material properties and taken as the properties of the sliding surface. Calibration of the reduction factor was conducted based on the measured run-out distance of the small-scale shaking table model test (Lin 2007) as shown in Fig. 6. Observing Fig. 6, the numerical simulation of run-out distance and deformation of sliding mass at the toe consist well with the testing results of small-scale shaking table when a reduction factor of 0.85 is adopted. The run-out distance composed of about 27.3 % of the total affected length of the slope in the horizontal projection. Further calibration tests were conducted on other set of model test, and it was found that typically a reduction factor of 0.85 provided a satisfactory result for the testing results. Thus, a reduction factor of 0.85 was used for the simulation of the field cases.

4 Analysis of Field Cases

Field cases of the landslides induced by the Chi-Chi Earthquake, 1999 in the May River Watershed, Nantou County, Taiwan were identified and investigated. The study area of the May River Basin with distribution of identified landslide scars for case study is as shown in Fig. 7. Among the identified cases, field investigations were conducted for Cases D01 through D03 where road traffic permitted. The major geological formation of the study area is Chiayoung Formation, which is composed of thick slate with thin sandstone/siltstone. In order to obtain the material properties for numerical simulation, the properties of Lushan Formation were used which is a slate formation in the neighboring area with similar properties. Topographic analysis of the field cases was conducted to construct the range and profile of the slope using digital terrain model. Numerical simulation was then conducted using the numerical model constructed in the previous section, calibrated reduction factor, and the properties of the Lushan Formation. The input acceleration record was

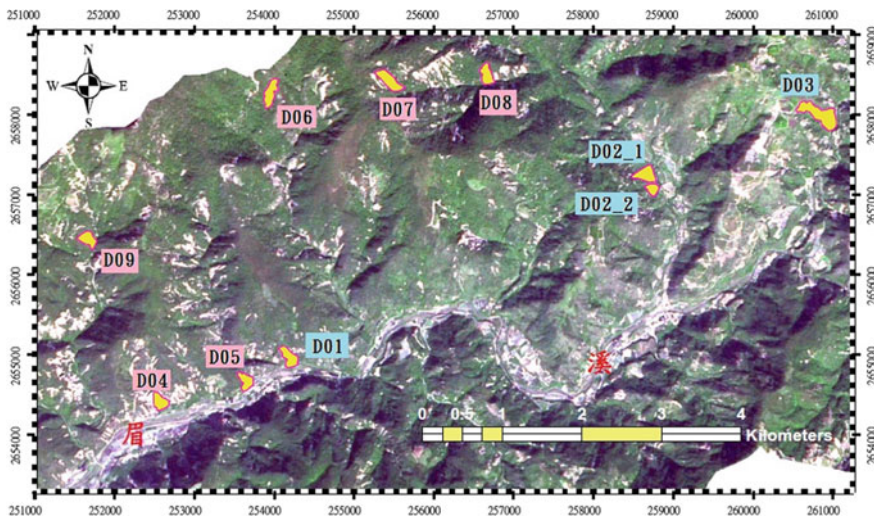


Fig. 7 Study area of the May River Basin with distribution of identified landslide scars

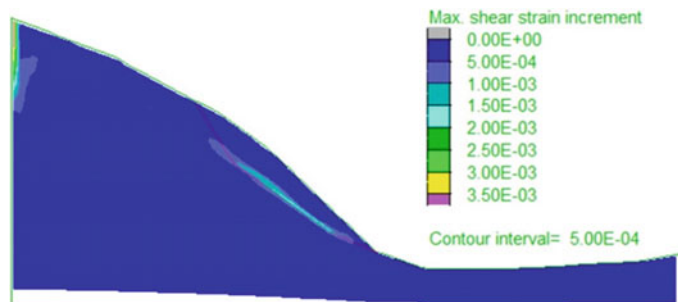


Fig. 8 Slope profile and distribution of shear strain and potential sliding surface of Case D01

interpolated from the Chi-Chi Earthquake records from nearby strong ground motion stations. The profile and distribution of shear strain corresponding to the maximum shear stress of Case D01 are illustrated in Fig. 8, and from which potential sliding surface and initiation time are determined as shown in the figure. The mesh for sliding simulation and the results of simulation of Case D01 are shown in Figs. 9 and 10, respectively.

The simulation results shown in Fig. 10 were verified using field data and comparisons to the aerial photo taken after the Chi-Chi Earthquake were made as shown in Fig. 11. In Fig. 11, the red arrow was used to illustrate the horizontal projection of simulated displacement from the crest along the analysis profile, and the blue arrow was used to illustrate the horizontal projection of simulated toe displacement. Observing Fig. 11, the analysis slope profile appears to be well taken, and representing the sliding direction well. The simulated displacements of both the

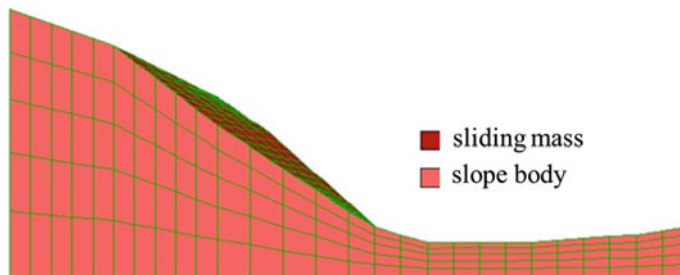


Fig. 9 Numerical model and mesh for sliding behavior simulation of Case D01

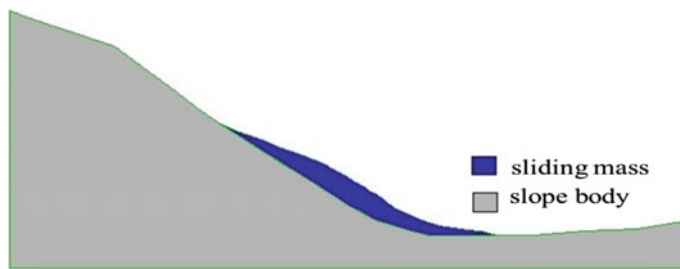


Fig. 10 Deformation of sliding mass and run-out distance from numerical simulation of Case D01

crest and toe match the mapped scar consistently, and provide good information for delineating the run-out distance especially at the toe area where roads and resident houses situated.

5 Run-Out Distances and Affected Area

Results of the run-out distance simulation for field investigation cases of D01, D02-1, D02-2, and D03 are listed in Table 1 as horizontal projection of the toe displacement and the overall affected length of slope. From Table 1, the projected toe displacement ranges from about 25–53.6 % of affected length of the slope. For Cases D01, D02-1, and D02-2, the results are quite consistent. However, for Case D03, the toe displacement was much larger compared to other cases. A close investigation of Case D03 revealed that D03 situated at a higher elevation with steep slope angle and to the left bank of May River compared to the other three cases. The mapped scar of D03 as shown in Fig. 7 appeared to be in an elongated shape and with steep slope angle, which were the characteristics of a shallow landslide or rock avalanche. In addition, the location of Case D03 is on the left bank of the May River as opposed to the other three cases, which may suggest differences in geological formation. Therefore, it is likely that the Case D03 is of a different

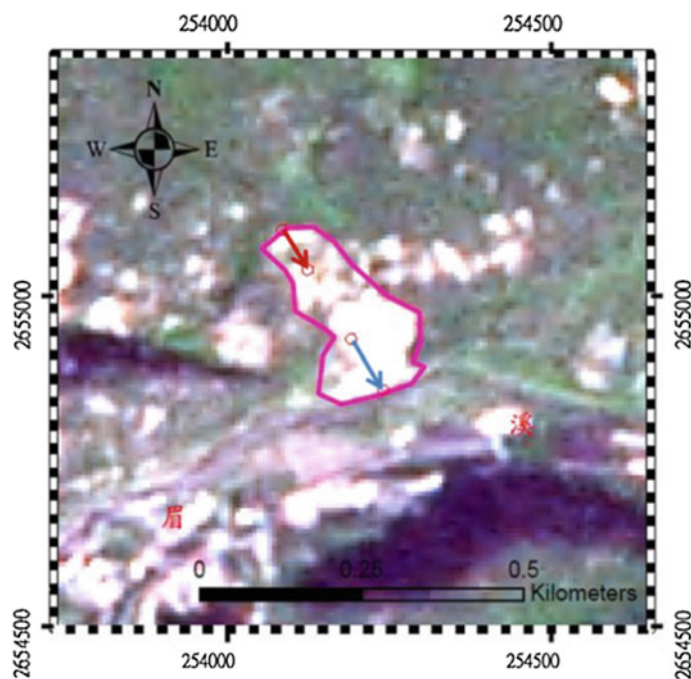


Fig. 11 Comparisons of mapped scar and horizontal projection of simulated displacements at crest and toe of Case D01

Table 1 Horizontal projection length of the toe displacement and the overall affected length of field cases

| Case ID | Toe displacement, m | Affected length, m | % of toe displacement to affected length |
|---------|---------------------|--------------------|--|
| D01 | 80 | 279 | 28.7 |
| D02-1 | 53 | 211 | 25.1 |
| D02-2 | 63 | 183 | 34.4 |
| D03 | 337 | 459 | 53.6 |

failure type and/or situates in different geological formation compared to the other three field cases. By omitting the result of Case D03, the average toe displacement as listed in Table 1 takes up about 30 % of the overall affected length of the landslide when projected in the horizontal direction. This result is also comparable to the ratio of about 27.3 % of the small-scale shaking table model test as shown in Fig. 6. The remaining two thirds of the affected length thus could be considered as the remaining sliding body situated on the slope. Such results could provide a viable method for estimation of the affected area and run-out distance, and which would be helpful for delineation of the potentially hazardous area when subjected to earthquakes.

6 Conclusions

A two-stage numerical model was developed in this study. In the first stage, the potential sliding surface was evaluated with the assigned ground motion record, and the initiation time of the sliding behavior was identified based on the shear strain corresponding to the maximum shear stress developed in the slope. The potential sliding surface then is assigned as a sliding surface. The slope mass deforms and slides along the surface and results in toe run-out displacement and over-all affected length. With the calibration of the small-shaking table model test, the numerical model provides satisfactory results for simulations of run-out behavior. It was found that the run-out distance generally composes about one third of the total length of the affected length for both the shaking table model test and field cases, and the remaining two thirds of the affected length are likely to be the sliding body situated on the slope. The hazard in the affected area of the earthquake-induced landslide thus can be estimated based on the simulation of the run-out distance using the proposed numerical model.

References

Agliardi F, Crosta GB, Zanchi A (2001) Structural constraints on deep-seated slope deformation kinematics. *Eng Geol* 59:83–102

Bruckl E, Brunner FK, Kraus K (2006) Kinematics of a deep-seated landslide derived from photogrammetric, GPS, and geophysical data. *Eng Geol* 88:140–159

Chen H, Lee CF (2003) A dynamic model for rainfall-induced landslides on natural slopes. *Geomorphology* 51:269–288

Crosta GB, Chen H, Frattini P (2006) Forecasting hazard scenarios and implications for the evaluation of countermeasure efficiency for large debris avalanches. *Eng Geol* 83:236–253

Finlay PJ, Mostyn GR, Fell R (1999) Landslide risk assessment: prediction of travel distance. *Can Geotech J* 36:556–562

ITASCA Consulting Group, Inc. (2000), FLAC Version 4.0 Manuals

Lin JH (2007) Model test of earthquake-induced landslide using small-scale shaking table. Master Thesis, National Taiwan University

Lin ML, Kao JJ (2005) The threshold displacement of landslides caused by Chi-Chi Earthquake. In: International symposium on the potential, risk, and prediction of earthquake-induced landslides

McAdoo BG, Pratson LF, Orange DL (2000) Submarine landslide geomorphology, US continental slope. *Mar Geol* 169:103–136

Wang KL and Lin ML (2007) The run-out and recessional distances of granular slope based on shaking table model tests. EGU General Assembly, Vienna, Austria, NSC94-2211-E-002-039

The Geometric Characteristics and Initiation Mechanisms of the Earthquake-Triggered Daguangbao Landslide

J.J. Dong, C.C. Tsao, C.M. Yang, W.J. Wu, C.T. Lee, M.L. Lin, W.F. Zhang, X.J. Pei, G.H. Wang and R.Q. Huang

Abstract The Daguangbao (DGB) landslide which triggered by the 2008 Wenchuan earthquake is one of the largest earthquake-triggered landslides in the world over the past century. In this study, remote sensing images analysis, field investigation, laboratory experiment and slope stability analysis were adopted to characterize this DGB landslide. We speculated the dominating structures of this landslide are folded bedding plane and a zigzag stepping-out joint system, which outcropped at the south and north of the landslide site, respectively. Accordingly, this landslide is a gigantic, atypical wedge failure. With the inferred slip planes, the intersection line is curved and counterclockwise rotated, which fit the trajectory of a mining tent pre and post this DGB landslide with a travel distance of 1.9 km. Meanwhile, the intersection line will be daylighted and rock mass shear-off on the toe of this landslide, as assumed by most of the researchers, is no more required. Based on the proposed wedge shape and DTMs, the volume of moving mass is about $10.51 \times 10^8 \text{ m}^3$. The characteristics of the sliding surface on the south part of the landslide site were carefully investigated. The identified slip zone was composed of breccia and gouge layers of several centimeters thick. The intact dolomite rocks adjacent to the slip zone and the thin gouges were sampled. The peak friction coefficient of the tested dry dolomite discontinuities and wet gouges are 0.52–0.96 and 0.73–0.86 and the steady-state friction coefficients of the two samples are 0.1–0.57 and 0.16–0.63, respectively. The wedge analysis shows that the slope is quite stable (F.S. = 4.14). However, the gigantic wedge can be

J.J. Dong (✉) · C.C. Tsao · C.M. Yang · W.J. Wu · C.T. Lee
Institute of Applied Geology, National Central University, Taoyuan, Taiwan
e-mail: jjdong@geo.ncu.edu.tw

M.L. Lin
Department of Civil Engineering, National Taiwan University, Taipei, Taiwan

W.F. Zhang · X.J. Pei · R.Q. Huang
The State Key Laboratory of Geohazards Prevention and Geoenvironment Protection,
Chengdu University of Technology, Chengdu, Sichuan, China

G.H. Wang
Research Center on Landslides, Disaster Prevention Research Institute,
Kyoto University, Gokasho, Uji, Japan

triggered by the Wenchuan earthquake based on the pseudo-static wedge stability analysis. Moreover, the friction coefficient of the gouges under large shear displacement will drop below 0.25 ($\sim \tan(14^\circ)$; the intersection line plunged 14°) when the shear velocity exceeds 1.3 m/s. That is, the gigantic wedge can be speeded up by the inertial force generated by the earthquake and keep moving rapidly with long run-out. Based on a simple one dimensional particle motion model, the DGB landslide traveled 52–67 s with a maximum velocity of 57–74 m/s.

Keywords Daguangbao landslide · Earthquake-triggered · Wedge failure · Rotary shear test · Friction coefficient

1 Introduction

The disastrous Wenchuan earthquake (M_w 7.9, 12 May 2008) was occurred in Sichuan province of western China (Fig. 1). The Wenchuan earthquake induced tens of thousands of landslides and Daguangbao (DGB) landslide is the largest one (Huang et al. 2008), which the range of estimated collapse volume is from 7.8×10^8 m³ to 11.99×10^8 m³ (Huang et al. 2008; Chigira et al. 2010; Yin et al. 2012). The volume of the DGB landslide is extremely huge and the toe of sliding surface was still buried by deposits with 600 m in depth. Hence, the geometry of the sliding surface are remained controversial. It has been proposed that the tensile cracks on the crown were initiated by the extremely strong ground shaking and follows the shattering of rock mass. Driven by the seismic force and gravity, the huge landslide mainly slid along the bedding plane and sheared-off the strata at the toe of the slope (Huang et al. 2012). Alternatively, this landslide could simply be a wedge failure. This hypothesis was testified with pre and post event DTMs and SPOT-5 satellite images (Fig. 2) and the field investigation. In this study, we aimed

Fig. 1 Location of the Daguangbao landslide (DGB). WMF Wenchuan-Maowen fault, YBF Yingxiu-Beichuan fault, PF Pengguan fault

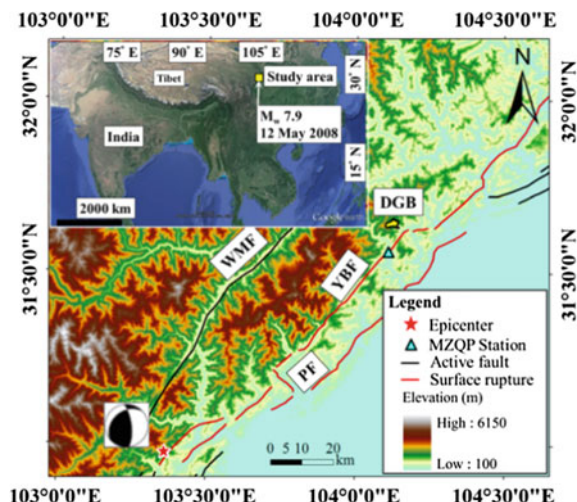
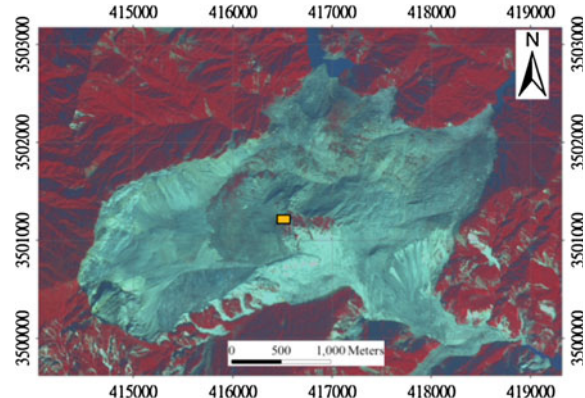


Fig. 2 Post-event SPOT-5 image of the Daguangbao region. The *orange box* is the slid mining tent after the earthquake



at exploring the failure mechanisms and kinematics of the DGB catastrophic landslide. The subjects includes: (1) to determine the geometry of sliding surface, (2) to study the initiation of the huge moving mass, we perform a series of low to high velocity rotary shear frictional tests and the pseudo-static slope analysis, and (3) to assess the kinematics of DGB landslide.

2 Geological Setting

The DGB landslide was located on the right bank of the Huangdongzi valley, which is located at the northwestern flank of the NE-striking Dashuizha anticline. The area was composed of interbed dolomite with subordinate shale; the thickness of the dolomite beds varied a few tens of centimeters to 10 m, shale from several centimeters to meters (Chigira et al. 2010). The lithology can be classified into Fig. 3 (revised from Huang et al. 2012). Zd3 of the Sinian system is constituted by limestone, red mudstone, and dolomitic rocks which is composed of the slip zone.

3 Results

3.1 Dominating Structures of Daguangbao Landslide

Field investigation results indicated most of the joints are distributed on the great circle of the bedding plane (Fig. 4a). These joints are common observed joint sets on limb of the anticline (Tension joint *T*, conjugated diagonal *A* and *B*, strike joint *C* and dip joint *D* in Fig. 4b). There are four planes bounded the DGB landslide: a bedding plane dipping to the north with an orientation of N86°E/35°N formed the southern boundary; north-eastward, south-eastward slopes, and northern slope. According to the geological map, there is dextral fault (blue box in Fig. 3) with a

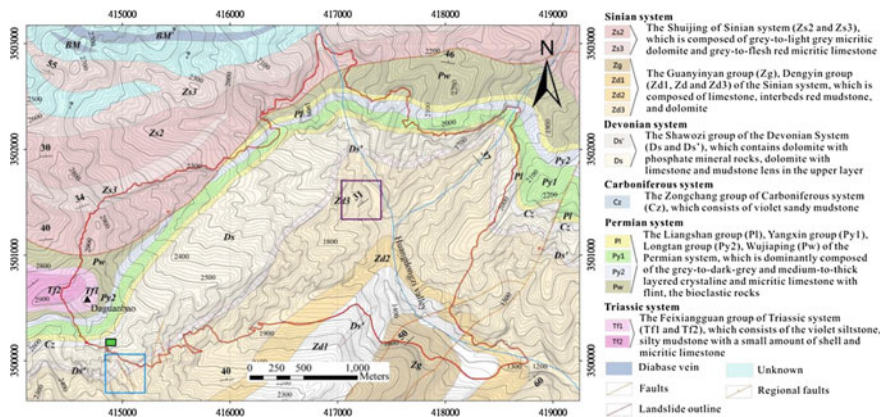


Fig. 3 Geological map of the DGB landslide (Huang et al. 2012). The green box is a mining tent before the event

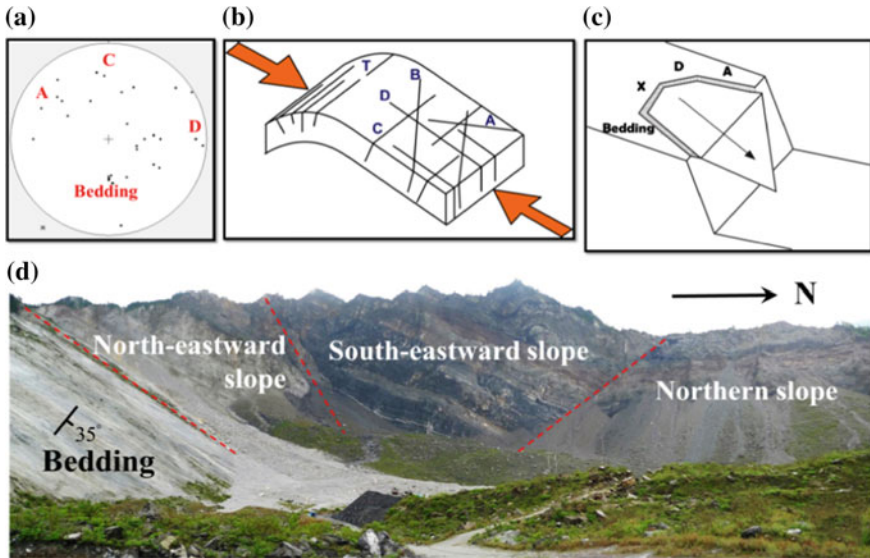


Fig. 4 **a** Stereonet with measured discontinuities. **b** Schematic diagram of the measured joint sets: diagonal joint A, strike joint C, and dip joint D. **c** Schematic diagram of the failure wedge of the DGB landslide. **d** Picture of the landslide scarp. Azimuth of the picture view is 245°

strike parallel to that of the south-eastward slope. This plane is numbered as X discontinuity (Fig. 4d). Southern plane is the bedding plane striking to N80° E-WE with a dip of 34°–38°. The orientation of the diagonal joint A and dip joint D are in accordance with the northern and north-eastward slopes. It is speculated that the sliding mass was bounded by the bedding plane and A, D, X planes. Figure 4c is

a schematic diagram of the failure wedge. Slickensides can be observed on the exposed bedding plane, having a pitch of 25° , which indicated the trend/plunge of the sliding direction here is N 67° E and 18° .

3.2 Determining the Geometry of the Sliding Surface

3.2.1 Typical Wedge Model

If the DGB landslide was a wedge failure dominated by bedding plane and Joint A, the trend and plunge of the intersection line will be N 70° E and 14° , based on the discontinuities characterization and stereonet analysis (Fig. 5). Combing the post-event image and post-event DTMs, structure contours of the sliding plane of the simple wedge were constructed (Fig. 6). The trend/plunge along of the intersection

Fig. 5 The stereonet of the bedding plane and Joint A. The trend along of the intersection line is N 70° E/ 14°

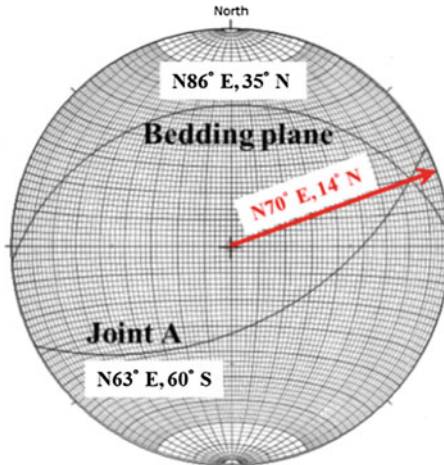


Fig. 6 Structure contours of the sliding plane of the simple wedge. The black arrow is the sliding direction of the wedge rock mass

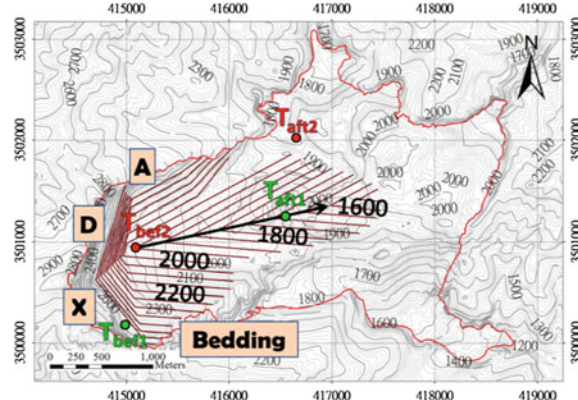
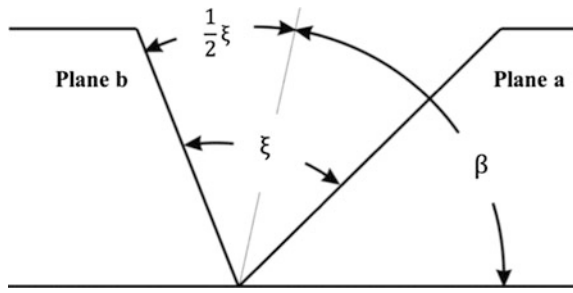


Fig. 7 Wedge geometry and definition of parameters involved in stability analysis. View along line of intersection



line of the structure contours is $N78^\circ E/11^\circ N$, which is identical to the vector of striation. The dominating structures of this gigantic wedge, bedding plane and joint A, are represented as planes “a” and “b” in Fig. 7. To check the movement trajectory of DGB landslide, we utilized the evidence provided by Huang et al. (2012). A mining tent moved more than 1 km without severe damage. The positions of this tent before and after the earthquake are listed in T_{bef1} and T_{aft1} (Fig. 6). If the position of the mining tent T_{bef1} moves to T_{bef2} , where is the source tip of the wedge, the trajectory of this tip of wedge should pass through T_{aft2} . This trajectory is deviated from the intersection line of the simple wedge model. Can we account for this discrepancy? A modification of the simple wedge model was proposed in the next section.

3.2.2 The Proposed Geometry of the Sliding Surface—An Atypical Wedge Model

Based on the geological map, the orientation of the bedding plane is turning from $N86^\circ E/35^\circ N$ near the crown of the landslide to $N52^\circ E/31^\circ N$ near the toe of the sliding mass (purple box in Fig. 3). Therefore, we speculated that the bedding plane buried under the deposit could be folded. That is, the dip direction of the bedding plane was rotated counterclockwise. To reduce the discrepancy of intersection line and inferred moving landslide trajectory of DGB landslide, a zigzag stepping-out joint system of joint A was assumed under the deposits. The averaged dipping angle of the stepped-out planes could be reduced (10° – 20° less than the outcropped north-eastward slope). The structure contours of the assumed surfaces (folded bedding plane and zigzag steeping-out joint system of joint A) were shown in Fig. 8a. Two cross sections I and II were illustrated in Fig. 8b, c. The sliding surface is within the $Zd3$ formation which is composed of dolomite. It is interesting to find that the intersection line of the folded bedding plane and zigzag joint system can be daylighted at the valley without shear-off the rock mass on the toe of the DGB landslide. This moving trajectory of the sliding mass, which is close to the inferred trajectory from the spatial variation of the mining tent before and after

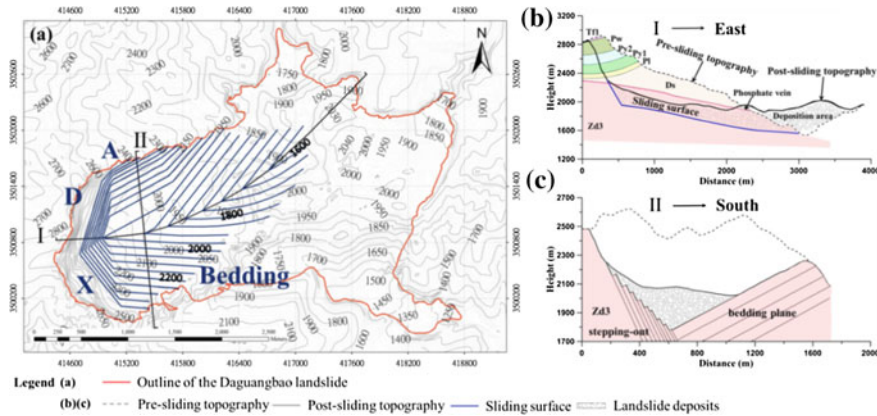


Fig. 8 a The modified wedge model. b, c Illustrated the profile I and II (locations are shown in a)

landslide, turned 20° counterclockwise compared with those from the typical wedge model. According to the proposed atypical wedge shape, the volume of moving mass is about $10.51 \times 10^8 \text{ m}^3$ with a travel distance of 1.9 km from the pre and post event DTMs.

3.3 Strengths on the Sliding Surface

This study utilizes two different kinds of samples to conduct the rotary shear tests. One is the artificial smooth joint of dolomite rock which represents the materials of joint A. The other one is the bedding parallel faults gouge which was sampled from a weak zone right above the outcropped bedding plane. Dolomite samples were prepared as core plugs and rock–rock shear tests were conducted. These experiments were performed at room humidity with shear velocity of 0.001–1.3 m/s and normal stress of 11.47 MPa (estimated from an average thickness of 420 m in source area). The shear velocities of gouge rotary shear tests were conducted at 0.01–1.3 m/s under normal stresses 1–3 MPa (difficult to increase the normal stress to 11.47 MPa) and water contents of 10 %. Slip weakening behaviors, which the friction coefficient decreased from a peak value (μ_p) to a steady-state value (μ_{ss}) with increasing slip distance (d), were observed. The μ_p of dolomite rotary shear tests are ranged from 0.52 to 0.96 with an average value of 0.71. The average peak friction coefficient of fault gouge is 0.79, where the lower and upper bound are 0.73 and 0.86, respectively (Fig. 9b). Generally, the steady-state friction coefficient μ_{ss} is decreased with increasing velocity (Fig. 9a, b). The steady-state friction coefficient is 0.1 and 0.16 for dolomite and fault gouge at shear velocity of 1.3 m/s.

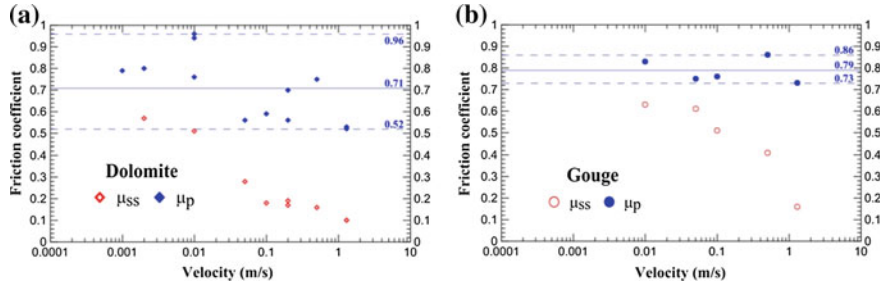


Fig. 9 **a** The friction coefficient of dolomite shear tests. μ_p are ranged from 0.52 to 0.96 and the average is 0.71. **b** The friction coefficient of gouge shear tests. μ_p are ranged from at 0.73 to 0.86 and the average is 0.79. The data points are averaged values of 2–3 tests

3.4 Pseudo-Static Analysis of Rigid Wedge

Since the planes X and D are assumed pre-existing before the landslide, the contributions of their strengths on the landslide initiation could be neglected. The peak friction coefficients (μ_p) of dolomite smooth joints and fault gouge of the bedding plane are used to represent the strength on joint A (plane “b” in Fig. 7) and bedding plane (plane “a” in Fig. 7). That is, $\mu_a = 0.79$ and $\mu_b = 0.71$.

3.4.1 Initiation of the DGB Landslide

The following analysis adopted the typical wedge analysis for simplicity. The safety factors of DGB wedge bounded by planes “a” and “b” can be calculated using rigid wedge method (Lee 1989) as follows:

$$F.S. = \frac{S_a + S_b}{P \sin \varphi} \quad (1)$$

where $S_a = N_a \mu_a$, $S_b = N_b \mu_b$. N_a and N_b can be calculated with Eqs. (2) and (3).

$$N_a = \frac{P \cos \varphi \sin(180^\circ - \frac{1}{2}\xi - \beta)}{\sin(180^\circ - \xi)} \quad (2)$$

$$N_b = \frac{P \cos \varphi \sin(\beta - \frac{1}{2}\xi)}{\sin(180^\circ - \xi)} \quad (3)$$

where P is the wedge weight, φ is the dip of the line of intersection, β and ξ are illustrated in Fig. 7. The parameters required in the pseudo-static analysis are listed in Table 1. The results show the wedge is stable ($F.S. = 4.14 > 1$) without seismic force.

Table 1 The values of the pseudo-static analysis parameters

| μ | | P (N) | β (°) | ξ (°) | φ (°) |
|-------------------------|----------------------------|--------------------|-------------|-----------|---------------|
| Fault gouge (μ_a) | Dolomite joint (μ_b) | | | | |
| 0.79 | 0.71 | 2.86×10^9 | 78 | 92 | 14 |

Lee (1989) proposed a pseudo-static rigid wedge method, which included the influence of the seismic force, to calculate the F.S. of wedge. Safety factor of a rock wedge under seismic condition can be expressed as follows:

$$\text{F.S.} = \frac{k}{\tan(\varphi + \tan^{-1} K_h)} \quad (4)$$

where K_h ($= \frac{a_h}{g}$, a_h is the horizontal acceleration and g is the acceleration of gravity) is the horizontal seismic coefficient, k is the wedge parameter which can be calculated as following if the friction coefficients of two planes are assumed as identical (μ):

$$k = \frac{[\sin(180^\circ - \frac{1}{2}\xi - \beta) + \sin(\beta - \frac{1}{2}\xi)]\mu}{\sin(180^\circ - \xi)}. \quad (5)$$

The influence of vertical force induced by earthquake was neglected, thus the F.S. could be slightly overestimated. The calculated F.S.s of the DGB wedge considering the seismic force are shown in Table 2. The horizontal seismic coefficients K_h will be 0.58 and 0.65 if the friction coefficients μ were assumed as 0.71 (dolomite joint) and 0.79 (fault gouge).

The record of Wenchuan earthquake of MZQP seismic station (Fig. 10a, b, location shown in Fig. 1) was adopted to evaluate the reasonability of the calculated K_h using friction coefficients from rotary shear tests. It can be read that the maximum horizontal acceleration is 837 gal. That is, the $K_{h,\text{max}}$ is about 0.85. A K_h of 0.58–0.65 to trigger the DGB landslide is about two thirds to three quarters of $K_{h,\text{max}}$, which is a reasonable estimation.

Table 2 Summary the results of rigid wedge method (F.S.), triggered K_h , travel time, final velocity and average velocity by dolomite and gouge samples under the different strength conditions

| | Friction coefficient | Static rigid wedge analysis (F.S.) | Triggered K_h (g) | Trigger time (s) | Friction coefficient after slide | Travel time (s) | Max/average V (m/s) |
|----------------|----------------------|------------------------------------|---------------------|------------------|----------------------------------|-----------------|---------------------|
| Dolomite joint | 0.71 | 4.14 | 0.58 | 39 | 0.1 | 52 | 74/37 |
| Fault gouge | 0.79 | | 0.65 | 46 | 0.16 | 67 | 57/28 |

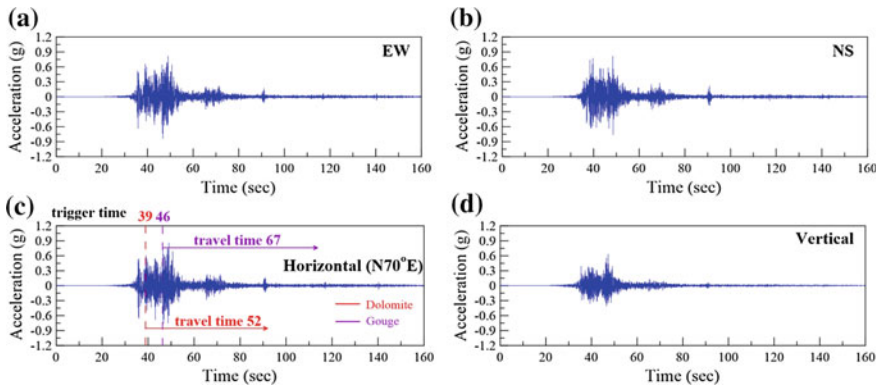


Fig. 10 Ground acceleration records of strong motion MZQP of the Wenchuan earthquake. **a, b**, **d** Are component of east-west (EW), north-south (NS) and vertical, respectively. **(c)** Is the component of the strike direction of the wedge intersection combined with **(a, b)**

3.4.2 Kinematics of DGB Landslide

The initiation and moving characteristics were evaluated using Eq. (4) and a one dimensional particle motion model incorporating the peak and steady-state friction coefficients obtained from the rotary shear tests. We calculated the required K_h to initial the DGB landslide (F.S. = 1). If the peak friction coefficients of dolomite joint and fault gouge were utilized, the triggered K_h will be 0.58 and 0.65 (Table 2), respectively. The trigger time of the landslide can be determined from the ground acceleration records (Fig. 10c) accordingly (39 and 46 s, Table 2). The friction coefficient on the bounded planes of the sliding wedge will drop to steady-state friction coefficient within several meters displacement. Since the friction coefficients of the dolomite joint and fault gouge are less than 0.25 ($\sim \tan(14^\circ)$; the intersection line plunged 14°) when the shear velocity exceeds 1.3 m/s (Fig. 9a, b), the gigantic wedge can be speeded up by the inertial force generated by the earthquake and keep moving rapidly with long run-out. The travel distance of DGB landslide project from the horizontal plane is about 1.9 km based on the position of the mining tent before (Fig. 3) and after (Fig. 2) the landslide event. The travel times and sliding velocities were calculated (Table 2) utilizing the travel distance and one dimensional particle motion model incorporating the steady-state friction coefficient of dolomite (0.1) and gouge (0.16) at shear velocity 1.3 m/s. Accordingly, the DGB landslide terminated at 91–113 s (travel 52–67 s) with a maximum velocity of 57–74 m/s. This study speculated that the signals at 90 s in Fig. 10c may induce by the sliding mass hit the opposite bank of the Huangdongzi valley.

4 Conclusions

1. The DGB landslide is an atypical wedge bounded by the folded bedding plane and zigzag stepped-out joint system. With the inferred slip planes, the intersection line is curved and counterclockwise rotated, which fit the trajectory of mining tent well. Meanwhile, the intersection line will be daylighted at the toe of the slope. Based on the proposed wedge shape, the landslide volume is $10.51 \times 10^8 \text{ m}^3$.
2. The average peak friction coefficient of dolomite joint is 0.71 and the steady-state friction coefficients are decreased from 0.57 to 0.1 under shear velocity increasing from 0.001 to 1.3 m/s under a normal stress of 11.47 MPa in room humidity condition. Meanwhile, the average peak friction coefficients of the bedding parallel fault gouges is 0.79 and the steady-state friction coefficients are decreased from 0.63 to 0.16 when the shear velocity increasing from 0.01 to 1.3 m/s under normal stresses 1–3 MPa in a water content of 10 %. The tested samples were characterized as slip weakening behavior which indicating the strengths on the sliding planes will decrease with increasing shear displacement and shear velocity.
3. The wedge analysis indicated that the slope is quite stable (F.S. = 4.14) before the Wenchuan earthquake based the strengths from rotary shear tests. Two thirds to three-quarters maximum horizontal acceleration is required to trigger the wedge failure. Once the failure initiated, the wedge can be speeded up for the positive regulation of the strengths on the sliding planes based on the measured friction coefficients. It is estimated that the DGB landslide traveled 52–67 s with a maximum velocity of 57–74 m/s.

References

Chigira M, Wu X, Inokuchi T, Wang GH (2010) Landslides induced by the 2008 Wenchuan earthquake, Sichuan, China. *Geomorphology* 118:225–238. doi:[10.1016/j.geomorph.2010.01.003](https://doi.org/10.1016/j.geomorph.2010.01.003)

Huang RQ, Pei XJ, Li TB (2008) Basic characteristics and formation mechanism of the largest scale landslide at Daguangbao occurred during the Wenchuan earthquake. *J Eng Geol* 17:730–741 (In Chinese with English abstract)

Huang RQ, Pei XJ, Fan XM, Zhang WF, Li SG, Li BL (2012) The characteristics and failure mechanism of the largest landslide triggered by the Wenchuan earthquake, May 12, 2008. *China, Landslides* 9:131–142. doi:[10.1007/s10346-011-0276-6](https://doi.org/10.1007/s10346-011-0276-6)

Lee CT (1989) Sensibility analysis of rock wedge stability, technical applied of engineering geology workshop, Taiwan (In Chinese)

Yin Y, Wang M, Lin B, Feng Z (2012) Dynamic response characteristics of DaGuangbao landslide triggered by Wenchuan earthquake. *Chin J Rock Mech Eng* 31:1970–1982 (In Chinese with English abstract)

Centrifuge Modeling of Relationships Between Earthquake Intensities and Scales of Post-quake Triggering Rainfall and Landslide

M.H. Wu, J.P. Wang and J.C. Yeh

Abstract The post-quake rainfall frequently induces large-scale landslides, which result in the loss of lives and economic damage. The observation of past slope-land disasters in Taiwan shows that the frequency of landslide occurrence increases remarkably after massive earthquakes. However, the understanding of correlation between seismic activity and post-quake slope stability is limited. As a result, the research on the influence of earthquake intensity on post-quake slope stability is vital for slope disaster prevention. This study is utilizing the self-developed hydrological environment testing box for slope model tests on the geotechnical centrifuge and shaking table. Through the static and dynamic modeling tests, the variations of landslide scales and rainfall intensities to trigger slope failures are investigated to understand the slope failure behavior due to post-quake rainfall.

Keywords Post-quake rainfall-induced slope stability · Centrifuge modeling · Landslide · Debris flow

1 Introduction

Taiwan is an island with abundant of rainfall. The torrential rainfall accompanied with typhoons frequently causes the events of slope instability. Besides, as located in the Circum-Pacific Seismic Belt, there are frequent earthquakes in Taiwan. Earthquake and rainfall are two of the critical driving forces for slope failures. For

M.H. Wu (✉) · J.C. Yeh
National University of Kaohsiung, Kaohsiung, Taiwan
e-mail: wuminhao@nuk.edu.tw

J.C. Yeh
e-mail: r123838338@yahoo.com.tw

J.P. Wang
Hong Kong University of Science & Technology, Clear Water Bay, Hong Kong
e-mail: jpwang@ust.hk

example, the 1999 M_w 7.6 Chi-Chi earthquake in Taiwan induced numerous landslides at that time, including a massive planer slope failure called the Chiu-Feng-Er-Shan landslide, which buried dozens of people alive. More importantly, after the earthquake in 1999, it seems that the frequency of landslides in central Taiwan is increasing, especially in typhoon seasons (Shou et al. 2011a, b; Liu et al. 2013; Lin et al. 2006), and the elevated rainfall-induced landslide probability is reflected on the increase in sediment discharges of the rivers in central Taiwan during the past decade (Shou et al. 2011a, b; Chen et al. 2011).

Based on the aforementioned observations, research to integrate the effects of hydrological, physiographic and seismic factors on slope instability is very important. As a result, the key scope of this study is to investigate the mechanisms causing the increasing frequency of rainfall-induced landslides after a major earthquake like the Chi-Chi earthquake. The study is mainly assisted with centrifuge modeling that has been commonly used in geotechnical studies (e.g., Ling et al. 2009; Ling and Ling 2012; Wong et al. 2012). The paper in the following is organized with an introduction to the centrifuge laboratory in National Central University Taiwan, followed by the testing program, results, and interpretations.

2 The Centrifuge Laboratory in National Central University Taiwan

This section is to introduce the centrifuge laboratory in National Central University (NCU) Taiwan where the tests of this study were conducted. The introduction includes the centrifuge-compatible shaking table, and the in-house water supply system for studying rainfall-induced slope stability after a major earthquake.

2.1 The Centrifuge Facility of NCU

The centrifuge of National Central University is model 665 of Acutronic. It has a rotating arm of 3 m, with its capacity in 100g-ton. The centrifuge can generate a gravity field as large as 200g, and it can carry a test model up to 550 kg on a 200-g level. Figure 1 shows a photo of the centrifuge, and the dimension of the platform carrying soil models is about 1.5 by 1.5 m.

2.2 The Shaking Table

The centrifuge-compatible shaking table of National Central University was designed and manufactured by PVL Technologies, which can simulate prescribed shakings in one dimension. The table is capable of generating a maximum



Fig. 1 The centrifuge of National Central University Taiwan

Table 1 Specifications of the shaking table used in this centrifuge study

| | |
|--------------------------------------|---|
| Payload area (mm) | ($L \times W \times H$) 800 \times 400 \times 500 |
| Maximum payload (kg) | 400 |
| Shaking direction | One direction |
| Shaking type | Periodic or random determined by input signal |
| Shaking force (kN) | ± 53.4 |
| Maximum shaking velocity (m/s) | 1 |
| Maximum table displacement (mm) | ± 6.4 |
| Working frequency range (Hz) | 0–250 |
| Maximum centrifugal acceleration (g) | 80 |

shaking velocity of 1 m/s, with its working frequency up to 250 Hz. Under a centrifuge environment, the shaking table can function properly under an 80-g level. Table 1 is a summary of the specifications of the shaking table.

2.3 Rainfall Simulations

The centrifuge laboratory was equipped with a rainfall simulation system designed and implemented in-house. The rate of water supply is controlled by air pressure with an air compressor, and the system is integrated with the centrifuge system operated and controlled from the outside of the centrifuge. The water pipes connecting to a water reservoir outside of the centrifuge were installed from the base of the centrifuge, and the pipes were mounted along its rotating arm, with water that can rain on soil models sitting on the platform of the centrifuge.



Fig. 2 The sand box with a honey-comb structure on the side

2.4 Sand Box

The sand box used in this study was in dimension $770 \times 150 \times 400$ mm ($L \times W \times H$), with one side made with a transparent plate for videotaping. In order to reduce the weight of the box, the box was fabricated with a honey-comb pattern on the side, as shown in Fig. 2, ensuring its rigidity and strength at the same time under the centrifuge testing condition.

3 The Centrifuge Tests

This section is to describe the program of the centrifuge tests to investigate post-quake rainfall-induced slope stability, including soil model setups and preparations, and the specifications of the test program.

3.1 Soil Slope Model Preparations

In order to prepare a slope model with high permeability and plasticity, this study used the soil mixture with 92 % silica sand and 8 % kaolinite to build soil slope models. Besides, as other centrifuge tests on slope stability (e.g., Ling et al. 2009), the water content was set at 10 % for building the soil slope models.

The soil mixture was then used to prepare a slope model inside of the sand box, as shown in Fig. 3. The slope model is 24-cm high, with a slope angle of 60°. The first step of the model slope preparation was to put certain weight of soil mixture in the box, followed by compaction to make the soil layer in a relative density of 80 %. Next, the soil layer was cut in the middle to form a 60° slope as shown in Fig. 3.



Fig. 3 The slope model with a 60° slope angle

3.2 The Centrifuge Tests

After the model preparation, the next step is to put the sand box on the platform of the centrifuge before the centrifuge simulation gets started. With the model or the sand box in place, the centrifuge starts spinning to gradually increase the gravity level to 60g as prescribed. After a few minutes, the shaking table was turned on to simulate earthquake shaking on slope models while the centrifuge is in-flight. After the shaking, we examined the soil model to make sure no slope failure was induced by shaking, before turning on the water supply system to simulate rainfall on the slope to trigger landslides.

3.3 Slope Failure Profile and the Scale of Landslide

After the test, we measured the slope profile to examine the scale of the landslide, or the volume of landslide debris. The task was assisted with a laser transducer scanning the slope profile after failure; then the measurements were utilized to construct a 3-D slope failure profile, and to estimate the volume of the landslide debris. Figure 4 shows the front view pictures of two set of testing models after failure.

Because some of the landslide debris will deposit at the toe of the slope, it increases the difficulty of measuring the volume of the landslide debris without a computer-aided analysis. Therefore, AutoCAD was employed for the task, utilizing its “Loft” functionality to calculate the volume of landslide by comparing the slope profiles before and after failure. Figure 5 shows an example of using AutoCAD in the estimating of landslide debris in this study.

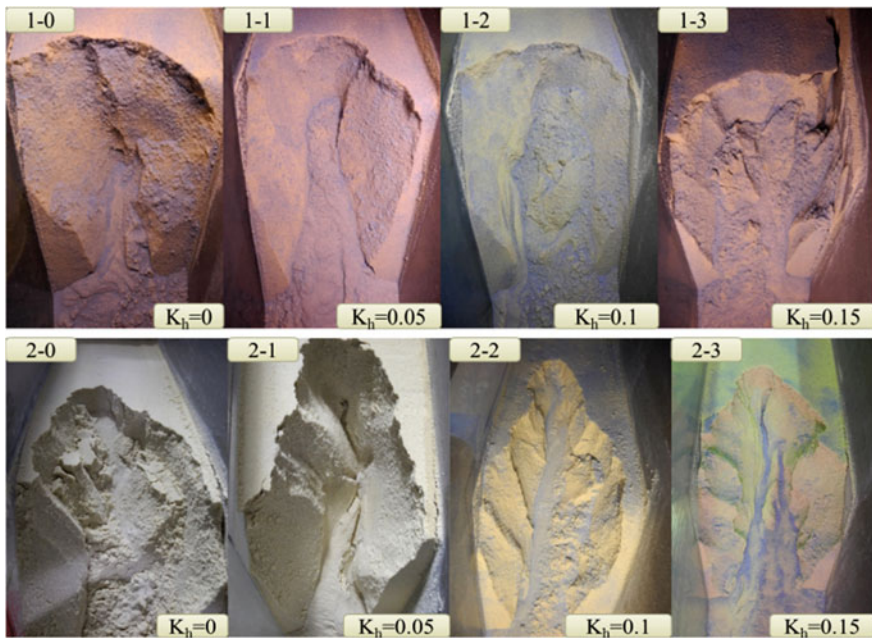


Fig. 4 Pictures of testing models after failure

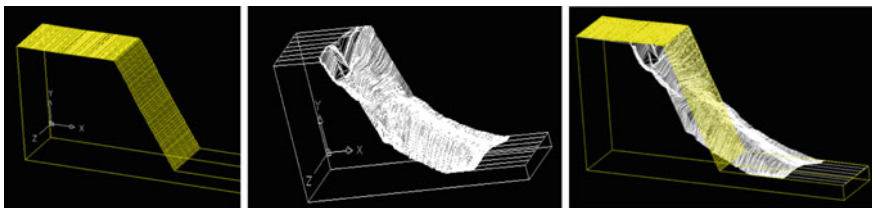


Fig. 5 The use of AutoCAD to calculate the volume of landslide debris

3.4 The Test Program

A total of eight centrifuge tests were carried out in this study, investigating the impact of earthquake shaking and rainfall intensity on slope stability. The test program is summarized in Table 2. For example, Test 1-0 was conducted on a no-earthquake and small-rainfall condition, in contrast to Test 2-3 to investigate the same slope's stability under larger rainfall intensity with the slope experiencing a horizontal shaking. As a result, Test 1-0 and Test 2-0 can be used to investigate the influence of rainfall intensity on rainfall-induced slope stability; by contrast, Test 1-0 and Test 1-3 aims to examine the influence of ground shaking on slope stability after a major earthquake.

Table 2 Summary of the eight centrifuge tests

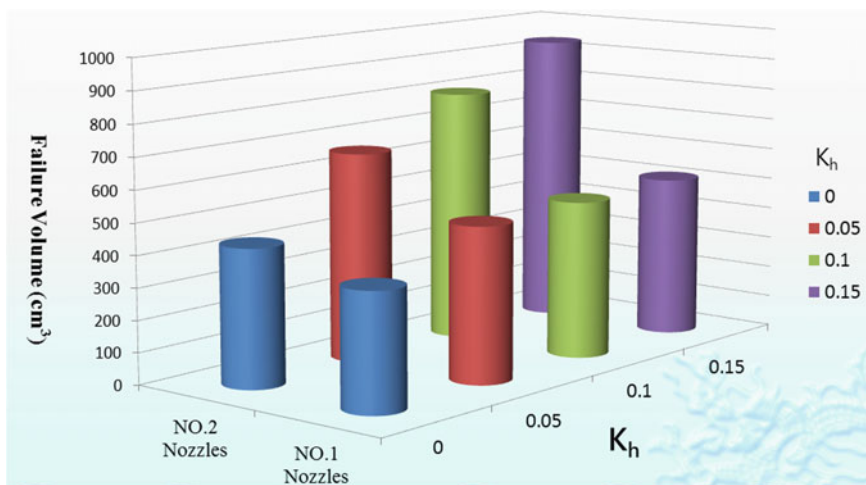
| | | | | | | | |
|--------------------------------------|-----|------|------|------|-----|------|------|
| Centrifugal acceleration (G) | 60 | | | | | | |
| Slope angle (degrees) | 60 | | | | | | |
| Duration of rainfall (mins) | 3 | | | | | | |
| Spraying nozzle openings (mm) | 0.1 | | | 0.2 | | | |
| Prototype accumulative rainfall (mm) | 126 | | | | 165 | | |
| Test no | 1-0 | 1-1 | 1-2 | 1-3 | 2-0 | 2-1 | 2-2 |
| Seismic horizontal coefficient | 0 | 0.05 | 0.10 | 0.15 | 0 | 0.05 | 0.10 |
| Prototype silt discharge (m^3) | 80 | 106 | 108 | 111 | 94 | 143 | 174 |
| | | | | | | | 202 |

4 Results and Discussions

4.1 The Volume of Landslide

Figure 6 shows the landslide volumes in each of the eight centrifuge tests. From the tests, we can see that the landslide volumes are increased with a large rainfall intensity and ground shaking. In other words, the first finding is that a deep-seated rainfall-induced landslide is more likely to occur after a major earthquake, and the possible reason could be that the water is allowed to penetrate deeper of the slope along with some earthquake-induced fractures, increasing pore water pressure in the slope to trigger the landslide.

On the other hand, when a slope is not experiencing earthquakes, most rainfall could accumulate on the slope surface, which becomes the driving force of the erosion type of slope failure observed in the test. And it is understood that more water accumulated on the slope surface should accompany more intensive erosion,

**Fig. 6** The volume of landslide debris in each of the eight centrifuge tests

so a large rainfall event could more possibly induce more erosion causing more debris washed out from the slope.

5 Conclusion

The study uses centrifuge modeling to examine the influence of earthquake ground shaking and rainfall intensity on slope stability. The key of the tests is to compare the volume of landslide debris under different levels of rainfall intensity and ground shaking. The result shows that a deeper and larger rainfall-induced landslide will be more possibly induced after a major earthquake, owing to the developments of earthquake-induced cracks in the slope that allows water to penetrate more deeply in the slope and to excite pore water pressure to trigger a deep-seated landslide.

References

Chen H, Lin GW, Lu MH, Shih TY, Horng MJ, Wu SJ, Chuang B (2011) Dynamic environment in the Ta-Chai River watershed after the 1999 Taiwan Chi-Chi earthquake. *Geomorphology* 133:132–142

Liu SH, Lin CW, Tseng CM (2013) A statistical model for the impact of the 1999 Chi-Chi earthquake on the subsequent rainfall-induced landslides. *Eng Geol* 156:11–19

Lin CW, Shieh CL, Yuan BD, Shieh YC, Liu SH, Lee SY (2006) Impact of Chi-Chi earthquake on subsequent rainfall-induced landslides in central Taiwan. *Eng Geol* 86:87–101

Shou KJ, Hong CY, Wu CC, Hsu HY, Fei LY, Lee JF, Wei CY (2011a) Spatial and temporal analysis of landslides in Central Taiwan after the 1999 Chi-Chi earthquake. *Eng Geol* 123: 122–128

Shou KJ, Wu CC, Fei LY, Lee JF, Wei CY (2011b) Dynamic environment in the Ta-Chai River watershed after the 1999 Taiwan Chi-Chi earthquake. *Geomorphology* 133:190–198

Ling HI, Wu MH, Leshchinsky D, Leshchinsky B (2009) Centrifuge modeling of slope stability. *J Geotech Geoenvir Eng ASCE* 135:758–767

Ling H, Ling HI (2012) Centrifuge model simulations of rainfall-induced slope stability. *J Geotech Geoenvir Eng ASCE* 138:1151–1157

Wong KS, Ng CWW, Chen YM, Bian XC (2012) Centrifuge and numerical investigation of pass failure of tunnel face in sand. *Tunn Undergr Space Technol* 28:297–303

Time-Prediction Method of the Onset of a Rainfall-Induced Landslide Based on the Monitoring of Surface Displacement and Groundwater Level in the Slope

Katsuo Sasahara

Abstract Analysis of monitored data of the deformation in sandy model slope under artificial rainfall was conducted in this study. The analysis revealed that the relationship between the surface displacement and the groundwater level in the slope was able to be modified as hyperbolic which is often adopted for the constitutive relation between the shear strain and the stress ratio under direct shear condition of loose sand. New prediction method for the time of the onset of a rainfall-induced landslide was proposed based on the relationship in the slope. Formula for predicting the relationship between time and surface displacement in the slope could be derived by combining regression equation between the time and the groundwater level to that between the surface displacement and the groundwater level at any time during the experiment in the model. The formula could simulate the actual deformation of the model slope well. It suggests the utility of the method for the time prediction of the onset of rainfall-induced landslides.

Keywords Rainfall • Landslide • Surface displacement • Groundwater level

1 Introduction

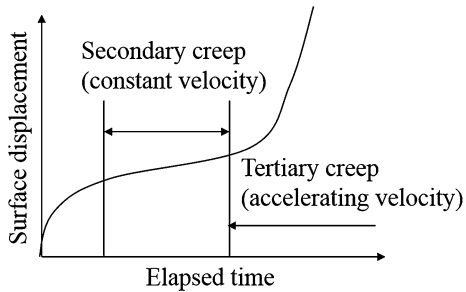
Existing methods for the early warning against rainfall-induced landslides are divided into two kinds. The first is a rainfall threshold such as Caine (1980), which is for the time prediction of landslides at an area while the second is monitoring of soil water or deformation in a slope for a prediction at a specific slope. Only the latter can treat the characteristics of a slope such as geometry, rainfall infiltration characteristics, and mechanical characteristics of the slope.

The sediment-related disaster prevention law (Uchida et al. 2009) was enacted at 2001 in Japan. A sediment-related disaster hazard area should be designated by prefectural governors based on the basic survey. It is defined as the area vulnerable

K. Sasahara (✉)

Kochi University, 200 Monobe Otsu, Nankoku, Kochi 783-8502, Japan
e-mail: sasahara@kochi-u.ac.jp

Fig. 1 Relation between time and displacement in a slope before failure



to sediment-related disasters. A warning and evacuation system should be established by municipal governors in the area according to the law. The monitoring of the soil water or the deformation of a slope can be an effective tool for the system.

Time-prediction methods based on the monitoring of the displacement of a slope have been proposed and are already in practice. The formulae proposed by Saitou (1965) or Fukuzono (1985) have been widely adopted to make time prediction of an onset of a landslide based on the monitoring of the slope. They are based on the empirical relationship between time and surface displacement in a slope before failure as expressed as Fig. 1. Various kinds of formulae have been proposed to express the relation between time and displacement at the secondary or tertiary creep stage and to predict the time of an onset of a landslide. Although time prediction could be successful based on the method in some cases, it could not succeed in other cases. The reason of the unsuccessful cases was identified to be the change of stress in the slope due to the change of the pore pressure according to rainfall infiltration or the change of geometry of the slope according to the cutting or filling works. The stress-strain relationship should be necessary to explain the deformation of the slope due to the change of stress in the slope.

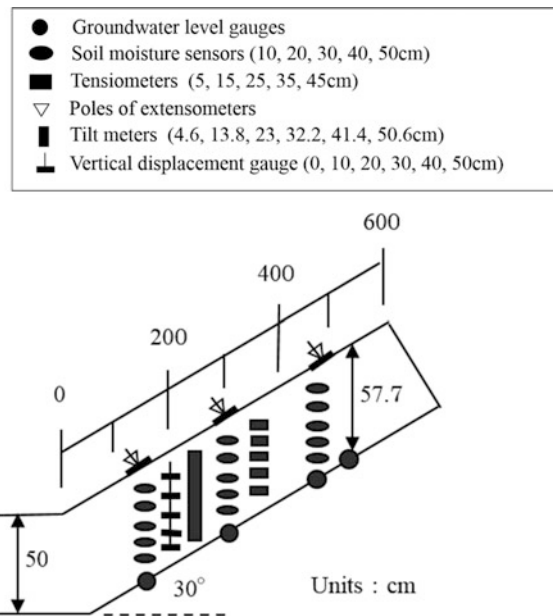
Monitoring of the surface displacements and the groundwater levels in a sandy model slope under artificial rainfall was carried out and the measured data was analyzed in order to establish a time-prediction method of the onset of rainfall-induced landslides based on the stress-strain relationship of a soil.

2 Methodology

2.1 Experimental Apparatus

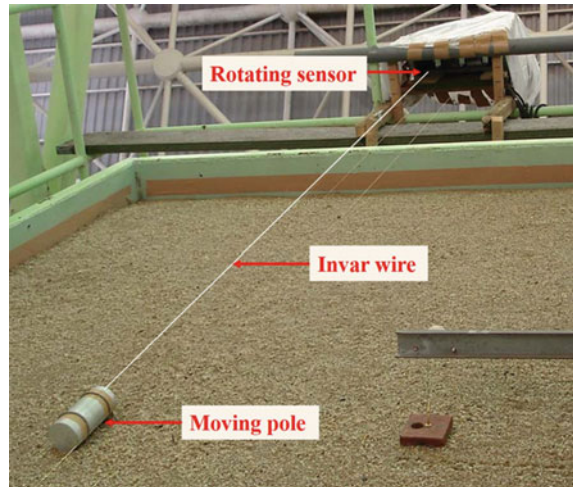
Figure 2 shows the longitudinal section of the model slope and the location of the monitoring devices. The model is 300 cm in length, 150 cm in width, and 50 cm in depth in the gravitational direction at the horizontal section; 600 cm in length, 150 cm in width, and 57.7 cm in depth at the slope section with an inclination of 30°. It was made in the Large-scale rainfall simulator room at National Research Institute for Earth Science and Disaster Prevention. The model is composed of

Fig. 2 Geometry of the model slope and the arrangement of the measurement devices



granite soil ($D_{50} = 1.3$ mm, $U_C = 22.23$, $F_C = 13.2\%$) and was made in a steel flume with vertical blades of 1 cm in height at every 50 cm in the longitudinal direction at the base of the slope to prevent slippage between the base of the model and the flume. The surface of the slope is parallel to the base of the slope. The inclination and the thickness of the model slope are determined based on the fact that most rainfall-induced landslides at the topsoil layer occur on slopes of 30–50° that are 0.5–1.5 m thick (Osanai et al. 2009). The soil is compacted horizontally by human stamping at every 20 cm to construct the model slope. The void ratio ranged from 0.65 to 0.68, and the water content of the soil layer was 3.7–4.4 %. The base and upper boundary of the flume were impermeable while the lower boundary was permeable. It is just like the structure of the slope layers with the top soil layer on the impermeable base rock.

The surface displacement was measured by an extensometer with a resolution of approximately 0.1 mm which was fixed at the upper boundary of the flume. The surface displacement was defined as the distance between the upper boundary of the flume and the moving pole at the surface of the slope (Photo 1). Moving poles move downward according to shear deformation of a slope due to rainfall infiltration and it results in the increase of the surface displacement. Moving poles were installed at 150, 300, and 450 cm from the toe of the slope. The groundwater level (hereafter G. W.L.) at the base of the slope was measured by a water level gauge with an accuracy of 1 cm H_2O . The gauges were installed at 0, 150, 300, 450, and 525 cm from the toe of the slope.

Photo 1 Extensometer

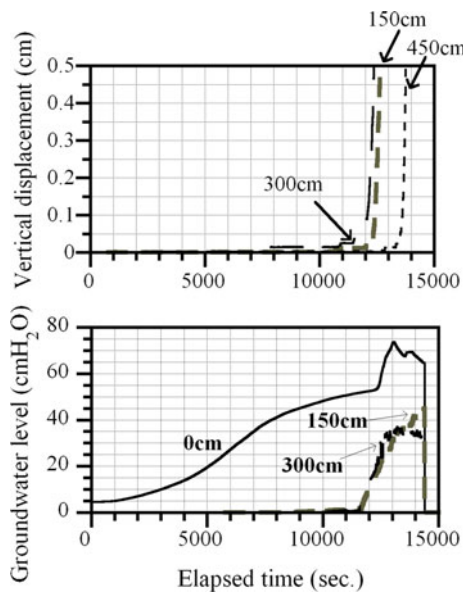
2.2 Experimental Conditions

To simulate the actual soil water condition in a natural slope which has experienced many rainfalls, three pre-rainfall events were conducted before the main rainfall event. The pre-rainfall events had rainfall intensity of 15–30 mm/h and the duration of 100–180 min. The main rainfall had intensity of 30 mm/h and continued until the onset of the failure of the model slope. The duration of the main rainfall is 240 min. The time interval between each pre-rainfall was 3 days and the interval between the last pre-rainfall and the main rainfall was 9 days. Rainfall intensity was determined based on the consideration that the rainfall-induced landslide occurs at the rainfall with rainfall intensity more than 30 mm/h in Japan (Osanai et al. 2009). The deformation was video recorded from the lateral side of the model slope, and no slip at the base of the flume could be observed.

3 Experimental Results

Figure 3 shows the time variation of the surface displacement and the G.W.L. at different distances from the toe of the model slope. The G.W.L. at 450 cm was zero throughout the experiment; therefore, it was not shown in this figure. The surface displacement at 150 and 300 cm showed significant increases from 12,000 s. A remarkable increase in the surface displacement at 450 cm started from 13,000 s, which was slightly later than the increases at 150 and 300 cm. And then the slope failed at 14,400 s. The G.W.L. at 150 and 300 cm increased significantly from 11,000 to 13,000 s when the surface displacement started to increase significantly. These facts suggested that the surface displacement increased significantly with the

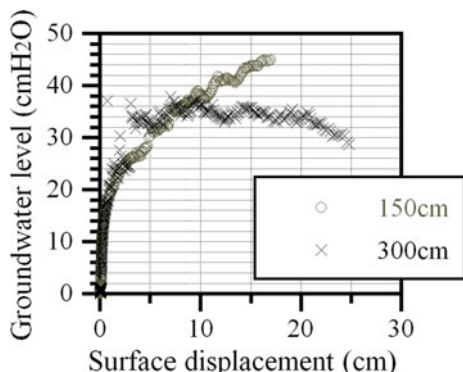
Fig. 3 Time variation of the surface displacement and the groundwater level at different distances from the toe of the model slope



generation of the G.W.L. at the base at the section between 150 and 300 cm while it increased without the generation of pore pressure at 450 cm. It is usually recognized that the behavior at 450 cm depends on the decrease of the suction in the soil while it cannot be denied that soil mass of the upper part of the slope moved only following the movement of the lower part of the slope without any influence of soil water condition. So the movement at 450 cm is out of scope in this paper.

The examination as above suggested the increase of the pore pressure generated the deformation of the slope. Thus, the dependency of the surface displacement on the pore pressure should be discussed. Figure 4 shows the relation between the surface displacement and the G.W.L. at 150 and 300 cm from the toe of the slope. The relation at 150 cm was almost same with that at 300 cm until 10 cm of the

Fig. 4 Relationship between the surface displacement and the groundwater level in the slope



surface displacement. The surface displacement increased slightly with the increase of the G.W.L. at first and then it developed significantly with the increase of the G.W.L. The relationship could be modified by hyperbolic function which is often adopted as stress-strain relationship of loose sand under direct shear condition. The relationship was examined in more detail in Sasahara and Sakai (2014) and they picked up some problems for the relationship to be adopted as the constitutive relationship for a slope. But the relationship is adopted for the basis of time prediction of rainfall-induced landslides in this paper instead of the problems.

4 Proposal of New Method for Time Prediction of a Rainfall-Induced Landslide

4.1 Basic Idea

It was made clear that the relation between the surface displacement and the G.W.L. in the slope could be modeled by the hyperbolic function. Based on the result, new procedure for time prediction of the onset of a rainfall-induced landslide is proposed. The relation between the surface displacement and the G.W.L. and that between the time and the G.W.L. is derived by the regression analysis of the measured data at any time during the experiment. The formula for simulating the relation between the time and the surface displacement is derived by combining these regression equations. All the formula for the prediction can be derived completely depending on the measured data of the surface displacement and the G.W.L. in this procedure.

4.2 Formula for the Prediction of Time–Surface Displacement Relation

4.2.1 Regression Analysis Between the Surface Displacement and the G.W.L

The relation between the surface displacement and the G.W.L. is derived by the regression analysis of the measured data until any time during the experiment. This analysis needed the surface displacement and the G.W.L. corresponding to the time of the surface displacement. The data are picked up at every 0.25–0.5 cm of the surface displacement. The hyperbolic function below is adopted for the relation between the surface displacement and the G.W.L.

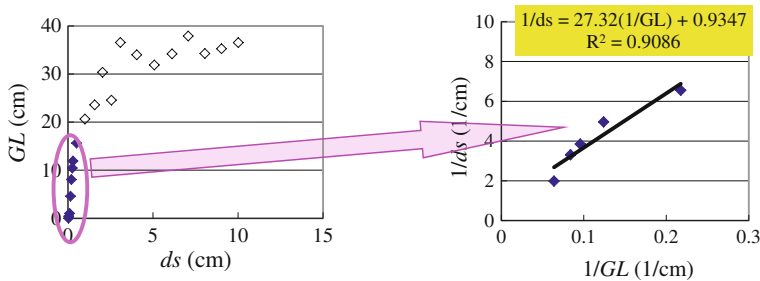


Fig. 5 Regression analysis of the relation between the surface displacement and the groundwater level with the measured data of $ds \leq 0.5$ cm

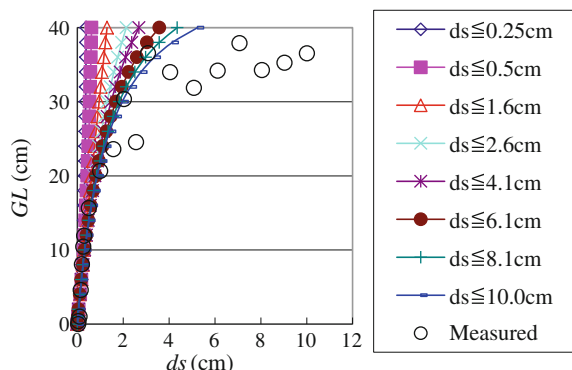
$$ds = \frac{1}{G_{\text{sur.}}} \frac{GL_{\text{max}} \cdot GL}{GL_{\text{max}} - GL} \quad (4.1)$$

Here, ds : the surface displacement, GL : the G.W.L., and $G_{\text{sur.}}$, GL_{max} : experimental constants. Left and right hands of Eq. (4.1) are inversed as below for linear regression analysis.

$$\frac{1}{ds} = \frac{GL_{\text{max}}}{\bar{G}} \frac{1}{GL} - \frac{1}{\bar{G}} \quad (4.2)$$

Here $\bar{G} = GL_{\text{max}}/GL_{\text{sur.}}$. Regression lines were derived in this study by using the ‘Add Trendline’ for the ‘XY(Scatter) chart’ on Microsoft EXCEL 2010. ‘Linear Trend/Regression type’ should have been selected for the linear regression analysis after selecting ‘Add Trendline’. Figure 5 shows the example of the regression analysis for the data of $ds \leq 0.5$ cm. Inversing the regression equation $1/GL - 1/ds$ results in the relations of $GL - ds$. Figure 6 shows the comparison of the relations of $GL - ds$ at every 0.5–1 cm of the surface displacement. Measured data are also shown

Fig. 6 Comparison of the regression curve for the relationship between the surface displacement and the groundwater level derived from the measured data of different ds



in the figure for the comparison. It is recognized that regression curve derived from the measured data of the larger ds can simulate the measured relation better.

4.2.2 Regression Analysis Between the Time and the G.W.L

The relation between the time and the G.W.L. is derived by the regression analysis of the measured data until any time during the experiment. Figure 7 shows the comparison of the relations derived from the measured data of the different ds during the experiment. Logarithmic function as below is selected for the regression analysis because this function simulates the relation well with the R^2 value of more than 0.9. T means the time; a_1 and a_2 in the equation below are the experimental constants in the equation.

$$GL = a_1 \cdot \ln(T) - a_2 \quad (4.3)$$

It is recognized that regression curve derived from the data of any ds shows small difference and any curve can simulate the measured data relatively well.

4.2.3 Time–Surface Displacement Relationship

Equation for the prediction of time–surface displacement at any time during the experiment is derived by the combining regression equation for the relation between the surface displacement and the G.W.L. and that for the relation between the time and the G.W.L. at the same time. After inserting Eq. (4.3) at a time to “ GL ” in Eq. (4.1) at the same time, Eq. (4.4) is derived as below.

$$ds = \frac{1}{G_{\text{sur.}}} \cdot \frac{GL_{\text{max}} \cdot a_1 \cdot \ln(T) - GL_{\text{max}} \cdot a_2}{(GL_{\text{max}} + a_2) - a_1 \cdot \ln(T)} \quad (4.4)$$

Fig. 7 Comparison of the regression curve between the time and the groundwater level derived from the measured data of different ds

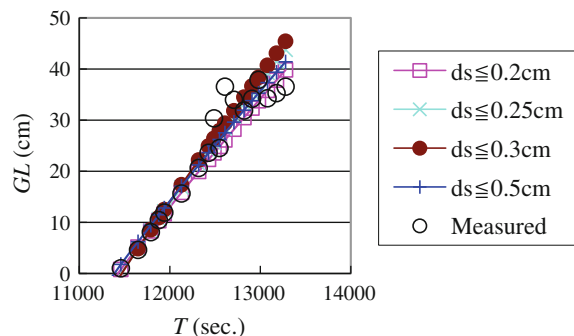


Fig. 8 Comparison of the relation between the time and the surface displacement derived from the measured data until different ds

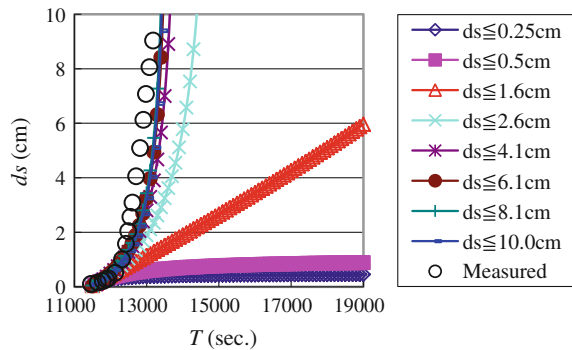


Figure 8 shows the relation between the time and the surface displacement derived by the equation with the data until different ds . It is recognized that the equation with the data until larger ds can simulate the measured data better. While the equations with the data of $ds \leq 4.1\text{--}10\text{ cm}$ show almost same relations and they simulate the measured data well.

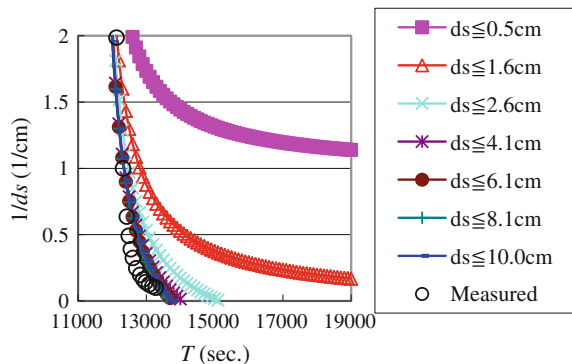
4.3 Time Prediction Based on the Time–Surface Displacement Relationship

Inserting Eq. (4.3) into Eq. (4.2) results in the relation as below. This equation explains the relation between the inverse of the surface displacement “ $1/ds$ ” and the time “ T ”. “ $1/ds$ ” decreases to zero as the surface displacement increases and approaches the failure state of the slope. Thus the time when “ $1/ds$ ” approaches almost zero can be regarded as the time of the failure of the slope.

$$\frac{1}{ds} = G_{\text{sur.}} \left(\frac{1}{a_1 \cdot \ln(T)} - \frac{1}{GL_{\max}} \right) \quad (4.5)$$

Figure 9 compares the relation between “ $1/ds$ ” and “ T ” derived by Eq. (4.5) with the data until a different ds . The relation with the data until larger ds can simulate the measured data better. In addition, the relations with the data of $ds \leq 4.1\text{--}10\text{ cm}$ are almost the same with the measured data. “ $1/ds$ ” seems to approaches zero at 13,500 s on the simulated relation while actual failure time of the slope was 14,400 s. It is recognized that the time prediction based on the relation between “ $1/ds$ ” and “ T ” can provide relatively good agreement with an actual phenomena.

Fig. 9 Relation between the time “ T ” and “ $1/ds$ ” derived from the measured data until different ds



5 Conclusions

Based on the monitored data of the groundwater and the surface displacement in the model slope under artificial rainfall, deformation characteristic of the model slope was examined and new time-prediction method for the onset of a rainfall-induced landslide is proposed based on the examination.

1. The surface displacement increased slightly with the increase of the G.W.L. at first and then the surface displacement increased remarkably with the increase of the G.W.L. The relation between the surface displacement and the G.W.L. can be modified as hyperbolic.
2. Based on the hyperbolic relation between the surface displacement and the groundwater level, new time-prediction method for the onset of a rainfall-induced landslide are proposed and examined. Regression analyses on the relationship between the surface displacement and the G.W.L. at a time and that between the time and the G.W.L. at the same time were carried out at first and then the second relationship is incorporated into the first relationship. This produces the equation for time–surface displacement relationship. Inversing the equation provides the relationship between the inverse of the surface displacement and time. This relationship can be used for the time prediction. Applying the procedure to the monitored data showed that this procedure could give good agreement with the actual relationship between the time and the inverse of the surface displacement even with the data until the half of the surface displacement at failure. It suggested that this procedure could give good prediction of the time of failure.

References

Caine N (1980) The rainfall intensity-duration control of shallow landslides and debris flows. *Geografiska Annalar Ser A Phys Geogra* 62:23–27

Fukuzono T (1985) A new method for predicting the failure time of a slope. In: Proceedings of IVth international conference and field workshop on landslides, Tokyo, Japan, pp 145–150

Osanai N, Tomita Y, Akiyama K, Matsushita T (2009) Reality of cliff failure disaster. Technical Note of National Institute for Land and Infrastructure Management No. 530 (in Japanese)

Saito M (1965) Forecasting the time of occurrence of a slope failure. In: Proceedings of 6th international conference on soil mechanics and foundation engineering Montreal, Canada vol 2, pp 537–541

Sasahara K, Sakai N (2014) Development of shear deformation due to the increase of pore pressure in a sandy model slope during rainfall. *Eng Geol* 170:43–51

Uchida T et al (2009) Countermeasures for sediment-related disasters in Japan using hazard maps. *Int J Erosion Control Eng* 2(2):48

Typhoon Rainfall Induces Slope Creep, Groundwater Variation, and Slope Movement

C.J. Jeng, C.Y. Yang and J.H. Lin

Abstract This study explores the behavior of long-term creep of a slope at the campus of Huafan University and changes in the groundwater level and displacements caused by typhoons. First, results from dozens of existing inclinometers on campus were used to observe long-term creep over a period extending beyond the past decade. Furthermore, the relations between the rainfall, groundwater variations during typhoons, and the surface displacement behaviors were analyzed. Additionally, a range of rainfall thresholds for issuing message were proposed. All monitored and analyzed results were compared to draw out more detailed potential sliding ranges; these may be used as a reference for future remediation. These findings will be used as a reference for slope disaster prevention and maintenance management.

Keywords Slope creep · Typhoon rainfall · Monitoring system · Groundwater · Rainfall threshold value

1 Introduction

The test site discussed in this research is located in the Talun mountain area of the Shiding District in New Taipei City, at an elevation of 550 m. The monitored slope displacement and water level changes caused by typhoon rainfalls were analyzed. Accordingly, the sliding range and sliding depth were determined and the information was used to evaluate the feasibility and priorities of counter measures. Finally, ranges of rainfall threshold values for slope instability were established to provide a reference for risk management.

C.J. Jeng (✉) · C.Y. Yang · J.H. Lin
Huafan University, New Taipei, Taiwan, ROC
e-mail: jcjh@cc.hfu.edu.tw

2 Literature Review

2.1 Inclinometer Displacement

According to a suggestion by the Japan Landslide Association, we can classify the different warning conditions of a landslide as shown in Table 1 (Shieh 2009):

2.2 Time Evolution of Creeping Landslide

Xu (2011) proposed that time evolution of a creeping landslide can be divided into three stages, namely the “initial stage,” “constant stage,” and “accelerated stage,” which has an obvious feature in its tangent angle when transferring from a S - t curve into a T - t curve, as shown in Figs. 1 and 2.

Table 1 Different warning conditions of a landslide (Japan Landslide Association 1978)

| Different kinds of warning | Monthly displacement (mm) | Tendency | Activities judgment | Notes |
|----------------------------|---------------------------|----------------------|---------------------|--|
| Emergency slide | More than 500 | Very significant | Rapid collapse | Collapse type, mudflow type |
| Accurate slide | More than 10 | Significant | Actively motion | Colluviums sliding, deep-seated creeping |
| Semi-accurate slide | More than 2 | Slightly significant | Slow motion | Clay sliding, backfill siding |
| Potential slide | More than 0.5 | Slightly | Remain to be seen | Clay sliding, talus sliding |

Fig. 1 Slope sliding displacement (S) versus time (t) relation curves and deformation stages (Xu 2008)

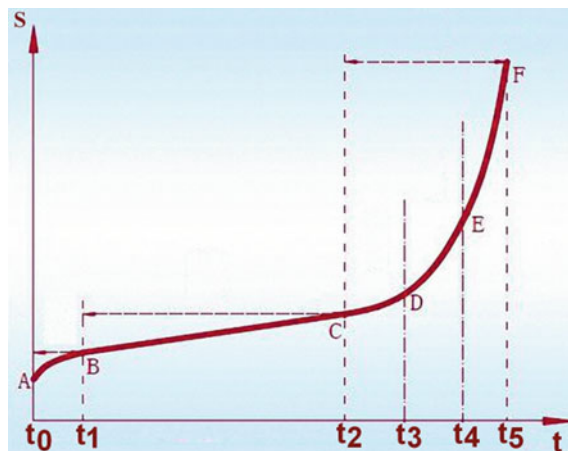


Fig. 2 Patterns of slope *S-t* curve (Xu 2011)

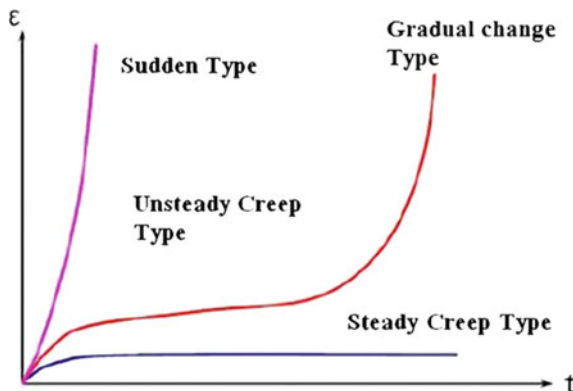


Table 2 Daily cumulative rainfalls versus deformation of inclinometers

| Item | Daily cumulative rainfall (mm/day) | Surface deformation from inclinometer (mm) |
|------|------------------------------------|--|
| 1 | 30–50 | 0.5–2.0 |
| 2 | 50–150 | 2.0–4.0 |
| 3 | 150–300 | 4.0–6.0 |
| 4 | 300–500 | 6.0–10.0 |
| 5 | >500 | >10.0 |

2.3 Cumulative Rainfall and Slope Deformation (Inclinometers)

Based on the monitoring results of inclinometers at Huafan campus, a preliminary relationship between daily cumulative rainfall and surface displacement from inclinometers has been analyzed. The results are shown in Table 2.

3 Geology and Topography Analysis

Figure 3 shows a satellite photo of the site. It indicates that the campus is located near the top of a hill and four waterways flow downwards from the top. The main strata outcropping at the site is *Mushan* strata, which mainly consists of sandstone and shale. The slope has an east-west strike with a dip angle about 10° – 20° toward to the south, thus making the slope a dip slope. Site investigations conducted by

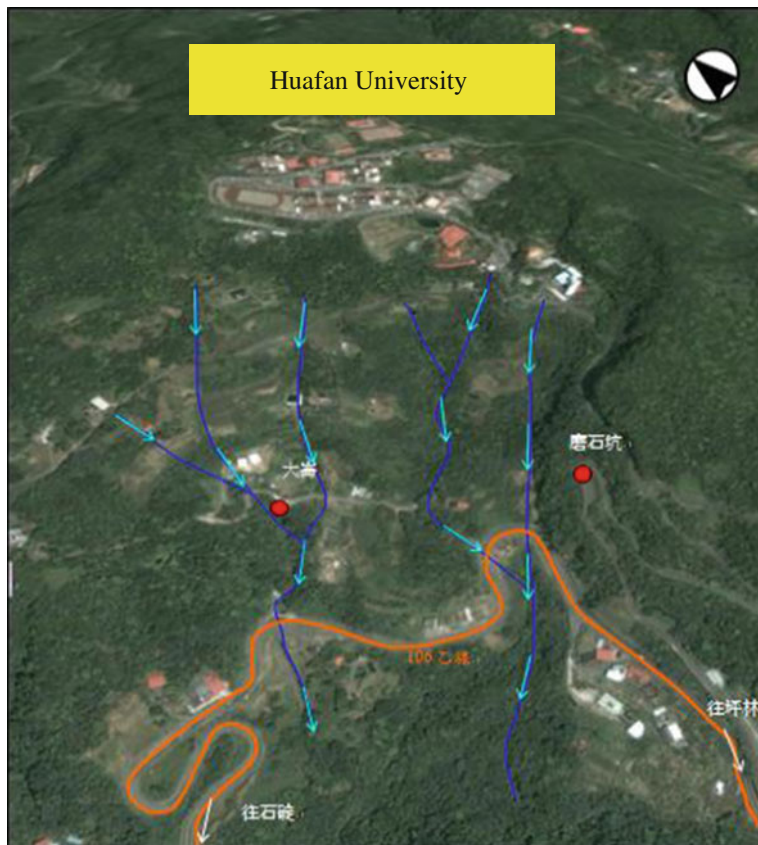


Fig. 3 Test site satellite photo (2006)

core drilling and 2D-resistivity image profiling determined with terrain features showed that the area has two small local faults. They are the Nanshikeng fault and an A-fault with a strike in the northwest direction (Fig. 4).

The geological conditions of the site are determined using the results obtained from a series of geological drilling surveys conducted over the years for the construction of building plans and installation of monitoring equipment for slope stability evaluation. Figure 5 shows the locations of inclinometers and self-recording water level gages. Based on these core drilling surveys, the required geological conditions for evaluating the slope stability were obtained.

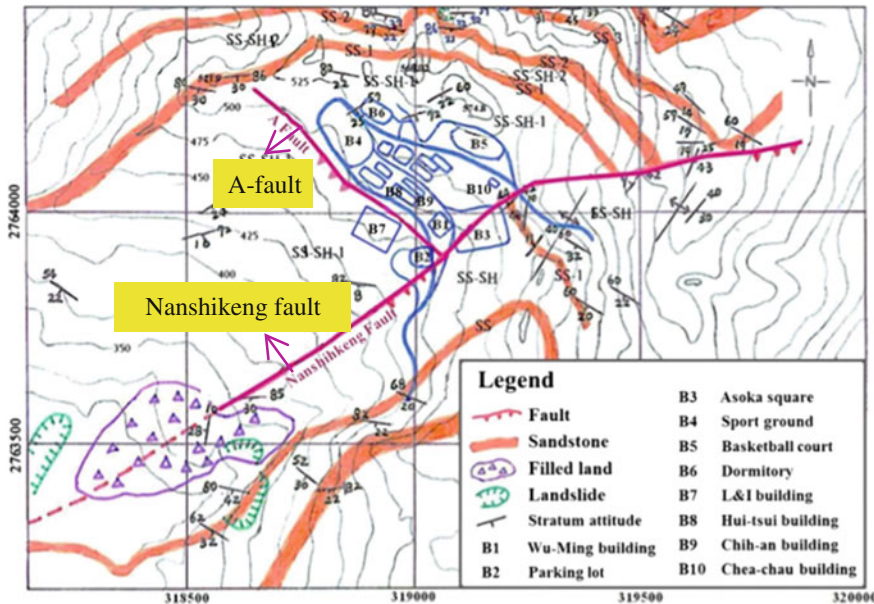


Fig. 4 Site geological map (Jeng et al. 2008)

4 Monitoring Data Analysis and Discussion

4.1 Groundwater Level Analysis

In this study, we used four self-recording water level gages to monitor the water table. The relationship between rainfall and groundwater was studied and the time lag of groundwater rise-up point to the peak rainfall was compiled. All rainfall and groundwater level data were taken from the field at the Huafan University test site.

Figure 6 shows the locations of four self-recording water level gages. Figures 7, 8, 9 and 10 show the curves of the relationship between rainfall and groundwater from April to October in 2013. These curves illustrate the changes in the water table caused by rainfall. The influence factors of groundwater depend on the rain type, rainfall amount, time lag, the slope location where the water level is observed, and which season it is. Taking into account all these factors, the relationship between peak rainfall intensity and time lag of the peak groundwater level response in these four self-recording water level gages (W1–W4) were drawn. Meanwhile, the peak rainfall intensity and the water table rise-up correlation diagrams are shown in Figs. 11, 12, 13 and 14.

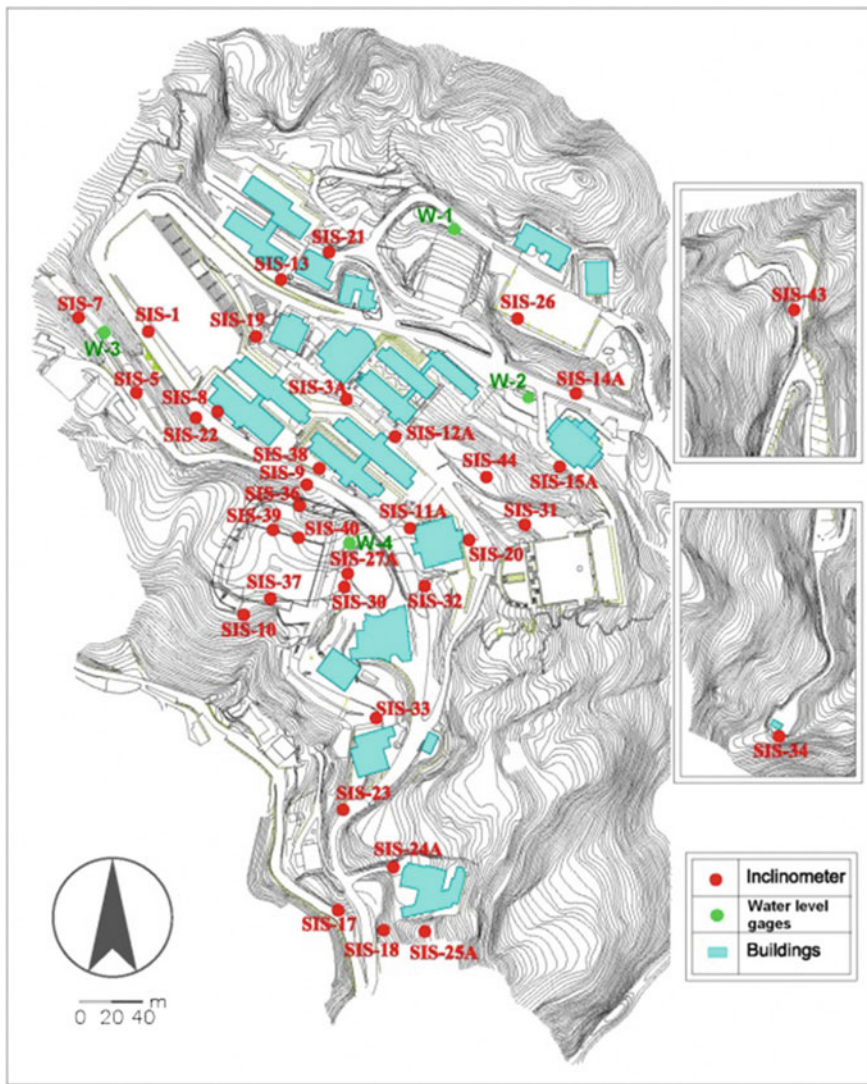


Fig. 5 Locations of inclinometers and self-recording water level gages

Using the above data, we were able to identify the changes in the water table caused by typhoon rainfalls. Influence factors discussed include the rainfall type, rainfall amount, water level time lag, the water level, and the season of the year.



Fig. 6 Locations of self-recording water level gages

Based on all these water level changes, the largest value of water level rise-up affected by the typhoon rainfall is near well W1. Therefore, the first priority for slope stability improvement should be near the W1 observation well.

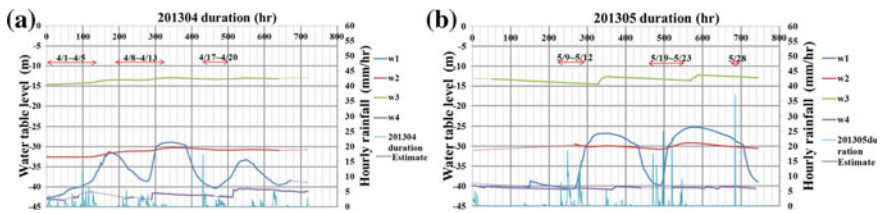


Fig. 7 The relationship between rainfall and groundwater (a) in April 2013 (b) in May 2013

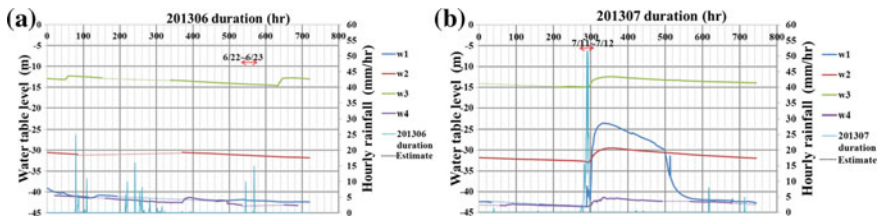


Fig. 8 The relationship between rainfall and groundwater (a) in June 2013 (b) in July 2013

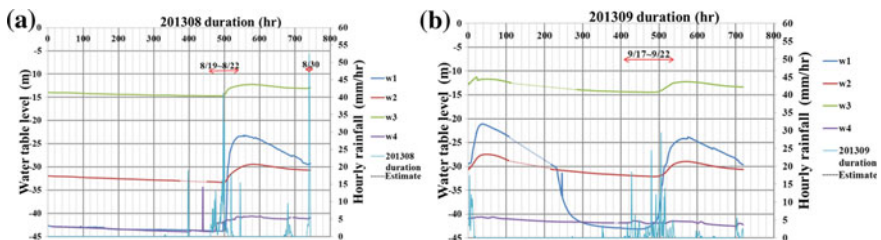


Fig. 9 The relationship between rainfall and groundwater (a) in August 2013 (b) in September 2013

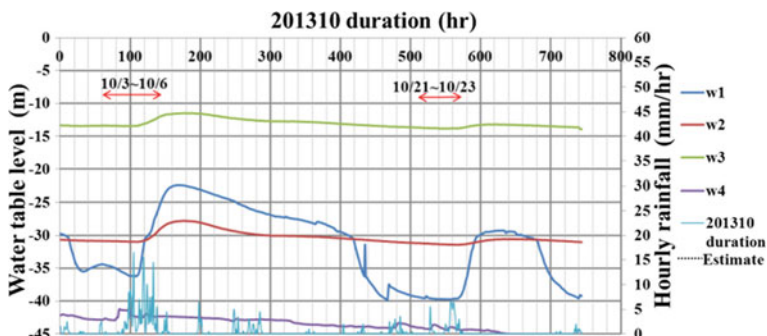


Fig. 10 The relationship between rainfall and groundwater in October 2013

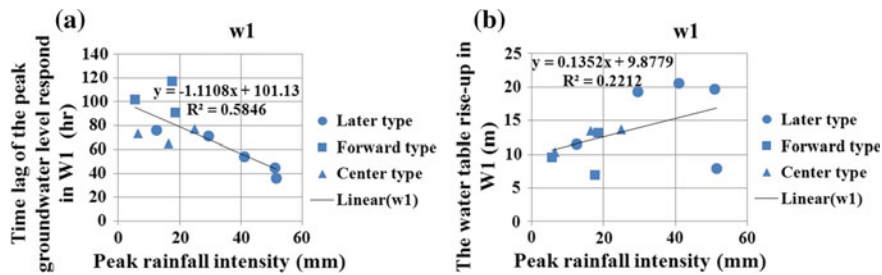


Fig. 11 **a** Peak rainfall intensity and time lag of the peak groundwater level response in W1. **b** Peak rainfall intensity and the water table rise-up in W1

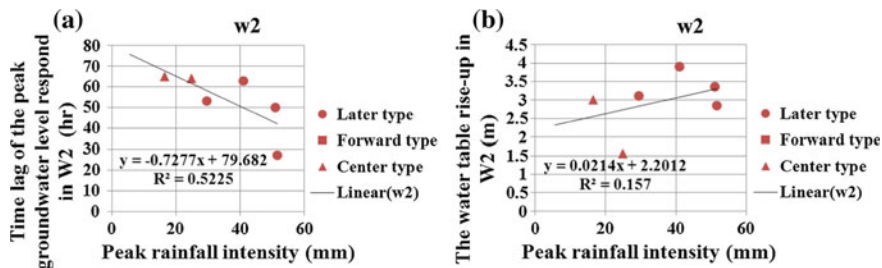


Fig. 12 **a** Peak rainfall intensity and time lag of the peak groundwater level response in W2. **b** Peak rainfall intensity and the water table rise-up in W2

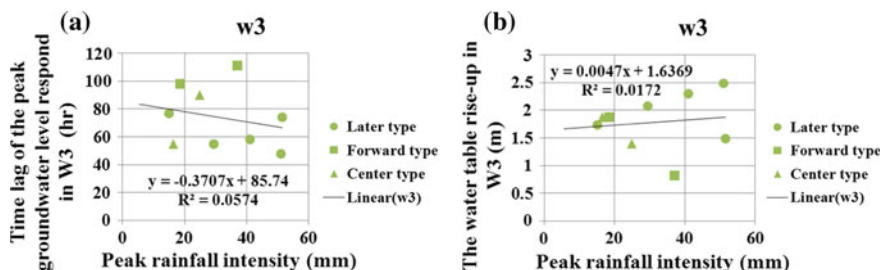


Fig. 13 **a** Peak rainfall intensity and time lag of the peak groundwater level response in W3. **b** Peak rainfall intensity and the water table rise-up in W3

4.2 Surface Displacement Analysis (Inclinometer)

The displacements of the slope during a typhoon were observed with 29 inclinometers and correlate with typhoon cumulative rainfall. Figure 15 shows the location of the inclinometers. Different locations may imply different slope

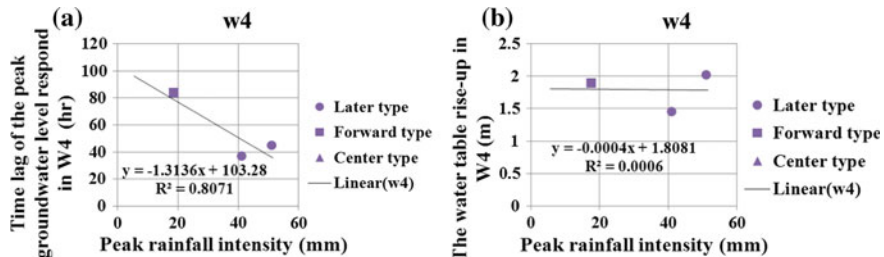


Fig. 14 **a** Peak rainfall intensity and time lag of the peak groundwater level response in W4. **b** Peak rainfall intensity and the water table rise-up in W4

geometries, loadings, and hydrogeological conditions. All displacements triggered by each typhoon were analyzed and the first nine inclinometers shows significant displacement were chosen and are shown in Figs. 16, 17 and 18. The data points of displacement for lower values are correlated separately with those for larger accelerated displacement points in each figure. The turning points of these two different correlation lines are obtained from each figure and marked on their horizontal axis values as the threshold of the typhoon alert rainfall for each inclinometer. Based on these correlation curves and with reference to the acceleration performance studies of critical sliding by Xu (2009), ranges of recommended threshold rainfall were determined as listed in Table 3 for various areas.

According to the acceleration trend of surface displacement, ranges of rainfall threshold for the nine inclinometers are proposed. Figure 19a shows the locations of the aforementioned nine inclinometers. The accumulated rainfall issuing warning message is approximately between 315–495 mm, and the lowest value is near the Wuming building and sports ground, which means that the risk is highest at this location.

Besides the value of inclinometer displacement discussed above, the displacement rates of inclinometers are determined from the time history curves of each inclinometer. The distribution of inclinometer displacement rate is shown in Fig. 19b. The interval of displacement rate shown in the figure is 1 mm per month. In the marked areas, the darker colors represent larger displacement rates, whereas the lighter colors indicate smaller displacement rates. The distribution of inclinometer sliding depth is shown in Fig. 19c. The interval of sliding depth shown in the figure is 10 m. A darker color represents sliding at a deeper depth, whereas a lighter color denotes a smaller sliding depth.

Comparison of the distribution area from Fig. 19a–c shows that the areas with significant surface displacements are the same as those with larger displacement rate areas, and similarly coincide with those of deeper sliding depth areas.

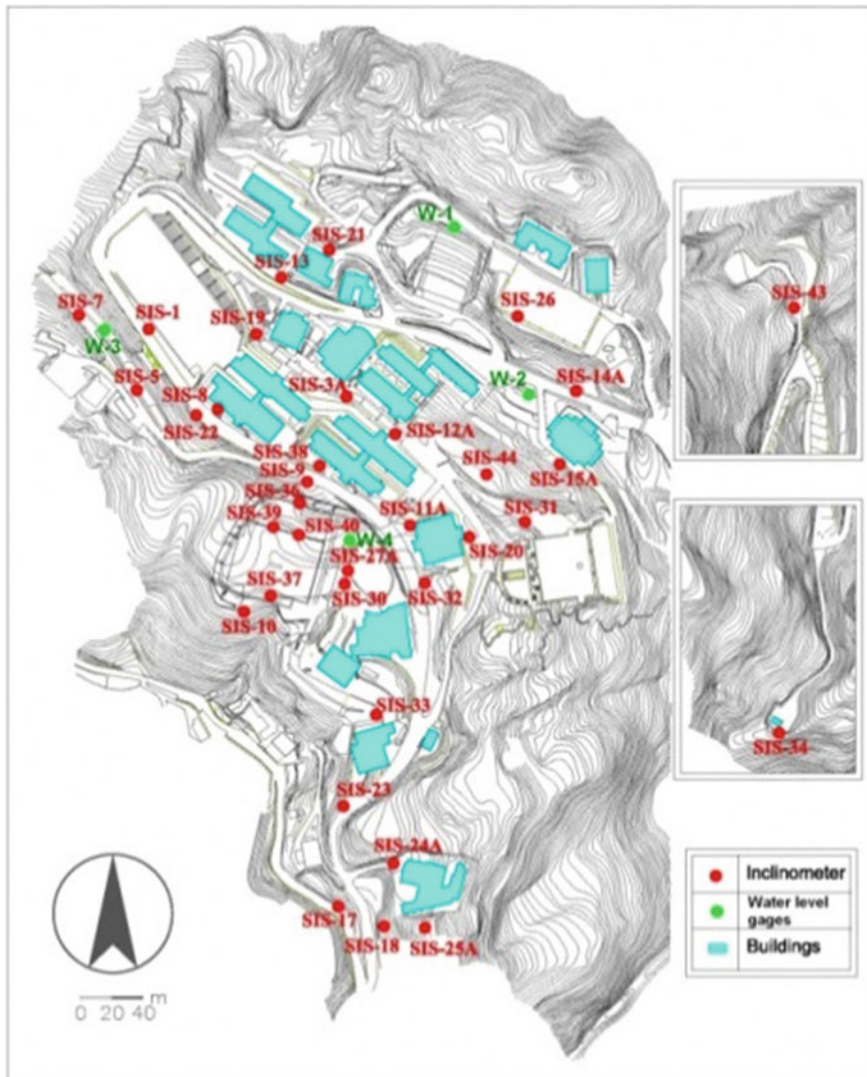


Fig. 15 Locations of inclinometers

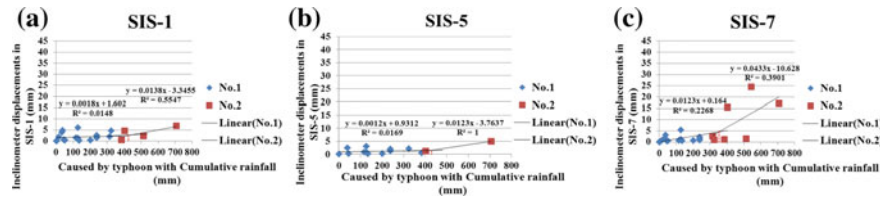


Fig. 16 Correlation of inclinometer displacements caused by typhoons with cumulative rainfall

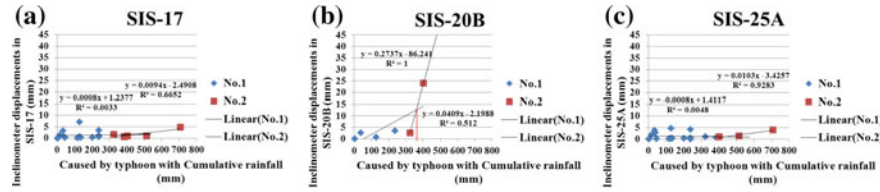


Fig. 17 Correlation of inclinometer displacements caused by typhoons with cumulative rainfall

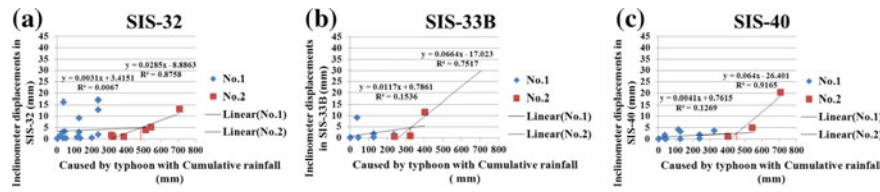


Fig. 18 Correlation of inclinometer displacements caused by typhoons with cumulative rainfall

Table 3 Threshold of the accumulated rainfall for slope instability

| Inclinometer number | Threshold rainfall (mm) | Inclinometer number | Threshold rainfall (mm) |
|---------------------|-------------------------|---------------------|-------------------------|
| SIS-1 | 420 | SIS-25A | 420 |
| SIS-5 | 420 | SIS-32 | 495 |
| SIS-7 | 350 | SIS-33B | 315 |
| SIS-17 | 420 | SIS-40 | 460 |
| SIS-20B | 370 | — | — |

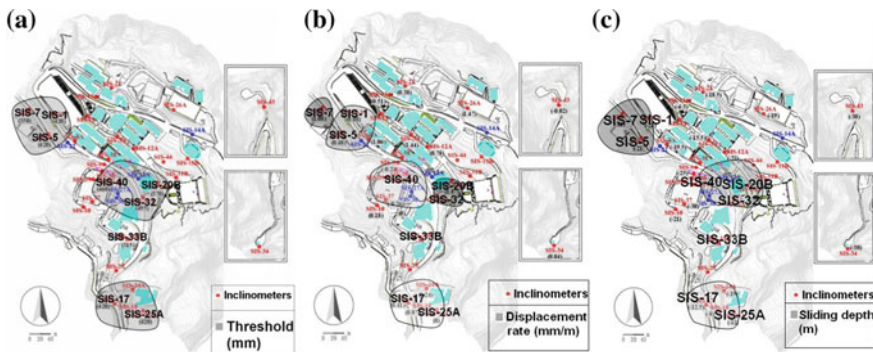


Fig. 19 **a** Location of the nine significant surface displacement area based on the measurement of inclinometers. **b** Distribution of inclinometer displacement rate. **c** Distribution of inclinometer sliding depth

5 Conclusions

1. When the peak rainfall is larger, the time lag of groundwater level rise-up will be shorter, and the rainfall pattern is almost a rear peak type rather than any other type of rainfall, which makes changes in the water table larger. Hence, special attention needs to be given to the rear peak type rainfall pattern.
2. Among four holes of water level changes, the water level changing in W1 indicates that W1 is largely affected by the typhoon rainfall. Therefore, the slope near the W1 observation well should be the first priority for slope stability improvement.
3. According to the acceleration trend of surface displacement, ranges of rainfall threshold in the nine inclinometers are proposed. The accumulated rainfall for issuing warning message is approximately between 315–495 mm, and the lowest value is near the Wuming building and sports ground, which means that the risk is highest at this location.

Acknowledgments The authors would like to thank the National Science Council of the Republic of China (No. NSC 102-2632-E-211-001-MY3) for financially supporting this research.

References

Japan Landslide Association (1978) Essential implementation of technical design for landslide countermeasures, vol 2, p 22 (in Japanese)

Jeng CJ, Huang CS, Shieh CY (2008) Case study of the application of in-situ geological mapping and 2D-resistivity image exploration for the slope in Huafan University. *J Art Des Huafan Univ* (4):166–180 (in Chinese)

Shieh CY (2009) A case study on the sliding surface judgment and the countermeasures for campus on slope land. Master thesis (in Chinese)

Xu Q (2008) Research on space-time evolution laws and early warning prediction of landslides. Chin J Rock Mech Eng 27(6):1104–1112 (in Chinese)

Xu Q (2011) Landslide hazard early-warning and emergency treatment. Presentation on Sichuan week: National Chung Hsing University Academic Report (in Chinese)

Topographic Characteristic of the Rainfall-Inducing Landslide in Slate Stratum—Case of Ai-Liao Catchment, South Taiwan

Tien-Chien Chen, Ping-Yuan Jhang and Huei-Jing Ciou

Abstract This paper describes the topographic characteristics of the landslides induced by 2009 Typhoon Morakot in Ai-Liao catchment, a slate geologic region. The topographic analysis on DEM shows 52 % of landslides were larger than 10 ha, the average slope of landslides was 20°–40°, and 81 % of the landslides were located at the hillside or the toe of slope. This was related to washing away by the river. For a massive landslide, the analysis results also demonstrate that a certain degree of deflection usually occurs before a sliding initiation. This suggests the deformation of a massive landslide is progressive. Moreover, when the profiles curvature of a landslide are close or above the curvature 1×10^{-4} (l/m), the sliding possibility of a massive landslide will increase.

Keywords Landslide · Rainfall · Topography · Curvature

1 Introduction

Previous studies indicated that the landslide locations can be quite different for different triggering forces. For example, landslides induced by the rainfall mostly distributed at the hillside and slope toe, so their scale is often greater than those induced by earthquakes (Pierson 1977; Fuchu et al. 1999; Chang et al. 2007). In order to explore the characteristics of the rainfall triggered landslides, we focus on the catchment of Ai-Liao River. There are 2327 landslides after Typhoon Morakot, as shown in Fig. 1 was identified. The geography information system and pre-event

T.-C. Chen (✉) · P.-Y. Jhang · H.-J. Ciou
National Pingtung University of Science and Technology,
#1 Shuefu Road, Neipu, Pingtung 912, Taiwan
e-mail: tcchen@mail.npust.edu.tw

P.-Y. Jhang
e-mail: moneyqq1992@gmail.com

H.-J. Ciou
e-mail: tzero7961@yahoo.com.tw

DEM were used to analyze the influence of the landslide depth, topography, and location of landslides. Accordingly, the characteristics of the rainfall triggered landslides were elucidated.

2 The Study Area

The Ai-Liao River flows through four towns at Pingtung County, South Taiwan. The catchments area of Ai-Liao River is about 34,025 ha, 80 % of which are hills, as can be seen in Fig. 1. Ai-Liao River is a consequent river on the western slope of a mountain located in southern Taiwan, with 90 km river form the source of the Zhi-ben Mountain (El. 2368.8 m).

The precipitation of the Ai-Liao River basin is very high, the average annual rainfall of up to 4500 mm. Tertiary Lushan formation is the main stratum in the basin that belongs to a class of sub-metamorphic rocks which consists of slate and phyllite. Figure 1 illustrates the landslide inventory and the geologic data of the study area.

3 The Topography of Landslides

The geographic information system (GIS) is utilized to delineate the landslides and to extract the topographic features from the DEM before typhoon event. Landslide locations are divided into ridge, hillside and foot. Landslide size are also classified into <1 ha, 1–10 ha, and 10–30 ha, and >30 ha as showing in Table 1. Landslides are also classified into dip, anti-dip, orthoclinal of dip, and orthoclinal of anti-dip (Table 2).

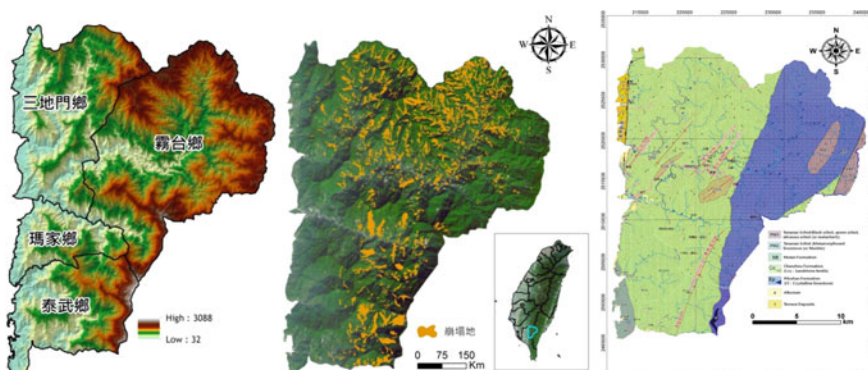


Fig. 1 Terrain, geology, and landslide inventory of Ai-Liao River

Table 1 The four categories of landslide size

| Landslide (ha) | Number | Number ratio (%) | Landslide area ratio (%) |
|----------------|--------|------------------|--------------------------|
| >30 | 24 | 1.0 | 24.6 |
| 10–30 | 92 | 4.0 | 27.4 |
| 1–10 | 701 | 30.2 | 37.5 |
| <1 | 1505 | 64.8 | 10.5 |
| Total | 2322 | 100.0 | 100.0 |

Table 2 The four categories of landslide slope type

| Slope type | Number | Number ratio (%) | Failure ratio (%) |
|-------------------------|--------|------------------|-------------------|
| Dip | 486 | 20.9 | 40.4 |
| Anti-dip | 251 | 10.8 | 7.4 |
| Orthoclinal of dip | 414 | 17.1 | 10.6 |
| Orthoclinal of anti-dip | 1171 | 51.2 | 41.6 |

3.1 Landslide Size and Slope Type

Table 1 contains the landslide number of different size categories in the area of Ai-Liao River after Typhoon Morakot. The total number of landslides is 2327. There were 24 landslides over 30 ha, and 92 landslides in 30–10 ha. There were 116 landslides over 10 ha in size, accounting for 5 % of the landslides. For the landslide area ratio (landslide area over total landslide area) in Table 1, the landslide smaller than 1 ha was 10.5 %; the landslides in 1–10 ha were 37.5 % showing that the landslides induced by rainfall have more middle and massive ones. For the landslides over 10 ha in size the landslide area ratio accounted for 52 %, showing that the large-scale landslides dominate the related hazards during Typhoon Morakot.

2322 landslides (5 entries of terraces are deleted) were classified into four types of slope. The location of dip slope is shown in Fig. 2. Table 2 shows that the landslides were mostly on orthoclinal of anti-dip slope, accounting for 51 %, followed by dip slopes. The orthoclinal slopes were 68.3 % in total. We inferred that the slate in Ai-Liao River catchment was highly jointed for the well develop cleavages and weak joints which not only reduced the rock strength but also enhanced the groundwater level caused by heavy rainfall infiltration. This led the shallow landslide on the orthoclinal slope apt to occur.

Furthermore, different slope type proportions of landslides for each landslide size category are shown in Fig. 3. The dip slopes often has a larger landslide size as shown in the figure. That is, the geological structure is the key influential factor of large-scale landslides. Moreover, as the downward cutting of Ai-Liao River was intense, stress releasing and cleavage are often founded in the hills. On the orthoclinal slopes, the rock mass is often highly jointed or covered by thick

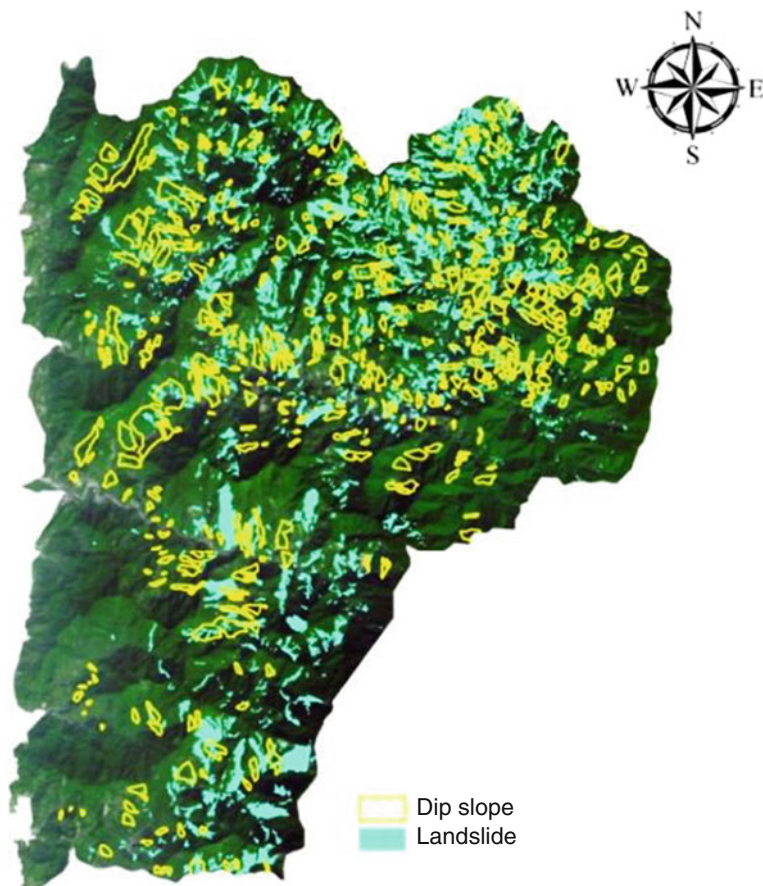
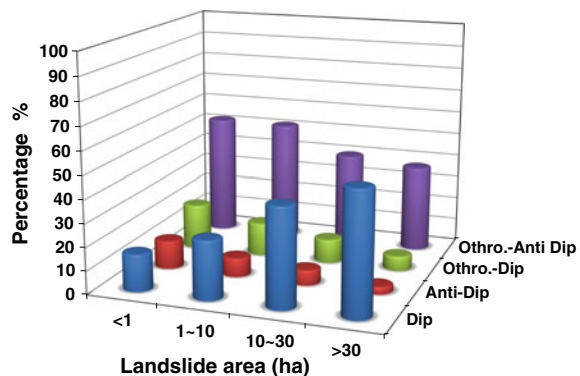


Fig. 2 Dip slopes and landslides distribution of the investigation area, the data of the dip slope were adopted from Lin (2010)

Fig. 3 The statistics of landslide size and type



colluvium; therefore, it tended to develop into middle and small-scale landslides (<10 ha).

3.2 Landslide Scale and Location

The statistics of the distribution of landslide locations at the Ai-Liao River are shown in Fig. 4. The methodology by Muenier et al. (2008) was applied to illustrate the distribution of landslide size and landslide location for the inventory. As shown in Fig. 4, landslides were 359 at the ridge, 784 at the hillside, 1101 at the foot, and 83 over the whole slope. The proportion of landslide locations was densely at the foot (47.31 %), followed by hillside (33.7 %), ridge (15.4 %), and whole slope (3.6 %). The landslide spot frequently distributed at the foot and the hillside of slope.

This study further investigated the distribution characteristics on large landslides and small landslides. The distribution of landslides located on the ridge, hillside, and foot are shown in Fig. 5 with separate figures for the landslide size larger or smaller than 1 ha. Comparing the events in Fig. 5, the landslide size bigger than 1 ha in ridge is 12.61 %; the one located at the foot is 54.71 %, and the whole slope landslides had 8.57 %. Large landslide areas triggered by Typhoon Morakot (>30 and 10–30 ha) were started at the foot of slope, then expanded up to the hillside, and extending over the whole slope at last. The landslides located on the hillsides were caused by deep slides resulting from the intense and long lasting rainfall. Otherwise, the landslides at the foot of slope were caused by the lateral erosion of river channel.

The distribution of small size landslides shows the similar characteristics to the big size landslides. Landslides were frequent and bigger at the foot of slope.

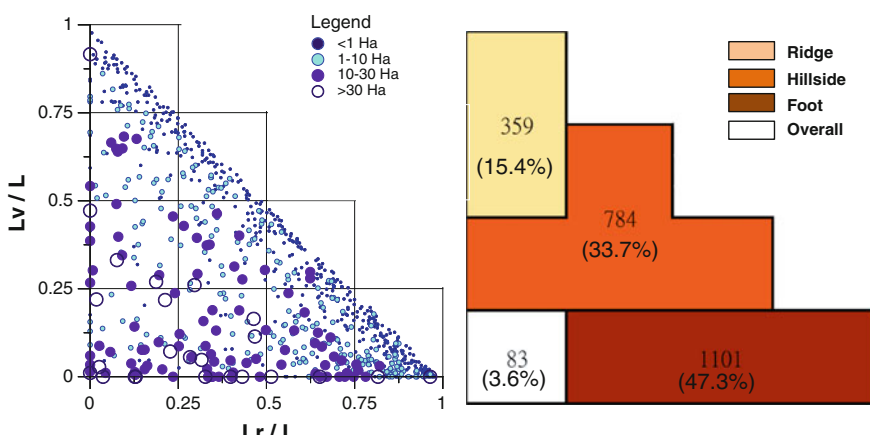


Fig. 4 The distribution of landslide size and location

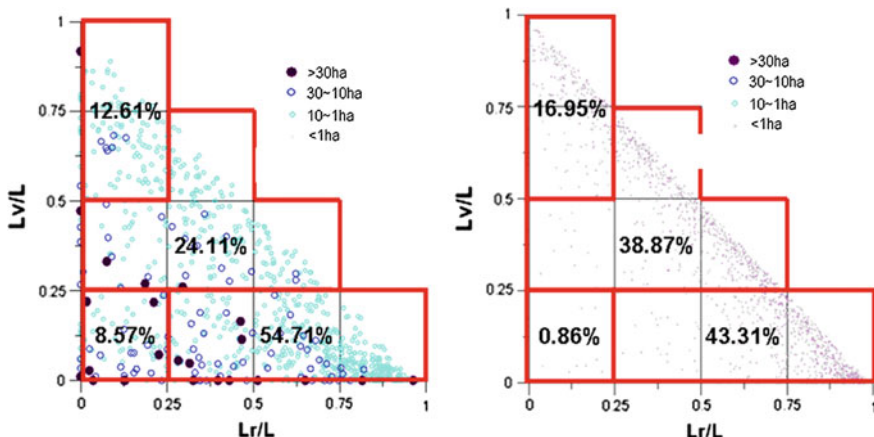


Fig. 5 Landslides location at ridge, hillside, and toe of slope for area >1 ha (left) and the area <1 ha (right)

3.3 Gradient of Landslides

The average slope angle of the landslides in the study area is shown in Fig. 6. The vertical axis is the percentage of the average slope angle of landslides. The histogram of each slope angle is the number of landslides. According to the statistics, the landslides induced by Typhoon Morakot are mainly distributed on the slopes with slope angles between 20° and 40° , accounting for 79 %. In general, the gradient of the rainfall-induced landslides are moderate.

The failure ratio of landslides is shown in Fig. 7. The failure ratio is the landslide area divided by the total area of each interval slope angles in the study area. The vertical axis shows the percentage of each interval failure ratio in total failure ratio. The histogram is the failure rate. It shows that the failure ratios are roughly similar

Fig. 6 The distribution of average slope angle of failure slopes in the catchment area of Ai-Liao River during Typhoon Morakot

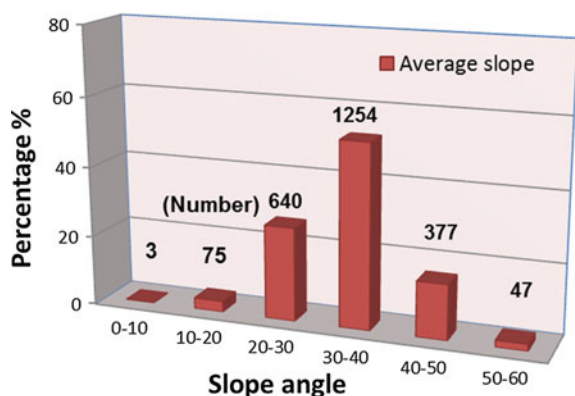
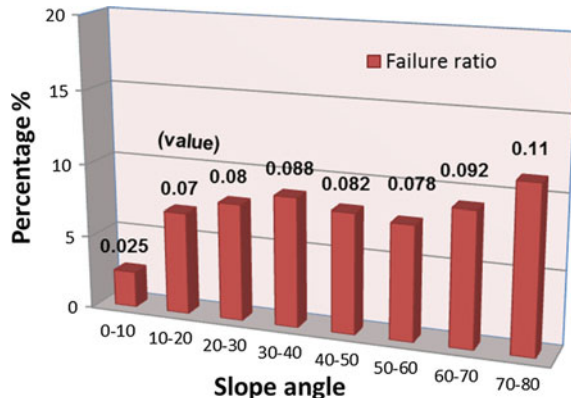


Fig. 7 The distribution of failure ratio for different slope angles in the catchment area of Ai-Liao River during Typhoon Morakot



to all slope angle intervals except the very gentle slope (slope angle small than 10°). The result elucidated that the potential of landslides are not so different for the gentle to the steeper slope in heavy rainfall events.

3.4 Shape of Large-Scale Landslides

The landslide size and location related to the shape of slope of large landslides were illustrated in Fig. 8. Landslides with size large than 5 ha were chosen in the figures, the plane and profile curvatures are set in the horizontal and vertical axis, respectively. The combinations of plane and profile curvatures were classified into nine blocks as shown in Fig. 8. Landslides were categorized into the location of ridge, hillside and foot, and also into the size in 5–10 ha, 10–30 ha and >30 ha.

Figure 8 shows the massive landslides are mostly located at hillside and foot of slope (left figure), and the landslides are mainly distributed at the foot of slope. The landslides on hillside and foot of slope with the area smaller than 30 ha is mostly distributed at convex and concave profiles; however, landslides greater than 30 ha in area are mostly in the convex profile and located at the foot of slope. This is significantly related to the headward erosion or valley stress releasing.

The large landslides are often formed as a deep seated landslide, the geological process and structures are the main controlling factors. In the right of Fig. 8, there were a pre-deflection for a massive landslide. The event in straight type slope in the figure (such as type 4, 5, 6) is few. In the left figure, the massive landslides (over 10 ha) were numerous distributed at 1 convex-damp, 2 convex-linear, 3 convex-mouth, 7 concave-damp, and 9 concave-mouth, indicated that the bigger the convex or concave topology before the collapsing, the bigger the landslide. The right Fig. 8 also shows that if the topography of most of the event point is not significant concave, it is significant convex, showing that the large scale of the

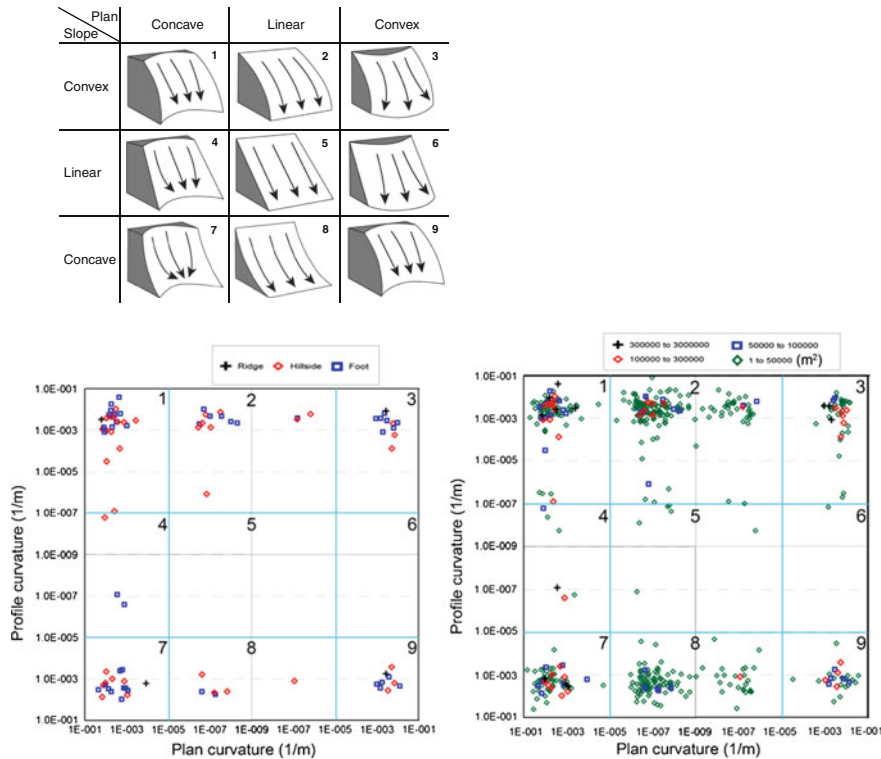


Fig. 8 Location—curvature distribution (1 ridge, 2 hillside, 3 foot of slope) (left) and landslide area (m^2)—curvature distribution (right) (reproduced from Ruhe 1975; Schaetzl 2013)

landslide are progressive failure, the mountain slope topography evolves gradually into a convex ridge or a concave valley, and are continue till failure.

The curvature of the landslide sector is shown in Fig. 9, showing that when the profile curvature reaches 1×10^{-4} (l/m), landslide events are elevated, in which case, the ridge location has significant sliding potential than the foot. The hillside and the foot of slope were more stable; the landslide percentage of the half of landslides increased till the curvature reached 1×10^{-3} (l/m).

3.5 Depth of Shallow Landslides

Figure 10 illustrates the average depth of the shallow landslide case which is defined as the landslide area of the event that is less than 1 ha. In general, the landslide depth varies from 4.6 to 6.3 m, the average depth of the dip slope is 6 m, and moreover the deepest of landslide depth is orthoclinal of anti-dip slope. Due to

Fig. 9 The statistics on the concave profile curvature and the location of large-scale landslides

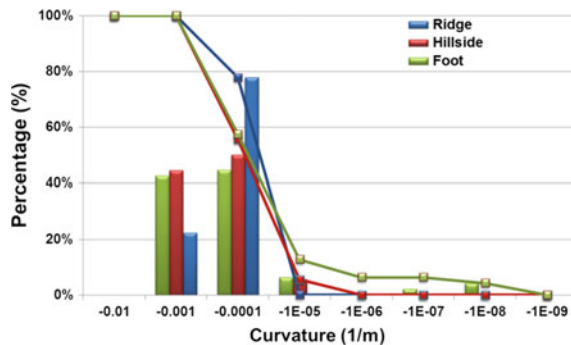
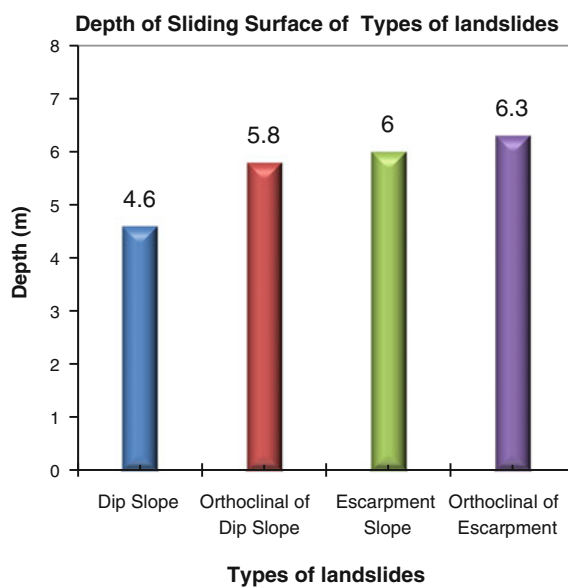


Fig. 10 The average depth of shallow landslides



the dip slopes act frequently as a translational failure mode, the depth of dip slope landslide is more uniform than the one of circular landslide.

4 Conclusion

The statistical analysis results of the landslides in Ai-Liao River catchment during Typhoon Morakot were summarized as follows:

1. The average slope angles of landslides triggered by the Typhoon Morakot was between 20° and 40° . The slope of rainfall-induced landslides is moderate.

2. 52 % of the rainfall triggered landslide areas were more than 10 ha. Large landslides accounts for 5 % in landslide number but took 50 % in area of all landslides. The geological structure is the key influential factor of large-scale landslides.
3. The rainfall triggered landslides were concentrated at the hillside and the foot of slopes. This was related to the lateral erosion of river channel.
4. Typhoon Morakot inducing landslide located mostly on the orthoclinal slopes. The result was related to the cleavage joints, intensive weak joints and the well developed groundwater pathways in the study slate terrain.
5. The hill shape analysis showed that large-scale landslides deflected before collapsing. The bigger the curvature the easier the occurrence of a large landslide. Most of large landslides is significant concave or convex before the events, indicated that large landslide are deformation gradually.
6. When the profiles curvature of a landslide are close or above the curvature 1×10^{-4} (l/m), the sliding possibility of a massive landslide will increase, and the ridge location has significant sliding potential than the foot and the hillside.

References

Chang KT, Chiang SH, Hsu ML (2007) Modeling typhoon-and earthquake-induced landslides in a mountainous watershed using logistic regression. *Geomorphology* 89:335–347

Fuchu D, Lee CF, Sijing W (1999) Analysis of rainstorm-induced slide-debris flows on natural terrain of Lantau Island, Hong Kong. *Eng Geol* 51:279–290

Lin CW (2010) The investigation results of sensitive geographic zone investigation of national land conservation. Central Geological Survey

Muenier P, Hovius N, Haines J (2008) Topographic side effects and the location of earthquake induced landslides. *Earth Planet Sci Lett* 275:221–232

Pierson TC (1977) Factor controlling debris-flow initiation on forested hillslopes in the Oregon coast range. Ph.D. dissertation, University of Washington, Seattle

Ruhe RV (1975) *Geomorphology: geomorphic processes and surficial geology*. Houghton Mifflin, Boston, Massa Chussets

Schaetzl RJ (2013) Catenas and soils. In: Shroder JF, Pope GA (eds) *Treatise on geomorphology, weathering and soils geomorphology*, vol 4. Academic Press, San Diego, pp 145–158

Site Investigation and In Situ Testing on Shallow Landslide Scars of Natural Slopes Covered by Volcanic Ash and Pumice Fall

Kentaro Yamamoto, Yukiyoshi Teramoto, Mizuki Hira and Katsuhisa Nagakawa

Abstract The slopes composed of Shirasu and other volcanic product often fail due to heavy rain in the rainy season. In order to prevent shallow landslides, six field test sites, where past occurrence of landslides due to heavy rainfall were identified, have been determined in the Takakuma experimental forest of Kagoshima University. In this study, site investigation and in situ testing on shallow landslide scars of natural slopes covered by volcanic ash and pumice fall are conducted to investigate the stability of the slopes and the effect of revegetation and soil development of forest topsoils from the viewpoint of forest ecology and geotechnical engineering. In the site investigation, the growth condition of forest trees, the measurement of dry density of topsoil and investigation using soil augers are carried out. Furthermore, simple dynamic cone penetration test and the investigation of slope topsoil using a soil strength probe are performed in situ. Finally, a judgment regarding the stability of slopes and the effect of revegetation and soil development could be made.

Keywords Natural slope • Site investigation • In situ test • Revegetation • Soil development

K. Yamamoto (✉)
Department of Civil and Environmental Engineering,
Nishinippon Institute of Technology, Fukuoka 800-0394, Japan
e-mail: kyama@nishitech.ac.jp

Y. Teramoto · M. Hira
Faculty of Agriculture, Kagoshima University, Kagoshima 890-0065, Japan

K. Nagakawa
Kiso-Jiban Consultants Company, Tokyo 870-0033, Japan

1 Introduction

In Japan, forest occupies about 70 % of the country. Approximately 90 % of slope failures occurring in Japan are shallow landslides and the trigger is usually rainfall in Southern Kyushu. Kagoshima Prefecture is located in the southern part of Kyushu Island. The surface ground in Kagoshima Prefecture is almost covered with volcanic products, such as pyroclastic flow deposits including volcanic ash and pumice fall and weathered igneous rock. The non-welded part of pyroclastic flow deposits is called Shirasu in Japanese, which is classified as a sandy soil. The density of Shirasu is lower than silica sand due to the porous properties of the particles. Thus, Shirasu is relatively susceptible to erosion by the surface flow of rainwater. When heavy rain falls every rainy season, shallow landslides often occur on the slopes composed of Shirasu on which a thin surface humus layer is present. It is well-known that these shallow landslides occur due to the flooding of forest soils, the seepage of rainwater and an increase in self-weight of the soil mass. But it is very difficult to predict quantitatively these shallow landslides due to natural disasters.

In this study, site investigation and in situ testing on shallow landslide scars of natural slopes covered by volcanic ash and pumice fall were conducted to investigate the stability of the slopes and the effect of revegetation and soil development of forest topsoils from the viewpoint of forest ecology and geotechnical engineering.

2 Field Test Sites

Six field test sites (Shirasu natural slopes covered by volcanic ash and pumice fall) have been determined in the Takakuma experimental forest of Kagoshima University as shown in Photo 1. The occurrence of landslides due to heavy rainfalls was identified by investigating past records of the Takakuma experimental forest, aerial photographs and the age of trees. In 2013, the elapsed years after the occurrence of landslides range from 8 to 58 years as shown in Table 1. No. 1 site has the shortest elapsed years and No. 6 site has the longest. These field test sites are situated in the same field as shown in Fig. 1, facing the north and the height above the sea level is about 520 m. The average inclination slope is over 37° and the area of landslide scars range from 29 to 114 m².

In Photo 1, No. 1 site is composed of various kinds of small trees and weeds, while large trees like evergreen broad-leaved trees are mostly seen in No. 6 site. Regarding the grain size in all field test sites, the percent finer by weight is approximately 100 % when the grain size is less than 2.0 mm and the vast majority is coarse sand (0.85–2.0 mm).

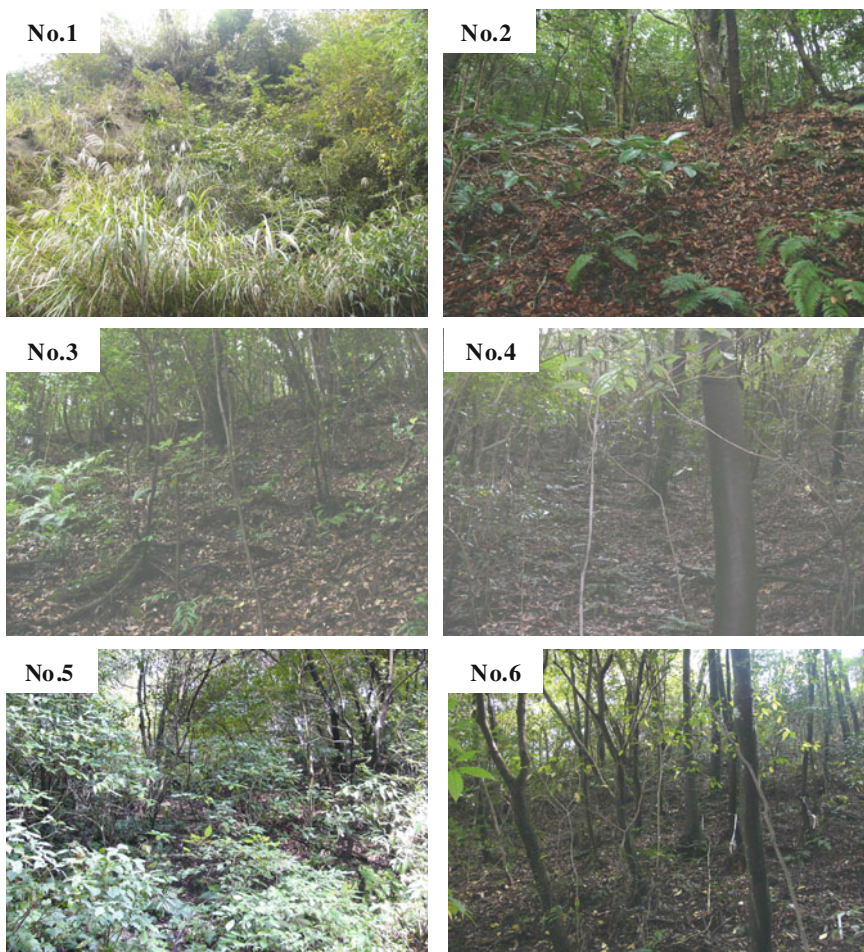


Photo 1 Photographs of six field test sites

Table 1 Properties of shallow landslide scars on six field test sites

| Test field point | No. 1 | No. 2 | No. 3 | No. 4 | No. 5 | No. 6 |
|---|-------|-------|-------|-------|-------|-------|
| Elapsed years after the occurrence of shallow landslide | 8 | 12 | 22 | 28 | 40 | 58 |
| Average inclination of slope (°) | 42 | 38 | 41 | 37 | 40 | 39 |
| Area of landslide scar (m ²) | 42 | 36 | 29 | 34 | 61 | 114 |

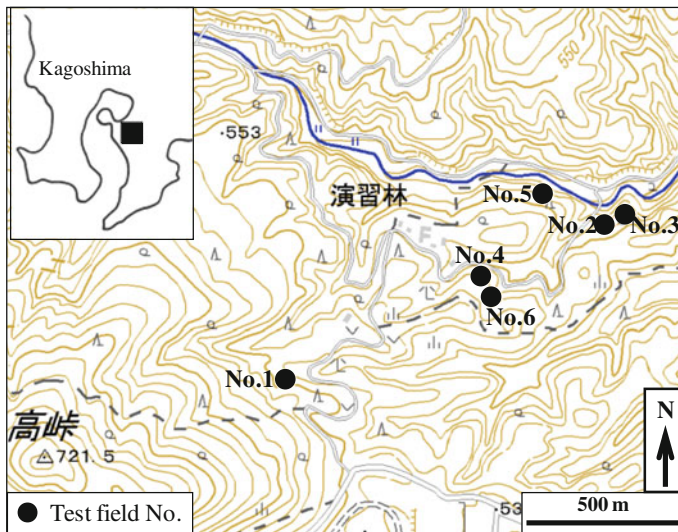


Fig. 1 Location of field test sites

3 Site Investigation

The identification of tree species, the growing conditions of forest trees, such as tree height and diameter at breast height, the measurement of dry density of forest topsoils and investigation using soil augers are carried out. Figure 2 shows the number of trees, tree species and tree basal area for the elapsed years after the occurrence of landslides. The number of trees and tree species peaked approximately 10 years after the occurrence of the shallow landslides, and then decreased with time. Approximately 40 years after the occurrence of the landslides, an apparent steady state was achieved. On the other hand, the tree basal area increases gradually with time.

The Fisher-Williams' index of diversity (Tagawa 1964) for forest trees and the appearance rate of evergreen broad-leaved trees for all trees are obtained as shown in Fig. 3. In the method of Fisher-Williams' index of diversity, α is calculated by solving the following equation:

$$S = \alpha \log(1 + N/\alpha) \quad (1)$$

where N and S are the number of all trees and all kinds of tree species, respectively. It is found that the tendency obtained from Fig. 3a has a good agreement with that from Fig. 2a, b, and α takes a value of approximately 8 when the elapsed years after the occurrence of landslides is over 40. Based on the temporal variation of the Fisher-Williams' index of diversity, the forest located in the shallow landslide scars reached a climax approximately 40 years after the occurrence of the landslides. In

Fig. 2 Number of trees, tree species and tree basal area for the elapsed years after the occurrence of landslides

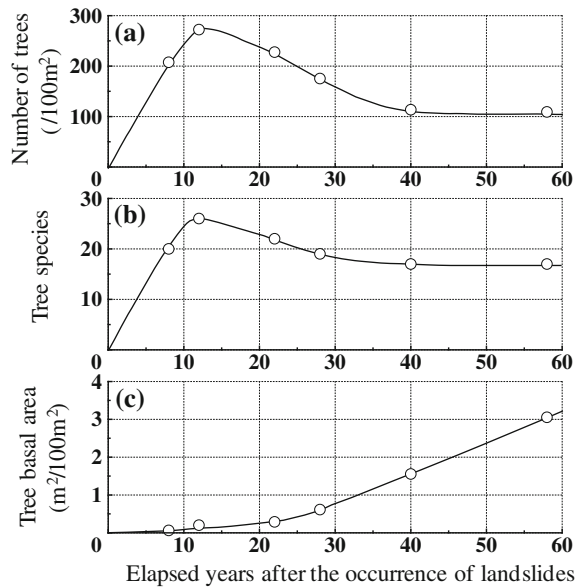


Fig. 3 Diversity index of forest trees and appearance rate of evergreen broad-leaved trees for the elapsed years after the occurrence of landslides

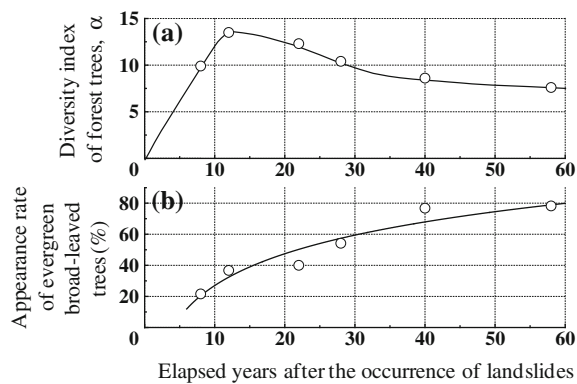
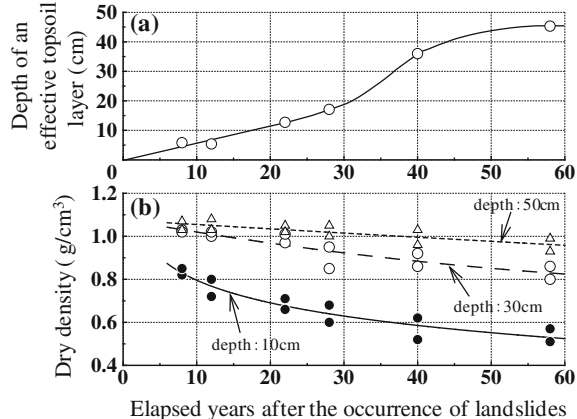


Fig. 3b, the appearance rate of evergreen broad-leaved trees increases with time, and about 80 % of all trees is occupied by evergreen broad-leaved trees when the forest reached a climax approximately 40 years after the occurrence of the landslides.

Next, Fig. 4 shows the depth of an effective topsoil layer and dry density of topsoils for the elapsed years after the occurrence of landslides. The depth of an effective topsoil layer is measured by soil augers, and the value is the average of test results at intervals of 1 m in vertical and horizontal directions on the area of each field test site. As shown in Fig. 4a, the development of a depth of an effective topsoil layer is relatively slow before approximately 30 years after the landslides, and after that the development becomes rapid. Revegetation developed on the forest

Fig. 4 Depth of an effective topsoil layer and dry density of topsoils for the elapsed years after the occurrence of landslides



soil and had grown to a thickness of approximately 40 cm by the time the forest reached a climax approximately 40 years after the landslides. The average value at No. 6 site (58 years have elapsed after the landslides) is 45.3 cm and the rate of development of depth of an effective topsoil layer is 0.78 cm/year. This value is higher than the average value 0.45 cm/year at shallow landslide scars on Shirasu in Kagoshima city for 80 years (Shimokawa et al. 1989). It is worthy to mention that the average inclination of slope is around 50° in Kagoshima city.

The soil profile is set for the upper and lower parts (2 points) at each shallow landslide scar to measure the dry density of forest topsoils. The dry density for each soil profile is measured by extracting the undisturbed sample at the depth of 10, 30, and 50 cm using 100 ml cylindrical sampling. Note that the data is composed of a pair of plots (the upper and lower parts of each shallow landslide scar). As shown in Fig. 4b, the dry density of forest topsoils tends to decrease with time after the occurrence of the landslide. Thus, the development of forest topsoils originates from shallow to deep depths due to the growing tree roots and the supply of organic substances followed by the revegetation of forest.

4 In Situ Testing

The simple dynamic cone penetration test and the investigation of slope topsoil using a soil strength probe (“dokenbou” in Japanese) are performed in situ (Sasaki 2010). Figure 5 shows the results of simple dynamic cone penetration test at No. 1 and No. 6 sites. Here, N_d value is the N value obtained from the simple dynamic cone penetration test. As shown in Table 1, 8 and 58 years have elapsed after the landslides at No. 1 and No. 6 sites, respectively. In Fig. 5a, the amounts of penetration at No. 1 site are 9 and 25 cm when the number of blow is 0 and 1, respectively. After that, the amount of penetration decreases and the value of N_d

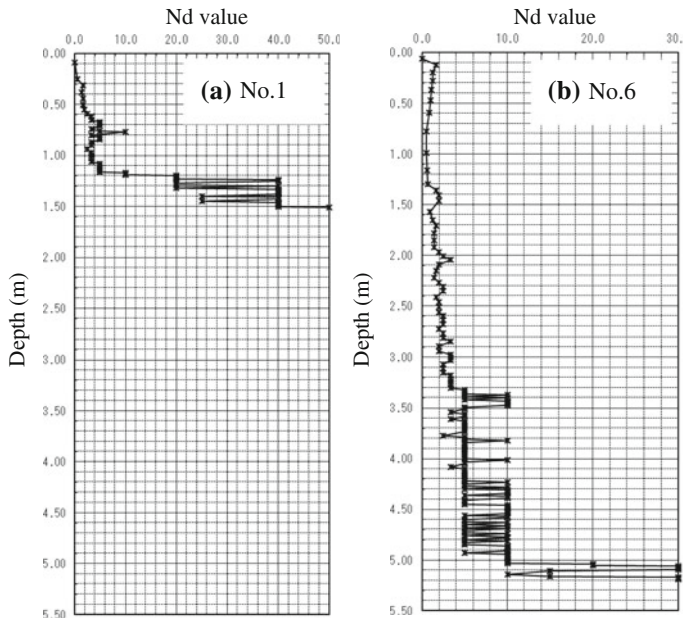


Fig. 5 Results of simple dynamic cone penetration test

tend to increase. Thus, it is supposed that the depth of an effective topsoil layer is approximately 9 cm. Also, the penetration is stopped when the penetration reached 1.5 m. This is because the amount of penetration is less than 20 mm even when 10 blows are applied. On the other hand, the amount of penetration at No. 6 site is 6 cm when the number of blows is 0 and, the value of N_d increases until the penetration depth is 10 cm as shown in Fig. 5b. After that, N_d decreases when the penetration depth is approximately 60 cm. Thus, the depth of an effective topsoil layer is around this depth. It is observed that the N_d value increases suddenly when the penetration depth is approximately 3.3 m. As the trend, the amount of penetration is relatively large even at few blows due to the forest topsoil, and the simple dynamic cone penetration test could generally be continued until the penetration depth is 5.0 m.

Next, Fig. 6 shows the results of vane cone shear test using “dokenbou.” This figure is the correlation between vertical load W_{vc} (N) and torque T_{vc} (N·m) when the shear test is conducted by changing the vertical load at least 4 times. These cases have quite a good agreement and the strength parameters c and ϕ of soils are calculated by the following conversion formula:

$$c = 10.16 \cdot Y_0 \quad (2)$$

$$\tan \phi = 12.04 \cdot X \quad (3)$$

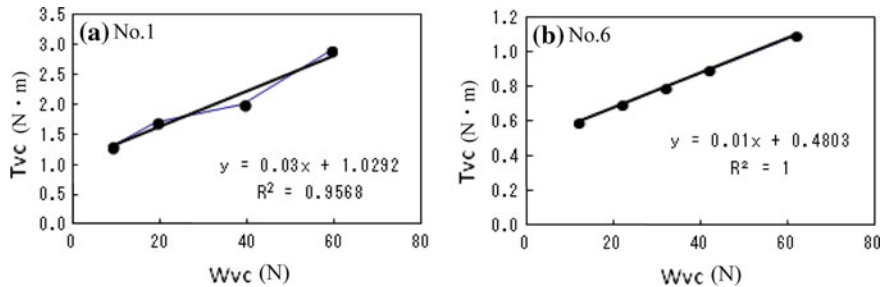


Fig. 6 Results of vane cone shear test

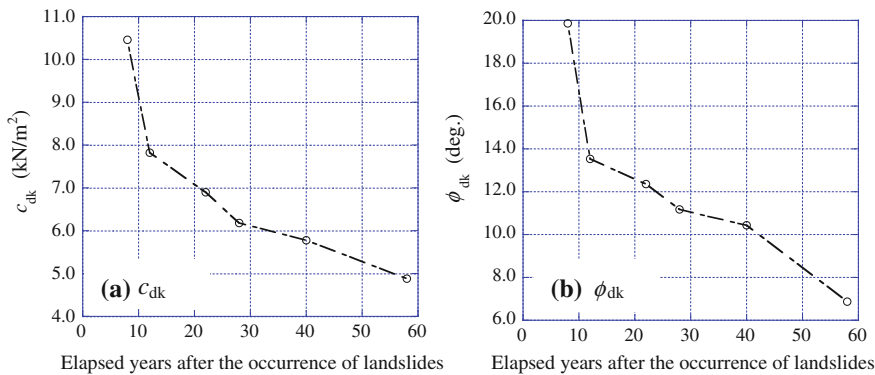


Fig. 7 Variation of c_{dk} and ϕ_{dk} for the elapsed years after the occurrence of landslides

where c and ϕ are the cohesion and internal friction angle, and Y_0 and X are the intercept and slope of approximate equation. Note that this conversion formula is based on the work by Sasaki (2010).

Finally, Fig. 7 shows the variation of cohesion, c_{dk} (kN/m^2) and internal friction angle, ϕ_{dk} (deg.) obtained from “dokenbou” for the elapsed years after the occurrence of landslides. The data are all field test sites and the subscript letter dk denotes the “dokenbou”. The values of c_{dk} and ϕ_{dk} decrease with the elapsed years after the occurrence of the landslides due to the effect of weathering, the growing tree roots and the soil development of forest topsoil followed by the revegetation of forest. In general, the strength parameters and dry density tend to become smaller from the surface layer when the elapsed years after the occurrence of the landslides are long. Additionally, it is found that the mixing of pumice and tree roots has a great effect on the results of the shear test when the test is actually conducted in situ.

5 Conclusions

It was possible to conduct a follow-up survey of forest trees on Shirasu natural slopes, since the period of shallow landslides is short, the age of some kinds of trees which cover the final stage of transitions is long and the growth of trees is relatively fast due to the geomorphological warm climates of the Southern Kyushu region. Most of the shallow landslides involve forest trees in Japan. Thus, several indicators can be proposed, such as, the diversity index of forest trees, the appearance rate of evergreen broad-leaved trees and the depth of an effective topsoil layer quantitatively. From the viewpoint of forest ecology and geotechnical engineering, a judgment regarding the stability of slopes and the effect of revegetation and soil development could be made. In general, the strength parameters (cohesion and internal friction angle) and dry density tend to become smaller from the surface layer when the elapsed years after the occurrence of the landslides are long. Furthermore, shallow landslides do not tend to occur regularly after 20 years have elapsed since the last landslide, due to the growing tree roots having a stabilising effect on the topsoil.

References

Sasaki Y (2010) Manual for the investigation of slope topsoil by soil strength probe. Technical Note of PWRI, No.4176 (in Japanese)

Shimokawa E, Jitousono T, Takano S (1989) Periodicity of shallow landslide on Shirasu steep slopes and prediction of potential landslide sites. *Trans Jpn Geomorphol Union* 10(4):267–284 (in Japanese)

Tagawa H (1964) A study of the volcanic vegetation in Sakurajima, South-West Japan I. Dynamics of vegetation. *Mem Fac Sci Kyushu Univ Series E (Biol)*, 3(3–4):166–228

Overhaul the Anchored Slopes in Taiwan

Hung-Jiun Liao and Shih-Hao Cheng

Abstract A catastrophic dip slope failure occurred suddenly at an anchored cut slope of Freeway No. 3 in 2010 after 13 years in service. Among the factors contributing to this landslide, serious corrosion on tieback anchors was the most obvious factor in addition to the groundwater hydrology inside the slope. In the past, most of the ground anchors in Taiwan were constructed with limited or no corrosion protection. So, it is likely that the tieback anchors on slopes are suffering similar corrosion problem under the humid weather condition. So, the Ministry of Transportation and Communication (MOTC) of Taiwan government launched an extensive island-wide investigation program to check the status quo of existing anchored slopes along the highways, railways, and public roads. Not surprisingly, corrosion is found to be a common problem for the existing ground anchors. A national overhaul program for the anchored slopes along the highways and railways has been launched. This paper covers the findings from the anchored slopes inspection and the measures taken to improve the corrosion protection of the existing anchors. In addition, some minor modification on anchor tendon assembly and cement grouting process has been suggested to upgrade the corrosion protection of the new anchors.

Keywords Ground anchor · Corrosion · Inspection · Remedial measures · Anchored slopes

H.-J. Liao (✉)

Department of Construction Engineering, National Taiwan University of Science and Technology, Taipei 10607, Taiwan
e-mail: hjiao@mail.ntust.edu.tw

S.-H. Cheng

Taiwan Building Technology Center, National Taiwan University of Science and Technology, Taipei 10607, Taiwan
e-mail: shcheng@mail.ntust.edu.tw

1 Introduction

A catastrophic dip slope failure occurred suddenly at an anchored cut slope of Freeway No. 3 in northern Taiwan after 13 years in service (Fig. 1). Originally, this slope was stabilized with a 20 m retaining structure and tied back with 10 levels of anchors. Totally, 572 ground anchors were installed with a prestressed load of 60 tons each. The findings from the forensic investigation taken after the landslide (CTGS 2011) had fundamentally changed the practice of anchored slope both in construction and maintenance.

From the remains of anchors on site, it was found that a large portion of anchors were seriously corroded (Fig. 2) due to improper corrosion protection under the anchor head. As a result of corrosion, the capacity of anchors decreased and a significant portion of tieback load was lost. Since ground anchors with the similar construction practice have been widely used to support the roadside slopes in Taiwan and are likely to suffer similar corrosion problem, the Ministry of Transportation and Communication (MOTC) of Taiwan government launched an extensive island-wide inspection program to check the status quo of existing



Fig. 1 Landslide on freeway No. 3 Taiwan (photo taken on April 25, 2010)



Fig. 2 Seriously corroded and broken steel strands found from at the landslide site



Fig. 3 Deformed rails next to a moving anchored slope

anchored slopes along the highways, railways (Fig. 3) and public roads. Up to now (July 2014), more than 30,000 anchors have been inspected. The preliminary results from the anchor inspection indicate that anchor corrosion is a systematic problem island-wide. The first aid remedial measure to protect anchors from further corrosion was on the existing anchors. Second, the stability of existing anchored slopes will be resumed by installing additional anchors to make up the loss of anchor capacity due to corrosion and other causes. Finally, comments on resuming the stability of existing anchored slopes will be discussed also.

2 Status Quo of Ground Anchors When Landslide Occurred

Fortunately, there were anchors and steel strands remained on the slope and can be used to examine the anchors condition 13 years after installation. When anchors were constructed, it was the standard operation procedure to inject the entire anchor hole with cement grout first and then inserted the tendon assembly to the hole later.



Fig. 4 Ungrouted free anchor end (inside and outside of plastic sheath) found from anchors left on sliding surface

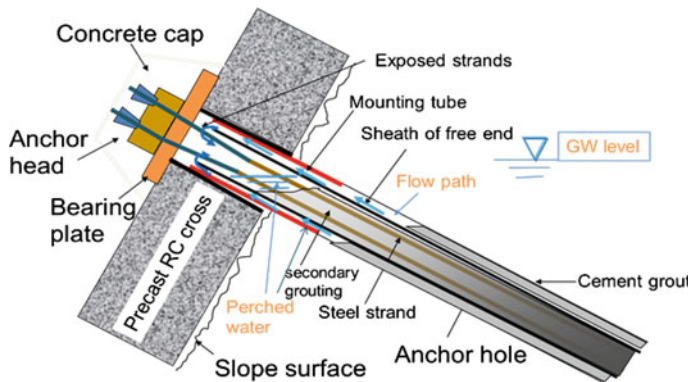


Fig. 5 Schematic diagram of ground anchor installed in the cut slope

However, the anchors left on the sliding surface (Fig. 4) showed that the annular space between anchor hole and plastic sheath of the free anchor end was not fully sealed with cement grout. Nor was the space inside the plastic sheath. Obviously, some cement grout might leak out through the cracks and joints inside the slope or might simply be a malpractice during anchor construction. As a result, steel strands with improper corrosion protection were exposed to groundwater and corroded later.

Figure 5 illustrates the voids in the free anchor length. Since all the anchors were inclined downward, the void and the annular space outside the plastic sheath could easily become a storage space for the perched groundwater inside the slope. The existence of perched water in the anchor hole caused the steel strands constantly exposed to or submerged under groundwater. Not for long, the steel components of anchor corroded quickly. It was confirmed by the endoscope images taken later when inspecting the steel strands under the anchor head. The majority of inspected anchors illustrated a serious to very serious corrosion on steel strands.

In addition to the corrosion problem on ground anchors, groundwater stored in anchor hole became a source of constant water supply to soften the material strength of slope and the sliding surface as well. It in turns transferred more load to the anchors. When the loading on corroded ground anchors reached the breaking point, a sudden and fast moving dip slope failure occurred.

3 Inspection Procedure of Existing Anchors

The following steps have been taken to inspect the existing anchored slopes and evaluate the residual stability of anchored slopes along freeways, major highways, and railways:

- 1. Visually inspect and hammer tap all the concrete protection cap of anchors** (Fig. 6): The integrity of concrete cap can be easily detected by hammer tapping. Special attention must be paid to the cracks on concrete cap and the sign of groundwater leaking out from the concrete cap. If there is a constant water flow from within the anchor hole, calcium carbonate (white stain) will deposit under the concrete cap and can be easily spotted.
- 2. Remove the concrete cap and inspect the steel strands and the wedges on the anchor head** (Fig. 7): If the integrity of concrete cap is good, normally the appearance of steel strands and wedges will also look good. Otherwise, a clear sign of corrosion can be observed on the strands and wedges.
- 3 Use endoscope to inspect the condition of steel strands beneath the anchor head** (Fig. 8): Usually, the appearance of anchor head components does not necessarily correspond to the extent of corrosion on steel strands beneath the anchor head. So, it is necessary to use endoscope to do a close up inspection on the corrosion condition of steel strands.



Fig. 6 Visual inspection and hammer tapping on the concrete cap of anchor



Fig. 7 Remove the concrete protection cap of anchor head



Fig. 8 Use endoscope to inspect steel strands under the anchor head



Fig. 9 Lift-off test for determining the residual anchor load

4. **Carry out the lift-off test to determine the residual anchor load** (Fig. 9): It is normal to have a residual anchor load varied within $\pm 20\%$ range of design load. If the residual load goes beyond 120 % of design load, it can be an indication of slope displacement; if the anchor load falls below 80 % of design load, it may be resulted by problems from fixed end, free end, and anchor head. For those anchors suffering serious strands corrosion problem, extra caution must be exercised to avoid breaking the rusty steel strands during lift-off test.

As demonstrated in Table 1, an example anchor is used to demonstrate the process to score the inspected anchor from the items evaluated. This example anchor got a score of 70.75 and graded as “Fair” (Table 2). However, it suffered severe strands corrosion and its residual load is between 0.8 and 1.1 Tw. This is the type of anchor which needs more caution. The high residual anchor load may be an indication of slope displacement and a sudden failure may occur due to strands breakage. Based on the anchor inspection results on the selected anchors, the overall safety of an anchored slope can be evaluated by adding up all the total score of inspected anchors and then divided by the number of inspected anchors. It yields a value of the anchored slope and can be used to grade the anchored slope using Table 3.

Table 1 Example case of an anchor inspection result

| No | Item | Weighting (%) | Score |
|-------------|---|---------------|-------|
| 1 | Visual inspection on concrete protection cap | 10 | 10 |
| 2 | Inspection on steel strands and wedges on anchor head | 15 | 11.25 |
| 3 | Endoscope inspection on steel strands beneath the anchor head | 30 | 4.5 |
| 4 | Determine the residual anchor load by lift-off test | 45 | 45 |
| Total score | | | 70.75 |

Table 2 Grading of single anchor based on the inspection score

| Total score | Grade | Remarks |
|----------------------|---------------------|---------|
| 0 | X (out of function) | |
| $\beta \leq 30$ | A (Very poor) | |
| $30 < \beta \leq 55$ | B (Poor) | |
| $55 < \beta \leq 80$ | C (Fair) | ■ |
| $80 < \beta$ | D (Normal) | |

Table 3 Grading of an anchored slope based on score summation of inspected anchors

| Overall score | Grade | Remarks |
|-----------------------|---------------|---------|
| $\alpha \leq 30$ | A (Very poor) | |
| $30 < \alpha \leq 55$ | B (Poor) | |
| $55 < \alpha \leq 80$ | C (Fair) | |
| $80 < \alpha$ | D (Normal) | |

Note $\alpha = \Sigma$ total score of inspected anchors/No. of inspected anchors

4 Comments on Anchored Slopes Inspection

After inspecting tens of thousands ground anchors in Taiwan, it is certain that almost all the anchors installed in Taiwan have suffered various degrees of corrosion. Where the ground anchors are below the groundwater surface, anchor corrosion can be severe; where anchors are above the groundwater surface or no groundwater present, anchor corrosion can be minor. However, following the above-mentioned steps to inspect the anchors on anchored slopes, there is no clear relationship among the findings from each step. For example, the visual inspection on the concrete cap of anchor could not unveil the results of the corrosion condition of steel strands under the anchor head. In addition, there is no clear relationship to link the visual inspection results from either concrete cap inspection or endoscopic

inspection of steel strands to the residual capacity determined from the lift-off test on ground anchors. In other words, good exterior condition of concrete cap cannot guarantee no corrosion on the steel strands and/or wedges. Minor corrosion on the steel strands observed from endoscope does not mean that the existing anchors can provide good residual load to withhold the slope from sliding. Finally, since only 10 % of total ground anchors on each slope are carried out the lift-off test, it is concerned that the test number is under representative, especially when there is a large variation among the residual loads of test anchors.

The lift-off tests carried out on the existing anchors showed a large majority of anchors, which were experiencing a prestressed load loss. In other words, the residual load of anchor is smaller than the design load. This is not a surprise to the local engineers because the high groundwater level and weak/fractured rock conditions of the anchored slopes are common problems in Taiwan and are likely to lead to a prestressed load loss of anchor. When the prestressed load is decreased, it should take a close look on not only the unusual surface and groundwater flow but also the cracks on the retaining structure and/or on the slope surface. If no sign of slope instability is observed, it indicates that slope is still under stable condition and the ground anchors are in balance with the current slope condition even though the prestressed anchor load had decreased. Under this situation, there is no need to re-stress the anchors back to the original design load.

On the other hand, if a majority of anchors on a slope showed an increase in prestressed load. Then it is necessary to study the causes of the anchor load increase and find the suitable remedial measures. However, it is not suggested to lower the residual load of overstressed anchors because it may deteriorate the stability of slope and trigger further slope displacement. In fact, if the anchor load of an anchored slope is increasing, it is an indication that the original anchor load is under designed and it is necessary to install additional anchors to keep the stability of the slope. For this case, more information about the slope is needed for reevaluating the stability of slope, including the geological and groundwater conditions of the slope.

It is also often to find that the residual load of anchors is lower than the design load and the steel strands are suffering corrosion problem. However, the slope still looks to be stable. Under this condition, the corrosion problem could be dealt with first by sealing the void in the anchor hole with cement grout. Since it is uncertain about how much anchorage capacity of the test anchor left and how much more loading can be taken beyond the residual load? Normally, a load reduction factor is applied to the corroded anchors and extra anchors are installed to make up the anchorage capacity loss due to corrosion and to resume the stability of slope. However, if no sign of slope instability is observed and the corrosion condition of anchor is still acceptable, it is possible to just do the first aid measure to stop the anchor from further corrosion and leave the anchors as they are. Then keep this anchored slope in the routine slope inspection list.

5 First Aid Measures for Corroded Anchors

As learned from anchor inspection, anchor corrosion is a common problem in Taiwan. Two major steps have been taken by the Highways and Freeways Authorities to deal with the problem: (1) to prevent the current anchor condition from getting worse, (2) to bring back the stability level of the existing tied back slopes. For the former, cement grout was injected to fill up the void underneath the head of existing anchor to stop further corrosion on steel strands. For the latter, additional ground anchors were installed to make up the loss of anchor capacity due to corrosion. Routine maintenance and monitoring program for the existing anchored slopes are also exercised.

The corrosion problem occurred on ground anchor is partly due to malpractice of anchor construction and partly due to the humid weather and geological condition of the site. Since the cause of corrosion is initiated from the ungrouted void under the head of existing anchors, it is essential to be sure that the void under the anchor head is filled up with cement grout to stop further corrosion on steel strands. This work was carried out by drilling two holes from outside to the void (Fig. 10). One hole is for cement grouting; the other is for air ventilation. Cement grout (water/cement ratio = 0.5) is injected to the void with grouting pump first. Since cement grout may settle or leak out from the anchor hole, such a pumping process takes time and may have to repeat several times. An intravenous injection method is adopted as the final step of the grouting work to make sure cement grout has filled up the anchor hole (Fig. 10). When the cement grout is effluent from the ventilation hole and is in balance with the grout supply bottle, then it can be certain that the void underneath the anchor head is fully filled with cement grout.

To facilitate the inspection work on anchor head later, the traditional concrete protection cap for the anchor head is replaced with a galvanized metal cap. The metal cap is mounted to the steel bearing plate with screws and sealed with an o-ring under it. So, it can be easily removed for the anchor head inspection later. Inside the metal cap, proper anticorrosion grease or mastic is used to protect anchor head from further corrosion.

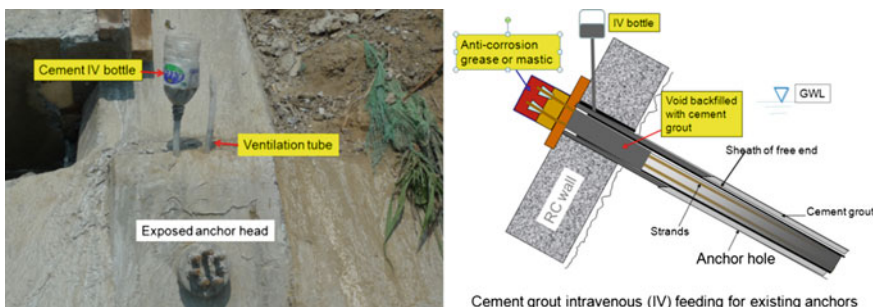


Fig. 10 Fill up the void under anchor head with cement grout

6 Modification of Tendon Assembly

For the new anchors installed to resume the stability of slope, the corrosion protection is the key issue to be taken care of (Fig. 11). Special attention is paid to the free anchor end right under the anchor head and the components of anchor head. To facilitate the cement grouting to the space outside the sheathing at free anchor end, a hole is predrilled on the bearing plate for cement grout injection together with some ventilation measure for grouting. Having done all of these, it can effectively prevent groundwater from seeping into the void underneath the anchor head.

The troublesome seal used to separate the fixed end and free end grouting is removed from the modified tendon assembly. It is replaced by sheathing each steel strand on free anchor end and sealed at the bottom of the sheathing with heat shrink tube (Fig. 11). Similar type of tendon assembly was also illustrated in the book by Hanna (1982) and BSI (1989). Without the seal between free end and fixed end, it can facilitate the process of anchor grouting a great deal. In addition, the modified tendon assembly uses only corrugated sheathing for both free end and fixed end of anchor. There is no connecting point in the entire sheathing and so no opening for cement grout to leak out. It is different from the traditional tendon assembly which uses smooth sheathing for the free end. At first, it is concerned that the load transfer mechanism of anchor with full length corrugated sheathing may be different from that of half corrugated—half smooth sheathing anchor. However, it has been pointed out by Lin (2014) that there is no obvious difference in the surrounding stress distribution around stressed anchors with either type of tendon assembly. So the anchor with full length corrugated sheathing is recommended for the anchors to be installed in the future.

To evaluate the current stability of existing anchored slopes, it needs to know the current anchor load applied on the slope. However, if no load cells were installed or no lift-off test was carried out, it is not possible to estimate the residual load of existing anchors. But it is also practically not possible to install a large number of load cells or to carry out many lift-off tests due to the high cost required. To solve

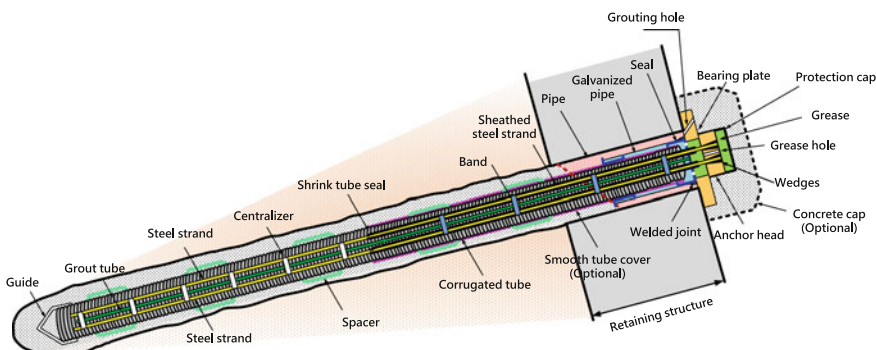


Fig. 11 Tendon assembly for supplement ground anchors

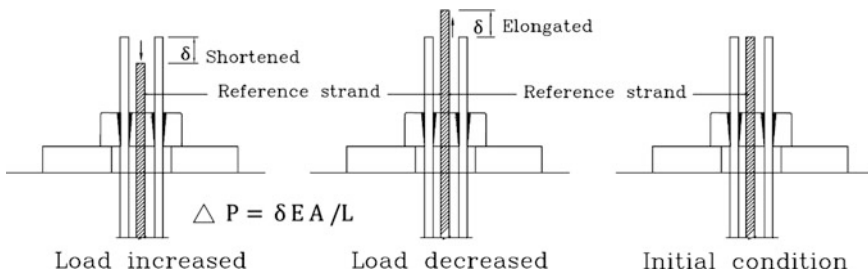


Fig. 12 Interpretation of anchor load change from the relative displacement of strands

this problem, a special arrangement of tendon assembly is adopted for the new anchors (Fig. 11). Among the strands in the tendon assembly, one strand was deliberately not locked with wedges and was used as the reference strand to measure the relative elongation (δ) of stressed steel strands. As the loading of anchor changes, the length of stressed strands in the free anchor end will change also (Fig. 12). Under this condition, the relative displacement between reference strand and stressed strands can be easily measured from the regular inspection on anchor head. Knowing the relative displacement (δ), the change of anchor load (ΔP) can be determined from the equation $\Delta P = \delta EA/L$, where E is the elastic modulus of steel strand ($= 2100 \text{ t/cm}^2$), A is the summation of cross section area of steel strand, L is the effective free length of strands. Knowing the residual anchor load will be very helpful reevaluate the stability of slope in the future (Lee et al. 2012; Liao et al. 2013).

7 Conclusion

Based on the findings from the nationwide anchored slopes inspection and the measures taken to resume the function of tieback anchors and the stability of slopes, the following conclusions can be drawn:

1. The findings from the investigation on the sudden failure of a roadside dip slope on Freeway No. 3 unveiled the serious corrosion problem of the anchors in Taiwan. Not properly sealed void underneath the anchor head is the main spot of steel strands corrosion. It requires immediate first aid treatment to stop further corrosion. For the new anchors, the corrosion protection of the anchor head and the strands underneath needs to be carefully treated.
2. Field anchors which suffered various extents of corrosion are in a delicate balance between residual tieback load and residual material strength of various anchor components. Any increase in loading or any further decrease in material strength due to corrosion may trigger a chain reaction failure among anchors. Because of unevenly redistributed loading among wires or strands and reduced elongation capacity of corroded steel strands, anchor tends to break suddenly

when the applied load becomes only marginally larger than the residual anchor load. The breakage of anchor strands will result in a sudden and fast moving dip slope landslide like the one occurred in Freeway No. 3.

3. To prevent the condition of corroded strands from getting worse, the void under the anchor head can be sealed with cement grout and cut off any contact between steel strands and air/water. Anchor heads should be protected with anticorrosion grease or mastic and covered with galvanized metal cap.
4. Normally, a reduction factor is applied to the corroded anchors and extra anchors are installed to make up the anchorage capacity loss due to corrosion. If no sign of slope instability is observed, the original design anchor load is usually applied to the slope again by installing additional anchors to the slope. Even though, the original anchor load was obviously over-designed. The new anchors should have good corrosion protection and hopefully can self detect the anchor load change.

Acknowledgments The Authors wish to thank the Ministry of Transportation and Communication of Taiwan Government for supporting an independent investigation on the Freeway No. 3 landslide; the Directorate General of Highways for providing financial support to carry out basic experiments on ground anchors and also contributing anchors inspection results from many anchored slopes in Taiwan.

References

British Standard Institute (BSI DD81, BS 8081) (1989) British standard code of practice for ground anchorage

Hanna TH (1982) Foundations in tension—ground anchors. Trans Tech Publications and McGraw-Hill Book Company

Lee WF, Liao HJ, Chang MH, Wang CW, Chi SY, Lin CC (2012) Failure analysis of a highway dip slope slide. *J Perform Constructed Facil* 27(SPECIAL ISSUE: Analysis of Structural Failures Using Numerical Modeling):116–131

Liao HJ, Lee Wei F, Wang CW (2013) A tale of Twin cut slopes in Taiwan. *Forensic Eng Proc Inst Civil Eng* 166(2):72–80

Lin S-J (2014) Influence of free end assembly on load transfer in anchor and stress distribution in surrounding ground. Master Thesis, National Taiwan University of Science and Technology, Taipei, Taiwan

Chinese Taipei Geotechnical Society (2011) Forensic study on the dip slope failure of freeway No. 3 at Chainage 3.1 k. Taipei, Taiwan

A Study by Field Measurement and Numerical Simulation About Rainfall Seepage Mechanism in Case of Torrential Rainfall

Toru Danjo, Tomofumi Koyama, Hideki Nakamura, Yuto Tsuruzawa and Naoki Fukuyama

Abstract To investigate the mechanism of rainwater infiltration into an unsaturated soil slope during torrential rainfall, we conducted a field measurement and monitoring of the rainfall for a year, pore water pressure, and pore air pressure on a natural slope located in Fukuchiyama city in Kyoto, Japan. In 2013, torrential rainfall was observed at the study site on August 31 and September 15. This study presents the measurement data collected during the two torrential rainfall events and compares them with a saturated–unsaturated flow simulation of fluctuations in water content inside the slope, which was performed using a two-dimensional (2-D) finite element method (FEM). The simulation results and field measurement data are then used to explore the influence of pore air pressure on the rainwater infiltration mechanism at different rain intensities.

Keywords Monitoring • Saturated–unsaturated flow simulation • Torrential rainfall • Rainwater infiltration • Pore water/air pressure

T. Danjo (✉)

National Research Institute for Earth Science and Disaster Prevention,
3-1 Tennodai, Tsukuba Ibaraki 305-0006, Japan
e-mail: t.danjo@bosai.go.jp

T. Koyama

Faculty of Safety Science, Kansai University, Osaka, Japan
e-mail: t-koyama@kansai-u.ac.jp

H. Nakamura

Chubu Electric Power Co. Inc., Aichi, Japan
e-mail: Nkamura.Hideki@chuden.co.jp

Y. Tsuruzawa

Department of Urban Management, Kyoto University, Kyoto, Japan
e-mail: tsuruzawa.yuto.38a@st.kyoto-u.ac.jp

N. Fukuyama

Fukuchiyama Office of River and National Highway,
Kinki Regional Development Bureau, MLIT, Kyoto, Japan

1 Introduction

Recently, landslide disasters have been reported in Japan due to torrential rainfall and the so-called guerrilla-like rainfall. Therefore, investigating the mechanism of rainwater infiltration during torrential rainfall to evaluate slope stability is important, and many researchers have undertaken investigations on these issues. For example, Raharjo et al. (2005) carried out an in situ field measurement of pore water pressure changes during infiltration. They reported on the relationship between total rainfall and runoff, the influence of initial condition of slope on this relationship, and the influence of rainfall patterns on changing pore water pressure. Kitamura et al. (2000) and Sako et al. (2006) carried out in situ field monitoring to predict rainfall-induced landslides and discussed the relationship between rainfall intensity and seepage behavior in unsaturated soil. However, these researches rarely considered rainfall infiltration into slopes under torrential rainfall with very high rainfall intensity. Since the geologies and geological structures of slopes are different, investigating soil/rock conditions and material properties in detail is necessary for a more accurate evaluation of slope stability during torrential rainfall. Measuring and/or monitoring the soil water content and saturation before rainfall is also necessary, because these initial conditions will significantly affect the flow simulation results. Field measurements of initial in situ moisture can also be used for data assimilation (back-analysis), thereby improving the accuracy of future slope stability analyses and predictions.

Therefore, the authors introduced an ongoing field monitoring system on the slope of a national road located in Fukuchiyama city in Kyoto, Japan. Measurements taken include the amount of rainfall and the pore water and pore air pressures. In the present study, saturated–unsaturated flow simulations of this slope were performed to investigate rainwater infiltration into the slope during rainfall at different intensities, with rainfall events in August and September 2013 serving as the subject cases. The flow simulation results were compared with field measurements, and the effects of pore air pressure on the rainwater infiltration mechanism were explored.

2 Field Measurements and Monitoring

2.1 *Outline of Field Measurements and Monitoring*

The subject slope in this study is located along a national road in Fukuchiyama city in Kyoto, Japan. Black clayslate and mudstone, which belong to the Maizuru and Yakuno groups (Maizuru Zone), are widely distributed in this area. These rocks are fractured, with relatively high permeability. The subject slope is also located near a past landslide area. The inclination of the slope is approximately 42°.

Rainfall, pore water pressure, and pore air pressure were measured. Pore water pressure sensors were installed along three different lines (upper, middle, and lower) of the slope at four different depths (0.2, 0.4, 0.6, and 0.8 m). Pore air pressure sensors were installed along the same lines at the depth of 0.8 m (see Fig. 1). A rain

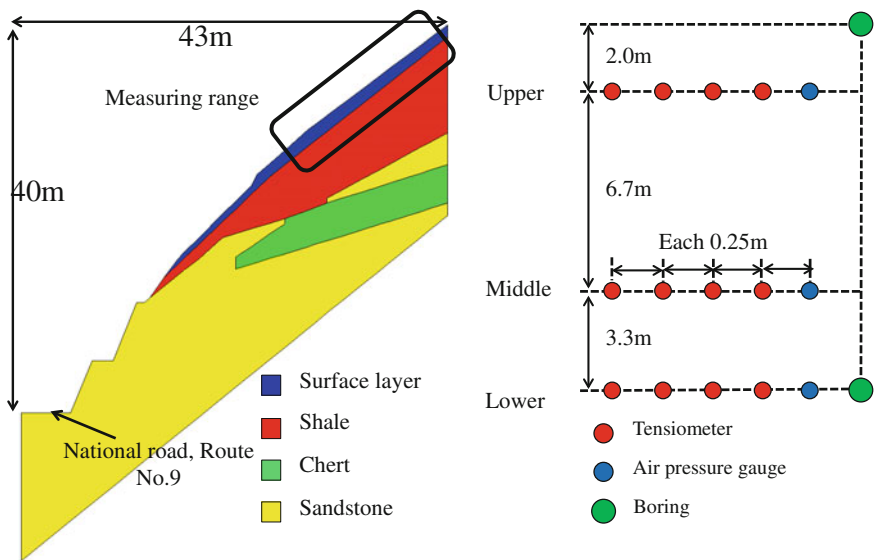


Fig. 1 Geological cross section of the slope based on the geological survey and measurement points

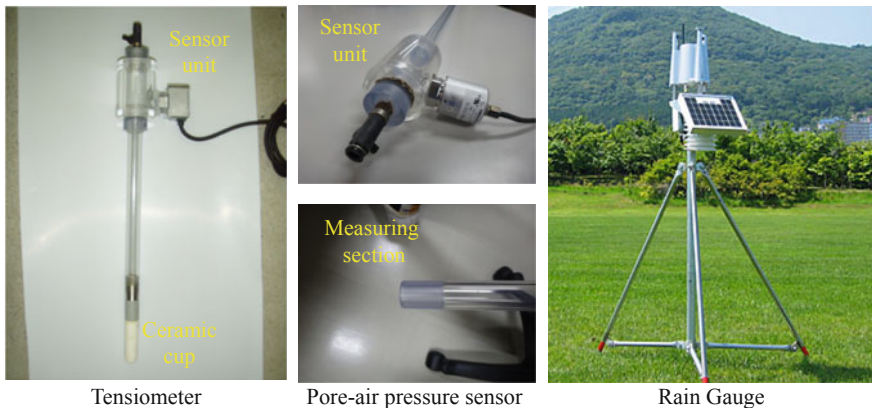


Fig. 2 Sensors and measurement tools used in the present study

gauge was set near the slope at a location where it would not be surrounded by tall obstacles such as trees. The measurement interval for the pore water and pore air pressure sensors was 1 min, and the interval for the rain gauge was 10 min.

The tensiometer used for measuring pore water pressure consists of a ceramic cup (DAIKIRIKA Ltd., DIK-3000-05), a semiconductor pressure sensor (Copal Electronics, PS7-102, 0 to -98 kPa, $\pm 0.3\%$ FS), and an acrylic pipe filled with degassed water (see Fig. 2). The pore air pressure sensor consists of an acrylic pipe and a pressure transducer (Kyowa Electronic Instruments Co. Ltd., PGM-02 kg, 0

to 20 kPa, $\pm 0.5\%$ RO). To measure pore air pressure, the measurement section of the pipe was set in the ground at the measurement depth, and a pressure sensor was installed at the top of the pipe (Sako et al. 2011). The rain gauge used was a tipping-bucket rain gauge (SEC Co., Ltd., TA-WL-2S).

2.2 Results and Discussion

Due to space limitations, this study discusses only the results obtained from the sensors installed at the upper part of the slope. The pore water and pore air pressure measurements taken during the short-term, high-intensity rainfall from August 31, 2013 to September 5, 2013 are shown in Fig. 3. The total amount of rainfall was 237.4 mm, and the maximum 10-min rainfall intensity was 8.2 mm. The pore water pressure began to increase from the shallow to the deep parts of the slope with rainwater infiltration into the slope. The pore air pressure measured at the depth of 0.8 m increased rapidly at the beginning of the rainfall. After the pore air pressure decreased at 12:30 AM on September 1, the pore water pressure at the depth of 0.6 m increased, suggesting that pore air may be compressed at depths between 0.6 and 0.8 m. Therefore, we conclude that rainwater infiltration is significantly affected by pore air pressure.

From September 15, 2013 to September 16, 2013, relatively long-term rainfall with low rain intensity was observed (see Fig. 4). This rainfall was caused by typhoon No. 18. The total amount of rainfall was 186.8 mm, and the maximum 10-min rainfall was 3.8 mm. The initial pore water pressure inside the slope was higher than that on August 31 and may have been affected by the rainfall observed on September 5, 2013. At 8:20 AM on September 15, the values of pore water

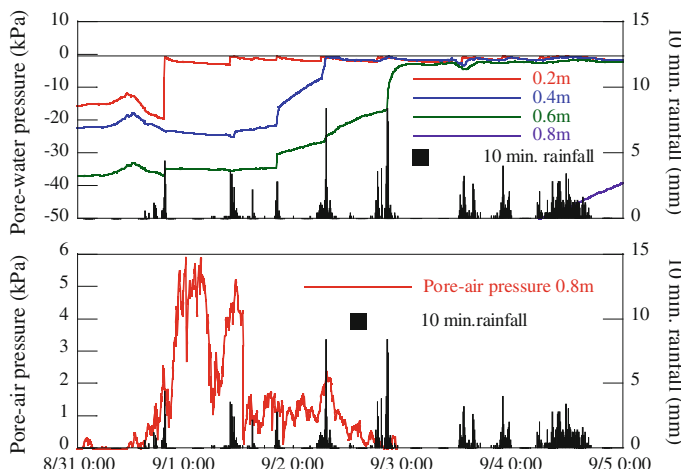


Fig. 3 Measurement results of pore water pressure and pore air pressure

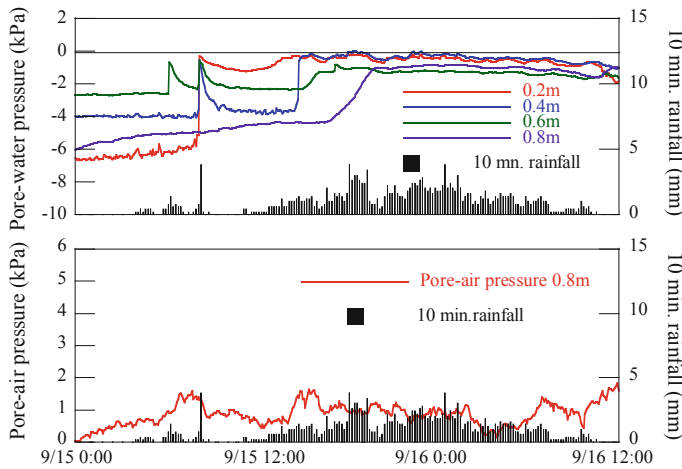


Fig. 4 Measurement results of pore water pressure and pore air pressure on

pressure measured by tensiometers installed at depths of 0.2, 0.4, and 0.6 m increased due to rainfall infiltration. The pore water pressure at the depth of 0.2 m then remained high, even though no rainfall was observed for the following 2 h (between 9:00 AM and 11:00 AM), suggesting that infiltrated rainwater was stored around the slope surface. Rainfall resumed at 11:00 AM, and the pore water pressure measured at the slope surface quickly increased. The tensiometers installed in the deeper part of the slope then showed increasing pore water pressure with rainfall infiltration. The pore air pressure observed from September 15 to September 16 was lower than that observed from August 31 to September 5. Therefore, we conclude that rainfall intensity significantly increases pore air pressure.

3 Numerical Simulations

3.1 Governing Equation for Saturated–Unsaturated Flow

The governing equation for saturated–unsaturated flow simulations can be derived from the mass conservation equation and Darcy’s law, as follows (Akai et al. 1977):

$$\frac{\partial}{\partial x_i} \left\{ K_r(\theta) K_{ij}^s \frac{\partial \psi}{\partial x_i} \right\} - q = \{c(\psi) + \beta S_s\} \frac{\partial \psi}{\partial t} \quad (1)$$

$$i, j = 1, 2 (1x, 2y)$$

In this equation, θ is the volume water content, ψ is the pressure head (matric suction), $K_r(\psi)$ is the relative permeability, K_{ij} is the hydraulic conductivity tensor for the saturated state, $c(\psi)$ is the specific water content (defined as $\partial n / \partial \psi$, where

n is porosity), β is 1 in the saturated area and 0 in the unsaturated area, S_s is the specific storage, and t is the time.

3.2 Numerical Model of the Slope

The analytical domain was 43 m wide and 40 m high. The lower part of the slope, defined as the region 8 m below the national road, was also included in the model. The geological cross section of the slope is shown in Fig. 5 and is defined on the basis of a geological survey, boring survey, and standard penetration tests. The rainfall boundary was applied along the ground surface of the slope, and the flow rate was fixed. The flow rate was calculated from the rainfall intensity records obtained from the on-site rain gauge. The boundary conditions of the slope in Fukuchiyama are shown in Fig. 6. The mechanical and hydraulic material properties of the surface soil and bedrock are shown in Table 1 (Tsuruzawa et al. 2014).

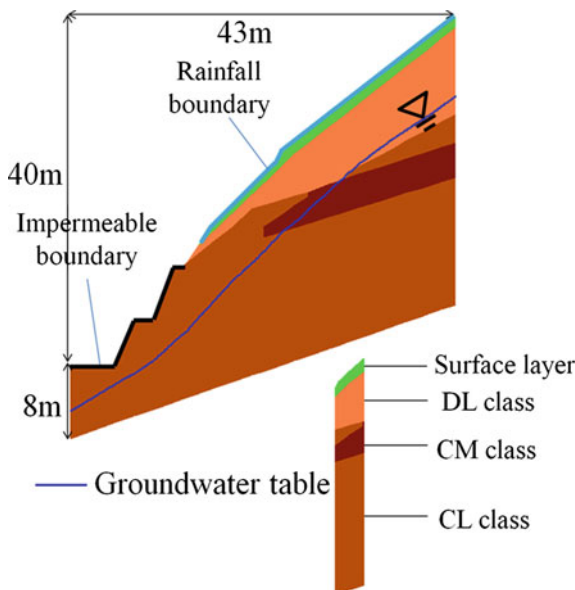


Fig. 5 Geological cross section and the location of groundwater table

Table 1 Mechanical and hydraulic properties for each layer of bedrock at the study slope

| | Weathering | γ (kN/m ³) | c (kN/m ²) | φ (°) | k (m/s) |
|--------------|------------|-------------------------------|--------------------------|---------------|-----------------------|
| Surface soil | | 18 | 2 | 33.72 | 9.62×10^{-5} |
| DL class | Highly | 20 | 100 | 30 | 1.0×10^{-7} |
| CM class | Slightly | 25 | 1000 | 40 | 5.0×10^{-8} |
| CL class | Moderately | 22 | 500 | 40 | 1.0×10^{-8} |

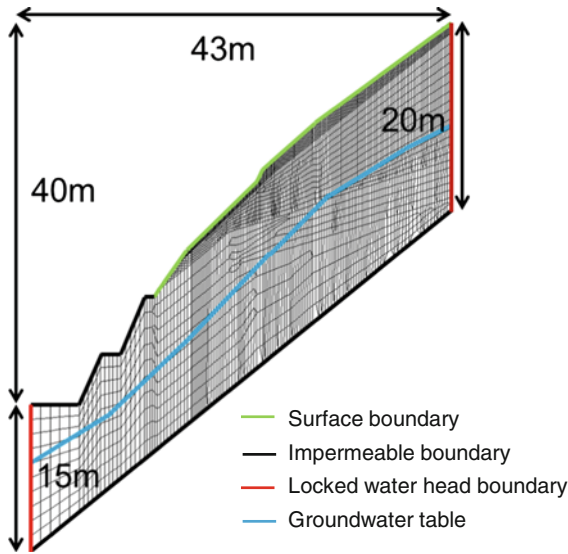


Fig. 6 Boundary conditions at the slope in Fukuchiyama

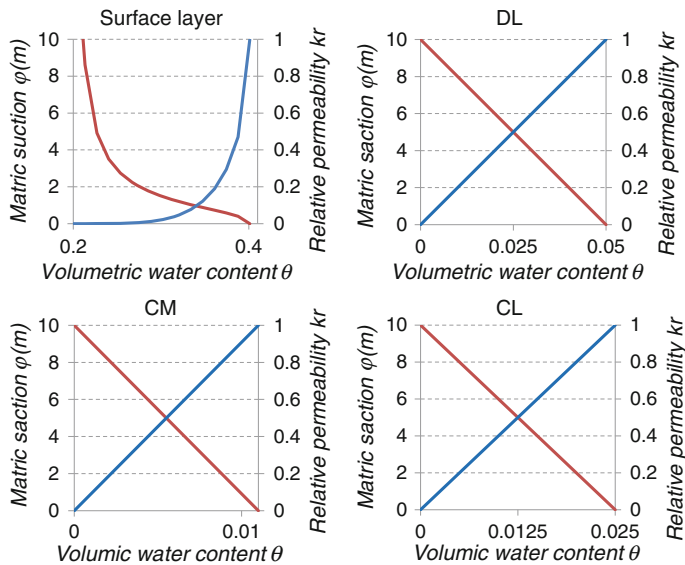


Fig. 7 Saturated characteristics of the surface soil and bedrock

The properties of the surface soil layer were obtained using in situ permeability tests. The bedrock was categorized as DL (highly weathered), CM (slightly weathered), or CL (moderately weathered) on the basis of the rock mass classification commonly used in Japan. The classifications were obtained from the

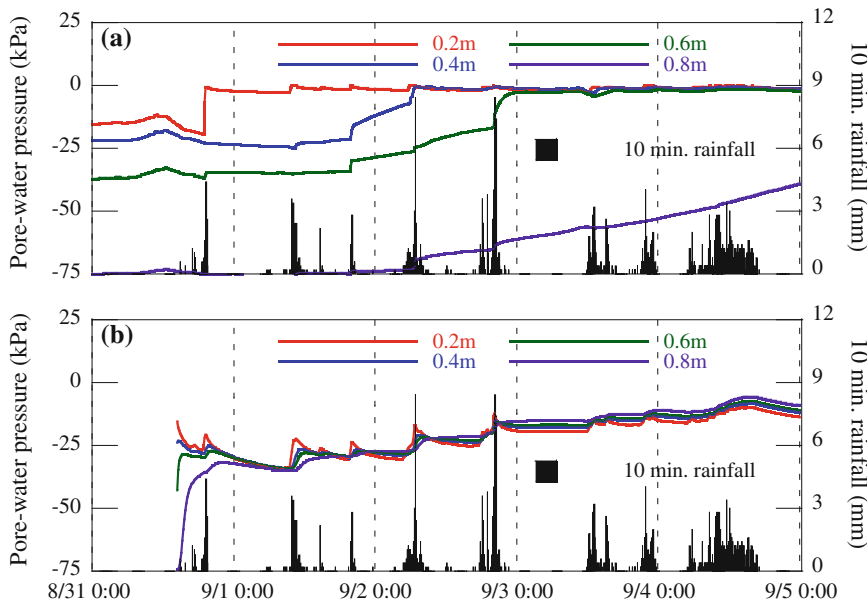


Fig. 8 Measurement (a) and analysis (b) results of pore water pressure

literature (Ministry of Land, Infrastructure, Transport and Tourism 2011). The lithological character is shell, chert, and sandstone distributed in the DL, CL, and CM class bedrocks, respectively. The unsaturated soil/rock properties of the surface soil and bedrock are shown in Fig. 7. In this study, as there were no laboratory data for unsaturated soil/rock properties, the linear relationship between the degree of saturation and suction/relative permeability for bedrock (DL, CM, and CL layers) was assumed for simplicity. The impact of this simplification on rainfall infiltration in the surface soil was small, because there is only one order of difference in saturated hydraulic conductivity between the surface soil and the DL class bedrock. The nonlinear relationship between the degree of saturation and relative permeability for the surface soil was given on the basis of the Van Genuchten (VG) model for sand, as the saturated hydraulic conductivity for surface soil is 8.25×10^{-5} m/s in the laboratory hydraulic conductivity test. The relationship between the degree of saturation and matric suction was assumed to be linear for simplicity.

4 Comparison of Measurement and Analysis Results

The measurement and analysis of pore water pressure and rainfall from August 31, 2013 to September 5, 2013 are shown in Fig. 8a, b. The results obtained by measurement and analysis at the depth of 0.2 m appeared to be relatively coincident. Analysis results for pore water pressure at depths of 0.4 and 0.6 m agreed with

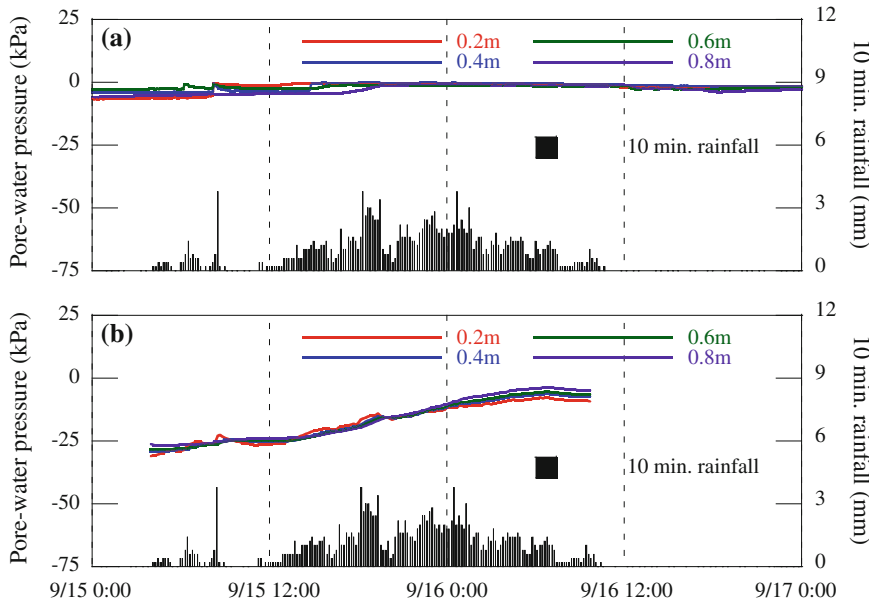


Fig. 9 Measurement (a) and analysis (b) results of pore water pressure on

the field measurement results. However, the arrival time of a phreatic line is different in the simulations and field measurements. The arrival time of the phreatic line is much earlier in the simulation than in the measurement. The time evolution of pore water pressure at the depth of 0.8 m is totally different in the simulations and the field measurements. This may be caused by the fact that rainwater infiltration was prevented by the increased pore air pressure. The increase in pore air pressure is not considered in the saturated–unsaturated flow simulations.

The results of the measurement and analysis of pore water pressure and rainfall on September 15, 2013 and September 16, 2013 are shown in Fig. 9a, b. As can be seen in the figure, the initial value of pore water pressure (9/14 4:00 AM) in the field is different from that in the analysis results. This is because the pore air pressure is not considered in the saturated–unsaturated flow simulations. It was found that if the seepage flow analysis without pore air pressure is analyzed for a long time, the infiltration behavior between the field measurement and the analysis differs.

5 Conclusion

In this study, saturated–unsaturated flow simulations using two-dimensional FEM were performed to investigate the rainwater infiltration mechanism during torrential rainfall. The simulation results were compared with the field measurement data. The findings obtained from this study are summarized as follows:

1. By installing a tensiometer and a pore air pressure sensor at the site, it was confirmed that the pore air pressure values increased during torrential rainfall, and the increase in pore air pressure significantly affected rainwater infiltration. Thus, the phreatic line does not arrive at the deeper part of the slope. [Remark 6]
2. The simulated pore water pressure did not agree well with the measurement data. This is possibly due to the pore air pressure not being considered in the saturated–unsaturated flow simulations.

In the near future, we plan to develop a methodology for simulating the two-phase (rainwater and air) flow to obtain more accurate simulation results.

References

Akai K, Ohnishi Y, Nishigaki M (1977) Finite element analysis of saturated-unsaturated seepage in soil. *J Geotech Eng JSCE* 264(8):87–96 (in Japanese)

Kitamura R, Kawaida M, Abe H, Jomoto K, Terachi T (2000) Development of field measurement system for suction in unsaturated soil with rainfall. *J JSCE* 652:287–292 (in Japanese)

Ministry of Land, Infrastructure, Transport and Tourism (2011). Report of research design for the slope around Heki and others along Route 9, 1–100 (in Japanese)

Rahardjo H, Lee TT, Leong EC, Rezaur RB (2005) Response of a residual soil slope to rainfall. *Can Geotech J* 42:340–351

Sako K, Kitamura R, Fukagawa R (2006) Study of slope failure due to rainfall, A comparison between experiment and simulation. In: Proceedings of the 4th International Conference on Unsaturated Soil, vol 2, pp 2324–2335

Sako K, Danjo T, Fukagawa R, Bui HH (2011) Measurement of pore-water and pore-air pressure in unsaturated soil. In: Proceedings of the 5th Asia Pacific conference on unsaturated soils. Pattaya, Thailand, pp 443–448

Tsuruzawa T, Koyama T, Nakamura H, Lee K, Fukuyama N, Yamada M (2014) Establishment of criteria for traffic regulations along the national road based on numerical simulations during torrential rainfall. XII International IAEG Congress, Torino, Italy

Numerical Simulation for the Earthquake-Induced Deformation of a Residential Land Slope Reinforced with Landslide Prevention Piles

Taisuke Watanabe, Akihiko Wakai, Takayuki Fukazu, Ryo Obuchi, Tomohiro Mori and Shingo Sato

Abstract In this study, a numerical simulation for the earthquake-induced deformation of a residential land slope reinforced with landslide prevention piles is presented. The objective slope is a real residential land slope in Sendai city, damaged at the time of the 2011 off the Pacific coast of Tohoku earthquake. The focus of the study is placed on the effectiveness of the landslide prevention piles in the slope which have been constructed before the earthquake. Reproduction analyses for the slope which has been constructed these piles are performed with 2D dynamic elasto-plastic finite element analysis considering strain-softening characteristics of the soils. In addition, analyses which assumed the slope without these piles are performed for a comparison, and the effectiveness of these piles is considered.

Keywords Residential land · Filled slope · Landslide prevention pile · The 2011 off the Pacific coast of Tohoku earthquake · Finite element analysis

1 Introduction

At the time of the 2011 off the Pacific coast of Tohoku earthquake (the 2011 earthquake), a large number of damages in residential lands of the Tohoku district with serious ground deformation were observed. In particular, the hillside

T. Watanabe (✉)
Jishin Kougaku Kenkyusho, Inc., 4-27-2, Yotsuya,
Shinjuku-ku, Tokyo 160-0004, Japan
e-mail: watanabe@flush.co.jp

A. Wakai · T. Fukazu · R. Obuchi
Gunma University, Kiryu, Japan

T. Mori
Tohoku University, Sendai, Japan

S. Sato
Fukken Gijyutsu Consultant Co., Ltd., Sendai, Japan

residential lands in Sendai City suffered serious damage (Wakai et al. 2012). Some of the residential lands had been damaged by the 1978 Miyagi-ken-oki earthquake (the 1978 earthquake) (Kawakami et al. 1978). Midorigaoka 1-chome and 3-chome district are districts that had been damaged, and just after the 1978 earthquake, several measures such as landslide prevention piles, and dewatering method were installed (Asada 2008). As a result, in the 2011 earthquake, there was no damage in 1-chome. It is probable that there was a certain effect on the measures. In contrast, in 3-chome district, long-distance movement of the whole fill slope as sliding collapse was prevented, but there was serious damage such as houses lean by ground deformation. In particular, by the displacement values measured after the earthquake (Wakai et al. 2012), it is estimated that the piles installed on upper part of the fill slope were greatly beyond the yield strength (Miyagi Prefecture 2011). Thus, in terms of conservation of houses on residential land, it is critical to verify the ground deformation quantitatively.

The purpose of this study is to verify the effect of the prevention piles by 2D dynamic elasto-plastic FEM (Finite Element Method), with reference to the 2011 earthquake disaster of the case in the 3-chome district.

2 Overview on Damages of Midorigaoka 3-Chome District

Midorigaoka 3-chome district is a residential area which was developed from 1961 to 1962 by cutting some parts of the hillside and using the materials as fill for the two deep valleys (Fig. 1; Wakai et al. 2012; Fukken Gijyutsu Consultant Co., Ltd. 2008). The residential land had suffered enormous damage due to landslide-type failure during the 1978 earthquake. After the 1978 earthquake, landslide prevention piles (steel pipe piles: $\phi = 318.5$ mm) were installed in five rows in zigzag to 1.5 m interval, and two groundwater drainage wells and horizontal drainage drilling were installed (Fig. 2; Wakai et al. 2012; Miyagi Prefecture 2011).

In Fig. 2, part of damage situation during the 2011 earthquake is shown. In the 2011 earthquake, some of the piles of 1–2 lines and 5 line were tilted to downhill side and they were exposed on the ground surface, and the surrounding ground became irregular. In addition, on the surface of top of the landslide block (around A in Fig. 2), numerous tension cracks and ground-level gaps in an arc were caused on the ground. From this situation, it is supposed that there are prevention effects on sliding collapse, but large deformation of the ground surface is caused. As a result, houses and the foundations suffered serious damages.

In Fig. 2, the residual displacement values (Horizontal displacement between the pile head and sliding plane) of steel pipe piles that have been measured are also shown (Miyagi Prefecture 2011). From the displacement level, it is estimated that the bending moment of many piles has been exceeded the yield strength.

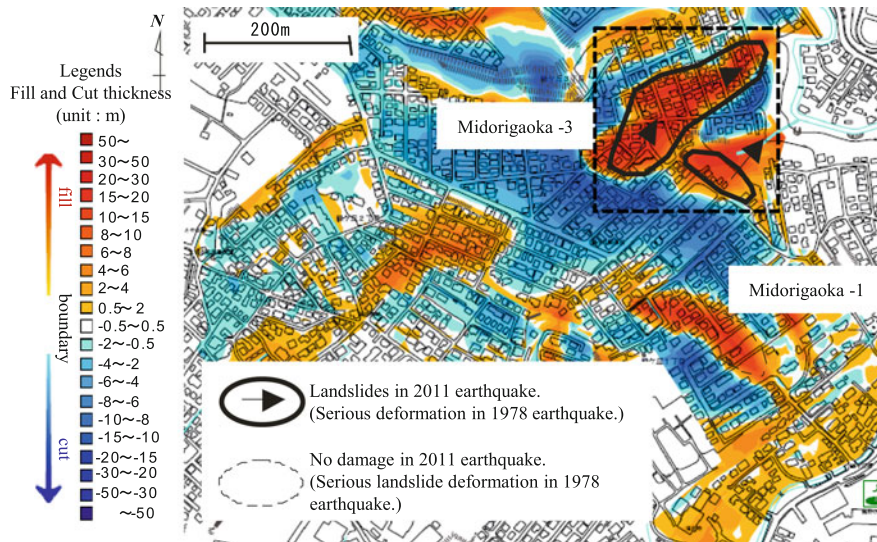


Fig. 1 The thickness distribution of cut and fill sections in Midorigaoka 3-chome

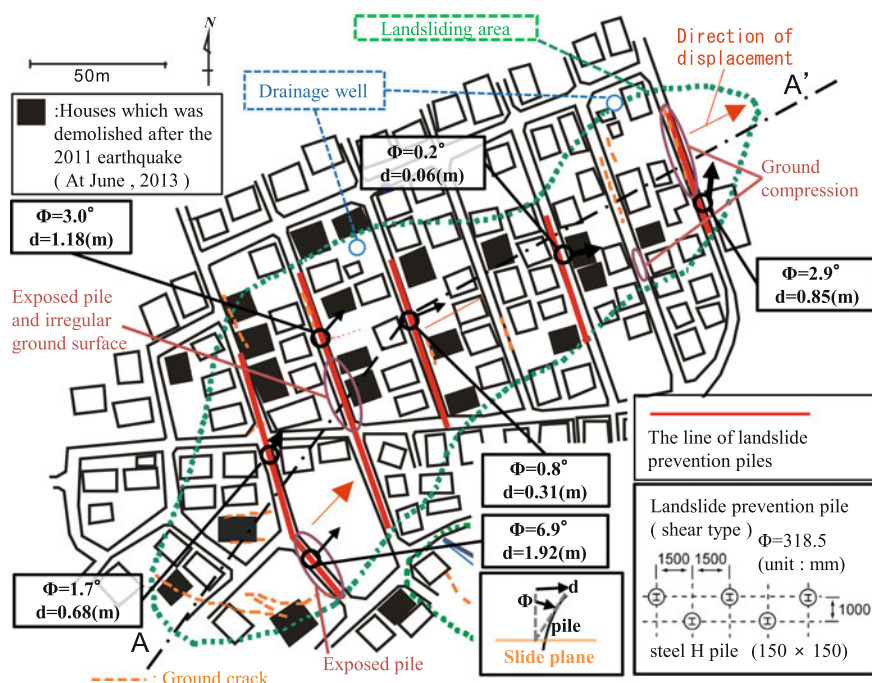


Fig. 2 Overview of countermeasures in 1978, and overview on damages in 2011 (Midorigaoka 3-chome district)

3 Verification of Effect on Landslide Prevention Piles

3.1 Analysis Model and Conditions

Figure 3 shows two-dimensional finite element meshes for the simulation. Object section is A-A' line in Fig. 2. It is estimated that the object of section for analysis consists of three layers, (A): detritus (fill), (B): weathered tuff, and (C): tuff. It is presumed that (A) is a soft ground by the N-values especially. However, the detailed soil test (such as cyclic triaxial test) in 3-chome has not been done. Therefore, the results of soil test (cyclic triaxial test) by samples which was collected in another residential land in Sendai City (Mori 2009) are determined by the parameters of constitutive equation of materials (a simple cyclic loading model incorporate strain-softening characteristics (Ugai and Wakai strain-softening model, total stress model)) (Wakai et al. 2010). However, about the deformation mode of whole slope after earthquake, it varies greatly with depth of layer causing the strength of soil to decrease sharply by cyclic loading. Based on the above, in this study, it is assumed that the ground conditions are in the following types, (a): there is a clear sliding surface at boundary between (A) and (B) (strain-softening type (B) in Fig. 3), (b): there is a possibility that whole fill slope can be sheared totally by strain-softening (strain-softening type (A) in Fig. 3) (Fig. 4 shows overview of two types of ground conditions).

Houses are assumed to be elastic bodies and their parameters are determined with the natural period of general wooden two storey houses (Japan 2 × 4 Home Builders Association 2007).

Landslide prevented piles are assumed to be elastic-perfectly plastic materials with critical moment values in bending moment. In addition, for comparisons, the

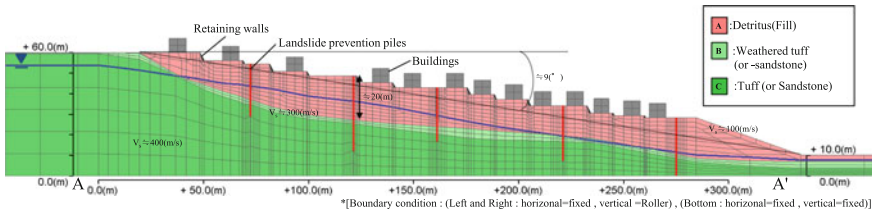


Fig. 3 Two-dimensional finite element meshes for the simulation

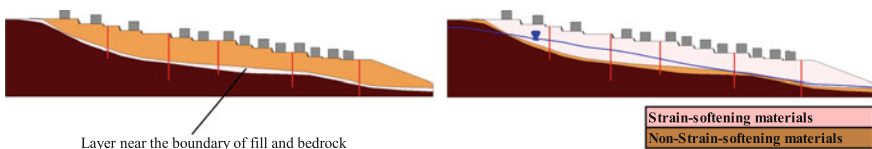
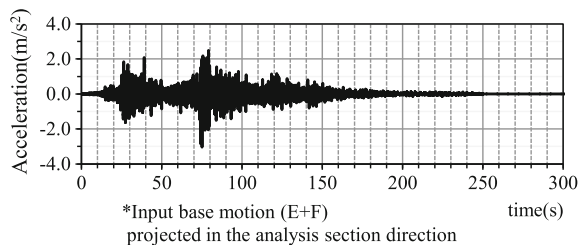


Fig. 4 Two types of ground conditions for the analysis

Table 1 Analysis cases for the simulation

| Case | Ground conditions | Type of prevention piles | Ground water |
|------|-------------------|--------------------------|--------------|
| 1 | A | — | — |
| 2 | A | Elasto-plastic | — |
| 3 | A | Elastic | — |
| 4 | B | — | × |
| 5 | B | Elasto-plastic | × |
| 6 | B | Elastic | × |

Fig. 5 Input motion

case where the piles are assumed to be elastic bodies, as well as the case without the piles are performed. Table 1 is the summary of the analytical cases.

Figure 5 shows input seismic wave motion which has been pullbacked to base. The motion is the observation waveform of nearby “Small-Titan” (Strong Motion Array of Local Lots by the Tohoku Institute of Technology Area Network).

In addition, to consider the 3D effect, the piles stiffness are set as a unit width to consider 1.5 m interval and pile diameter ($\Phi = 318.5$ m) for flexural rigidity per pile.

3.2 Analytical Results

Figure 6 shows the residual deformation of ground conditions (a) (case1–case3). In the case1 (without the piles), the layer near boundary between bedrock and fill are sheared largely, and the displacement is caused in the ground surface. On the other hand, in the case2 and case3 (with the piles), deformation is suppressed, it is estimated that the effect of the prevention piles appears. In particular, in the case3 (assuming elastic body piles), the deformation is smaller than case2 (assuming elasto-plastic body piles). Thus, it is suggested that the strength of stiffness of piles is important.

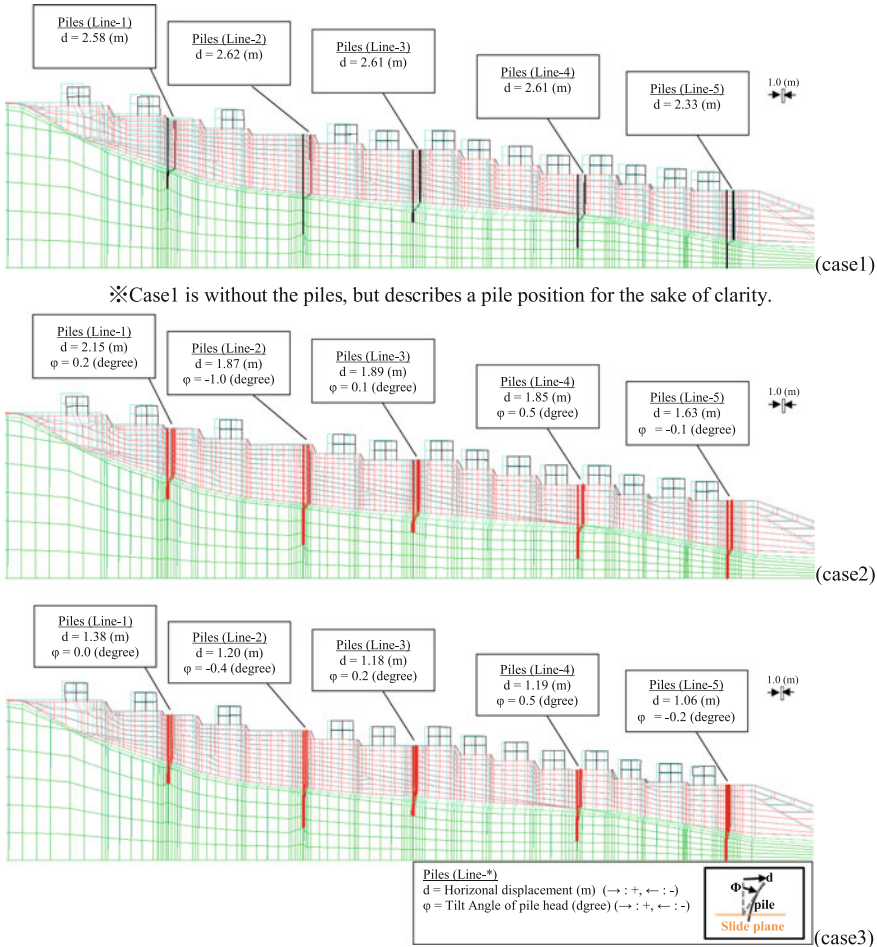
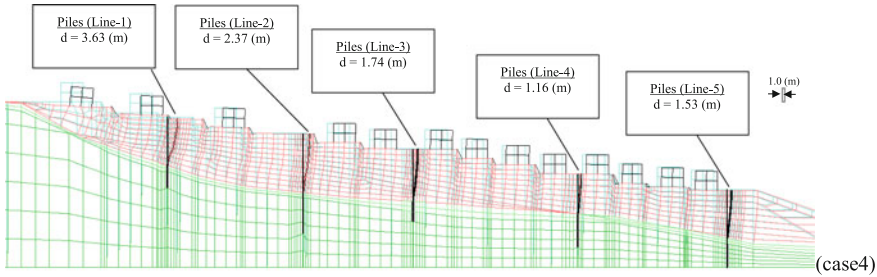


Fig. 6 Residual deformation after the motion by the simulation [ground conditions (a)]

Figure 7 shows the residual deformation of ground conditions (b) (case1–case3). Because of the fill layer is softened throughout, shear deformation is caused largely in the shallow ground. In this ground conditions, deformation have no major differences between with and without piles. Rather, the displacement of the ground surrounding the piles is larger. The displacement of the head of piles is greater than the measured displacement. However, it can be presumed that ground conditions (b) are results close to the actual damage trends.

Then, it compares distribution of the bending moment and shear force of the piles (Figs. 8 and 9). Comparing distribution of the bending moment (In Figs. 8



※Case4 is without the piles, but describes a pile position for the sake of clarity.

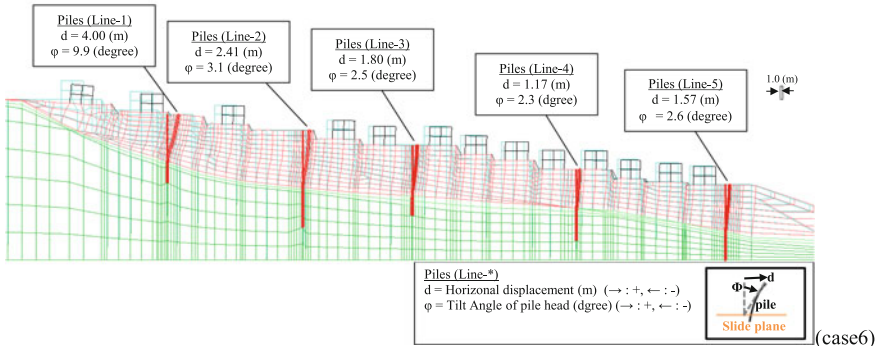
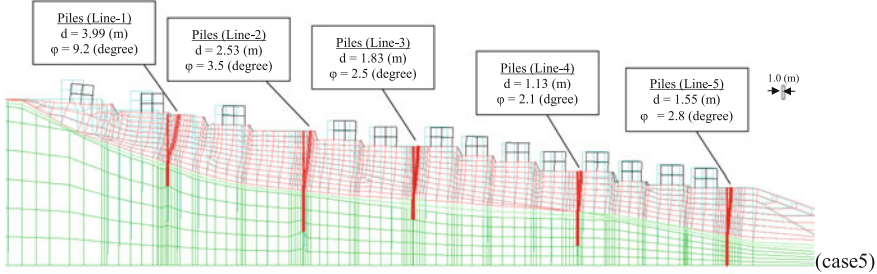


Fig. 7 Residual deformation after the motion by the simulation [ground conditions (b)]

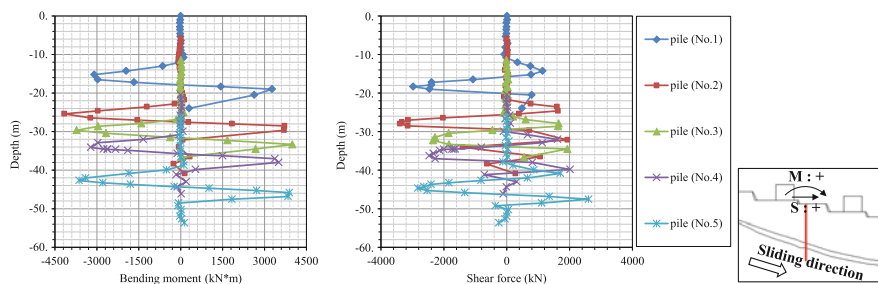


Fig. 8 Distribution of the residual bending moment and shear force [ground conditions (a); case3]

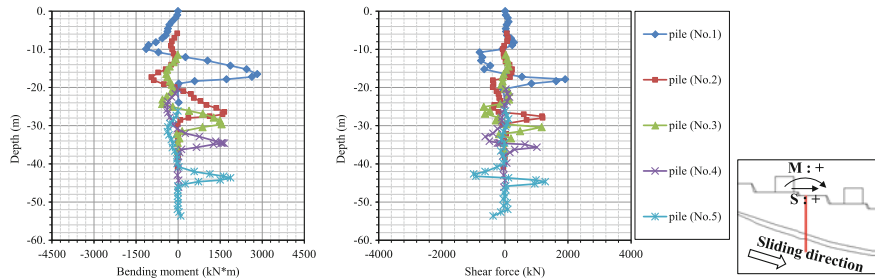


Fig. 9 Distribution of the residual bending moment and shear force [ground conditions (b); case6]

and 9), in the case of ground conditions (a), the pile deformation modes are in S-shape around the sliding surface at the softened layer. On the other hand, in the case ground conditions (b), the pile deformation modes are in bending deformations similar to cantilevers, and the shear force in the direction of suppressing are small (negative value in the shear force). As a result, it was confirmed that the pile effect of resistance on landslide is greater in the former conditions. From the above, it can be presumed that difference of landslide preventive effect of the piles is caused by ground conditions.

4 Conclusion

The primary results of the present study are as follows:

- (1) In the series of the analyses demonstrated in this study, it is probable that the mechanical properties of the actual soil are not simulated exactly, but the results which show the tendency similar to actual damage situation was obtained. As an example, in the ground conditions (b) (the fill materials are strain-softening type), there may be mentioned that displacement and tilt angle of the piles in the upside slope is larger, in comparison with them of the piles in the downside slope.
- (2) Comparing the distributions of the bending moment of the piles obtained from the analysis, in the case ground conditions (a), the pile deformation modes are in S-shape around the sliding surface at the softened layer. On the other hand, in the case ground conditions (b), the pile deformation modes are in bending deformations similar to cantilevers. As a result, it is confirmed that the pile effect of resistance on landslide is great in the former conditions.
- (3) According to the results, it is clear that the deformation reduction effects of the landslide prevention piles are affected by the mechanical conditions of the ground. The measures considering the ground condition and the ground deformation are desired.

References

Asada A (2008) What should be feared is not an earthquake but a weak ground (reviews and proposals), *Jiyu-Kobou* (Japanese Publication), pp 83–111

Fukken Gijyutsu Consultant Co., Ltd. (2008). Map for developed residential ground in southern Sendai city and Natori city (1/25,000)

Japan 2×4 Home Builders Association (2007) Structural design guidelines for wood frame construction, pp 46–48

Kawakami F, Asada A, Yanagisawa E (1978) Damage to embankments and earth structures due to Miyagiken-oki earthquake of 1978. *J Jpn Soc Soil Mech Found Eng* 26(12):25–31

Miyagi Prefecture (2011) Report of landslides disaster surveying design in Midorigaoka and others districts

Mori T (2009) A study on seismic response of fill slope considered soil water characteristics. Ph.D. thesis, Tohoku University, pp 99–129

Wakai A, Ugai K, Onoue A, Kuroda S, Higuchi K (2010) Numerical modeling of an earthquake-induced landslide considering the strain-softening characteristics at the bedding plane. *Soils Found* 50(4):515–527

Wakai A, Sato S, Mitsuji K, Mori T, Kazama M, Koseki J (2012) Investigation of damage caused by the 2011 off the Pacific coast of Tohoku earthquake—brief report on the residential lands in Sendai city-. *Jpn Geotech J* 7(1):79–90

Centrifuge Model Test on Slope Reinforcement by Rock Bolt with Facing Plate

Shion Nakamoto and Jiro Takemura

Abstract Rock bolt with facing plate is a kind of reinforcement of soil slope. By adding prestress to the slope through facing plate, slope strength of shearing is increased to restrain the slope from unstable. However, the effect of prestress on the slope stability and its variation when the slope moves have not been well studied. In this research, a centrifuge model test system which can simulate the preloading process of the bolts in a slope and apply the horizontal load to the slope was developed to study the mechanical behaviour of the slope with this type of reinforcement.

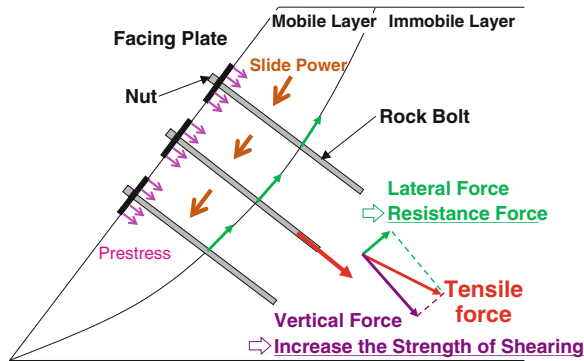
Keywords Centrifuge modelling · Slope reinforcement · Rock bolt · Prestress

1 Introduction

Rock bolt is used as a kind of soil nailing method which is one of reinforcement method for natural slopes. If a deformation occurs on the slope, a tensile force will be generated in the rock bolts, which works for the stability of the slope. The vertical component of the tensile force increases the shearing strength of the soil, and the horizontal component works as a resistance against the sliding. But for a slope with weak soils, such as highly weathered rocks, a large deformation is needed for mobilization of the force. For such slopes, a kind of prestressed rock bolt has been considered. It has a facing plate. Prestress is added to the slope through the plate by tightening the nut as shown in Fig. 1. To study the reinforcement mechanisms of this kind of soil nailing method and the reinforcing effect of the facing plate and prestress in this kind of reinforcement, many researches have been done on the reinforced slope using small scale 1 g physical models (Hayashi et al. 1986; Sasahara and Nakamura 1997). However, it is difficult to simulate mechanical behaviour of soil caused by the self-weight, like failure of slope, in a small scale

S. Nakamoto (✉) · J. Takemura
Tokyo Institute of Technology, Tokyo 152-8552, Japan
e-mail: zhao.s.aa@m.titech.ac.jp

Fig. 1 Mechanism of rock bolt with facing plate slope reinforcement



physical model under normal gravity (1g) conditions, because stress levels in the model are much smaller than those in the prototype structures.

Under these situations, centrifuge modelling has been used. Centrifuge modelling is a kind of experimental technique that can replicate the gravity-induced stresses of a prototype in a $1/n$ reduced model by test in a high gravitational field n times larger than that of prototype. The main advantage of using centrifuge modelling is that the magnitude and distribution of stress can be simulated in small scale model. From previous studies done in centrifuge, reinforcing effects of this kind of method and facing plate have been confirmed for various conditions (Tei et al. 1998; Viswanadham and Deepa 2010; Inagawa and Yamamoto 2012). However, because of the difficulty in controlling the preloading to the facing plate in centrifuge, the effects of the prestress on the stability of reinforced slope have not been well studied.

In this study, a centrifuge model test system which can simulate the preloading process of the rock bolts with facing plate in a slope was developed. Using the system, I conducted static loading tests by an inclining table in centrifuge to study the mechanical behaviour of the slope with this type of reinforcement, and the effect of prestress on the slope stability and its variation when the slope moves.

2 Centrifuge Model Test

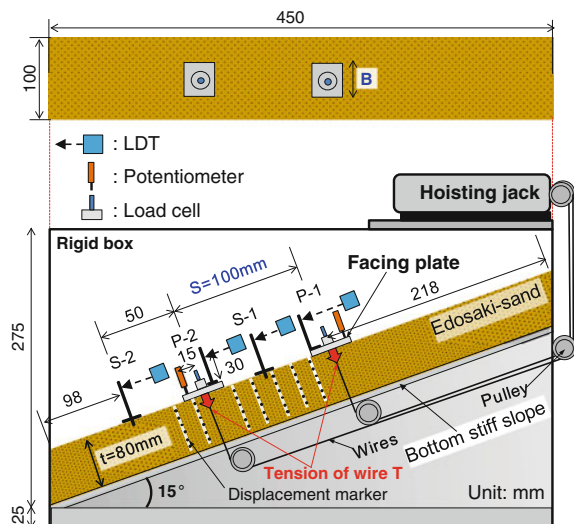
In these tests, a container with inner dimension of 450 mm in length, 100 mm in width, and 300 mm in depth, accommodated model slope with 2 rock bolt models installed at intervals of 100 mm [prototype: 3.7 m] was prepared on 15° sloping base fixed to the inclination table. Because the model slope also has 15° inclination, the initial slope angle was 30° . The mobile layer of model slope was made of Edosaki sand with the index and mechanical properties shown in Table 1. White noodles with black dots are inserted in front of the slope for visual observation of ground deformation. The immobile layer was made of aluminum with Edosaki sand pasted on the surface to create a rough surface. Preload was applied by pulling wire, which connected to the facing plate and hoisting jack, under 37 g centrifugal acceleration. After applying the

Table 1 Properties of compacted Edosaki sand used in the test

| | |
|--|------------------------|
| Specific gravity: G_s | 2.72 |
| Mean grain diameter: D_{50} | 0.219 mm |
| Uniformity coefficient: U_C | 9.85 |
| Maximum dry density: ρ_{dmax} | 1.78 g/cm ³ |
| Optimum water content w_{opt} | 15 % |
| Bulk density of compacted sand: ρ_t | 1.43 g/cm ³ |
| Water content of compacted sand: w | 15 % |
| Degree of compaction: D_c | 70 % |
| Friction angle*: ϕ' | 29.4° |
| Cohesion*: c' | 2.7 kPa |

*: strength parameters obtained from direct shear test under vertical stresses from 9 to 41 kPa

Fig. 2 Front and top view of model slope

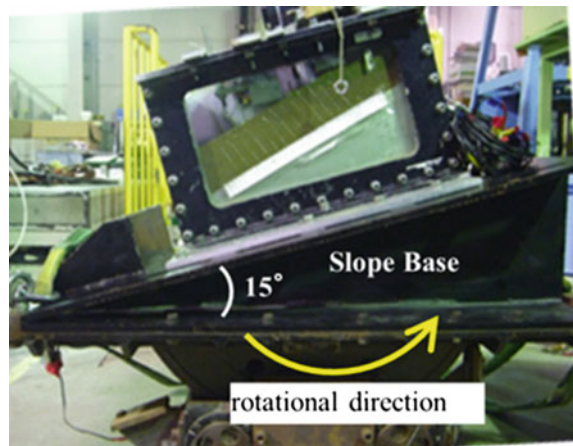
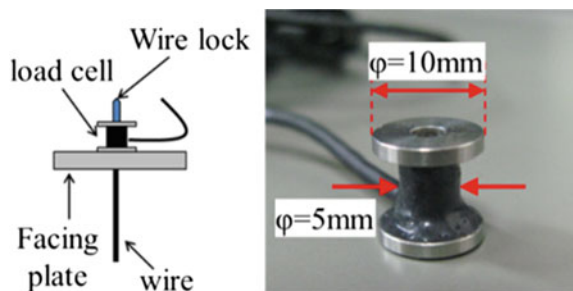


preload, the model slope was inclined up to 50° from 30° by the inclination table. The inclination table has been used in centrifuge model studies to impose the pseudo-static seismic force to model slopes (Saito et al. 1995; Izawa et al. 2003). Equivalent seismic intensity α_h by the inclination angle $\Delta\theta$ is given by the following expression:

$$\alpha_h = \tan \Delta\theta \quad (1)$$

Lateral displacement ($\delta_{P-1}, \delta_{P-2}$) and settlement (S_{P-1}, S_{P-2}) of facing plate, lateral displacement of the slope surface ($\delta_{S-1}, \delta_{S-2}$) and tensile forces applied to the wires (T_{P-1}, T_{P-2}) were measured by potentiometers, laser displacement transducers (LDT) and miniature load cells on the facing plate. Deformation of the slope was monitored by video camera during the inclining test.

Figure 2 shows the model set-up and location of sensors. Figures 3 and 4 show inclination table with 15° slope base and miniature load cell. Table 2 shows

Fig. 3 Inclination table**Fig. 4** Miniature load cell placed on the facing plate**Table 2** Condition of test cases and results

| Test case | B/S | Prestress: σ_{pi} (kPa) | $R^p = \sigma_{pi}/t\gamma_t$ | $\Delta\theta_y^a$ (°) | $\Delta\theta_f^b$ (°) |
|-----------|--------------------|--------------------------------|-------------------------------|------------------------|------------------------|
| Case NR | – | – | – | 1.9 | 8 |
| Case 1 | 0.4 ($B = 40$ mm) | 54 | 1.3 | 2.0 | 15 |
| Case 2 | 0.4 ($B = 40$ mm) | 89 | 2.1 | 3.5 | 16 |
| Case 3 | 0.4 ($B = 40$ mm) | 112 | 2.7 | – | – |
| Case 4 | 0.4 ($B = 40$ mm) | 136 | 3.2 | 3.9 | 20 |
| Case 5 | 0.2 ($B = 20$ mm) | 136 | 3.2 | 3.5 | 16 |

$\Delta\theta_y^a$: the increment of inclination at onset of the deformation

$\Delta\theta_f^b$: the increment of inclination when displacement of slope measured between the plates is 4 mm

condition of test cases. B and R_p showed in Table 2 is the width of facing plate and the ratio of prestress σ_{pi} to overburden pressure $t\gamma_t$. The main parameter of this study is prestress. One case with smaller facing plate was also conducted to study the effect of facing plate size.

3 Test Results and Discussions

Figure 5 shows the relationships between the contact pressure $\sigma_p (= T_p/B^2)$ and settlement S of the facing plate observed in the preloading process. Pull-in loading tests, with 20 and 40 mm wide facing plate, were conducted under the same ground condition. The $\sigma_p - S$ relationships observed in the pull-in loading tests are also shown in Fig. 5. From this figure, some scattering in the relation can be observed especially in the case with larger facing plates ($B = 40$ mm). This could be partly attributed to heterogeneity of the slope and rotation of the facing plate. Because of the space limitation, the settlement and lateral displacement were only measured by one potentiometer and one LDT, respectively, which could not detect the rotation. In all the cases, the pressures decreased to some extent after the loading process became constant. These constant values are considered as the prestress in this study and shown in Table 2.

Figure 6 shows observed ground deformation of the no reinforcement slope (Case NR) and reinforced slopes (Case 1, 4 and 5) after inclining tests. Broken line in the figures shows slip line observed in the slope. No reinforcement case (Case NR) shows deep deformation with clear slip line. For the case with large prestress and facing plate (Case 4), only shallow and local deformation occurred. While the cases with small prestress and large plate (Case 1) shows deep and large deformation, but no clear slip surface. Furthermore, deep deformation without clear slip surface is also shown in the case with large prestress but small plate (Case 5).

Figure 7 shows the displacement of markers along the needles placed right under the upper side facing plate ($N-1$) and the mid-part of two facing plates ($N-2$). In Case NR, a large displacement occurred near the observed slip line shown

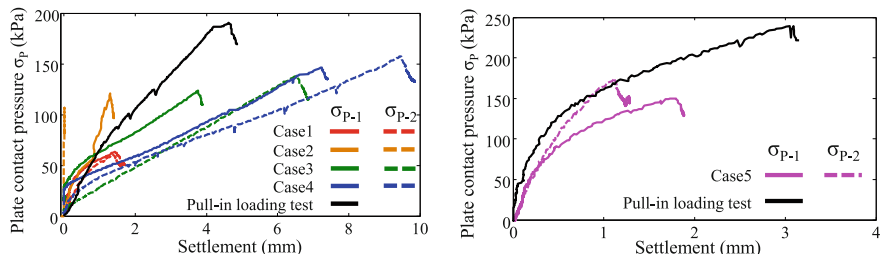


Fig. 5 Relationships between the contact pressure and settlement of facing plate observed in the pull-in loading test and preloading process before the inclination test

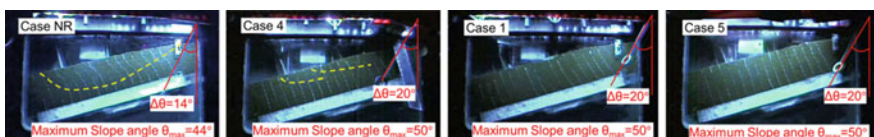


Fig. 6 Observed slope deformation

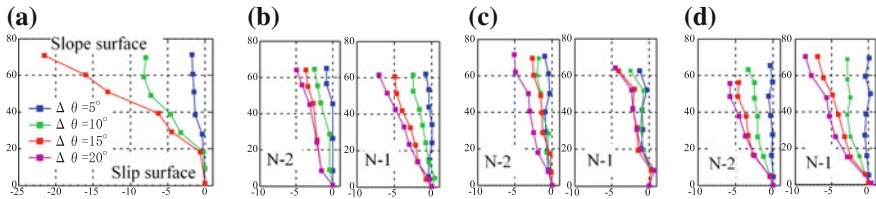
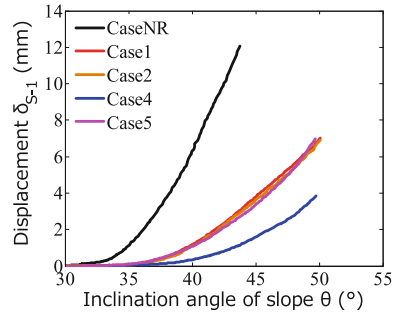


Fig. 7 Observed displacement form marker. **a** Case NR. **b** Case 1. **c** Case 4. **d** Case 5

Fig. 8 $\theta - \delta_{S-1}$ in inclination tests



in Fig. 6 after $\Delta\theta = 5^\circ$. In the reinforced cases, simple shear type deformation was observed and the displacement gradually increases with increase of inclination without showing abrupt increase of displacement. The effect of prestress can be seen especially from the marker right under upper side facing plate ($N-1$). The larger the prestress is, or the larger the facing plate is, the smaller the deformation become.

Figure 8 shows the inclination angle θ and lateral displacement relationships measured at mid-part of two facing plates (δ_{S-1}). From this figure, it can be confirmed that displacement can be greatly reduced by the reinforcement, and the effects of prestress can be seen for the onset of the deformation. The larger the prestress is, the smaller the displacement become. To compare Case 4 and Case 5 (the two cases with same prestress but different facing plate width), it also can be said that lateral displacement in case with large facing plate was much smaller than that in case with small facing plate.

Figure 9 shows the inclination angle θ and lateral displacement δ relationships measured at each location in Case 2, 4 and 5. In the case with small prestress (Case 2) and the case with small facing plate (Case 5), large displacement was measured at each location; while in the case with large facing plate and large prestress (Case 4), the movement of the lower part of the slope was smaller than that of upper part. These differences in the deformation patterns with different prestress and facing plate width are also can be observed in Fig. 7.

$\tan \Delta\theta - \delta$ relationships measured at the mid-part of facing plate are shown on a log-log graph in Fig. 10. $\tan \Delta\theta$ is equivalent to the horizontal seismic intensity

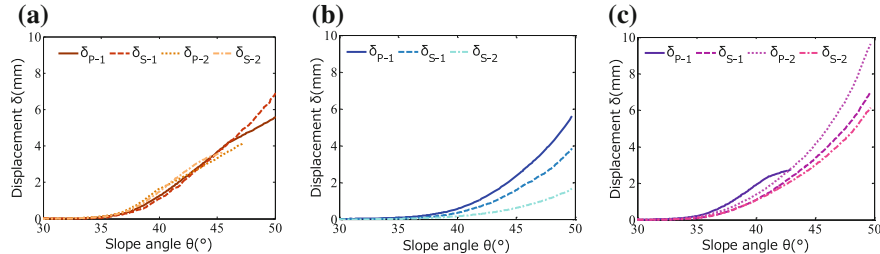


Fig. 9 $\theta - \delta$ in inclination tests. **a** Case 2. **b** Case 4. **c** Case 5

Fig. 10 $\log \Delta - \log(\tan \Delta \theta)$ and defined $\Delta \theta_y$

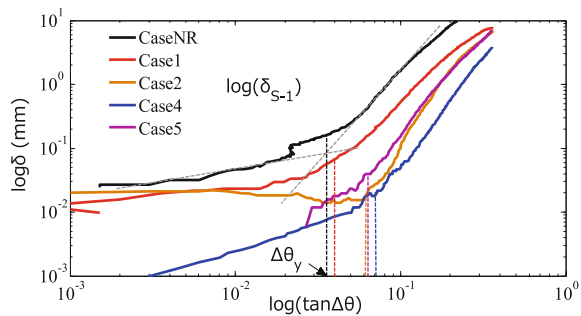
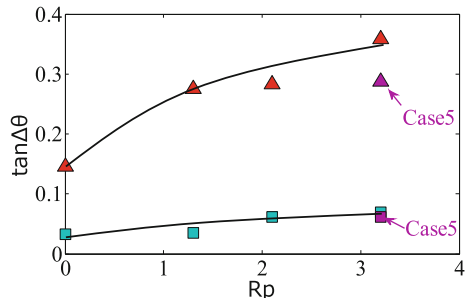


Fig. 11 Effect of the prestress on the movement slope



when the increment of inclining angle is $\Delta\theta$ as shown in Eq. (1). From Fig. 10, a rapid increase of the displacement in the relationship can be obtained at very small δ , which is defined as onset of the deformation and the increment of inclination at this point is denoted by $\Delta\theta_y$. As Fig. 8 shows, no abrupt increase of displacement was observed, 4 mm displacement of slope measured between the plates (δ_{S-1}) is defined as a failure point, and the inclination increment at this point ($\Delta\theta_f$) is employed as an index of the stability of the slope. 4 mm displacement at the surface corresponds to shear strain of 5 % of the slope. Both of $\Delta\theta_y$ and $\Delta\theta_f$ are also shown in Table 2. The $\Delta\theta_f$ and the $\tan \Delta\theta_y$ measured at upper plate and mid-part of facing plate are plotted to R_p in Fig. 11. Some data points are missing because of the fault

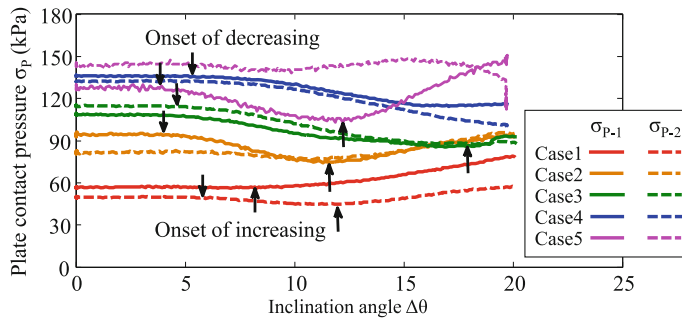


Fig. 12 Variation of facing plate contact pressure by inclination

of measurements. The larger the R_p , that is the larger the prestress, the larger the effects of reinforcement could be obtained. However, the increase of $\tan \Delta\theta$ becomes smaller as R_p increases.

Figure 12 shows the variation of face contact pressure σ_p measured at both the upper and lower facing plates during the inclination test. In the cases with R_p greater than 2.1, the contact pressure started decreasing at some $\Delta\theta$ slightly larger than $\tan \Delta\theta_y$ after and then turned to increase. Because mobile layer was made with relatively low compaction degree, the decrease of facing plate contact pressure is supposed to be due to volumetric shrinkage of the weak soils. After a large displacement occurred at the surrounding areas of facing plate as shown in Fig. 7 (N-1), facing plate contact pressure turned to increase. In the case of $R_p = 1.3$ (Case 1), the upper facing plate contact pressure did not decrease but increased. $\Delta\theta$ values of the onsets of decreasing and increasing of the contact pressure are smaller for the case with increasing R_p (prestress of the facing plate). This variation of facing plate contact pressure could be a reason why the increase of $\tan \Delta\theta_f$ becomes smaller as R_p increases.

4 Summary and Conclusions

In this study, inclination tests were carried out in centrifuge to investigate the effects of prestress and facing plate size of rock bolt with facing plate in slope with weak soils. Following conclusions are reached.

- (1) Reinforcement of slope by rock bolts with facing plate can effectively prevent the deformation and failure.
- (2) The larger the prestress is the better reinforcement effect. However, the effect of the prestress on the stability becomes smaller as the prestress increases. This can be attributed to the variation of face plate contact pressure as the deformation of slope progresses.

(3) The deformation of the slope depends on the prestress and the size of facing plate. It is deeper and wider for the reinforcement with smaller prestress and smaller plate, and shallower limited in local areas for the reinforcement with larger prestress and larger plate.

References

Hayashi S, Ochiai H, Tayama S, Sakai A (1986) Effect of top-plates on mechanism of soil-reinforcement cut-off slope with steel bars. Proc. JSCE 367/VI-3:62–70 (in Japanese)

Inagawa Y, Yamamoto A (2012) Evaluation of slope protection work in reinforced embankment by soil nailing method with regard to stability, Rep Obayashi Corp Techn Res Inst 76 (in Japanese)

Izawa J, Ishihama Y, Kuwano J (2003) Effect of particle size on seismic stability of the reinforced soil wall. Geosynth Eng J 19:183–190 (in Japanese)

Saito K, Katagami N, Ishii T, Tanaka M, Nomoto K, Sugimoto T (1995) Centrifuge model study on the seismic stability of high embankment constructed by volcanic ash. In: Proc. 23th JSCE earthquake engineering symposium, vol 23, pp 615–618 (in Japanese)

Sasahara M, Nakamura H (1997) The effect of facing plate on the reinforcement of rebar nailing. In: Proc. 50th annual conference of Japan association of erosion control engineering, pp 816–817 (in Japanese)

Tei K, Taylor NR, Milligan GWE (1998) Centrifuge model tests of nailed soil slopes. Soils Found 38(2):165–177

Viswanadham BVS, Deepa V (2010) Evaluation of performance of soil-nailed slopes subjected to seepage in a centrifuge. In: Proceedings of the 7th international conference on physical modelling in geotechnics 2010, vol 2, pp 1151–1156

Numerical Simulation of Post-Entrainment Debris Flow at Alluvial Fan Using FLO-2D Model

Zheng Han, Guangqi Chen, Yange Li, Linrong Xu and Fusong Fan

Abstract The FLO-2D model has long been validated as an efficient tool to simulate the motion behavior of debris flow, but could not consider bed-sediment entrainment in the simulation. Bed sediment entrainment is an important feature of debris flow and sometimes amplifies the debris flow magnitude manifold. In this paper, we present a simple preliminary approach to evaluate the potential entrainment and incorporate it into the FLO-2D model. In the presented approach, the bed sediment entrainment is simplified as the process that bed shear stress of the flow is sufficiently high to overcome the basal resistance of the bed and incorporate this part of the bed into the flow. In this way, we obtain a solution to calculate the potential entrainment depth of bed sediment by debris flow. To estimate the total entrainment volume along the path, as well as the variation of hydraulic condition of post-entrainment debris flow, we divide the path into finite segments, calculate the entrainment volume of each segment, and obtain the variation of hydraulic condition by a discrete algorithm. In order to demonstrate this approach, a debris flow event occurred at Yohutagawa region, Japan, 2010, is selected as a case study. We calculate the post-entrainment volume and hydraulic condition of debris flow of this case. Furthermore, we also reproduce this event by the FLO-2D model. Results show that both the calculated total erosion volume and simulated deposition results are in good agreement with the field investigation.

Keywords Debris flow · Bed sediment entrainment · Numerical simulation · FLO-2D model · Yohutagawa

Z. Han (✉) · G. Chen · F. Fan
Kyushu University, Fukuoka 819-0395, Japan
e-mail: zheng.han@aol.jp

Y. Li · L. Xu
Central South University, Changsha 410075, China

1 Introduction

Debris flow is a common phenomenon in mountainous regions worldwide. It is widely accepted that debris flow plays an important role in landscape evolution (Hung et al. 2005; Han et al. 2014a, b). The immense impact by debris flows requires reliable predicting technique using numerical ways. Among the numerical models, FLO-2D is a flood routing model that simulates channel flow, unconfined overland flow, and street flow over complex topography (O'Brien et al. 1993). It is adapted to simulate the debris flow motion behavior in the valley. As a principle, FLO-2D model requires a user-defined outlet of debris flow at the downstream of the channel, and performance well to simulate debris flow spreading extent and deposition process. In other words, it alternatively neglects the bed sediment entrainment along the path when running down the slope. In fact, besides FLO-2D model, some of the numerical model also could not take into account the entrainment simulation. However, several lines of evidences suggest an important role of bed sediment entrainment that debris flows can grow dramatically in magnitude (Berti et al. 1999; Breien et al. 2008). In this sense, simulation results are significantly influenced if entrainment simulation could not be implemented in the model.

At the current stage, entrainment can be predicted in the three major ways. (a) Established empirical laws by in situ surveys, in which measured data can help to form the empirical laws. (b) Empirical laws by the laboratory experiments, manipulated conditions in the experiments make it possible to link the entrainment process with flow dynamics or flow structure (e.g., Farin et al. 2014). (c) Theoretical laws by process-based analysis (e.g., Iverson 2012). However, on the one hand, the commonly used entrainment laws are sometimes empirically or semiempirically based, the elaboration of these laws lacks deep physical understanding of the entrainment processes. For example, RAMMS simulation method (Christen et al. 2010) based on Voellmy-Salm model and KANAKO-2D based on Takahashi's diluent model, only empirical-determined entrainment coefficient or rate is adopted to simulate the erosion process, which more or less causing the simulation results vary and affect the simulation accuracy.

Thus, the limitation of the theoretical research about erosion mechanism restrict not only the hazard magnitude assessment and zone delineation, but also the debris flow model and numerical simulation research.

2 Analysis of the Entrainment Model

Given the established roles of the governing factors, we describe an entrainment model in this section. Previous studies revealed the primary condition for bed entrainment that the bed shear stress of flow is sufficiently high to overcome the basal resistance of bed and incorporate this part of the bed into the flow. In this process, objects including debris flow, erodible bed, and substrate are involved.

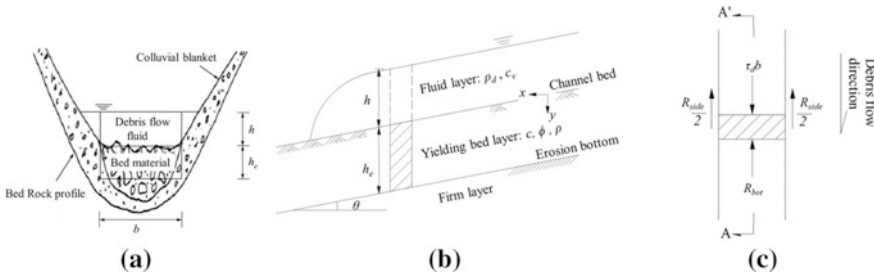


Fig. 1 Schematic illustration of the static model: **a** channel cross section; **b** A–A' cross section; **c**. Top view of the bed layer

Herein, we employ a three-layer model to conduct the static analysis as shown in Fig. 1. Analogous models have been described by Iverson (2012) and Medina et al. (2008), they usually consists of a flow layer with a free top surface, an erodible bed layer with a moveable bottom, and a deeper substrate that cannot be entrained.

The static approach can be described with the soil mechanics concepts. It considers a static equilibrium between the drag forces of debris flow and resistance forces of sides and bottom. This equilibrium reduces to

$$\tau_d b + h_e b \rho g \sin \theta = R_{\text{bot}} + R_{\text{side}} \quad (1)$$

where τ_d denotes the basal shear stress applying by moving mass; ρ is the density of bed sediment; R_{bot} is the basal resistance at the depth of h_e ; R_{side} is the side resistance. We limit our approach to a much simpler relation—the turbulent flow resistance law. It is given by

$$\tau_d = \frac{\rho_d g v_x^2 n_c^2}{h^{1/3}} \quad (2)$$

where ρ_d is the density of debris flow mass, g is the gravity acceleration, v_x is the depth-averaged velocity, n_c is the Manning's roughness coefficient, and h is the flow depth of debris flow. Turbulent flow may be suitable to describe the water or granular mixtures with low solids concentration.

The resistance forces of the bed sediment include the basal resistance and side resistance. Mohr–Coulomb failure criterion can be used since the recent experiment substantiated the frictional behavior near the bed surface. The basal resistance force and side resistance are given by

$$R_{\text{bot}} = \sigma(1 - r_u)b \tan \phi + cb \quad (3)$$

$$R_{\text{side}} = 2 \left(\frac{\rho g h_e^2}{2} \cos \theta + \rho_d g h h_e \cos \theta_c \right) k_0 \tan \phi + 2 c h_e \cos \theta \quad (4)$$

where σ is the bed-normal stress; c is the effective cohesion at potential failure; ϕ is internal friction angle in degree; b is the width of the erodible bed; r_u is the pore pressure ratio. By incorporating Eqs. (2), (3) and (4), Eq. (1) becomes

$$A_1 h_e^2 + A_2 h_e + A_3 = 0 \quad (5a)$$

where:

$$A_1 = \rho g k_0 \cos \theta \tan \phi \quad (5b)$$

$$A_2 = [(1 - r_u) \rho g b + 2 \rho_d g h k_0] \cos \theta \tan \phi + 2c \cos \theta - \rho g b \sin \theta \quad (5c)$$

$$A_3 = (1 - r_u) \rho_d g h b \cos \theta \tan \phi + c b - \tau_d b \quad (5d)$$

The quadratic Eq. (5a) yields a positive solution to the entrainment depth, it is written as,

$$h_e = \frac{-A_2 + \sqrt{A_2^2 - 4A_1 A_3}}{2A_1} \quad (6)$$

Prediction of Eq. (6) can be compared with the entrainment depth of 0.1–5.0 m as commonly measured by the in situ survey. Applicable parameter values were assumed as $\rho_d g = 16.00 \text{ kN m}^{-3}$, $\rho g = 22.00 \text{ kN m}^{-3}$, $h = 2 \text{ m}$, $\theta = 21^\circ$, $c = 3 \text{ kPa}$, $\phi = 26^\circ$, $b = 8 \text{ m}$, and $r_u = 0.5$. The use of these values in Eq. (6) yields an entrainment depth of 0.81 m.

3 Concept of the “Critical Line”

Let us discuss the critical condition of bed sediment entrainment by debris flow. The critical condition mentioned here denotes that the bed sediment is becoming unstable and is about to be eroded by the overriding debris flow. To achieve this condition, the entrainment depth should satisfy the criteria $h_e = 0$. One of the solutions applied if the term A_3 in Eq. (5a) exclusively equates 0. Then Eq. (5d) reduces to

$$(1 - r_u) \rho_d g h_{\text{cri}} \cos \theta \tan \phi + c = \tau_d \quad (7)$$

Rearrangement of this equation shows that the critical condition depends on a certain thickness of the debris flow, if the other parameters are constant.

$$h_{\text{cri}} = \frac{c}{\rho_d g [\sin \theta - (1 - r_u) \cos \theta \tan \phi]} \quad (8)$$

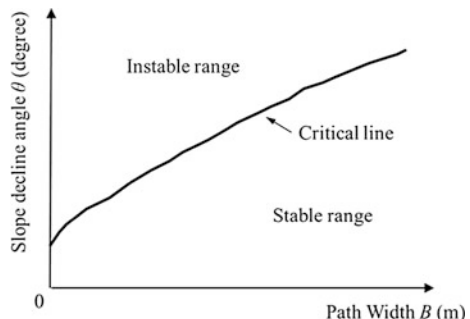
This may be somewhat questionable since the parameters in Eq. (8) varies spatially (e.g., cohesion c and friction angle ϕ) and temporally (e.g., pore pressure ratio r_u). However to continue the analysis, we regard the parameters involved as constant. The meaning of Eq. (8) is that the thickness of the debris flow mass overriding the bed should be greater than the critical value h_{cri} to provoke the basal entrainment.

However, for the hazard prediction, the thickness of the debris flow mass is sometimes difficult to measure directly unless conducting numerical modeling. Therefore, we employ a more intuitive variable—the peak discharge Q —to represent the thickness of debris flow. It is generally accepted that the peak discharge Q is the product of the velocity and the area of cross section where debris flow passes, it obeys,

$$Q_{\text{cri}} = \frac{b}{n_c} h_{\text{cri}}^{5/3} \sin^{1/2}(\theta) = g(b, \theta) \quad (9)$$

Parameters (θ, b) are defined as microtopographic variables. The occurrence of entrainment applies when the discharge Q of the event is greater than Q_{cri} . Equation (9) can be plotted in Fig. 2. Up-to-date studies have provided available approach to estimate the discharge Q of a debris flow event. It is worth mentioning the work done by Rickenmann (1999), who provided a detailed insight into this parameter and summarized equations to predict the peak discharge, in which $Q = aM^b$, and a and b are the coefficients depending on the type of debris flow and geometry of the temporary reservoir, as illustrated in Rickenmann (1999); M denotes the debris flow volume (m^3). In this way, the critical condition of the bed sediment can be represented by this discharge criterion.

Fig. 2 Illustration of the concept of the critical line



4 Debris Flow Peak Discharge Amplification Due to Erosion

Discretized analysis is used here for illustrating the peak discharge enlarging process inducing by erosion. That is to say, as shown in Fig. 3, for each discretized reach segment i during a certain time interval Δt_i , total cumulative duration of debris flow is,

$$T_i = T_0 + \sum_{i=1}^i \Delta t_i \quad (10)$$

where T_0 is initiation time for transition from source landslide to debris flow (s), Δt_i is the time interval (s) and can be expressed as $\Delta t_i = \Delta L/v_{mi}$, where ΔL_i is the path distance of the discretized channel segment (m), v_{mi} is the mean velocity of debris flow in the segment i (m/s). When flowing over the discretized channel segment i , outflow volume V_i of debris flow in this segment is consisted of inflow volume V_{i-1} , rainfall runoff gathering $Q_w\Delta t_i$, and total erosion volume ΔV_i .

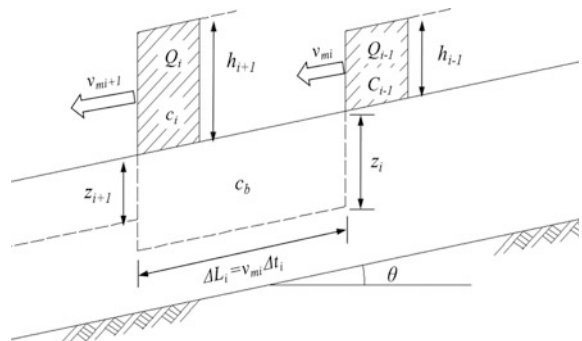
$$V_i = V_0 + \sum_{i=1}^i (\Delta V_i + Q_w\Delta t_i) \quad (11)$$

Thus because the supplement inducing by erosion process, for the outflow debris flow peak discharge of this segment Q_i and volume concentration c_i are varying,

$$Q_i = \frac{V_0 + \sum_{i=1}^i (z_i B v_{mi} \Delta t_i + Q_w \Delta t_i)}{T_0 + \sum_{i=1}^i \Delta t_i} \quad (12)$$

$$c_i = \frac{Q_{i-1} T_{i-1} c_{i-1} + c_b z_i B \Delta L_i}{Q_{i-1} T_{i-1} + z_i B \Delta L_i + Q_w \Delta t_i} \quad (13)$$

Fig. 3 Debris flow developing process between two discretized channel segments



Then for the next channel segment, calculated Q_i and c_i are inputted in Eqs. (12)–(13), volume concentration, and erosion depth z_{i+1} can be solved. By this iteration procedure, peak discharge and volume concentration of each discretized channel segment can be obtained until to the node where erosion process ends. Since no erosion and entrainment are proceeding, debris flow behaves as viscous regime fluid, it can be described by FLO-2D rheological model and same model based commercial software FLO-2D is used to simulate deposition process.

5 Case Study

5.1 *Introduction of the Yohutagawa Terrain, Japan*

The Yohutagawa torrent (28°24' N, 129°32' E) is located in Amami Oshima Island, southwest Japan. The torrent has a catchment area of 0.24 km² and elevation varying from 20 to 250 m. From a geological point of view, the massif consists of sandstone and mudstone, mainly composed of fragmented plates and flakes packed in the clayey matrix. The bedrock on most slopes is covered with amount of colluvium deposits, which is typically a few meters thick. Large parts of the catchment were covered with forest before debris flow occurred. The incised channel has an average slope of about 16°, range from 33° in the higher part to 10° on the alluvial fan. The total length of the channel is approximately 750 m.

The selected event was triggered on October 20, 2010, by intense rainfall accompanying by Typhoon Megi. The intense rainfall had a maximum intensity of 131 mm h⁻¹, and an accumulated intensity of 601 mm. It provoked a failure of the colluvium deposits in the highest part of the massif, with a volume of 5843 m³. Field observations and subsequent interpretation of aerial photographs indicate that the initially failed mass was rapidly transformed into a debris flow. Being overridden by the debris flow, the entire superficial deposits along the trajectory PA-PB, was impacted, eroded, and then incorporated into the flow. A total volume of 8697 m³ was estimated in the elongated deposition region, from which we speculate that the volume of entrained bed sediment was 2854 m³. The heavy deposits at the alluvial fan caused two building damages, but luckily without death.

5.2 *Critical Line and Entrainment Estimation*

The digital contours data of the Yohutagawa terrain with 5.0 m interval provided by Geospatial Information Authority of Japan, was interpolated to 2.5 m resolution and then compiled to DEM data in the ArcGIS 9.0 environment as shown in Fig. 4. We divided the primary trajectory into 17 segments with the length of 10–20 m (shown in Fig. 5), and extracted the slope and channel width of each individual

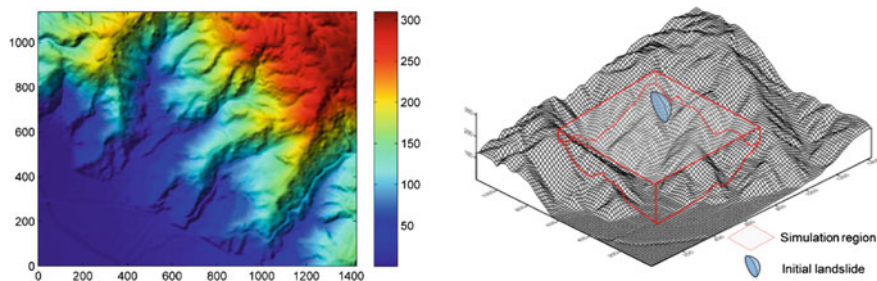


Fig. 4 Topography of the Yohutagawa terrain and DEM data generation

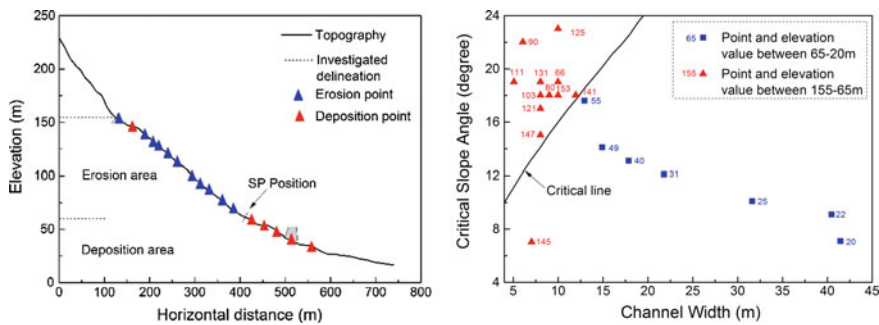


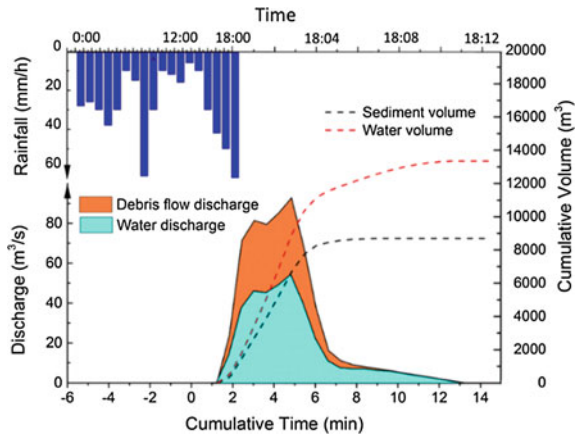
Fig. 5 Delineation of the entrainment reaches using the “critical line”

Table 1 Parameters used for the analysis (notations are explained in the main text)

| Debris flow initiation condition | | Bed material property | |
|----------------------------------|--------|---------------------------------|-------|
| Parameter | Value | Parameter | Value |
| γ_d (KN/m ³) | 17.3 | γ (kN/m ³) | 23 |
| γ_w (KN/m ³) | 10 | γ_s (kN/m ³) | 26.5 |
| c_0 | 0.44 | c_b | 0.79 |
| Q_0 (m ³ /s) | 79.71 | c (kPa) | 12 |
| V_0 (m ³) | 13,280 | ϕ (°) | 28 |
| V_{s_0} (m ³) | 5843 | n | 0.25 |
| T_0 (s) | 167 | | |
| Q_w (m ³ /s) | 45.35 | | |

reach using the ArcGIS environment. The value of input parameters used in the model is listed in Table 1. Given the conditions above, the critical line can be plotted applying values of the input parameters to Eq. (9). As shown in the right column of Fig. 5, the black line is the critical line of the 2010 event, it denotes the critical peak discharge to provoke the entrainment. The extracted topographic data b and θ locate each individual segment in the graph. As anticipated, the entrainment

Fig. 6 Hydraulic condition of the 2010 debris flow after entrainment as calculated by the proposed approach



and nonentrainment segments are delineated by the critical line and critical line. It is clearly indicated that entrainment occurred only on the higher slope beyond the elevation of 55 m. Evidence revealed by the in situ survey after the debris flow event also support this delineation.

In addition, Eqs. (11)–(13) are used to estimate the variation of the hydraulic condition of the 2010 debris flow. The total entrained volume was computed as 2861.5 m^3 . This value is consistent with the investigated value 2854 m^3 after the event. Due to the erosion and entrainment of bed material, peak discharge Q of debris flow increases from 79.71 to $92.25 \text{ m}^3 \text{ s}^{-1}$, while volume concentration c_i decreases from 0.44 to 0.414 due to the run-off gathering by heavy rainfall, as shown in Fig. 6.

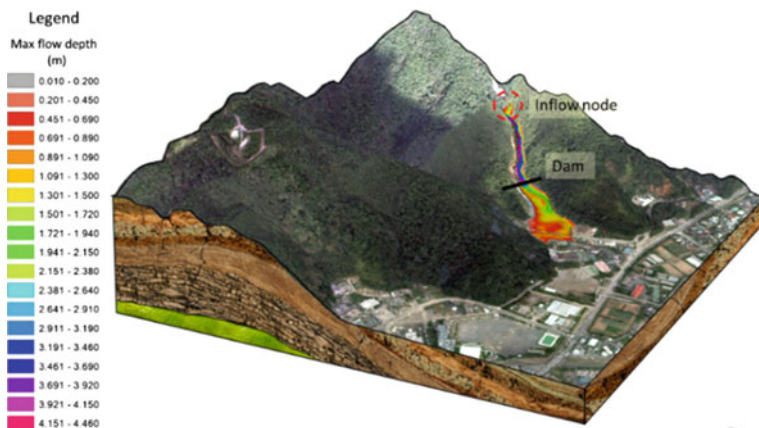
5.3 Deposition Simulation Using FLO-2D Model

To simulate Yohutagawa debris flow and delineate the hazard zone, the DEM of Yohutagawa watershed with a resolution of $2.5 \times 2.5 \text{ m}$ and aerial photos with resolution of $0.5 \times 0.5 \text{ m}$ are imported into the commercial numerical simulation software, FLO-2D. Node at the path of debris flow with the elevation of 55 m where erosion process ends is selected as the inflow element with the hydrograph condition as shown in Fig. 6. However, due to the lack of the data of rheological parameters, exponent equations proposed by O'Brien et al. (1993) were used to estimate the yield stress and viscosity in FLO-2D rheological model. Referring to FLO-2D User's Manual coefficient α_1 , α_2 and exponent β_1 , β_2 , as well as resistance parameter for laminar flow K are listed in Table 2.

Proceeding with debris flow simulation as shown in Fig. 6, the deposition process is simulated. Based on these results shown in Fig. 7, the potential debris flow hazard zone and hazard magnitude can be delineated and identified. Comparing with aerial photos taken at post-hazard event, it can be seen that

Table 2 Rheological parameters used in FLO-2D simulation

| Rheological parameter | Initial value | | |
|--|---------------|--------|----------|
| Bingham yield stress τ_y (Pa) | α_1 | 1202.0 | 0.0811 |
| | β_2 | | 13.72 |
| Bingham dynamic viscosity η (Pa s) | α_1 | 1.21 | 0.000462 |
| | β_2 | | 11.24 |
| Specific gravity of debris flow γ_s (t/m ³) | | 2.65 | |
| Resistance parameter for laminar flow K | | 2285 | |

**Fig. 7** Numerical simulation process by FLO-2D with the given data (maximum flow depth obtained from numerical simulation within FLO-2D)

simulated contour of deposition matches well with field investigation result. The simulated deposition run-out volume is 7869.08 m³ of grain–water mixture including 3147.63 m³ of sediment, which indicates the error between simulation and investigation is 2.27 % considering 3069 m³ sediment in deposition as investigated. Both simulated run-out distance and flow depth are in good agreement with observation. However, simulated inundated area is as large as 13,783 m², compared with observation result 11,644 m², error may count to 15.5 %. One possible explanation may turn to the lack of accurately measured rheological parameters, which affects the flowing behavior simulated in FLO-2D.

6 Conclusions and Discussion

Bed sediment entrainment by debris flow is important for the debris flow simulation work, but it is sometimes neglected by the current models, including FLO-2D model. We presented an elementary approach to estimate the entrainment of the bed

sediment by a debris flow, and incorporated the approach to the FLO-2D model to implement the bed sediment entrainment. The approach is based on a static equilibrium model of the bed sediment when overridden by debris flow. Analyzing the critical condition of the equilibrium model, we subsequently propose a new concept of “Critical line” to delineate the erodible reaches of the whole channel. The approach was further incorporated into the FLO-2D model, and deposition of the post-entrainment debris flow can be simulated. The 2010 Yohutagawa debris flow event was chosen as the case study. Results shown that the simulated debris flow spreading extent and deposited depth well reproduced the event. With these verifications, it is believed that the described methodology represents a rational approach to consider the bed sediment entrainment and can be incorporated into FLO-2D model.

References

Berti M, Genevois R, Simoni A, Tecca PR (1999) Field observations of a debris flow event in the dolomites. *Geomorphology* 29:265–274

Breien H, Fabio D et al (2008) Erosion and morphology of a debris flow caused by a glacial lake outburst flood, Western Norway. *Landslides* 5:271–280

Christen M, Kowalski J, Bartelt P (2010) RAMMS: numerical simulation of dense snow avalanches in three-dimensional terrain. *Cold Reg Sci Technol* 63:1–14

Farin M, Mangeney A, Roche O (2014) Fundamental changes of granular flow dynamics, deposition, and erosion processes at high slope angles: Insights from laboratory experiments. *J Geophys Res Earth Surf* 119:504–532. doi:[10.1002/2013JF002750](https://doi.org/10.1002/2013JF002750)

Han Z, Chen G, Li Y, He Y, Zhang H (2014a) Elementary analysis on the bed-sediment entrainment by debris flow and its application using the TopFlowDF model. *Geomat Nat Hazards Risk*, in press. doi:[10.1080/19475705.2014.966868](https://doi.org/10.1080/19475705.2014.966868)

Han Z, Chen G, Li Y, Xu L, Zheng L, Zhang Y (2014b) A new approach for analyzing the velocity distribution of debris flows at typical cross-sections. *Nat Hazards* 74(3):2053–2070

Hungr O, Dougall S et al (2005) Entrainment of material by debris flow, debris-flow Hazards and related phenomena. Springer, Berlin, Heidelberg, pp 136–137

Iverson RM (2012) Elementary theory of bed-sediment entrainment by debris flows and avalanches. *J Geophys Res* 117

Medina V, Hurlimann M, Bateman A (2008) Application of FLATModel, a 2D finite volume code, to debris flows in the northeastern part of the Iberian Peninsula. *Landslides* 5:127–142

O’Brien JS, Julien PY, Fullerton WT (1993) Two-dimensional water flood and mudflow simulation. *J Hydraul Eng ASCE* 119(2):244–261

Rickenmann D (1999) Empirical relationships for debris flows. *Nat Hazards* 19:47–77

Photomicrograph Investigation of Rock Thin Sections Taken from Landslides Scree by the Eastern Honshu Earthquake, 2008

Tsuneo Ohsumi

Abstract An earthquake with a magnitude of 7.2 occurred on June 14, 2008. Housing damage due to this earthquake was quite light. On the other hand, heavy damage was sustained due to landslides. It was pointed out that large-scale landslides occurred around the Aratozawa area which lies to south of the Kurikoma mountain caldera. Since the first activity of Kurikoma volcano 50,000 years ago, the volcanic ash has been spread widely throughout the western area from the volcano. In this article, the scale of the caldera is compared to that of the landslides. At Aratozawa landslide point, the estimated ground acceleration was approximately 3G. Thus, large acceleration caused landslides in this area. Seismic waveform at the Aratozawa landslide was estimated based on empirical site amplification and phase effects. Site amplification characteristics at the Aratozawa landslide were evaluated based on the aftershock observation records. Moreover, a characterized source model for strong ground motion prediction was constructed based on the results of waveform inversion for this earthquake. A sample of mudstone from Aratozawa point consisted of lamination, and sand mud alternating strata. Diatoms can be seen clearly in the mudstone taken from Aratozawa Point. Thus, this proves that sediments from the caldera period accumulated on the large-scale pyroclastic flow sediments which filled the caldera. Based on the photomicrograph investigations, factors for each scale of collapse pattern and rock materials are investigated. Aratozawa landslide was lateral spread and attributed to the fact that many landslides were translational slides of the bedding plane slide type, and a slippery stratum were caused by the earthquake. The upper part of the gliding slope of the Aratozawa Point consists of high density welded tuff due to gravity. This is evidence that water above the present ground water level used to exist. On the other hand, below the high density sediments low density pumice exists causing instability.

Keywords Eastern Honshu earthquake • Landslides • Photomicrograph • Rock thin section • Plane-polarized • Crossed-polarized

T. Ohsumi (✉)

Disaster Risk Research Unit, National Research Institute for Earth Science and Disaster Resilience, 3-1 Tennodai, Tsukuba, Ibaraki 303-0006, Japan
e-mail: t_ohsumi@bosai.go.jp

1 Introduction

An earthquake with a magnitude of 7.2 occurred on June 14, 2008. As a member of the Emergency Survey joint team of the Japan Society of Civil Engineers, the Japanese Geotechnical Society, the Japan Association for Earthquake Engineering and the Japan Landslide Society, the author investigated into the damaged area mainly in Iwaigawa, Ichihazamagawa, and Aratozawa from June 15 the day after the earthquake happened. The joint survey team prepared reports from each society and they are submerged in Nakamura (2008) and Miyagi (2008). Focusing on slope failure that caused extensive damage, this paper observed the collapse phenomenon from various viewpoints. Housing damage due to this earthquake was quite light. On the other hand, heavy damage was sustained due to landslides. There was a strong possibility that the landslide dams left over had been able to cause debris flow. Since the first activity of Kurikoma volcano 50,000 years ago, volcanic ash has been widely spread throughout this area. It was pointed out that large-scale landslides occurred around the Aratozawa area which lies to the south of the Kurikoma mountain caldera. In this study, in order to investigate the lake data was taken from geotechnical viewpoints. In addition, typical rock samples were obtained from small, middle, and large-scale landslides.

2 Characteristics of This Earthquake

The characteristic of this earthquake were: housing was lightly damage, on the other hand, landslide was heavily damage. The characteristics of the ground motion were calculated by waveforms and response spectrum estimated by empirical Green's function at Aratozawa.

2.1 *Characteristics of the Ground Motion*

For the characteristics of the ground motion, as the yield of housing damage was very slight (Fig. 1). Although, Landslides were enormous. According to Goto (2008), Fig. 2 shows the pseudovelocility response spectra ($h = 0.05$) of these components. Goto (2008) was also shown for comparison to the three K-NET and KiK-net records, which were IWATE25 (Ichinoseki-nishi), IWATE 26 (Ichinoseki-higashi) and MYG005 (Naruko), during the 1995 Hyogoken-Nambu (Kobe) earthquake and 2004 Niigata Chuetsu-Oki earthquake in the severely damaged areas. Generally, a peak is located in the record of an earthquake in periods less than 0.5 s, whereas a severe earthquake has the peak value in periods 1–2 s. Hayashi and Mori (2008) compared of earthquake records to wooden housing damage. This case also features experienced such past results as the housing damage.



Fig. 1 Comparison of the lightly damaged house, which was built in 1980, Iwate–Miyagi inland earthquake, 2008 (M_j 7.2), Ishinomaki, Miyagi prefecture (left photo taken in 15 June, 2008) and the collapsed house in Niigata Chuetsu-Oki earthquake, 2004 (M_j 6.8), Kawaguchi, Niigata, prefecture, (right photo taken in Oct., 2004)

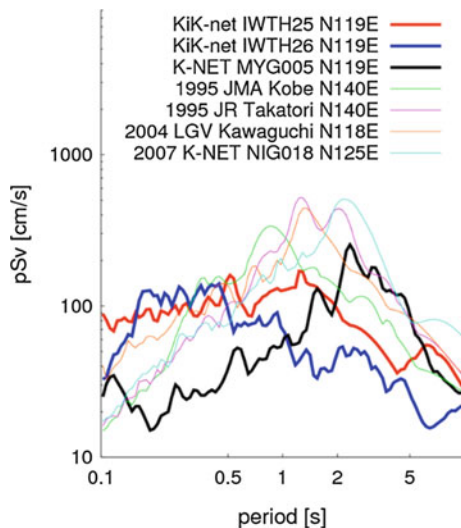


Fig. 2 The pseudo velocity response spectra ($h = 0.05$) of these components. Goto (2008)

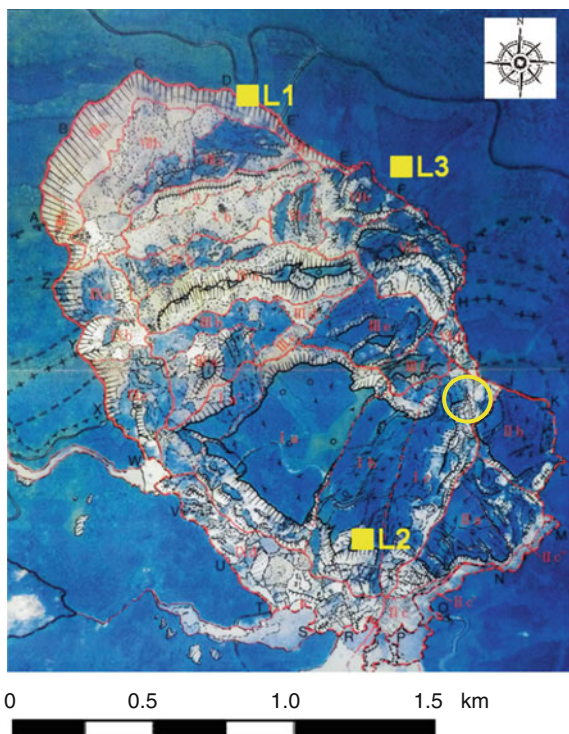
2.2 Estimated Earthquake Ground Motions at Aratozawa

Extremely high accelerations were recorded at the KiK-net IWTH25. The peak acceleration in the vertical component of the surface record was about 4G. Hata et al. (2010) was estimated based on empirical site amplification and phase effects by seismic waveform at the Aratozawa landslide. Site amplification characteristics at the Aratozawa landslide were evaluated based on the aftershock observation records. Moreover, a characterized source model for strong ground motion prediction was constructed based on the results of waveform inversion for this earthquake. In this study, two sites (L1, L2: Fig. 3) were observed using the

Fig. 3 Bird's-eye view of the Aratozawa landslide and survey points (Photo taken by Kamae)

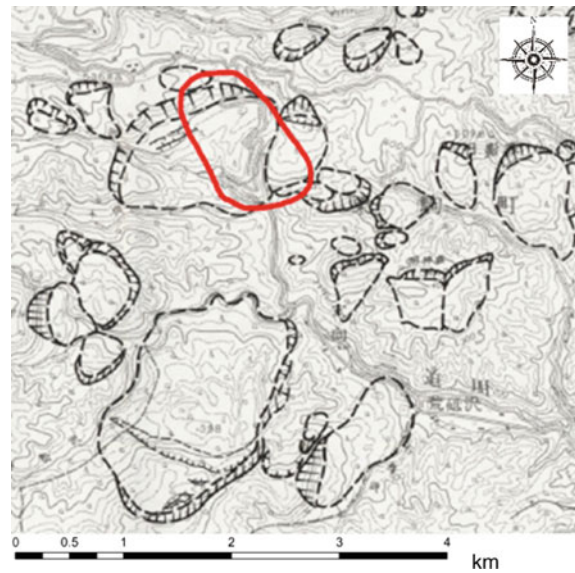


Fig. 4 Aerial photo interpretation (after Ohyagi, N, Photo taken at 16 June, 2008). Yellow squares are seismograph setting points. Yellow circle is rock thin section sampling point



aftershock records. According to Ohyagi's aerial photo interpretation (Fig. 4), L1 was the point of extended collapse after a few days from the landslide and L3 was the point of unmoved area. Inoguchi et al. (2010) showed landslide map of Kurikoma mountain and source area of the Aratosawa landslid (Fig. 5). In this map, the red line is the landslide area, some of the other landslides also occurred on landslide landform features and L3 point is out of the landform feature area.

Fig. 5 Landslide map of Mt. Kurikoma and source area of the Aratosawa landslide



As a result, the maximum horizontal acceleration was estimated L1 at 841 Gal and L3 at 2931 Gal during the main shock at the Aratozawa survey points (Fig. 6). The comparison of the acceleration spectrum shown in Fig. 7. Reasons for the estimated large ground motion at the L-3 point: the effect of differences in the surface layers thickness of shallower engineering basement, the effect of the seismic characteristic of the gliding slopes and Influence by the topography effect, etc.

At L3, the estimated ground acceleration was approximately 3G, which is dominant period was 0.16 s. The Great Wenchuan earthquake's dominant frequency was 4 Hz (Zifa 2008). The Chi-Chi earthquake's dominant frequency was 4 Hz (Chen and Yanxiang 2007). Dominant frequency around 5 Hz might be a relationship with landslides.

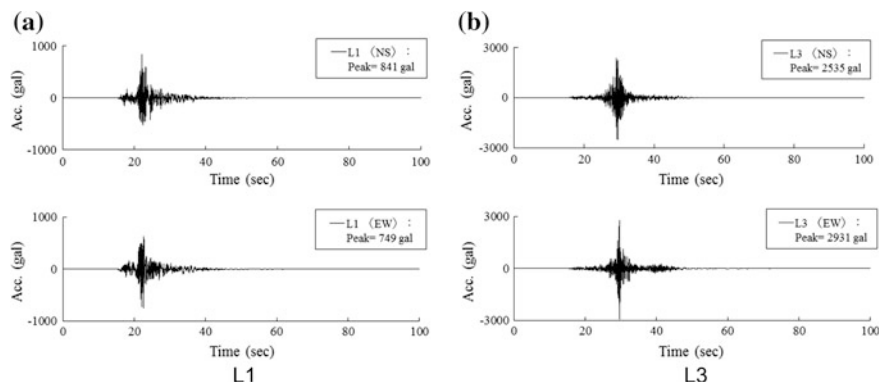
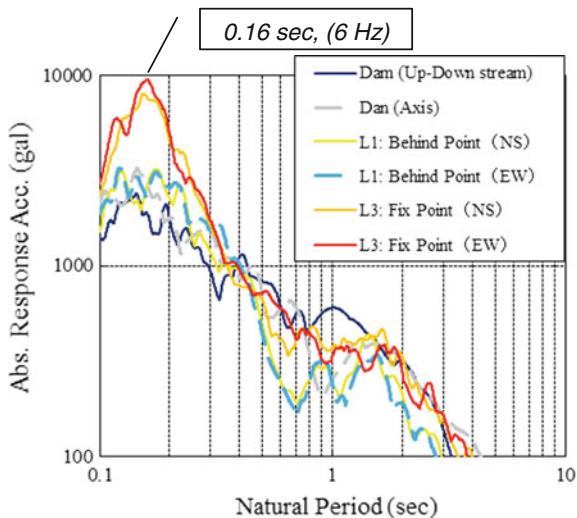


Fig. 6 The estimation of the acceleration waveform at the Aratosawa landslide during the main shock

Fig. 7 The comparison of the acceleration response spectrum



3 Large-Scale Collapse: Aratozaw Dam Site

The large-scale collapse at Aratozaw dam site lies to the south of the Kurikoma mountain caldera. Since the first activity of Kurikoma volcano 50,000 years ago, the volcanic ash has been spread widely throughout the western area from the volcano. In this article, the scale of the caldera is compared to that of the landslides. The collapsed area estimates the quantity of sediment. Sediments from the caldera period accumulated on the large-scale pyroclastic flow sediments which filled the caldera. Based on the photomicrograph investigations, rock materials are investigated.

3.1 Characteristics of the Aratozawa Landslide

Since the first activity of Kurikoma volcano 50,000 years ago, the volcanic ash has been spread widely throughout the western area of the volcano. Large-scale collapse occurred at the Aratozawa dam. The first activity of Kurikoma volcano 50,000 years ago, the volcanic ash had been spread widely to the western area from the volcano. Large-scale collapse occurred at the Aratozawa dam, in the upper stream part which is located in Kurihara, Miyagi Prefecture. In the collapsed area was estimated of the quantity of sediment to be 1.2 km long and 0.9 km wide, and a maximum thickness was over 50 meters with $70,000,000 \text{ m}^3$. The pumice moved and it continuously filled up the four or five mass movements caused from the quake (Fig. 8).

The collapsed gliding slopes were mainly white pumice tuff, others were grain tuff and welded tuff. These were regarded as pyroclastic flow sediment. The

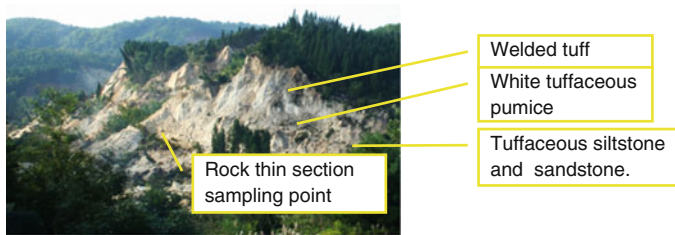


Fig. 8 Full view of the Aratozawa landslide and rock section sampling point (*Photo* taken at 10 Sep., 2008)

landslide topography existed in this area before this earthquake occurred. The collapse was in the upper part of the welded tuff. In the middle part of alternation of strata were white tuffaceous pumice. In the bottom of the laminated retainer consisted of tuffaceous siltstone and tuffaceous sandstone. The upper part of the welded tuff used to be water level surface. The welded tuff was created by the deadweight of a high density layer. The region that collapsed was formed in strata of about 5 million years ago, called Ono Matsuzawa layer. This layer is composed of pumice tuff substantially horizontal primarily.

According to Nunohara et al. (1999), Yoshida et al. (1999), the large-scale landslide which occurred in the Aratozawa Dam upper stream part is located near the caldera rim of the Kurikoma Mts. south crest caldera (Fig. 9). In this Figure, the Aratozawa landslides is a small 1/20 part of the caldera of about 15 km width. Moreover, the minor scale landslides also occurred inside the caldera. The lacustrine deposit of the late caldera phases appears on the large-scale pyroclastic flow sediment which fills up the inside of the caldera. By this large-scale collapse, it is observed in the higher rank of the massive pumice tuff, which has a thickness more than 50 m and is covered by the 60-m-thick welded tuff of dacite.

The upper part of the gliding slope is consists of high density welded tuff due to gravity. On the other hand, below the high density sediments low density pumice exists causing instability.

3.2 Photomicrograph Investigation of Rock Thin Sections

Typical rock samples were obtained from small, middle, and large-scale landslide. Based on the photomicrograph investigations, factors for each scale of collapse pattern and rock materials are verified. A piece of the mudstone at the Aratozawa point (Fig. 8) consisted of lamination and sand-mud alternating strata. Alternating strata of sand and mud are also distributed which are useusuallyfound at the bottom of the lakes. This sedimentation is thought to be from the Quaternary Period. A piece of sandstone at the same point consisted of quartz, pumice, volcanic fragments, feldspar, pyroxene, and diatom (Fig. 10). Diatoms can be clearly seen in the

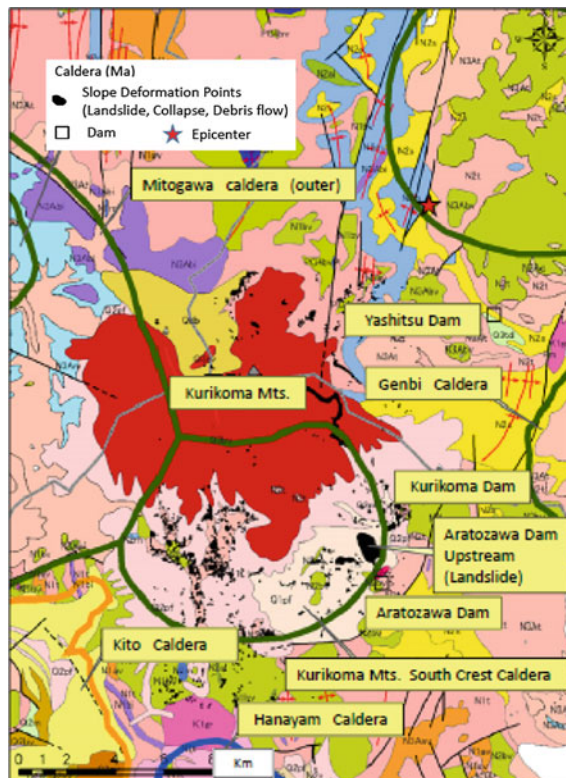


Fig. 9 The GIS database suggested that the caldera structure is closely related to the distribution of the large-scale landslides

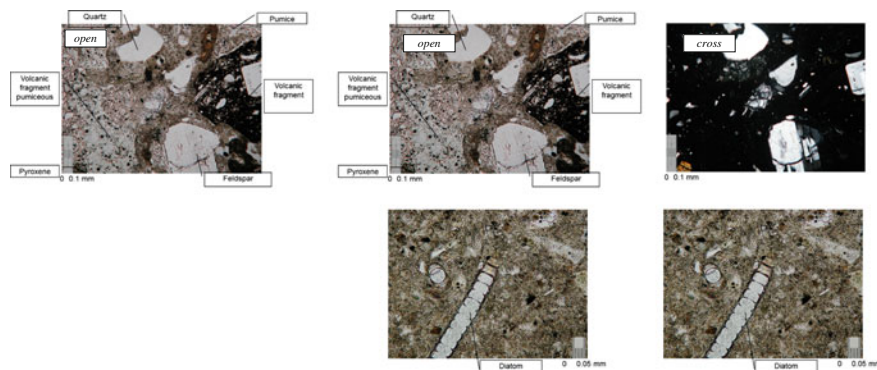


Fig. 10 Photomicrography of rock thin sections from Aratozawa landslide point

mudstone at the Aratozawa landslide point. Thus, this proves that sediments from the caldera period accumulated on the large scale pyroclastic flow sediments, which filled the caldera.

4 Characteristic of This Earthquake Summary and Conclusions

1. At Aratozawa landslide point, the estimated ground acceleration was approximately 3G. Thus, large acceleration caused landslides in this area. Since the first activity of Kurikoma volcano 50,000 years ago, the volcanic ash has been spread widely throughout the western area from the volcano.
2. A sample of mudstone from the Aratozawa point consisted of lamination, and sand mud alternating strata. This shows evidence that it is very similar and probably from the alternating strata of sand and mud that were distributed at the bottom of a lake in the past. This sedimentation is thought to be from the Quaternary Period. Diatoms can be seen clearly in the mudstone at Aratozawa Point. Thus, this proves that sediments from the caldera period accumulated on the large-scale pyroclastic flow sediments which filled the caldera.
3. During the volcanic activity period the pyroclastic flow widely covered the surface due to the fact that the gliding slope was not very steep as section Fig. 11 A-A' solid line. The extensive area of gentle slope caused a wide collapse as section Fig. 11 B-B' broken line. The landslide slope was found by boring exploration by MAFF (2008).
4. Aratozawa landslide was lateral spread and attributed to the fact that many landslides were translational slides of the bedding plane slide type, and a slippery stratum were caused by the earthquake.

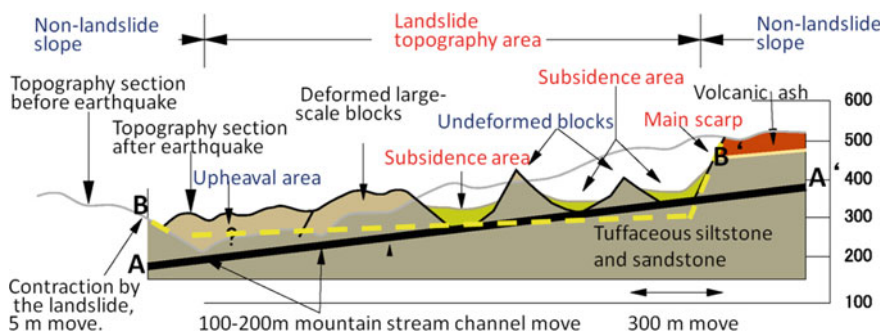


Fig. 11 Aratozawa landslide cross section (Modified from JGS; Miyagi 2008). JGS defined very steep as section A-A'. MAFF defined widely collapse as section B-B' from the boring exploration

5. The upper part of the gliding slope of the Aratozawa Point consists of high density welded tuff due to gravity. This is evidence that water above the present ground water level used to exist. On the other hand, below the high density sediments low density pumice exists causing instability.

Acknowledgments This research of photomicrograph investigation for rock thin sections was supported by Prof. Yujiro Ogawa with Tsukuba University. I also thank Dr. Norio Ohyagi from the Fukada Geological Institute who provided valuable geological information from the Aratozawa landslide.

References

Chen Y, Yanxiang Y (2007) Characteristics of response spectra for long-periods of main-shock recordings of the Chi-Chi earthquake. *Earthq Eng Eng Vibr* 6(2):111–121

Forestry Agency Tohoku Forest Management Bureau, Ministry of Agriculture (2008) Forestry and fisheries (MAFF), mountains disaster study measures handouts of the 2008 Iwate-Miyagi Nairiku earthquake (in Japanese)

Goto H (2008) A summary of an earthquake/earthquake ground motions in the 2008 Iwate-Miyagi Nairiku earthquake (in Japanese)

Hata Y, Ohsumi T, Nozu A, Kamai T (2010) Evaluation of the strong motion at the Aratozawa site induced by the 2008 Iwate-Miyagi Nairiku earthquake based on empirical site amplification and phase effects. *Jpn Landslide Soc* 47(5):247–254. ISSN:1348-3986 (in Japanese with English abstract)

Hayashi Y, Morii Y (2008) The 2008 Iwate-Miyagi Nairiku earthquake (in Japanese)

Inoguchi T, Oyagi N, Uchiyama S, Snimizu F (2010) Topographical and geological features of landslide disasters caused by the 2008 Iwate-Miyagi Nairiku earthquake. *Nat Disaster Res Rep Nat Res Inst Earth Sci Disaster Prev* 43 (in Japanese with English abstract)

Miyagi T (2008) Flash report of the 2008 Iwate-Miyagi Nairiku earthquake. *Jpn Geotech Soc* (in Japanese)

Nakamura S (2008) Flash report of the 2008 Iwate-Miyagi Nairiku earthquake, emergency survey on joint team of the Japanese geotechnical society, the Japan association for earthquake engineering and the Japan landslide society. *JSCE Mag* 93(8):42–45 (in Japanese)

Nunohara K, Yoshida T, Yamada R (1999) Relationship between earthquake disasters and caldera structures using of GIS. *Geol Soc Jpn* (in Japanese with English abstract), <http://www.geosociety.jp/hazard/content0035.html>

Yoshida T, Nagahashi Y, Oguchi T, Ohira H, Aizawa K, Sato H et al (1999) Geohistory of the active periods of volcanoes and the formation of late Neogene calderas in northeastern Honshu *Arc. Chikyu Monthly Extra* 27:123–129 (in Japanese)

Zifa W (2008) A preliminary report on the Great Wenchuan earthquake. *Earthq Eng Eng Vib* (2008) 7:225–234. doi:[10.1007/s11803-008-0856-1](https://doi.org/10.1007/s11803-008-0856-1)

An Extension to Weiler–Atherton Clipping Algorithm for the Face-to-Face Contact in Three-Dimensional Discrete Element Method

H. Zhang, G. Chen, S.G. Liu, P.D. Jing and Z. Han

Abstract This paper proposes a comprehensive method to resolve the problem existing in three-dimensional (3D) general discrete element method (GDEM) that is detecting contact area between any two general 3D polyhedral blocks. The presented method even supports generations of more than one contact area between two approaching faces. Avoidance of transfer of global coordinates to local ones and vice versa make the new method more efficient and applicable in 3D GDEM.

Keywords Contact detection · Contact area · Polyhedral block · Discrete element method · Weiler–Atherton

1 Introduction

Numerical approaches capable of computing contacts between individual discrete elements mainly involve the explicit scheme distinct element method (DEM) introduced by Cundall and Strack (1979), Cundall (1988) and Hart et al. (1988), and the implicit scheme discontinuous deformation analysis (DDA) developed by Shi and Goodman (1985, 1989) and Shi (1988, 2001), which mainly consist of the family of general discrete element method (GDEM).

In the available method of 3D DEM, the calculation of mutual area of face-to-face contact is a straightforward but lengthy procedure that only available for two convex polygons comprising the contact (Liu and Lemos 2001). As a result, the mutual area of the contact is also a convex, simply connected polygon, as is illustrated in Fig. 1a. Although Keneti et al. (2008) make some improvements to Liu and Lemos method to confirm proceeding order in the case of vertex-to-vertex

H. Zhang (✉) · G. Chen · P.D. Jing · Z. Han
Kyushu University, Fukuoka 819-0395, Japan
e-mail: wudizh@gmail.com

H. Zhang · S.G. Liu
Tongji University, Shanghai 200092, China

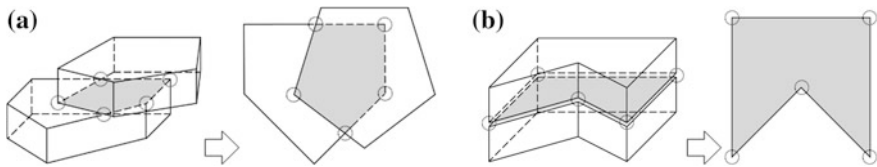


Fig. 1 Comparison of mutual area in original 3D DEM and 3D DDA. **a** 3D DEM, **b** 3D DDA

and vertex-to-edge, the modified method still does not work well for concave polygons.

In comparison, 3D discontinuous deformation analysis (DDA) allows blocks to be arbitrarily shaped, through introducing a delicate method, *simplex integration*, developed by Shi (1988, 2001) for oriented volume integration on a block (Wu 2010), as well as geometric analyses for contact detection between two blocks in shapes of arbitrary polyhedrons. However, the original 3D DDA identify face-to-face contacts through marking “pair polygons” bisected by joint polygon in the preprocessing cutting algorithm developed by Shi (2006), rather than calculating in main program. The facets of the blocks can be cut into the shape of arbitrary polygons, no matter convex or concave, but necessarily geometrically symmetric with respect to the joint polygon and locate all their pair vertices within a tolerance, as illustrated in Fig. 1b. Obviously, these pair polygons allow tensile contacts only occurring between these pair vertices and thus no tensile strength will be applied to even when they are simply partly overlapped as processed in 3D DEM.

In conclusion, a general algorithm for detecting face-to-face contacts between any two 3D arbitrarily shaped blocks in any case of relative position, has not yet been available. Hereinafter, a new algorithm to identify two approaching faces and determine the mutual area is developed based on the contact theory by Zhang et al. (2015, 2016). The comprehensive algorithm can be applied to any two 3D blocks with arbitrarily shaped polygons of faces (no matter convex or concave) in any relative position, with even more than one mutual area.

2 An Extension to Weiler–Atherton Clipping Algorithm

Weiler–Atherton clipping algorithm is a method sufficiently general to clip a concave polygon to the borders of another (Weiler and Atherton 1977), as shown in Fig. 2a. The algorithm represents each polygon as a chain of points in the same clockwise or counter-clockwise order, as shown in Fig. 3b. The clipping process is as follows:

1. Producing vertices of the each polygon and intersecting points of two polygons linking two chains.
2. Ranking these points in the same order to form the chain of points.

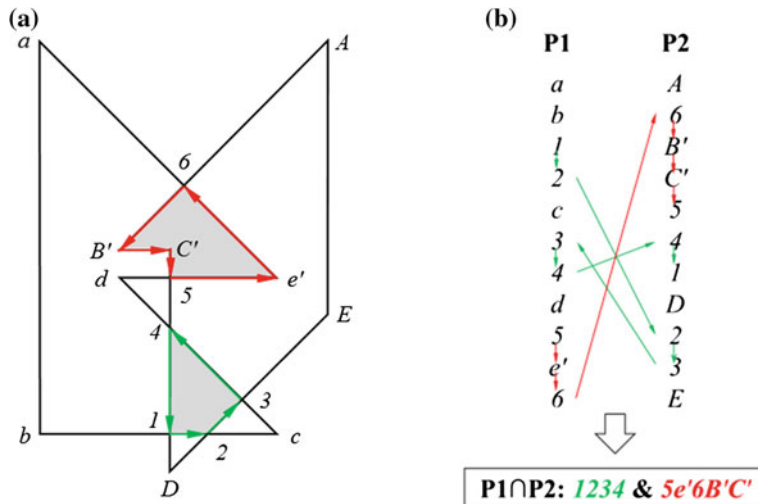
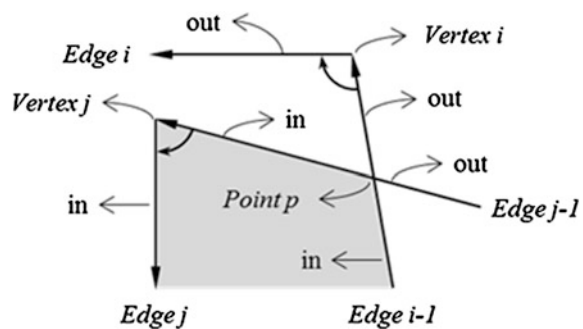


Fig. 2 Intersection generated by the Weiler–Atherton clipping algorithm. **a** Proceeding order, **b** chains of points

Fig. 3 General intersecting modes in original Weiler–Atherton clipping algorithm



3. Labelling these points as entries inside or outside the other polygon.
4. Copying an inside point of the chain or jumping to the other chain when an outside point is reached.
5. Repeating step (4) until the starting point has been reached.

In the process of clipping, the point will be kept in storage when it is inside the other polygon, while it will be ignored when it is outside the other polygon; and intersecting points of two edges will be found to alternate along any given chains, as shown in Fig. 3.

In general, when the searching of proceeding order is performed along one chain and an intersecting point is found, one segment of two candidates which intersects the other polygon will be qualified as the proceeding order and the other one will be ignored. However, attention should be paid where any vertex of a polygon is very

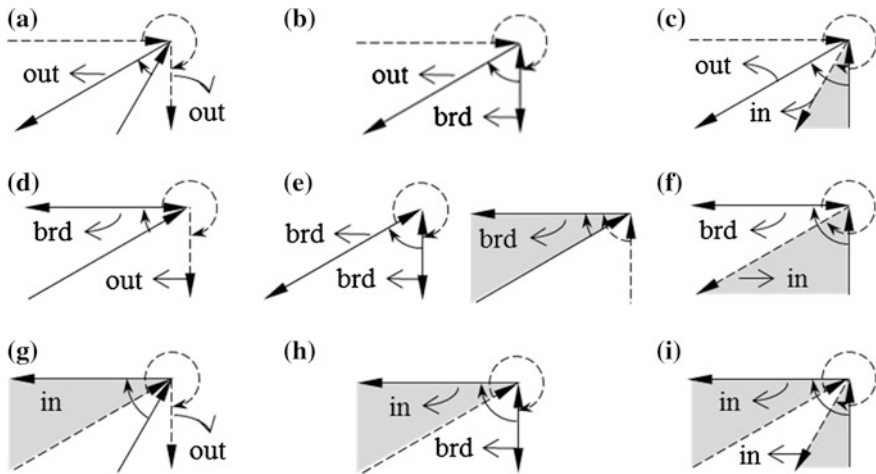


Fig. 4 Intersecting modes in the case of a vertex of a polygon very close to the border of the other polygon. **a** Outside-and-outside, **b** outside-and-border, **c** outside-and-inside, **d** border-and-outside, **e** border-and-border, **f** border-and-inside, **g** inside-and-outside, **h** inside-and-border, **i** inside-and-inside

Table 1 Proceeding order with respect to the intersecting mode

| The other chain | Outside | Border | | Inside |
|------------------|----------|------------|----------|--------|
| Proceeding chain | | | | |
| Outside | Ignore | Ignore | | Switch |
| Border | Ignore | Coincident | Continue | Switch |
| | | Otherwise | Ignore | |
| Inside | Continue | continue | | Switch |

close to the vertex or edge of the other polygon, because they may be considered as both in and out until their status is confirmed after their intersecting modes have been verified, as shown in Fig. 4.

In particular, when the intersecting point has no proceeding segment intersecting with the other polygon, it should be actually considered as an outside point. These intersecting modes that make no contribution on the formation of intersecting area involve outside-and-outside, outside-and-border, border-and-outside and border-and-border (not in coincident case), as shown in Fig. 4a–e.

Another dilemma may be encountered is the intersecting mode of inside-and-inside, as shown in Fig. 4i. When two parts of mutual area share a common vertex of a concave angle, proceeding path could bifurcate at this vertex. Under this condition, two separate common areas can be gained, respectively, if proceeding path switch to the other chain at that vertex.

In summary, the inside point will be kept while in opposite the outside point will be ignored. As for intersecting points, correct proceeding order could be selected with respect to the intersecting mode, as listed in Table 1.

3 Conclusions

A new algorithm is developed for detection of face-to-face contact between any two 3D blocks with faces in arbitrary shape of no matter convex or concave polygons. The new algorithm is implemented with a generalized polygon clipper called Weiler–Atherton clipping algorithm, capable of clipping concave polygons with several intersecting polygons, incorporated with vector geometry analyses for contact detection between two blocks in shapes of arbitrary polyhedrons. In order to produce correct proceeding order of intersecting area of two arbitrary polygons in any relative position, eligibility of the potential proceeding segment is distinguished from pair of intersecting segments by the relative positions of the segments. Instead of identifying proceeding segment left or right to the other intersecting one, a more robust and comprehensive method to locate proceeding segment inside or outside the other approaching face is proposed.

Acknowledgements This study is funded by the National Science & Technology Pillar Program of the Ministry of Science and Technology of China (Grant No. 2014BAL05B01).

References

Cundall PA (1988) Formulation of a three-dimensional distinct element model—Part I. A scheme to detect and represent contacts in a system composed of many polyhedral blocks. *Int J Rock Mech Mining Sci Geomech Abstracts* 25(3):107–116

Cundall PA, Strack OD (1979) A discrete numerical model for granular assemblies. *Geotechnique* 29(1):47–65

Hart R, Cundall PA, Lemos J (1988) Formulation of a three-dimensional distinct element model—Part II. Mechanical calculations for motion and interaction of a system composed of many polyhedral blocks. *Int J Rock Mech Mining Sci Geomech Abstracts* 25(3):117–125

Keneti AR, Jafari A, Wu JH (2008) A new algorithm to identify contact patterns between convex blocks for three-dimensional discontinuous deformation analysis. *Comput Geotech* 35(5):746–759

Liu XL, Lemos JV (2001) Procedure for contact detection in discrete element analysis. *Adv Eng Softw* 32(5):409–415

Shi GH (1988) Discontinuous deformation analysis: a new numerical model for the statics and dynamics of block systems. Doctoral dissertation, University of California, Berkeley

Shi GH (2001) Three dimensional discontinuous deformation analyses. In: The 38th US symposium on rock mechanics (USRMS), DC Rocks 2001. American Rock Mechanics Association

Shi GH (2006) Producing joint polygons, cutting joint blocks and finding key blocks for general free surfaces. *Chin J Rock Mech Eng* 25(11):2161–2170

Shi GH, Goodman RE (1985) Two dimensional discontinuous deformation analysis. *Int J Numer Anal Meth Geomech* 9(6):541–556

Shi GH, Goodman RE (1989) Generalization of two-dimensional discontinuous deformation analysis for forward modelling. *Int J Numer Anal Meth Geomech* 13(4):359–380

Weiler K, Atherton P (1977) Hidden surface removal using polygon area sorting. In: *ACM SIGGRAPH computer graphics*, vol 11, No. 2. ACM, pp 214–222

Wu JH (2010) Compatible algorithm for integrations on a block domain of any shape for three-dimensional discontinuous deformation analysis. *Comput Geotech* 37(1):153–163

Zhang H, Chen G, Zheng L, Han Z, Zhang Y, Wu YQ et al (2015) Detection of contacts between three-dimensional polyhedral blocks for discontinuous deformation analysis. *Int J Rock Mech Min Sci* 78:57–73

Zhang H, Liu SG, Zheng L, Zhong GH, Lou S, Wu YQ et al (2016) Extensions of edge-to-edge contact model in three-dimensional discontinuous deformation analysis for friction analysis. *Comput Geotech* 2016(71):261–275

Application of Three-Dimensional Discontinuous Deformation Analysis to Simulate Characteristics of Planar Translational Slope Failure

P.D. Jing, G. Chen, H. Zhang and W. Wang

Abstract This paper analyses some characteristics of planar translational slope failure using 3D-DDA. The focus of this paper is only on two factors that influences the failure pattern, boundary condition, and dip angle of discontinuity sets. The 2D-DDA has been developed maturely both in theory and computational code. The usage of 3D-DDA is somewhat rare according to the literature search. This paper demonstrates the power of DDA method, especially the feasibility of using 3D-DDA with many blocks. This article also illustrates the great influence of boundary condition and dip angle of discontinuity set on the stability of rock slope.

Keywords 3D-DDA · Planar translational slope · Boundary condition · Discontinuity set

1 Introduction

Discontinuous deformation analysis (DDA) method was originally developed by Shi (1988). This method has drawn many researchers and engineers' attention because its rigorous scheme of block kinematics and equilibrium conditions achieved by minimizing the total potential energy. The 2D-DDA has been developed maturely both in theory and computational code. Many papers have been published to show its availability in the two-dimensional problems just like the literature reviews by MacLaughlin and Doolin (2006) and Hatzor and Bakun-Mazor (2011) showed. However, the usage of 3D-DDA is somewhat rare according to the literature search. This perhaps due to the difficulty in developing a complete contact theory that governs the interaction of many 3D blocks. Although some papers have published on completing the contact theory of 3D-DDA, using it to simulate a system containing many blocks is still a huge challenge we have to conquer.

P.D. Jing (✉) · G. Chen · H. Zhang · W. Wang
Kyushu University, Fukuoka 819-00367, Japan
e-mail: jingpeideng@gmail.com

Planar translational sliding pattern is the main form of failure although accompanied by toppling failure sometimes. The reason of choosing the planar translational sliding is not only its simplicity and also “sliding along an adversely orientated rock face or block edge will invariably occur if the kinematic conditions for such sliding are met” (Goodman and Kieffer 2000). Although the sensitivity of the failure mechanism to the orientation of discontinuity sets has been previous investigated using two-dimensional distinct element method like Kimber et al. (1998), the relevant research by 3D method is not very mature especially by 3D-DDA.

2 Evaluation Process

This paper will show the availability of application of 3D-DDA to simulate the planar translational slope with hundreds of blocks. The attention is put on two main kinds of factors that have great influence on the failure pattern. These two factors are (1) boundary condition. Two kinds of boundary condition has been taken into consideration, confined lateral boundary and fixed lateral boundary separately; (2) Dip angle of the discontinuity sets, which, in detail, can be divided into two: (a) dip angle of basal discontinuity set, (b) dip angle of rear release discontinuity set; In this paper, the dip direction and angle of lateral release discontinuity set keep constant during all the simulation. An example of the 3D model can be found in Fig. 1.

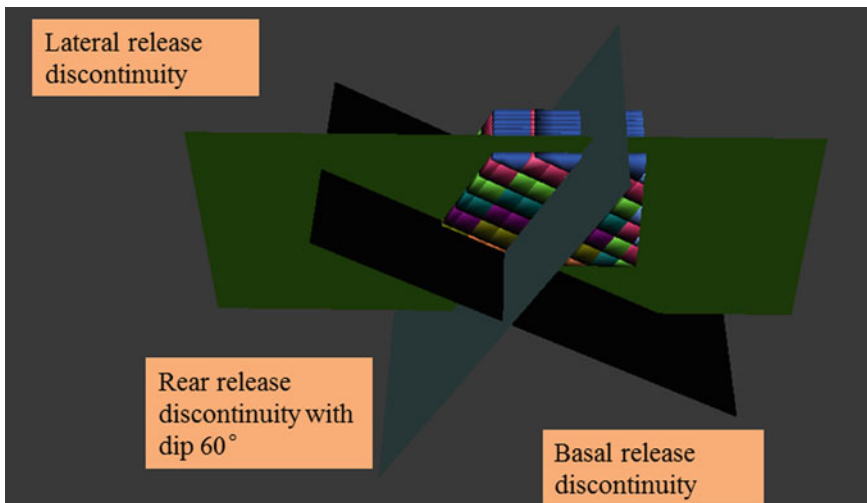


Fig. 1 One conceptual 3D model used in the 3D-DDA analysis

Table 1 Parameters used in the 3D-DDA simulation

| Parameters | Unit weight (kN/m ³) | Young's modulus (kPa) | Poisson's ratio | Friction angle (°) | Cohesion (kPa) | Contact spring stiffness (kN/m) | Time interval (s) | SOR value | Total time steps |
|------------|----------------------------------|-----------------------|-----------------|--------------------|----------------|---------------------------------|-------------------|-----------|------------------|
| | 2000 | 5E07 | 0.2 | 5 | 0 | E08 | 0.001 | 1.3 | 10,000 |

In the conceptual 3D model, the rear release discontinuity and basal release one are always orthogonal. The lateral release discontinuity is fixed vertically. There are totally three kinds of discontinuity condition, with the release discontinuity dip angle changes by 30°, 60°, and 90°. There are two kinds of boundary conditions, lateral free or fixed.

The simulation parameters used in this paper are showed in Table 1. It should be illustrated that the cohesion and friction angle are conceptual because the focus of this paper is not on these two parameters.

There are totally six 3D-DDA models were built and analyzed. In the below picture, the color bar represents the value of velocity. Figures 2 and 3 showed the influence of lateral boundary condition on the failure characteristics when the rear release discontinuity dip is 60°. Figures 4 and 5 showed that when the dip angle is 90°.

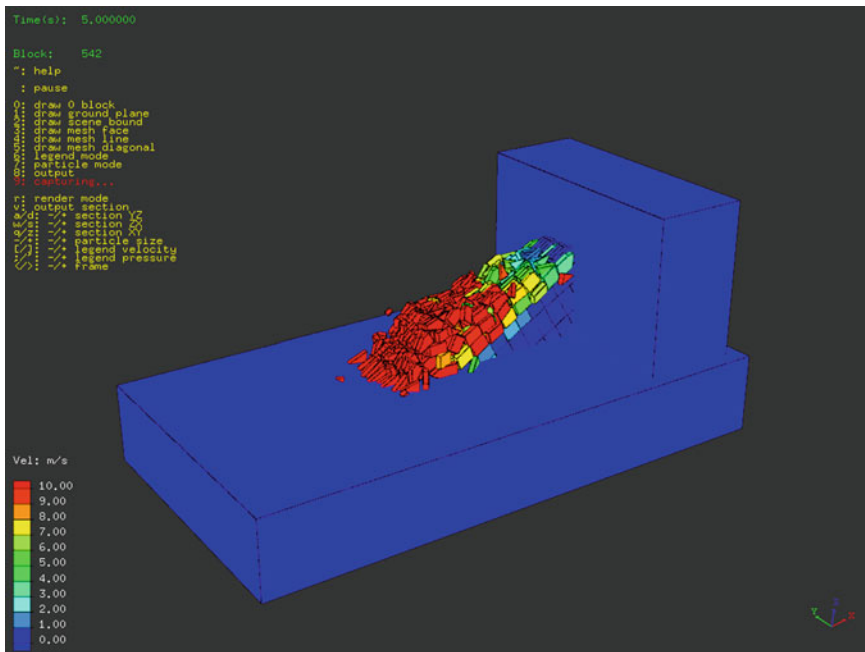


Fig. 2 Free lateral condition—the velocity pattern of the slope with rear release discontinuity dip 60° at 5000 steps

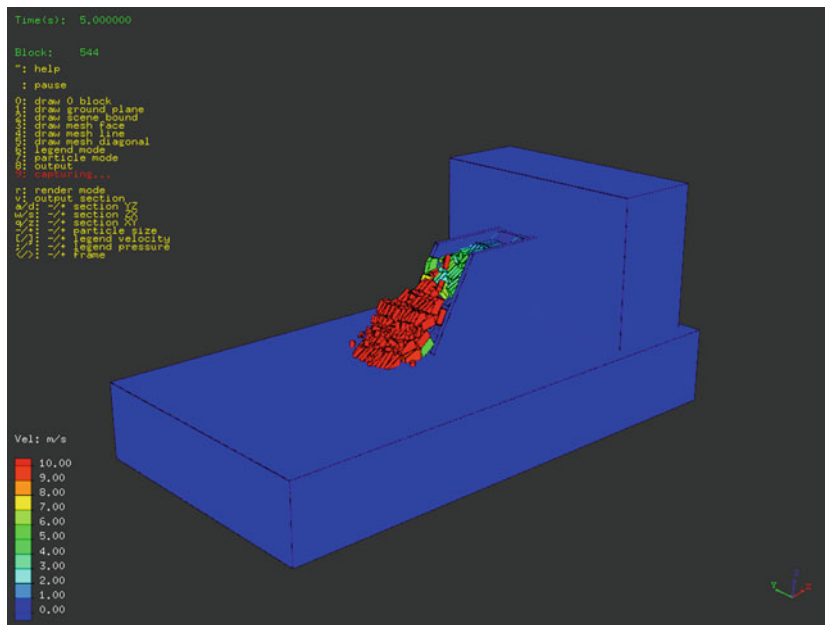


Fig. 3 Fixed lateral condition—the velocity pattern of the slope with rear release discontinuity dip 60° at 5000 steps

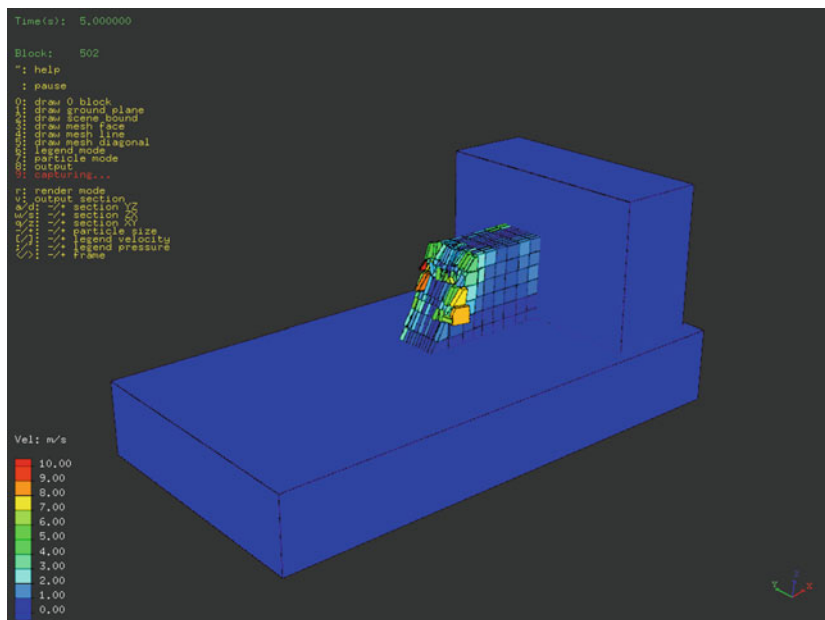


Fig. 4 Free lateral condition—the velocity pattern of the slope with rear release discontinuity dip 90° at 5000 steps

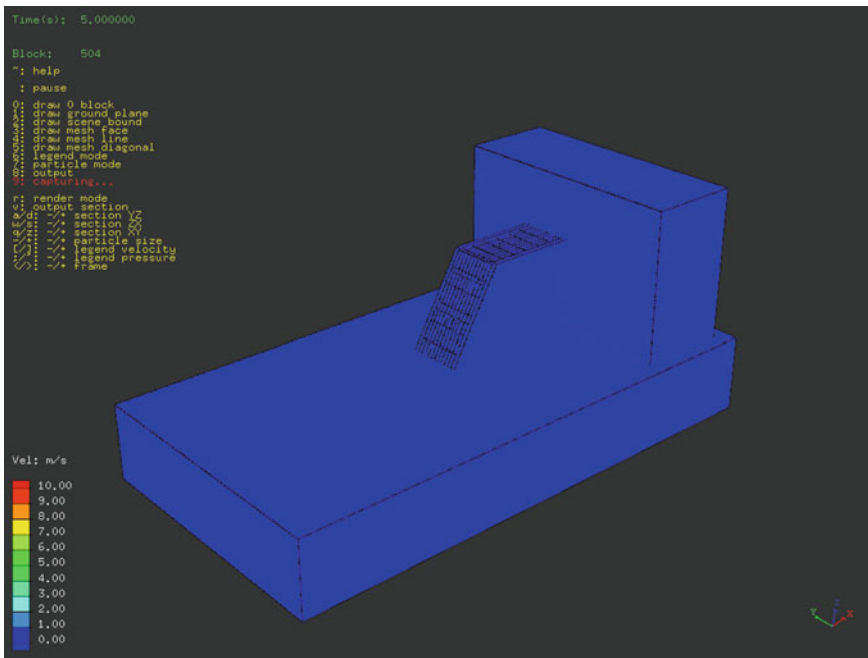


Fig. 5 Fixed lateral condition—the velocity pattern of the slope with rear release discontinuity dip 90° at 5000 steps

Figures 6 and 7 showed the different velocity pattern when the dip angle of the joint set changes. It can be found that the most dangerous pattern happened when the dip angle of rear release discontinuity is 60° .

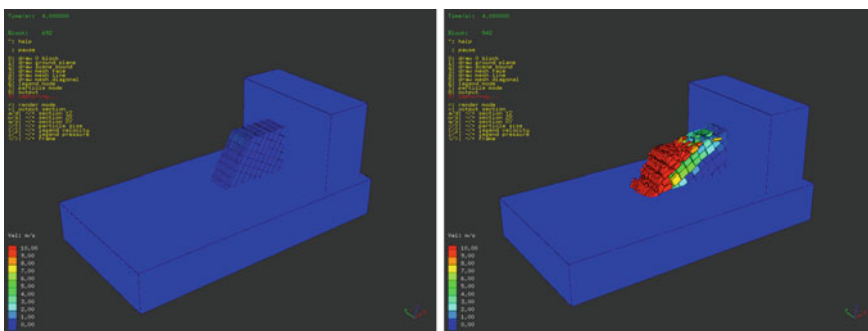


Fig. 6 The velocity pattern of the slope with rear release discontinuity dip angle of 30° and 60° separately

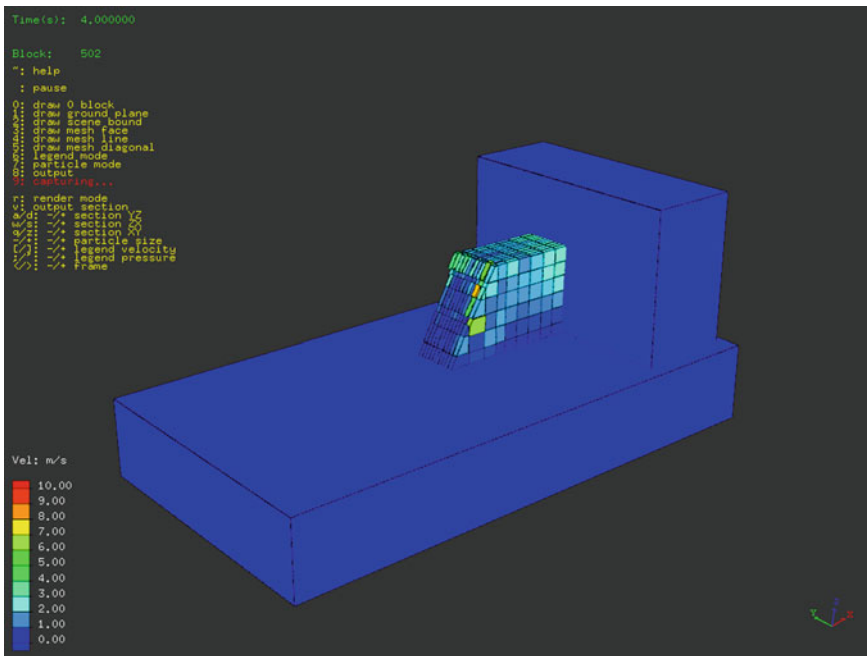


Fig. 7 The velocity pattern of the slope with rear release discontinuity dip angle of 90°

3 Conclusions and Discussion

Dip angle of joints have great influence on the planar translational slope. Change of dip angle of rear release discontinuity set has great influences on the slope failure, like the change from slide-topping to sliding. With the increasing of dip angle of basal joint sets, the failure pattern may change from topping mixed with sliding to toppling.

The confining condition is of great importance in the rock slope analysis. The simulation results showed that it has huge influence on the slope stability when increasing the rear release joint dip angle.

The simulation code used in this paper is developed directly from the original edition keeping the core algorithm constant and some details are improved and modified. Details about the improvement on the original DDA code are out of the range of this paper and not discussed. This paper limits the blocks numbers to hundreds because as the block numbers increased to a thousand, the simulation turns to be very time consuming.

The focus of this paper is only on two factors that influences the failure pattern. It does not take other important factors into consideration, like the shear strength of joint, block size and et al., which leads to the necessary of the future deeply study. This paper also demonstrates the powerful of DDA method, especially the feasibility

of using 3D-DDA with many blocks. Moreover, in order to expand the 3D block number from hundreds to thousands, maybe tens of thousands, to development the 3D-DDA based on the CUDA (Compute Unified Device Architecture) platform may be a future development direction.

References

Goodman RE, Kieffer DS (2000) Behaviour of rock in slopes. *J Geotech Geoenviron Eng* 126 (8):675–684

Hatzor YH, Bakun-Mazor D (2011) Modelling dynamic deformation in natural rock slopes and underground openings with DDA: review of recent results. *Geomech Geoenviron Eng* 6(4):283–292

Kimber OG, Allison RJ, Cox NJ (1998) Mechanisms of failure and slope development in rock masses. *Trans Inst Br Geogr* 23(3):353–370

MacLaughlin MM, Doolin DM (2006) Review of validation of the discontinuous deformation analysis (DDA) method. *Int J Numer Anal Meth Geomech* 30:271–305

Shi G (1988) Discontinuous deformation analysis—A new numerical method for the statics and dynamics of block system. PhD thesis, University of California

Part IV

Evaluation and Mitigation of Geohazards

Hazard Mapping for Earthquake-Induced Geo-disaster Chain

Guangqi Chen, Yanan Fan and Yange Li

Abstract Dammed lakes are considered as the most subsequently dangerous post-earthquake geo-hazard because the lakes not only flooded human habitats in upstream areas but also posed threats to potentially inundated downstream areas with large populations. Therefore, it is necessary and important to pay attention on prediction of earthquake-induced landslides and landslide dams in order to mitigate or avoid the secondary disasters occurrence. This study proposes a landslide dam prediction system over a regional scale. The prediction procedure is carried out in slope unit-based mapping unit, and utilizing four filters to remove steady slopes to obtain landslides dam prone slopes. A practical application is presented to show the usefulness of the hazard mapping system.

Keywords Geo-disaster chain · Landslide dams · Prediction system · Hazard mapping

1 Introduction

A strong earthquake can not only cause catastrophic damage on structures directly but also result in series of secondary geo-disasters indirectly for a long period of time. These secondary disasters occur as a disaster chain, i.e., “disaster triggering disaster.” The chain starts from earthquake-induced landslides, and an extensive landslides can create landslide dams when their debris fill into and stops a river. While the dam is being filled, the surrounding water level rises and causes

G. Chen (✉) · Y. Fan · Y. Li
Kyushu University, Fukuoka 819-0395, Japan
e-mail: chen@civil.kyushu-u.ac.jp

Y. Li
School of Civil Engineering, Central South University, Changsha, China

back-flooding (upstream flooding). Due to its loose nature and absence of controlled spillway, a landslide dam can easily fail catastrophically and lead to debris flows or downstream flooding.

Many reports show that these post-earthquake disasters would cause catastrophic damages. For example, the 2008 Wenchuan Earthquake (Ms 8.0) induced approximately 60,000 landslides, which ran down into river valleys and blocked drainages, raising the water level and flooding roads, villages and towns. The earthquake also created 828 landslide dams, and the subsequently dammed lakes are considered as the most dangerous post-earthquake geo-hazard because the lakes not only flooded human habitats in upstream areas but also posed threats to potentially inundated downstream areas with large populations. The direct economic loss from the earthquake is estimated at approximately 150 billion USD, while it is recorded that more than one-third of the total loss (both property and life) came from the post-earthquake disaster chain other than earthquake shaking itself (Chen et al. 2012). Therefore, it is necessary and important to pay attention on prediction of earthquake-induced landslides and landslide dams in order to disclose the geo-disaster chain to mitigate or avoid the secondary disasters occurrence.

Effective countermeasures to disclose the geo-disaster chain rely on accurate information about the location of landslide dam prone slopes (LDPSs). Because an accurate landslide dam hazard map can provide useful information for these countermeasures. For example, we can determine which slope needs to be reinforced based on the hazard map before an earthquake. Also, it would be easy for us to detect landslide dams immediately after an earthquake if we know the potential places from an accurate landslide dam hazard map. However, few studies focus on landslide dam hazard mapping up to now, although several mapping methods have been applied on landslides. Thus, it is important and essential to develop landslide dam hazard mapping system.

In this paper, we present a hazard mapping system for landslide dam over a regional scale. The system is carried out in slope unit-based mapping unit, which utilizing four filters to remove steady slopes to obtain LDPSs. The filters including (1) slope safety factor filter using a 3-D slope stability analysis (SSA) model; (2) a volume filter to exclude impossible LDPS by defining a threshold volume of slide mass based on field investigation; (3) several spatial filters for eliminating slopes that are impossible to reach a river or block a river.

The mapping system has been developed with C# language and tested for mapping LDPSs caused by the Wenchuan earthquake in the catchment of Tongkou River. The predicted result is validated through comparing with an existed landslide inventory which is interpreted from some aerial photographs. The detected LDPSs show good agreement with interpreted landslides inventory. It indicates that the proposed approach is effective and efficient for landslide dam hazard mapping against a strong earthquake.

2 Hazard Mapping Method

Few studies have carried out landslide dam hazard mapping up to now, although several mapping methods have been applied on landslides (Van Westen et al. 2006, 2008; Pradhan and Lee 2007). A landslide dam hazard map shows slopes that have high possibility of collapsing and blocking a river. A LDPS should meet with the following conditions: (1) it will be unstable caused by a strong earthquake; (2) its debris will reach a river; (3) the volume of reached debris is large enough to block the river.

Therefore, in order to identify all the LDPSs in a wide area, we need (1) to identify all the slopes in the area; (2) to find unstable slopes; (3) to judge whether its debris can reach a river and is enough to block a river. Thus, we propose the following procedures for hazard mapping.

2.1 Slope Identification

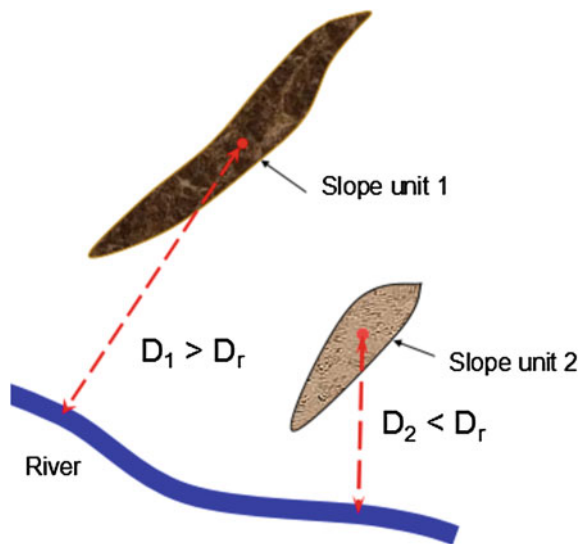
For hazard mapping within a wide area, the first and essential step is to define the mapping units which affect uncertainties of the input data, the fitness of the assessment model and the reliability of calculated susceptibility zonation. Each mapping unit, the portion of land surface that contains maximum internal homogeneity differing from adjacent units, should have relative similar topographic and geological characteristics, respectively. In this study, slope unit-based landslide dam mapping is selected. Since the page limitation, the detail processing procedure can be found in our previous work (Fan et al. 2013).

After slope unit identification, next process for predicting landslide dam is the extraction of LDPSs, which can be performed by the following filters to erase irrelevant slope units step by step.

2.2 River Buffer Filter

Landslide dam is a natural damming of a river by some kind of mass wasting, e.g., landslide, debris flow, or rock avalanche. Considering that the formation of a landslide dam cannot happen without a river, we can remove the slopes, from where the sediment material cannot reach to the river using a defined certain distance, to obtain possible LDPSs. The central point of each slope unit is first need to be calculated, and then the distance from each central point to the target river can be derived within GIS. Next the distance larger than a given threshold can be excluded as non-LDPS. We call this step as a river buffer filter and its sketch map is shown in Fig. 1, in which D_1 and D_2 are distances from slope center to the river, D_r is the buffer width.

Fig. 1 A sketch map of river buffer filter to show the distance from each slope unit to the river



2.3 Aspect Filter

After step 2.2, most of slopes which are with the distance to river larger than a given threshold are erased. Among the rest slopes, it is necessary to consider whether their runouts can reach to the valley or not according to slope aspect. This could be carried out by extending a runout path toward the slide direction and then checking if it is conjoined with the stream line. We call this step as an aspect filter, which means to exclude the slopes that could not reach to the river with slope directions not toward the river. The runout path and direction can be derived by linking the highest point to the lowest point in each slope unit. A sketch map of the aspect filter is shown in Fig. 2.

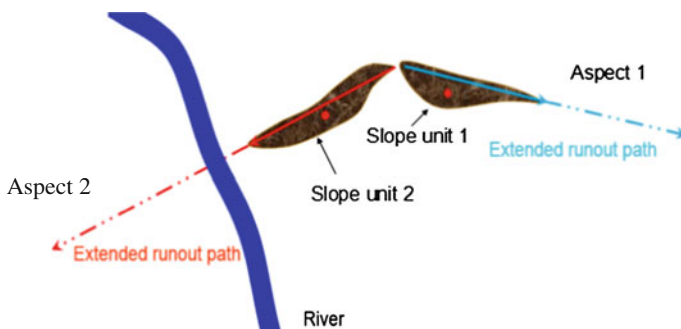


Fig. 2 A sketch map of aspect filter to show extended runout paths and the dammed river

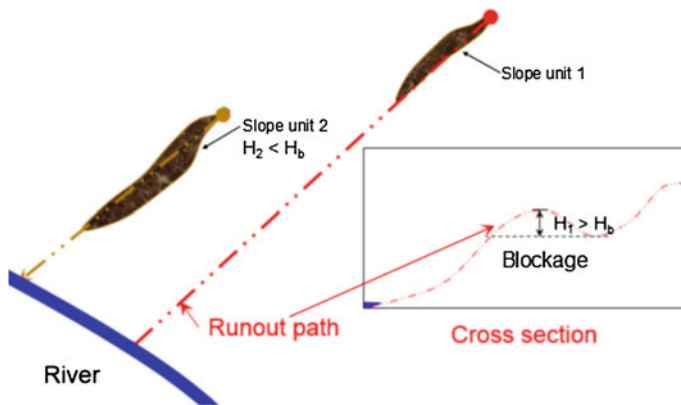


Fig. 3 A sketch map of blockage filter to show blockage of slopes along runout path

2.4 Blockage Filter

Another decisive factor of whether the slide runouts can reach to the valley or not is the blockage height of sedimental material along the runout path toward river. A module named by blockage filter is developed, which excludes impossible LDPSs by defining a threshold of debris height, the slopes with height larger than the threshold would be removed as non-LDPSs. Its sketch map is shown in Fig. 3. From the cross section in Fig. 3, slide direction starts from the highest point to the lowest one in each slope unit. Thus, a GIS module is developed to count the risen topography along slide direction and records the highest location. Any slope unit with a height H greater than a given height H_b is excluded from the LDPSs, like the slope 1 in Fig. 3 shows.

2.5 Slope Safety Factor Filter Using a 3-D Limit Equilibrium Analysis

Slope safety factor is an essential index for landslide dam analysis, because it indicates landslide-prone or non-prone slopes. The most used method for determining the slope safety factor in a GIS environment is one-dimensional infinite plain slope modeling (IPSM) (Ward et al. 1982; Van Westen and Terlien 1996). However, following major problems need to be solved for using infinite plain slope modeling. (1) The failure depth should be assumed in advance. It is very difficult to determine the failure depth since it varies from place to place and its value affects the calculated results very much. (2) The scale of a landslide with slip surface and volume information cannot be obtained but they are necessary in predicting LDPS. (3) IPSM assumes that the slope is extended infinitely in all directions and slide

occurs along a plane parallel to the face of the slope. In practice, most failure slip surfaces are not planes. Thus, SSA based on a circular slip mode (CSM) is more popular than IPSM in geotechnical engineering. Also the use of 2-D slope stability programs in a GIS environment is seldom used (Van Asch et al. 1992), because this method requires the selection of a number of slope profiles from a digital terrain model. Moreover, 2-D method cannot replicate the 3-D geological structures of nature slopes. Since all slope failures show a 3-D geometry, it is reasonable to use a 3-D model to calculate slope safety factor.

For this reason, we develop a GIS module for 3-D SSA based on CSM. The module is actually an extension of the well-known Swedish Method with a 2-D limit equilibrium analysis. Thus before we carry out the 3-D stability analysis, we need to introduce the 2-D model at first.

2.5.1 The 2-D Slope Stability Analysis

Considering that the tendency of a landslide is to go along the flow line, from the top to the bottom, thus by recording the positions of the highest point and lowest point in each slope unit, the cross line module embedded in GIS, which can calculate the sliding direction, is created by using the C# computer language in this study.

The cross line is extended by 10 and 20 % of the total projected length at the top and bottom, respectively, so as to include plenty of topography features. The Interpolate function of GIS is used to extract the elevation data into the cross line in a 1 m-interval. Each point of the path line stores an elevation data. The elevations of the points are arranged within an array to obtain the cross section of a possible landslide (Fig. 4).

The slope surface is split into two equal parts. 10 head points of A are distributed from the upper part and 10 toe points of B from the lower part through a simple enumeration algorithm. For each pair of A and B, radii R takes 10 different values (Fig. 5). By means of permutation and a combination of their sample groups, 1000 different slip surfaces are analyzed for critical slip surface searching.

Through the 2-D SSA, the center point $O(x_o, y_o)$, position of the head point and toe point can be derived. Thus, the angle and inclination of slip surface can be derived.

2.5.2 The Extending 3-D Slope Stability Analysis

For the column-based 3-D SSA model, usually it is needed to determine the ellipse center $O(x_o, y_o, z_o)$, lengths x, y, z of the X, Y, Z axes, angle and inclination of slip surface. Contrastively, except of the parameter z , all the other parameters have been calculated from 2-D slope stability analysis in this study. Thus, 10 different lengths z are assumed to determine the 3-D slip surface.

Fig. 4 Interpolation of the extracted cross section of each slope unit from DEM

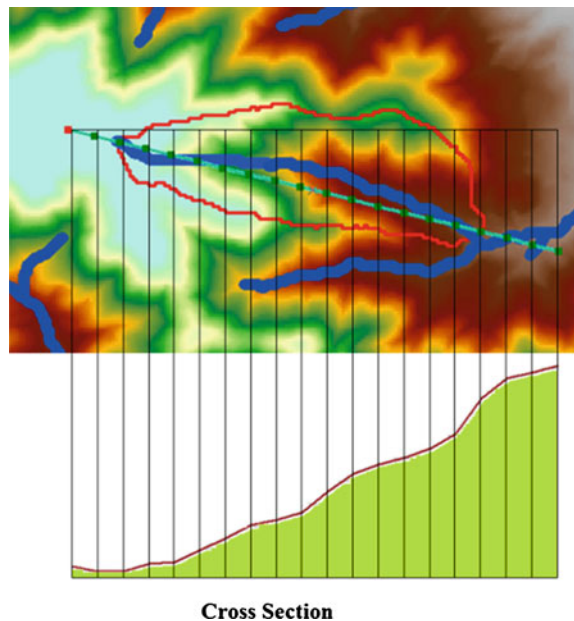


Fig. 5 One case of slip surfaces

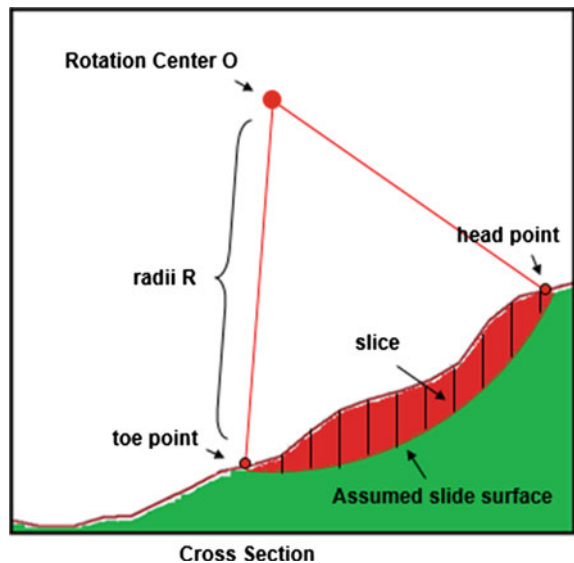
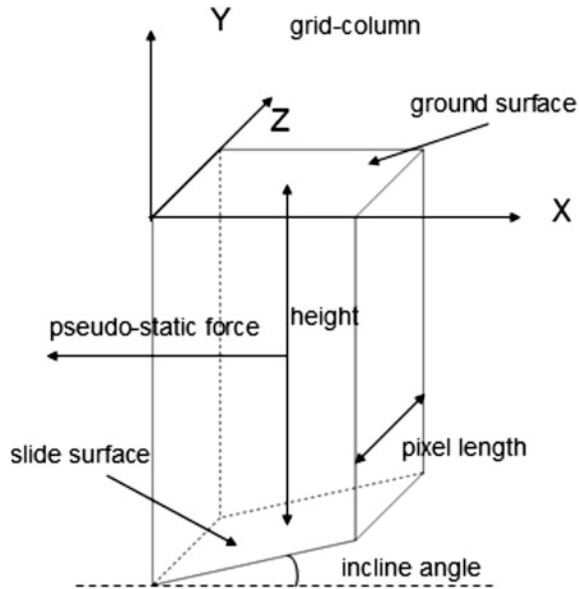


Fig. 6 3-D view of one grid-column for deriving factor of safety equation



2.5.3 The Revised Hovland's Model

The GIS-based data is selected because it can be easily managed in the column-based model (Fig. 6). The revised Hovland's model is selected to calculate the safety factor

$$SF_{3D} = \frac{\sum_j \sum_i (c A_{i,j} + W_{i,j} \cos \theta_{XYi,j} \tan \phi)}{\sum_j \sum_i (W_{i,j} \sin \theta_{XYi,j} + E_{i,j})}, \quad (1)$$

where, F_{3D} = 3D slope safety factor; $W_{i,j}$ = weight of the i th, j th grid-column; $A_{i,j}$ = area of the slip surface of the i th, j th grid-column; c = cohesion; ϕ = friction angle; θ = normal angle of the slip surface; $E_{i,j}$ = the earthquake forces of the i th, j th grid-column.

2.6 Volume Filter

After a landslide occurs, the volume of its sediment material directly determines whether a landslide dam forms or not. It is clear that large-scale landslides have significantly likelihood for forming landslide dams. In the developed 3-D SSA module, the volume of landslide for each slope unit can be calculated simultaneously. Thus, by defining a certain threshold beforehand, the slope unit with slide volume greater than the threshold can be considered as LDPS.

3 Case Study

3.1 Study Area and Data Source

The new hazard mapping method is applied to an area of the 2008 Wenchuan earthquake where five large-scale landslide dams were formed (Fig. 7), including the largest Tangjiashan Dam with a volume of 20.37 million m³. The basic data used in this study consists of a DEM with resolution of 10 m and a satellite image with resolution of 2.5 m.

3.2 Results

Following the slope unit identification method, a total of 10,186 slope units were derived. Then the non-LDPSs can be removed by the above-mentioned filters step by step.

1. Eliminate the non-LDPS by the river buffer result.

As we know, if a slope is far from a river, it will not form a LDPS. We use the buffer function of ArcGIS to attract 3996 slopes along the Tongkou river. Figure 8 shows the slopes in the whole area by blue lines and the slopes within 2 km along the river by red lines.

2. Eliminate the non-LDPS by the aspect filter.

If the aspect of a slope is not toward the river, the slope should not be a LDPS since the debris cannot reach the river. We developed the so-called aspect filter

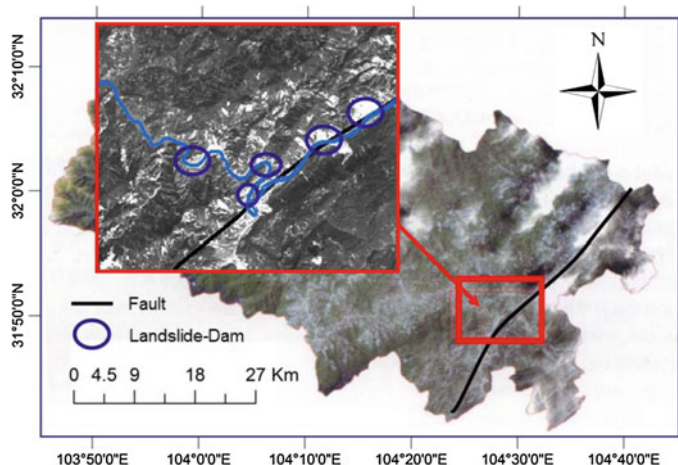
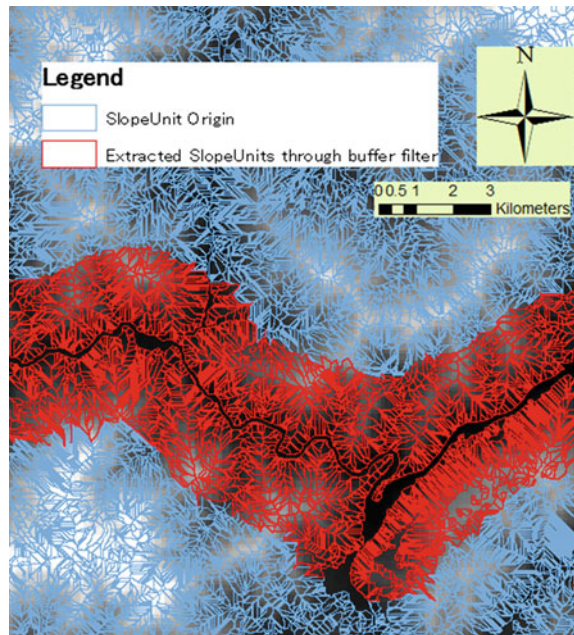


Fig. 7 The study area shows five large-scale landslide dams

Fig. 8 Remained LDPSs after filter 1



to eliminate non-LDPS. As a result, 2400 slopes are eliminated from the remained 3996 slopes in step (1), and 1596 slopes remained in this step (Fig. 9).

3. Eliminate the non-LDPS by the blockage filter.

If there is another slope between a target slope and the river, and it is tall enough to hinder the slope debris, the target slope will be eliminated since the debris could be blocked by the midway slope. We developed the so-called blockage filter for this purpose. 460 slopes are eliminated and 1136 slopes remained in this step (Fig. 10).

4. Eliminate the non-LDPS by 3-D slope stability analysis.

According to field investigation, the parameters used for calculation of slope safety factor are defined as: the soil unit weight $\gamma = 22 \text{ kN/m}^3$, the cohesion strength $c = 20 \text{ kN/m}^3$ and the internal friction angle of slope material $\Phi = 32^\circ$. Finally, 524 slopes are eliminated according to the safety factors calculated by the newly developed 3-D SSA tool and 612 slopes remained in this step (Fig. 11).

5. Eliminate the non-LDPS based on the volume filter.

The failure volume is estimated by 3-D SSA, and the volume threshold of debris moves to river which is defined by the field investigation of existed landslide dams caused by the Wenchuan earthquake in previous research (Fan et al. 2012). As a result, 28 slopes are eliminated and 584 slopes are determined as the LDPSs (Fig. 12).

Fig. 9 Remained LDPSs after filter 1 and 2

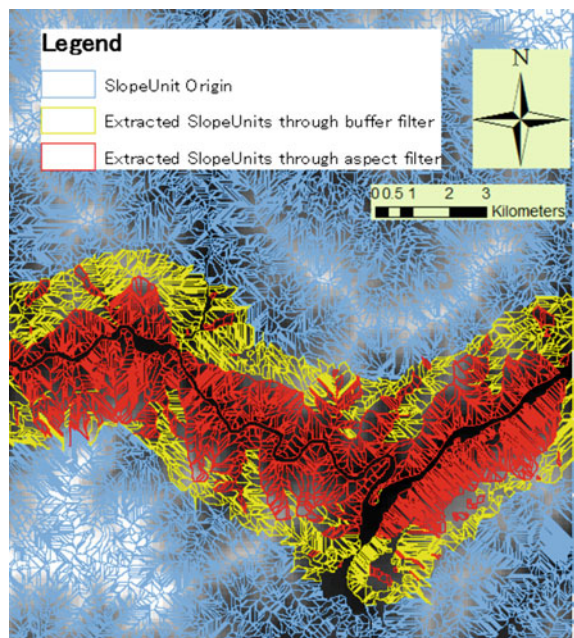


Fig. 10 Remained LDPSs after filter 1, 2 and 3

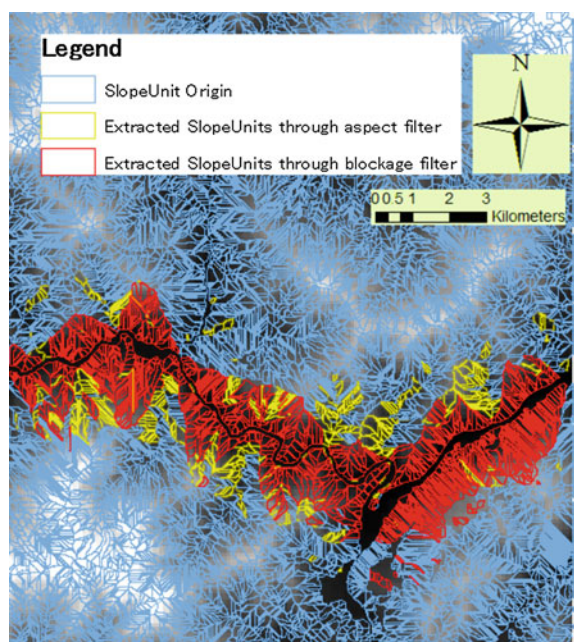


Fig. 11 Remained LDPSs after filter 1, 2, 3 and 4

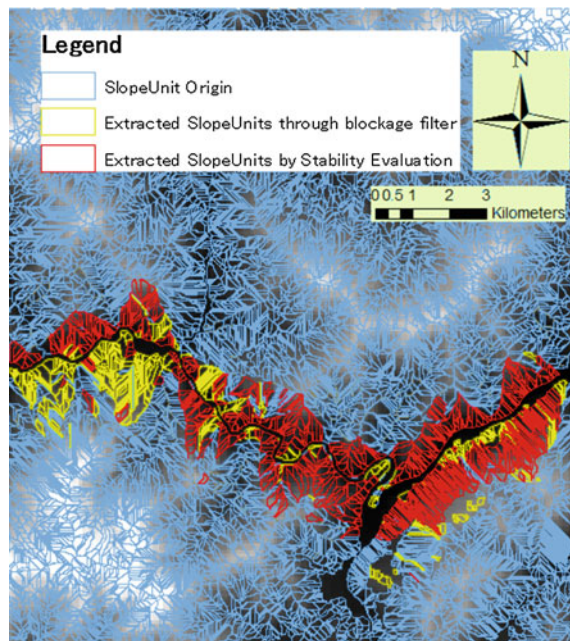


Fig. 12 Remained LDPSs after filter 1, 2, 3, 4 and 5

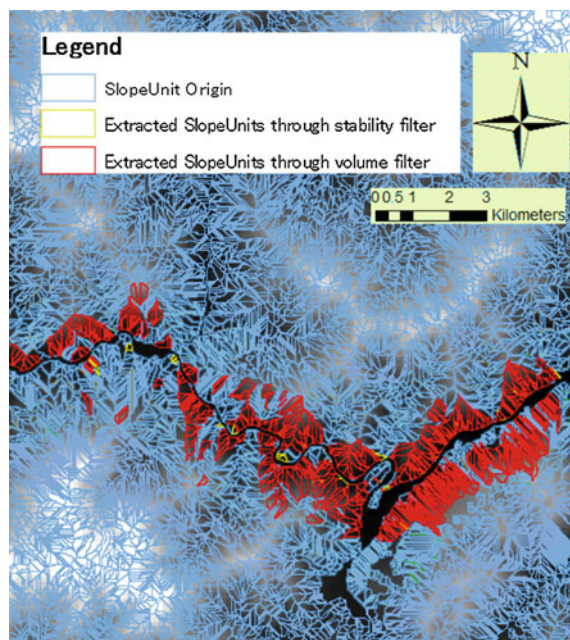


Fig. 13 Hazard map of landslide dam

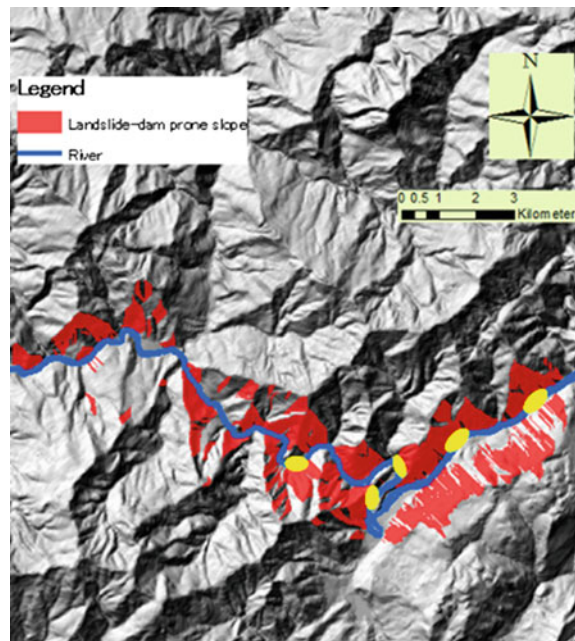


Figure 13 shows the landslide hazard map. The five landslide dams caused by the Wenchuan earthquake are also shown by the yellow areas. It can be seen that the results are quite reasonable.

4 Conclusions

A strong earthquake can induce landslide dam disaster chain which may cause more serious damage than earthquake-induced direct damage. A landslide dam hazard map can provide necessary and essential information for effective countermeasures against the disaster chain since it shows the location, possibility, and dangerousness of potential landslides and landslide dams.

In this paper, we have proposed a hazard mapping method for landslide dam induced by earthquake according to the slope stability analysis, possible slide volumes, together with topography data and river conditions. The hazard mapping system includes a 3-D slope stability analysis GIS module which aims for calculating safety factors and estimating failure volumes with high accuracy, an aspect filter and a blockage filter which are used to exclude non landslide dam prone slopes combining with the geographical data.

The proposed prediction system has been developed with C# computer language and tested for mapping LDPS caused by the Wenchuan earthquake in the catchment of Tongkou River. The predicted result is validated through comparing with an

existed landslide inventory which is interpreted from some aerial photographs. Results show that the detected LDPSs show good agreement with interpreted landslides inventory. It indicates that the proposed approach is effective and efficient for landslide dam hazard mapping.

References

Chen GQ, Li Y, Zhang YB et al (2012) Earthquake induced a chain disasters. In: *Earthquake research and analysis—Statistical studies, observations and planning*. InTech—Open Access Publisher, pp 383–416

Fan X, van Westen CJ, Xu Q et al (2012) Analysis of landslide dams induced by the 2008 Wenchuan earthquake. *J Asian Earth Sci* 57:25–37

Fan YN, Chen GQ, Kasama K, Li Y (2013) Susceptibility zonation of earthquake induced landslide-dams at the catchment of Tongkou River, China. *Mem Fac Eng Kyushu Univ* 73(2):57–70

Pradhan B, Lee S (2007) Utilization of optical remote sensing data and GIS tools for regional landslide hazard analysis by using an artificial neural network model. *Earth Sci Front* 14(6):143–152

Van Asch TWJ, Van Westen CJ, Blijenberg H, Terlien M (1992) Quantitative landslide hazard analyses in volcanic ashes of the Chinchina area, Colombia. In: *Proc ler Simposio Int sobre Sensores Remotes y Sistemas de Informacion Geografica para el estudio de Riesgos Naturales*, Bogota, Colombia, pp 433–443

Van Westen CJ, Terlien MTJ (1996) An approach towards deterministic landslide hazard analysis in GIS. A case study from Manizales (Colombia). *Earth Surf Proc Land* 21:853–868

Van Westen CJ, Van Asch TWJ, Soeters R (2006) Landslide hazard and risk zonation—Why is it still so difficult? *Bull Eng Geol Environ* 65:167–184

Van Westen CJ, Castellanos E, Kuriakose SL (2008) Spatial data for landslide susceptibility, hazard, and vulnerability assessment: an overview. *Eng Geol* 102:112–131

Ward TJ, Ruh-Ming L, Simons DB (1982) Mapping landslide hazards in forest watershed. *J Geotech Eng Div Proc Am Soc Civil Eng* 108(GT2):319–324

Monitoring Techniques for Sediment Disaster in Mountaint Area

**Lin Bing Shyan, Lien Hei Pan, Liu Yi Chen,
Li Cheng Yang and Chen Ping Sen**

Abstract In Taiwan, disaster prevention work has become an important issue for government agency which works for mountain area conservation, especially when disaster has become a complex kind of slope disaster combining landslide, debris flow, and flooding. In order to increase the ability of these complex disaster monitoring prewarning system in Taiwan area, one is to gain the prewarning time in which we can put much power-saving monitoring system more upstream, and the other way is to make the monitoring site much densely covered with disaster prevention class order low cost detecting instruments apply by low-frequency radio transmitter and mesh transfer technique for accurate data transmit. Another use of watershed prewarning technique is the UAV image providing different time of slope and riverbed landscape and also provides high-resolution DTM and DSM in order to calculate and provide numerical modification resources for different construction suggestions and monitoring sensor position replacement. In result, we use Han-Shi watershed in Yi-Lan County in northwest of Taiwan, and Li-Yi in Pin-Tung County in southern Taiwan has accomplished this goal and makes effort by the use of 158, 433 and 900 MHz all three different frequencies of radio transmission, and successfully transmit including five major collecting site, and 19 different signals for upstream debris flow of potential river monitoring for slope sliding amount, ground movements, ground moisture, rain amount, water level, and also site visions. From measurement result, we can assure that sediment transportation in this watershed can be measured in all three directions, and for protection site, large mass of sediment movement occurrence can be measured by these low-cost direct instruments and by the use of low-frequency radio network,

L.B. Shyan (✉) · L.H. Pan

Department of Water Resources Engineering and Conservation CDPRC,
Feng Chia University, Taichung 5960, Taiwan
e-mail: bslin@fcu.edu.tw

L.B. Shyan · L.Y. Chen
CDPRC, Feng Chia University, Taichung, Taiwan

L.C. Yang · C.P. Sen
SWCB, Nanto, Taiwan

prewarning alert can be proposed and old estimations for rainfall induced amount can be fixed more correctly.

Keywords Sediment disaster • Monitoring • Warning system • Low-frequency radio transmitter

1 Introduction

In Taiwan, typhoon and earthquake are the most common hazardous events that cause serious slope land disaster; therefore, large amount of sediment transport downstream and flooding threaten the resident or protection target alongside the riverbed. Therefore, when heavy rainfall event or earthquake occurs, demands for efficiently monitoring the widely spread protection target arose quickly. To obtain the required information for prewarning system, different monitoring methods are proposed according to different purpose

1. Debris flow sites:

Normally, debris flow site is in the upper part of the watershed, where slope is steep, no road reachable, accompanied by bedside landslide which provides the sediment to supply the debris flow. If the watershed does not have new sediment supply point, it will be difficult to find the monitor point, then, indirect way to define debris flow will be important. Instruments like vibration sensor, wire sensor, ground moisture instruments, rainfall amount, underground water level, and also the sliding amount are useful. From other indirect guarding method for defining landside we can use tilt meter, tension crack meter, displacement meter, ground vibration sensor, and also slope type wire sensor can be used and CCD camera and rain gauge is used for evidence proof.

2. Landslide sites:

Landslide could occur in any place in the watershed area. For creeping sliding site, the tilt meter, tension crack meter, displacement meter, ground vibration sensor, and also slope type wire sensor are useful. For potential landslide sites, surface acceleration sensor and ground vibration sensor which detect frequency can be changed and are helpful to detect the landslide activity for prewarning.

3. Riverbed scouring and depositing sites

Riverbed water level, scouring, and deposition are also important to define the slope disaster. Different types of water level sensors are available (laser type, infrared sensor, radar type). Those sensors are normally setup on fixed structures, such as check dams and weirs.

Based on the above-mentioned method, we can collect monitored data in different places and send it to the web cloud to calculate and demonstrate the result, as shown in Fig. 1. Accordingly, the distributed data was obtained, from the upstream to the downstream of a watershed.

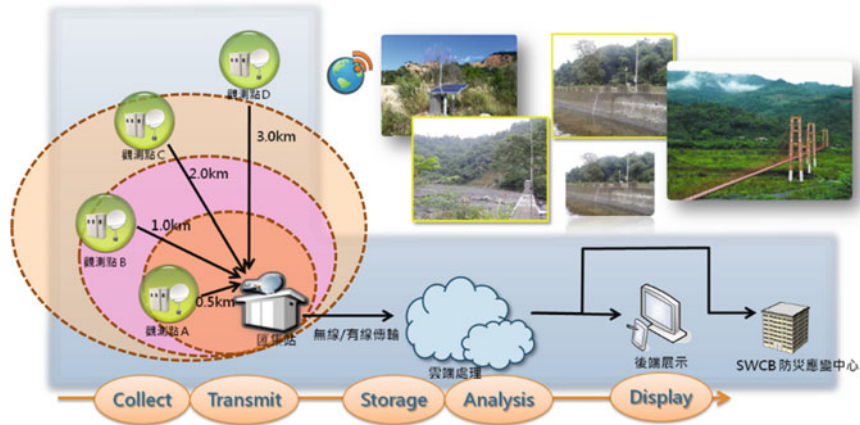


Fig. 1 Monitoring and data transmission structure

2 Analysis Methodology

For each kind of detecting instrument, analysis of the transmitted data is essential. The results monitored by different sensors can be illustrated in different ways according to different purpose as listed below (SWCB 2013b):

1. Rain gauge data: This data (include accumulated rainfall, rainfall intensity, and duration) affects the slope stability directly. Usually, the empirical critical lines (function of rainfall intensity, rainfall duration, or cumulative rainfall) are used to issue the warning message (Fig. 2).
2. Wire Sensor: The place and timing of the wire broken is the most critical information. If the broken succession (temporally and spatially) was detected, the travel speed of landslide or debris flow surge can be evaluated (Fig. 3).
3. Water level: This data can be used for calculating the discharge. In addition, it can be used to indicate the occurrence of landslide. From water level, we can conduct rainfall data to calculate the watershed discharge and also (Fig. 4).
4. Soil Moisture: This data show the amount percentage of water contained in the soil which provides the result in different area (Fig. 5).
5. Geophone/Seismic meter: This instrument is based on different angle of ground acceleration meter analysis, under different detect frequency, the detect range differs, and with real time transmission, the entire surge event can be detected (Fig. 6).
6. Tilt meter: The rotation angle of a rotational sliding and the rate of rotation can be used to indicate the slope instability.
7. Ground Placement meter: This data include tension crack or soil and tree movement for slope failure potential area and old landslide site.

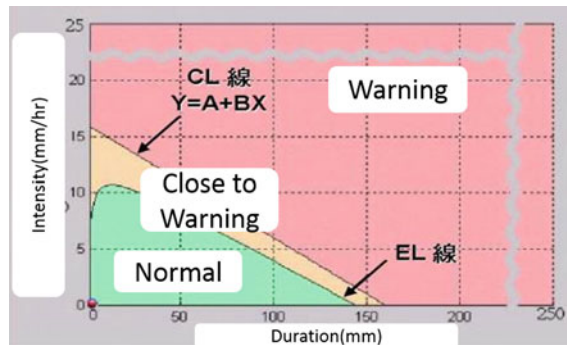


Fig. 2 Critical line for issuing a warning message of landslide or debris flow during heavy rainfall

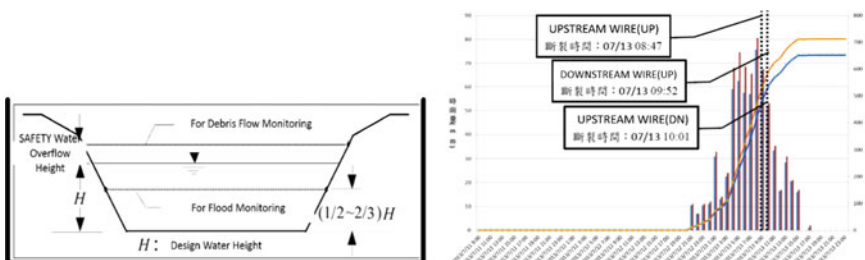


Fig. 3 Wire sensor placement illustration

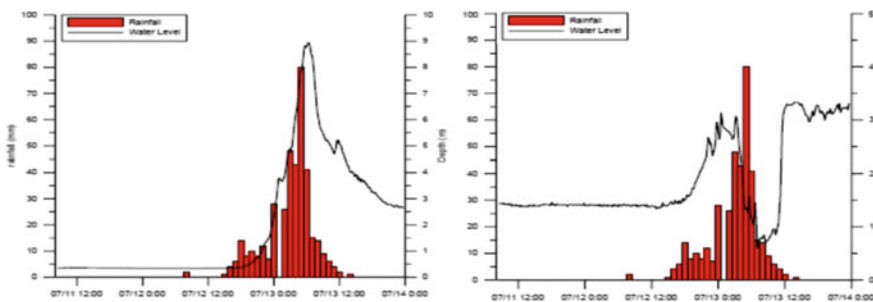


Fig. 4 Water level dropped at certain place of river might indicate the occurrence of landslide

8. Groundwater Level: This data is collected when a borehole is made in slope failure area and the data is normally conducted with borehole tilt amount and movement speed.
9. CCD image: This data is the most important proof for the occurrence of slope failures and debris flows.

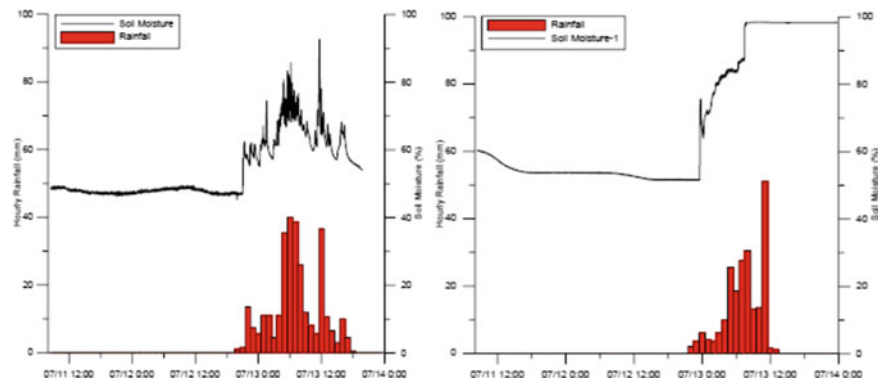


Fig. 5 Soil moisture at different area reaction

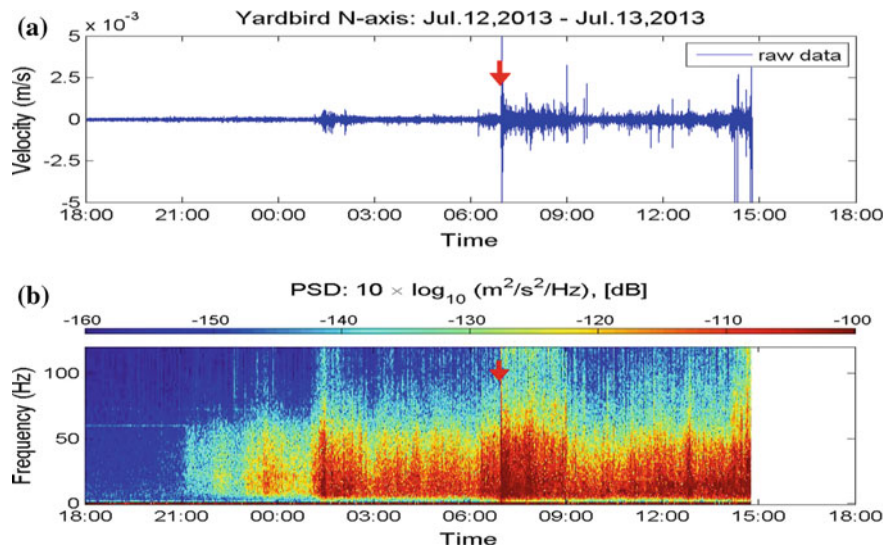


Fig. 6 Geophone data under typhoon debris flow event

Aforementioned slope soil observation instruments, including biaxial inclinometer, surface displacement meter, soil moisture meter, taking into account the water table, combined with rainfall hydrograph, can analyze the changes observed values for each observation instrument trend. However, the specific view of these observations and the slope of the department of slope stability (or stability) between, we must continue to accumulate more information and experience, in order to establish the value of assets can alert management applied. When the event ends, the relevant information about statistical analysis stage of the event must be observed not only can accumulate in the sediment observation stations where

sediment catchment evolution trends, and experience will also help future decision-making contingency event occurs. But consider the incident, the communication data transfer operations or omissions circumstances may occur, so before making observations statistical analysis must be downloaded on the observational data, time alignment, Addendum and correction, classification, storage and archiving, etc., the work.

3 Correlation Analysis of the Observational Data

In addition to in situ imaging (i.e., visual class), other equipment can be divided into pre-sediment disasters (i.e., predicted class) and after the occurrence (i.e., analysis class) of observation instruments; so the observation instrument between the observations should be certain that the correlation can interpret relevant information between various observations and sediment disaster by checking calculation and analysis in order to enhance the efficiency of the alert notification of changes in the sediment during the flood. Figures 6, 7 and 8 for the observation and analysis instruments in predicting debris flow correlation can be divided into the slope and sediment transport in the two types of debris flow dynamics, hereby comprehensive analysis below (SWCB 2013c).

4 Monitoring Site Introduction

Under consideration of past disaster distribution and local landscape features, we selected Han-Si as our monitoring site. Han-Si is located at the northeast part of Taiwan, located in Da-Tung district of Yi-Lan County. The averaged accumulated

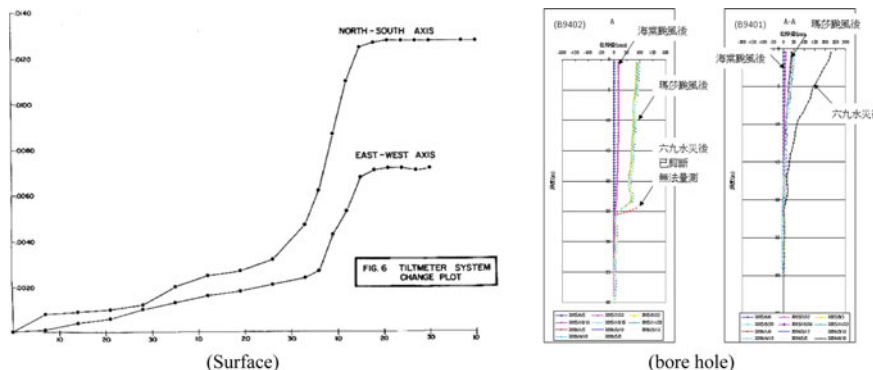


Fig. 7 Tilt meter placement result the right hand side is the monitored results of inclinometers

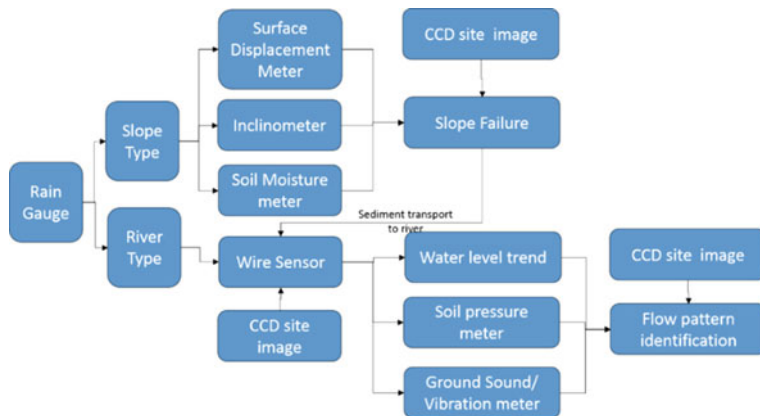


Fig. 8 Sediment observation stations (network-based) figures observation instruments and landslides occurred forecasts and judgments of the association graph functions and observation instruments and relationships



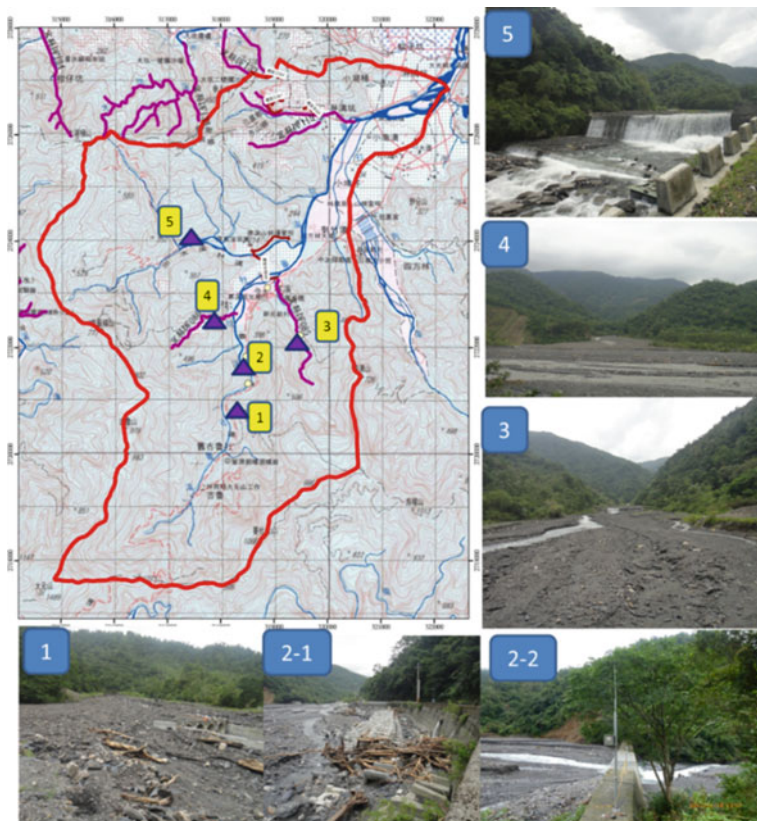


Fig. 10 Monitoring site picture

Another site is Lai-Yi, located in Ping-Dong County, southern Taiwan, which suffered from large amount of sediments and flooding during Typhoon Morakot in 2009. Landslides were continuously monitored to prevent sediment disaster against Lai-Yi east village.

Each site has different detecting instruments, including rain gauge, water leveler, soil moisture sensor, ground vibration sensor, wire sensor, and also CCD camera. The instruments are all linked to individual wireless transmitter. The data are collected at a merge point shown in Fig. 10. The purpose is to monitor the hazard input source, such as landslide origin and structure reaction during heavy rainfall. In Fig. 5, different instruments are wireless connected at distributed hazardous sites and these efficient devices are all powered by solar plates and batteries (Fig. 11).



Fig. 11 LaiYi monitoring site

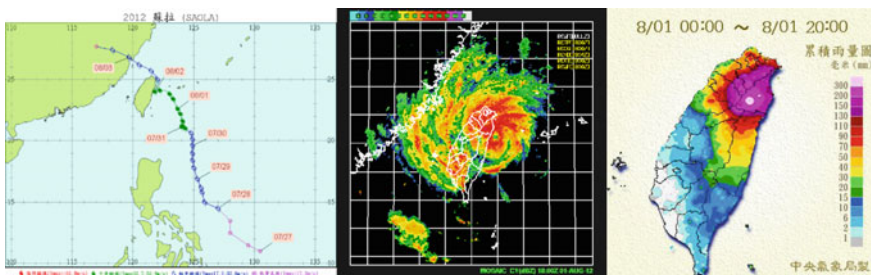


Fig. 12 Typhoon Sao-la route and satellite and rainfall graphic image

5 Event Monitor Result

During July 31 to August 2, typhoon Sao-la struck northeast Taiwan and brought heavy rainfall, especially in Yilan county (Fig. 12). The typhoon brought heavy rainfall and induced huge disaster in this area, including landslide and debris flow and also flooding. From rain gauge monitor shown in Fig. 13, maximum 1 h

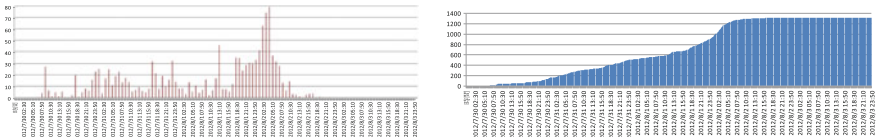


Fig. 13 Rainfall amount during typhoon Sao-la at Han-Si monitoring site

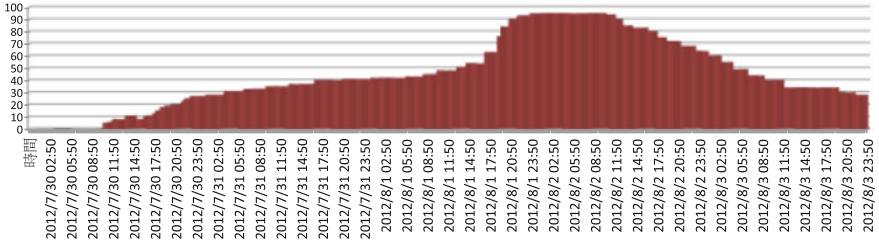


Fig. 14 Soil moisture changes during typhoon Sao-la at Han-Si monitoring site

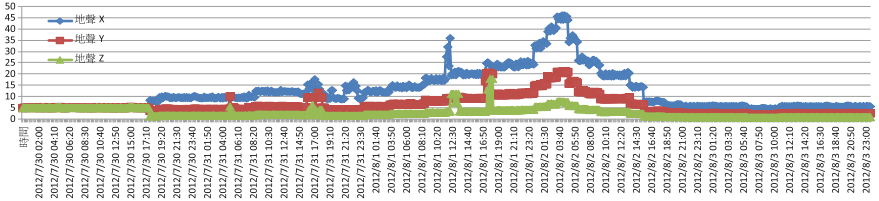


Fig. 15 3D ground vibration limit changes during typhoon Sao-la at Han-Si monitoring site

rainfall is 80 mm/h, 10 min maximum rainfall is 16 mm, total rainfall for three days is 1320 mm, almost one-third of year precipitation. In Fig. 14, the soil moisture attained 93 % around 9 pm on August 1, just before the occurrence of debris flow at around 2:30 a.m., August 2. Figure 15 shows that the largest ground vibration occurred at around 2:30 a.m., August 2. Before the debris flow event, at around 10:30, August 1, the landslide might have occurred. After rainfall accumulated, the debris started moving at 4:30 a.m.

Another tool for site monitoring is UAV. The pre- and post-event DTM of the riverbed and slope can be collected and analyzed. The results are illustrated in Fig. 16. Using simulation model such as CCHE-2D, the sediment dredging and transport can be reproduced.

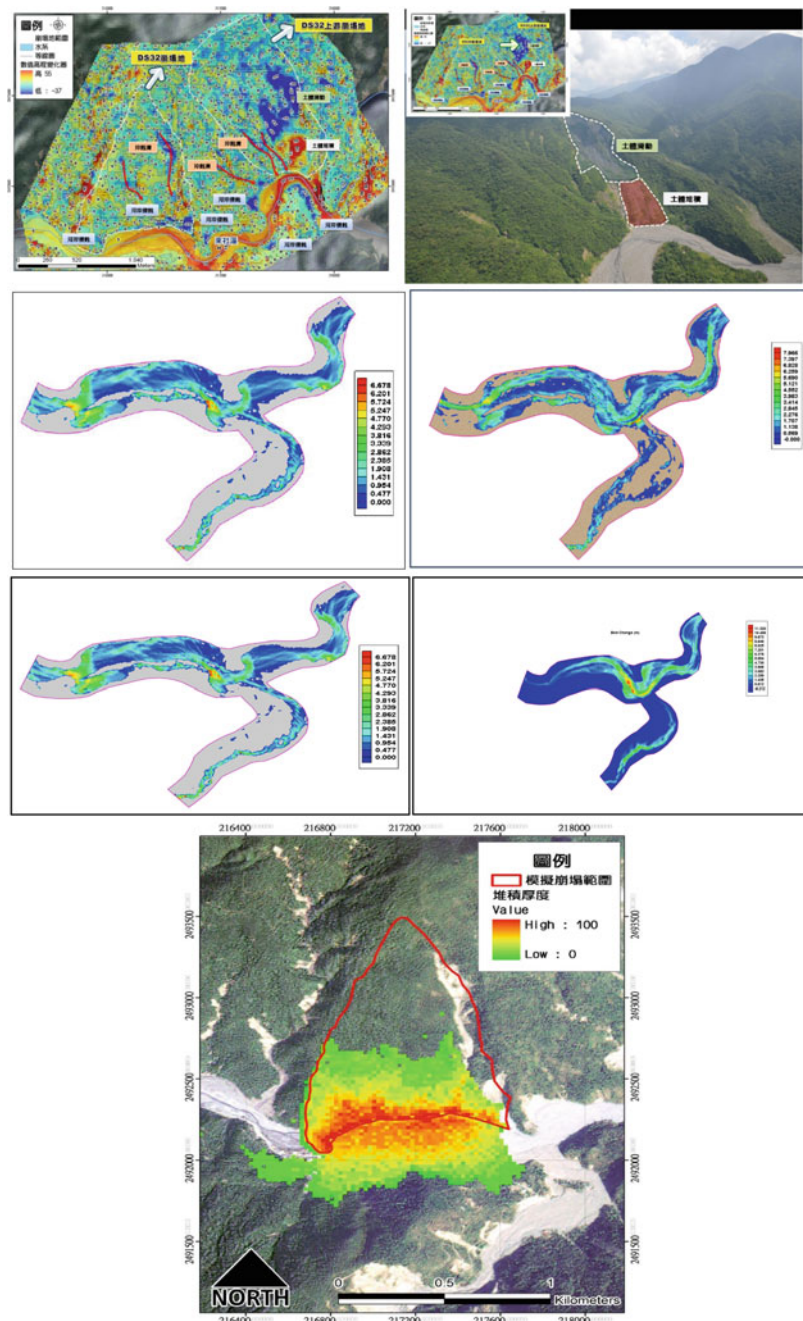


Fig. 16 Lai-Yi riverbed simulation using CCHE2D and the comparison to the results derived from the pre- and post-event DTMs made by UAV

6 Conclusion

From different wireless monitoring instruments distributed in the monitor site, we can gain more temporal and spatial information related to the hazardous phenomena. Therefore, during certain hazard event, we can earn more time for self-saving. The issuing of warning messages becomes reliable. In addition, the hazard mitigation measures can be correctly established.

References

- SWCB (2013a) Dredging operations project management plan of Tainan Branch of Soil and Water Conservation Bureau, SWCB-102-221, pp 1–472
- SWCB (2013b) LaiYi large scale landslide potential area field investigation and monitoring project, SWCB-103-028, pp 1–284
- SWCB (2013c) Yilan Hansi and Miaoli HoYanSan sediment observation and maintain research, SWCB-103-017, pp 1–274

Seismic Performance of Piles from EQWEAP and Monte Carlo Simulation Analyses

D.W. Chang, Y.H. Lin, C.H. Liu, S.C. Chu and H.C. Chao

Abstract This paper discusses the seismic performance-based design (PBD) analysis on piles using one-dimensional stress wave equation and Monte Carlo Simulation. Seismic responses of the piles were monitored at a wider spectrum of earthquake intensities rather than the target ones. To obtain appropriate estimations, weights of the intensities were calculated from the probability density function determined from the seismic hazard curve. Probabilities of failure of the piles were evaluated for uncertainties of soil parameters and seismic records, and then calibrated with the weights. The result of the numerical study indicates that the seismic force is the most dominant factor. Large diameter pile sometimes exerts cracks around pile head under moderate earthquakes. Therefore, the assessment would become very critical in that case. For design and maximum consideration (MCE) earthquakes, the piles were found satisfied because of performance based on ductility resistance and ultimate moment capacity. Probabilities of failure of the piles were also found sensitive to horizontal load from the superstructure. Comparing the correspondent reliability indexes with those required for acceptable foundations, the seismic performance of the piles can be assessed. With the suggested factor of safety, the seismic performance of the piles was found to be greater than 2.0 for design and MCE quakes in this study.

Keywords Performance based seismic design · Piles · EQWEAP analysis · Reliability approach

D.W. Chang (✉) · Y.H. Lin · C.H. Liu · S.C. Chu
Tamkang University, New Taipei, Taiwan
e-mail: dwchang@mail.tku.edu.tw

H.C. Chao
Moh and Associates, Inc., New Taipei, Taiwan

1 Seismic PBD of Piles

For any geotechnical structure, Honjo et al. (2002) suggested that the PBD analysis can be conducted using (1) LRFD method, (2) reliability method, and (3) probability method. Applications of the first two methods were frequently adopted on pile foundations. Performance of the piles at both ordinary and seismic conditions can be evaluated. For the seismic investigations, usually the target PGAs from the design code were considered. The uncertainties are mostly related to seismic records, soil parameters, and spatial variability. Reliability methods such as first-order second moment (FOSM), first-order reliability method (FORM), and Monte Carlo Simulation (MCS) can be adopted to estimate the probability of failure and reliability index of the pile.

For probability-based method, the so called PBEE (Performance-Based Earthquake Engineering) analysis suggested by US Pacific Earthquake Engineering Research Center (PEER) is referable. Such analysis has been conducted by research teams on NEES project with 3D FEM program-OpenSees (2009). Excellent overview of the PBEE analysis can be found in Kramer (2008). It suggests that the annual rate of exceedance (λ) for a decision variable (DV) on any engineering structure can be analyzed as a triple-integral on probabilities of intensity measured (IM), engineering demand parameter (EDP), and the damage measure (DM). For seismic hazard curve in hand, the integral is able to be decomposed in finding the annual rate of exceedance for EDP, DM, and DV, respectively. Based on log-normal distributions, analytical expressions of this rate exceedance for EDP, DM, and DV can be found. Simplified methods to compute the statistics of the data were suggested. This approach can ideally include all possible earthquake influences with the uncertainties of soil parameters and spatial variability. According to Shin (2007), the effects of the uncertainties of seismic forces are much larger than those from soil parameters and spatial variability. The record-to-record uncertainty was found to be 90–95 % of the total uncertainty involved in the seismic assessment.

From the stress and deformation analysis of the structure, the piles can be monitored using either static (or pseudo-static) or dynamic analysis. While the former is easier to conduct, the latter requires longer computation time and pre-processing. In order to reduce the time for dynamic computations, a rather fast solution EQWEAP was suggested by Chang et al. (2006, 2008). It solves the free-field ground responses (with the lumped mass analysis) and using them to obtain the corresponding pile deformations from 1D wave equations. With such solution, the PBD analysis based on dynamic modeling becomes more applicable. Details of the EQWEAP analysis can be found in Chang et al. (2014a). This solution was found agreeable with 2D and 3D FEM analyses using PLAXIS (2012) and Midas-GTS (2012) with simple geometry conditions.

The EQWEAP analysis has been combined with the PBEE procedures in evaluating the seismic performance of piles in Taipei (Chang et al. 2010). The dynamic impacts of the ground motions can be monitored through this solution.

According to the local design code, seismic level-I, -II, and -III required for moderate earthquake, design earthquake and the maximum consideration earthquake (MCE), respectively, were considered. For 50-year design life, the corresponding probabilities of the occurrence of these quakes are 80, 10, and 2 %, whereas the seismic return periods are 30, 475, and 2500 years. Cheng (2002) suggested that the corresponding target PGA_t at these seismic levels in Taipei could be 0.12, 0.29, and 0.51g.

With the target PGA_t and acceleration records from nearby stations, seismic PBD on bridge-piles ($D = 2$ m and $L = 60$ m) of an expressway at the Sin-Jhuang District in Taipei was analyzed by Chang and Lee (2013) and Chang et al. (2013). Tri-linear moment-curvature relationship of the concrete pile was suggested based on the approximate Bouc-Wen model. To keep the piles remain elastic at moderate earthquakes, the maximum bending moment (M_{max}) needs to be less than M_{cr} , at which the concrete starts to crack. For design EQ, M_{max} should be less than M_y , where the steel bar starts to yield. For MCE quakes, the ultimate moment, M_{ult} in which the plastic hinge occurs must not be exceeded. By analyzing experimental data or results from analytical computations, one can apply the model equation to compute model parameters α and Z for the line-segments and then find out the correspondent secant stiffness, EI for the use of nonlinear analysis.

By taking the internal moments of pile as DM and comparing it with these moment capacities (i.e., M_{cr} , M_y , and M_{ult}), the engineers can evaluate the seismic PBD of piles. Figure 1a, b reveals the result for seismic assessments of the piles in Taipei Basin (details of the site conditions and pile foundation are described in following paragraphs). In Fig. 1b, the maximum absolute pile displacements (solid points in dash curve) found at the pile head are about 20, 50, and 80 cm, respectively, for moderate, design and MCE quakes. In Fig. 1a, comparing the maximum pile moments (solid point in dash line) with the moment capacities shows that the seismic level-I is difficult to satisfy since the predicted maximum bending moment at the pile head will exceed

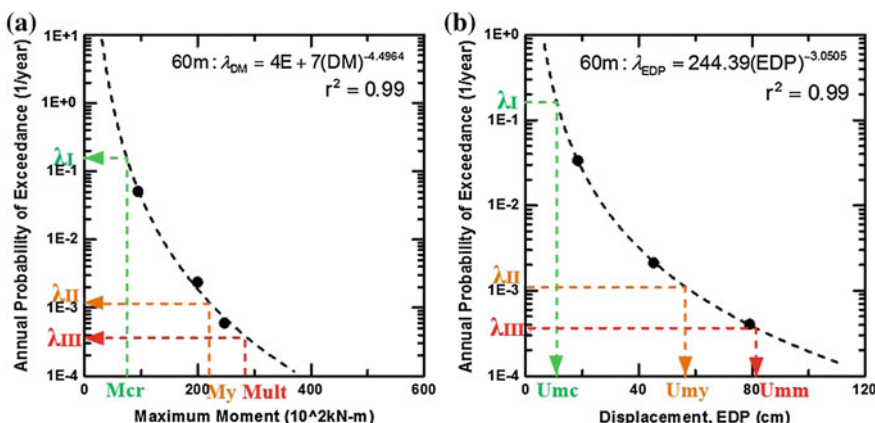


Fig. 1 Annual rate of exceedance for **a** the maximum displacements and **b** bending moments of the piles

M_{cr} at moderate earthquakes. On the other hand, matching the requirements for design and MCE quakes are relatively easier providing that M_{cr} and M_{ult} of the pile are carefully estimated. The engineers can also use these figures to find the allowable pile displacements under different seismic levels, i.e., U_{mc} , U_{my} , and U_{mm} . A factor of safety (FS_p) for seismic performance of the piles from PBEE analysis can be suggested as the ratios of the moment capacities divided by the maximum moments obtained from the PBEE procedures, i.e., M_{cr}/M_{max} , M_y/M_{max} , and M_{ult}/M_{max} . Chang et al. (2014b) have reported that the piles located at Taipei could be greater than 1.1 with the concerns of design and MCE quakes.

2 Monte Carlo Simulations

On the other hand, one can simply conduct Reliability analysis for structural responses at the target PGAs from probability seismic hazard analysis (PSHA), the results are generally acceptable in engineering practice. Such approach is often followed by LRFD and other type of design methods. In general, the seismic influences of the earthquakes are only focusing on few target intensities. However, in considering the design life of the structure, it will be more objective to include all quake influences rather than a few ones. With such concern, the influences of every PGAs should be found. The annual rate of exceedance, λ of any PGA is subtracted from 1.0 in order to obtain the probability of occurrence for any intensity less than or equal to that PGA during the design life, i.e., the cumulated density function (CDF). The probability density function (PDF) of the PGAs can be computed by differentiating CDF. For the seismic intensities from “not noticeable to person” to “danger to structure,” one can thus compute the weights of these intensities and use them to calibrate the corresponding probability of failure for the structure. The probability of failure is strongly dependent on the performance requirement at arbitrary seismic level. Using the central difference formulas, the weights of every possible PGA can be calculated from the PDF as follows:

$$P_A(a) = \frac{d}{da} F_A(a) = \frac{d}{da} (|1 - R_A(a)|) = \frac{dR_A(a)}{da} \quad (1)$$

where $P_A(a)$ is the probability density function, F_A is the cumulated density function, $R_A(a)$ is the function of seismic hazard curve, and a is the variable of intensity measure. Table 1 lists the weights for PGAs from seismic hazard curve in Taipei (Chang et al. 2014b).

The accuracy of Monte Carlo Simulation (MCS) depends on the number of simulations considered. For seismic intensities between 0.01 and 0.51g, an increment of 0.01g is used. Totally 51 intensities (PGAs) were analyzed for the uncertainties of seismic forces. Alternative methods to produce the seismic records for the structural response analysis have been discussed by Kramer (1996). For simplicity, the acceleration time history recorded at a nearby seismic station can be

Table 1 Calculated weights of the intensities for PGAs in between 0.01 and 0.51g

| PGA (g) | Return period (year) | λ (%) | Probability of occurrence for $a > \text{PGA}$ | Probability of occurrence for $a \leq \text{PGA}$ | Numerator of the central difference formula | Weights |
|------------|----------------------------|---------------|--|---|---|----------|
| 0.01 | 1 | 100.00 | 1.0 | 0.000 | 5.00E-03 | 2.50E-03 |
| 0.02 | 1.005 | 99.50 | 0.995 | 0.005 | 1.00E-02 | 5.00E-03 |
| 0.03 | 1.01 | 99.00 | 0.99 | 0.010 | 4.95E-01 | 2.48E-01 |
| 0.04 | 2 | 50.00 | 0.50 | 0.500 | 7.50E-01 | 3.75E-01 |
| 0.05 | 4 | 25.00 | 0.250 | 0.750 | 3.33E-01 | 1.67E-01 |
| 0.06 | 6 | 16.67 | 0.167 | 0.833 | 1.25E-01 | 6.25E-02 |
| 0.07 | 8 | 12.50 | 0.125 | 0.875 | 6.67E-02 | 3.33E-02 |
| 0.08 | 10 | 10.00 | 0.100 | 0.900 | 5.36E-02 | 2.68E-02 |
| 0.09 | 14 | 7.14 | 0.071 | 0.929 | 5.00E-02 | 2.50E-02 |
| 0.10 | 20 | 5.00 | 0.050 | 0.950 | 2.98E-02 | 1.49E-02 |
| 0.11 | 24 | 4.17 | 0.042 | 0.958 | 1.67E-02 | 8.33E-03 |
| 0.12 | 30 | 3.33 | 0.033 | 0.967 | 1.31E-02 | 6.55E-03 |
| 0.13 | 35 | 2.86 | 0.029 | 0.971 | 9.52E-03 | 4.76E-03 |
| 0.14 | 42 | 2.38 | 0.024 | 0.976 | 8.57E-03 | 4.29E-03 |
| 0.15 | 50 | 2.00 | 0.020 | 0.980 | 7.42E-03 | 3.71E-03 |
| 0.16 | 61 | 1.60 | 0.016 | 0.984 | 6.11E-03 | 3.06E-03 |
| 0.17 | 72 | 1.40 | 0.014 | 0.986 | 5.03E-03 | 2.51E-03 |
| 0.18 | 88 | 1.14 | 0.0114 | 0.9886 | 3.89E-03 | 1.94E-03 |
| 0.19 | 100 | 1.00 | 0.0100 | 0.990 | 3.36E-03 | 1.68E-03 |
| 0.20 | 125 | 0.80 | 0.0080 | 0.992 | 3.01E-03 | 1.50E-03 |
| 0.21 | 143 | 0.70 | 0.0070 | 0.993 | 1.90E-03 | 9.51E-04 |
| 0.22 | 164 | 0.61 | 0.0061 | 0.9939 | 1.73E-03 | 8.65E-04 |
| 0.23 | 190 | 0.53 | 0.0053 | 0.9947 | 1.57E-03 | 7.86E-04 |
| 0.24 | 221 | 0.45 | 0.0045 | 0.9955 | 1.29E-03 | 6.47E-04 |
| 0.25 | 252 | 0.40 | 0.0040 | 0.996 | 1.03E-03 | 5.14E-04 |
| 0.26 | 286 | 0.35 | 0.0035 | 0.9965 | 9.65E-04 | 4.83E-04 |
| 0.27 | 333 | 0.30 | 0.003 | 0.997 | 9.33E-04 | 4.66E-04 |
| 0.28 | 390 | 0.26 | 0.0026 | 0.9974 | 8.98E-04 | 4.49E-04 |
| 0.29 | 475 | 0.21 | 0.0021 | 0.9979 | 5.64E-04 | 2.82E-04 |
| 0.30 | 500 | 0.20 | 0.002 | 0.998 | 2.30E-04 | 1.15E-04 |
| 0.31 | 533 | 0.19 | 0.0019 | 0.9981 | 2.61E-04 | 1.30E-04 |
| 0.32 | 575 | 0.17 | 0.0017 | 0.9983 | 2.50E-04 | 1.25E-04 |
| 0.33 | 615 | 0.16 | 0.0016 | 0.9984 | 3.19E-04 | 1.59E-04 |
| 0.34 | 704 | 0.14 | 0.0014 | 0.9986 | 3.75E-04 | 1.87E-04 |
| 0.35 | 800 | 0.13 | 0.0013 | 0.9987 | 2.80E-04 | 1.40E-04 |
| 0.36 | 877 | 0.11 | 0.0011 | 0.9989 | 2.50E-04 | 1.25E-04 |
| 0.37 | 1000 | 0.10 | 0.0010 | 0.999 | 2.05E-04 | 1.02E-04 |

(continued)

Table 1 (continued)

| PGA (g) | Return period (year) | λ (%) | Probability of occurrence for $a > \text{PGA}$ | Probability of occurrence for $a \leq \text{PGA}$ | Numerator of the central difference formula | Weights |
|------------|----------------------------|---------------|--|---|---|----------|
| 0.38 | 1069 | 0.09 | 0.0009 | 0.9991 | 1.43E-04 | 7.15E-05 |
| 0.39 | 1167 | 0.09 | 0.0009 | 0.9991 | 1.35E-04 | 6.77E-05 |
| 0.40 | 1250 | 0.08 | 0.0008 | 0.9992 | 1.29E-04 | 6.43E-05 |
| 0.41 | 1373 | 0.07 | 0.0007 | 0.9993 | 1.21E-04 | 6.05E-05 |
| 0.42 | 1473 | 0.07 | 0.0007 | 0.9993 | 1.17E-04 | 5.84E-05 |
| 0.43 | 1635 | 0.06 | 0.0006 | 0.9994 | 1.13E-04 | 5.66E-05 |
| 0.44 | 1767 | 0.06 | 0.0006 | 0.9994 | 9.16E-05 | 4.58E-05 |
| 0.45 | 1923 | 0.05 | 0.0005 | 0.9995 | 7.35E-05 | 3.68E-05 |
| 0.46 | 2031 | 0.05 | 0.0005 | 0.9995 | 5.85E-05 | 2.92E-05 |
| 0.47 | 2167 | 0.05 | 0.0005 | 0.9995 | 5.78E-05 | 2.89E-05 |
| 0.48 | 2301 | 0.04 | 0.0004 | 0.9996 | 5.39E-05 | 2.69E-05 |
| 0.49 | 2453 | 0.04 | 0.0004 | 0.9996 | 3.04E-05 | 1.52E-05 |
| 0.50 | 2475 | 0.04 | 0.0004 | 0.9996 | 7.69E-06 | 3.84E-06 |
| 0.51 | 2500 | 0.04 | 0.0004 | 0.9996 | 4.79E-05 | 2.39E-05 |

used to produce the bedrock motions with any target PGA (PGA_t). Varying with other variables (e.g., material parameters and geologic conditions), the database of MCS can be optimized. The total probabilities of failure, P_{FT} at different seismic levels (PGA_t) with the required performance can be computed summing up all the individual probabilities of failure at the PGAs less than and equal to the PGA_t .

$$P_{\text{FT}} \text{ at any } \text{PGA}_t = \sum P_{\text{fi}} \quad \text{where } \text{PGA} \leq \text{PGA}_t \quad (2)$$

Assuming that the probability densities of the maximum pile moments at the PGAs can be analyzed as normal or log-normal distributions, the reliability index, β of the MCS can be achieved. Note that β can be calculated by

$$\beta = \mu/\sigma \quad (3)$$

where μ is the mean value and σ is the standard deviation of the data.

3 Case Study

Numerical model of a bridge pile foundation at an expressway located in Sin-Jhuang district at New Taipei City is again studied. Based on the previous study by Chang and Lee (2013) and Chang et al. (2013), the acceleration records producing largest

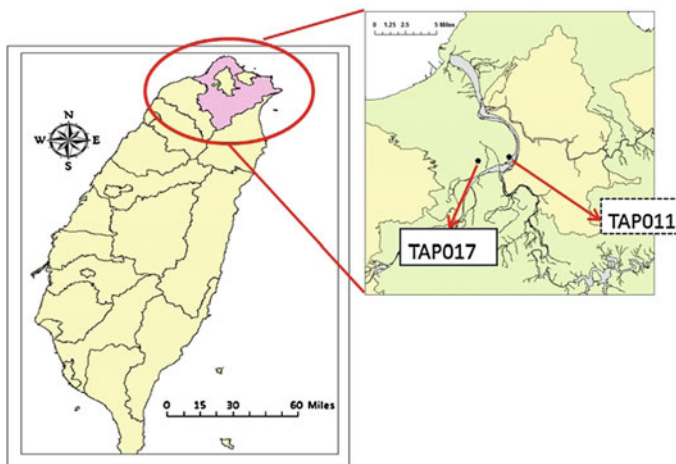


Fig. 2 Locations of seismic stations near the pile foundation site

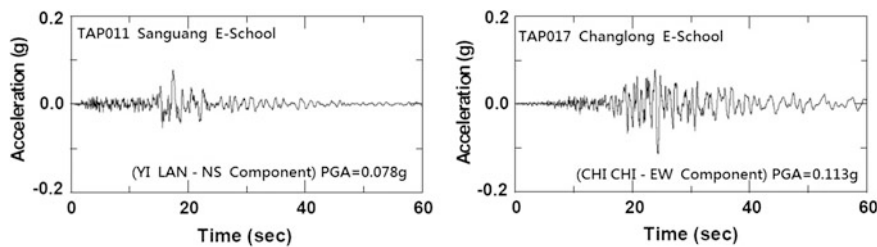


Fig. 3 Acceleration time history selected from stations TAP011 and TAP017

deformations and smallest deformations of the piles were selected. Records at stations TAP017 for 1999 Chi-Chi earthquake (in-land/active faulting triggered quake, $M_L = 7.3$) and at TAP011 for 2002 Yi-Lang earthquake (east coast offshore/subduction plate triggered quake, $M_L = 6.8$) were in use. Figures 2 and 3 show the locations and the acceleration time histories used. A typical 3×3 pile foundation with piles of 2 m diameter and 60 m length was investigated. The EI value of the pile is 2.4×10^4 MPa. Geological condition of the site is presumed based on in situ borehole data and representative studies. Table 2 shows the information of the ground site. According to the designer, the maximum vertical loads at the single piles were designed as 9MN and 18MN for ordinary and seismic cases. Horizontal loads were kept as 15 % of the maximum vertical loads. The moment capacities of M_{cr} , M_y , and M_{ult} were able to obtain from LPILE analysis. With 1.94 % reinforced bar ratio and 18MN vertical loads, M_{cr} , M_y , and M_{ult} were obtained as 7.35, 22.15, and 28.68 MN-m, respectively. Varying the unit weight, SPT- N value, friction angle, and cohesion of the layered soils with presumed averages and standard deviations (see Table 2), 5000 combinations of the soil layers were randomly generated. Varying 51 PGAs on two seismic records, the

Table 2 Geological condition and soil parameters for the numerical model of the site

| Depth (m) | H (m) | Soil layers | γ (kN/m ³) | | SPT-N | | ϕ (°) | | c (kPa) | | Vs (m/s) |
|-----------|-------|---------------|-------------------------------|----------|-------|----------|------------|----------|---------|----------|----------|
| | | | Avg. | σ | Avg. | σ | Avg. | σ | Avg. | σ | |
| 0–4 | 4 | Surface fill | 18.0 | 1.5 | 3 | 1 | 30 | 1 | – | – | 115 |
| 4–10 | 6 | SS-IV (ML) | 18.5 | 0.7 | 5 | 1 | 6 | 1 | 7 | 1 | 171 |
| 10–20 | 10 | SS-V (SM) | 18.9 | 1.3 | 14 | 3 | 34 | 2 | – | – | 192 |
| 20–40 | 20 | SS-IV (CL-ML) | 18.8 | 1 | 11 | 2 | 14 | 1 | 5 | 1 | 222 |
| 40–50 | 10 | SS-III (SM) | 18.6 | 0.9 | 21 | 4 | 34 | 2 | – | – | 221 |
| 50–60 | 10 | SS-II (CL-ML) | 19.0 | 0.7 | 14 | 2 | 21 | 1 | 6 | 1 | 241 |
| 60–70 | 10 | SS-I (SM) | 19.3 | 0.7 | 30 | 4 | 42 | 1 | – | – | 248 |

Note SS means Songshan formation

total number of simulations is 5.1×10^5 . Note that according to the local seismic design code for seismic level-I, -II, and -III, the performance functions depend on M_{cr} , M_y , and M_{ult} respectively. The EQWEAP analysis is efficient to provide fast solutions within limited time period. The probability of failure, P_f is defined as the ratio of number for cases at failure ($M_{max} \geq M_{cr}$ or $\geq M_y$ or $\geq M_{ult}$) divided by the total number of cases. The reliability indexes, β are computed accordingly.

Detailed results for the probabilities of failure at each PGA from EQWEAP analysis can be found in Chang et al. (2014b). Note that the static horizontal load from the superstructure is defined as F_H . Calculating the probabilities of failure, P_f at every PGA and multiplying them with the weights, the calibrated P_f can be obtained. Summation of the calibrated P_f up to the target PGA_t gives the total probability of failure, P_{fT} at different seismic levels. It can be obviously seen that the horizontal structural load is very significant to the results. For F_H applied statically, the failures will increase dramatically. If no static horizontal force is considered, then the predictions will become much safe. The effects of soil parameters varying the number of simulations at each PGA (only the soil parameters were changed) were studied and it was found that the effects of soil parameters are relatively insignificant compared to PGAs (Chang et al. 2014b).

Following the assumptions of log-normal distribution, the corresponding reliability indexes, β can be calculated. Reliability indexes for seismic performance of the numerical piles were found between 2.8 and 5 under design earthquake and MCE quakes. Following the foundation performance and reliability index of 2.3 suggested by Whitman (1984), the piles are acceptable for the seismic design requirements. However, for moderate earthquake concern, the reliability indexes were found less than 2, which is unacceptable to the design. This is attributed to the fixed-head condition of piles and the static load applied at the pile head.

Similarly, the factor of safety (FS_R) for seismic performance of the piles from Reliability analysis can be suggested as the ratio of computed reliability index divided by reliability index required β_r , i.e., $\beta_{moderate\ EQ}/\beta_r$, $\beta_{design\ EQ}/\beta_r$, and β_{MCE}/β_r . The FS_R of the example study is summarized in Table 3. It can be found that the factors of safety calculated from reliability method using MCS approach showed

Table 3 Factor of safety for seismic performance of the numerical piles

| Method | Factor of safety, FS_P and FS_R | | |
|------------------|--|---|---|
| | Moderate EQ | Design EQ | MCE quakes |
| MCS w/o F_H | 0.696 ($\leq 0.12g$) and 1.08 @ 0.12g | 2.17 ($\leq 0.29g$) and 2.17 @ 0.29g | 2.17 ($\leq 0.51g$) and 2.1 @ 0.51g |
| MCS w F_H | 0.43 ($\leq 0.12g$) and 1.08 @ 0.12g | 1.17 ($\leq 0.29g$) and 1.6 @ 0.29g | 1.79 ($\leq 0.51g$) and 2.08 @ 0.51g |

Note β_R is kept as 2.3 according to the suggestion of Whitman (1984)

that the assessment for moderate EQs were too conservative by only checking the damages at the pile head and taking the horizontal structural loads as a static one. The minimum safety factor of the seismic PBD of the piles can be accordingly made at various design levels. In this case, a factor of safety on the order of 2.0+ of the seismic PBD on piles under design and MCE quakes can be obtained.

4 Summary and Conclusions

For seismic level-I corresponding to the moderate earthquakes, the piles were found very critical due to large bending moment encountered at the pile head with fixed-head connection. Although the most part of shaft remains elastic, the occurrence of the cracks at pile head would fail the assessment. For design earthquake with seismic level-II concern, the piles of the numerical model can sustain the seismic forces and remain under ductility resistance (M_y). For level-III concern under the maximum consideration earthquake, it is found that the internal moments can be controlled under the ultimate moment capacity (M_{ult}). Calibrating the probabilities of failure under the intensities smaller than PGA_t and summing them up, the total probability of failure, P_{ff} at that PGA_t can be found. In this study, P_{ff} were reported as 0.054 % (96.9 %), 0.0 (0.343 %), and 0.0 (0.002 %) for moderate, design and MCE seismic levels without (or with) the static horizontal superstructural load. The foundation performance for design and MCE concerns were found acceptable based on the suggestion of Whitman (1984). Again, the assessment on seismic level-I will lead to a critical result. The factor of safety (FS) for seismic PBD of the piles was suggested based on the ratios of reliability indexes. It can be found greater than 2.0 for the numerical piles under design and MCE quakes. The results seem to be more optimistic than those suggested by PBEE analysis.

References

Chang DW, Lee SM (2013) Performance based design of piles due seismic ground motions. In: Proceedings of international symposium on safety of foundation engineering (ISAFE), Singapore, December 5–6, pp 313–316

Chang DW, Lin BS (2006) EQWEAP~a simplified procedure to analyze dynamic pile-soil interaction with soil liquefaction concerns. In: Proceedings of second Taiwan-Japan joint workshop on geotechnical hazards from large earthquake and heavy rainfall, Nagaoka, Japan, May, pp 155–162

Chang DW, Cheng SH, Lin BS (2008) Discrete wave equation analysis for seismic responses of piles. In: Proceedings of stress wave 2008—8th international conference on the application of stress wave theory to piles, Lisbon, Portugal, September, pp 285–292

Chang DW, Yang TY, Yang CL (2010) Seismic performance of piles from PBEE and EQWEAP analyses. *Geotech Eng J SEAGS-AGSSEA* 41(2):79–86

Chang DW, Sung SH, Lee SM, Zhussupbekov A, Saparbek E (2013) On seismic performance and load capacities for pile design. In: Proceedings of 18ICSMGE, Paris, France, September 2–6, pp 1455–1458

Chang DW, Cheng SH, Wang YL (2014a) One-dimensional wave equation analyses for pile responses subjected to seismic horizontal ground motions. *Soils Found* 54(3):313–328

Chang DW, Lin YH, Chao HC, Chu SC, Liu CH (2014b) Seismic PBD on piles from Monte-Carlo simulation using EQWEAP analysis and weighted intensities. *Geotech Eng J SEAGS-AGSSEA*, 45(2):62–69

Cheng CT (2002) Uncertainty analysis and deaggregation of seismic hazard in Taiwan, PhD thesis, Department of Earth Science and Institute of Geophysics, National Central University, Chung-Li, Taiwan

Honjo Y, Kusakabe O, Matsui K, Kouda M, Pokhard G (2002) Foundation design codes and soil investigation in view of international harmonization and performance based design, IWS Kamakura. A.A. Balkema Publishers, 457 pp

Kramer SL (1996) Geotechnical earthquake engineering. Prentice Hall

Kramer SL (2008) Performance-based earthquake engineering: opportunities and implications for geotechnical engineering practice. *Geotechnical earthquake engineering and soil dynamics*, vol IV. ASCE GSP, p 181

OpenSees (2009) OpenSees 2.4.3. Download website: <http://opensees.berkeley.edu/>

Shin HS (2007) Numerical modeling of a bridge system and its application for performance-based earthquake engineering. PhD thesis, Department of Civil and Environmental Engineering, University of Washington

Whitman RV (1984) Evaluating calculated risk in geotechnical engineering. *J Geotech Eng ASCE* 110(2):145–188

The Overflow Model Experiment Using the Waterway for Examining the Countermeasure Effect Against the Tsunami-Induced Tide Embankment Scouring

**Tomohiro Mori, Hiroaki Kabuki, Motoki Kazama, Peter K. Hutapea,
Jongkwan Kim, Ryuji Sakamoto and Koujirou Takao**

Abstract In this study, the anti-erosion effect of the countermeasure and the erosion extent were considered using the model canal and the model soil ground when the concrete panel with nailing and cement development soil were used as the countermeasure. As the result, the following knowledge were obtained: (1) The erosion depth and extent of the landside ground of the tide embankment decreased markedly due to placing the countermeasure at the landside toe of the tide embankment. (2) The concrete panel with nailing and the cement development soil as the countermeasure had the similar anti-erosion performance. (3) Collapse of the tide embankment due to the Tsunami overflow was caused by the erosion of the landside foundation and the water permeation to the inside of the tide embankment from the seaside.

Keywords Scouring · Tide embankment · Tsunami · Model experiment

1 Introduction

When the tide embankment which suffered damage from Tsunami of the 2011 East Japan Great Earthquake is restored, the tough structure which can resist tenaciously is expected, even when the designed Tsunami height is exceeded. NILIM (National Institute for Land and Infrastructure Management, Japan) examined the tough tide embankment structure for Tsunami overflow, and showed the experimental result in

T. Mori (✉) · H. Kabuki · M. Kazama · P.K. Hutapea · J. Kim
Department of Civil and Environmental Engineering, Graduate School of Engineering,
Tohoku University, 6-6-06, Aramaki, Aoba-ku, Sendai, Miyagi 980-8579, Japan
e-mail: mori@soil1.civil.tohoku.ac.jp

R. Sakamoto · K. Takao
Hirose Co., LTD., Reinforced Earth Division, Tokyo, Japan

which the soil improvement was installed in the toe of back slope of tide embankment as a scouring countermeasure (Kato et al. 2012, 2013). On the other hand, the soil nailing is often applied as an alternative method of soil improvement in the field of reinforced soil. In this study, the overflow and scouring experiments which used the model canal and model embankment were performed to examine the effectiveness of soil nailing method, and the influence of the variation of countermeasure upon the scouring process was studied.

2 Testing Methods

2.1 Model Embankment and Countermeasures

The model embankment was made imitating the embankment shape which was adopted as the actual tide embankment with countermeasure at the coastal area of Tohoku District. The size of model embankment was 1/25 of the actual one. The model diagram of the model embankment, ground, and canal is shown in Fig. 1. The two types of embankment, the fixed embankment and the sand embankment, were used in this model experiment. The soil improvement and the soil nailing were installed in the toe of back slope as the anti-scouring countermeasure. The four concrete blocks 5 cm in length, 15 cm in width, and 17 cm in depth were used as a substitute of soil improvement. And the hollow aluminum pipe 5 mm in diameter, 1 mm in thickness, and 17 cm in length was used as the model pile of soil nailing, and the concrete panel was set at the head of model pile (refer to Photo 1). The sand particles were bonded to the pile surface, and the roughness was progressed, for imitating an actual pile of soil nailing.

The “Watari sand,” it was deposited soil by Tsunami and picked in coastal area of Watari town, Miyagi prefecture, was used for the sand embankment and the model ground. The soil compaction was performed into the portion of Watari sand, and the dry density of Watari sand was unified into 1.59 g/cm^3 (the relative density was 63.3 % and the degree of compaction was 93.5 %). The soil property of Watari sand, the grain size accumulation curve of Watari sand, and the compaction curve of Watari sand are shown in Table 1; Figs. 2 and 3, respectively. The mean diameter of Watari sand was 0.42 mm. The overflow depth of



Fig. 1 The size of the model embankment, the ground, and the canal

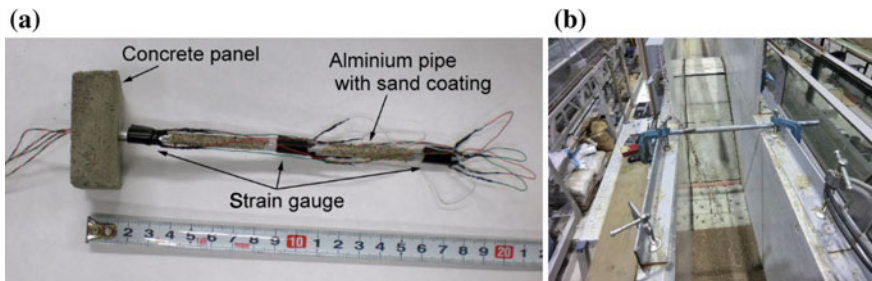


Photo 1 **a** The model pile and concrete panel. **b** The covering panel and the pile with concrete panel

Table 1 The soil property of Watari sand

| Soil particle density (g/cm ³) | Max. dry density (g/cm ³) | Optimum moisture content (%) | Coefficient of permeability (m/s) |
|--|---------------------------------------|------------------------------|---|
| 2.596 | 1.67 | 15.0 | $5.5-7.0 \times 10^{-5}$ |
| – | Compaction: A-a method | – | Compaction: A-a method $w = 15.0 \%$, $\rho_d = 1.59 \text{ g/cm}^3$ |

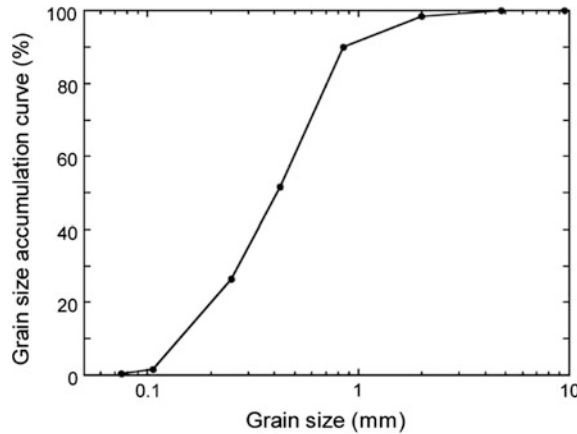


Fig. 2 The grain size accumulation curve of Watari sand

model Tsunami was set to 8.6 cm at the top of slope on the upper stream side. The average velocity of waterflow at the center of back slope during the experiment was 1.62 m/s. The nine cases of experiment were performed changing the kind of embankment and countermeasure. The model diagrams of each experiment case are shown in Fig. 4.

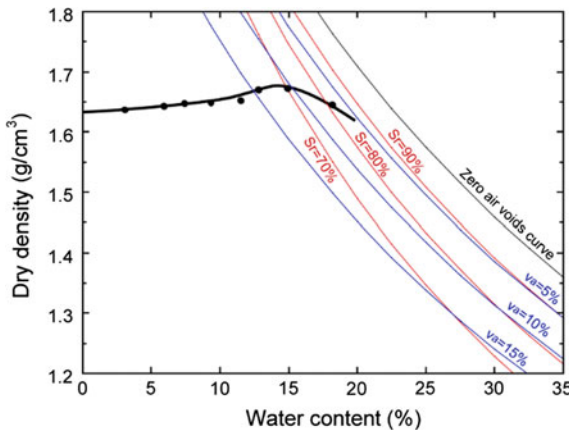


Fig. 3 The soil compaction curve of Watari sand

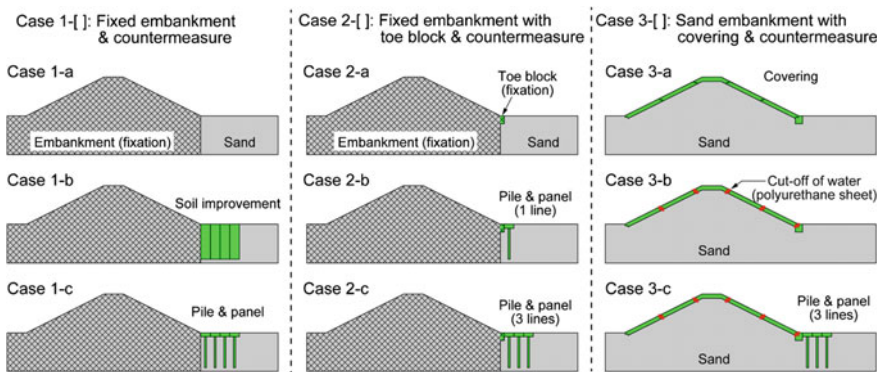


Fig. 4 The model diagrams of each experiment case

In the case 1-a, 1-b, and 1-c, the embankment was considered as fixation, having assumed that a tide embankment was not scoured. The three types of countermeasure, the non-countermeasure, the soil improvement, and the pile and concrete panel (4 rows), were installed in the toe of back slope, and the scouring situation according to the change of countermeasure was measured. In the case 2-a, 2-b, and 2-c, the embankment was considered as fixation, but the shape of embankment was different from the case 1-a, 1-b, and 1-c. The fixed toe block was installed at the toe of back slope in the case 2-a, 2-b, and 2-c. Its shape was adopted actually to the restoration work of tide embankment in coastal area of Tohoku district. The kind of countermeasure were the non-countermeasure, the

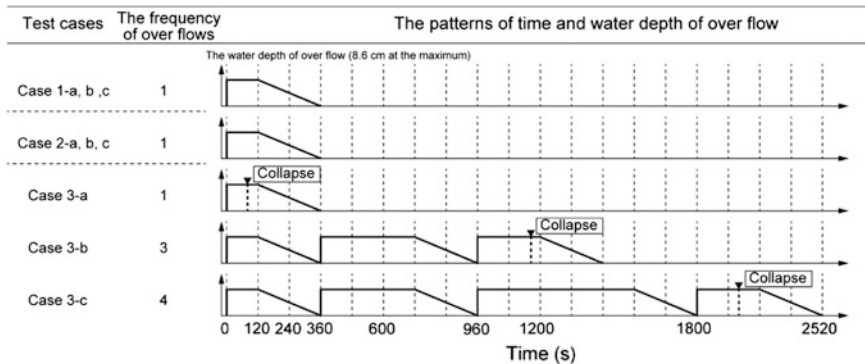


Fig. 5 The relation between the time and the overflow depth of each experiment case

pile and concrete panel (1 row), and the pile and concrete panel (3 row). In the case 3-a, 3-b and 3-c, the embankment was made of Watari sand, having assumed that a tide embankment was scoured by waterflow. The covering concrete panels with engagement mechanics were installed on the surface of sand embankment (refer to Photo 1b). The non-countermeasure, the cut-off of water between covering panels, and the cut-off of water between covering panels and the pile and concrete panel (3 rows), were installed as the countermeasure in the case 3-a, 3-b, and 3-c.

The diagram of relation between the time and the depth of overflow is shown in Fig. 5. In the case 3-b and 3-c, 3 or 4 times experiment were performed because the embankment did not collapse by the overflow of 360 s.

2.2 Compatibility of Similarity Rule in the Model Experiment

It is important to make the similarity rule identical between the prototype and the model when the force and the amount of eroding sand are talked on by a model experiment. The similarity rule on 1G condition is shown in Table 2. As mentioned above, the model embankment was made with the reduced scale 1/25, and had non-distortion. In this chapter, the influence of the scaling upon the result of model experiment is considered by referring to the similarity rule.

At first, the overflow depth and the velocity of water are considered. In the model experiment, the overflow depth and the water velocity at the back slope were 8.6 cm and 1.62 m/s, respectively. When these values are converted into the proto model, the overflow depth is 2.15 m (scale: n), the water velocity at the back slope is 8.10 m/s (scale: $n^{1/2}$).

Table 2 The similarity rule on 1G condition

| Value | | Scale |
|-----------------|-----|-----------|
| Length | L | n |
| Area | A | n^2 |
| Volume | V | n^3 |
| Velocity | v | $n^{1/2}$ |
| Flux | Q | $n^{5/2}$ |
| Time | t | $n^{1/2}$ |
| Frequency | f | $n^{1/2}$ |
| Force | F | n^2 |
| Pressure | P | n |
| Bending moment | M | n^3 |
| Elastic modules | E | n |
| Section modules | Z | n^3 |

$$n = L_{(\text{model})}/L_{(\text{prototype})} = 1/25$$

Next, the force and pressure applied to the countermeasures are considered. The force F that the waterflow exerts on the concrete panel is calculated from e.g. Eq. 1.

$$F = \rho \cdot Q \cdot v \quad (1)$$

where ρ is the specific gravity of water, Q is the flux of water, and v is the velocity of waterflow. Because ρ is constant regardless of scale, the force F that the waterflow exerts on the concrete panel is n^3 times of the proto model. On the other hands, the force of pull-out resistance of pile (F_{res}) is calculated from e.g. Eq. 2.

$$F_{\text{res}} = \mu \cdot k_h \cdot \sigma' \cdot A \quad (2)$$

where μ is the coefficient of static friction, k_h is the horizontal coefficient of earth pressure, σ' is the effective overburden pressure, and A is the area of pile surface. Because μ and k_h are constant regardless of scale, the force of pull-out resistance of pile (F_{res}) is n^3 times of the proto model. From these things, the similarity rule about the pull-out of pile is formed.

Next, the similarity about eroding sand is considered. It is said that the mean diameter of the embankment material which was used in the retrieved tide embankment in the coastal area of Tohoku district is about 1–10 mm (Ono et al. 2014). The mean diameter of sand which used in the model experiment was 0.42 mm. It is necessary to make the mean diameter of sand in the model experiment 1/25 of the prototype for optimizing the amount of eroding sand (Watanabe et al. 2012). Then, except when the assumed mean diameter of prototype is 10 mm, the similarity rule is not formed. The phenomenon of eroding sand is controlled by the critical friction velocity applied to sand particle by waterflow. The relationship between the mean diameter of sand (d_s) and the critical friction velocity (u_{*c}) was calculated from Eq. 3 (Iwagaki 1956).

$$\begin{aligned}
 d_s > 0.303; \quad u_{*c}^2 = 80.9 d_s & \quad \text{unit : } d_s \text{ (cm)}, u_{*c}^2 \text{ (cm/s)} \\
 0.303 \geq d_s > 0.118; \quad u_{*c}^2 = 134.6 d_s^{31/22} & \quad \text{when...} \\
 0.0118 \geq d_s > 0.0565; \quad u_{*c}^2 = 55.0 d_s & \quad \text{Specific gravity of sand particle} = 2.65 \\
 0.0565 \geq d_s > 0.0065; \quad u_{*c}^2 = 8.14 d_s^{11/32} & \quad \text{Coefficient of kinematic viscosity} = 0.01 \text{ cm/s} \\
 0.065 \geq d_s; \quad u_{*c}^2 = 226 d_s & \quad \text{Acceleration of gravity} = 980 \text{ cm/s}^2
 \end{aligned} \tag{3}$$

The critical friction velocity (u_{*c}), when the mean diameter of sand (d_s) are 0.42, 1.0, and 10.0 mm, are 1.68, 2.35, and 8.99 cm/s, respectively. However, the waterflow velocity on the back slope is 162 cm/s, and is fast enough compared with the critical friction velocity. Therefore, the strict influence of velocity of waterflow upon the eroding rate of sand is able to ignore.

The comparable phenomena in this model experiment are the waterflow (similarity), the force, and stress about the countermeasures (similarity), the eroding rate (qualitatively), and the eroding volume (qualitatively).

3 Results

3.1 Scouring Situation According to the Countermeasure (Fixation Embankment)

The scouring situation at the time of 100 s after starting overflow is shown in Fig. 6a-c. The countermeasure and the scouring front of model ground are indicated as green portions and red lines, respectively. The size of black grid on the side of model canal is 5 cm in height, 5 cm in width. And the relationship between the time and the scouring area in Fig. 7.

In the case 1-a, 1-b, and 1-c, in which the embankment is fixation and does not have the toe block, the waterflow which flowed down the back slope struck the model ground or the countermeasure without weakening force. In the case 1-a with non-countermeasure, the model ground was scouring greatly, and the scouring front reached to the bottom of model canal. In the case 1-b with soil improvement, the direction of waterflow which flowed down the back slope was changed into horizontally by the soil improvement. Because of horizontal direction of waterflow, while the scouring depth was small compared with the case 1-a, the scouring range spread to the lower stream more. In the case 1-c with the pile and concrete panel (4 rows), the scouring range was almost the same as the case 1-b, but the ground under the concrete panel was scoured by the inflowing water from the gap between concrete panels. However, the countermeasure was kept by the pull-off resistance of pile, and was not lost by scouring. The scouring area at the time of 100 s in the case 1-a, 1-b, 1-c were 950, 505, and 533 cm², respectively, and the scouring area and velocity in the case 1-b and 1-c were almost the same.

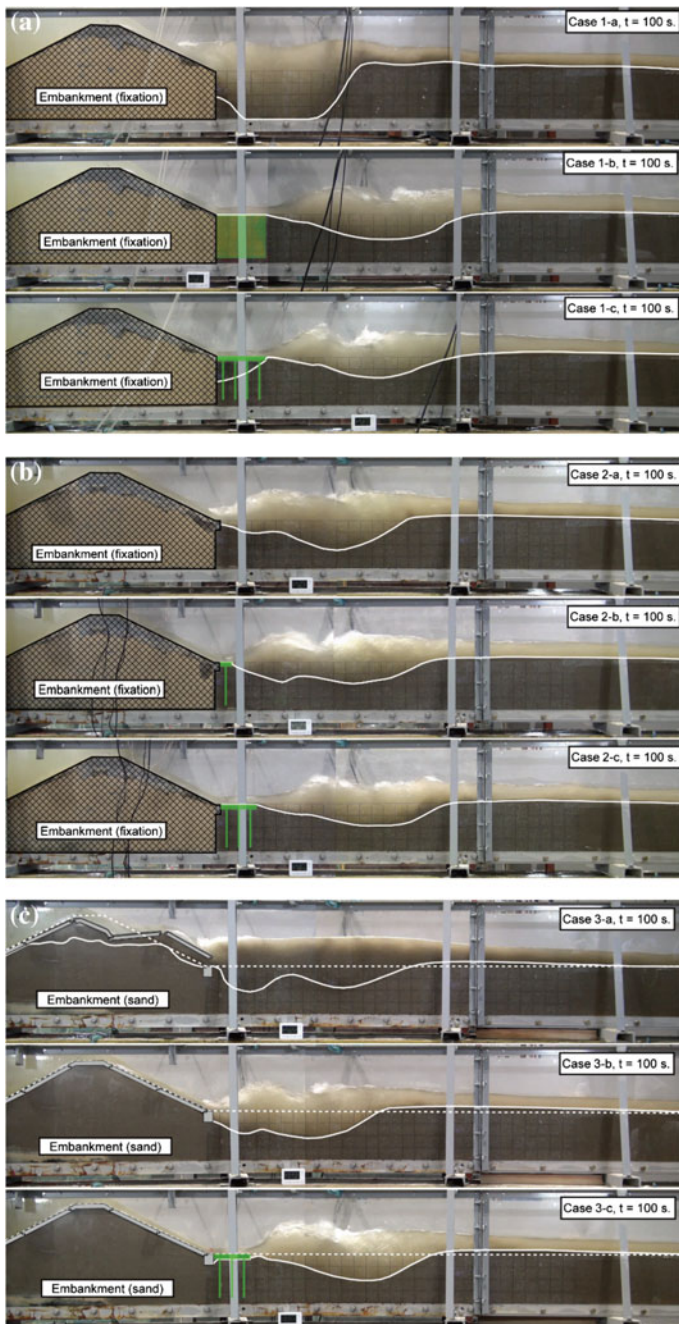


Fig. 6 The scouring situation at the time of 100 s after starting overflow. **a** Case 1-a, 1-b, and 1-c, **b** Case 2-a, 2-b, and 2-c. **c** Case 3-a, 3-b, and 3-c

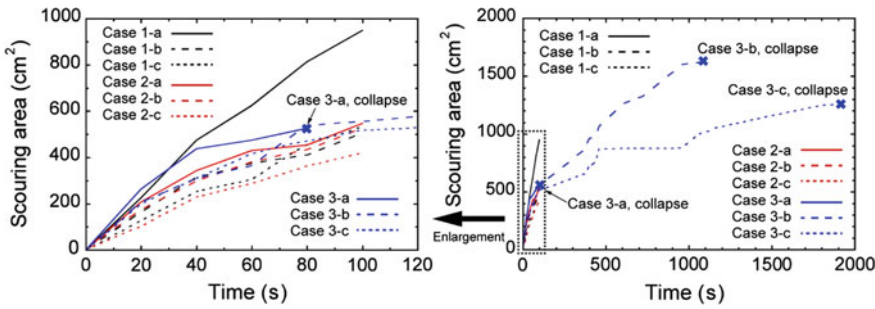


Fig. 7 The relationship between the time and the scouring area

In the case 2-a, 2-b, and 2-c, in which the embankment is fixation and have the toe block, the direction of waterflow which flowed down the back slope was changed into horizontally by the toe block. Although the width of toe block was only 2 cm, the effect of changing direction of waterflow was large. The scouring depth in the case 2-a (with the toe block) decreased greatly than that in the case 1-a (without the toe block). In the case 2-b with pile and concrete panel (1 row), the tendency of horizontal waterflow increased, and the scouring depth decreased while the scouring range increased. In the case 2-c with pile and concrete panel (3 rows), the waterflow at the lower stream end of countermeasure became almost horizontally, the scouring range was the same as the case 1-c. However, the scouring under the concrete panel did not occur because the direction of waterflow changed horizontally and the inflow of water became difficult from the gap between the concrete panels. These result shows that the toe block has large effect to decrease the scouring damage by changing the direction of waterflow. The scouring area at the time of 100 s in the case 2-a, 2-b, 2-c were 548, 526, and 420 cm², respectively. The scouring area became small when the installation distance of countermeasure was lengthened.

3.2 Scouring Situation According to the Countermeasure (Soil Embankment)

In the case 3-a, 3-b, and 3-c, in which the embankment was made of Watari sand and was covered by the concrete panel, the embankment collapsed at the time of 80 s in the case 3-a, at the time of 1160 s in the case 3-b, and at the time of 1960 s in the case 3-c. Even if the embankment was fixed and made of Watari sand, the scouring situation of model ground was almost the same if the embankment kept

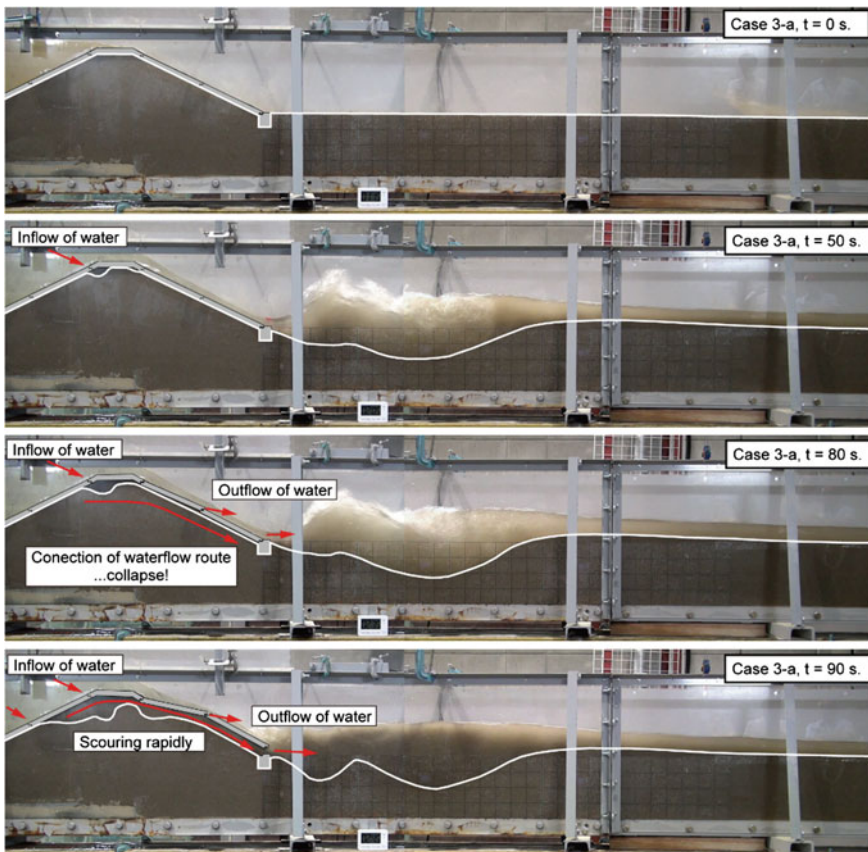


Fig. 8 The progress of scouring in the case 3-a

good condition. The scouring situation became equivalent in the case 2-a and 3-a, and in the case 2-c and 3-c, because of the similarity of shape of countermeasure.

The collapse of embankment in the case 3-a was triggered by the inflow of water from the gap between covering concrete panels at the top of slope of upper stream side (refer to Fig. 8).

The inflowed water was scouring the sand in the boundary between the embankment and the covering concrete panel, the scouring region progressed from the top of slope of the upper stream side to the slope of the lower stream side. When the scouring region reached to the toe of back slope, the covering concrete panel floated up, the sand was sucked out quickly from the gap between covering concrete panels, and the embankment collapsed.

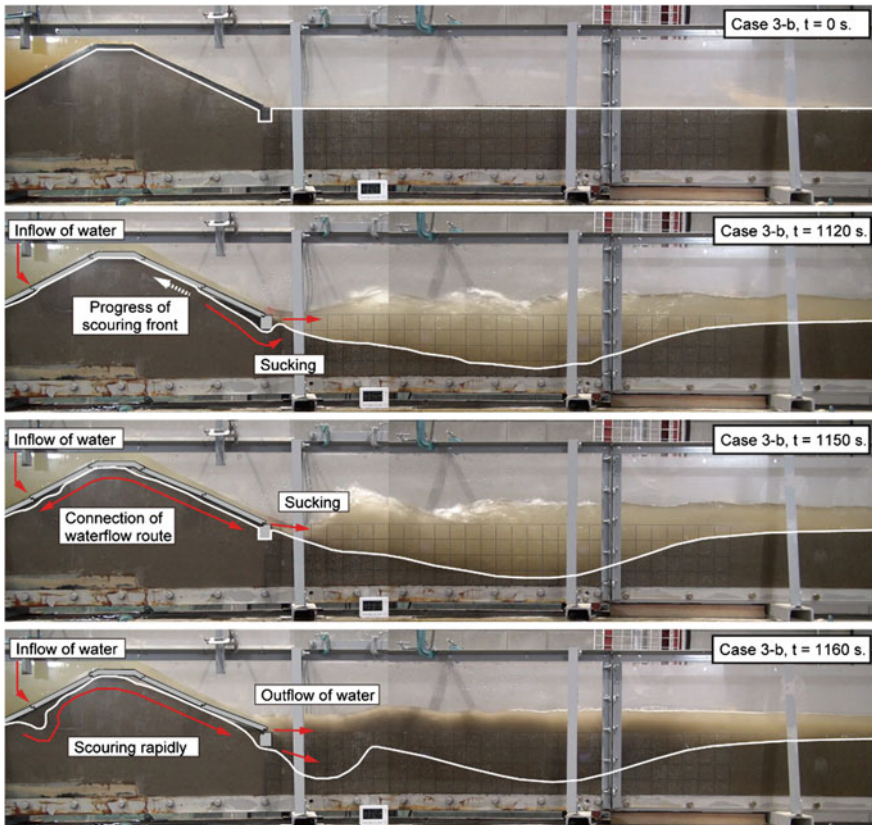


Fig. 9 The progress of scouring in the case 3-b

Then, the cut-off water treatment by putting a polyurethane sheet was performed at the gap between the covering concrete panels. As a result, the inflow of water from the top of slope of upper stream side stopped, and the scouring of embankment progressed from the lower stream side in the case 3-b, 3-c. The scouring of embankment triggered by sucking out the sand under the toe of slope (refer to Figs. 9 and 10). The scouring front progressed from the toe of slope to the slope of lower stream side, and after a while, the inflow of water from the slope of upper stream side began. When the scouring front from the upper stream side and the lower stream side connected, the waterflow route from the upper stream side and the lower stream side was built. Afterwards the scouring velocity of embankment accelerated and the embankment collapsed rapidly.

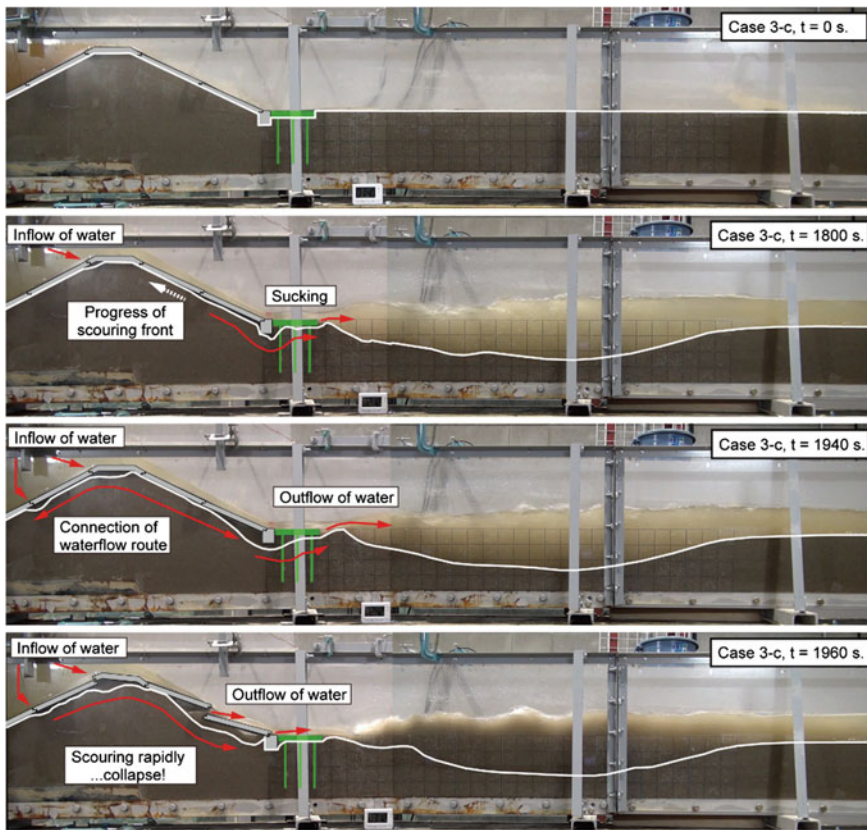


Fig. 10 The progress of scouring in the case 3-c

4 Conclusion

From the experimental results, the following knowledge were obtained:

1. The scouring region is different according to the direction of waterflow after flowing down the back slope. Installing the countermeasure in the toe of slope and changing the waterflow horizontally are able to make the scouring depth small, while the scouring range progressed to the direction of the lower stream.
2. The soil improvement and the pile and concrete panel as the countermeasure in the toe of slope showed an almost equivalent effect. However, in the case of installing the pile and concrete panel, it is necessary to pay attention that a waterflow does not enter from the gap between concrete panels because of prevention of the scouring around the pile and concrete panel. When the toe block was installed in the toe of slope, the direction of waterflow was changed

horizontally by the toe block, and the scouring around the pile and concrete panel did not occur.

3. Two kinds of mechanism of embankment collapse were observed in this experiment. One was the inflow of water from the embankment of upper stream side. The other was the sucking from the embankment of lower stream side. If the cut-off of water of the gap between the covering concrete panels was insufficient, the water entered from the embankment of upper stream side, and the embankment collapsed with short time. On the other hand, if the cut-off of water of the gap between the covering concrete panels was sufficient, the embankment was sucked from the lower stream side, and the embankment kept good condition for a long time.

It was clear that the prevention of inflow of water to the inside of embankment as well as the installing of the anti-scouring countermeasure in the toe of back slope were important for preventing the embankment collapse by Tsunami overflow.

References

Iwagaki Y (1956) Hydrodynamical study on critical tractive force. Trans JSCE 41:1–21 (in Japanese)

Kato F, Suwa Y, Watanabe K, Hatogai S (2012) Mechanism of coastal dike failure induced by the Great East Japan Earthquake Tsunami. In: Proceedings of the 33rd international conference on coastal engineering, structures, vol 40, 9 p

Kato F, Suwa Y, Watanabe K, Hatogai S (2013) Damages to shore protection facilities induced by the Great East Japan earthquake tsunami. J Disaster Res 8(4):612–625

Ono I, Shishido H, Kaneko T (2014) Activities for supplying embankment materials which are used in retrieval works of coastal embankment. Reports of Tohoku regional bureau of Ministry of Land, Infrastructure and Transport. (<http://www.thr.mlit.go.jp/Bumon/B00097/K00360/happyoukai/H26/5-2.pdf>) (in Japanese)

Watanabe Y, Yamamoto M, Hayakawa H, Shimada T (2012) Reproducibility of the hydraulic experiments on overflow-induced collapse by the different scales. J JSCE Ser B1 68(4): I_1123–I_1128 (in Japanese)

Analysis of a Coastal Structure Damaged Due to Compound Effect of Earthquake and Tsunami

**H. Hazarika, T. Hara, K. Kuribayashi, S. Kuroda, T. Nishi,
H. Furuichi, K. Takezawa and T. Ohsumi**

Abstract This paper analyzes the cause of damage to the Yoshihama river dike located in Ofunato city of Iwate prefecture, which were damaged due to strong shaking of the 2011 off the pacific coast of Tohoku earthquake and subsequent tsunami. Analyses were based on the past field investigations and numerical simulations. Investigations revealed that the dike body had low liquefaction resistance and the volume change after liquefaction was rather large. Two dimensional effective stress analyses showed that due to main shock and aftershock, there is a likelihood of liquefaction in dike body and the reliquefaction possibilities are high even under small ground motion.

Keywords The 2011 off the Pacific Coast of Tohoku Earthquake · Field survey · Liquefaction numerical analysis · River dike

H. Hazarika (✉)

Kyushu University, 744, Notooka, Nishi Ku, Fukuoka 819-0395, Japan
e-mail: hazarika@civil.kyushu-u.ac.jp

T. Hara

Kochi University, Kochi, Japan

K. Kuribayashi · S. Kuroda

Eight-Japan Engineering Consultants Inc., Okayama, Japan

T. Nishi

Construction Project Consultants, Tokyo, Japan

H. Furuichi

Giken Ltd., Tokyo, Japan

K. Takezawa

Newjec Inc., Osaka, Japan

T. Ohsumi

National Research Institute for Earth Science and Disaster Prevention, Tsukuba, Japan

1 Introduction

Amongst the scientist, engineers, planners and policymakers, mega disaster caused by the 2011 off the pacific coast of Tohoku earthquake ($M_w = 9.0$) is a major cause of concern toward future protection of geotechnical structures. Geotechnical structures such as dikes and railway embankments in the vicinity of the eastern coasts suffered scouring and erosion due to overtopping of the highest ever tsunami which far exceeded the design head levels (JGS 2011). According to investigation by the Ministry of Land, Infrastructure, Transport and Tourism (MILIT), Japan, there were more than 1195 damage in the river bank that Tohoku district maintenance office directly manages (MILIT 2011a). In the river mouth, the damage was mostly by the tsunami. In the other parts of river banks, the damage was mostly due to the subsidence by either earthquake motion or the liquefaction of soils in the dike body. Especially in those areas under the jurisdiction of the Tohoku Regional Bureau of MILIT, extensive investigations were carried out to determine the damage characteristics (MILIT 2011b). Based on those damage patterns and characteristics and analyses of dikes due to the earthquake and tsunami, appropriate reconstruction measures were suggested. Furthermore, many researchers (Imai et al. 2013; Wakinaka et al. 2013) conducted case study analysis of river dikes damaged due to liquefaction, and reported the damage patterns and the extent of deformation.

Hara et al. (2012), based on their investigation in southern central part of Iwate prefecture, came to conclusion that the level of damage by the tsunami on river banks varies according to the structural forms, such as existence of surface covering, materials, and topographical features. Investigation conducted by Hazarika et al. (2012) in Aomori prefecture and northern part of Iwate prefecture, revealed that most of the damage of the river banks or coastal dikes were mainly due to scouring at the back of the structures. Scouring was found to be caused not only by the overtopping tsunami itself, but also the force of the backrush of tsunami.

In this research, Yoshihama river dike located in the southern central part of Iwate prefecture was picked up as a target for our study. The purpose was to analyze the performance of river dike under the compound effects of earthquake and tsunami. Several field investigations, in situ testing, and laboratory testing were conducted in the past (Hazarika et al. 2013; Yamanaka et al. 2012) for investigating the cause of damage. Based on those, the damage analyses of the dike due to ground shaking were performed, which are reported in Hara et al. (2014a). Numerical simulations of the dike were performed considering the history of the earthquakes and tsunami, and the performance of the dike before the arrival of tsunami.

2 A Brief Review on Field Investigations

The investigated site is located in the Yoshihama area of Ofunato city, Iwate Prefecture. Due to the 2011 Off the Pacific Coast of Tohoku Earthquake, many parts within 102.4–138.5 m of the upstream of both the right and left banks of the river

Fig. 1 State of damage of the Yoshihama dike



were damaged and the dike revetments were tilted towards the river. The road embankment, situated perpendicular to the dike also completely collapsed. However, there was no sign of damage to the nearby buildings. The state of damage of the dike is shown in Fig. 1. In the upstream of the river, several connecting parts of the vertical buttress wall were moved away by about 30 m due to damage to the crown and protective cover of the dike as shown in the Figure. Close to the damaged parts of the dike, the crown of the dike body (referred hereafter as embankment) subsided by about 0.6–1 m. Near the drainage ditch of the sloping side, sand boils were observed (these resemble sand with fine contents that may have formed from granite) in several places. No sign of scouring related damage was observed in those areas, and also there were no damage to the drainage ditches.

Three surveys were conducted on the damaged dike after the disaster (Hazarika et al. 2013; Yamanaka et al. 2012). The first one was after two months (May 2011), the second one was after six months (September 2011), and the third one was after almost two years and four months (July 2013). As shown in Fig. 2, surveyed locations were mainly the top of the damaged part of the dike and the foundation soils.

The cross section surveyed point of the Yoshihama dike along the A–A' line (Fig. 2) is shown in Fig. 3. The dike is having the standard shape typically used in Japan with 5.15 m in height, 2.0 m in width at the crown, and 1:1.2 in gradient at the back. The structure of the dike consists of a concrete wall with counterfort on the river side, and a dike body with filled soil covered with concrete blocks on the back side of the slope. As of July, 2013, the crown height of the embankment was T.P. + 5.10 m. Wide area around the epicenter of the 2011 Off the Pacific Coast of Tohoku Earthquake suffered huge tectonic subsidence. About 73 cm subsidence was recorded in the Yoshihama area of Ofunato city (GIA 2011). According to the standard cross section used in design (1968) of Yoshihama dike (TDL 2011), the design crown height was T.P. + 6.15 m. Therefore, it can be inferred that in the concerned location, the crown subsided by about 1 m as compared to the original height at the time of completion of the embankment.

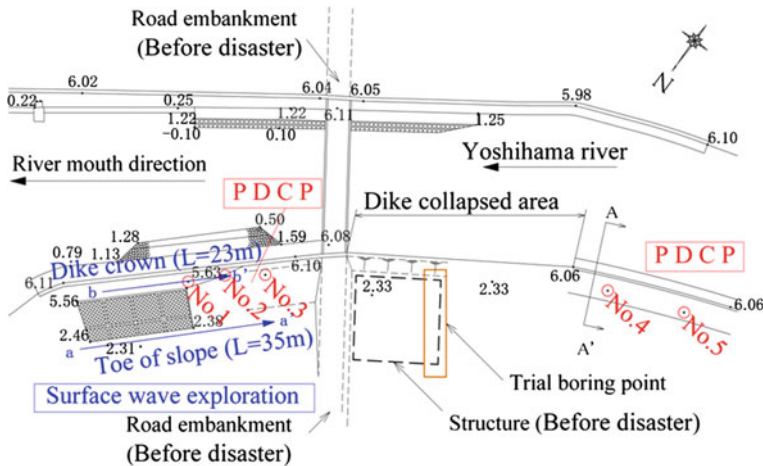


Fig. 2 Plan of Yoshihama dike surveyed area (numbers in the figure shows the altitude during July, 2011)

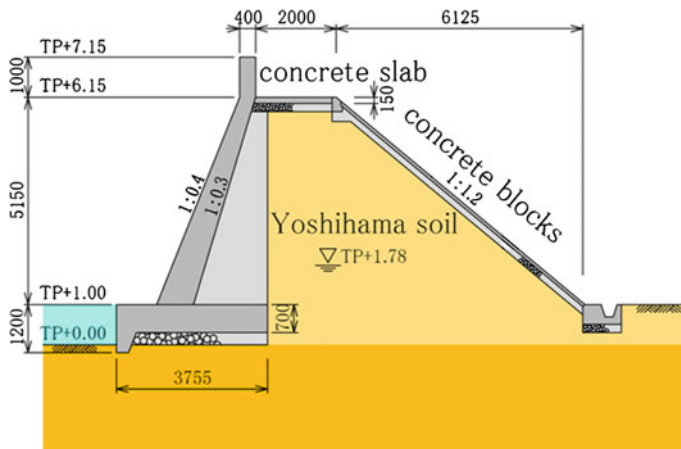


Fig. 3 Cross section of the dike at the surveyed point (left bank of the Yoshihama dike)

Figure 4 shows the N -value converted from N_d obtained from the PDCP test conducted on the soils of the dike body. The N -values of the fill soils range between 1 and 4, which implies that the soil was in very loose state. However, the N -value increases along the bottom of the body, implying a dense state. From the PDCP test the ground water level was confirmed to be at 2 m below the ground surface. Therefore, it can be said that the fill soil was almost at the saturated state.

Figure 5 shows the S-wave velocity distribution analyzed from the surface wave exploration data of the ground near the embankment. The S-wave velocity ranges

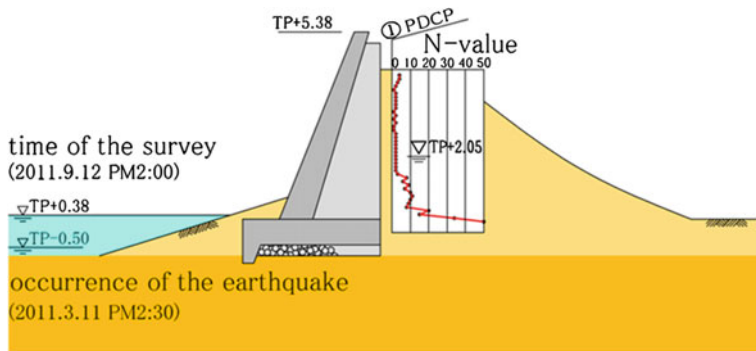


Fig. 4 Cross section of the dike after the earthquake

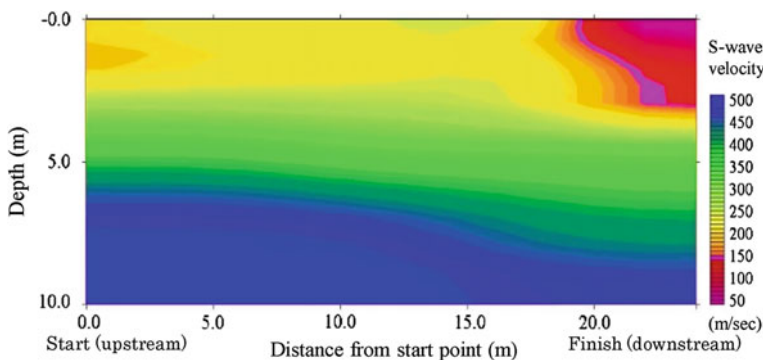


Fig. 5 Distribution of the shear wave velocity

from 200 to 250 m/s near the surface, and the converted N -value was about 20 (Imai and Tonouchi 1982), which implies that the surface soil is very dense. Near the end of the measured zone, the S-wave velocity was found to be low. Based on the observations of the topography and the deposited sand due to tsunami, it can be said that the lower velocity was due to the reclaimed soils used in construction.

3 Numerical Simulations

In order to analyze the cause of damage of the embankment due to the strong ground motion and tsunami, numerical analyses were conducted for the damaged parts of the dike. The numerical model is shown in Fig. 6. The parameters used in the analyses were determined based on the in situ and laboratory tests as described in Hazarika et al. (2013). Simulations were performed for the damaged dike by considering the history of the main shock, aftershocks, and the tsunami that attacked the dike.

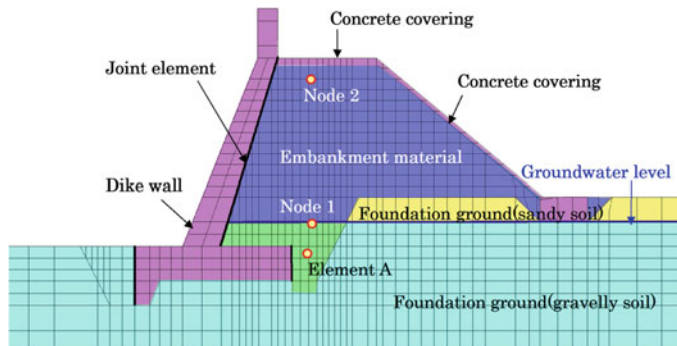


Fig. 6 Model of numerical analyses

Two dimensional effective stress analyses were performed that can take into the account the post liquefaction settlement due to drainage (Oka et al. 1994). Here, attention was paid to the influence of long continuation time of the main shock and several aftershocks that followed within a short time. In the analyses, timing of the peeling off of the concrete cover on the crown and at the back slope of the embankment as well as the settlement and the gap at the crown of the embankment that were observed in the field test were evaluated in the time scale (Kuribayashi et al. 2013; Hara et al. 2014b).

The target structure is the damaged part of the Yoshihama dike shown in Fig. 6. The bottom of the analysis model was set in the location, where the measured shear wave velocity (V_s) exceeded 350 m/s. Regarding the boundary conditions, the bottom was taken as viscous boundary and the sides were set as equal displacement boundary. The input parameters are shown in Table 1. The input parameters were determined based on the undrained cyclic test of the materials collected from the surveyed site (Ueno et al. 2012), and using the simulations of the element tests. Embankment soils and foundations soils were modeled as elasto-plastic materials proposed in Oka et al. (1994). The retaining wall, concrete covers at the top, and the back of the embankment were modeled as linear elastic materials. The input parameter of the concrete was determined that is equal to the design strength of 18 N/mm². The interface between the wall and embankment was simulated using joint elements. The contact and separation between the wall and the embankment were also simulated. The ground water level was considered to be at T.P. + 1.78 that was observed when it had passed enough time after the earthquake.

Figure 7 shows the earthquake record of KiK-net that was recorded near the surveyed area, which was adopted as the input ground motion in the analyses. It is to be noted that the area around our case study experienced the main shock at 14:46 h and the two aftershocks at 15:06 h and 15:09 h. Ground motion observed at KiK-net Kamaishi (IWTH23), which has almost the same V_s as the base of analysis model, was used in the analyses. The ground motions (NS direction and EW direction) were synthesized by changing to direction normal to the dike.

Table 1 List of input properties

| | Elasto-plastic model | | | Elastic model Concrete | |
|---|----------------------|----------------------|----------------------|---------------------------|--|
| | Embankment material | Foundation ground | | | |
| | | Sandy soil | Gravelly soil | | |
| Unit weight, γ (kN/m ³) | 14.31 | 14.00 | 20.00 | 24.00 | |
| Permeability, k (m/s) | 7.0×10^{-6} | 7.0×10^{-6} | 1.0×10^{-4} | — | |
| Initial void ratio, e_0 | 0.99 | 0.95 | 0.45 | — | |
| N -value | 2.00 | 2.00 | 50.00 | — | |
| Fines fraction content, F_c (%) | 20.50 | 15.50 | — | — | |
| S-wave velocity, V_s (m/s) | 175 | 155 | 350 | 2000 | |
| Initial mean effective stress, σ'_m (kN/m ²) | 98.00 | 98.00 | 66.67 | — | |
| Initial shear modulus, G_0 (kN/m ²) | 45,625 | 35,022 | 255,102 | 8,750,000 | |
| Cohesion, c' (kN/m ²) | 0.00 | 0.00 | 0.00 | — | |
| Internal friction angle, ϕ' (°) | 36.60 | 37.00 | 40.00 | — | |
| Bulk modulus, K_f (kN/m ²) | 2,200,000 | 2,200,000 | 2,200,000 | — | |
| Compression index, λ | 0.01610 | 0.02051 | 0.00142 | — | |
| Swelling index, κ | 0.00161 | 0.00205 | 0.00014 | — | |
| Pseudo overconsolidation ratio, OCR* | 1.000 | 1.000 | 1.000 | — | |
| Normalized initial shear modulus, G_0/σ'_m | 466 | 357 | 3827 | — | |
| Phase transformation stress ratio, M_m^* | 0.909 | 0.909 | 0.909 | — | |
| Failure stress ratio, M_f^* | 1.215 | 1.229 | 1.336 | — | |
| Hardening parameter, B_0^* | 1533 | 5000 | 11,458 | — | |
| Hardening parameter, B_1^* | 15 | 100 | 115 | — | |
| Hardening parameter, C_f | 0.00 | 0.00 | 0.00 | — | |
| Reference value of plastic strain | 0.0100 | 0.0070 | — | — | |
| Reference value of elastic strain | 0.020 | 0.015 | — | — | |
| Parameter of dilatancy, D_0^* | 1.000 | 3.000 | — | — | |
| Parameter of dilatancy, n | 4.000 | 6.000 | — | — | |

The deformation of the dike is shown in Fig. 8. Due to the main shock and two aftershocks, the embankment subsided by about 0.67 m and the back slope suffered displacement and peeling off of the concrete covers as observed in the in situ survey. However, near the toe of the embankment no large deformations were observed due to the ground motions.

Figure 9 shows the distribution of the maximum excess pore water pressures developed inside the embankment due to the main shock and aftershocks. The domain of the reliquefied zone due to aftershocks is shown in the same figure. As

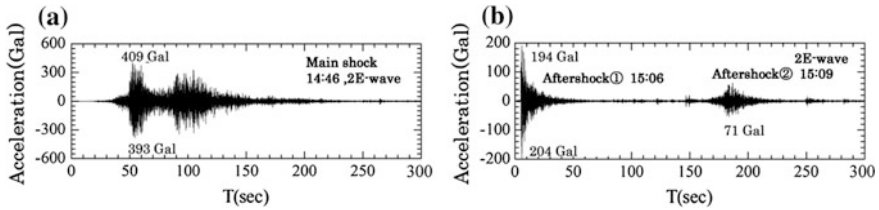


Fig. 7 Input ground motion recorder at KiK-Net Kamaishi (IWTH 23). **a** Main shock **b** aftershocks

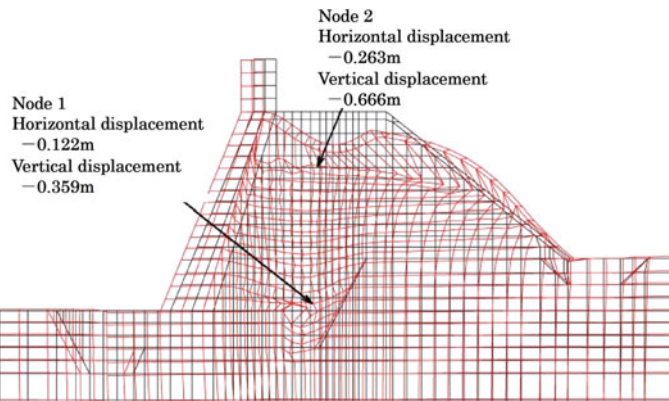


Fig. 8 Deformation of the dike due to the main shock and aftershocks

seen in the Figure, in Y Line the value of $\Delta u/\sigma'_c$ reaches 1.0, however, in X Line the value of $\Delta u/\sigma'_c$ reaches up to 0.6–0.8 without any liquefaction. We can infer from such phenomena that due to the main shock, bottom parts of the embankment located under the water table, suffered local liquefaction. The excess pore water pressure dissipated in some cases, and in some cases not. Therefore, even though the aftershock ground motions are small as compared to the main shock, the excess pore water pressure built up again leading to reliquefaction of the soils.

Figure 10 shows the development and dissipation of the excess pore water pressure due to the ground motions in the element A within the embankment located below the ground water level. It can be seen that in spite of the sound bed rock that supports the dike, due to the maximum ground motion of about 400 Gal, almost whole of the bottom part of the embankment reached the excess pore water ratio of 1.0, and as result many locally liquefied zones were observed. However, within 20 min of the main shock (before the aftershock), the excess pore water pressure almost dissipated. During the first aftershock when the maximum acceleration was about 200 Gal, the excess pore water pressure within the embankment built up again, and the $\Delta u/\sigma'_c$ value reached 1.0. The pore water pressure dissipated before the second after shock (maximum acceleration 70 Gal) and $\Delta u/\sigma'_c$ values

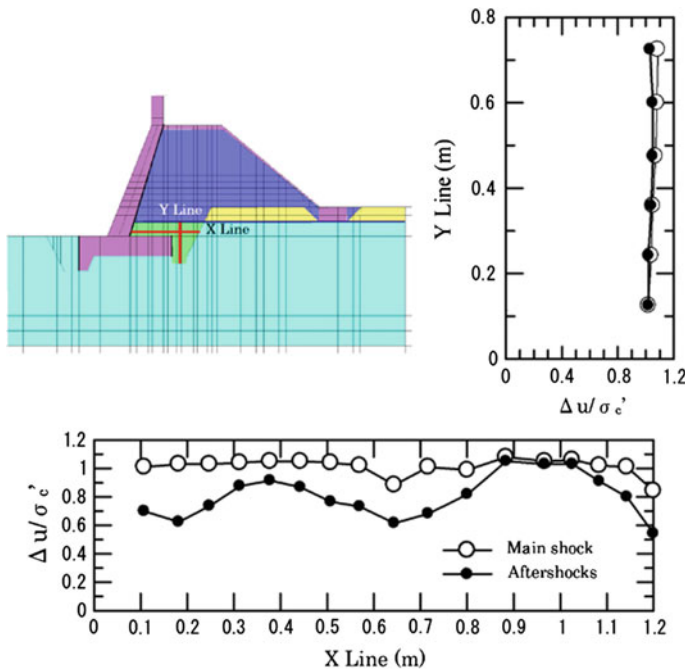
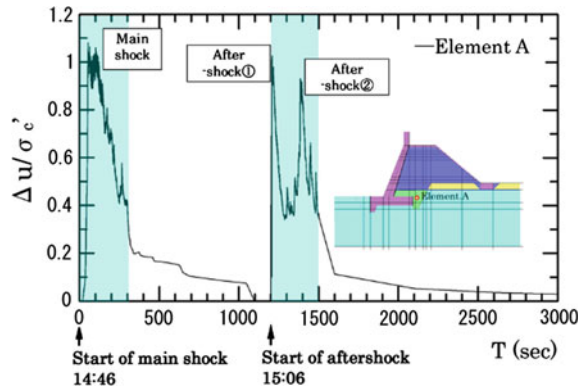


Fig. 9 Maximum excess pore water pressures distribution at the bottom of the embankment

Fig. 10 Time history of the excess pore water pressure (Element A of Fig. 6)



came down to 0.4. However, the second aftershock brought the $\Delta u/\sigma'_c$ value again to 0.9, and as a result a part of the embankment experienced reliquefaction.

The distribution of the volumetric strain inside the embankment due to dissipation of the excess pore water pressure is shown in Fig. 11. This figure reveals that

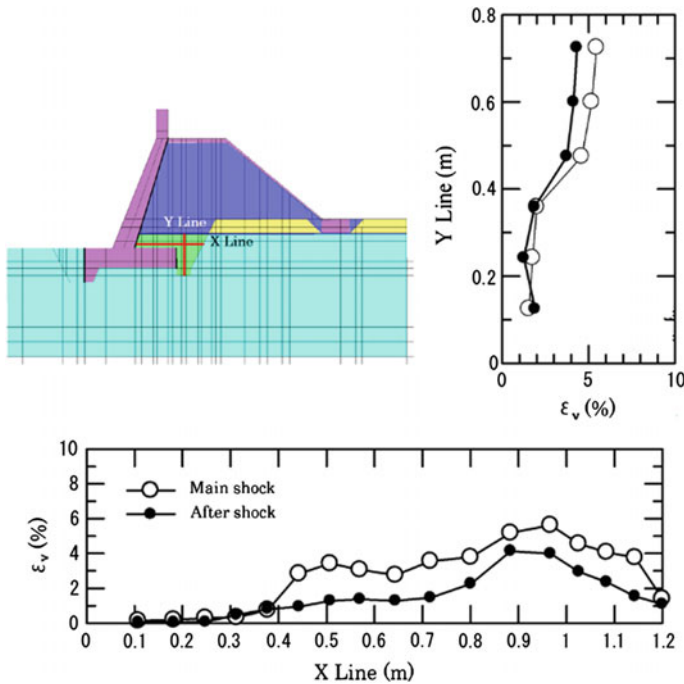


Fig. 11 Post liquefaction volumetric strain due to dissipation of the water pressures at the bottom of the embankment

during the main shock when $\Delta u/\sigma'_c$ attains 1.0, the volumetric strain becomes 2–5 %. During the aftershocks, in the parts where $\Delta u/\sigma'_c$ attains 1.0 almost the same amount of volumetric strains were generated. In parts where $\Delta u/\sigma'_c$ is 0.6–0.8 without any liquefaction, volumetric strain is 1–2 %. This is consistent with the results from the reconsolidation test results conducted after the cyclic undrained test (Ueno et al. 2012).

The vertical displacements of the embankment at two points (node 1 and node 2 of Fig. 8) due to dissipation of the excess pore water pressure after the main shock and the aftershocks are shown in Fig. 12. The vertical displacement δ_v in the surface of the embankment were calculated to be 0.52 m after the mainshock, 0.60 m after the first aftershock, and 0.67 m after the second aftershock. Therefore, it can be inferred that the subsidence of the embankment progressed due to repeated dissipation of the pore water pressures, and as a result even before the arrival of the tsunami, the embankment suffered huge deformation. It is to be noted that the subsidence at the end of the second aftershock calculated from the simulation agrees with the value recorded in the field survey (Hara et al. 2014a, b).

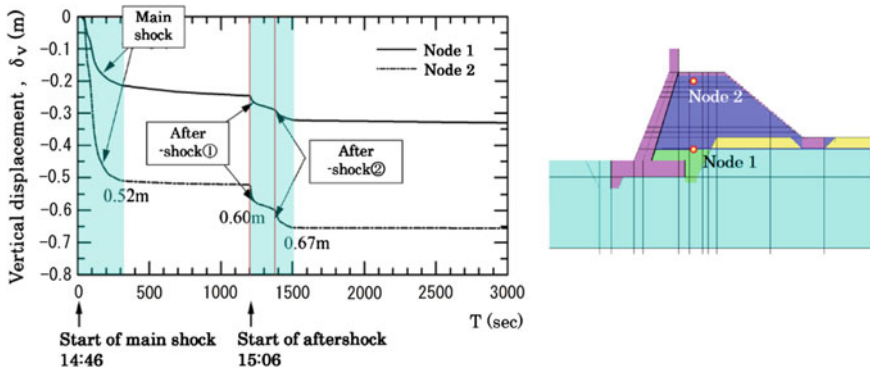


Fig. 12 Subsidence of the embankment due to the ground motions

4 Conclusion

In this paper, the cause of damage to the Yoshihama river dike located in Ofunato city of Iwate prefecture, due to strong shaking of the 2011 off the pacific coast of Tohoku earthquake and subsequent tsunami were analyzed. Based on the field investigations and subsequent numerical simulation, the following conclusions could be drawn:

1. The dike body had low liquefaction resistance similar to those of alluvial soils and decomposed granite.
2. When several ground motions from the main shock and the aftershocks act on the dike, in the saturated zone of the foundation soils a large change of the excess pore water pressure develops. As a result even under small aftershocks, the foundation soils undergo reliquefaction.
3. The subsidence of the dike body due to dissipation of the excess pore water pressure after liquefaction increases due to repeated loads under the main shock and aftershocks.

Acknowledgments The authors greatly appreciate the contributions of the following individuals in the in situ testing, field survey and data analysis of this research: Dr. Minoru Yamanaka, Kagawa University; Mr. Nozomu Kosaka, JAFEC USA, U.S.A.; Mr. Hiroshi Takenaka and Masaaki Fujii of Japan Foundation Engineering Co., Ltd., Sendai Branch, Japan.

References

Geospatial Information Authority (GIA) of Japan 2011: Reference point browsing service, <http://www.gsi.go.jp/kyusyu/kokyo-index.html>
 Hara T, Okamura M, Uzuoka R, Ishihara Y, Ueno K (2012) Damages to river dikes due to tsunami in south-central coastal area of Iwate Prefecture in 2011 off the Pacific Coast of Tohoku Earthquake. Japan Geotech J Japan Geotech Soc 7(1):25–36 (in Japanese)

Hara T, Hazarika H, Kuroda S, Kuribayasi K, Nishi T, Furuichi H, Takezawa K, Ohsumi T (2014a) Damage Analysis of the compound disaster suffered by a river dike due to ground motion and tsunami. In: Special symposium of the Great East Japan Disaster, Tokyo CD-ROM

Hara T, Hazarika H, Kuroda S, Kuribayasi K, Nishi T, Furuichi H, Takezawa K, Ohsumi T (2014b) Analysis of the compound disaster suffered by a river dike due to the 2011 off the pacific coast of Tohoku earthquake. *Geotech Eng J Japan Geotech Soc* 9(4):645–658 (in Japanese)

Hazarika H, Kasama K, Suetsugu D, Kataoka S, Yasufuku N (2012) Damage to geotechnical structures in waterfront areas of northern Tohoku due to the March 11, 2011 tsunami disaster. *Indian Geotech J Indian Geotech Soc* 43(2):137–152

Hazarika H, Hara T, Furuichi H (2013) Soil-structure interaction during earthquake and tsunami— Two case studies from the latest disaster in Japan. In: Proceedings of the special workshop on challenges of soil-structure interaction and retaining walls, 18th ICSMGE, Paris, pp 131–142

Imai T, Tonouchi K (1982) Correlation of N-value with s-wave velocity and shear modulus. In: Proceedings of 2nd European Symposium on Penetration Testing, pp 67–72

Imai Y, Suzuki A, Tobita T (2013) Case study analysis of river embankment caused by the Great East Japan Earthquake. In: 48th Annual Meeting of the Japanese Geotechnical Society, Toyama, pp 1129–1130 (in Japanese)

Japanese Geotechnical Society (JGS) (2011) Joint survey of Tohoku Branch, and Shikoku branch investigation team: damages in South-central Coastal Area of Iwate Prefecture in 2011 off the Pacific Coast of Tohoku earthquake. *Geotech Eng Mag* 59(6):30–35 (in Japanese)

Kuribayashi K, Kuroda S, Hara T, Sakabe A, Furuichi H, Hazarika H (2013) Liquefaction behavior of the river dike in consideration of the aftershock. In: Proceedings of the 2013 JGS Shikoku Branch Annual Scientific Conference, pp 57–58 (in Japanese)

Ministry of Land, Infrastructure, Transport and Tourism (MILIT) (2011a) Restoration and damage of rivers and coastal facilities in the Great East Japan Earthquake. Report of the River section of the Tohoku Regional Bureau (in Japanese)

Ministry of Land, Infrastructure, Transport and Tourism (MILIT) (2011b) Kitakami river dike restoration, technical review group report, The Tohoku Regional Bureau (in Japanese)

Okada F, Yashima A, Shibata T, Kato M, Uzuoka R (1994) FEM-FDM coupled liquefaction analysis of a porous soil using an elasto-plastic model. *Appl Sci Res* 52:209–245

Tsunami Digital Library (TDL) (2011) http://tdl.civil.tohoku.ac.jp/TSUNAMI/TDL_top_e.html, http://tsunami-dl.jp/docimg/080/chile80_125.jpg/medium

Ueno M, Hara T, Hazarika H, Ohsumi T, Yamanaka M, Furuichi T (2012) Shear strength and deformation properties before and after liquefaction of the tsunami-affected river dike. In: Proceedings of the 67th JSCE Annual Meeting, III, pp 39–40 (in Japanese)

Wakinaka Y, Ishihara M, Sasaki T (2013) Case study analysis of River dike damage caused by liquefaction during the Great East Japan Earthquake. In: 48th Annual Meeting of the Japanese Geotechnical Society, Toyama, pp 1701–1702 (in Japanese)

Yamanaka M, Hara T, Hazarika H, Ohsumi T, Furuichi H, Ueno M, Yamazaki T, Okada H (2012) Stability of Earth structures against overflow of Tsunami during the 2011 off the Pacific Coast of Tohoku Earthquake. *Japan Assoc Earthq Eng* 12(5):89–101 (in Japanese)

An Example of the Restoration Method of Levees Damaged by the Great East Japan Earthquake

Tohru Yanagihata, Osamu Nakayama, Yasushi Sasaki,
Ryosuke Uzuoka and Tetsuya Nakamura

Abstract Following the Great East Japan Earthquake, the aseismatic construction method featuring a combination of sheet pile and drain was adopted as the construction method for recoveries of the levees in Ajiki district along the Tone River. Water seepage and aseismatic effects on the levees in the district by the adopted construction method were evaluated based on the results of the measurements of their observed groundwater level, two dimensional saturate–unsaturated seepage flow analysis, and liquefaction-induced deformation analysis. As a result, it was found that the levels of water infiltration into the bodies following insertion of aseismatic sheet piles along the toes of the back slopes of these levees were reduced by installing drains along the top of the piles inserted. And it was demonstrated that the levees will not be affected by the potential external forces assumed in the post-earthquake flood control plan, if the construction method was used for them. Also, even when the earthquake about the same acceleration scale with the Great East Japan Earthquake occurred, it was also demonstrated that the aseismatic sheet piles inserted along the toes of the back slopes would prevent lateral displacement.

Keywords Levee • Liquefaction • Seismic engineering measures • Seepage flow analysis • Liquefaction-induced deformation analysis

T. Yanagihata (✉) · O. Nakayama
Japan Institute of Country-ology and Engineering, 105-0001 Tokyo, Japan
e-mail: t.yanagihata@jice.or.jp

Present Address:
O. Nakayama
Kitac Corporation, Tokyo, Japan

Y. Sasaki
Hiroshima University Professor Emeritus, Ibaraki, Japan

R. Uzuoka
The University of Tokushima, Tokushima, Japan

T. Nakamura
Tonegawa-Karyu River Office, Chiba, Japan

1 Introduction

The Great East Japan Earthquake caused significant damage in and around river levees over a vast area in the Northeastern and Kanto regions. The Tone River is one of the biggest rivers in Japan. In its Ajiki district at R70.0 k neighborhood, the river levees of the extension about 2 km were damaged along the Tone River. This area is located in a compound of a flood plain and natural levees. In modern times, river levees have made filling made of dredging soil of river channels or cutting soil of old disappearance levees.

In Ajiki district, two kinds of deformations levee damaged were observed on the Great East Japan Earthquake. One of the deformations has subsidence of levee crest, and another one has distortion of levee berm on protected lowland side. The aseismatic construction method featuring a combination of sheet pile and drain was adopted as the construction method for recoveries of the levees in this area along the Tone River.

Water seepage and aseismatic effects on the levees in the district by the adopted construction method were evaluated based on the results of the measurements of their observed groundwater level, two-dimensional saturate–unsaturated seepage flow analysis, and liquefaction-induced deformation analysis.

2 Feature of District for Examination

2.1 *Transition of Levee, Topography, and Geology*

The levee of Ajiki district was under consideration; the Tone River right bank levee is shown in Fig. 1. Beginning with the second phase of construction of the Tone

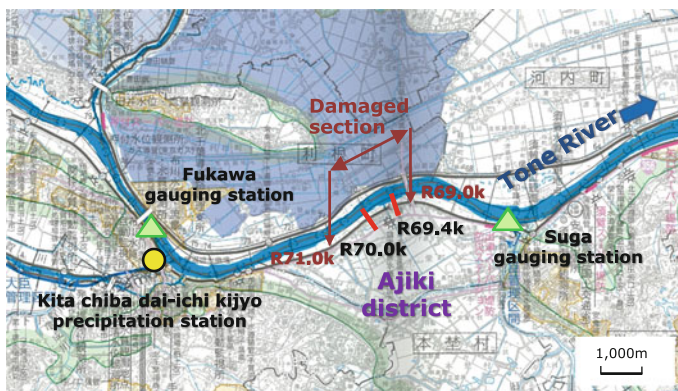


Fig. 1 Consideration district

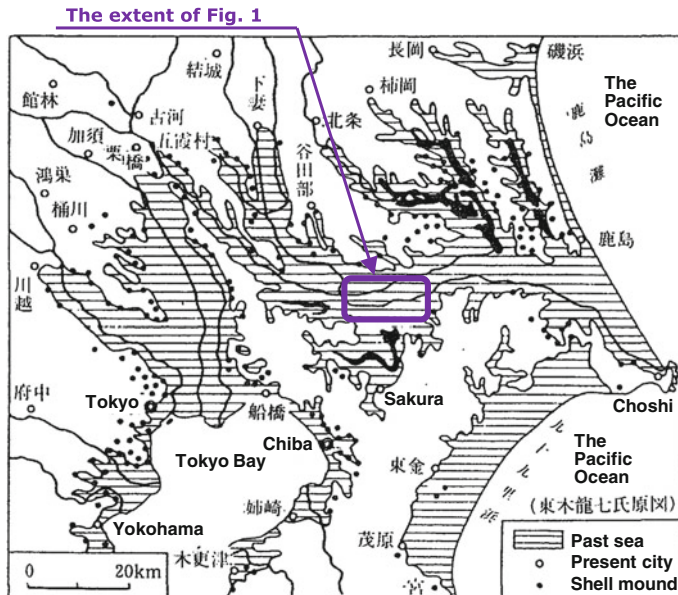


Fig. 2 Old coastline and distribution of shell mounds in the Kanto region lowland

River renovation that started in 1900, the river improvement full-scale upstream and downstream sections, including the Tone River right bank Ajiki district are going on till now.

The Levee excluding a portion of the Ajiki district is assumed to be expanded or raised compared to the old levee that existed before the times mentioned above. In addition, as the levee body of these materials, excavated soil of the river channel and the old levee that was removed due to renovation are mainly used.

Further, the consideration district, as shown in Fig. 2, is the sea during the time of the Holocene glacial retreat; clay is the distributed thick foundation ground and a layer of sand thin between the thick clay is sandwiched.

In recent years, it is the section in which the foundation groundwater leakage and the levee body water leakage occurred in many places in 1982, 1983, and 1985.

2.2 Levee Disaster of the Great East Japan Earthquake

The levee of Ajiki district, where damage occurred for about 2 km between the neighborhood (69 k and neighborhood 71 k) by the Great East Japan Earthquake. In cross section in the deformation of the damaged levee, there was little in the face of front slopes. On the other hand, deformation was concentrated between the crest and the face of back slopes. Deformation of the levee affected by the disaster can be

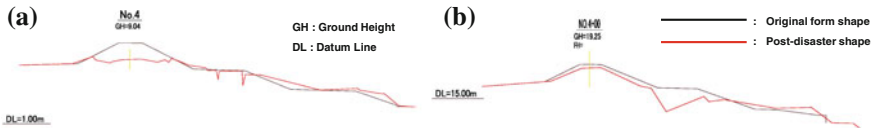


Fig. 3 The deformation shape of post-disaster. **a** Neighborhood R70.0 k. **b** Neighborhood R70.75 k

classified into deformation of two types. By subsidence and depression of the levee crest a type of the face of back slopes is deformed, and one of the variant types is shown in Fig. 3a. Almost no subsidence of the levee crest which is the type that is part between the face of back slopes and the toes of back slopes deformed, and another type is shown in Fig. 3b.

In addition, sand boiling in the protected inland has not been confirmed. It is filed as an emergency disaster; the levees that were classified as large-scale disaster place and was restored to predisaster shape during emergency restoration.

2.3 Disaster Recovery Method

Kanto Regional Development Bureau has been set up after the Great East Japan Earthquake by the “Kanto river levee restoration technical committee”; design conditions and considerations and basic policy of this restoration has been proposed (Kanto River Levee Restoration Technical Committee 2011). In the disaster recovery method of damaged levee of Ajiki district, in the light of proposed above, for steel sheet pile method and the consolidation process and gravel drain method, comparative study construction and economy, etc., is carried out and steel sheet pile method has been selected. In the Ajiki district perforated sheet pile are installed and provided with a water flow hole height foundation ground sand in order to prevent the steel sheet pile laying seepage capabilities of levees from being reduced. Further, in order to facilitate the drainage water level in the levee body, the drains shown in Fig. 4 were installed along the top of the sheet piles and along the toes of the back slopes of these levees.

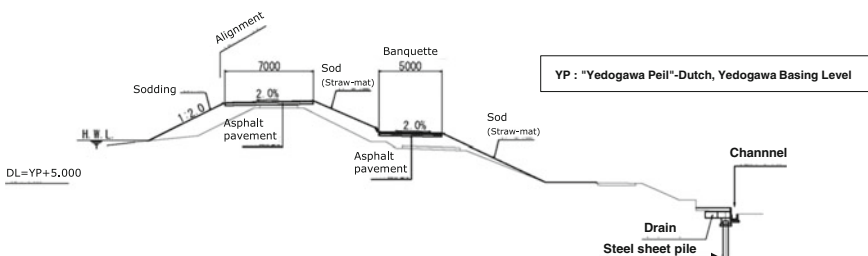


Fig. 4 The aseismatic construction method featuring a combination of sheet pile and drain

3 Evaluation of Ground-Water-Level Observation Result

The groundwater level observation well was set up in five places inside the cross sections shown in Fig. 5a, R70.0 k, and in Fig. 5b, is shown R69.4 k, each of constructed section and non-constructed aseismatic construction method. In both sections, four groundwater level observation wells were set up inside the levee body, and the remaining one was set up in the protected inland. The groundwater level has been observed until February 25, 2014 since November 8, 2012 as shown in Figs. 6 and 7. The cross section of the levees of Ajiki district, the seawall and the sheet pile was in the front of the river levees before the Great East Japan Earthquake embankment. In the constructed section, the sheet piles along the toes of the back slopes and the drains of width 2 m along the top of the piles have been installed from observation before the start. On the other hand, up to November 2013 was a state that was not the construction of these measures in the non-constructed section.

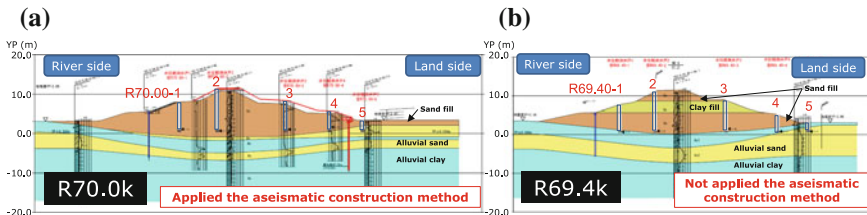


Fig. 5 Placement of the groundwater level observation well. **a** At the R70.0 k. **b** At the R69.4 k

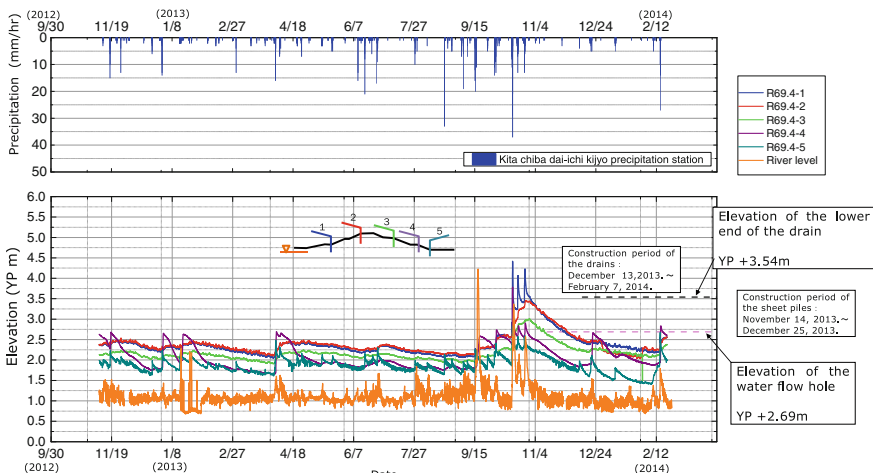


Fig. 6 Time history of the groundwater level observations at the R69.4 k

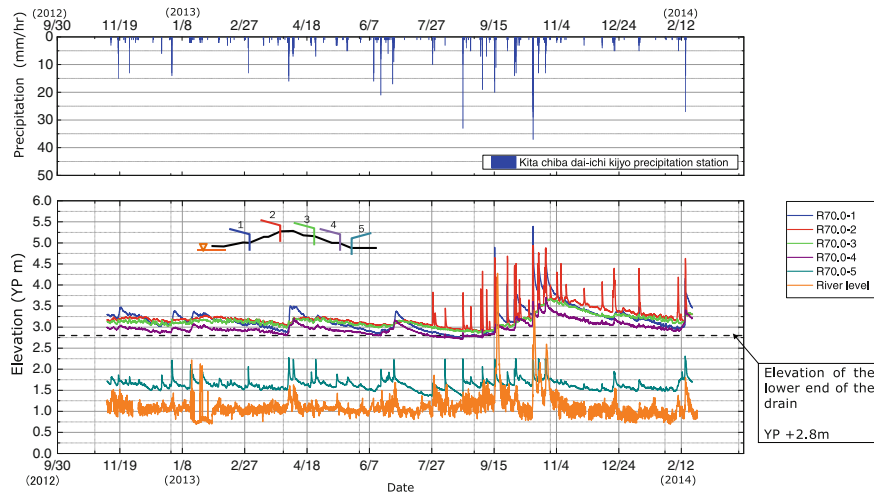


Fig. 7 Time history of the groundwater level observations at the R70.0 k

In the observation well of the ground-water-level in the drain neighborhood, it was confirmed that the decrease speed of the water level was fast compared with other observation wells in the same section. Therefore, it is thought that the drainage effect by the drain was demonstrated.

The groundwater level in the levee inside the body is higher than the water level of the Tone River and the groundwater level of protected lowland regardless of the aseismatic construction method existence.

4 Evaluation of Seepage Flow Analysis

The levee was modeled for the levee cross section in the aseismatic construction method, and two-dimensional saturation-unsaturated seepage flow analysis was executed. The analysis cases are shown in Table 1. As a result of using the seepage flow analysis, results were summarized for the variables defined in Fig. 8 and is shown in Fig. 9.

Table 1 The list of case study of saturation unsaturated seepage flow analysis

| Code | (Along the toes of the back slopes) | | |
|------|-------------------------------------|-------------|-------------|
| | Hydraulic conductivity (cm/sec) | | Width (m) |
| | Steel sheet piles | Drains | |
| 1 | 10^{-6} | 10^{-1} | 2 |
| 2 | (Not exist) | (Not exist) | (Not exist) |
| 3 | 0 | 10^{-2} | 4 |
| 4 | 0 | 10^{-2} | 8 |

Fig. 8 Definition of the state variables of the levee

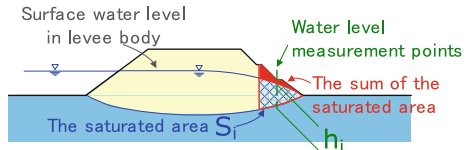
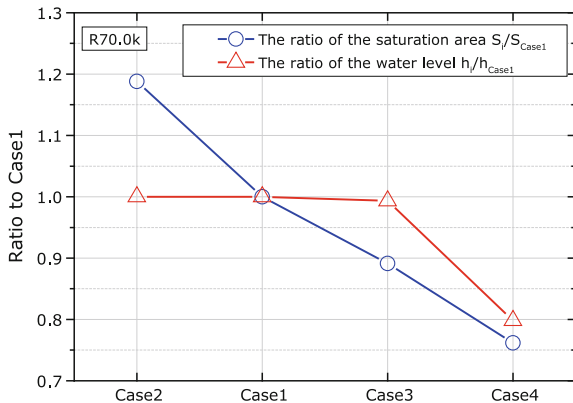


Fig. 9 Evaluation results of the seepage capabilities of levees



As a result, it was demonstrated that the levees will not be affected by the potential external forces (Japan Institute of Country-ology and Engineering 2012) assumed in the post-earthquake flood control plan, if the construction method was used for them.

According to the analysis result, it was found that the levels of water infiltration into the bodies following insertion of aseismatic sheet piles along the toes of the back slopes of these levees were reduced by installing drains along the top of the piles inserted. In this situation, groundwater level observations described above are also consistent.

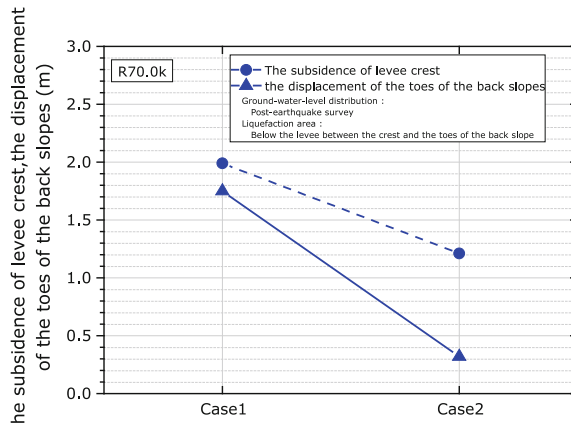
5 Evaluation of Liquefaction-Induced Deformation Analysis

The levee was modeled for the levee cross section in the aseismatic construction method, and two-dimensional liquefaction-induced deformation analysis was executed. Liquefaction-induced deformation analysis, LIQCA (LIQCA Liquefaction Geo-Research Institute 2013), was performed for the deformation caused by the Great East Japan Earthquake of the levee in the Ajiki district of the ground configuration and earthquake disaster form. The analysis cases are shown in Table 2. In addition, groundwater level distribution in levee body was set from the shape that had been confirmed in post-earthquake survey carried out in May 2011. The

Table 2 The list of case study of liquefaction-induced deformation analysis

| Code | (Along the toes of the back slopes) | |
|------|-------------------------------------|-----------|
| | Steel sheet piles | Drains |
| 1 | Not exist | Not exist |
| 2 | Exist | Exist |

Fig. 10 Evaluation results of the seismic performance of levees



subsidence of levee crest and the displacement of the toes of the back slopes were organized from liquefaction-induced deformation analysis results as shown in Fig. 10.

As a result, reproducibility of the case was high, when liquefaction parts are assumed to have been existed from the levee bottom to the under parts of back slopes, or the under parts of back slopes.

According to the analysis result, even when the earthquake of the same acceleration scale with the Great East Japan Earthquake occurred, it was also demonstrated that the aseismatic sheet piles inserted along the toes of the back slopes would prevent lateral displacement.

6 Conclusion

Following the Great East Japan Earthquake, the aseismatic construction method featuring a combination of sheet pile and drain was adopted as the construction method for recoveries of the levees in Ajiki district along the Tone River.

Water seepage and aseismatic effects on the levees in the district by the adopted construction method were evaluated based on the results of the measurements of their observed groundwater level, two-dimensional saturate–unsaturated seepage flow analysis, and liquefaction-induced deformation analysis.

This study revealed following conclusion:

1. It was found that the levels of water infiltration into the bodies following insertion of aseismatic sheet piles along the toes of the back slopes of these levees were reduced by installing drains along the top of the piles inserted. And it was demonstrated that the levees will not be affected by the potential external forces assumed in the post-earthquake flood control plan, if the construction method was used for them.
2. Also, even when the earthquake about the same acceleration scale with the Great East Japan Earthquake occurred, it was also demonstrated that the aseismatic sheet piles inserted along the toes of the back slopes would prevent lateral displacement.

In this study, it should be noted that it is considered based on the limited data of a limited duration. Issues such as verifying the soil conditions used for the numerical analysis and continuation of groundwater level observation remains in the future.

In considering the seismic engineering measures, it is insufficient in the study of improving the seismic performance and workability. The reason is because it should not reduce the seepage capabilities of levees by installing seismic engineering measures.

References

Japan Institute of Country-ology and Engineering (2012) Guideline for design of river levees (in Japanese)

Kanto River Levee Restoration Technical Committee (2011) For the correspondence towards flood period of April 2012 to March 2013 <For the real restoration> (3rd Committee material No. 5) (in Japanese)

LIQCA Liquefaction Geo-Research Institute (2013) Manual of LIQCA2D13 (in Japanese)

Remediation of a Failed Slope Located at Fault Fracture Zone

San-Shyan Lin, Jen-Cheng Liao, Sheng-Der Yang
and Li-Yuan Huang

Abstract Earthquake-triggered faulting frequently causes fracture zone due to shearing along both sides of the fault. Fracture zone is then becoming the flow path of groundwater, resulted from weak and loose material properties inside. However, low permeability of fault gouge also becomes barrier easily to lift groundwater to the soil and rock interface in the fracture zone. Slope located at the fracture zone is unstable and easily causes disaster. In this paper, remediation of a tea product factory, located at a fault fracture zone in Taipei that failed due to slope failure is reported. The characteristics of the fault fracture zone and the slope sliding mechanism are investigated first. The remediation of the failed slope is then introduced. Effectiveness of the remediation is then checked by observation of the ground displacement. It is expected that this example can provide a good reference for future similar practical cases.

Keywords Slope slide • Fault fracture zone • Drilled shaft • Ground anchor

S.-S. Lin (✉)

Department of Harbor and River Engineering, National Taiwan Ocean University,
Keelung 20224, Taiwan
e-mail: sslin46@gmail.com

J.-C. Liao

Taiwan Construction Research Institute, New Taipei, Taiwan

S.-D. Yang

Artech Engineering, Taipei, Taiwan

L.-Y. Huang

Public Works Department, Geotechnical Engineering Office,
Taipei City Government, Taipei, Taiwan

1 Introduction

Studies on the effect of fault on a slope have been focusing on the distance between epicenter and the slope, the relationship of distance between fault and slope, and the relationship between ground surface acceleration and dynamic behavior of the slope and so on. Due to shearing along fault, the geological materials inside the faulting are often fragmental, loose, and weak, which easily become the flow path of groundwater. However, existence of the fault gouge with impervious property results in aquiclude to raise the groundwater up to the interface of the soil and rock. Study on the stability of the slope located at fault fractured zone is not common. This paper presents a case study on remediation of a building sitting on an unstable slope located at the fault fractured zone.

The building is located at the east side of the Tafung rural road with elevation of 360 m along the east side of the Nan-Gang district of Taipei city (DOED 2006). The site is on the west slope of the NS hill connecting Wufen mountain in the north and Tukuyue mountain in the south. Both mountains stretch along the ENE direction. The hill on the east side of the building site is the watershed of the Takung creek on the west and Yungding creek on the east, as shown in Fig. 1. Based on the surveying, as shown in the Fig. 1, variation of the elevation of the site is 403 m on the east down to 345 m on the west.

2 Site Investigation

Based on the Central Geological Survey in Taiwan, geological zonation of the building site is on the western foothill containing the Mushan formation and Taliao formation of Miocene epoch. The geological structure includes folds and reverse faults, which stretch along the ENE. During site investigation, some fountains or gushing groundwater were found along the hanging wall of the fault. A circular type slope failure on the west side of the hill was observed. Irregular attitudes of the

Fig. 1 Site topographic map

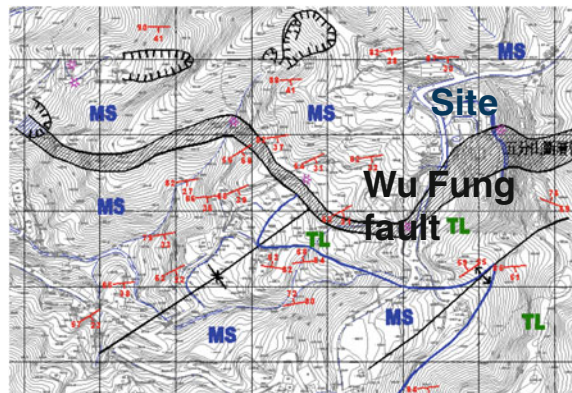
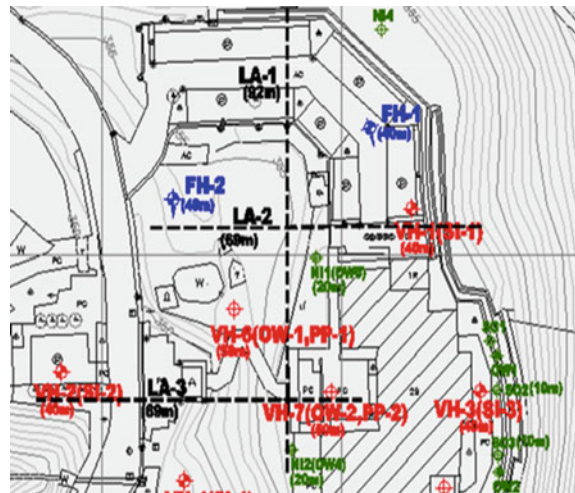


Fig. 2 Site monitoring instruments map



rock layer, fault gouge, and fault breccia were also observed at the failed slope site. One more evidence of the fault was found at a creek located at 250 m of the SW side of the building, where fault gouge and breccia were also found. Irregular rock strata, shearing fold, fault breccia, fault gouge, and slickenside were also observed from coring at the Wufen mountain fault zone. Hence, it was confirmed the building site is sitting on the Wufen mountain fault. Because of higher elevation of the Wufen mountain on the N and NE corner of the building, groundwater of the fault zone areas often seeps into ground becoming fountain. The fault gouge stops the groundwater running foot wall of the fault in the south side. Hence, we could find some fountain seeps out of the ground in the surrounding area of the building.

Seismic prospecting was also conducted for the purpose to gain more ground information of the studied site. In general, the ground condition can be divided into two layers. The top layer is the surface layer containing surface soil and backfill with P wave velocity of 0.7–1.28 km/s. The thickness surrounding the building is around 6–7 m. Below the surface layer, most of the investigated area are highly fractured rock with P wave velocity of 2.05–2.75 km/sec, except the investigating line along LA-2 between 0k+63 and 0k+69, where better rock properties were found with P wave velocity of 2.75 km/sec. Detailed investigation results are given in Table 1.

Table 1 Seismic prospecting results

| | Layer | Stratum judgments | P wave (km/sec) | Thickness (m) |
|------|-------|-------------------|-----------------|---------------|
| LA-1 | 1 | Backfill | 0.70–1.02 | 6.32–14.66 |
| | 2 | Fractured rock | 2.35–2.54 | – |
| LA-2 | 1 | Backfill | 0.72–0.96 | 5.26–9.30 |
| | 2 | Fractured rock | 2.10–2.75 | – |
| LA-3 | 1 | Backfill | 0.83–1.28 | 6.03–25.50 |
| | 2 | Fractured rock | 2.05–2.21 | – |

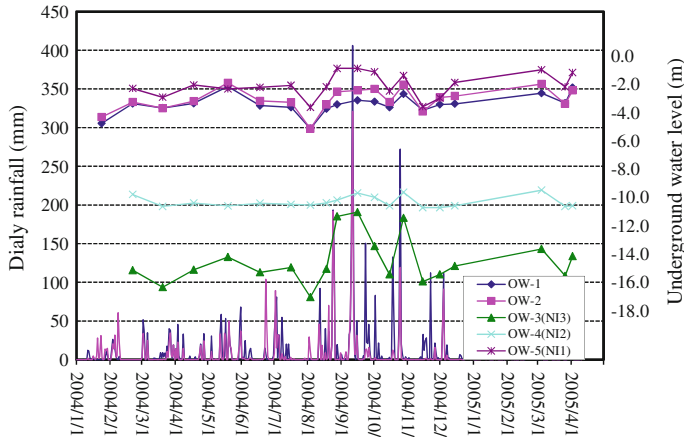


Fig. 3 The relationship of rainfall versus groundwater level

Three water level gages and three piezometers were installed at the site. Variation of the observed water table level and the precipitation or the daily rainfall is given in Fig. 3. The comparison shows that the precipitation has little influence on groundwater level inside the fault fractured zone, such as the station OW1, OW2, OW4(NI2), and OW5(NI1) as shown in Fig. 2. However, outside the fault fracture zone the groundwater level is highly influenced by the precipitation, such as the station OW3(NI3).

3 Observation

Twelve inclinometers were installed surrounding the building site area. Variation of the accumulated displacement with time is shown in Fig. 4. As shown in the figure, most of the observation location appeared to have some degree of displacement with rate of 0.15–0.30 cm/month, except VH-1 and VH-3 showed almost no movement. During heavy rainfall, the rate of displacement was even higher. The displacement direction was all perpendicular to the surface of the slope. In addition, the displacement on east side of the building was minimal, however larger displacement on the west side of the building was observed.

Based on the investigated information and the measured inclinometer data, the slope condition can be summarized in the following:

1. The sliding of the slope on the west side of the building was the main reason for the settlement of the building;
2. Sliding surface of the slope was along the soil/rock interface;
3. Heavy rainfall often accelerated the sliding;
4. The north side of the building was sitting on the hanging wall of the fault, where is also the location draws groundwater.

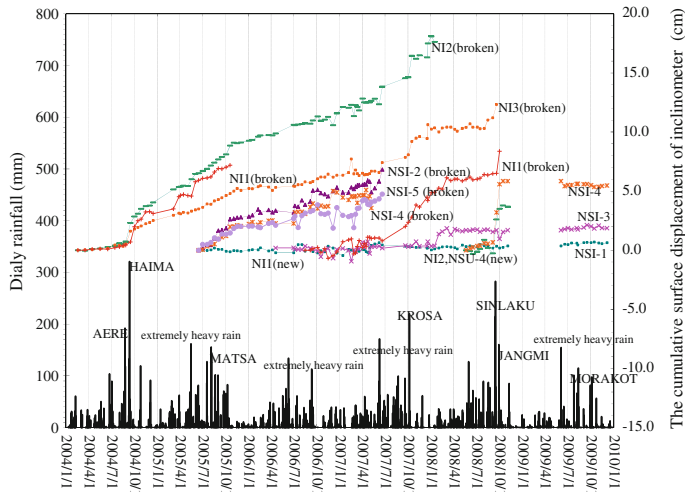


Fig. 4 The cumulative surface displacement of inclinometer in A direction

4 Mitigation

The strategy for stabilizing the slope was proposed as in the following:

1. Use of drilled shaft and ground anchor to stabilize the slope;
2. Install groundwater collecting well and horizontal drainage conduit for lowering of the groundwater table;
3. Long term monitoring.

Analyses were conducted at several different cross sections. Considering the safety factor of 1.5, the cross sections along 1, 2, and 3 needed additional resistance of 228–256 kN to stabilize the slope, as given in Fig. 5. The size of the drilled shafts, 60 cm in diameter, was 14, 17, and 20 m long. The center to center distance between the drilled shafts was 1 m. The free and the fixed length of the designed ground anchor were 12.5 and 15 m, respectively. The design load of the anchor was 300 kN.

In order to collect the large area of groundwater at hanging wall of the fault on the north side, groundwater collecting wells, collecting conduits, and drainage pipes were installed as shown in Fig. 6. Two 13.5 m deep collecting wells with diameter of 3.5 m were installed at the SW side of the building and at the parking lot of the building. Installed horizontal collecting conduits, with diameter 5 cm, were 40 m long. In addition, each collecting well was accommodated with two drainage pipes of 10 cm in diameter. With all the equipped groundwater lowering system, the safety factor of the protected slope was 1.3 as shown in the analytical result of Fig. 7.

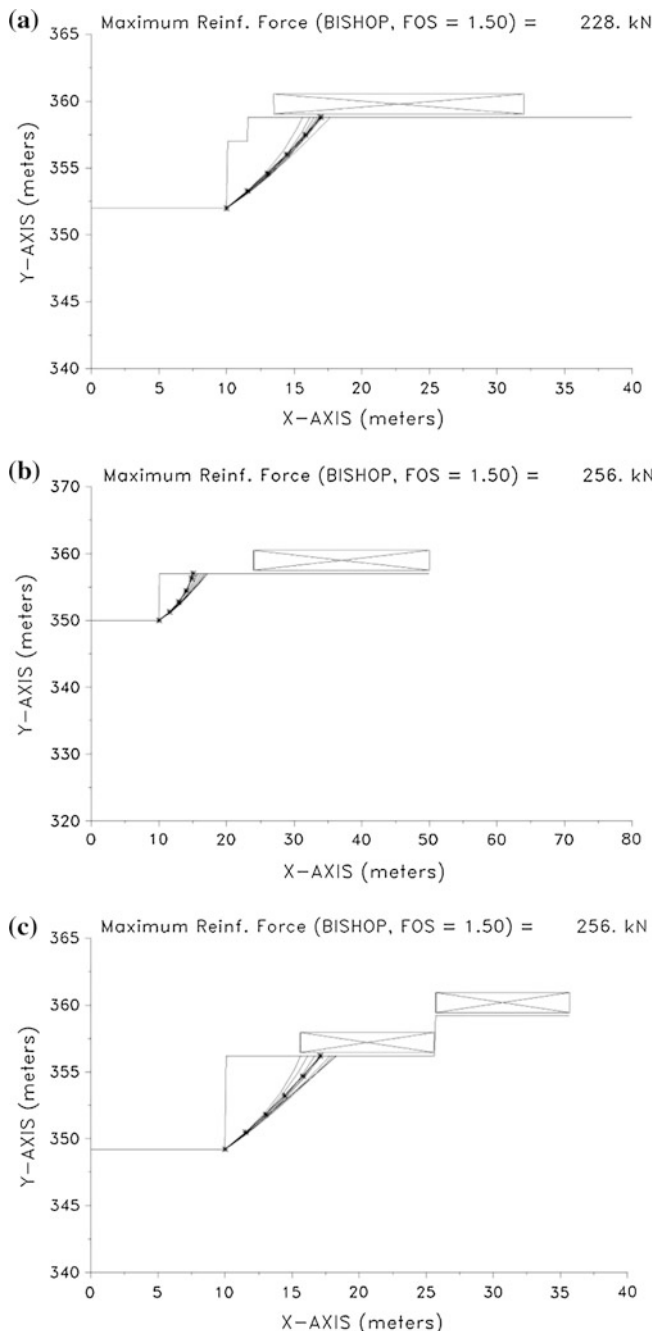


Fig. 5 The essential resistance force of different pile length for FS = 1.5, **a** pile length 14 m, **b** pile length 17 m, **c** pile length 20 m

Fig. 6 Arrangement of the mitigation

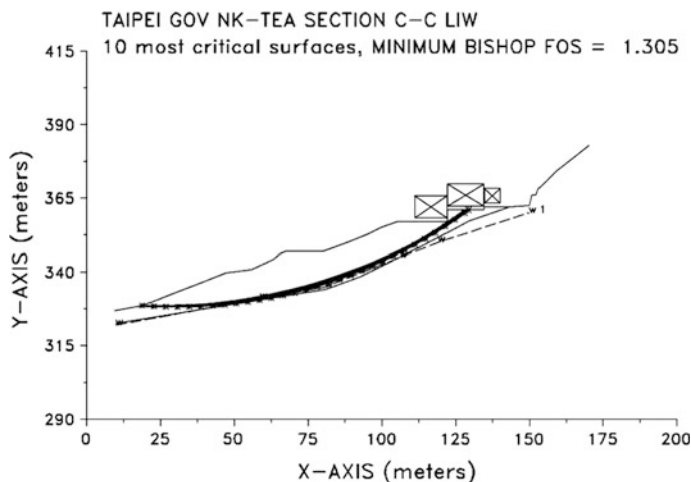
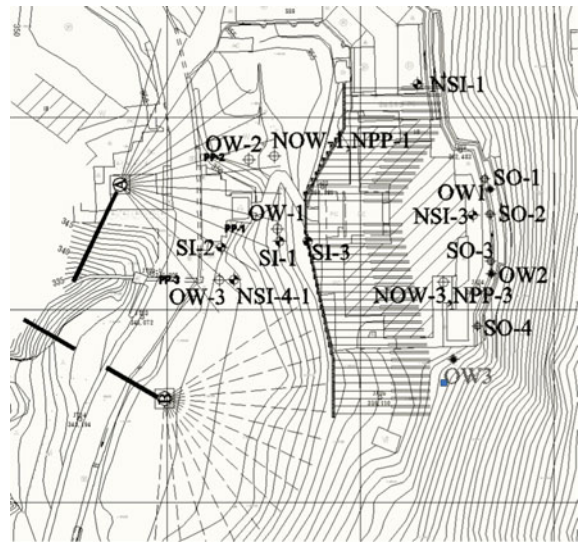


Fig. 7 The slope stability analysis using stable

5 Discussion of the Mitigation Works

Geotechnical mitigation works of the project started from August of 2010 until April of 2011 (GEO 2009, 2010). During the mitigating works, monitoring on the stability of the slope was continuous as shown in Fig. 6 (GEO 2011a, b). The time history of the groundwater level and the precipitation relations during the mitigating

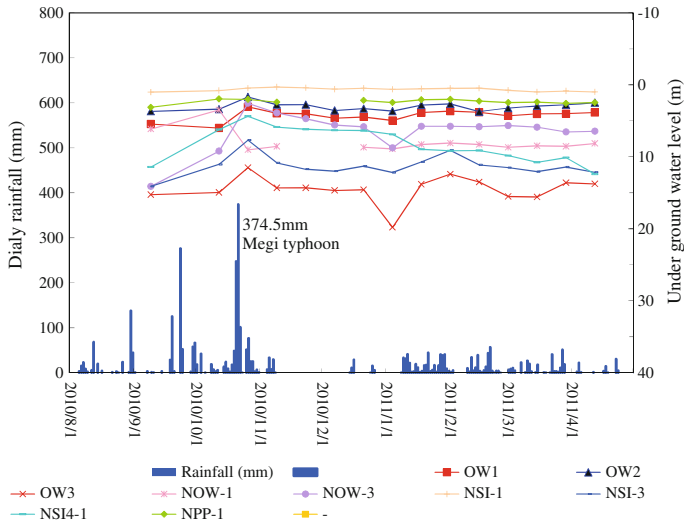


Fig. 8 The rainfall versus groundwater level during construction

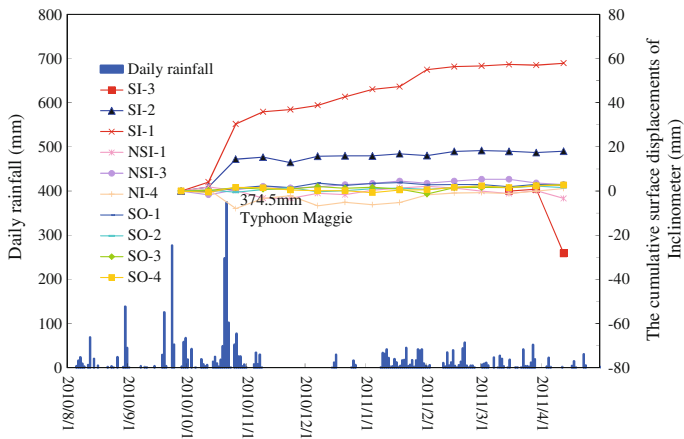


Fig. 9 Rainfall versus ground surface displacements during construction

work using the old and the newly installed monitoring system are shown in Fig. 8. When the collecting well A finished in December 2010, the groundwater level dropped 5.5–6.5 m. However, similar trends were not found for OW-1 and OW-2.

As shown in Fig. 9 for the ground surface displacement changing with time, when typhoon Maggie hit Taiwan (2010/10/22) and accumulated 374.5 mm of rainfall in 24 h, the ground surface displacement at SI-1 and SI-2 jumped from 0.86 cm/month and 0.397 cm/month, respectively, to 5.638 cm/month and 2.696 cm/month. However, after the drilled shafts and ground anchors were

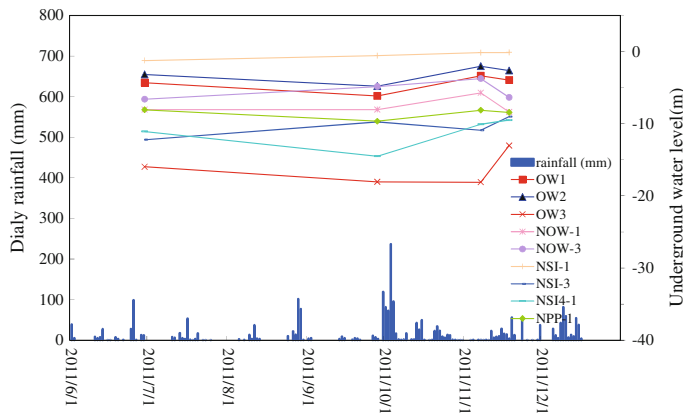


Fig. 10 The rainfall versus underground water level after slope reinforcement (old monitoring system)

installed, the displacement speed was down to 0.085 cm/month and 0.006 cm/month for SI-1 and SI-2, respectively.

Monitoring results on the ground displacement of the inclinometers between June and November of 2011 are shown in Fig. 10. The observed maximum displacement of SI-1 and SI-2 were only 0.55 and 0.61 mm, respectively. The observed accumulated maximum displacement, based on the SI-3 installed inside the drilled shaft, located at 7.0 m below ground surface was only 1.05 mm.

6 Conclusions

Geotechnical mitigation work of a building located at an unstabled slope sitting on the fractured zone was carried out by installation of groundwater collecting wells, retaining drilled shafts, and ground anchors. Based on the engineering works discussed in this paper, the following conclusions are drawn:

1. After the remediation work was finished, the water pressure gage readings of NPP-1 and PP-2 dropped 6.0 and 4.0 m, respectively. In addition, the observation well of OW-2 dropped 1.4 m. It is concluded that the collecting well installation was a correct decision.
2. Based on the inclinometer data installed in the drilled shaft SI-3, the accumulated maximum displacement was only 1.05 mm at 7.0 m below ground surface. In addition, maximum displacement based on the observation from SI-1 and SI-2 was only 0.55 and 0.61 mm, respectively. Hence, the installed drilled shaft and ground anchor system also had good performance.

References

DOED (2006) The building and geological survey of the Taipei Nangang tea manufacturing demonstration farm-finial report, Department of Economic Development, Taipei City Government (in Chinese)

GEO (2009) Slope restoration work of the Nangang Tea manufacturing demonstration farm-design report, Geotechnical Engineering Office, Taipei City Government (in Chinese)

GEO (2010) Slope Improvement work of the Nangang Tea Manufacturing Demonstration Farm-Supervisor Report, Geotechnical Engineering Office, Taipei City Government (in Chinese)

GEO (2011a) Slope restoration work of the Nangang Tea Manufacturing Demonstration Farm-the Monitoring Report (2010/09–2011/04), Geotechnical Engineering Office, Taipei City Government (in Chinese)

GEO (2011b) Slope restoration work of the Nangang Tea Manufacturing Demonstration Farm-the Monitoring Report (2011/04–2011/11), Geotechnical Engineering Office, Taipei City Government (in Chinese)

Case Study of Using the Low-Pressure Grouting Method to Uplift a Tilted Building

C.J. Kuo, Y.K. Lin, S.C. Shieh and C.H. Chen

Abstract A case of using the grouting method to uplift a tilted building is reported in this paper. This building is a nine-storey reinforced concrete structure with a one-storey basement. After the completion of constructional works, the building was found to be settled a little bit and tilted about 1/270. Two stages of grouting were conducted. The first stage was the compact grouting, aimed to consolidate the soft soils underneath the foundation slab. Then, the second stage low-pressure grouting was applied to uplift the building. After the completion of grouting, the maximum tilt angle was reduced to 1/787, which fulfills the requirement of serviceability of the building.

Keywords Grouting · Building tilt · Foundation retrofit · Soft ground · Soil improvement

1 Introduction

The case reported thereafter is a newly constructed nine-storey reinforced concrete structure, which is located at Xizhi, New Taipei City, Taiwan. This building has a one-storey basement of depth 5 m. The southeastern side of the basement is closely adjacent to an old five-storey building without any basement, as shown in Fig. 1. For basement construction, the sheet pile of length 10 m was penetrated surrounding the construction site for protection during the basement excavation. After the completion of constructional works, the building was found to be settled a little bit and tilted to the northwestern direction about 1/270. It is believed to be resulted from the pulling-out of sheet piles used for the basement excavation. Afterwards, the maximum settlement of the foundation was increased to 6.5 cm and the max-

C.J. Kuo (✉) · Y.K. Lin · S.C. Shieh
Mice Engineering Consultants Co. Ltd, Taipei, Taiwan
e-mail: kuo06@ms28.hinet.net

C.H. Chen
Department of Civil Engineering, National Taiwan University, Taipei, Taiwan



Fig. 1 Plan of foundation and tilting measured for the building

imum tilting was increased to 1/230 after the shaking of a very small earthquake. The measurements of building tilting are indicated in Fig. 1. Therefore, it is decided to uplift the foundation using the grouting method.

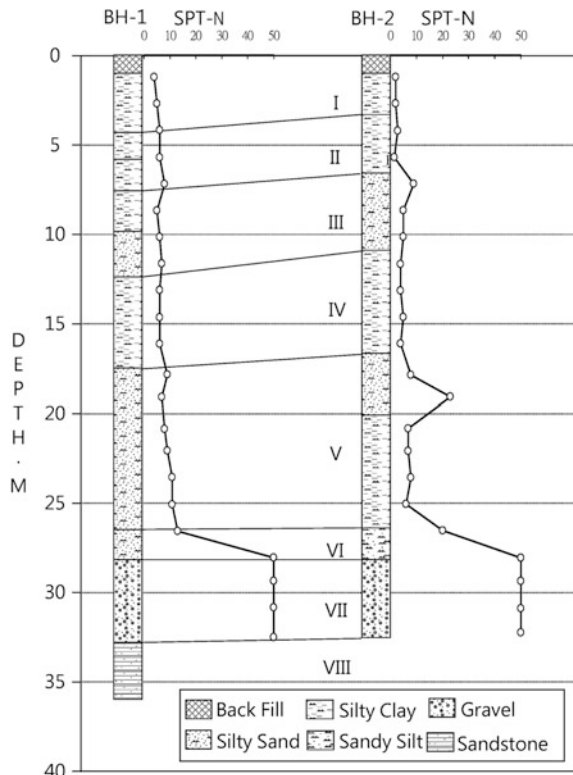
2 Geological Condition

According to the site investigation report (Mice Engineering Consultants 2007), the geotechnical conditions at the site had be summarized and simplified as shown in Table 1. It shows that the soils underneath the foundation slab are alternating layers

Table 1 Geological profile

| Layer | Depth (m) | Soil description | SPT-N | g_t (t/m ³) | w_n (%) |
|-------|-----------|------------------|-----------|---------------------------|-----------|
| I | 0.0–3.8 | SF/CL | 2–6 (4) | 1.90 | 33.0 |
| II | 3.8–7.1 | CL | 2–8 (5) | 1.91 | 31.7 |
| III | 7.1–11.7 | SM/CL | 5–9 (6) | 1.94 | 28.6 |
| IV | 11.7–17.1 | CL | 4–6 (5) | 1.86 | 33.8 |
| V | 17.1–26.5 | SM/CL | 6–23 (10) | 1.94 | 26.7 |
| VI | 26.5–28.2 | SM/ML | 13–20 | 1.96 | 25.0 |
| VII | 28.2–32.8 | GW | >50 | 2.25 | – |
| VIII | 32.8– | SS | >50 | 2.40 | – |

Fig. 2 Geological loggings and SPT-N values



of silty clays and silty sands, till the depth of 17.1 m. Those layers have very low SPT-N values, as shown in Fig. 2, and can be characterized as a soft ground, which is believed to have not enough bearing capacity to be adopted as a base-layer for uplift grouting. Therefore, ground improvement or compact grouting on these soft layers are necessary before the uplift grouting can be applied.

3 Method of Grouting

The plan of the basement along with the grouting holes is shown in Fig. 3. From the geological loggings shown in Fig. 2, it can be seen that the soils beneath the foundation slab to the depth of 17 m are mainly very soft clay layers interbedded with silty sands. For grouting, a total of 16 grouting holes of depth 19 m were installed through the foundation slab inside the building as shown in Figs. 4, 5, 6 and 7. In addition, four grouting holes of depth 18 m were installed on the ground surface surrounding the southwestern side of the building. The method of

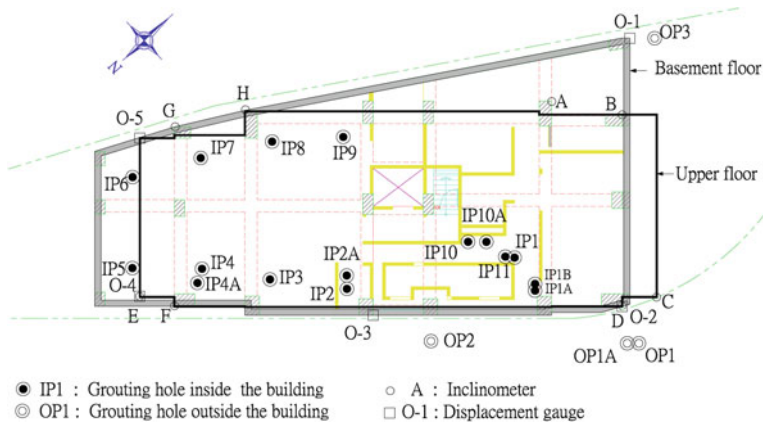


Fig. 3 Layout of grouting holes and instrumentations



Fig. 4 Picture of TAM tube

low-pressure grouting with the double packer Tube-A-Manchette (TAM) was applied. The procedure for installing the TAM grouting tube is shown in Fig. 8.

Two stages of grouting were conducted in this project. The first stage work was to grout the soils from the depth GL.-19 m upwardly to the depth GL.-5 m as shown in Fig. 9, which aimed to infill the voids in the ground, as well as to compact the loose soils using the water-cement-waterglass mixture of quick-solidify or fast-penetration type. For the second stage, the water-cement-waterglass grouting, with a maximum pressure of 30 kg/cm^2 , was applied to the upper 5 m soils to uplift the foundation slab and to compensate the tilt of the building. The materials used for the first and second stage groutings are shown in Tables 2 and 3, respectively. It can be seen that the contents of waterglass used in the second stage grouting has been increased to 35 % to enhance the effects for uplifting.

Fig. 5 Drilling hole on the foundation slab



Fig. 6 Pre-embeded outer pipe



Fig. 7 Pressure grouting



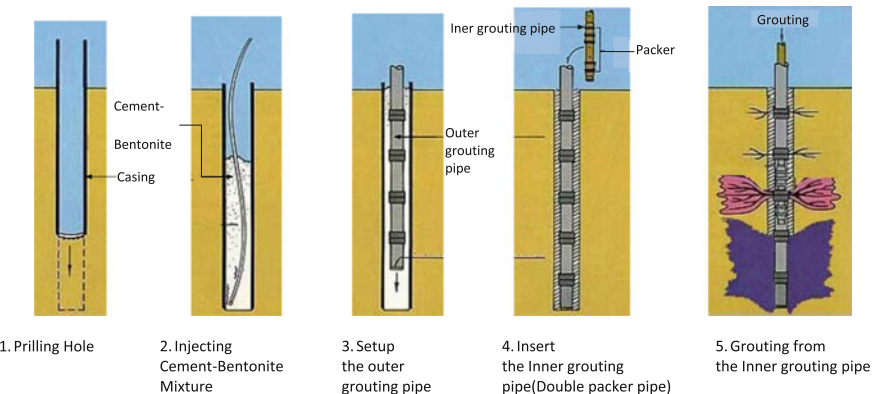


Fig. 8 Procedure of installing the Tube-A-Manchette (TAM)

Fig. 9 Pressure grouting by using TAM method

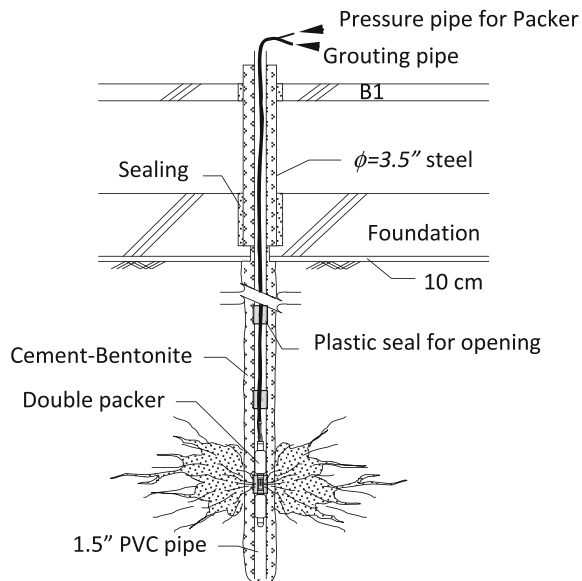


Table 2 Material used for the first-stage grouting

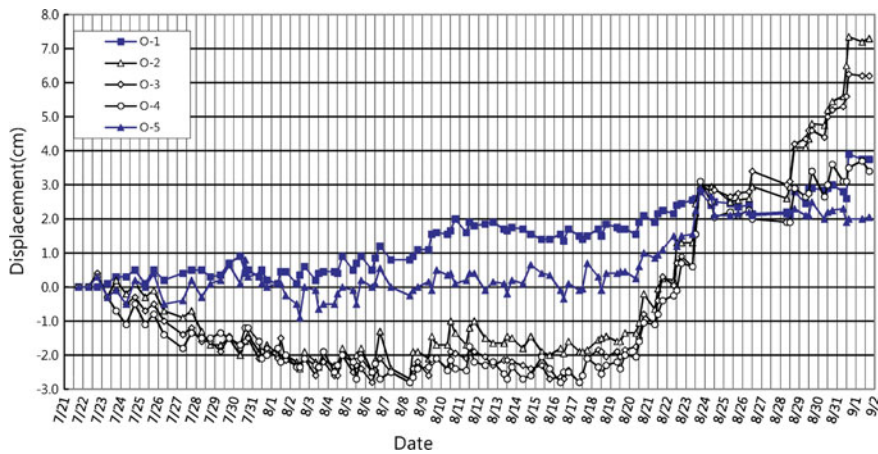
| Cement | Water | Waterglass | Water |
|--------|--------|------------|-------|
| 241 kg | 217 kg | 75 L | 225 L |
| 300 L | | 300 L | |
| 600 L | | | |

Table 3 Grouting material at the second stage

| Cement | Water | Waterglass | Water |
|--------|--------|------------|-------|
| 263 kg | 210 kg | 105 L | 195 L |
| 300 L | | 300 L | |
| 600 L | | | |

4 Monitoring

In order to monitor and control the movement of the structure during the process of grouting, five displacement gauges (O-1 to O-5) and six inclinometers (A, B, C, F, G, and H) were installed on the structure as shown in Fig. 3. The results of monitored displacements and tilt angles are shown in Figs. 10 and 11, respectively. The first stage grouting, started from July 21 and ended on August 20, used grouting material of volume 255 m^3 . From Fig. 10, it can be seen that the O-2, O-3, and O-4, which located on the northwestern side of the structure, suffered additional settlement during the first-stage grouting. However, during the second stage of grouting, very rapid and significant uplifts at these three locations were observed, even though only a volume of 67 m^3 was grouted during this stage. A total volume of 322 m^3 was grouted in 42 days. After the completion of grouting, the maximum tilt of the building was reduced to $1/787$ as shown in Fig. 12, which fulfills the requirement of $1/600$ as requested by the client (Mice Engineering Consultants 2009).

**Fig. 10** Results of foundation uplift

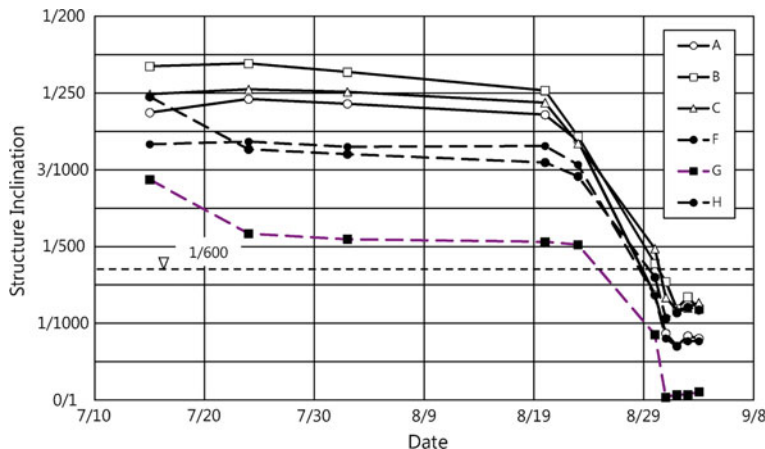


Fig. 11 Results of structure inclination, locations as indicated in Fig. 12

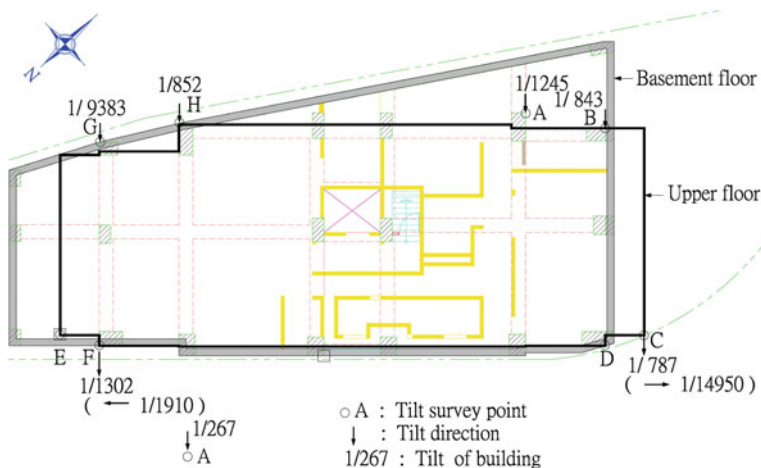


Fig. 12 Tilt of building after uplift grouting

5 Summary and Conclusions

1. The method of low-pressure grouting with the double packer TAM tube was successfully used to uplift a tilted nine-storey building with a one-storey basement of depth 5 m. The maximum tilt of the building was reduced from 1/230 to 1/787 after the completion of grouting.
2. Two stages of grouting were conducted. The first stage used a volume of 255 m³ for compaction grouting, which resulted additional settlement due to

compaction of soils at deeper depth. However, the second stage of grouting used only a volume of 67 m³ grouted for the top 5 m soils under and near the foundation slab, which resulted a rapid uplift of the foundation slab.

References

Mice Engineering Consultants (2007) Soil investigation report of Xizhi Site, New Taipei City.
Mice Engineering Consultants Co. Ltd, Taiwan

Mice Engineering Consultants (2009) Construction report of uplifting a titled building. Mice Engineering Consultants Co. Ltd, Taiwan

A Study on the Bio-treatment Technique of Ground Improvement with Urease Microorganisms Which Live in Japan

Seiji Kano, Takeo Moriwaki and Kyohei Ochi

Abstract Soil improvement techniques using microorganisms have recently been focused on as the low cost and environmentally friendly technique (Mitchell and Santamaria in *J Geotech Geoenviron Eng* 131:1222–1233, 2005; De Jong et al. in *Bio-soils interdisciplinary science and engineering initiative: meeting societal needs through international transforming research*, 85 pp, 2007) for practical use in Japan. *Sporosarcina pasteurii* is mainly used for this technique in almost all researches. But it has not yet been clarified how much this microorganism affects the environment in Japan because it is imported from the USA. In this paper, three laboratory tests were carried out to examine urease microorganisms which live in Japan for this bio-treatment technique. Results revealed that the urease microorganisms were found in all natural beach rocks from Okinawa that these microorganisms could reproduce calcium carbonates in soil. Especially microorganisms picked up from Yomitan Beach show a high rate of productivity of calcite to help the treatment. It was also found that the unconfirmed compression strength of the specimen treated with microorganism from Yomitan Beach showed almost the same strength as the one with *S. Pastuerii*. Therefore this microorganism is useful for the bio-treatment technique, instead of *S. pasteurii*.

Keywords Bio-treatments · Urease microorganisms · Beach rock

S. Kano (✉) · T. Moriwaki · K. Ochi
Kure College, National Institute of Technology,
2-2-11, Agaminami, Kure, Hiroshima 737-8506, Japan
e-mail: kanou@kure-nct.ac.jp

T. Moriwaki
e-mail: moriwaki@kure-nct.ac.jp

K. Ochi
e-mail: smoriwaki@kure-nct.ac.jp

1 Introduction

Recently the climate situation has been changed by global warming. Very heavy rainfalls of more than 100 mm/h are observed in Japan. Because of heavy rainfalls, many slope failures occur all over Japan every year. One way to prevent slope disasters is slope stabilization. However the amount of area which should be stabilized is too large and the construction takes place on steep slopes. Therefore a cheap and easy stabilization technique should be developed.

Many slope failures induced by rainfall in Japan occur in the shallow part of ground. This part is very loose because the overburden pressure is small and it is weathered. Thus that technique does not need such a high solidification capacity, but should be low cost and environmentally friendly.

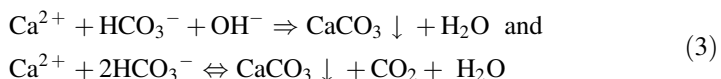
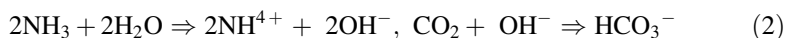
On the other hand, a soil improvement technique using microorganisms has been recently focused on as the low cost and environmentally friendly technique. According to the report by De Jong, the shear wave velocity of bio-treated soil reached to more than 300 m/s (DeJong et al. 2010). In considering the shallow part of a slope, this treatment technique can be useful for the slope stabilization.

Some problems, however, should be solved before it is put to practical use in Japan, such as which kind of microorganism is best to use. Many studies on this bio-treatment technique are also conducted in Japan but a microorganism, *Sporosarcina pasteurii*, which is imported from USA, is used in almost all studies. But it is not clarified how much this microorganism affects the environment in Japan. In order to use this technique in practice, the microorganism which exists in Japan must be used.

This study aims to examine whether urease microorganisms which live in Japan can be used for this bio-treatment technique or not.

2 Mechanism of Ground Improvement

A calcium carbonate, Calcite, precipitates by the chemical reaction induced by biological activity in the ground has the following reactions. Bio-treatment technique exploits this reaction.



Calcite can be precipitated in the solution with containing carbonate ions under an alkaline environment. Microorganisms having urease activity, such as *Bacillus pasteurii* or *S. pasteurii* are used for many studies on bio-treatment techniques.

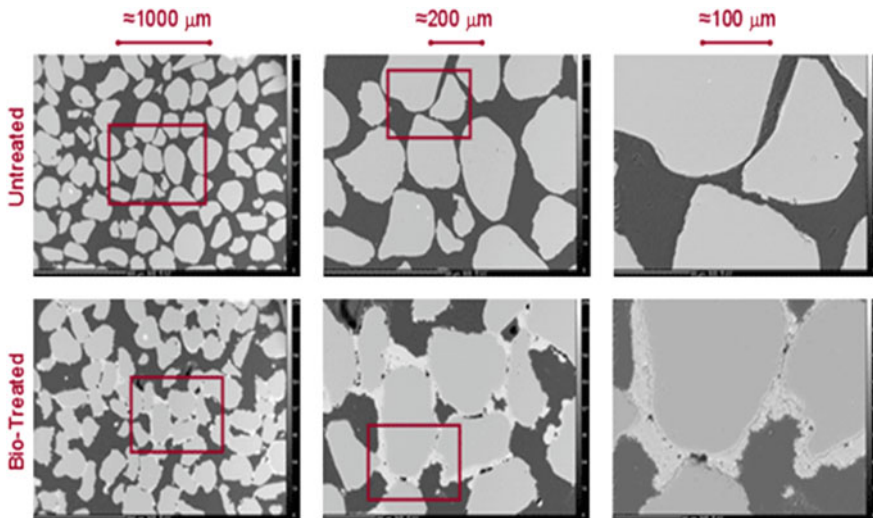


Photo 1 SEM images of bio-treated soil

However these microorganisms cannot be used in Japan because they are imported from the United States. So an investigation on urease microorganisms which live in Japan should be performed.

Photo 1 shows SEM Images of bio-treated soil (UC Davis 2007). As shown in this photograph, Calcite was observed between soil particles in bio-treated soil.

3 Laboratory Tests

This study aims to examine whether urease microorganisms which live in Japan can be useful for a bio-treatment technique or not.

Several beach rocks were collected and microorganisms which live in them were harvested. An examination whether cultured microorganisms have urease activity or not was performed. If urease microorganisms existed in it, the examination of how much Calcite they could reproduce in the soil was done. Finally, a series of unconfirmed compression tests were carried out to check whether they could be useful for bio-treatment technique.

3.1 Harvesting the Urease Microorganism from Beach Rock

According to the report by Yonetani (1964), there are many rocks, called Beach rock, which were cemented from sand on the beach in the southern part of Japan (Photo 2). They have strong cementation. If it is possible to make them artificially,



Photo 2 Beach rock (at Yomitan son, Nakagami County, Okinawa)

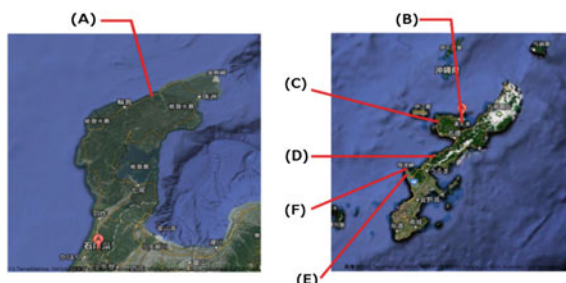


Fig. 1 Maps of the location of beach rocks. *A* Mituko-hama Beach, Wajima, Ishikawa. *B* Kori Bridge, Nagijin son, Kunigami County. *C* Emerald Beach, Motobu town, Kunigami county. *D* Manza Beach, Onna son, Kunigami County. *E* Yomitan son, Nakagami County. *F* Nikko Alivila Beach, Yomitan son, Nakagami County son

the technique is useful for ground improvement. In this study, one beach rock from Ishikawa prefecture (A) and five beach rocks from Okinawa Island (from B to F) were picked out as shown in Fig. 1.

Small particles of each beach rock were added to a culture solution for *S. pasteurii* in a beaker. Then microorganisms were harvested in an incubator at 30 °C and the optical density of the solution was measured. Figure 2 shows growth curves of harvested microorganisms from beach rocks. This figure shows the microorganisms of B, E, and F rise a little bit faster than *S. pasteurii*, but the microorganism of D rises more slowly than that.

3.2 Test of Urease Activity

In order to investigate whether urease microorganisms live in beach rocks or not, small spall from each beach rock, urea, and yeast extract were put in a small tube.

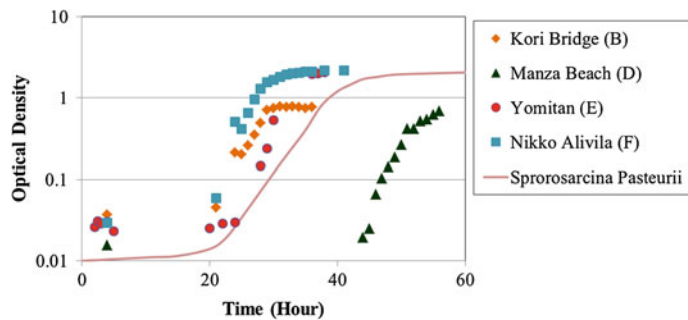


Fig. 2 Growth curves of harvested microorganisms from beach rocks

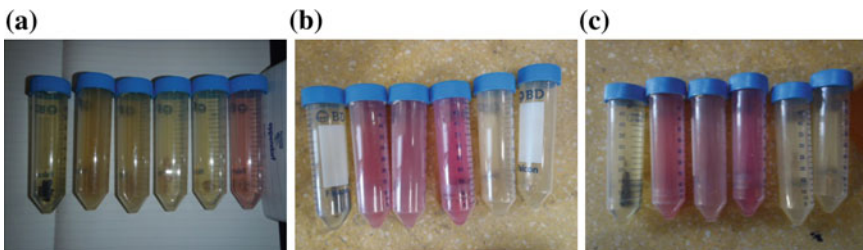


Photo 3 Color of tubes after 48 h (a), 72 h (b) and 1 week (c)

Table 1 Results of urea activity tests

| | A | B | C | D | E | F |
|--------|---|---|---|---|---|---|
| 48 h | × | × | × | × | × | ○ |
| 72 h | × | × | ○ | ○ | ○ | ○ |
| 1 week | × | ○ | ○ | ○ | × | × |

Tubes were kept in an incubator with shaking at 30 °C. If urease microorganisms live in it, the pH of the solution rises. The phenolphthalein reagent was used to check the pH. When the color turns red, it means urease microorganisms live in that beach rock. The color of tubes was checked after 48 h, 72 h, and 1 week.

Results are shown in Photo 3 and Table 1. As shown in the photographs below, tubes in which beach rocks from Okinawa were put, showed urease activity but the one from Ishikawa did not show urease activity. This indicated that urease microorganisms lived in Okinawa's beach rock. However the Ishikawa's beach rock is not made by urease microorganisms. In fact, it is said that the Ishikawa's beach rock is made from silica (Ogasawara et al. 2004).

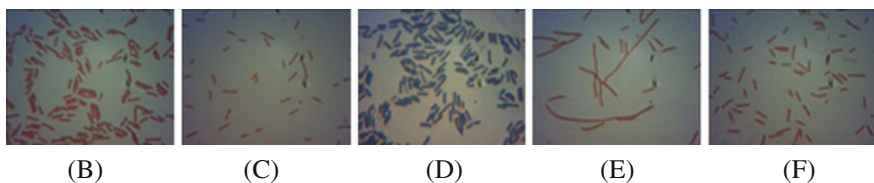


Photo 4 Pictures of harvested microorganisms in laboratory

Table 2 Results of calcite reproduction

| | B | C | D | E | F |
|--------------------------|-------|-------|-------|-------|---|
| CaCO ₃ (g) | 0.231 | 0.496 | 0.442 | 0.878 | – |
| Rate of reproduction (%) | 22.9 | 49.2 | 43.9 | 87.2 | – |

3.3 Gene Analyses of Harvested Microorganisms

Photo 4 shows the pictures of harvested microorganisms in the laboratory. It has found that all microorganisms were rod-shaped bacillus. Gene analyses of harvested microorganism were conducted to identify the urease microorganism. As a result, microorganism from B was *Paenibacillus fonticola* (99 %), microorganism from D was *Lysinibacillus sphaericus* (99 %), microorganism from E was *Sporosarcina sphaericus* (99 %) (values mean the degree of occurrence of RNA). Unfortunately, the microorganisms of C and F were not identified.

3.4 Test of Calcite Precipitation

A series of beaker tests were carried out to know how much the harvested microorganisms could reproduce Calcite. Microorganisms were added to the culture solution containing calcium ion in a beaker. Beakers were kept in the incubator with shaking at 30 °C for 48 h. After that, Calcite was filtered from the solution and was weighed.

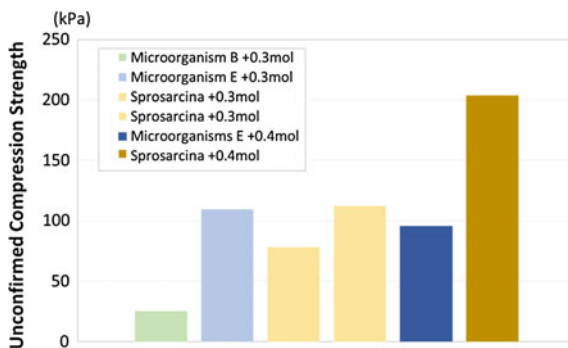
Table 2 shows the result of beaker tests. As shown in this, all microorganisms, with the exception of F, reproduced Calcite. Microorganism E showed the highest rate of reproduction of calcium carbonate. This result inspires that these microorganisms can be used for bio-treatment technique, instead of *S. pasteurii*.

3.5 Unconfirmed Compression Tests

In order to clarify the effect of bio-treatment using the harvested microorganisms, a series of unconfirmed compression tests was performed. Specimens made of

Table 3 Conditions for unconfirmed compression tests

| No. | Microorganism | Moisture content (%) | Calcium chloride (mol/l) |
|--------|---------------|----------------------|--------------------------|
| Test 1 | C | 27.8 | 0.3 |
| Test 2 | E | 22.7 | |
| Test 3 | Sporosarcina | 19.6 | |
| Test 4 | Sporosarcina | 24.1 | 0.4 |
| Test 5 | E | 18.5 | |
| Test 6 | Sporosarcina | 14.9 | |

Fig. 3 Relationships between axial strain and principal stress differences of triaxial tests

Toyoura sand were treated using Microorganism C, E, and *S. pasteurii*. The size of specimen was 5 cm in diameter and 10 cm in height. The relative density of the specimen was 65 %. 0.3 mol/l of calcium chloride was added to the culture solution from Test 1 to Test 4, and 0.4 mol/l of calcium chloride was added in Test 5 and 6. Overburden pressure during the treatment was 200 kPa. Conditions for tests are shown in Table 3.

Figure 3 shows the unconfirmed compression strength in each test. It is found that the unconfirmed compression strength of the specimen treated with Microorganism E shows almost the same strength as the one with *S. pasteurii* from this figure. But the unconfirmed compression strength of the specimen treated with Microorganism C was less than the one with *S. pasteurii*. Therefore Microorganism E is useful for the bio-treatment. By comparing the results of 0.3 mol/l calcium and 0.4 mol/l calcium, the unconfirmed compression strength of specimen with Microorganism E and 0.4 mol/l of calcium ion varied only slightly from the one with 0.3 mol/l. However, the one with *S. pasteurii* and 0.4 mol/l calcium ion increased. The reason why this happened is considered that *S. pasteurii* has a higher salt tolerance than Microorganism E.

4 Conclusions

This paper aims to examine whether urease microorganisms which live in Japan are useful for a bio-treatment technique or not. The following results were obtained from this study:

1. It was found that the urease activity was confirmed in all beach rocks from Okinawa, and all urease microorganisms can reproduce calcium carbonates. Urease microorganisms from Beach rock E show the highest rate of reproduction of calcite to help the treatment.
2. The unconfirmed compression strength of the specimen treated with this microorganism was almost the same as the specimen treated with *S. pasteurii*. Therefore this microorganism is useful for the bio-treatment technique, instead of *S. pasteurii*, as it is locally sourced. This treatment is intended to prevent further landslides in Japan.

Acknowledgments This work was supported by JSPS KAKENHI Grant Number 24560614.

References

De Jong JT, Mortensen BM, Martinez BC (2007) Bio-soils interdisciplinary science and engineering initiative: meeting societal needs through international transforming research. NSF final report on 2007 workshop (NSF Grant #CMS-0628782), 85 pp

DeJong JT, Mortensen BM, Martinez BC, Nelson, DC (2010) Bio-mediated soil improvement. Ecological Eng 36:197–210

Mitchell JK, Santamaría JC (2005) Biological considerations in geotechnical engineering. J Geotech Geoenvir Eng 131(10):1222–1233

Ogasawara H, Yoshidomi K, Jiju K (2004) Beachrock from the Sosogi Coast in the Wajima City, northern part of Noto Peninsula, Chushikoku Branch of Japan Society of Engineering Geology. <http://www.jseg.or.jp/chushikoku/ronnbunn/ronnbunn16.html> (in Japanese)

Soil Interactions Laboratory of UC Davis (2007). <http://www.sil.ucdavis.edu/index.htm>

Yonetani S (1964) The beach rock on the south-west of Japan. The Bunka Hokoku, Shigaku-hen, Kagoshima University, vol 12, pp 83–94 (in Japanese)

Behavior of Breakwater Foundation Reinforced with Steel Sheet Piles Under Seismic Loading

**Babloo Chaudhary, Hemanta Hazarika, Naoya Monji,
Kengo Nishimura, Ryohei Ishikura and Kiyonobu Kasama**

Abstract Waterfront structures such as breakwater, coastal dike, sea wall, etc., suffer serious damage from the earthquake and tsunami. The breakwaters are designed to protect coastline and seaport from the devastation effect of wave and current of tsunami by absorbing their wave energy and reducing overtopping. The port of Kamaishi (Iwate Prefecture, Japan) suffered heavy causalities due to the Great East Japan Earthquake in March 2011 mainly due to the damage of breakwater mound/foundation which was caused due to collapse of the breakwater. On the other hand, mitigation of compound disaster due to predicted future earthquakes such as Tokai earthquake, Nankai Earthquake, and Tonankai-Nankai Earthquake is a matter of great concern. The stability and safe performance of breakwater is very important for the protection of structures and population living near to coastline. It is, therefore, necessary to develop a new earthquake and tsunami resistant reinforcement technique for breakwater foundations which will make the breakwater resilient against the earthquake and tsunami forces. This paper deals with the development of an effective reinforcement technology for breakwater foundation which provides resiliency to the mound against earthquake. The technique involves use of steel sheet piles and gabion type mound (gravel wrapped up in steel wired mesh), which is effective in preventing breakwater subsidence and horizontal displacement. As a part of the study, a series of shaking table test in 1 g of gravitational field were performed and through the tests, the reinforcement effect by the steel sheet pile and gabion under earthquake loading and its influence on breakwater performance was made clear.

Keywords Steel sheet pile · Gabion · Earthquake · Mitigate · Resilient structure · Breakwater

B. Chaudhary (✉) · H. Hazarika · N. Monji · K. Nishimura · R. Ishikura · K. Kasama
Kyushu University, W2-1108, 744 Motooka, Nishi-Ku, Fukuoka 819-0395, Japan
e-mail: babloomit@gmail.com

1 Introduction

Tsunami is frequently generated by strong earthquake with $M_L \geq 6.5$ in open sea due to quick dislocation of a seismological fault. Tsunami carrying huge energy always could lead to great catastrophic losses for the structures and population living near the coastline where tsunami wave could reach. Japan has many experiences of tsunami disasters such as the 1896 Meiji Sanriku tsunami that caused 22,000 dead and missing. Even after improvement of coastal defense systems which have been significantly implemented since the 1960s, the 1983 Nihon-kai Chubu earthquake tsunami (the Japan Sea tsunami) killed 100 persons, and 1993 Hokkaido Nansei-oki earthquake tsunami (the Okushiri tsunami) caused 230 dead and missing including casualties by the seismic damage. The Great East Japan earthquake ($M_w = 9.0$) stroked off the east coast of Japan on 11th March 2011 at 14:46 (local time). The Tohoku Earthquake occurred in the subduction zone where the Pacific plate subducts beneath the North American plate or the Okhotsk plate. It was the most powerful earthquake that ever hit Japan, and the fifth most powerful earthquake in the world since modern record keeping began in 1900. The earthquake triggered powerful tsunami waves that reached run-up heights of up to 40.50 m in Miyako in Tohoku (Iwate Prefecture) and in the Sendai area, traveled up to 10 km inland. The maximum inundation height was 19.5 m, and inundation area was 400 km² (approximate). The Great East Japan earthquake generated a higher tsunami (the 3.11 tsunami) than the tsunami level determined for tsunami disaster management in communities such as the 1896 Meiji Sanriku tsunami. Lots of coastal structures (breakwaters, sea wall, embankment, etc.) were damaged by the Great East Japan Earthquake (Hazarika et al. 2012, 2013a, b). It caused devastated damage in wide areas by not only inundation but also tsunami debris. More than 20,000 people were killed and a large number of structures were collapsed.

Breakwaters are designed to protect coastline and seaport from the devastation effect of wave and current of tsunami by absorbing their wave energy and reducing overtopping. The Kamaishi breakwater (Iwate Prefecture, Japan), which was completed in 2009 and recognized as world's deepest (63 m) breakwater, collapsed and failed to block tsunami generated by the Great East Japan Earthquake. The Caissons were moved and sanked. This happened due to large difference in water level between the front and back of the breakwater during tsunami, which creates high water pressure on the breakwater. The tsunami wave also imposed a huge horizontal force on the breakwater. The main reasons of failure of the breakwater were (Takahashi et al. 2011; Arikawa et al. 2012) (i) Scouring of foundation mound, (ii) Sliding and turning of breakwater, (iii) Toe erosion and Joint failure, (iv) Decrease in bearing capacity due to increase in pore water pressure, (v) Dynamic water pressure as wave force (vi) Water level difference between the front and back of the breakwater. The stability and safe performance of breakwater is very important for the protection of structures and population living near to coastline. After the 2011 Great East Japan disaster, development of geotechnical structures which can provide resiliency to the structures against earthquake and

tsunami became top priorities of scientists and researchers. It is therefore, necessary to develop a new earthquake and tsunami resistant reinforcement technique for breakwater foundations which will make the breakwater resilient/resistant against the earthquake and tsunami forces. This study deals with the development of an effective reinforcing technique of the mound and foundation which provides resiliency to breakwater by improving the earthquake resistant properties of the breakwater foundation. Steel sheet piles and gabion type mound (gravel wrapped up in wired mesh) are used in the foundation as a reinforcing measure. A series of shaking table test were performed to evaluate the effect of using steel sheet pile and gabion under earthquake loading. The main purpose of the research is to find a new reinforcing technique for breakwater foundation against earthquake and show effectiveness of the reinforcement technique (using sheet piles and gabion) in improving the earthquake resistant properties of the breakwater foundation.

2 New Technology for Breakwater Foundation

The port of Kamaishi (Iwate Prefecture, Japan) suffered heavy casualties due to the Great East Japan Earthquake in March 2011 mainly due to the collapse of breakwater. The Kamaishi breakwater collapsed and failed to block tsunami generated by the Great East Japan Earthquake in March 2011. The breakwater collapsed due to damage/failure of its mound/foundation. The future earthquakes such as Tokai earthquake, Nankai Earthquake, and Tonankai-Nankai Earthquake is a matter of great concern. According to the central disaster mitigation council of the ministry of Japan (Central Disaster Mitigation Council 2003), about 2 m ground sinking is expected in the Kochi area of Shikoku island, Japan, by the Nankai earthquake (Central Disaster Mitigation Council 2003), which is predicted to occur any time in the near future. These earthquakes may generate big tsunamis. In order to mitigate the damage from such future devastating earthquakes and tsunami, it is necessary to take appropriate measures that can protect the infrastructures from the compound disasters instigated by the combined effect of events such as an earthquake and tsunami. So for the protection of coastal lives and structures, it is necessary to develop a new technology to make the breakwater safe against the future earthquakes and tsunamis. A new reinforcing technology is proposed for the foundation and mound of breakwater which will make the breakwater resilient against the earthquake and tsunami forces. The sheet piles and Gabion mound was used in the foundation (Fig. 1). The gabion mound foundation was adopted in addition to the rubble mound (for conventional breakwater, generally rubble mound was used in the foundation). The gabion covered the entire mound. The purpose of use of gabion mound is to protect it from the scouring and toe erosion due to tsunami and earthquake. It will also improve its bearing capacity due to constraint effect. Due to these properties, subsidence and lateral displacement of breakwater can be prevented/reduced. In addition to gabion, steel sheet piles were also used in the foundation as shown in Fig. 1.

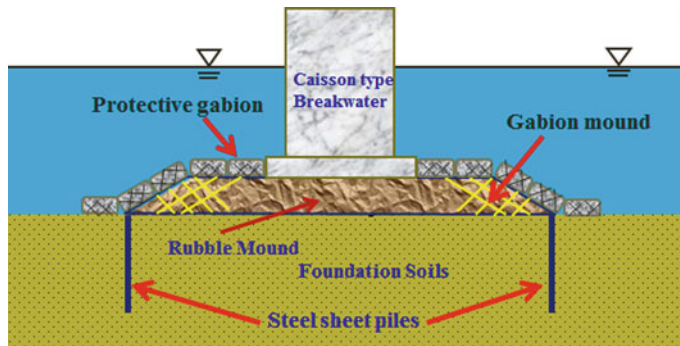


Fig. 1 Model of caisson type breakwater

These sheet piles behave like a cut off wall and reduce flow/seepage of water below the foundation during tsunami. It controls scour of the foundation as well as reduces uplifting force due to seepage of water, and thus prevent/reduce scour, subsidence, and lateral displacement. They will improve the bearing capacity also due to its confinement effect. The purpose of the study is to find effectiveness of the new reinforcing technique against earthquake and tsunami. This paper deals with effectiveness of the new reinforcing technique against earthquake. Through the shaking table tests, the reinforcement effect due to the steel sheet pile and gabion under earthquake loading and its influence on breakwater performance was made clear.

3 Shaking Table Test

A series of shaking table test in 1 g gravitational field were performed for the model breakwater. Shaking table tests were done under different field conditions and loading conditions. The pore water pressure, water pressure, horizontal displacement, and settlement were monitored during the experiments. The effect of reinforcement on breakwater performance was evaluated based on reduction of pore water pressure, horizontal displacement, and settlement.

3.1 Model Breakwater

A model of breakwater at Miyazaki port (Miyazaki Prefecture, Japan), which is likely to be affected by the Nankai trough earthquake, is chosen for the experiment. The prototype to model ratio was 64 and the similitude relationship proposed by Iai (1989) was used for this experiment. A tank, made with acrylic plates and steel

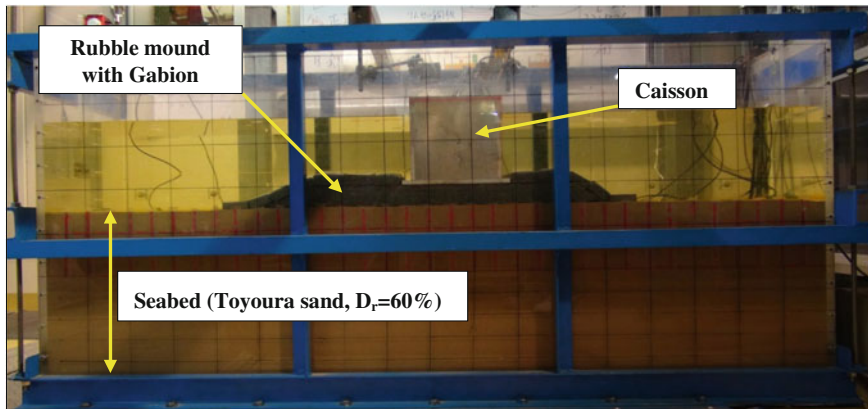


Fig. 2 Shaking table test for breakwater

frames, was used to make the model for the shaking table test. The size of the tank was 1830 mm (length) \times 430 mm (width) \times 865 mm (height). The photographic view of the shaking table is shown in Fig. 2.

3.2 Test Materials

The seabed was modeled with Toyoura sand of relative density, $D_r = 60\%$. The rubble mound was made of number 6 gravel ($D_r = 70\%$). The relative density $D_r = 70\%$ for rubble mound was achieved by tamping method. The grain size accumulation curve of Toyoura sand and number 6 gravel (Rubble mound) is shown in Fig. 3. The gabion was made of number 7 gravel and wire mesh. The wire mesh was made of steel wire of diameter 0.63 mm.

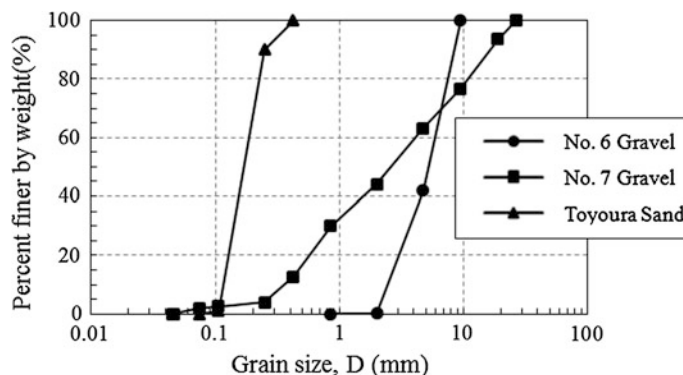


Fig. 3 Grain size distribution curve of sample A (No. 6 gravel) and Toyoura sand

Fig. 4 Number 6 gravel (rubble mound)



Table 1 Basic property of the foundation materials

| Materials | Sat. density ρ_s (g/cm ³) | Dry density ρ_d (g/cm ³) | Min. dry density $\rho_{d\min}$ (g/cm ³) | Max. dry density $\rho_{d\max}$ (g/cm ³) | Uniformity coefficient U_c | U_c' | Mean grain size D_{50} (mm) | Plastic limit I_p |
|--------------|--|---|--|--|------------------------------|--------|-------------------------------|---------------------|
| No. 6 gravel | 1.620 | 1.416 | 1.781 | 2.773 | 1.5 | 1.4 | 4.7 | NP |
| No. 7 gravel | 2.727 | 1.980 | 1.768 | 2.143 | 11.4 | 0.5 | 2.7 | NP |
| Toyoura sand | 2.640 | 1.506 | 1.336 | 1.639 | 1.7 | 3.8 | 0.16 | NP |

Photographic view of number 6 gravel (Rubble mound) is shown in Fig. 4. Basic properties of foundation materials are given in Table 1. The breakwater (caisson type) was fabricated box type model, and it was made of aluminum. The silica sand and lead ball were filled in the box type caisson to adjust the weight and center of gravity. The silica sand was medium packed of specific gravity 2.3. Three caissons, in a row, were used as breakwater in the experiment. The horizontal displacement and settlement were monitored for middle caisson. Both side caissons were used as dummy caisson to prevent effect (e.g., side friction between caisson and acrylic tank) of acrylic tank. Two sheet piles, used in the foundation, were made of steel plates (200 mm height, 400 mm width and 3.2 mm thickness).

3.3 Test Conditions

The shaking table tests were conducted for different field conditions (like—no reinforcement, reinforced by gabion only and reinforced by gabion, and sheet piles together). The earthquake loading was applied in the form of sinusoidal wave.

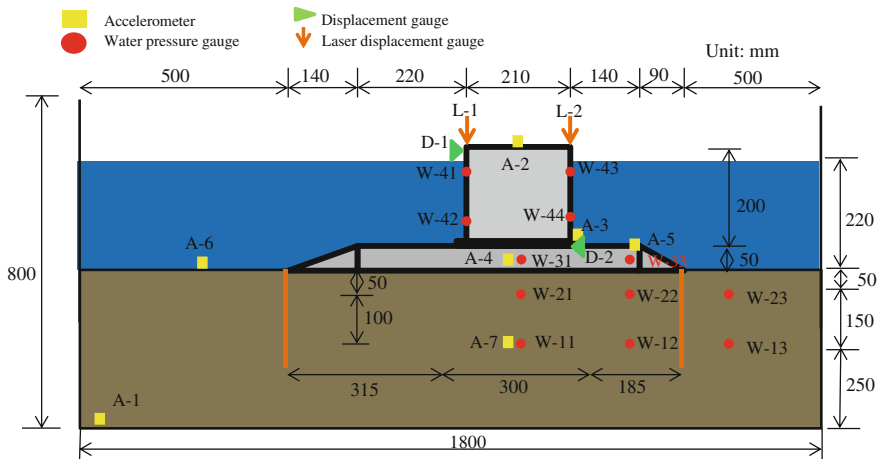


Fig. 5 Experimental set up of the shaking table test for breakwater

A sinusoidal wave of acceleration 400 Gal, frequency 15 Hz and time duration 8 s was used in the experiment. The acceleration, water pressure, and deformation of caisson breakwater were measured during the experiment. The acceleration and pore water pressure inside foundation soils and rubble mound were also monitored. The settlement of the breakwater was measured by laser displacement gauge, and horizontal displacement of the breakwater was measured by displacement gauge. The accelerometers were established to record acceleration at seven locations (A-1 to A-7) as shown in Fig. 5. A-1 was the acceleration of the shaking table, which was assumed as the input acceleration. The water pressure gauges were used to measure pore water pressure inside the seabed and mound, and water pressure gauges were used to measure water pressure on the caisson breakwater. They were installed at twelve locations (W-11 to W-43). The displacement gauge was installed at two locations (D-1 and D-2) to measure horizontal displacement. The laser displacement gauges were used at two locations (L-1 and L-2) to monitor settlement of the caisson breakwater.

4 Results and Discussions

Two types of reinforcements were used for the breakwater foundation (i) gabion only and (ii) combination of gabion and two steel sheet piles. The comparisons are made between the reinforced and conventional (unreinforced) breakwater foundation. The time history of acceleration for conventional (unreinforced) breakwater and developed new breakwater (reinforced with gabion and two sheet piles) are shown in Figs. 6 and 7 respectively. As compared with A-1, acceleration is amplified in inner portion of the seabed (A-7). While on the surface of seabed (A-6)

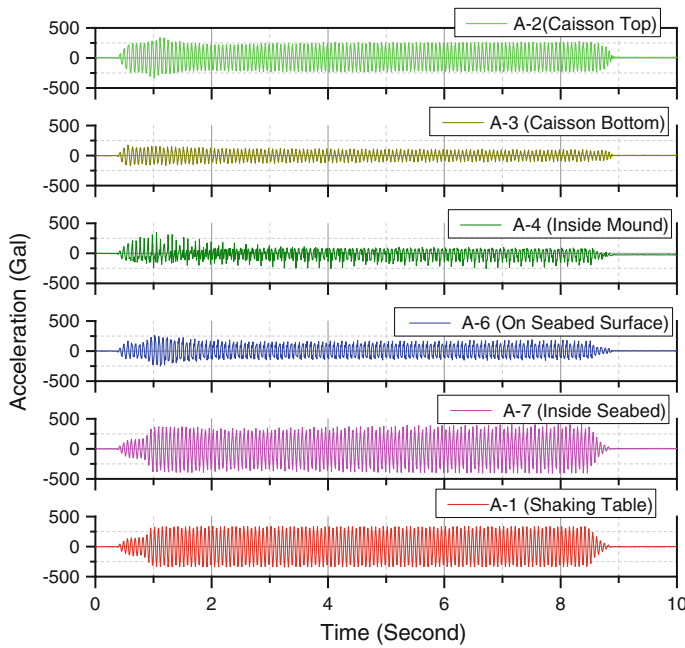


Fig. 6 Acceleration history at different locations of conventional breakwater

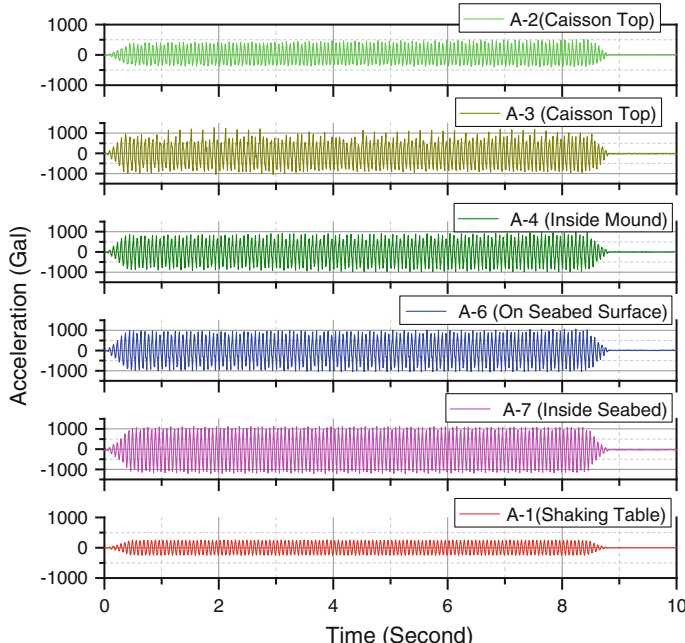


Fig. 7 Acceleration history at different locations of developed BW (compound reinforced with gabion and two sheet piles)

amplification is there but its value is lower as compared to the inner portion of seabed (A-7). It may be due to the fact that inner layer of seabed may be densified by the weight of upper layers, thus lower layer amplified the acceleration more than upper layer. In the mound (A-4), acceleration was amplified but its value is less than that of inside the seabed and on the surface of seabed. The mound was made of number 6 gravel ($D_r = 60\%$). Due to the low relative density ($D_r = 60\%$) and high void, vibration energy might be dissipated and so acceleration inside mound decreases compare to seabed. For the caisson, as compared the acceleration at A-3 and A-2, it is clear that acceleration is amplified within the caisson.

The settlement with respect to time at L-1 (top left corner of caisson) is shown in Fig. 8. The BW reinforced with gabion only gives less settlement than unreinforced BW. The gabion BW reduces final settlement by 63 %. But when BW was reinforced with combination of gabion and two steel sheet piles, settlement reduces much and final settlement is reduced by 74 %. Figure 9 shows the settlement of breakwater at L-2 (top right corner of caisson). The BW reinforced with gabion give less settlement than unreinforced BW while combination of gabion and two steel sheet piles give lesser settlement. The gabion only, as reinforcement, reduces final settlement by 62 %, while combination of gabion and two sheet pile, as compound reinforcement, reduce final settlement by 84 %. It is clear that combination of gabion and two sheet pile, as reinforcement, is more effective to reduce settlement of the breakwater. From Figs. 8 and 9, it is clear there is tilting of caisson occurred which was observed during experiment also.

The graphs are drawn for horizontal displacement of breakwater with respect to time. Horizontal displacement at D-1 (top left corner of caisson) is shown in

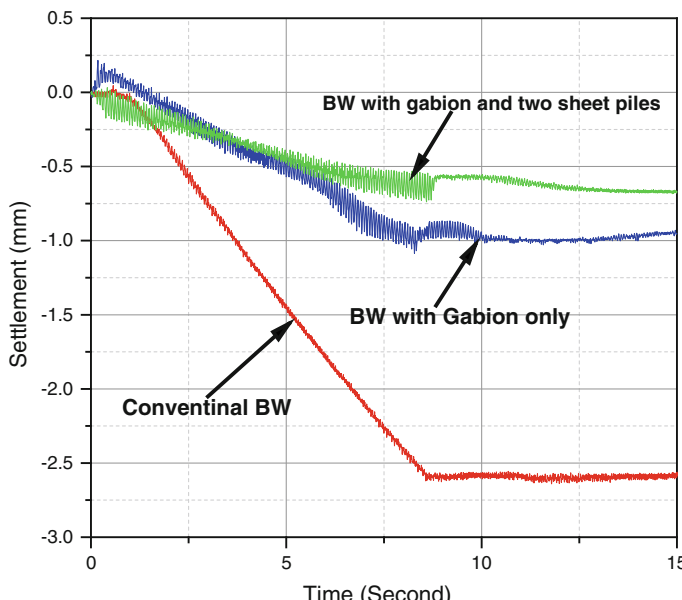


Fig. 8 Settlement measured at L-1 for different layouts of breakwater under earthquake loading

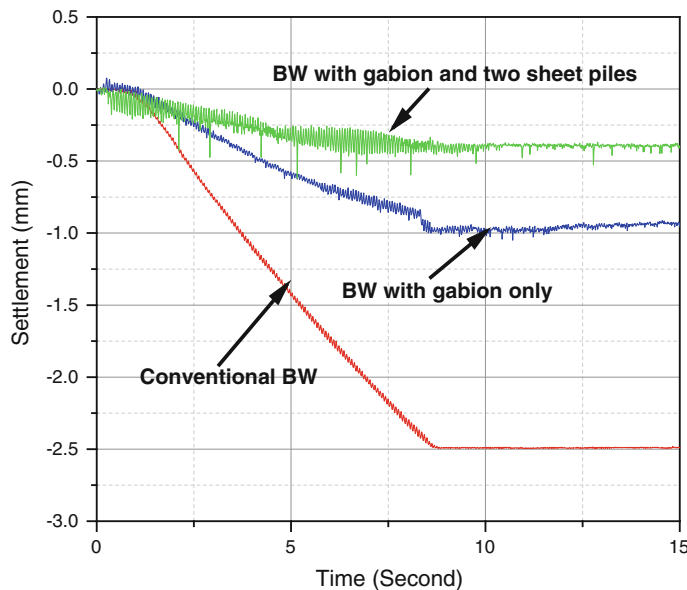


Fig. 9 Settlement measured at L-2 for different layouts of breakwater under earthquake loading

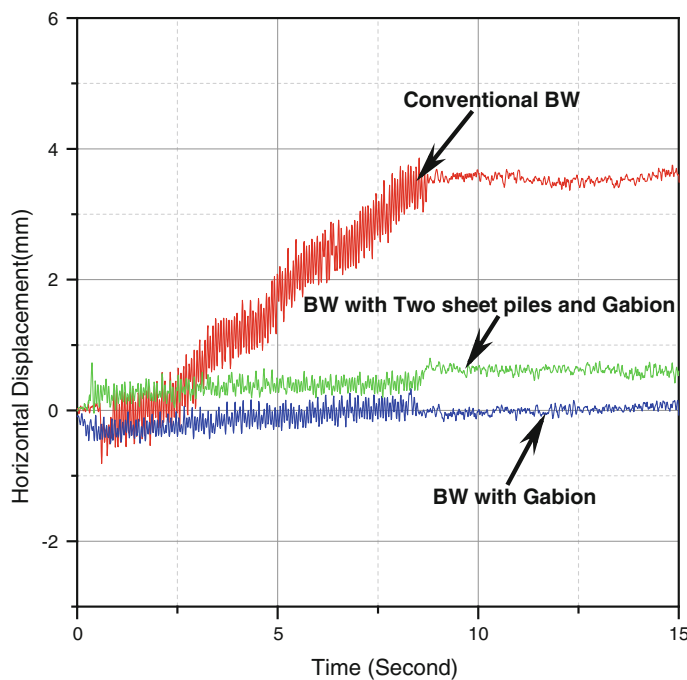


Fig. 10 Horizontal displacement measured at D-1 for different layouts of breakwater under earthquake loading

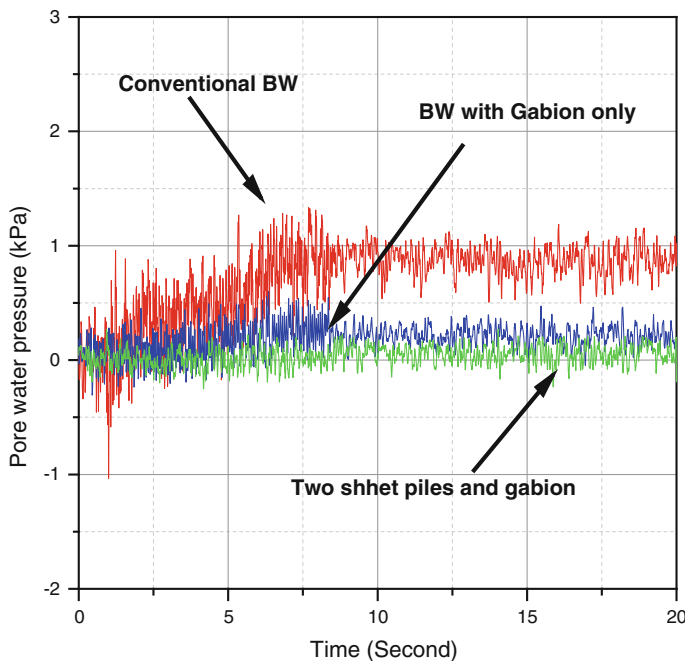


Fig. 11 Pore water pressure measured at W-31 for different layouts of breakwater under earthquake loading

Fig. 10. The BW reinforced with gabion only gives less horizontal displacement compared to unreinforced BW. The gabion BW reduces final horizontal displacement by 95 %. But when BW was reinforced with gabion and two steel sheet piles together, horizontal displacement reduces but final horizontal displacement is reduced by 83 %, which is less than that for gabion BW.

Figure 11 shows the pore pressures at W-31 (inside the mound and beneath the caisson) for reinforced and unreinforced BW. The BW reinforced with gabion has less pore water pressure than unreinforced BW. Its final value reduces by 63 %. When BW was reinforced with combination of gabion and two sheet piles, pore pressures reduces much more and its final value reduces by 81 %. It is clear that combination of gabion and two sheet piles, as reinforcement, is more effective in reducing pore water pressure, settlement. Results come out from the experiment show that the combination of gabion and two steel sheet piles as reinforcement is most suitable reinforcement for breakwater foundation against earthquake. Hence combined reinforcement (gabion and two sheet piles together) is proposed as an effective reinforcement for the breakwater foundation against the earthquake.

5 Conclusions

A new reinforcement technique was developed for foundation of the breakwater, which gives resiliency/resistant against earthquake to the breakwater. A prototype model of breakwater at Miyazaki port (Miyazaki Prefecture, Japan), which is likely to be affected by the Nankai trough earthquake in the near future was chosen for the experiment. The prototype to model ratio of 64 was adopted. The gabion mound foundation was adopted in place of the rubble mound. In addition to gabion, two steel sheet piles were also used in the foundation. In this paper, the effectiveness of a new reinforcing technique for breakwater foundation against earthquake induced forces was evaluated. The results show that the reinforced breakwater performed well during high earthquake (400 Gal) loading and long duration (8 s). The following conclusions could be derived based on this research.

1. The new reinforced breakwater could prevent/reduce breakwater tilting/overturning during earthquake.
2. The new reinforced breakwater reduced lateral displacement of breakwater during earthquake.
3. One of the major causes of breakwater settlement is the lateral flow of foundation soils. Sheet pile can restrict the lateral flow, and thus could prevent/reduce differential settlement.
4. The proposed reinforcing technique provides better mitigation effect as the vertical settlement as well as lateral displacement of the breakwater could be reduced significantly.
5. Pore water pressure below the breakwater (inside the mound) reduced in reinforced breakwater with comparison to conventional breakwater.

It is believed that the reinforcement will reduce the scouring effect of the tsunami wave also. One of the most important benefits of the model is that the reinforcement (sheet piles and protective gabion) can be used in existing breakwater also. For an effective reinforcing technique for breakwater foundation more detailed studies are needed. Further studies are going on for detail analysis (e.g., embedded depth and location of sheet piles, size and weight of breakwater, etc). Researches are also ongoing to evaluate the tsunami resistant characteristics of the proposed technique through hydraulic model test and centrifuge test. Numerical analyses are also carried out.

Acknowledgments This study was funded by the Japan Iron and Steel Federation under priority themes research grant. The authors express their deep gratitude for this financial support.

References

Arikawa T, Sato M, Shimosako K, Hasegawa I, Yeom GS, Takashi T (2012) Failure mechanism of Kamaishi breakwaters due to the Great East Japan Earthquake Tsunami. *Coast Eng* 1–13

Central Disaster Mitigation Council (2003) Report of the 16th committee meeting. Investigation Committee on Tonankai Earthquake and Nankai Earthquake, Cabinet Office, Government of Japan (in Japanese)

Hazarika H, Kataoka S, Kasama K, Kenji K, Daisuke S (2012) Composite ground disasters caused by the earthquake and tsunami in Aomori, Iwate Prefecture, northern. *Geotech Eng J (Spec Issue “2011 Great East Japan Earthquake”)* 7(1):13–23

Hazarika H, Hara T, Furuichi H (2013a) Soil structure interaction during earthquake and tsunami —Two case studies from the latest disaster in Japan. In: 18th international conference on soil mechanics and geotechnical engineering, Paris, France, pp 131–142

Hazarika H, Kasama K, Suetsugu D, Kataoka S, Yasufuku N (2013b) Damage to geotechnical structures in waterfront areas of northern Tohoku due to the March 11, 2011 tsunami disaster. *Indian Geotech J* 43(2):137–152

Iai S (1989) Similitude for shaking table tests on soil-structure-fluid model in 1 g gravitational field. *Soils Found* 29(1):105–118

Takahashi S, Kuriyama Y, Takashi T, Kawai Y, Arikawa T, Tatsumi D and Negi T (2011) Urgent survey for 2011 Great East Japan Earthquake and Tsunami disaster in ports and coasts—Part I (Tsunami). Technical note of Port and Airport Research Institute No. 1231, pp 1–9

Shaking Table Model Tests on Mitigation of Liquefaction-Induced Distortion of Shallow Foundation

Rouzbeh Rasouli, Ikuo Towhata and Hadrien Rattez

Abstract Recent earthquakes of Japan and New Zealand have revealed that there is no concrete and reliable solution for liquefaction-induced settlement and tilting of light surface structures. In this study, qualification of three possible mitigations against this problem is examined by conducting shaking table tests: (1) installation of sheet-pile walls surrounding the building's foundation. (2) Lowering ground water level and (3) installation of diagonal drainage pipes under the foundation. Experiments showed that all mitigations reduced the settlement to some extent, while some considerations in implementation of each of them should be taken into account. In the end, the experiments were solved mathematically to provide a theoretical basis for the proposed mitigations performance prediction.

Keywords Settlement · Mitigation · Shaking table test · Numerical analysis

1 Introduction

The historical development of geotechnology for mitigation of liquefaction problems has addressed important structures that require perfect prevention of the onset of liquefaction. Although many reliable techniques in this perspective have been developed in the past decades, limitations have been pointed out in the recent times. One of the limitations is the mitigation of liquefaction-damage of private houses

R. Rasouli

Penta-Ocean Institute of Technology, 1534-1, Yonkucho, Nasushiobara-shi,
Tochigi 329-2746, Japan
e-mail: rouzbeh.rasouli@gmail.com

I. Towhata (✉)

Kanto Gakuin University, 1-50-1, Mutsu-ura Higashi, Kanazawa-ku,
Yokohama 236-8501, Japan
e-mail: towhata.ikuo.ikuo@gmail.com

H. Rattez

École normale supérieure de Cachan, Paris, France



Fig. 1 Examples of liquefaction-damaged buildings: *left* tilted building after 1990 Luzon earthquake (Orense et al. 2011), *right* settlement of building due to liquefaction after 2011 earthquake of Japan

which rest on liquefaction-prone subsoil and require damage mitigation with acceptable cost. Figure 1 shows that this problem has been suffering cities and people since several years ago and it repeated during the 2011 earthquake of Japan. The difficulties lying herein is the subsoil improvement under existing fragile houses and the limited budget that individual house owners can afford. Several studies have been initiated recently to deal with this problem (e.g. Tsukamoto et al. 2012; Kuriki et al. 2012; Yasuda et al. 2013; Towhata and Rasouli 2013). In this study, a series of shaking table tests as well as numerical analyses on the mitigation of such distortion as settlement and tilting of houses have been conducted. Based on some previous empirical and experimental studies (e.g. Ishihara 1985; Mizutani and Towhata 2001) the possibly appropriate techniques including installation of sheet pile walls around the house foundation, installation of drainage pipes under the foundation and limited lowering of ground water table as well as their combinations were proposed. These techniques were examined by running shaking table tests in 1-G environment in which the similitude was considered by employing looser-than-reality sand so that the extent of dilatancy might be made equivalent. The experiments were later solved mathematically by a previously developed closed form solution, based on principle of minimum potential energy.

2 Method of Shaking Table Tests

The experiments were conducted in a large soil container of 2.65 m length, 0.6 m height, and 0.4 m width. Shock absorbers were installed at both rigid ends of the container. Silica sand No. 7 with the geotechnical properties of $\rho_s = 2.64$, $e_{\max} = 1.252$ and $e_{\min} = 0.749$ were used for making model ground. Height of model ground was 0.5 m. The first 10 cm was compacted to reach 80 % relative density and was considered as non-liquefiable layer. The rest of ground was made by water pluviation method and was set to 46 % relative density. Several pore water pressure

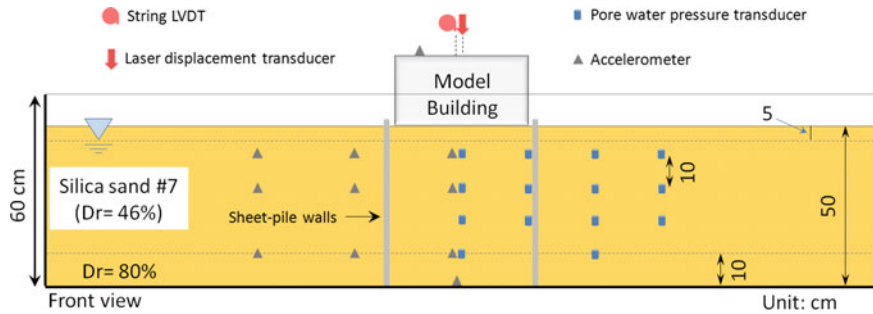


Fig. 2 Schematic illustration of experimental setup in one typical experiment with sheet-pile walls with low GWL

transducers and accelerometers were installed in the model ground to record the behavior of ground accurately. Aluminum plates were used as sheet-pile walls. Strain gauges were pasted to plates for recording induced bending moment in plates. Ground water level (GWL) was at surface, -5 cm, and -10 cm below surface in different cases. In cases of low GWL a 2 cm layer of gravel was placed on the last layer of liquefiable ground to prevent saturation of surface non-liquefiable layer by capillary effects. Drainage pipes were made of plastic pipes. Many holes were made around the pipe and they were covered by metal mesh to prevent inflow of liquefiable sand into the holes. A rigid wooden box filled with sand was used as a model building. A laser displacement transducer was used to record time history of subsidence accurately. Figure 2 shows the setup of experiments schematically for experiments with sheet-pile walls with low GWL. All models were shaken by sinusoidal waves of 300 Gal and 10 Hz frequency. Shaking duration was 25 s. For more details of model preparation and input motion refer to Rasouli (2014).

3 Discussion on Experimental Results

As a comprehensive research program, around 70 shaking table experiments were conducted on this issue (Rasouli 2014). Different variables were examined in these experiments including: Effects of sheet-pile's bottom and top fixity (Rasouli et al. 2012), configuration of drainage pipes (Towhata and Rasouli 2013), and performance of sheet-piling with gaps (Rasouli et al. 2014). In this paper, a comparative discussion on performance of each of these mitigations is made.

3.1 Lowering Ground Water Level

Empirical data demonstrated that where there is a deep non-liquefiable layer at surface, liquefaction does not damage the surface structures (see e.g. Ishihara 1985). Figure 3 shows deformation of liquefied soil in cases of low GWL. It is observed

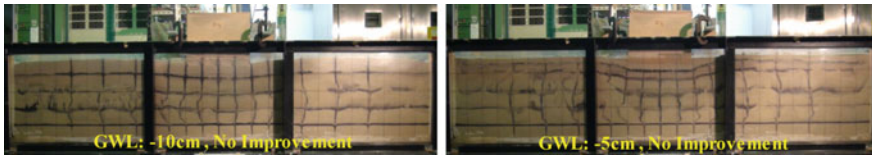


Fig. 3 Deformation of model ground in cases of low GWL

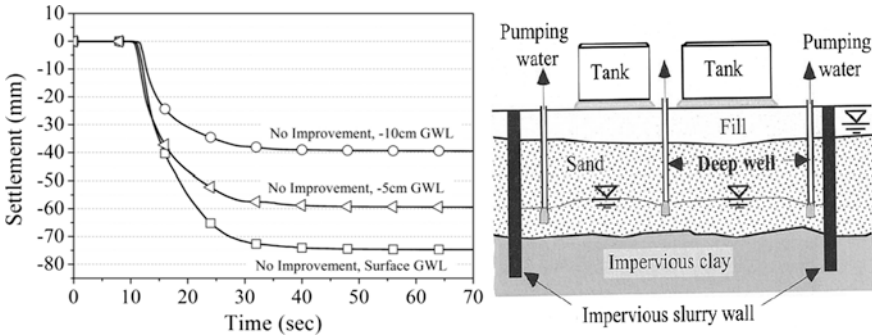


Fig. 4 *Left* Settlement of model building in different GWLs. *Right* An example of lowering GWL in practice

that considerable lateral displacement of liquefied soil took place in bottom liquefiable layers. Lowering GWL changes the stress distribution of the surface structure. In other words, lower surface pressure on a wider area on liquefiable layer causes lower settlement of structures. In addition, lowering GWL controls the upward flow of liquefied soil during the dissipation of excess PWP. Figure 4(left) shows that lowering GWL for several centimeters considerably reduced settlement of model building. From practical point of view, lowering GWL is possible by installation of a horizontal network of drains or pumping water from a constrained area (Fig. 4(right)).

3.2 Installation of Sheet-Pile Walls

Installation of sheet-pile walls in order to reduce settlement of river dikes were utilized previously (e.g. Mizutani and Towhata 2001). Nowadays, advances in technology made it possible to install sheet-piles in dense urban area. Installation of sheet-pile walls under structures reduces the lateral displacement of liquefied soil and consequently reduces the settlement of structure (Rasouli et al. 2012). There are many factors which affect performance of this technique against settlement of structure. Rasouli et al. (2012) examined effects of sheet-piles top and bottom fixity

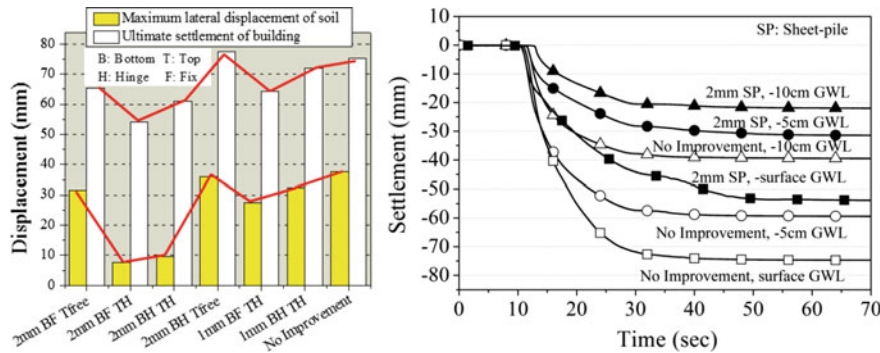


Fig. 5 *Left* Correlation between prevention of lateral displacement of liquefied soil and settlement of building (thickness of wall = 1 or 2 mm). *Right* Time history of settlement in cases of sheet-pile walls

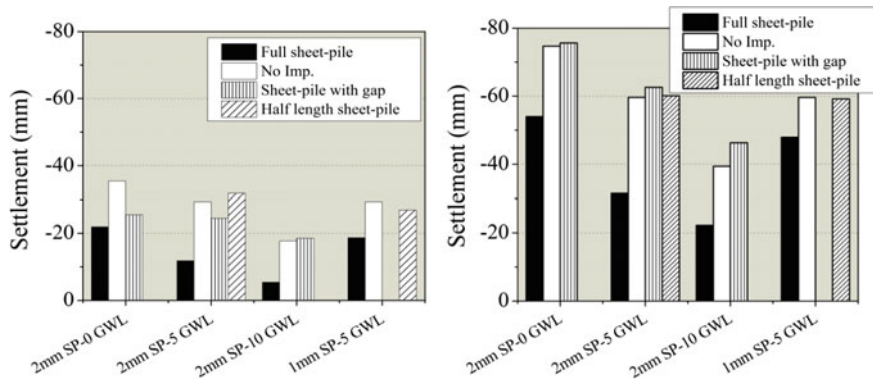


Fig. 6 Settlement of structure: *left* after 70 cycles, *right* ultimate settlement

on their performance. Based on that study, reaching non-liquefiable layer at the bottom is a key requirement for having good performance of sheet-piles. In addition it was found that constraining sheet-pile's head from lateral displacement considerably enhances its mitigative effects. Figure 5(left) shows the meaningful correlation between reduction of lateral displacement of liquefied soil and ultimate settlement of building. Figure 5(right) shows time history of model building settlement in experiments of 2 mm sheet-piles in different GWLs. Considering 20 mm of free-field settlement it can be expressed that installation of sheet-pile walls along with 10 cm of lowering GWL prevented building's settlement completely.

In order to reduce the cost of this mitigation, performance of sheet-piling with gaps and half-length sheet-piling were also examined. Although ultimate settlement of model building was not reduced in these cases, the settlement at early stages of shaking was slightly reduced (Fig. 6).

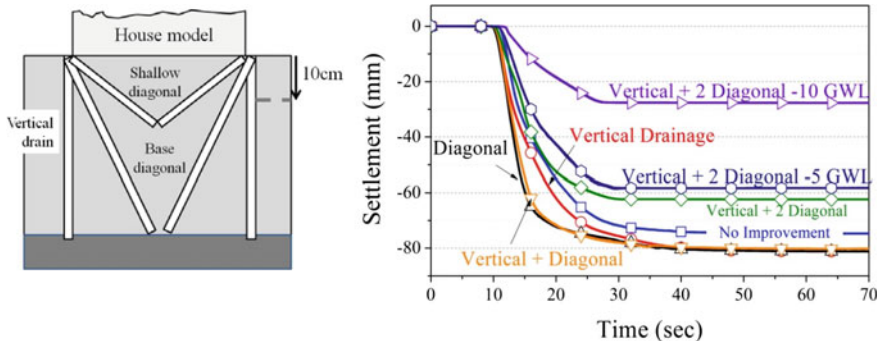


Fig. 7 *Left* Proposed configuration of installation of drains. *Right* Time history of settlement in cases with drains

3.3 Installation of Drainage Pipes

Installation of drainage pipes is a conventional mitigation against onset of liquefaction. However, experiments revealed that installation of only vertical drains around the building's foundation is not sufficient to prevent building's settlement (Towhata and Rasouli 2013). Figure 7(left) schematically shows the proposed configuration of drains to make this mitigation effective against settlement of buildings. It consists of two sets of diagonal drains under the building's foundation. The results of experiments with different configurations are shown in Fig. 7(right). It is observed that settlement of building is not mitigated unless the full set of drains are installed under the building in a relatively low GWL. It implies that prevention of liquefaction immediately under the structure is more important than prevention of liquefaction in the surrounding area and at deeper depths.

3.4 Performance Against Tilting

In addition to settlement of building, tilting of building can also cause many problems to its residents' life. Based on Architectural Institute of Japan (2003), tilting of building over 0.6° causes dizziness and headache to residents and leveling retrofitting is needed in such cases. Figure 8(right) shows ultimate tilting of model building in different cases. Installation of sheet-pile walls does not prevent onset of liquefaction under the model structure (Rasouli et al. 2014). Therefore, in cases of non-uniform loaded buildings, the liquefied soil under the structure could deform easily in its constrained area and this led to considerable tilting of model building in experiments with sheet-pile walls. In contrast, installation of drainage pipes

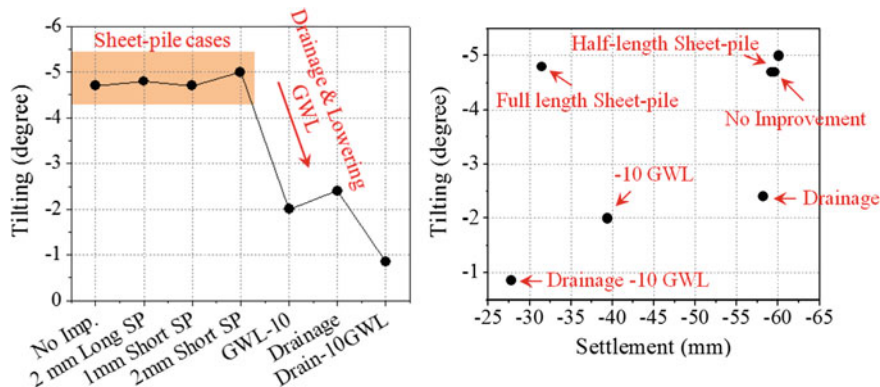


Fig. 8 *Left* Performance of different mitigations against tilting of structures. *Right* Reduction of model building settlement versus its tilting in different cases

prevents onset of liquefaction. Thus, the soil under the building does not deform due to the surface pressure easily. Therefore, tilting of structure was mitigated perfectly in this case. Lowering GWL, provides a non-liquefiable layer at surface. Thus, the tilting of the structure was reduced as compared with experiments of surface GWL (No improvement and cases with sheet-pile walls). However, tilting is less in the case of low GWL in combination with drainage pipes.

Figure 8(right) shows settlement of model building versus its tilting. It is observed that full-length sheet-piles reduced settlement of building substantially but its performance against tilting of structure was not promising. Installation of drainage pipes reduced tilting of structure and also reduced the settlement of structure when combined with lowering GWL. Lowering GWL reduced both settlement and tilting of structure to some extent.

4 Numerical Analysis

To have a numerical basis for prediction of model building behavior in practice, the model experiments are solved mathematically. For this purpose, displacement of model building and liquefied ground is calculated based on principle of minimum potential energy. It is assumed that the volume of the soil is constant before and after liquefaction. It means that the consolidation of liquefied soil is not considered in calculations. However, based on experimental observations, 20 mm of subsidence of free-field is added to calculated values to consider the consolidation of liquefied soil. Some residual shear stiffness is considered for the liquefied soil. It can be applied when the soil did not completely liquefy. However, for modeling

present experiments no residual stiffness is considered (the residual stiffness (E) is set to 1 kPa). The friction between the model structure and the surface soil is the other energy dissipation which is considered in the calculations. The mitigations, including sheet-pile walls and drainage pipes are also considered in the calculations. The area of drainage pipes is considered as a non-liquefiable zone. The strain energy of sheet-pile walls are also included in the calculations. The head of sheet-piles were considered as a hinge supported condition. This is due to the prevention of lateral displacement of walls at the top. The piles were mechanically fixed at the bottom. However, the first 10 cm above the fixed point is buried in compacted soil. Therefore, the sheet-pile is considered as hinged from the point where liquefiable soil starts. Details of equations and calculations are presented in Rasouli (2014). The considered energies which were solved to reach the minimum energy are as below:

$$Q = Q_s + Q_f + Q_g + Q_w - \varsigma \left(\int_0^H \rho dz - \frac{uB}{2} \right) \rightarrow \text{Min.}$$

$$\left(\varsigma \left(\int_0^H \rho dz - \frac{uB}{2} \right) : \text{Lagrangean multiplier for flux continuity} \right)$$

where Q_s is strain energy of soil, Q_f , the energy of friction, Q_g , the energy of gravity and Q_w , strain energy of sheet-pile walls ρ , sheet-pile deflection B , width of foundation. Finally, the equation of the motion for the subsiding building $\left(m \frac{d^2u}{dt^2} + 2\zeta \sqrt{mk} \frac{du}{dt} + ku = f \right)$ is solved to have the time history of subsidence. The subsidence of model structure after 30 s is taken into account to be compared with the results of experiments. The details of this solution are presented in the appendix. Figure 9 compares experimental results with numerical predictions which shows a good consistency between experiments and calculations.

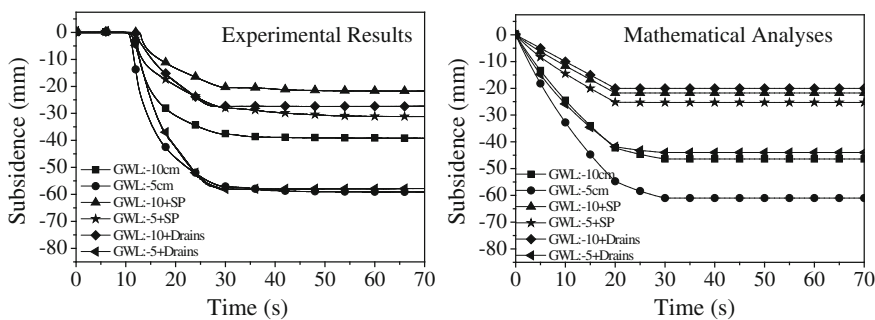


Fig. 9 Comparison of the mathematical analyses (right) versus experimental results (left)

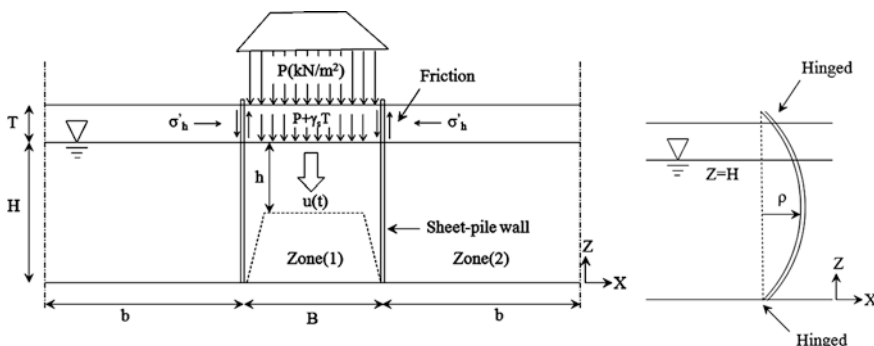
5 Conclusions

The following conclusions can be drawn from the results of this study:

1. Lowering GWL reduces both settlement and tilting of structures by changing the stress distribution of surface structure and prevention of sand boiling.
2. Reduction of lateral displacement of liquefied soil by installation of sheet-pile walls leads to reduction of settlement of structure. It was observed that presence of openings between sheets or not reaching the non-liquefiable layer disturbs the performance of this mitigation. However, liquefied sand under the model building could deform easily in the constrained area by sheets and consequently tilting of structure was not reduced in experiments with sheet-pile walls.
3. It is found that prevention of liquefaction immediately under the structure is more important than prevention of liquefaction in the surrounding area and at deeper depths. Installation of complete set of drainage pipes (vertical and diagonal drains) in combination with lowering GWL prevent onset of liquefaction under the building. Thus, the soil under the building does not deform due to the surface pressure easily. Therefore, the building does not settle down and tilting of structure was mitigated perfectly in this case as well.

Appendix: Details of Numerical Analysis

Details of mathematical solution:



Boundary: Horizontal displacement = 0

Below the house (Zone 1, non-liquefiable in cases with diagonal drains),

Strain $\epsilon_z = \frac{u}{h}$, $\epsilon_x = -v' \epsilon_z = -v' \times \frac{u}{h}$, Poisson ratio, $v' = 1.0$ (Undrained, constant volume in 2-D analysis)

$$\text{Lateral displacement: } |\varepsilon_x| \times \frac{B}{2} = \frac{v' u(t) B}{2h} \quad (1)$$

$$\text{Volume of lateral soil flow: } h \times \frac{v' u(t) B}{2h} = \frac{v' u(t) B}{2} \quad (2)$$

Below Free-field (Zone 2),

Volume of flow-in: (2)

$$\text{Lateral displacement below the house edge} \times H = \frac{v' u(t) B}{2}$$

$$\text{Lateral displacement} = \frac{v' u(t) B}{2H}, \quad \text{Lateral strain} = \varepsilon_x = \frac{v' u(t) B}{2Hb} \text{ (compression)}$$

$$\text{Vertical strain} = \varepsilon_z = -(v')^2 \varepsilon_z = \frac{(v')^2 u(t) B}{2hb} \text{ (extension),}$$

$$v' = 1.0 \text{ (constant volume)}$$

$$\text{Uplift of the ground surface} = H |\varepsilon_z| = \frac{(v')^2 u(t) B}{2b}$$

Elasticity theory in 2-D plane strain conditions:

$$\varepsilon_x = \frac{1}{E} (\sigma_x - v \sigma_y - v \sigma_z)$$

$$\varepsilon_y = \frac{1}{E} (\sigma_y - v \sigma_z - v \sigma_x) = 0, \quad \text{Plane strain condition: } \sigma_y = v(\sigma_z + \sigma_x)$$

$$\varepsilon_x = \frac{1}{E} (\sigma_z - v \sigma_x - v \sigma_y)$$

strain energy = $\frac{1}{2} (\varepsilon_x \sigma_x + \varepsilon_z \sigma_z)$. Because $\varepsilon_x = -\varepsilon_z$ (constant volume)
strain energy = $\frac{\varepsilon_z}{2} (\sigma_z - \sigma_x)$

$$E \varepsilon_x = \sigma_x - v^2 (\sigma_z + \sigma_x) - v \sigma_z = (1 - v^2) \sigma_x - v(1 + v) \sigma_z$$

$$E \varepsilon_z = \sigma_z - v^2 (\sigma_z + \sigma_x) - v \sigma_x = (1 - v^2) \sigma_z - v(1 + v) \sigma_x$$

$$E(\varepsilon_z - \varepsilon_x) = (1 + v) \sigma_z - (1 + v) \sigma_x, \quad \frac{E}{1 + v} (\varepsilon_z - \sigma_x) = \sigma_z - \sigma_x$$

Because of constant volume and $v = 0.5$: $\sigma_z - \sigma_x = \frac{4E}{3} \varepsilon_z$

Strain energy = $\frac{2E}{3} \varepsilon_z^2$ in both zones (1) and (2)

Strain energies in zones (1) and (2) are:

$$Q_s = \frac{2E}{3} \left\{ \left(\frac{u}{h} \right)^2 \times Bh + \left(\frac{uB}{2Hb} \right)^2 bH \times 2 \right\} = \frac{2E}{3} \left(\frac{B}{h} + \frac{B^2}{2Hb} \right) u^2$$

Friction energy $Q_f = 2 \times (\text{Frictional stress}) \times (\text{relative displacement between house and dry soil}) \times T$

$$\text{Friction stress} = \sigma_h \tan \varphi = K_0 \sigma_v \tan \varphi = K_0 \frac{\gamma_s T}{2} \tan \varphi$$

Relative displacement = garden uplift - house subsidence

$$= \frac{u(t)B}{2b} + u(t) = \left(\frac{B}{2b} + 1 \right) u$$

$$Q_f = K_0 \frac{\gamma_s T}{2} \tan \varphi \left(\frac{B}{2b} + 1 \right) u$$

Potential energy due to gravity Q_g is negative (decrease);

$$Q_g = -(p + \gamma_s T)Bu + 2\gamma_s Tb \frac{Bu}{2b}$$

$$Q_g = -(p + \gamma_s T)Bu + 2\gamma_s Tb \frac{Bu}{2b} + \left[\frac{\gamma_l}{2} \left\{ (H - u)^2 - (H - h)^2 \right\} - \frac{\gamma_l}{2} \left\{ H^3 - (H - h)^2 \right\} \times B \right] + 2 \left[\frac{\gamma_l}{2} \left(H + \frac{Bu}{2b} \right)^2 - \frac{\gamma_l}{2} H^2 \right] \times b$$

$$Q_g = (\gamma_s TB - PB - \gamma_s TB)u + \frac{\gamma_l}{2} [-2Hu + u^2]B + \gamma_l \left[\frac{HBu}{b} + \frac{B^2 u^2}{4b^2} \right] b = \gamma_l \left(\frac{B}{2} + \frac{B^2}{4b} \right) u^2 + (-PB - \gamma_l HB + \gamma_l HB)u = \frac{\gamma_l B}{2} \left(1 + \frac{B}{2b} \right) u^2 - PBu$$

$$\text{Volume of soil flow} = \int_0^H \rho dz = \frac{uB}{2}, \quad v' = 1.0$$

$$\text{Strain energy } Q_w = 2 \times \int_0^H \frac{EI}{2} \left(\frac{d^2 \rho}{dz^2} \right)^2 dz,$$

Boundary condition at $Z = 0$ & $Z = H$, $\rho = 0$ & $M = 0$

Conditional minimization of energy:

$$Q = Q_s + Q_f + Q_g + Q_w - \varsigma \left(\int_0^H \rho dz - \frac{uB}{2} \right) \rightarrow \text{Min.}$$

$$\left(\varsigma \left(\int_0^H \rho dz - \frac{uB}{2} \right) : \text{Lagrangean multiplier} \right)$$

$$\begin{aligned} & \frac{2E}{3} \left(\frac{B}{h} + \frac{B^2}{2Hb} \right) u^2 + K_0 \gamma_s T^2 \tan \varphi \left(\frac{B}{2b} + 1 \right) u + \frac{\gamma_l B}{2} \left(1 + \frac{B}{2b} \right) u^2 \\ & - PBu + EI \int_0^H \left(\frac{d^2 \rho}{dz^2} \right)^2 dz - \varsigma \left(\int_0^H \rho dz - \frac{uB}{2} \right) \rightarrow \text{Min.} \end{aligned}$$

$$\begin{aligned} & \left\{ \frac{2E}{3} \left(\frac{B}{h} + \frac{B^2}{2Hb} \right) + \frac{\gamma_l B}{2} \left(1 + \frac{B}{2b} \right) \right\} u^2 + \left\{ K_0 \gamma_s T^2 \tan \varphi \left(\frac{B}{2b} + 1 \right) - PB \right\} u \\ & + EI \int_0^H \left(\frac{d^2 \rho}{dz^2} \right)^2 dz - \varsigma \left(\int_0^H \rho dz - \frac{uB}{2} \right) \rightarrow \text{Min.} \end{aligned}$$

$$\begin{aligned} & \frac{1}{2} \left\{ \frac{2E}{3} \left(\frac{2B}{h} + \frac{B^2}{Hb} \right) + \gamma_l B \left(1 + \frac{B}{2b} \right) \right\} u^2 \\ & + \left\{ K_0 \gamma_s T^2 \tan \varphi \left(\frac{B}{2b} + 1 \right) - PB \right\} u + EI \int_0^H \left(\frac{d^2 \rho}{dz^2} \right)^2 dz \\ & - \varsigma \left(\int_0^H \rho dz - \frac{uB}{2} \right) \rightarrow \text{Min.} \left\{ \frac{2E}{3} \left(\frac{2B}{h} + \frac{B^2}{Hb} \right) + \gamma_l B \left(1 + \frac{B}{2b} \right) \right\} : K_1, \\ & \left\{ K_0 \gamma_s T^2 \tan \varphi \left(\frac{B}{2b} + 1 \right) - PB \right\} : K_2 \end{aligned}$$

$$Q = \frac{1}{2} K_1 u^2 + K_2 u + EI \int_0^H \left(\frac{d^2 \rho}{dz^2} \right)^2 dz - \varsigma \left(\int_0^H \rho dz - \frac{uB}{2} \right) \rightarrow \text{Min.}$$

$\delta Q = 0$ for any small change of $u \rightarrow u + \delta u$ & $\varsigma \rightarrow \varsigma + \delta \varsigma$

$$K_1 u \delta u + K_2 \delta u + 2EI \int_0^H \left(\frac{d^2 \rho}{dz^2} \right) \left(\frac{d^2 \delta \rho}{dz^2} \right) dz$$

$$- \varsigma \left(\int_0^H \delta \rho dz - \frac{\delta u B}{2} \right) - \varsigma \left(\int_0^H \rho dz - \frac{u B}{2} \right) = 0$$

for any δu & $\delta \rho$ & $\delta \zeta$, this satisfies the boundary condition at $Z = 0$ and $Z = H$.

By partial integration,

$$K_1 u \delta u + K_2 \delta u + 2EI \left[\left(\frac{d^2 \rho}{dz^2} \right) \left(\frac{d^2 \delta \rho}{dz^2} \right) \right]_0^H - EI \int_0^H \left(\frac{d^3 \rho}{dz^3} \right) \left(\frac{d \delta \rho}{dz} \right) dz$$

$$- \varsigma \left(\int_0^H \delta \rho dz - \frac{\delta u B}{2} \right) - \varsigma \left(\int_0^H \rho dz - \frac{u B}{2} \right) = 0$$

$$K_1 u \delta u + K_2 \delta u + 2EI \left[\left(\frac{d^2 \rho}{dz^2} \right) \left(\frac{d \delta \rho}{dz} \right) \right]_0^H - 2EI \left[\left(\frac{d^3 \rho}{dz^3} \right) \delta \rho \right]_0^H + 2EI \int_0^H \left(\frac{d^4 \rho}{dz^4} \right) \delta \rho dz$$

$$- \varsigma \left(\int_0^H \delta \rho dz - \frac{\delta u B}{2} \right) - \delta \varsigma \left(\int_0^H \rho dz - \frac{u B}{2} \right) = 0, \quad \frac{d \delta \rho}{dz} = \delta \rho = 0 \text{ at } Z$$

$$= H \text{ & } 0 \text{ (Boundary condition)}$$

$$K_1 u \delta u + K_2 \delta u + \int_0^H \left(2EI \frac{d^4 \rho}{dz^4} - \varsigma \right) \delta \rho dz - \varsigma \frac{\delta u B}{2} - \delta \varsigma \left(\int_0^H \rho dz - \frac{u B}{2} \right) = 0$$

for any δu & $\delta \rho$ & $\delta \zeta$

$$K_1 u \delta u + K_2 \delta u + \frac{\varsigma B}{2} = 0 \quad (3)$$

$$2EI \frac{d^4 \rho}{dz^4} = \varsigma \quad (4)$$

For Compatibility of volume flux,

$$\int_0^H \rho dz = \frac{u B}{2} \quad (5)$$

Integration of (4) for four times:

$$\begin{aligned}\frac{d^3\rho}{dz^3} &= \frac{\varsigma}{2EI}z + C_1 \\ \frac{d^2\rho}{dz^2} &= \frac{\varsigma z^2}{EI} + C_1z + C_2 \\ \frac{d\rho}{dz} &= \frac{\varsigma z^3}{3EI} + \frac{C_1}{2}z^2 + C_2z + C_3\end{aligned}$$

$$\begin{aligned}\rho &= \frac{\varsigma z^4}{12EI} + \frac{C_1}{6}z^3 + \frac{C_2}{2}z^2 + C_3z + C_4, \text{ at } Z = 0 \text{ & } Z = H, \rho = 0 \text{ & } M = 0 \\ \rho &= \frac{\varsigma z^4}{48EI} - \frac{\varsigma H z^3}{24EI} + \frac{\varsigma Z H^3}{48EI} \text{ by using (5): } \varsigma = \frac{120EIBu}{H^5} \\ \text{using (3):}\end{aligned}$$

$$u = \frac{PB - K_0\gamma_s T^2 \tan \varphi \left(\frac{B}{2b} + 1 \right)}{\frac{2E}{3} \left(\frac{2B}{h} + \frac{B^2}{Hb} \right) + \gamma_l B \left(1 + \frac{B}{2b} \right) + \frac{60EIB^2}{H^5}}$$

This equation gives the maximum possible displacement. For having the time history of the subsidence the equation of motion should be solved:

$$\begin{aligned}m \frac{d^2u}{dt^2} + 2\zeta \sqrt{mk} \frac{du}{dt} + ku &= f \\ u &= A \exp \left\{ -w_0 \left(\zeta - \sqrt{\zeta^2 - 1} \right) t \right\} + B \exp \left\{ -w_0 \left(\zeta + \sqrt{\zeta^2 - 1} \right) t \right\} + \frac{f}{k} \\ m &= \frac{\gamma_l B}{6g} (2h + B) + \frac{\gamma_l B^2}{6gHb} (H^2 + b^2) + \frac{b}{g} \left\{ P + \gamma_s T \left(1 + \frac{B}{4b} \right) \right\} \\ k &= \frac{2E}{3} \left(\frac{2B}{h} + \frac{B^2}{Hb} \right) + \gamma_l B \left(1 + \frac{B}{2b} \right) + 60 \frac{EIB^2}{H^5} \\ f &= PB - K_0\gamma_s T^2 \tan \varphi \left(1 + \frac{B}{2b} \right)\end{aligned}$$

According to the Lagrangean equation of motion

References

Architectural Institute of Japan (2003) Textbook for registered architects (in Japanese)

Ishihara K (1985) Stability of natural deposits during earthquakes. In: Proceedings of 11th international conference of soil mechanics and foundation engineering, vol 1, San Francisco, USA, pp 321–376

Kuriki A, Tamura S, Zhou Y, Tokimatsu K (2012) Centrifuge model test of liquefaction countermeasure for existing houses. In: Proceedings of 47th conference of Japanese Geotechnical Society, Hachinohe, Japan, pp 1497–1498

Mizutani T, Towhata I (2001) Model tests on mitigation of liquefaction-induced subsidence of dike by using embedded sheet-pile walls. In: Proceedings of 4th international conference of recent advances in geotechnical earthquake engineering and soil dynamics, San Diego, USA, Paper No. 5.24

Orense RP, Kiyota T, Yamada S, Cubrinovski M, Hosono Y, Okamura M, Yasuda S (2011) Comparison of liquefaction features observed during the 2010 and 2011 Canterbury earthquakes. *Seismol Res Lett* 82(6):905–918

Rasouli R (2014) Experimental study on mitigation of liquefaction-induced settlement of structures with shallow foundations. PhD dissertation, The University of Tokyo, Tokyo, Japan

Rasouli R, Hayashida T, Towhata I (2012) Experimental study on subsidence of surface structures due to liquefaction and its mitigation. In: Proceedings of 1st international symposium on earthquake engineering, Tokyo, Japan, 8–10 Nov 2012, pp 199–208

Rasouli R, Towhata I, Hayashida T (2014) 1-g shaking table tests on mitigation of seismic subsidence of structures. In: Proceedings of 8th international conference on physical modeling in geotechnics, vol 2, Perth, Australia, pp 1001–1007

Towhata I, Rasouli R (2013) Attempts to protect personal houses from seismic liquefaction problem. In: Proceedings of 4th international seminar on forensic geotechnical engineering, Bangalore, India

Tsukamoto Y, Ishihara K, Sawada S, Fujiwara S (2012) Settlement of rigid circular foundations during seismic shaking in shaking table tests. *Int J Geomech ASCE* 12(4):462–470

Yasuda S, Sasaki S, Noguchi C, Ozawa N (2013) Shaking table tests to study the possibility to prevent liquefaction-induced damage of houses by installing sheet-piles. In: Proceeding of 48th conference of Japanese Geotechnical Society, Toyama, Japan, pp 1759–1762

Study on the Effect of Union Basement on Decreasing Destruction During Liquefaction

G. Liu, R. Ishikura, N. Yasufuku, K. Kasama and N. Matsuo

Abstract One of the greatest earthquakes in human's history (9.0 M_ω) occurred in Japan on March 11, 2011, which also took a tsunami sweeping the Tohoku region. In this major disaster, around 27,000 personal houses were damaged by liquefaction. On the principle of higher safety and lower cost for the engineering of preventing liquefaction, a new structure form, Three-Union house with basement, is introduced in this study. Aiming at liquefaction inhibition and the increasing of stability of foundation, the function of basement for preventing liquefaction is evaluated by shaking table tests. The factors considered in the test are as follows, with or without substructure, individual basement or union forms, the weights of different model. The test result showed that higher stability can be achieved by Three-Union house with basement.

Keywords Sand · Liquefaction · Shaking table · Excess pore pressure · Basement · Settlement

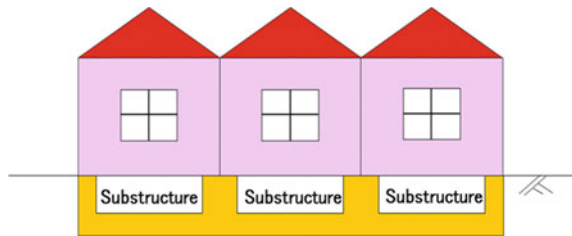
1 Introduction

Liquefaction occurred in a wide range from Tohoku to Kanto in Tohoku-Pacific Ocean earthquake especially in Urayasu City built in a reclaimed land. The superficial zone of ground in this city is mainly consisted of sand with a high groundwater level around -2.0 to -0.5 m. Since many countermeasures of preventing liquefaction have been developed and applied in the construction of large buildings, there was relatively less damage to large buildings. On the other hand, the slower development of protection countermeasures for personal house resulted in more damages in this earthquake.

G. Liu (✉) · R. Ishikura · N. Yasufuku · K. Kasama
Kyushu University, Fukuoka, Japan
e-mail: liuguojunj0@163.com

N. Matsuo
Daiken Co. Ltd, Fukuoka, Japan

Fig. 1 Three-Union house with substructure model



In this study, a new type of structure form named Three-Union house with basement shown in Fig. 1 (Tajima 2013) is introduced to analysis the response of personal house to the liquefaction. In order to look for a structure form with most effective function of preventing liquefaction, a series of tests were conducted. Furthermore, the factors were evaluated to analyse the damage of liquefaction, which includes settlement and inclination of house model, and the excess pore pressure inside of the ground base. The substructure existing and not, individual or union forms, the weights of different model are considered when implementing the shaking table tests.

2 Test Conditions

Ground condition and each sensor setting were depicted in Fig. 2, all tests were operated in earth's gravity field. The container is 1800 mm in length and 400 mm in width. Toyoura sand was adopted as the test material. By water falling method (Wang 2012), the ground could nearly reach full saturation that was the initial

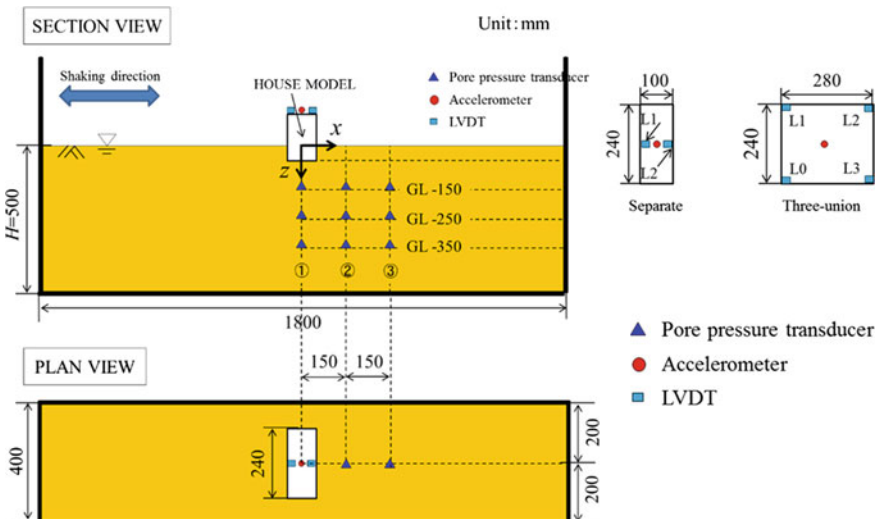


Fig. 2 Schematic diagram of the container

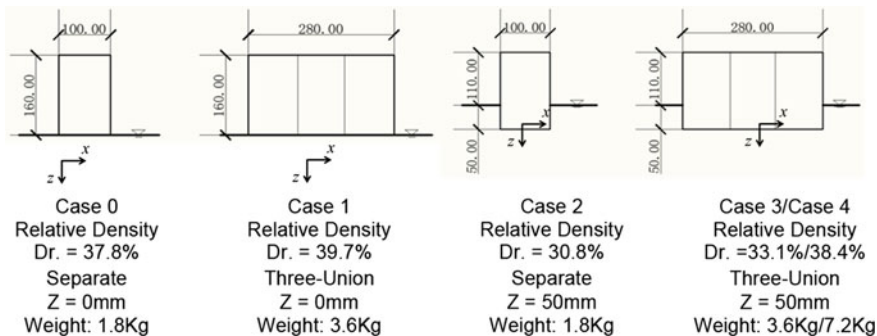


Fig. 3 Dimensions of test models

condition. Adjusting the height of the sandy ground in the container up to 500 mm, the relative density (Dr) got to around 35 % (Fukutake et al. 2013). The seismic wave was input in sinusoidal with frequency $f = 3$ Hz, and the maximum acceleration was set to 400 Gal during 10 s for detecting the house performance in the completely liquefaction environment (Suzuki et al. 2013). The pore pressure transducers were set inside the ground. The accelerometer was installed on the top of house model which was used to measure the acceleration in horizontal direction, while linear variable differential transformer was used to record the history of settlement.

House model were made of acrylic fibre by 1/50 scale from the size of specified house. Ground condition and each sensor setting were depicted in Fig. 2 and all tests were operated in earth's gravity field (Hayashi et al. 1997). Depending on the substructure existence or not, individual basement or union forms, and different weights of models, five patterns was considered in the testing, and the details are shown in Fig. 3.

3 The Performance of the Patterns Without Substructure

First, the response of Case 0 is analysed in. Figure 4a shows the seismic wave input to the container, which was recorded by an additional accelerometer from the table. Figure 4b depicts the acceleration varying with time on the top of house. It reaches the maximum magnitude around 150 Gal rapidly when the shaking started, then decreased and kept in a limited range. Note that the acceleration curve deviated from X-axis, which indicates that the house over turned after 5 s. Figure 4c reveals that 2–3 s after shaking, the settlement occurred. Then the settlement increased to 30 mm. After that, the house started to incline. But a high angle lean does not appear in Case 1, and final average settlement is about 21 mm.

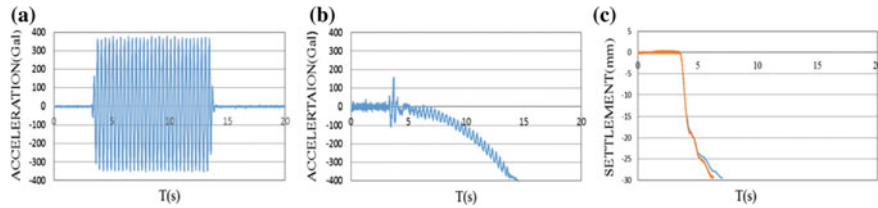


Fig. 4 Responses on shaking test in Case 0. **a** Seismic wave input. **b** Acceleration on house top. **c** Settlement

The magnitude of pore water pressure (Excess pore pressure ratio) is used to estimate the extent of the liquefaction, which is defined as (Kasama et al. 2010):

$$\text{Excess pore pressure ratio} = \frac{u}{\sigma'_z} \quad (1)$$

In which, σ'_z is effective stress, determined by the upper load, u is the pore water pressure.

Figure 5 shows the pore water pressure of Case 0 versus time. Figure 5a reveals that the pore water pressure raised promptly following the shake starting, and was in a constant level for almost 40 s in spite of the shaking ending at 15 s. The deeper the soil, the higher the pore water pressure performed. Moreover, it is noted that, the pore pressure decreased slowly with time, meanwhile, the beginning of dissipating presents sequential order by depth. Similar phenomenon can be observed in Case 1 as shown in Fig. 6a. It can be found from Figs. 5b and 6b that the excess pore pressure ratio of Case 0 and Case 1 almost achieved 1.0 in each depth, that is to say, liquefaction occurred in entire ground. Since the most maximum excess pore pressure ratio reach 1.0, a relation between the depth and distance from house can be drawn as Fig. 7.

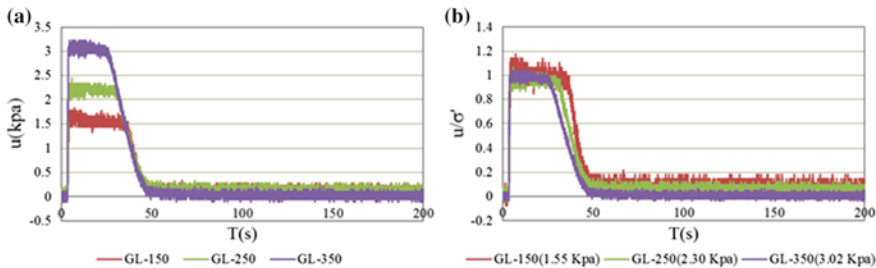


Fig. 5 The pore water pressure versus time in Case 0. **a** Excess pore pressure. **b** Excess pore pressure Ratio

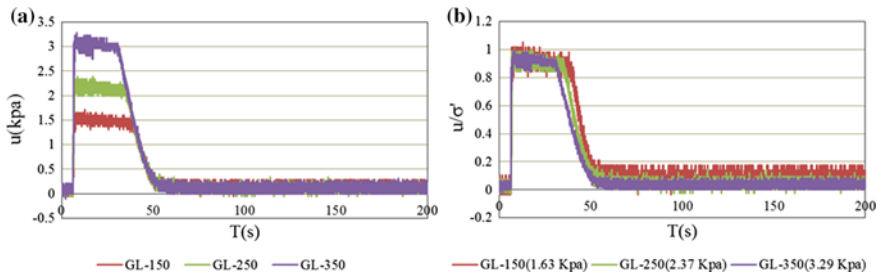


Fig. 6 Case 1 the pore water pressure versus time. **a** Excess pore pressure. **b** Excess pore pressure ratio

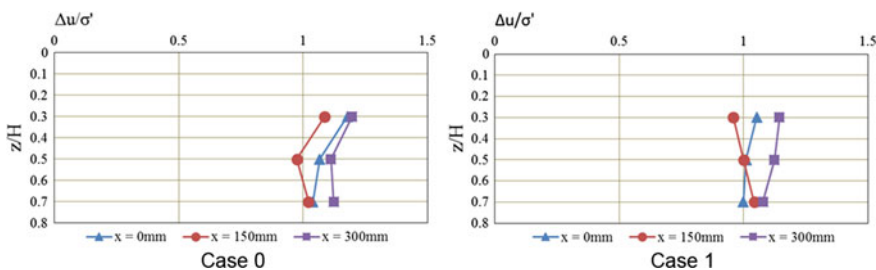


Fig. 7 Maximum excess pore water pressure ratio distribution by depth

4 The Performance of the Patterns with Substructure

In Case 2, Fig. 8 shows the pore water pressure of each depth versus time, it kept increasing instead of holding a steady level when the shaking stopped at 15 s, thereafter, the pore pressure dissipated slowly. Furthermore, note that the pore pressure u did not return back to zero but maintained at a constant value. It is considered that pore pressure transducers were not of fixed result in declining during liquefaction occurred in the ground. As a result, hydrostatic pressure went on

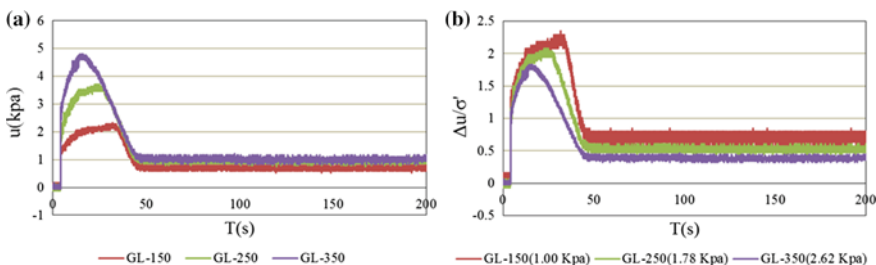
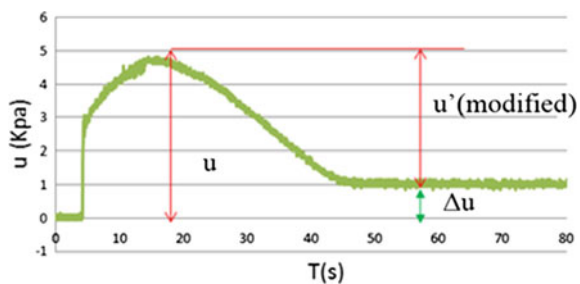
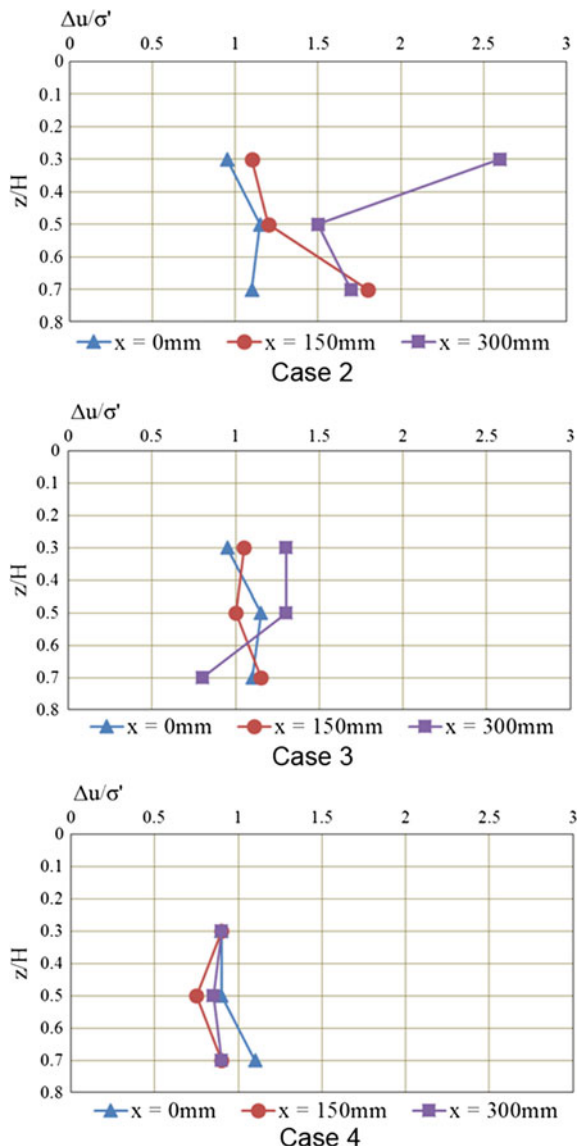


Fig. 8 The pore water pressure versus time in Case 2. **a** Excess pore pressure. **b** Excess pore pressure ratio

Fig. 9 Modification method**Fig. 10** Maximum excess pore pressure ratio distribution

increasing, so the pore pressure u still kept increasing with these transducers dropping down. The result of Case 3 and Case 4 is similar to that of Case 2.

To solve this problem in Fig. 9, a new equation form is adopted as,

$$u' = u - \Delta u,$$

Here u is the original maximum pore pressure, Δu is the residual pore pressure, u' the modified maximum pore pressure (Yoshiaki 1998). The results are rearranged as shown in Fig. 10. Considering the Case 2, Case 3 and Case 4, most maximum pore water pressure ratio reached 1.0, which indicates that the ground was completely liquefied after inputting the seismic load. The comparison of the three cases reveals that the preventing effect becomes more effective by the order of Case 2, Case 3 and Case 4. This provides the evidence that Three-Union form have a better performance than Separate structure form.

5 Weight Effect

Focusing on acceleration on top of house together with the settlement, Case 1, Case 3, and Case 4 will be discussed in this section. The weight of the house model in Case 4 was changed from 3.6 to 7.2 kg for analysing the weight effects.

As shown in Fig. 11, the settlement increased sharply as shaking started and reached 15 mm. After that, the settlement increased gradually with time. Final

Fig. 11 Case 1 acceleration and settlement varies with time

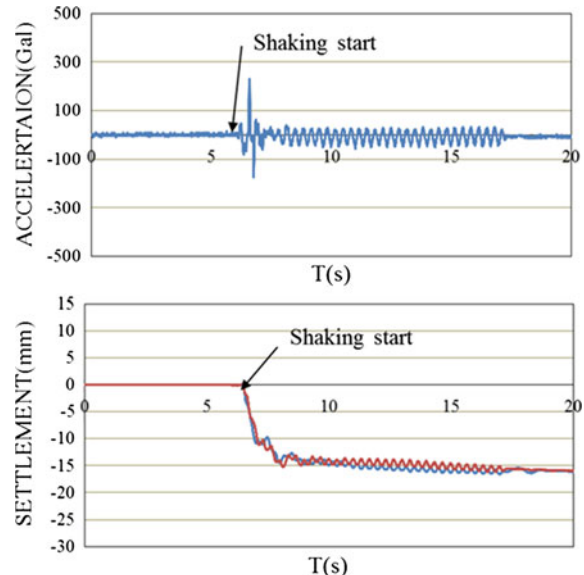
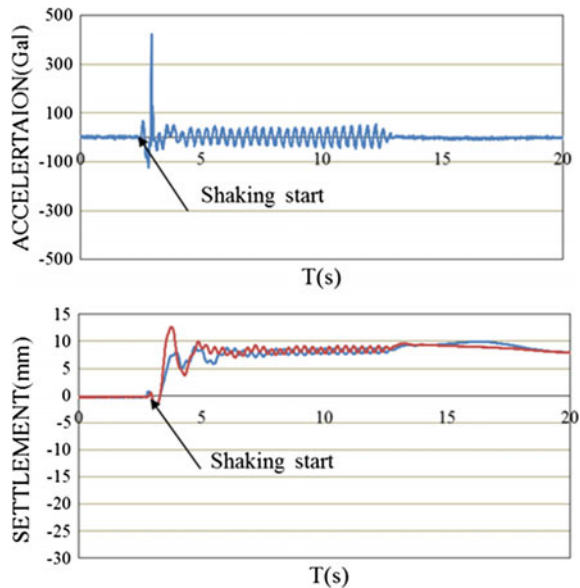


Fig. 12 Acceleration and settlement versus time in Case 3



settlement was stabilised at 20.9 mm, meanwhile uneven settlement of house was less than 1.5 mm in Case 1 (Three-Union house without basement). On the contrary, if the substructure exists, the height was 50 mm, such as Case 3 (Three-Union house with basement), the buoyant force can be calculated to about 3.6 kg, which equals to the weight of house. As a result, the house was uplifted about 10 mm in maximum and stabilised at 2.85 mm higher than original position. The uneven settlement of this case is around 3.05 mm, shown as Fig. 12. For limiting the uplift problem, the weight of house model in Case 4 added to 7.2 kg which was 2 times greater than the former Cases. As is expected, the position of house mostly remained during the test, and settled about 4.67 mm finally, whereas the non-uniform settlement was up to 9.5 mm as shown in Fig. 13. Larger leaning happened compared with Case 1 and Case 3.

The comparison on the accelerations is depicted in Fig. 14. Case 1 shows a lowest response that is only half of the input wave. Both Case 3 and Case 4 exceed 400 Gal and as a result of that, the substructure was embedded into ground foundation. Substructure weight and height will be discussed in the future to decrease the settlement and acceleration response.

Fig. 13 Acceleration and settlement versus time in Case 4

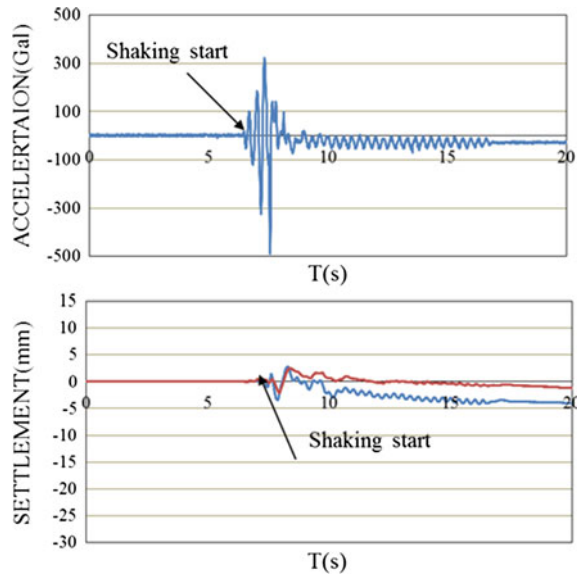
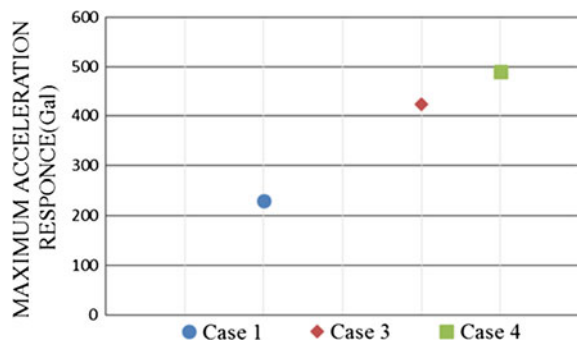


Fig. 14 Maximum acceleration response



6 Conclusions

Five different structural performances have been investigated by shaking table test in gravity field. Several primary results are summarised as follows:

1. Comparing with separate house, three-union form shows higher stability and lower settlement on liquefied ground condition during earthquakes.
2. Settlement is reduced greatly with the help of substructure. However, the uneven settlement occurred in this case produced by the buoyancy uplifting the house during liquefaction. So that water level and model weight become significant factors to balance the vertical force, which will be considered in the future study.
3. Liquefaction occurred on all patterns in this test condition. It could not indicate a clear function of basement to restrict the pore water pressure increasing on

sandy ground. In order to detect the advantage of Three-Union house with basement, the lower seismic load condition will be carried out in further study.

Acknowledgments This study achieves the financial support from Kyushu Bureau of Economy, Trade and in Industry of Japan. Thanks laboratory technician Mr. NAKASHIMA, Mr. YAHIRO and graduated student Miss. TAJIMA for their helps on making the house models and equipment utilizations. Gratitude is given to Professor HAZARIKA of Kyushu University for his many valuable advices.

References

Fukutake T, Yasuhiro S, Tokimatsu K (2013) Discussing the Inhibitory effects of ground water draining and decreasing by numerical analysis for existing housing. The 48th annual meeting of Japanese Geotechnical Society, Toyama, Japan, 7 July, pp 1607–1608 (in Japanese)

Hayashi K, Fujii N, Muramatsu T, Houjyou K (1997) Direct comparison of gravity model and centrifuge model for the seismic problem. *J Geotech Eng*, No. 582/III-41, 207–216

Kasama K, Zen K, Chen GQ, Hayashi K (2010) Shaking table model test on seismic stability of caisson type quay wall in application of cement-mixing method. *J Geotech Eng* (c) 66 (1):196–201 (in Japanese)

Suzuki Y, Tokimatsu K, Hidekawa T, Adachi N (2013) Dynamic centrifuge model test of liquefaction countermeasures using both dewatering and drainage method for existing houses. The 48th annual meeting of Japanese Geotechnical Society, Toyama, Japan, 7 July, pp 1603–1606 (in Japanese)

Tajima T (2013) Discussion the function of basement on seismic resistance with liquefaction problem, Bachelor Dissertation, Kyushu University, Japan (in Japanese)

Wang B (2012) Experimental and analytical studies on the mechanism of ground deformation after liquefaction in terms of soil permeability, Ph.D. Thesis, Kyushu University, Japan

Yoshiaki Y (1998) Simplified design of structures buried in liquefiable soil. *Soil Found* 38 (1):235–240

Part V
Piles and Retaining Walls

Analysis of the Lateral Force on Stabilizing Piles in $c\text{-}\varphi$ Soil

Yi He, Hemanta Hazarika, Noriyuki Yasufuku and Ryohei Ishikura

Abstract In the past, the lateral force on stabilizing piles has been studied by many researchers. In this study, the lateral force loading on stabilizing piles per unit thickness is analyzed in a semi-infinite $c\text{-}\varphi$ soil ground ($\varphi > 0$, $c > 0$). The soil arching effects between two neighboring piles are considered. A new formula is proposed to estimate the lateral load acting on the stabilizing piles. When the proposed approach is applied on some kinds of $c\text{-}\varphi$ soil, an invalid value would be obtained on the failure plane. However, the invalid value can be ignored since it has little impact on the solution. The in situ observed tests from the literatures are introduced to validate the proposed approach. The comparison charts illustrate that the prediction from the proposed approach shows a better agreement with the test results comparing with the solution from plastic deformation theory.

Keywords Stabilizing piles · Landslides · Soil arching · Slope

1 Introduction

During the past decades, installing rows of drilled shafts for slope stabilization has been proved to be the reliable and effective technique to prevent excessive slope movement (Liang and Zeng 2002; Lirer 2012). Such piles are installed through the unstable soil layer and embedded into the stable layer below the sliding surface. The slope is enhanced by piles, which are able to transfer part of the force from the failing mass to the stable soil layer. For passive piles, the lateral force applied on the piles by the unstable layer is dependent on the soil movement, which is in turn affected by the presence of the piles.

Evaluating the lateral force loading on the stabilizing piles is of great significance for the study of slope stabilization. Referring to the previous research on estimation of the lateral force of the stabilizing piles, an analysis of piles in a single

Y. He (✉) · H. Hazarika · N. Yasufuku · R. Ishikura
Kyushu University, Fukuoka 819-0395, Japan
e-mail: dell811@163.com

row through plastically deforming ground was described by Ito and Matsui (1975) based on the theory of plastic deformation, simultaneously, the interaction between piles and soil are considered. The approach can roughly agree with the observed values. However, the linear distribution of the lateral force predicted by this method appears different from many experimental results (Chen and Poulos 1997; Lirer 2012; Fukumoto 1972), which present the nonlinear distribution of the force due to arching effects in the soil-piles system. Recently, the soil arching theory has been successfully introduced in soil-structure engineering, such as retaining walls and piles embankments. Authors believe that Ito and Matsui's method can be got further improvement by soil arching theory as well.

In this study, a new formula is proposed to estimate the lateral load acting on the stabilizing piles in c - ϕ soil ground. The distribution of the soil stress exerted on the piles is nonlinear based on the soil arching theory. To validate the proposed approach, the in situ tests are introduced. The results indicate that the prediction by the proposed formula agrees with measured data, but some limitation still exists. Nevertheless, comparing to Ito and Matsui's methods (1975), it shows that the proposed approach has advantage in estimating the lateral force acting on stabilizing piles.

2 Analysis of the Piles

2.1 Soil Arching Effects

In order to estimate the lateral force acting on stabilizing piles, a set of assumptions in the soils between two neighboring piles were developed in plastically deforming ground by Ito and Matsui (1975). In this analysis, comparing with the assumptions of the soil deforming adjacent to piles in Ito and Matsui's theory, the soil arching zone in the rear of piles is introduced (Fig. 1). As shown in Fig. 1, the deformation in the unstable soil layer of thickness H yields the soil arching, whose area is described by the shaded portion. The plane view of soil deforming between two neighboring piles is depicted in Fig. 2. Furthermore, a typical cross section, UU', as shown in Fig. 3, is employed to display the state of the soil stress in the rear of the plane AA' (Fig. 2). In the present paper, the analysis is conducted in two stages. First, the soil pressure acting on the plane AA' is analyzed based on the soil arching theory. Second, considering the squeezing effect between the piles, the lateral force acting on the piles is calculated.

The soil arching theory has been developed to study on retaining wall based on the catenary and circle shaped arch respectively (Handy 1985; Wang 2000; Paik and Salgado 2003). In this paper, some concept of previous study is adopted to investigate the state of soil stress behind a row of stabilizing piles. The trajectory of soil arch is assumed to be an arc of a circle, and the direction of major and minor principal stress in the rear of piles is discussed. Furthermore, in order to inquire into the state of soil stress in the rear of the plane AA' (Fig. 2), two main assumptions are made as follows:

Fig. 1 The soil arching zone in the rear of stabilizing piles

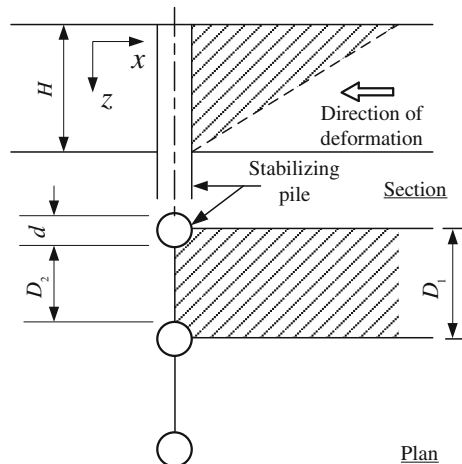
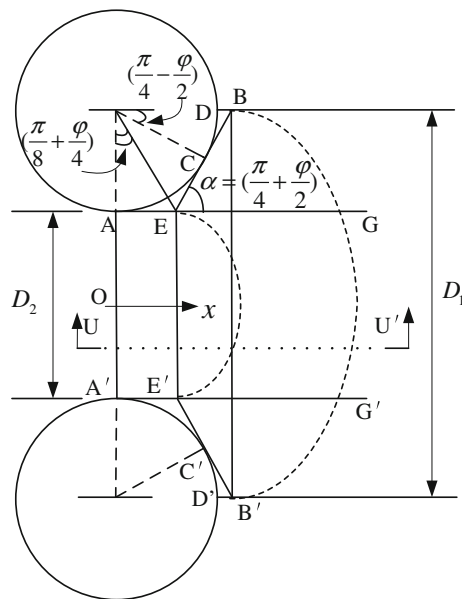


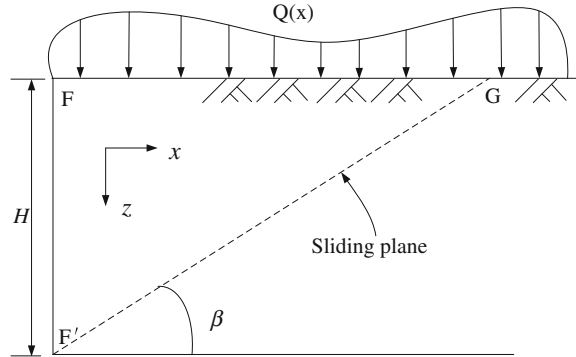
Fig. 2 Plastic deformation of soil between neighboring piles [after Ito and Matsui (1975)]



1. When soil layer deforms, the plane AA' (Fig. 2) is in active condition.
2. When the active stress on the plane AA' is analyzed, only the area between the two parallel lines AG and A'G' (Fig. 2) is considered, the actual sliding surface between two piles is ignored.

It is noted that assumption 1 is same as that of Ito and Matsui (1975). Furthermore, they assumed that the Coulomb's active earth pressure was applied on the plane. However, some researches (Janssen 1895; Marston and Anderson 1913;

Fig. 3 Cross section of deformation in $c\text{-}\varphi$ soil with non-uniform pressure on the top surface

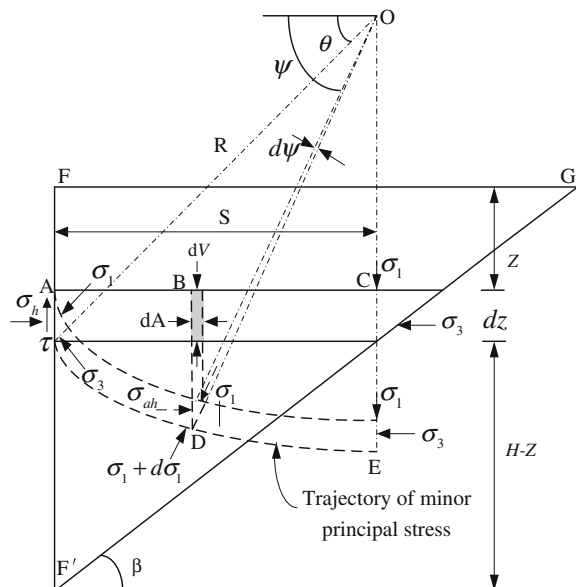


Paik and Salgado (2003) indicate that the active earth pressure predicted by soil arching theory provides more accurate result than that by Coulomb's method. In this paper, the active stress on plane AA' (Fig. 2) in $c\text{-}\varphi$ soil is discussed based on soil arching theory.

When soil layer deforms, the actual soil arching zone would be complicated. In this study, assumption 2 is utilized to simplify the analysis. The cross section UU' is shown in Fig. 3, where the angle between the sliding plane and the horizontal is assumed to be β . It is noted that a nonuniform pressure $Q(x)$ is applied on the top surface FG in Fig. 3, which aims at eliminating the effect of tensile zone in $c\text{-}\varphi$ soil.

The rotation of the principal stress on the line FF' (Fig. 3) is described as Fig. 4. The trajectory of minor principal stress on the differential element is represented by the dotted lines, while the major principal stress is the normal of the arch.

Fig. 4 State of stress on differential element in the soil arching zone [after Paik and Salgado (2003)]



Considering the force equilibrium in the triangular element at point A in Fig. 4, the lateral stress is obtained as

$$\sigma_h = \sigma_1 \cos^2 \theta + \sigma_3 \sin^2 \theta \quad (1)$$

At an arbitrary point D of the arch, whose original location is point B, a similar equation is given by

$$\sigma_{ah} = \sigma_1 \cos^2 \psi + \sigma_3 \sin^2 \psi \quad (2)$$

where ψ is the angle between the normal of the arch at point D and the horizontal, σ_{ah} the lateral stress at point D. Considering that the soil is in active state, the Mohr–Coulomb's yielding criterion is applied:

$$\sigma_3 = \sigma_1 K_a - 2cK_a^{1/2} \quad (3)$$

where, $K_a = \tan^2(\pi/4 + \varphi/2)$, c is the cohesion of soil. Substituting Eq. (3) into Eq. (1), the lateral stress at point D is obtained

$$\sigma_{ah} = (\cos^2 \psi + K_a \sin^2 \psi) \sigma_1 - 2cK_a^{1/2} \sin^2 \psi \quad (4)$$

Since $\sigma_{ah} - \sigma_3 = \sigma_1 - \sigma_{av}$, substitution for σ_{ah} gives

$$\sigma_{av} = (\sin^2 \psi + K_a \cos^2 \psi) \sigma_1 - 2cK_a^{1/2} \cos^2 \psi \quad (5)$$

where σ_{av} is the vertical stress at an arbitrary point D. As depicted by Eq. (5), the vertical stress varies with angle ψ , which changes from θ to $\pi/2$. In this problem, it seems to be impossible to calculate the vertical stress at every point in the analyzing zone, so the average vertical stress $\bar{\sigma}_v$ is introduced, which can be expressed as

$$\bar{\sigma}_v = \frac{V}{S} \quad (6)$$

in which V is the total vertical stress across the differential element and S the width of the differential element. The total vertical stress V of the differential element can be calculated by the following formula:

$$\begin{aligned} V &= \int_{\theta}^{\pi/2} dV = \int_{\theta}^{\pi/2} \sigma_{av} dA \\ &= \int_{\theta}^{\pi/2} \left[\sigma_1 (\sin^2 \psi + K_a \cos^2 \psi) - 2cK_a^{1/2} \cos^2 \psi \right] (R \cdot d\psi \cdot \sin \psi) \end{aligned} \quad (7)$$

where dV is the differential vertical force on the shaded portion at arbitrary point B, and dA the width of the shaded portion at point B.

Substituting Eq. (7) into Eq. (6), and considering $S = R \cdot \cos \theta$, the average vertical stress is obtained as follows

$$\bar{\sigma}_v = \int_{\theta}^{\pi/2} \sigma_1 (\sin^2 \psi + K_a \cos^2 \psi) \frac{\sin \psi}{\cos \theta} \cdot d\psi - \int_{\theta}^{\pi/2} 2cK_a^{1/2} \cos^2 \psi \frac{\sin \psi}{\cos \theta} \cdot d\psi \quad (8)$$

Integration of Eq. (8) yields

$$\bar{\sigma}_v = \sigma_1 \left(1 - \frac{1 - K_a}{3} \cos^2 \theta \right) - \frac{2c}{3} K_a^{1/2} \cos^2 \theta \quad (9)$$

Equation (9) can be rewritten as

$$\sigma_1 = \frac{3\bar{\sigma}_v + 2cK_a^{1/2} \cos^2 \theta}{3 - (1 - K_a) \cos^2 \theta} \quad (10)$$

Substituting Eqs. (3) and (10) into Eq. (1), the lateral stress is obtained

$$\sigma_h = \frac{3(\cos^2 \theta + K_a \sin^2 \theta)}{3 - (1 - K_a) \cos^2 \theta} \left(\bar{\sigma}_v + \frac{2c}{3} K_a^{1/2} \cos^2 \theta \right) - 2cK_a^{1/2} \sin^2 \theta \quad (11)$$

in which $\theta = 45^\circ + \varphi/2$ when the line FF' is in the active condition. In order to predigest the expression of Eq. (11), let

$$K_{an} = \frac{3(\cos^2 \theta + K_a \sin^2 \theta)}{3 - (1 - K_a) \cos^2 \theta} \quad (12)$$

and

$$\begin{aligned} T &= \frac{3(\cos^2 \theta + K_a \sin^2 \theta)}{3 - (1 - K_a) \cos^2 \theta} \cdot \frac{2c}{3} K_a^{1/2} \cos^2 \theta - 2cK_a^{1/2} \sin^2 \theta \\ &= \frac{2c}{3} K_a^{1/2} \cos^2 \theta \cdot K_{an} - 2cK_a^{1/2} \sin^2 \theta \end{aligned} \quad (13)$$

Then Eq. (11) can be expressed as

$$\sigma_h = K_{an} \bar{\sigma}_v + T \quad (14)$$

2.2 Limit Equilibrium Equation for $c\text{-}\varphi$ Soil

As mentioned previously, when the $c\text{-}\varphi$ soil is in active condition, a tensile zone exists in the soil, which leads to a complicated analysis for the active stress. To simplify the analysis, as shown in Fig. 5, a nonuniform load $Q(x)$ is assumed acting on the top surface of the soil, which would erase the tensile zone. Furthermore, it is assumed that the angle between the yielding plane and the horizontal in the loaded cohesive soil is assumed $\beta = 45^\circ + \varphi/2$.

Figure 5 shows the state of the differential element in loaded $c\text{-}\varphi$ soil. In the vertical direction, considering the effect of cohesion at the left edge, the limit equilibrium equation is set up

$$\gamma S \cdot D_2 dz = (K_{an} \bar{\sigma}_v + T) \tan \varphi \cdot D_2 dz + c D_2 dz + S \cdot D_2 d\bar{\sigma}_v \quad (15)$$

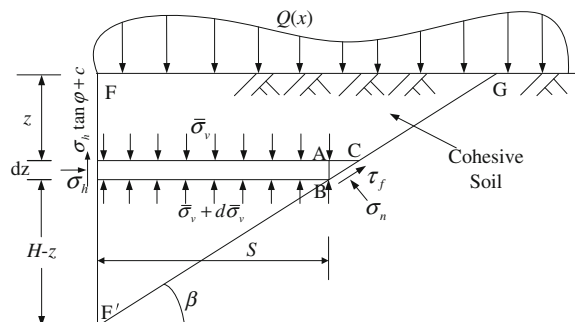
in which T is calculated by Eq. (13), $\bar{\sigma}_v$ the average vertical stress, S the width of the differential element ($S = (H - z)/\tan \beta$), D_2 the clear interval between two neighboring piles, dz the thickness of the differential element. Solving this equation, the average vertical stress at arbitrary depth in the loaded $c\text{-}\varphi$ soil is obtained as follows

$$\bar{\sigma}_v = \frac{\gamma H \left[\left(1 - \frac{z}{H}\right)^{K_{an} \tan \varphi \tan \beta} - \left(1 - \frac{z}{H}\right) \right]}{1 - K_{an} \tan \varphi \tan \beta} + \frac{(T \tan \varphi + c)}{K_{an} \tan \varphi} \left[\left(1 - \frac{z}{H}\right)^{K_{an} \tan \varphi \tan \beta} - 1 \right] + \bar{Q}(x) \left(1 - \frac{z}{H}\right)^{K_{an} \tan \varphi \tan \beta} \quad (16)$$

Let

$$\bar{\sigma}_{v1} = \frac{\gamma H \left[\left(1 - \frac{z}{H}\right)^{K_{an} \tan \varphi \tan \beta} - \left(1 - \frac{z}{H}\right) \right]}{1 - K_{an} \tan \varphi \tan \beta} + \frac{(T \tan \varphi + c)}{K_{an} \tan \varphi} \left[\left(1 - \frac{z}{H}\right)^{K_{an} \tan \varphi \tan \beta} - 1 \right] \quad (17)$$

Fig. 5 Soil stress on differential element in loaded cohesive soil



Eliminating the average nonuniform pressure $\bar{Q}(x)$ with some simplifying method, the active lateral stress on the plane AA' (Fig. 2) in $c\text{-}\varphi$ soil is presented by

$$\sigma_h = K_{an} \left([\bar{\sigma}_{v1}]_{z=z_i} - [\bar{\sigma}_{v1}]_{z=0} \right) \quad (18)$$

in which z_i is the arbitrary depth of the soil layer, $\bar{\sigma}_{v1}$ is calculated by Eq. (17).

It is noted that, when Eq. (18) is utilized to estimate the active lateral stress in cohesive soil whose internal friction angle equals to zero, parameter φ should be substituted by a value close to 0, such as 0.01° .

2.3 The Squeezing Effects of the Soil Between Neighboring Piles

Ito and Matsui (1975) have proposed a plastic deformation model to evaluate the squeezing effects between two neighboring piles. In the present paper, the concept used herein is similar to the method used by Ito and Matsui (1975). Furthermore, all the assumptions given by them are adopted. Equation (18) is substituted for Eq. (8) in Ito and Matsui's research (1975), the lateral forces acting on stabilizing piles in the $c\text{-}\varphi$ soil is expressed as

$$\begin{aligned} p = cD_1 \left(\frac{D_1}{D_2} \right)^{N_\varphi^{1/2} \tan \varphi + N_\varphi - 1} & \left\{ \frac{(2N_\varphi^{1/2} \tan \varphi + 1)}{N_\varphi \tan \varphi} \right. \\ & \times \left[\exp \left(\frac{D_1 - D_2}{D_2} N_\varphi \tan \varphi \tan \left(\frac{\pi}{8} + \frac{\varphi}{4} \right) \right) - 1 \right] \\ & + \left. \frac{2 \tan \varphi + 2N_\varphi^{1/2} + N_\varphi^{-1/2}}{N_\varphi^{1/2} \tan \varphi + N_\varphi - 1} \right\} - cD_1 \frac{2 \tan \varphi + 2N_\varphi^{1/2} + N_\varphi^{-1/2}}{N_\varphi^{1/2} \tan \varphi + N_\varphi - 1} \\ & + \left(K_{an} \left([\bar{\sigma}_{v1}]_{z=z_i} - [\bar{\sigma}_{v1}]_{z=0} \right) \right) \\ & \times \left[D_1 \left(\frac{D_1}{D_2} \right)^{N_\varphi^{1/2} \tan \varphi + N_\varphi - 1} \times \exp \left(\frac{D_1 - D_2}{D_2} N_\varphi \tan \varphi \tan \left(\frac{\pi}{8} + \frac{\varphi}{4} \right) \right) - D_2 \right] \end{aligned} \quad (19)$$

In $c\text{-}\varphi$ soil, when Eq. (19) is utilized to calculate the lateral force acting on a stabilizing pile, an invalid value would be obtained in when z_i is very close to the height of the unstable soil layer H . In other words, the predicted lateral force by Eq. (19) may be as a negative value when z_i approximates to H . It is considered to be limitation of this approach since the lateral force of the pile in the ground between the tensile zone and the failure plane should not be negative. An adjustment for this problem is that, if the calculated value is negative in the invalid-value-area above H , we let it to be 0. That is to say, in a tiny range above the

failure plane, the lateral force on the piles would be 0 when the invalid-value-area exists in the soil ground. Since the invalid-value-area is very small and the lateral force on the pile at $z_i = H$ generally approximate to 0 for rigid piles, this treatment of the negative force is reasonable. Furthermore, the range of the invalid-value-area will be discussed in the following section. On the contrary, if the calculated value on the failure plane is not negative, it means there is no invalid-value-area in this kind of soil. In this soil, the lateral forces around the depth $z_i = H$ can be calculated by Eq. (19) directly.

3 Parameter Analysis (The Range of Invalid-Value-Area)

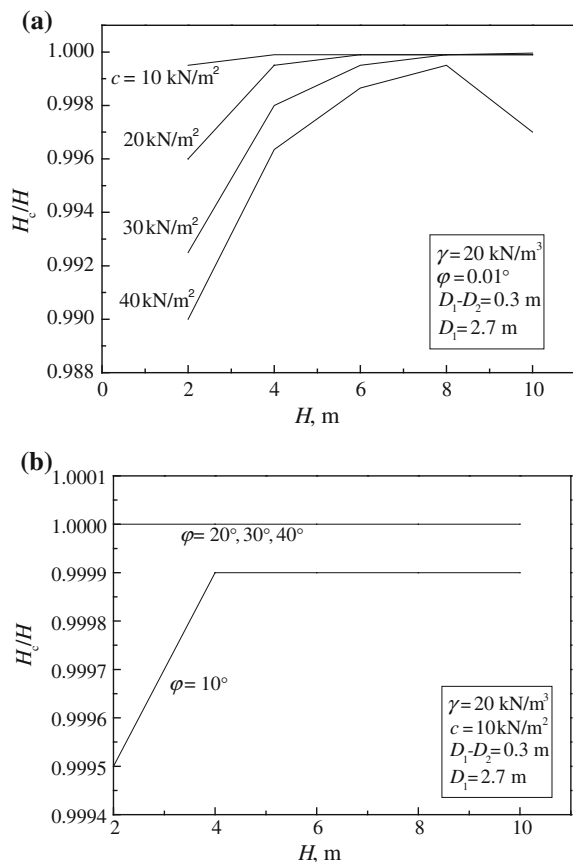
As noted previously, in some kinds of $c\text{-}\varphi$ soil, an invalid value would be obtained near the potential failure plane. The area in which the invalid value obtained is called invalid-value-area. Effective height is defined as the accurate height that the positive lateral force on piles can be calculated along by Eq. (19). That is to say, when Eq. (19) is utilized, once the height exceeds effective height the lateral force would be negative. The ratio H_c/H versus H with respect to different mechanical parameters is shown in Fig. 6, in which H_c is the effective height, H the height of the unstable soil layer. Figure 6 displays that the effective height varies with the mechanical parameters, and the ratio H_c/H changes from 0.99 to 1. The variation of the ratio H_c/H indicates that the only a tiny discrepancy exists between effective height and the height of unstable soil layer.

In some kinds of soil, when Eq. (19) is utilized the invalid-value-area indeed exists, it is the limitation of this approach. However, as shown in Fig. 6, this area is so tiny that it is considered reasonable to neglect it. So in both cohesionless and cohesive soil, the proposed approach is available for estimating the lateral force on pile at every depth within H .

4 Experimental Verification

In Ito and Matsui's research (1975), the theoretical values were compared with the observed ones, which were obtained by Fukumoto (1972, 1973) in the typical landslides areas in Japan, including Higashitono, Kamiyama landslides areas. In this research, for the purpose of comparison, one of the measured data of Fukumoto (1972, 1973) is used again. The condition of the stabilizing piles in Kamiyama areas is summarized as follows. The steel pipe piles with the diameter of 318.5 mm, and wall thickness of 6.9 mm were adopted. All the piles were set up zigzag in two rows at 4 m intervals, and the line space between two rows was 2 m. The friction angle, cohesion and unit weight of the soil are 0.01° , 0.41 kg/cm^2 , 19 t/m^3 respectively. Note that the internal friction angles in Kamiyama landslide area is set 0.01° , while the original values of the angles are 0° . As mentioned previously, in

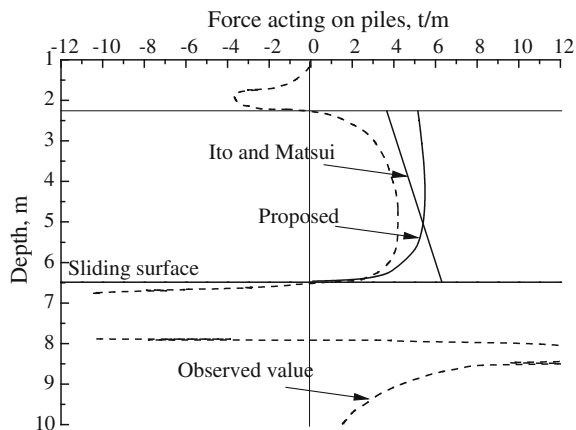
Fig. 6 Change of effective height with mechanical parameters for (a) cohesive soil with internal friction angle approximates to 0° and (b) $c\text{-}\varphi$ soil with $\varphi = 10^\circ$. **a** Change of effective height with cohesion. **b** Change of effective height with internal friction angle



the cohesive soil, when the internal friction angle equals to zero, a value approximated to 0 is substituted. It is a mathematic approach to make sure Eq. (19) can still be used in the case of $\varphi = 0^\circ$.

In Fig. 7, it is obvious that the distribution of the lateral force computed by Ito and Matsui's approach is linear along the stabilizing piles from top of the soil to the sliding surface. Furthermore, the maximum value calculated by Ito and Matsui's method is on the sliding surface, but the observed data shows that the value on the sliding surface usually is minimum, namely 0. Contrarily, the lateral force from the proposed method shows the nonlinear distribution, which results from the soil arching effect. Both the values due to the two theoretical methods are in the same order of magnitude with the observed ones. Since in the $c\text{-}\varphi$ soil, the angle of the soil arching zone is simply assumed to be $45^\circ + \varphi/2$, and the assumption of tensile zone is simplified, some discrepancies still exist in the solution. Nevertheless, the proposed approach shows a more accurate solution for estimating the lateral force acting in stabilizing piles than Ito and Matsui's.

Fig. 7 Comparison between the observed and the theoretical values of lateral force acting on stabilizing piles in typical landslide area (Kamiyama No. 2 pile, height of unstable soil layer H is 6.47 m; effective height H_c is 6.460 m)



5 Conclusions

The estimation of the lateral force acting on the stabilizing pile due to the soil layer movement is discussed in this paper. Former theoretical methods proposed by other researchers show the linear distribution of the lateral force along the unstable soil layer, which is quite different from the observed value. In this paper, the plastic deformation theory proposed by Ito and Matsui is modified by considering the soil arching effect between two neighboring piles, which results in the nonlinear distribution of the lateral force.

For the purpose of checking the accuracy of the proposed methods, a comparison is conducted on the cohesive soil between the observed values and this model. The comparison shows that the proposed formula produces satisfactory results for $c\text{-}\varphi$ soil.

References

Chen LT, Poulos HG (1997) Piles subjected to lateral soil movements. *J Geotech Geoenviron Eng* 123(9):802–811

Fukumoto Y (1972) Study on the behavior of stabilization piles for landslides. *J JSSMFE* 12 (2):61–73 (in Japanese)

Fukumoto Y (1973) Failure condition and reaction distribution of stabilization piles for landslides. In: Proceedings of 8th annual meeting of JSSM, pp 459–462 (in Japanese)

Handy RL (1985) The arch in soil arching. *J Geotech Eng ASCE* 111(9):1321–1325

Ito T, Matsui T (1975) Methods to estimate lateral force acting on stabilizing piles. *Soils Found* 21:21–37

Janssen HA (1895) Versuche über getreide druck in silozellen. *Z. Ver. Deut. Ingr.*, vol 39, 1895, pp 1045–1049 (partial English translation in Proceeding of the Institute of Civil Engineers, London, England, 1896, p 553)

Liang R, Zeng SP (2002) Numerical study of soil arching mechanism in drilled shafts for slopes stabilization. *Soils Found* 42(2):83–92

Lirer S (2012) Landslide stabilizing piles: experimental evidences and numerical interpretation. *Eng Geol* 149–150:70–77

Marston A, Anderson AO (1913) The theory of loads on pipes in ditches and tests of cement and clay drain tile and sewer pipe. *Iowa Engineering Experiment station Bulletin*, Iowa State College, Ames, Iowa, No. 31, 181 p

Paik KH, Salgado R (2003) Estimation of active earth pressure against rigid retaining walls considering arching effects. *Geotechnique* 53(7):643–653

Wang YZ (2000) Distribution of earth pressure on a retaining wall. *Geotechnique* 50(1):83–88

Application of Close-Range Photogrammetry for Post-Failure Reconnaissance of a Retaining Wall

Yung-Yen Ko, Jen-Yu Han and Jun-Yun Chou

Abstract Typhoons and earthquakes are common natural disasters in Taiwan, and both tend to cause failures of geotechnical structures. Consequently, there is much demand for rapid post-failure reconnaissance. Because the failure sites of geotechnical structures are usually not easily accessible and direct measurements will be not possible in such situations, close-range photogrammetry, which gives accurate spatial information about an object at a certain distance, is utilized in this research to develop an indirect reconnaissance method for geotechnical structures. For any object that is recorded in a pair of images from different viewpoints, its relative three-dimensional geometry can be reconstructed without ground control points using relative orientation between conjugate points in the image pair, along with a reference scale provided by any in situ object with a known length. Consequently, the local displacement and deformation of a geotechnical structure can be solved using this method and its damage state can be evaluated accordingly. A retaining wall, which was damaged in an $M_L = 6.5$ earthquake occurred on June 2, 2013 in middle Taiwan, is chosen as a case study. Results show that the forward displacement on the top of the wall can be obtained using close-range photogrammetry based on the relative orientation between an image pair with good precision. Thus, the proposed method is verified to be applicable for the rapid reconnaissance of geotechnical structures after failures occurred.

Keywords Geotechnical structures • Post-failure reconnaissance • Close-range photogrammetry • Relative orientation

Y.-Y. Ko (✉)

National Center for Research on Earthquake Engineering,
200, Sec. 3, Hsinhai Rd., Taipei 10668, Taiwan
e-mail: yyko@ncree.narl.org.tw

J.-Y. Han · J.-Y. Chou

National Taiwan University, Taipei, Taiwan

1 Introduction

In Taiwan, typhoons and earthquakes are common natural disasters that tend to cause failures of geotechnical structures. This is because the heavy rainfalls brought by typhoons reduce the strength of soil material, and the inertial forces generated by earthquakes may damage structures. Consequently, there is much demand for rapid reconnaissance after these failures to assist in the emergency response.

The displacement and deformation of geotechnical structures are important for evaluating their damage state. However, it is sometimes difficult to approach the failure site of a geotechnical structure because there could have been no access originally or access could have been interrupted as the failure occurred. In this case, the displacement and deformation cannot be closely observed and directly measured. Thus, indirect inspection techniques are required. Close-range photogrammetry has been well developed over past years and is capable of giving useful spatial information about an object at a certain distance away with satisfactory precision using a nonmetric camera. Therefore, it can be applied in this situation.

In this research, close-range photogrammetry using the relative orientation technique was applied. This technique is designed to reconstruct the three-dimensional geometry of any object recorded in a pair of images from different viewpoints. Compared to classical photogrammetry based on the absolute orientation technique, this approach requires no ground control points and is particularly useful for rapid measurement of geotechnical structures in an inaccessible site. It merely requires a pair of partially overlapping images taken from different exposure stations and a reference scale provided by any *in situ* object with a known length. Next, by identifying conjugate points in the image pair, their relative geometry in the object space can be uniquely solved.

In order to verify the feasibility of close-range photogrammetry using the relative orientation technique for the damage assessment of geotechnical structures, a retaining wall failure in an $M_L = 6.5$ earthquake in Nantou County in the middle of Taiwan was chosen for a case study. The wall and its backfill were separated as a result of shaking with a seismic intensity of up to intensity *V* on the intensity scale of the Central Weather Bureau (CWB) of Taiwan, which means the peak ground acceleration (PGA) ranges from 80 to 250 Gal. The forward displacement on the top of the wall was estimated using the proposed method with a pair of photographs that were taken on site and then compared to a direct tape measurement. The results will be presented later.

2 Close-Range Photogrammetry Using the Relative Orientation Technique

2.1 Concept of Relative Orientation

By taking two photographs of the same scene from different viewpoints, a stereomodel can be created. To this end, the fact that the projected image rays through conjugate points (image points in an image pair that correspond to the same object point) will intersect in space is used to reconstruct the original epipolar geometry of the image pair. This procedure is known as relative orientation, and can be performed by adjusting the orientation elements of an analog stereoplottor, or by solving the orientation parameters by measuring corresponding image points.

Assuming that the interior orientation parameters of the images are known, each image still has six unknown exterior orientation parameters, which are three position parameters (X_L , Y_L , Z_L), and three rotation parameters (ω , ϕ , κ). Thus, for an image pair, there will be a total of 12 unknown parameters. These parameters can be solved by several approaches, such as dependent relative orientation and independent relative orientation.

As an example, in dependent relative orientation, six parameters of one image along with one position parameter of the second image are first fixed and then the remaining five parameters of the second image are still to be solved. As illustrated in Fig. 1, the six parameters of the first image are fixed if the model coordinate system is defined to be parallel to the coordinate system of the first image. The only fixed position parameter of the second image is used for the calculation of the model scale. Consequently, there will be two position parameters and three orientation parameters of the second image that remain to be determined (Mikhail et al. 2001).

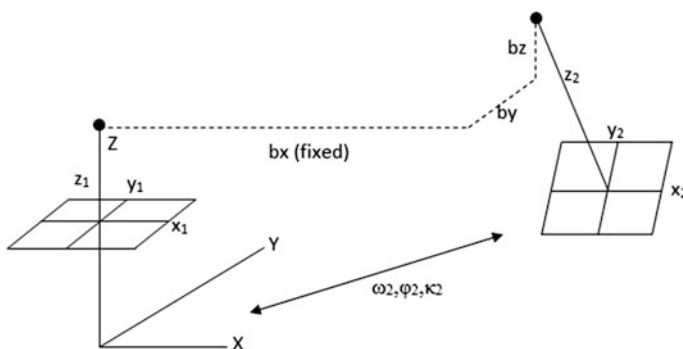


Fig. 1 Dependent relative orientation

2.2 Coplanar Condition and Coplanarity Equation

Figure 2 illustrates a pair of partially overlapping images and a pair of conjugate image points. If the relative orientation of the two images has already been determined, then the two image rays defined by each image point and its corresponding perspective center will exactly intersect. The corresponding positions of these two image points in model space, which correlates to the object space but usually at a reduced scale, can be defined by this intersection (Mikhail et al. 2001).

The two image rays and the vector connecting the two perspective centers form a triangle, as shown in Fig. 2. The three sides of the triangle can be expressed as follows:

$$\vec{a}_1 = \begin{bmatrix} u_1 \\ v_1 \\ w_1 \end{bmatrix} = \frac{1}{k_1} \begin{bmatrix} X - X_{L1} \\ Y - Y_{L1} \\ Z - Z_{L1} \end{bmatrix} = \frac{1}{k_1} M_1^T \begin{bmatrix} x - x_0 \\ y - y_0 \\ -f \end{bmatrix} \quad (1)$$

$$\vec{a}_2 = \begin{bmatrix} u_2 \\ v_2 \\ w_2 \end{bmatrix} = \frac{1}{k_2} \begin{bmatrix} X - X_{L2} \\ Y - Y_{L2} \\ Z - Z_{L2} \end{bmatrix} = \frac{1}{k_2} M_2^T \begin{bmatrix} x - x_0 \\ y - y_0 \\ -f \end{bmatrix} \quad (2)$$

$$\vec{b} = \begin{bmatrix} b_X \\ b_Y \\ b_Z \end{bmatrix} = \begin{bmatrix} X_{L2} - X_{L1} \\ Y_{L2} - Y_{L1} \\ Z_{L2} - Z_{L1} \end{bmatrix} \quad (3)$$

where

\vec{a}_1 denotes the object space vector that forms the image point on the left image;
 \vec{a}_2 denotes the object space vector that forms the image point on the right image;

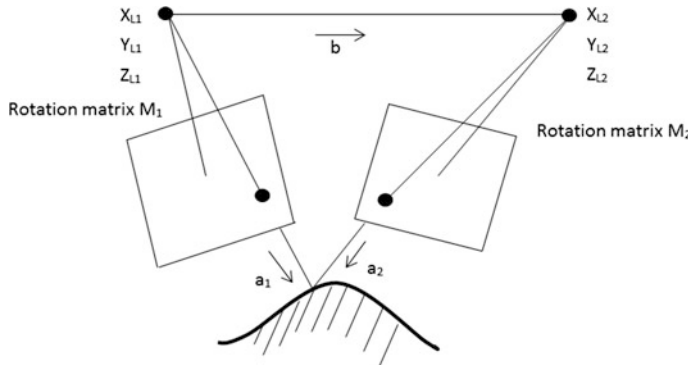


Fig. 2 Geometry of the coplanar condition

\vec{b} denotes the base vector, which is the displacement between the two perspective centers;

(X_{L1}, Y_{L1}, Z_{L1}) and (X_{L2}, Y_{L2}, Z_{L2}) are the position parameters of the left image and the right image, respectively;

(x_0, y_0, f) are the interior orientation parameters in the camera;

M_1 and M_2 are the rotation matrices of the left image and the right image, respectively. For example, the elements of M_1 are functions of the rotation parameters $(\omega_1, \phi_1, \kappa_1)$ and can be expressed as follows:

$$\begin{aligned} m_{11} &= \cos \phi_1 \cos \kappa_1; & m_{12} &= \cos \phi_1 \sin \kappa_1; & m_{13} &= -\sin \phi_1; \\ m_{21} &= \sin \omega_1 \sin \phi_1 \cos \kappa_1 - \cos \omega_1 \sin \kappa_1; \\ m_{22} &= \sin \omega_1 \sin \phi_1 \sin \kappa_1 + \cos \omega_1 \cos \kappa_1; \\ m_{23} &= \sin \omega_1 \cos \phi_1; \\ m_{31} &= \cos \omega_1 \sin \phi_1 \cos \kappa_1 + \sin \omega_1 \sin \kappa_1; \\ m_{32} &= \cos \omega_1 \sin \phi_1 \sin \kappa_1 - \sin \omega_1 \cos \kappa_1; \\ m_{33} &= \cos \omega_1 \cos \phi_1. \end{aligned}$$

The triangle formed defines a unique plane and the relationship between the three vectors \vec{a}_1 , \vec{a}_2 , and \vec{b} is called the coplanar condition:

$$\vec{b} \cdot (\vec{a}_1 \times \vec{a}_2) = 0 \quad (4)$$

This coplanarity equation can be used to determine the relative orientation between an image pair. As mentioned, this is usually achieved by fixing seven of the 12 orientation parameters and then solving for the remaining five.

2.3 Projective Geometry

In independent relative orientation, projective geometry can be used to reconstruct the original epipolar geometry of an image pair (Cheng 2007). If a point m' is located on the right image, then its conjugate point m on the left image should be located on the epipolar line, of which the line equation can be expressed as follows:

$$l = Fm'^T = 0 \quad (5)$$

where F denotes the fundamental matrix (abbreviated as F -matrix hereafter) that describes the epipolar geometry of the image pair.

As $m \cdot l = 0$, the constraint of the epipolar geometry can be expressed as follows:

$$mFm^T = 0 \quad (6)$$

If the interior parameters are known, a C -matrix containing the interior parameters can be defined as follows:

$$C = \begin{bmatrix} 1 & 0 & -x_0 \\ 0 & 1 & -y_0 \\ 0 & 0 & -f \end{bmatrix} \quad (7)$$

The F -matrix can be decomposed by the C -matrix and Eq. (6) can be rewritten as:

$$mFm'^T = mC^T E C m'^T = 0 \quad (8)$$

where E denotes the essential matrix (abbreviated as E -matrix hereafter).

If the vectors \vec{a}_1 and \vec{a}_2 in Eqs. (1) and (2) are rewritten as:

$$\vec{a}_1 = \frac{1}{k_1} M_1^T \begin{bmatrix} 1 & 0 & -x_0 \\ 0 & 1 & -y_0 \\ 0 & 0 & -f \end{bmatrix} \begin{bmatrix} x \\ y \\ 1 \end{bmatrix} = \frac{1}{k_1} M_1^T C \begin{bmatrix} x \\ y \\ 1 \end{bmatrix} \quad (9)$$

$$\vec{a}_2 = \frac{1}{k_2} M_2^T \begin{bmatrix} 1 & 0 & -x_0 \\ 0 & 1 & -y_0 \\ 0 & 0 & -f \end{bmatrix} \begin{bmatrix} x \\ y \\ 1 \end{bmatrix} = \frac{1}{k_2} M_2^T C \begin{bmatrix} x \\ y \\ 1 \end{bmatrix} \quad (10)$$

\vec{b} in Eq. (3) is modified into an skew-symmetric matrix K_b :

$$K_b = \begin{bmatrix} 0 & -b_z & b_y \\ b_z & 0 & -b_x \\ -b_y & b_x & 0 \end{bmatrix} \quad (11)$$

Thus, the coplanarity equation in Eq. (4) can be expressed as follows:

$$\vec{b} \cdot (\vec{a}_1 \times \vec{a}_2) = \vec{a}_1 \cdot (\vec{b} \times \vec{a}_2) = \vec{a}_1^T K_b \vec{a}_2 = [x_1 \ y_1 \ 1]^T C^T M_1 K_b M_2^T C [x_2 \ y_2 \ 1]^T \quad (12)$$

Upon comparison of Eqs. (8) and (12), the E -matrix can be expressed as follows:

$$E = M_1 K_b M_2^T \quad (13)$$

2.4 Analysis Procedure

The procedure for solving the relative orientation between a pair of images using projective geometry is as follows:

- According to dependent relative orientation, six orientation parameters of the left image, X_{L1} , Y_{L1} , Z_{L1} , ω_1 , ϕ_1 , and κ_1 , and one orientation parameter of the right image, X_{L2} , are first fixed.
- Using Eq. (13) and the coordinates of the conjugate points in the image pair, the E -matrix can be obtained.
- Introducing the singular value decomposition technique (Faugeras and Luong 2001) to decompose the E -matrix, the remaining five orientation parameters, Y_{L2} , Z_{L2} , ω_2 , ϕ_2 , and κ_2 , can be determined, and the relative geometry between the two images can be solved.

If an object on the image pair with a known size in the object space and its observed size in the image space are given, the model scale from image space to object space can be computed, which can then be used to estimate the actual distance in the object space from the distance in the image space.

A software for close-range photogrammetry using the procedure proposed above as well as the minimum square method was developed. Using this software, as long as a pair of partially overlapping images are imported, a sufficient number of conjugate points are manually specified, and the distance between two of the conjugate points is given, the distance between any two conjugate points can be solved. Figure 3 shows the snapshot of the software execution.

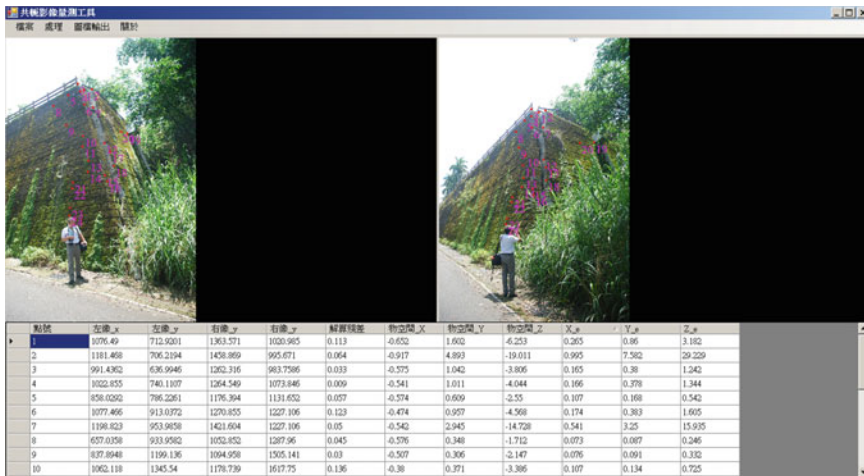


Fig. 3 Snapshot of the execution of the software for close-range photogrammetry developed in this study

3 Case Study of a Retaining Wall Failure

On June 2, 2013, an $M_L = 6.5$ earthquake occurred in Nantou County, Taiwan. The seismic intensity in most areas of Nantou County reached CWB intensity V (80–250 Gal) and a retaining wall at Lugu Junior High School was damaged as a result of this intense shaking. The retaining wall and its backfill were separated and a huge crack on its wing wall was induced, as shown in Fig. 4. If the top of the retaining wall had not accessible, then it would have been difficult to accurately estimate its forward displacement, which is important for the evaluation of the damage state of the retaining wall. Thus, this damage case was chosen to investigate the feasibility of the method proposed in the previous section for the damage assessment of geotechnical structures.

A pair of images as shown in Fig. 5 were first acquired in the field. About 20 pairs of conjugate points that were well distributed over the images were chosen to minimize the error. Using the software developed based on the procedure proposed in Sect. 2.4, all the relative coordinates of these conjugate points were solved. With the sizes of some of the objects in the images given (the height of the man in Fig. 5 is 172 cm, and the depth of the unit segment of the wall is 30 cm), the displacement vector from point B to point A was calculated, and a 31.6-cm forward displacement



Fig. 4 Retaining wall failure case in Lugu Junior High School (left the crack on the wing wall; right the separation of wall and backfill)



Fig. 5 Image pair for solving relative orientation of the retaining wall failure case



Fig. 6 Tape measurement of forward displacement on the top of the retaining wall

was thus obtained. This value is close to the 30-cm tape measurement on the top of the retaining wall, as shown in Fig. 6. The error is less than 10 % and therefore the accuracy of the close-range photogrammetry using the relative orientation

technique is considered high enough for the rapid reconnaissance after the failure of geotechnical structures.

4 Conclusions

In this research, close-range photogrammetry using the relative orientation technique was introduced for post-failure reconnaissance of geotechnical structures, and a retaining wall damaged in an $M_L = 6.5$ earthquake was chosen for case study. Some conclusions can be drawn as follows:

1. By identifying conjugate points in a pair of partially overlapping images taken from different exposure stations, their relative geometry in the object space can be uniquely solved using the coplanar condition among the two image rays and the vector connecting the two perspective centers.
2. Projective geometry accompanied with the singular value decomposition technique can be utilized to reconstruct the original epipolar geometry of an image pair. Then, using a reference scale provided by any in situ object with a known length, the actual distance in the object space can be estimated from the distance in the image space.
3. According to the case study, the proposed method was demonstrated to be practical and gave a result that is accurate enough for the requirement of post-failure rapid reconnaissance.

References

Cheng KW (2007) Projective geometry in photogrammetry. MD thesis, Department of Civil Engineering, National Taiwan University (in Chinese)

Faugeras OD, Luong QT (2001) The geometry of multiple images. The MIT Press, Cambridge, MA

Mikhail EM, Bethel JS, McGlone JC (2001) Introduction to modern photogrammetry. Wiley, New York

Seismic Response of a Newly Developed Geocell-Reinforced Soil Retaining Wall Backfilled with Gravel by Shaking Table Model Test

Han Xinye, Mera Tomoharu, Katagiri Toshihiko and Kiyota Takashi

Abstract A new type of geocell, called square-shaped geocell having straight longitudinal members with transversal walls at separated locations has been developed to alleviate the potential problem of geogrid when used as tensile reinforcement in GRS RWs. In this paper, to check whether geocell-RS RW backfilled with poorly graded gravels has a substantially high seismic stability, two shaking table model tests on geocell-RS RW and geogrid-RS RW backfilled in poorly graded gravels were carried out. A conventional-type RW (i.e., T-shape RW) was also tested for comparison. It was found that geocell-RS RW model exhibited more ductile behavior than geogrid-RS RW model and T-shape RW model from the evaluation of residual sliding displacement and residual overturning angle of the wall facing. In addition, the dynamic behavior of RW models was analyzed as a damped single-degree-of-freedom system. The geocell-RS RW shows similar dynamic strength to the geogrid-RS RW, but a slightly higher dynamic ductility and damping capacity than geogrid-RS RW.

Keywords Geocell · Geogrid · Reinforced soil · Retaining wall · Shaking table model test · Dynamic stability

1 Introduction

For the past two decades, geosynthetic-reinforced soil retaining walls (GRS RWs) with a stage-constructed full-height rigid (FHR) facing have been constructed for railways, highways, and other facilities and have shown greater seismic resistance than conventional retaining wall structures (Tatsuoka et al. 2009). Geogrids are commonly used as planar reinforcements to tensile-reinforce the backfill of RWs, embankments, and other soil structures.

H. Xinye (✉) · M. Tomoharu · K. Toshihiko · K. Takashi

Institute of Industrial Science, University of Tokyo, 4-6-1,
Komaba, Meguro-ku, Tokyo, Japan

e-mail: hanxinye@iis.u-tokyo.ac.jp

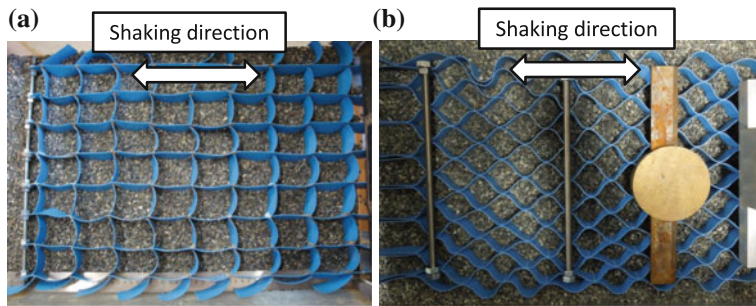


Fig. 1 **a** Square-shaped geocell model; **b** diamond-shaped geocell model

However, the GRS RWs with geogrids may encounter the following potential problems: (1) the geogrid reinforcement is required to use high-quality backfill soil (i.e., sandy soil with good compaction), while the local soil materials which may be poorly graded or include larger particles would be inevitably used as backfill. This would result in a decrease in its deformability, since the bond stress along the interface between geogrid and the backfill becomes lower than the shear strength of the backfill to a larger extent with an increase in the backfill soil particle size; (2) for other GRS structures such as GRS integral bridge (Tatsuoka et al. 2009), the reinforcement is required to provide a higher pullout resistance due to the larger earthquake induced by inertial force. In order to alleviate these problems and improve the seismic performance of GRS RWs, a new type of geocell (Fig. 1a) was developed by Han et al. (2013), which has a different cell shape compared with traditional type geocell (diamond-shaped geocell, Fig. 1b), named square-shaped geocell having straight longitudinal members with transversal walls at separated locations. The pullout test results indicated that square-shaped geocell shows negligible progressive deformation and therefore exhibiting higher pullout resistance and initial stiffness than diamond-shaped geocell. Han et al. (2014a) conducted a series of pullout tests using square-shaped geocell models and a prototype geogrid (i.e., Tensar SS-35) embedded in gravelly soils. The results indicate the important benefit of square-shaped geocell which can confine large soil particles in their three dimensional cells and respective cells provide large anchorage capacity when pull laterally compared with geogrids. What's more, the seismic performance of GRS RW using square-shaped geocell (i.e., geocell-RS RW) backfilled with sandy soil was evaluated comparing to conventional type RW (i.e., T-shape RW) and geogrid-RS RW by shaking table model tests (Han et al. 2014b), showing that geocell-RS RW model exhibited slightly higher seismic performance than geogrid-RS RW model.

In order to check whether geocell-RS RW has a substantially high seismic stability when backfilled with poorly graded gravels, two shaking table model tests on geocell-RS RW and geogrid-RS RW backfilled with poorly graded gravels were carried out. In addition, a T-shape RW model was also tested for comparison.

2 Experiment Outlines

The model tests were carried out using a shaking table at IIS, the University of Tokyo. Figure 2a, b shows the cross-sections of geocell (or geogrid)-RS RW model and T-shape RW model, respectively. Assuming a scale down factor of 1/10, both geocell-RS RW model and geogrid-RS RW model were constructed by a full-height rigid (FHR) facing panel having a size of 39.5 cm in width, 50 cm in height, and 3 cm in thickness. The T-shape RW was constructed by a FHR facing (39.5 cm-wide \times 45 cm-high \times 4.5 cm-thick) strongly connected with a spread-footing foundation (39.5 cm-wide \times 5 cm-high \times 20 cm-thick). All of these walls were made of duralumin with a similar density of concrete ($\rho_d = 2.7 \text{ g/cm}^3$). The back faces of RWs and the bottom surfaces of the foundation directly contact with the subsoil and were made rough by being covered with a sheet of sand paper (No. 150).

As shown in Fig. 2c, geogrid reinforcements used in actual field cases were simulated by a set of regular grids comprising longitudinal members (made of thin and narrow phosphor-bronze strips, 0.2 mm-thick and 3 mm-wide) welded at nodes to transversal members (made of mild steel bar, 0.5 mm in diameter) at intervals of 35 mm. To effectively mobilize friction between the reinforcement and the backfill, sand particles were glued on the surface of the strips. The geogrid model reinforcement was 360 mm (length) \times 350 mm (width). As shown in Fig. 2d, the square-shaped geocell reinforcement consisted of six square cells in the longitudinal direction and seven square cells in the transverse direction. The height of transverse

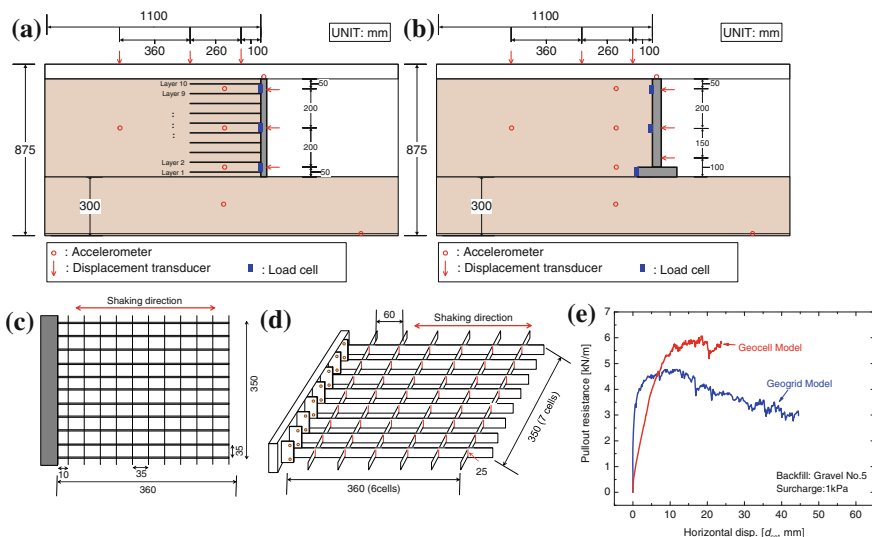


Fig. 2 a GRS RW model; b T-shape RW model; c geogrid model; d geocell model; and e pullout behavior of reinforcements

member is 25 mm and the size of each cell is 60 mm by 50 mm. It was made from polyester (PET) covered with PVC for protection which is a relatively weak material that can be used in scaled-down model test. Ten layers of reinforcements were horizontally placed at a vertical spacing of 5 cm in the backfill which was set by reducing them to a scale of one-tenth of that of actual reinforced soil retaining walls with a full-height rigid facing constructed in Japan.

As shown in Fig. 2a, b, the thickness of subsoil was 30 cm. The subsoil and backfill soil were produced by Gravel No. 5 ($D_{50} = 14.2$ mm; $U_c = 1.44$). The compaction degree was controlled to 100 % ($\rho_d = 1.78$ g/cm³) by manual hand-held plate compaction method. Gravels were placed in a number of layers with each layer compacted to a prescribed dry unit weight while its density is controlled by adjusting the height of the layer. After filling the gravels, a surcharge of 1 kPa was applied by placing lead shots on the surface of the backfill to simulate the weight of the road base for railways or highways. Each retaining wall model was subjected to harmonic sinusoidal base acceleration motion at predominant frequency of 5 Hz having 20 cycles per stage. The acceleration amplitude was increased stage by stage with a target increment of 100 gal from 100 gal to until the failure or collapse occurs.

3 Results and Discussions

3.1 Failure Patterns of Models

Figure 3 shows the residual displacement of the wall the backfill, which was observed at the end of the final shaking step. The values of input base acceleration required to cause significant deformation of RWs are about 417, 755, and 843 gal for T-shape RW, geogrid-RS RW, and geocell-RS RW, respectively. Figure 4 shows the cumulative lateral displacements of the wall facing along the height of the wall as the increasing of the input base acceleration. Due to the rigidity of the wall facing, the displacements of the top of the wall (i.e., d_{total} , at 50 cm height of the wall) and the bottom of the wall (i.e., $d_{sliding}$, at 0 cm height of the wall) can be obtained from the linear extrapolation of the displacements recorded at the height of 5, 25, and 45 cm from the bottom of the wall, as shown the dashed line in Fig. 4. The lateral displacement at the top of the wall, d_{total} , comprised overturning

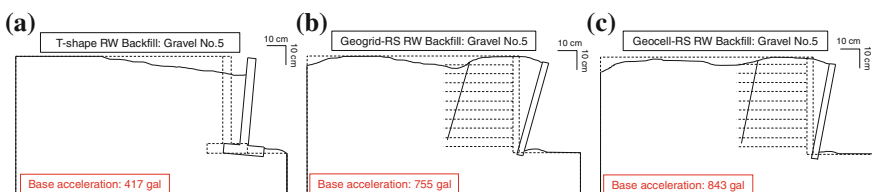


Fig. 3 Residual deformation of wall at failure state: **a** T-shape RW; **b** geogrid-RS RW; **c** geocell-RS RW

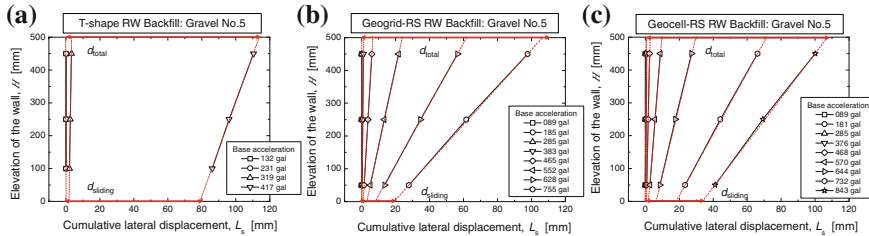
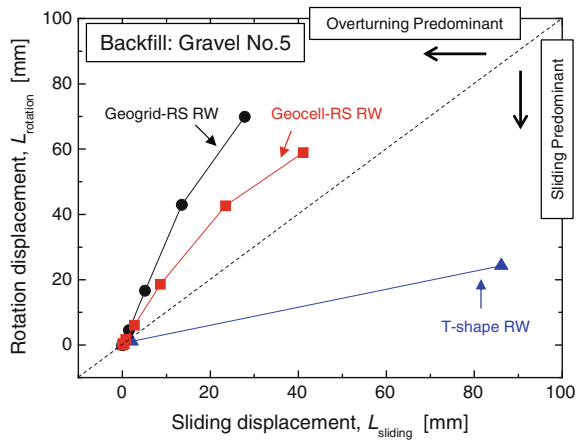


Fig. 4 Lateral displacements of the wall facing for: **a** T-shape RW; **b** geogrid-RS RW; **c** geocell-RS RW

Fig. 5 Relationship between sliding component and overturning component



component (i.e., $d_{overturning}$) and sliding component (i.e., $d_{sliding}$). Therefore, the actual overturning component can be calculated as the difference between the top wall displacement and the bottom wall displacement, $d_{overturning} = d_{total} - d_{sliding}$. Figure 5 shows the relationship between the overturning component and sliding component with the increasing of the input base acceleration. From Figs. 4 and 5, it is clear to see that the predominant failure pattern of T-shape RW was sliding, associated with some small component of overturning. For geogrid-RS RW and geocell-RS RW, the predominant failure pattern was overturning with small component of sliding. This can be attributed to different deformation mechanisms, which will be explained in the next section.

3.2 Residual Deformation of the Wall

Figure 6a compares the residual overturning angle of the facing wall for three types of RW models. As can be seen, up to a base acceleration value of around

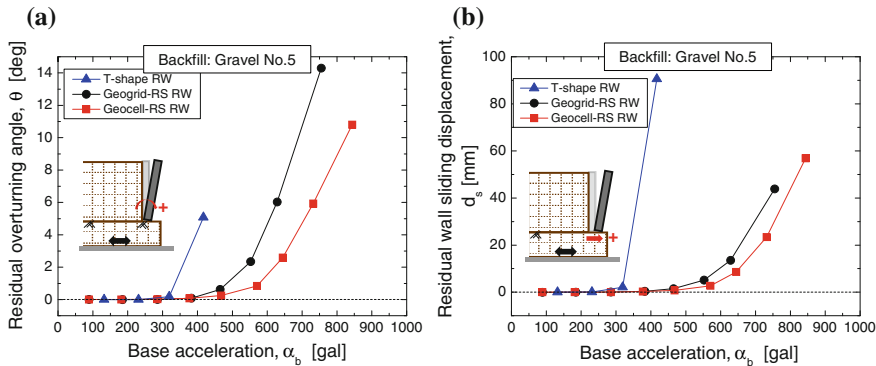


Fig. 6 Relationship between sliding component and overturning component

319 gal no significant difference could be observed. However, under higher base accelerations (i.e., when the base acceleration was larger than 319 gal), the residual wall overturning angle accumulated rapidly with T-shape RW. In contrast, the geogrid-RS RW and geocell-RS RW exhibited more ductile behavior, particularly geocell-RS RW showed smaller residual overturning angle for increasing base acceleration indicating a higher resistance against seismic loading. The overturning of the facing wall of GRS-RW is mainly induced by the shear deformation of the reinforced backfill (Nakajima et al. 2010). As can be seen in Fig. 2e, geocell reinforcement provides a larger pullout resistance than geogrid reinforcement which increases the stability of reinforced backfill, therefore a smaller overturning or more ductile behavior of geocell-RS RW with gravel backfill comparing to geogrid-RS RW.

Figure 6b presents the residual base sliding of facing wall against input base acceleration for three types of RW models. The T-shape RW, geogrid-RS RW, and geocell-RS RW showed very limited sliding displacements and no significant difference could be observed prior to the base acceleration of around 319 gal. Afterwards, the sliding displacement of T-shape RW was larger than that of geogrid-RS RW and geocell-RS RW. The sliding displacement of wall facing mainly depends on the friction between the bottom surface of the wall foundation and the subsoil. The foundation of T-shape RW is roughed by sand paper No. 150 and has size of 39.5 cm by 20 cm. However, the foundation of geogrid-RS RW and geocell-RS RW can be regard as the sum of width of facing wall and the reinforced backfill zone, which have not only a higher friction angle between reinforced soil and subsoil but also a wider interaction area, thereby inducing a lower sliding displacement comparing to T-shape RW. The sliding displacements of geogrid-RS RW and geocell-RS RW were the same each other until a base acceleration value of around 468 gal, after which a larger sliding displacement of geogrid-RS RW occurred. This may be due to the fact that the

sliding displacement of facing wall of GRS RW is mainly induced by the shear deformation of the subsoil beneath the reinforced backfill (Nakajima et al. 2010).

In this study, the subsoil conditions were the same for the two types of GRS RWs resulting in the same sliding displacement before large overturning occurred, after which the bottom layers of reinforcement (i.e., Layer 1 and 2 shown in Fig. 2a) may restrict the sliding of the wall to different extents by different reinforcements, which result in different sliding displacements.

4 Dynamic Behavior as a Damped SDOF System

4.1 A Brief Introduction of SDOF System

From the observation of the dynamic behaviors of the RW in shaking table model tests, three types RW models (T-shape RW, geogrid-RS RW, and geocell-RS RW) were modeled as a damped single-degree-of-freedom (SDOF) following the method developed by Shinoda et al. (2003) and extended by Muñoz et al. (2012). Equation 1 expresses the motion for a damped SDOF system subjected to base acceleration, \ddot{u}_b , measured at the shaking table in this study. The total response acceleration at the mass, \ddot{u}_t , measured at the top of the wall, is the sum of \ddot{u}_b and the acceleration of the mass relative to the base, \ddot{u} , as shown in Eq. 2.

$$m\ddot{u}_t(t) + c\dot{u}_t(t) + ku(t) = 0 \quad (1)$$

$$\ddot{u}_t = \ddot{u}_b + \ddot{u} \quad (2)$$

where m , k , and c are the mass, the stiffness, and the coefficient of viscosity of the system, and t is time. In this study, \ddot{u}_b is the input harmonic sinusoidal, shown in Eq. 3.

$$\ddot{u}_b = -\alpha_b \sin(\omega_b t) \quad (3)$$

where α_b is the amplitude of \ddot{u}_b . \ddot{u}_t is comprised of the transient response, which is controlled by the initial conditions and decays with time, and the steady-state response (Eq. 4), which becomes \ddot{u}_t (Eq. 1) after the transient response dies out.

$$\ddot{u}_t = -\alpha_t \sin(\omega_t t + \varphi) = -\alpha_b M \sin(\omega_b t + \varphi) \quad (4)$$

where α_t is the amplitude of \ddot{u}_t , $M = \alpha_t/\alpha_b$ is the magnification ratio of acceleration and φ is the phase difference.

In this study, the transient response is recognized only at the first cycle and ignored in the analysis shown below. For the steady-state response, the values of M and φ can be obtained as

$$M = \sqrt{\frac{1 + 4\xi^2\beta^2}{(1 - \beta^2)^2 + 4\xi^2\beta^2}} \quad (5)$$

$$\varphi = \arctan\left(\frac{-2\xi\beta^3}{1 - (1 - 4\xi^2)\beta^2}\right) \quad (6)$$

where ξ is the damping ratio of the system, β is the tuning ratio.

The values of M and φ at each cycle are obtained from a single exact sinusoidal wave acceleration recorded at the shaking table and the top of the wall. From these values for M and φ , the values for β and ξ in each cycle are back-calculated. These values for β and ξ represent the transient stiffness and the energy dissipation capacity of the respective wall models, which are the two crucial parameters for analysis of the seismic stability of RWs.

4.2 Dynamic Behaviors of RW Models

Figures 7 and 8 show the dynamic performances of T-shape RW, geogrid-RS RW, and geocell-RS RW backfilled with gravel in terms of M - β relation and φ - β relation. It can be seen that, with each model, the value of β and the value of ξ increased with an increase in the number of shaking cycles and with an increase in input base acceleration. These trends were different among different models.

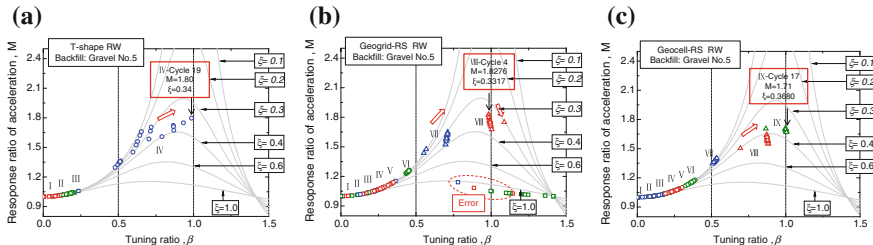


Fig. 7 M - β relations for: a T-shape RW; b geogrid-RS RW; and c geocell-RS RW

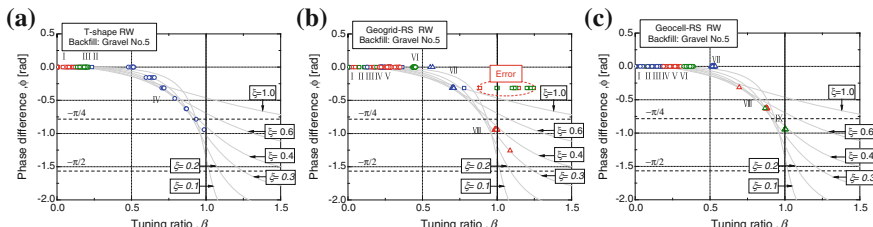


Fig. 8 φ - β relations for: a T-shape RW; b geogrid-RS RW; and c geocell-RS RW

4.3 Comparison of Dynamic Stability of Different RW Models

The dynamic stability of the retaining wall models was evaluated from the following aspects: (1) dynamic strength; (2) dynamic ductility (or softening rate); (3) damping capacity at failure state.

4.3.1 Dynamic Strength

The failure of full-scale retaining wall structures is usually defined as the deformation of the wall (i.e., sliding of the wall or overturning of the wall), settlements or bumps of the backfill, cracking of the concrete walls, etc., which exceed the specified serviceability limit values. In this study, the dynamic strength of a RW model against failure is defined as the value of response acceleration amplitude at the top of the wall, α_t , at resonance state, where the magnification ratio, M , becomes maximum; and the value of β becomes $\beta = \beta_{\text{resonance}}$. At this state, the retaining wall model exhibits significant deformation.

Figure 9a shows the relationship between tuning ratio, β , and response acceleration at the top of the wall, α_t . It is shown that, with an increase of tuning ratio, β , the response acceleration at the top of the wall, α_t , increased and the largest α_t takes place as β approached unity. As can be seen, geocell-RS RW showed almost similar dynamic strength with geogrid-RS RW, but both showed higher dynamic strength than T-shape RW.

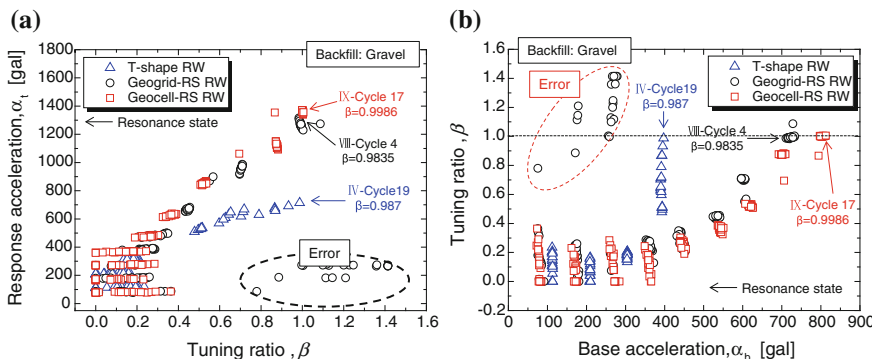


Fig. 9 a Relationship between tuning ratio, β , and response acceleration at the top of the wall, α_t ; b relationship between base acceleration, α_b , and tuning ratio, β

4.3.2 Dynamic Ductility

Tatsuoka et al. (2007, 2012) has demonstrated that a higher dynamic ductility means a lower speed to reach resonance state, at which failure of the structure may occur. Figure 9b shows the relationship between base acceleration, α_b , and tuning ratio, β . Smaller increasing rate of tuning ratio, β , with the input base acceleration level and number of cycles implies a higher dynamic ductility. Therefore, the increasing rates of tuning ratio, β , with the input base acceleration level and number of cycles of geogrid-RS RW and geocell-RS RW were much smaller than that of T-shape RW, indicating that GRS RWs with geogrid and geocell reinforcements have higher dynamic ductility than conventional type RW (i.e., T-shape RW). Furthermore, the increasing rate of β of geocell-RS RW became smaller than that of geogrid-RS RW when the base acceleration, α_b , was larger than around 500 gal. This result indicates that GRS RW with geocell reinforcements can decrease the rate approaching to resonance state, thus increase the dynamic ductility, comparing to that with geogrid reinforcements.

4.3.3 Damping Capacity

As shown in Figs. 7 and 8, at resonance state, the value of damping ratio of geocell-RS RW ($\xi = 0.368$) was relative larger than that of geogrid-RS RW ($\xi = 0.3317$), which resulted in a relative smaller M value for geocell-RS RW ($M = 1.71$) compared with geogrid-RS RW ($M = 1.83$), therefore a slightly higher dynamic capacity of geocell-RS RW. In GRS RW system, the damping ratio, ξ , is controlled by the following factors: (1) the material damping (i.e., facing wall material, backfill soil and subsoil material, and the reinforcement material); (2) the interaction among the components of GRS RW system (i.e., the connection between the wall and reinforcements, the interaction between the reinforcements and backfill soil). In this case, under otherwise the same conditions, factor (2) becomes more significant due to the fact that geocell reinforcement may provide a relative better confinement of larger backfill soil particles, which make a good contact of the wall facing with the backfill soil.

5 Conclusions

The seismic performance of geocell-RS RW backfilled with poorly graded gravels was evaluated by shaking table model tests, as well as geogrid-RS RW, T-shape RW. The geocell-RS RW exhibits the most stable seismic behavior and the conventional type RW (i.e., T-shape RW) shows the least stable seismic behavior among three RW models. The main conclusions can be summarized as follows:

- The predominant failure mode of geocell-RS RW is overturning which is similar with geogrid-RS RW, but the seismic resistance of geocell-RS RW is slightly higher than that of geogrid-RS RW from the evaluation of input base acceleration which induce the failure of the RW. Meanwhile, the predominant failure mode of T-shape RW is sliding.
- From the evaluation of overturning angle of facing wall, geocell-RS RW shows more ductile failure behavior than geogrid-RS RW due to higher pullout resistance of geocell reinforcements compared with geogrid reinforcements when backfilled with gravel. T-shape RW shows brittle failure behavior.
- The dynamic behavior of RW models is analyzed as a damped single-degree-of-freedom system. It is found that geocell-RS RW shows similar dynamic strength, but a slightly higher dynamic ductility and damping capacity than geogrid-RS RW.

References

Han X, Kiyota T, Tatsuoka F (2013) Pullout resistance of geocell placed as reinforcement in gravelly soil backfill. In: Proceedings of the 10th international conference on urban earthquake engineering, Tokyo Institute of Technology, Tokyo, vol 1, pp 533–538

Han X, Kiyota T, Tatsuoka F (2014a) Comparison of pullout behaviors between geogrid and a newly-developed geocell. In: Proceedings of 10th international conference on geosynthetics, Berlin (To appear)

Han X, Kiyota T, Mera T, Katagiri T (2014b) Shaking table model tests on reinforced soil retaining walls by using newly-developed geocell reinforcements and geogrid reinforcements. Bulletin of Earthquake Resistance Structure Research Center, No. 47 (To appear)

Muñoz H, Tatsuoka F, Hirakawa D, Nishikiori H, Soma R, Tateyama M, Watanabe K (2012) Dynamic stability of geosynthetic-reinforced soil integral bridge. *Geosynthetics Int* 19(1): 11–38. doi:[10.1680/gein.2012.19.1.11](https://doi.org/10.1680/gein.2012.19.1.11)

Nakajima S, Koseki J, Watanabe K, Tateyama M (2010) Simplified procedure to evaluate earthquake-induced residual displacement of geosynthetic reinforced soil retaining walls. *Soils Found* 50(5):659–678. doi:[10.3208/sandf.50.659](https://doi.org/10.3208/sandf.50.659)

Shinoda M, Uchimura T, Tatsuoka F (2003) Improving the dynamic performance of preloaded and prestressed mechanically reinforced backfill by using a ratchet connection. *Soils Found* 43(2):33–54

Tatsuoka F, Tateyama M, Mohri Y, Matsushima K (2007) Remedial treatment of soil structures using geosynthetic-reinforcing technology. *Geotext Geomembr* 25(4 & 5):204–220. doi:[10.1016/j.geotexmem.2007.02.002](https://doi.org/10.1016/j.geotexmem.2007.02.002)

Tatsuoka F, Hirakawa D, Nojiri M, Aizawa H, Nishikiori H, Soma R, Tateyama M, Watanabe K (2009) A new type of integral bridge comprising geosynthetic-reinforced soil walls. *Geosynthetics Int* 16(4):301–326. doi:[10.1680/gein.2009.16.4.301](https://doi.org/10.1680/gein.2009.16.4.301)

Tatsuoka F, Tateyama M, Koseki J (2012) GRS structures recently developed and constructed for railways and roads in Japan. In: Proceedings of 2nd international conference on transportation geotechnics (ICTG), Hokkaido, Japan, pp 63–85

Ultimate Lateral Resistance of Piles in Soils Based on Active Pile Length

Mary Roxanne Aglipay, Kazuo Konagai,
Takashi Kiyota and Hiroyuki Kyokawa

Abstract Simulation of the in situ behavior of pile foundation is necessary in the seismic design and assessment of piles for target structural integrity and performance during earthquakes. Having the mere presence of the soil and the pile in this foundation system, the complex behavior of piles is generally captured by the soil-pile interaction. In this research, a simple parameter called the active pile length, L_a , which is reflective of the deformation of pile relative to the stiffness of the soil, is explored to describe the ultimate lateral resistance of the soil. The idea is based upon the deformation of flexible piles commonly used in engineering practice. When piles are induced by a lateral load, the pile deforms significantly in the region near the ground surface and decreases with increasing depth. This region of significant deformation down to the negligible point along the pile depth is defined as the active pile length, L_a . During the event of nonlinear excitation, a soil wedge is formed in the passive region along this active pile length. This soil wedge is indicative of the ultimate side soil resistance, and thus can be inferred to be described by L_a . To simply investigate, a simple plane strain condition using 2-D finite element method in nonlinear analysis is done to obtain the behavior response of a single pile embedded in a homogeneous soft soil. The elasto-plastic behavior of the soil is modeled using the subloading t_{ij} model and the pile is modeled as a 2-D continuum based beam element. Deformation of the pile and corresponding surrounding lateral soil deformation are analyzed. The potential of this simple concept of active pile length to describe the nonlinear response of piles embedded on soft soils is presented for more practical approach in the seismic design and assessment of piles.

Keywords Ultimate lateral resistance • Active length • Soil pile interaction

M.R. Aglipay (✉) · T. Kiyota
Institute of Industrial Science, University of Tokyo, 4-6-1 Komaba,
Meguro-ku, Tokyo 153-8505, Japan
e-mail: aglipay@iis.u-tokyo.ac.jp

K. Konagai
Yokohama National University, Yokohama, Japan

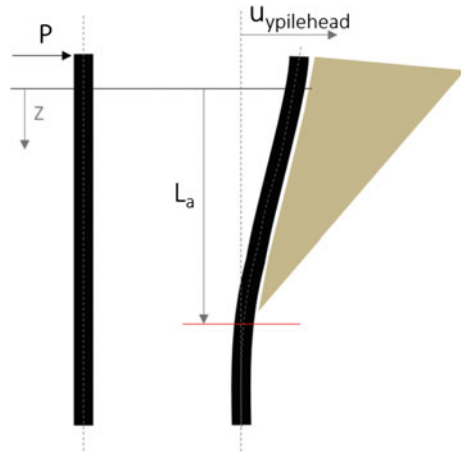
H. Kyokawa
Kajima Corporation, Tokyo, Japan

1 Introduction

Piles are usually used as deep foundations for important structures, or structures supported by soft soils. These piles are most susceptible against external lateral loads like the seismic waves induced by occurrence of earthquakes. In this case, the definition of ultimate lateral resistance of piles is necessary for design and assessment of piles for target structural integrity and performance during earthquakes.

The lateral resistance of piles is governed by the soil-pile interaction, since the piles and the soil are mutually dependent from each other, such that when the pile is induced by a lateral load, it deforms relative to the deformation of its surrounding soil (Konagai et al. 2003). Many researches on soil pile interactions have been done especially in the advent of high computing powers where rigorous solutions can be done for any complex soil-pile configuration. However, it is still warranted especially in the engineering practice that simple yet high caliber solutions can be available. In this study, it is aimed that a simple parameter, active pile length L_a , reflective of the soil-pile interaction, is used to rationally define the side soil resistance. For flexible piles commonly used in engineering practice, the deformation of the vertical beam when induced by a lateral load at its pile head, is observed to be significantly prominent in the region near the ground surface and decreases with increasing depth. Within this region of deformation, the pile can be described as a cantilever beam, assuming fixity at negligible deformation. This region is called the active pile length (see Fig. 1). During a nonlinear event, a soil wedge is pushed up in the passive region along this active pile length. Thus, the ultimate lateral resistance, represented by the soil wedge, is inferred to be described by the simple concept of active pile length.

Fig. 1 Formation of soil wedge along the active pile length, L_a (fixed head)



2 Numerical Modeling

To simply investigate the idea of the nonlinear response of piles against the surrounding soil, the pile-soil system is modeled as 2-D plane strain condition using the finite element method. A single pile is embedded in a homogeneous soil. In this case, the head of the pile is assumed fixed. The subloading t_{ij} model (Nakai et al. 2011) is used to describe the elasto-plastic behavior of soils. The beam is modeled using a continuum-based beam element (Yoon et al. 2012) in elastic case. The pile head is slightly protruding from the ground level for the application of the lateral loading. The lateral load is applied monotonically until the pile head reaches 1 m displacement. A joint element is introduced between the soil and the pile to simulate the slipping of soil against the pile during nonlinearity though separation between the soil and pile is not taken into account. The angle of internal friction used in the pile-soil interface is 25° (Wakai et al. 1999). The bottom ends are fixed in x and y directions, while the sides are fixed at x direction only. Figure 2 shows the soil-pile configuration. The actual length of the pile, L_p , is equal to 10 m and the soils at each side of the pile are dimensioned as 19 m \times 10 m. There are a total of 1660 quadrilateral isoparametric elements for soil, 21 beam elements and 40 joint elements.

The pile and soil parameters used are shown in Tables 1 and 2, respectively. In this study, eight cases were simulated varying the initial void ratio of the soil and the elastic Young's modulus of the pile. The soils were taken into account using initial void ratios of 0.9 and 1.0 for Toyoura sand (TS) and 0.7 and 0.8 for the Fujinomori clay (FC). These material parameters were calibrated from the drained triaxial results (Kyokawa 2011). While the initial void ratios are varied, the Young's moduli were also varied to account the effect of change of pile rigidity. Elastic Young's moduli, E_p , 0.30 and 3.0 GPa, were considered in this study.

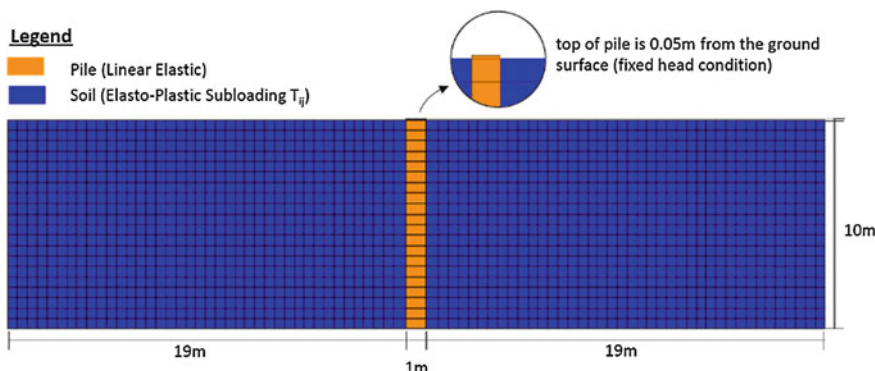


Fig. 2 Soil-pile system

Table 1 Pile parameters

| | |
|--------------------------------------|----------|
| Elastic young's modulus, E_p (GPa) | 0.30/3.0 |
| Width, b (m) | 1.0 |

Table 2 Soil parameters

| Material parameters | | Fujinomori clay (FC) | Toyoura sand (TS) |
|--|-----------|----------------------|-------------------|
| Compression index | λ | 0.104 | 0.070 |
| Swelling index | κ | 0.010 | 0.0045 |
| Stress ratio at critical state | R_{cs} | 3.50 | 3.20 |
| Shape of yield surface | β_s | 1.50 | 2.00 |
| Void ratio at normal consolidation at $P_a = 98$ kPa | e_{NC} | 0.83 | 1.10 |
| Atmospheric pressure (kPa) | P_a | 98 | 98 |
| Controlling decay rate of the influence of density | a | 500 | 33 |
| Poisson ratio | ν | 0.2 | 0.2 |
| Unit weight (kN/m) | γ | 20.2 | 19.5 |
| Initial void ratio | e_o | 0.80/0.70 | 1.0/0.9 |

3 Active Length

The behavior of piles embedded in soil is generally governed by the deformation along its length. For flexible piles, which are commonly used in practice, when the pile head is induced by a lateral loading, the deformation at the upper region along its length is significant and decreases along increasing depth until it reaches a point where it becomes negligible or can be considered as zero bending. Within this region of significant deformation, pile can be described as a cantilever beam, assuming fixity at negligible deformation.

In the engineering practice, the active length used for pile design is derived from Chang's formula (Eq. 1) (Chang 1937). This provides the measure of the stiffness of piles relative to the surrounding soil. Having a unit of m^{-1} , the inverse of this was thought of as characteristic length of the pile, L_o as expressed in Eq. 2 (Van Impe and Reese 2001)

$$\beta = \sqrt{4} \frac{k_h b}{4E_p I_p} \quad (1)$$

$$L_o = \frac{1}{\beta} \quad (2)$$

where k_h is the coefficient of horizontal subgrade soil modulus, b is the pile width and $E_p I_p$ is the pile stiffness.

From Eq. 1, the characteristic length in this case is a function of the coefficient of the horizontal subgrade soil modulus and the width of the pile. However, $k_h b$ is not an inherent characteristic of the soil but rather dependent on the pile geometric properties. Therefore, a more rational definition was proposed by Konagai et al. (2003) to describe the pile deformation in terms of its stiffness with the surrounding soil stiffness given in Eq. 3.

$$L_o = \sqrt{4 \frac{E_p I_p}{\mu}} \quad (3)$$

where μ is soil shear modulus, and $E_p I_p$ is the pile stiffness.

This characteristic length is closely related to the active length by factor α as given by Eq. 4 as generally observed in some formulas proposed by proposed Randolph, Velez, and Gazetas (Konagai et al. 2003; Velez et al. 1983; Randolph 1981; Gazetas and Dobry 1984).

$$L_a = \alpha L_o \quad (4)$$

However, practical classification of soil profiles is necessary to provide α for different soils (Konagai et al. 2003). Nevertheless, there are studies that provide definition of cutoff point for the active pile length to be considered as negligible deformation or zero bending. Velez et al. defined the active pile length, L_a , to be the length until it reaches a point along the pile length where the pile's lateral displacement is 5 % of the pile head displacement. Wang and Liao used 0.3 % of the pile head displacement as the fixity point. In this paper, the point of fixity or zero bending is based on the study of Velez et al. (1983).

The deformation of piles along the soil depth is observed along progressive pile head deformation. Active pile length is derived at lateral pile head displacements: 0.05, 0.1, 0.2, 0.3, 0.4, 0.5, 1.0, and 1.8 m as seen in Fig. 3. The y-axis in Fig. 3 is the soil depth with zero as the bottom of the soil layer. As seen in the case of piles embedded in FC with initial void ratio, $e_0 = 0.7$ with pile elastic Young's moduli

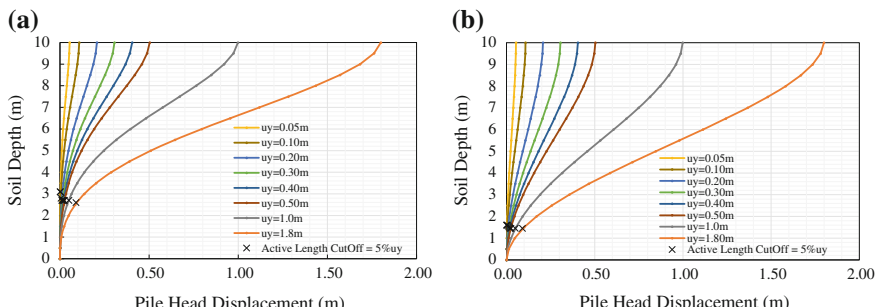


Fig. 3 Pile deformation along the soil depth at different pile head displacements for FC with initial void ratio $e_0 = 0.7$ and **a** $E_p = 0.3$ GPa and **b** $E_p = 3.0$ GPa

(E_p) equal to 0.3 and 3.0 GPa, the active pile length is observed to be longer with piles having higher E_p . It is to be noted that for piles having higher E_p , the active pile length comes closer to the actual pile length, i.e., L_a/L_p is near 1. Thus, the bottom boundary condition may affect the pile deformation such as restricting the pile deformation, consequently restraining the supposed progression of the active pile length. This should be further investigated in the next studies.

Generally, for this case with actual pile length, $L_p = 10$ m, the active pile length seems to be constant despite progressive pile head deformation as seen in Fig. 4. In Fig. 4, considering the piles having $E_p = 0.3$ GPa embedded in FC and TS, it can be observed that at smaller pile head deformations, the active length are generally the same, then it starts to deviate from each other. For piles with small pile stiffness and embedded in the lowest initial void ratio of both type of soils, the active length continues to progress with increasing pile head deformation. The reason for this is that the low pile stiffness gives small resistance against the deformation of their surrounding soil, thus, inevitably follows the deformation of their surrounding soil. With the soil having high initial void ratio, it entails larger deformation capacity. So it can be observed that with looser soil, the longer the active pile length is. For the case of Toyoura sand, while there is a difference in the active pile length for piles embedded in soils with $e_o = 0.9$ and 1.0, the difference is very small. This is due to the soil being too loose and with piles having very low stiffness. Significant difference can be seen by increasing the E_p of flexible piles, reflective of the actual E_p used in engineering practice, shown in the next papers.

Looking closely at the piles with $E_p = 3.0$ GPa, it can be observed that for the same type of soil, there is no difference in the active pile length. This is attributed to the effect of the bottom boundary condition, restraining the supposed active length of the pile, thus a saturation point is reached. In the next studies, this will be discussed together with the other parameters that affect the active pile length.

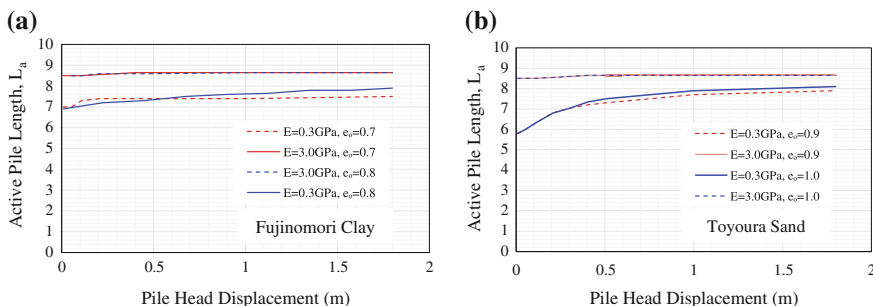


Fig. 4 Active pile length at progressive lateral pile head displacements for the eight cases of piles embedded in **a** FC and **b** TS

4 Soil Displacements Around Laterally Loaded Pile

Based from the numerical simulations, upon application of lateral load to the pile head at a rate of 0.002 m/s, a triangular wedge is progressively formed at the passive region, at the same time an active wedge is moving with the pile. Along with the deformations of the pile, a local bulging around the pile surface appears upon reaching large deformations. In this event, soil in the passive region is being pushed upward with the soil surface not even with the pile head, indicating spillage over the pile in the real scenario (see Figs. 5 and 6).

The load-deformation response is derived at the pile head and the natural responses can be observed for all the cases seen in Fig. 7. In these figures, it can be

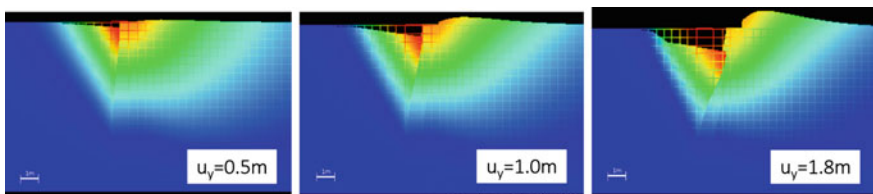


Fig. 5 Progressive deformation around a laterally loaded pile (FC, $E_p = 0.3$ GPa, $e_o = 0.8$, u_y = pile head lateral deformation)

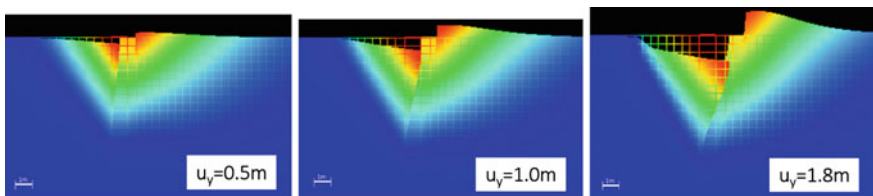


Fig. 6 Progressive deformation around a laterally loaded pile (TS, $E_p = 0.3$ GPa, $e_o = 1.0$, u_y = pile head lateral deformation)

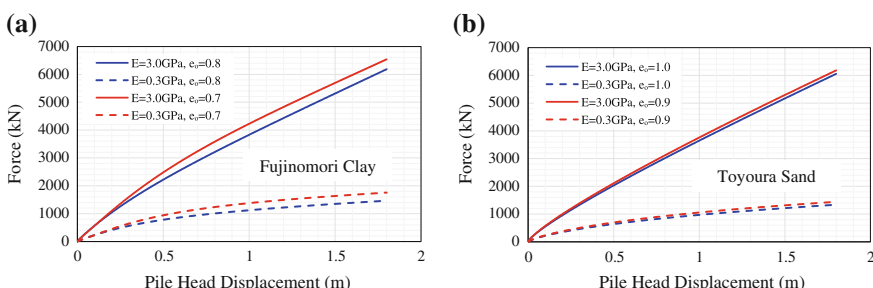


Fig. 7 Lateral force at the pile head with progressive pile head deformation of piles embedded in **a** FC and **b** TS

observed that the lateral load–pile head deflection curves for the same type of soil is only affected by the pile stiffness and not a function of initial void ratio at small deformations around 0.1 m (less than 1 % of the pile width). Beyond such a point, the curves deviate and the following characteristics are generally observed: (1) Having the same pile stiffness, the looser soils have lower response curve than the relatively denser soil, and (2) Having the same type of the soil, the stiffer piles have higher response curve than the piles with lower pile stiffness. The difference of the response curves in the Toyoura sand for piles of different stiffnesses are not significant due to the relatively smaller stiffnesses of piles used embedded in loose sand.

In Fig. 7, as the lateral force at the pile head reaches higher deformations, a straight line starts to appear after the nonlinear region indicating the point of ultimate lateral resistance. This is emphasized in the lateral load–pile head displacement curves for the cases of: (1) FC having $E_p = 0.3$ GPa and $e_o = 0.8$ and (2) TS having $E_p = 0.3$ GPa and $e_o = 1.0$ (see Fig. 8). In this case, the induced displacement is increased to 1.8 m to see clearly the formation of the straight line right after the nonlinear region. This appeared at 1.0 m for piles embedded in FC (Fig. 8a) and 0.7 m for piles embedded in TS (see Fig. 8b).

Given the active length, the pile resistance can be derived assuming a cantilever beam of that length. The side soil reaction is derived from getting the difference between the lateral force–pile head displacement curve and the pile resistance based on active pile length. In Fig. 8, we can observe that the side soil reaction becomes constant despite increasing pile head deformation. This constant value is the ultimate lateral resistance of piles which is derived for all cases. The plateau region of the side soil resistance curve is found to be coincident at the starting point of the appearance of straight line after the nonlinear region of the lateral force–pile head displacement curve. Thus, the active pile length is a key parameter to describe the ultimate lateral resistance of piles.

However, some softening behavior can be observed in the side soil reaction curve. This can be attributed with the soil pushed up at very large deformation. In this condition, the soil surface is not in contact with the pile head. Thus, it loses its

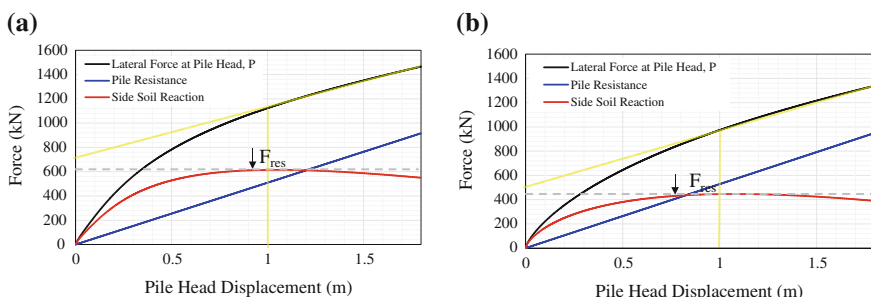


Fig. 8 Lateral force-pile head deformation curves for **a** FC, $e_o = 0.8$, $E = 0.3$ GPa and **b** TS, $e_o = 1.0$, 0.3 GPa

support to the pile interface. These are manifested in Figs. 5 and 6 which show the soil behavior around the laterally loaded pile between piles embedded in Fujinomori Clay and Toyoura Sand. Nevertheless, the peak side soil reaction force is assumed as the point where the side soil reaction becomes constant despite increasing pile head displacement.

5 Conclusion

Within this range of soil properties considered for clay and sand, the lateral force at the pile head is not affected by the initial void ratio but a function of the pile stiffness at smaller deformations, less than 1 % of the pile width. In addition, the active pile lengths are generally the same at smaller deformation for piles having the same stiffness, and starts to deviate from each other as the pile head displacement increases. For piles embedded in the same soil, the active pile length is longer for piles with higher elastic Young's modulus or higher pile stiffness. In view of this, a saturation point may exist for piles with active pile length coming close to the actual pile length because of the restraint given by the bottom of the pile. Parametric analysis on the pile length, pile width, and other factors deemed to affect the active pile length is to be done on the next study.

The use of active pile length to get the pile resistance along the deformed length and derive the side soil reaction from the load-deflection response curve at the pile head is indicative that the active pile length is a key parameter to define the ultimate lateral resistance. In the event of the nonlinear scenario, the wedge is pushed up in the passive region along the deformed region of the pile. This soil wedge can be described by its weight, size, and shape, which could be represented by the unit weight of the soil and the failure plane between the pile and soil using Rankine coefficient of passive earth pressure. Therefore, the active pile length together with these important soil parameters has the potential to evaluate the soil wedge, indicative of the ultimate lateral resistance of piles.

References

Chang YL (1937) Discussion on 'lateral piles loaded tests'. *Feagin Trans ASCE* 1959:272–278

Gazetas G, Dobry R (1984) Horizontal response of piles in layered soils. *J Geotech Eng ASCE* 110 (1):20–40

Konagai K, Yin Y, Murono Y (2003) Single beam analogy for describing soil-pile group interaction. *Soil Dyn Earthq Eng* 23:213–221

Kyokawa H (2011) Elastoplastic constitutive model for saturated and unsaturated soils considering deposited structure and anisotropy. Ph.D. thesis of Nagoya Institute of Technology

Nakai T, Shahin H, Kikumoto M, Kyokawa H, Zhang F, Farias M (2011) A simple and unified three-dimensional model to describe various characteristics of soils. *Soils Found* 51(6): 1149–1168

Randolph MF (1981) Response of flexible piles to lateral loading. *Geotechnique* 315(2):247–259

Van Impe W, Reese L (2001) Single piles and pile groups under lateral loading. Taylor and Francis Group. A.A.Balkema, Rotterdam

Velez A, Gazetas G, Krishnan R (1983) Lateral dynamic response of constrained head piles. *J Geotech Eng ASCE* 109(8):1063–1081

Wakai A, Gose S, Ugai K (1999) 3-D elasto-plastic finite element analyses of pile foundations subjected to lateral loading. *Soils Found* 39(1):97–111

Yoon K, Lee Y, Lee P (2012) A continuum mechanics based 3D beam finite element with warping displacements and its modelling capabilities. *Struct Eng Mech* 43(4):411–443

Effect of Backfill Reinforcement on Retaining Wall Under Dynamic Loading

Babloo Chaudhary, Hemanta Hazarika and A. Murali Krishan

Abstract This paper presents numerical analysis of a reinforced soil retaining wall under static and dynamic loading. Finite difference programme, FLAC, was used to analyze behaviour of the reinforced soil retaining wall. In the analysis, behavior of soil–wall interaction, soil–reinforcement interaction has been considered. Analyses were conducted using different backfill conditions and loading conditions. The lateral displacement and earth pressure were analysed in order to evaluate the effect of reinforcement on the retaining wall. Comparisons were made between unreinforced (conventional) and reinforced soil retaining wall. The results show that length of the reinforcing layer affects earth pressures as well as lateral displacement significantly. Incremental dynamic earth pressure was affected by length of reinforcing layer.

Keywords Retaining wall · Reinforced soil · Seismic earth pressure · Lateral displacement

1 Introduction

Use of reinforced soil retaining wall has been increased tremendously during past few decades. The soil reinforcement, either relatively inextensible metallic or extensible polymeric reinforcement, performed well during earthquake. But few retaining walls were damaged during past earthquakes (Bathurst and Cai 1995). The stability analysis of reinforced soil retaining walls under dynamic loading is very important for the safe performance of these structures in earthquake prone area and has drawn attention of researchers. Accurate prediction of earth pressures and

B. Chaudhary (✉) · H. Hazarika
Kyushu University, W2-1108-2, 744 Motooka, Nishi-ku, Fukuoka 819-0395, Japan
e-mail: babloomit@gmail.com

A.M. Krishan
Indian Institute of Technology Guwahati, Guwahati 781039, India

deformation; these are the essential parameters for the safe design of these structures.

There are various methods to analyse the retaining structures (e.g. Pseudo static method, Pseudo dynamic method, Horizontal slice method, etc.). The Pseudo static method (Bathurst and Cai 1995; Greco 2014; Hazarika 2009; Mononobe and Matsuo 1929; Okabe 1924) is a popular method in which inertia forces acting on soil mass during earthquake is taken into account. Earthquake forces will be considered as equivalent static forces using horizontal and vertical acceleration coefficients. Mononobe and Matsuo (1929) and Okabe (1924) developed a limit equilibrium approach using Coulomb's earth pressure theory. The earthquake forces were considered as equivalent static forces using horizontal and vertical acceleration coefficients. This method is known as Mononobe-Okabe (MO) method. Bathurst and Cai (1995) discussed the seismic stability analysis of geosynthetic reinforced segmental retaining wall. The dynamic earth pressure was derived using MO method for pseudostatic approach. The dynamic earth pressures can be obtained as follows:

$$p_{AE} = C(1 \pm K_V)K_{AE} \cdot \gamma H(1 \pm K_V)K_{AE} = K_A + \Delta K_{dyn} \quad (1)$$

$$\Delta p_{dyn} = p_{AE} - p_A, \quad (2)$$

where p_{AE} = Seismic active earth pressures on the wall, C = Constant, K_V = Vertical seismic coefficient, K_{AE} = Dynamic active earth pressure coefficient, γ = Unit weight of the soil, H = Height of the wall, K_A = Static active earth pressure coefficient, ΔK_{dyn} = Incremental dynamic active earth pressure coefficient, Δp_{dyn} = Incremental dynamic active earth pressure and p_A = Static active earth pressure on the wall.

Hazarika (2009) proposed a new formulation by taking into account of progressive failure of backfill soil as well as shape of failure plane (combination of a curved lower part and a straight upper part). It was observed that the MO method underestimates seismic active earth pressure and overestimates domain of failure zone, especially under intense seismic excitation. Pseudostatic method does not consider time effect and shear and primary wave propagation through body of soil mass. This demerit of the method has been solved in the pseudo-dynamic method (Choudhury and Nimbalkar 2006; Nimbalkar et al. 2006). Choudhury and Nimbalkar (2006) and Nimbalkar et al. (2006) discussed pseudo-dynamic method and analysed retaining wall considering time effect and shear and primary wave propagation through body of soil mass. It was observed that pseudo-dynamic method gives better result than pseudostatic method.

Researchers performed experimental studies to understand behavior of reinforced soil retaining walls including studies of full-scale structures (Kazimierowicz-Frankowska 2005) and reduced-scale models (El-Emam and Bathurst 2007; Krishna and Latha 2007; Krishna and Latha 2009; Wu and Pham 2013). El-Emam and Bathurst (2007) performed a reduced-scale model shaking table tests and show that reinforcement design parameters (i.e. stiffness, length and

vertical spacing) affect the earth pressures and lateral displacement. The earth pressure and lateral displacement decreases with increase in number and length of reinforcing layers. Bilgin and Mansour (2014) discussed effect of reinforcement type on mechanically stabilised soil retaining wall and show that length as well as spacing of the reinforcement affects the performance of reinforced soil retaining wall. Krishna and Latha (2007) suggested that seismic deformation is inversely proportional to initial relative density of backfill. Hazarika (2000) used lightweight deformable geofoam/EPS for soil retaining walls, which was proved effective to reduce earth pressure on the retaining wall.

Numerical analysis of reinforced soil retaining wall is more economical than those from physical model tests. Numerical analyses are much more rigorous than conventional limit equilibrium approach as they satisfy force equilibrium condition, strain compatibility condition and constitutive material laws. Both qualitative and quantitative performances could be obtained from numerical investigations. Rajeev (2012) showed results of an investigation aimed to assess the appropriateness of using the MO method for determining dynamically induced lateral earth pressures on the retaining walls having a granular backfill. Reliability of the results obtained with DIANA was assessed through a comparison with available results of analyses performed using FLAC. Chen et al. (2013) performed a numerical analysis for behaviour of geocell-reinforced retaining structures using FLAC and show that the structure with longer length of geocells performs well in reducing deformation of the structure and decreasing potential slip zone. El-Emam et al. (2004) performed a series of reduced-scale shaking table tests to investigate response of reinforced soil retaining walls for different base accelerations. They performed parametric numerical studies using FLAC to evaluate the effect of base acceleration on the performance of reinforced soil retaining wall.

Since considerable interest has been shown in reinforced soil retaining walls with normal spacing between layers of reinforcement (Bathurst and Cai 1995; Bilgin and Mansour 2014; El-Emam and Bathurst 2007; Krishna and Latha 2007) but there is no sufficient information available for the reinforced soil retaining walls with larger spacing between layers of reinforcement. For better understanding of the reinforced soil retaining walls with larger spacing between reinforced layers, this paper discusses the earth pressures and lateral displacement of reinforced soil retaining walls using FLAC under static and dynamic conditions. Several numerical model tests were performed under different field conditions and different loading conditions. Parametric studies were also carried out to understand the behavior and mechanics of soil wall system.

2 Numerical Modelling

A two-dimensional finite difference numerical model was developed by using FLAC (Itasca 2008). Foundation and backfill soil was modelled using elasto-plastic and Mohr-Coulomb constitutive model. Height of the wall was 5.00 m, width

0.30 m and of unit length in plane strain direction. The retaining wall facing was assumed to be made of concrete and was modelled as linear elastic material. Properties of the material of the wall facing are given in Table 1. The backfill and foundation soil was modelled as a dry, cohesionless and homogeneous material with elastic plastic response and Mohr–Coulomb failure criterion. Properties of backfill soil and foundation soil are shown in Table 2. The soil profile was assumed as homogeneous throughout retaining wall and the water table was assumed to be at a great depth so there was no effect of water table on the model response. The reinforcement was made of strips of phosphorous bronze material and was modelled as cable element with zero compressive strength. The length of the reinforcement is kept same (either 2 m or 4 m) in each reinforced soil retaining wall (cantilever type retaining wall) model. No relative movement was permitted between backfill grid points and reinforcement nodes. The soil-reinforcement interaction was incorporated in the model. At the bottom plane of the model, all movements were restrained. Stability of the retaining wall was checked every time when a new layer was placed. Quiet boundary condition is applied during dynamic motion to avoid wave reflections. A damping ratio of 5 % was taken into account. Dynamic loading was applied in the form of sinusoidal velocity wave (Eq. 3) at the base of foundation soil corresponding to 3 Hz frequency and 0.2 g acceleration amplitude. This wave was acting on the model for the time duration 2.0 s (6 cycles). The equation of velocity wave used for dynamic loading in the analysis is

$$V_x = V_0 \cos(2\pi\eta t) \quad (3)$$

where V_0 = velocity amplitude = 0.01 m/s, V_x = velocity in x direction at time (t), η = frequency, and t = time.

There was a surcharge of 1 kPa at top of the backfill soil as shown in Fig. 1. For verification of the model under static condition, earth pressure on the wall was calculated using classic Rakine's earth pressure theory and it was compared with pressures obtained from the numerical analysis. There was a good agreement between them, which confirms verification of the model under static condition. After attaining the static equilibrium, dynamic loading was applied to the numerical model. For verification of the model under dynamic condition, the dynamic earth pressure was obtained from numerical analysis and analytical analysis. The pseudostatic method (Eq. 1) was used for analytical analysis to obtain the dynamic earth pressure. There was a good agreement between them. The model was verified under both the static and dynamic conditions

3 Results and Discussions

In order to evaluate effect reinforcing layers on performance of the retaining wall, earth pressures on the wall (having three reinforcing layers) for different lengths (0, 2 and 4 m) of layers under static and dynamic conditions were determined and

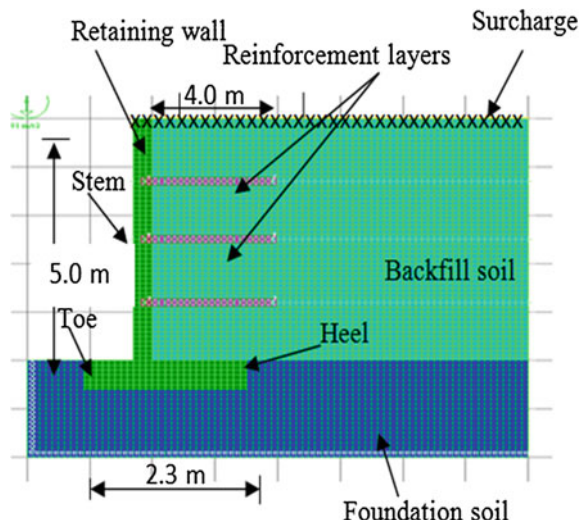
Table 1 Properties of material of the retaining wall facing

| Properties | Values |
|---------------------------|----------------------|
| Young's modulus (E) | 25.00 GPa |
| Shear modulus (G) | 10.87 GPa |
| Density (γ) | 25 kN/m ³ |
| Poisson's ratio (μ) | 0.15 |

Table 2 Properties of the soil

| Properties | Value |
|------------------------------|----------------------|
| Young's modulus (E) | 60.00 MPa |
| Unit weight (γ) | 17 kN/m ³ |
| Poisson's ratio (μ) | 0.33 |
| Angle of friction (ϕ) | 37° |
| Dilatance angle (ψ) | 0° |
| Cohesion (C) | 0 kPa |

Fig. 1 Model of the reinforced soil retaining wall



shown in Fig. 2. The earth pressures were obtained with respect to elevation (from base of retaining wall). It can be seen that static earth pressures are less than dynamic earth pressures. Reinforced soil retaining wall shows less earth pressure compared with unreinforced (conventional) soil retaining wall under static and dynamic conditions. The dynamic and static earth pressures on the reinforced soil wall having reinforcement length 2 m is less than that of conventional retaining wall, but when length of reinforcement was increased to 4 m, both type of pressures (dynamic and static) are reduced much. The earth pressures (static and dynamic) decreases with the increase in length of the reinforcing layers. The lateral

displacement for different lengths (0, 2 and 4 m) of reinforced soil retaining wall (three reinforcing layers) under static and dynamic conditions is shown in Fig. 3. It can be observed that lateral displacement under static condition is less than that in dynamic condition. The reinforced soil retaining wall shows less lateral displacement compared with unreinforced (conventional) soil retaining wall. The lateral displacement decreases with increase in length of the reinforcing layers of the reinforced soil retaining wall. From Figs. 2 and 3 it can be said that change in lateral displacement is almost linear but change in earth pressures is nonlinear.

Incremental dynamic earth pressures can be determined using Eq. (2). The plots are drawn for incremental dynamic pressures with respect to the elevation for one and three layers of reinforcement, which are shown in Figs. 4 and 5 respectively. The comparisons are shown between different lengths of reinforcement (2 and 4 m), no reinforcement and its analytical value in these plots. The incremental dynamic

Fig. 2 Earth pressures reinforced (three layers) soil retaining wall

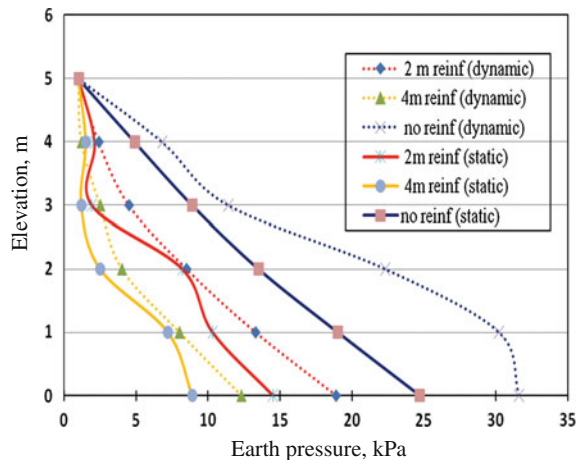


Fig. 3 Lateral displacement reinforced (three layers) soil retaining wall

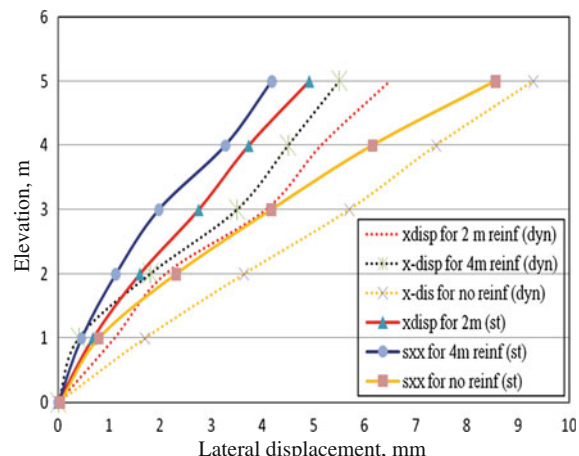


Fig. 4 Incremental dynamic earth pressures on one layer of reinforced soil retaining the wall

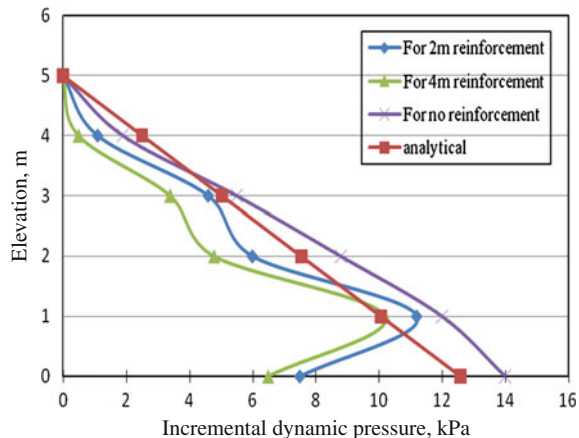
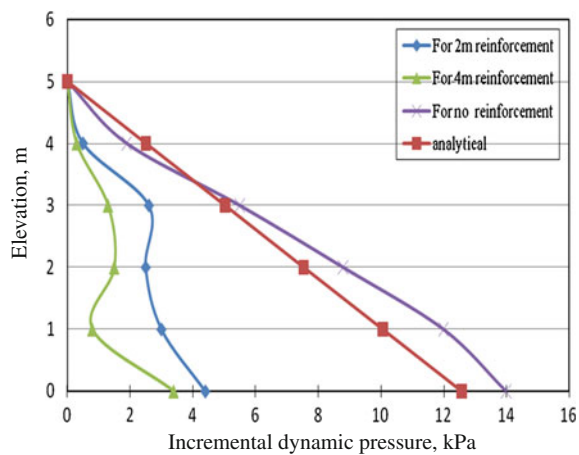


Fig. 5 Incremental dynamic earth pressures on three layers of reinforced soil retaining the wall

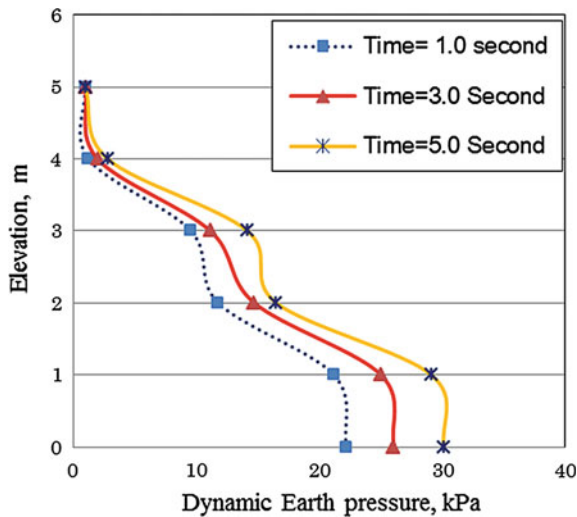


earth pressure for no reinforcement and analytical value is linear but for reinforcement it is nonlinear. The incremental dynamic earth pressure for one layer (length—2 and 4 m) shows more nonlinearity than that of three layers. The incremental dynamic earth pressure for three layers of reinforced retaining wall of the wall is less than that of one layer of reinforcement. It can be noted that incremental dynamic earth pressure decreases with increase in length of the reinforcement layers.

4 Parametric Studies

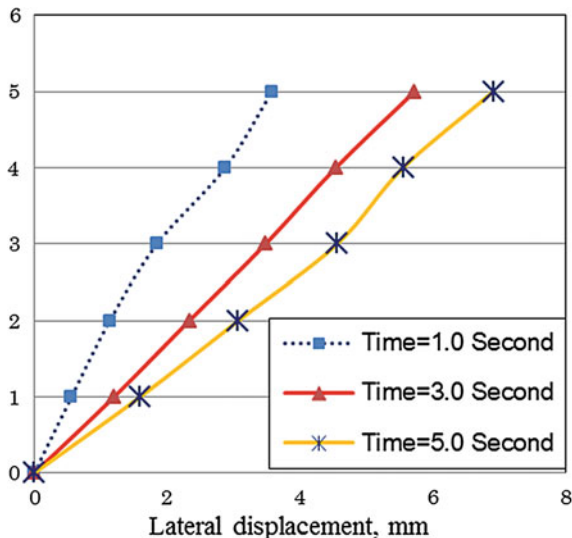
To evaluate the effect of time duration of dynamic loading on the performance of reinforced soil retaining wall, parametric studies were carried out for different time durations (1.0, 3.0 and 5.0 s) of dynamic loading. The reinforced soil retaining wall

Fig. 6 Dynamic earth pressures on the reinforced soil retaining wall for different time intervals



of three layers was used in parametric studies. The length of the each reinforcement was 2 m. The dynamic earth pressures on the reinforced soil retaining wall for different time duration (1.0, 3.0 and 5.0 s) of dynamic loading are shown in Fig. 6. The dynamic earth pressures increases with increase in time duration of dynamic loading. It can be noted that change in dynamic earth pressures is nonlinear. The change in dynamic earth pressures between time duration $t = 1.0$ s and $t = 3.0$ s is and between time duration $t = 3.0$ s and $t = 5.0$ s is same. The lateral displacement of reinforced soil retaining wall for different time duration of dynamic loading is shown in Fig. 7. It can be observed that the lateral displacement increases with

Fig. 7 Lateral displacement of the reinforced soil retaining wall for different time intervals



increase of time duration of the dynamic loading. The change in lateral displacement is almost linear and change in lateral displacement between time duration $t = 1.0$ s and $t = 3.0$ s is more than that of between $t = 3.0$ s and $t = 5.0$ s.

5 Conclusions

The numerical analyses of a reinforced soil retaining wall were performed by finite difference programme, FLAC. The earth pressures and lateral displacement (deformation) were observed under static and dynamic conditions. The comparisons were made between conventional (unreinforced) soil retaining wall and reinforced soil retaining wall. The study shows that the reinforced soil retaining wall performed well in reducing the earth pressure and lateral displacement of wall under static and dynamic conditions. The number of reinforcement layers and its length affects earth pressure as well as lateral displacement significantly under static and dynamic conditions. The earth pressure and lateral displacement of the retaining wall decrease with increase in length of the layers. Incremental dynamic earth pressure reduced significantly using soil reinforcement compared to unreinforced (conventional) soil retaining wall. Incremental dynamic earth pressure decreases with increase in number and length of reinforcing layers.

References

Bathurst RJ, Cai Z (1995) Pseudo-static seismic analysis of geosynthetic reinforced segmental retaining walls. *Geosynthetics Int* 2(5):787–830

Bilgin O, Mansour E (2014) Effect of reinforcement type on the design reinforcement length of mechanically stabilized earth walls. *Eng Struct* 59:663–673

Chen RH, Wu CP, Huang FC, Shen CW (2013) Numerical analysis of geocell reinforced retaining structures. *Geotext Geomembr* 39:51–62

Choudhury D, Nimbalkar SS (2006) Pseudo-dynamic approach of seismic active earth pressure behind retaining wall. *Geotech Geol Eng* 24(5):1103–1113

El-Emam MM, Bathurst RJ (2007) Influence of reinforcement parameters on the seismic response of reduced-scale reinforced soil retaining walls. *Geotext Geomembr* 25(1):33–49

El-Emam, MM, Bathurst, RJ, Hatami K (2004) Numerical modeling of reinforced soil retaining walls subjected to base acceleration. In: 13th world conference on earthquake engineering, Vancouver, BC, Canada, pp 621–635

Greco VR (2014) Analytical solution of seismic pseudo static active thrust acting on fascia retaining walls. *Soil Dyn Earthq Eng* 57:25–36

Hazarika H (2000) Modeling the application of EPS as compressible buffer in soil-structure interaction. In: Proceedings of the 2nd international summer symposium of JSCE, Tokyo, Japan, pp 261–264

Hazarika H (2009) Prediction of seismic active earth pressure using curved failure surface with localized strain. *Am J Eng Appl Sci* 2(3):544–558

Itasca (2008) FLAC—Fast Lagrangian analysis of continua, version 6.0. Itasca Consulting Group, Minneapolis, USA

Kazimierowicz-Frankowska K (2005) A case study of a geosynthetic reinforced wall with wrap-around facing. *Geotext Geomembr* 23(1):107–115

Krishna AM, Latha GM (2007) Seismic response of wrap-faced reinforced soil retaining wall models using shaking table tests. *Geosynthetics Int* 14(6):355–364

Krishna AM, Latha GM (2009) Seismic behaviour of rigid-faced reinforced soil retaining wall models: reinforcement effect. *Geosynthetics Int* 16(5):364–373

Mononobe N, Matsuo H (1929) On the determination of earth pressures during earthquakes. In: *Proceedings of world engineering congress*, vol 9, pp 177–185

Nimbalkar SS, Choudhury D, Mandal JN (2006) Seismic stability of reinforced soil wall by pseudo-dynamic method. *Geosynthetics Int* 13(3):11–119

Okabe S (1924) General theory of earth pressure and seismic stability of retaining wall and dam. *J Jpn Soc Civ Eng* 10(5):1277–1323

Rajeev P (2012) Numerical modeling of seismic response of cantilever earth retaining structures. In: SAITM research symposium on engineering advancements, Malabe, Sri Lank, pp 7–10

Wu JTH, Pham TQ (2013) Load carrying capacity and required reinforcement strength of closely spaced soil-geosynthetic composites. *J Geotech Geoenviron Eng* 139(9):1468–1476

Numerical Study on the Seismic Response of Waterfront Retaining Wall Reinforced with Cushion

Amizatulhani Abdullah, Hemanta Hazarika, Noriyuki Yasufuku
and Ryohei Ishikura

Abstract This paper describes the findings on the effectiveness of waterfront retaining structure reinforced with cushion made of tire chips, which has been analyzed using commercial software, PLAXIS 2D. The numerical model was subjected to the real earthquake recorded during the 1995 Hyogo-ken Nanbu earthquake. The results of the numerical analysis were presented in term of the deformation of the mesh, the displacement of the quay wall horizontally and vertically, and the settlement of the soil behind the quay wall. In general, the utilization of tire chip as a cushion behind a waterfront retaining wall was able to improve the behavior of the wall against an earthquake loading.

Keywords Quay wall · Seismic response · Numerical analysis

1 Introduction

Japan suffered a lot from the series of earthquakes that struck in this country frequently. Earthquakes lead to the destruction not only to the substructures, but to superstructures as well. For instance, The 1995 Hyogo-ken Nanbu earthquake had damaged quite a huge number of waterfront retaining walls. Retaining walls are reported to be settled and tilted in the seaward direction as the result of a very strong earthquake motion while soil liquefaction was also observed in the backfill area (Inagaki et al. 1996). The above-mentioned earthquake was the eye-opener to the researchers to start thinking about how to reduce the severity of the damage of the waterfront retaining structures as a result from an earthquake.

On the other hand, the continuous generation of scrap tires globally seems to be an important issue. In Japan, the volume of scrap tires generated in the year 2013

A. Abdullah (✉) · H. Hazarika · N. Yasufuku · R. Ishikura
Kyushu University, 744 Motooka, Nishi-ku 819-0395, Fukuoka, Japan
e-mail: amihaniabdullah@gmail.com

A. Abdullah
Universiti Malaysia Pahang, Lebuhraya Tun Razak, Gambang, 26300 Kuantan, Pahang,
Malaysia

has been reported to increase by 3 millions of tires from the previous year. Meanwhile, the method of disposing such material also should be concerned. The material, if being dumped conventionally in the landfill, will potentially be a ground for breeding diseases. Moreover, the conventional way of dumping such materials consumed much space. Therefore, recycling of this material is one of the alternative methods of disposal. In Japan, although the scrap tires generation shows an increasing trend, the recycling rate of such waste also shows good signs in order to balance the amount of waste tires generated in each year. The trend of recycling efforts since 2009 until 2013 shows that at least 57 % of the scrap tires were used for thermal recycling while the rest were reused as material recycling and also were exported in the form of either used or cut tires (JATMA 2014). Thermal recycling, however, was harmful to the environment because it releases more carbon dioxide (CO_2) compared to other efforts of recycling. Therefore, in order to encourage the material recycling of scrap tire, which is more environmentally friendly, the utilization of such waste in construction projects seems to be a good approach.

In connection to that, research regarding the utilization of tires in construction projects has gained its popularity for the past few years. Due to its advantageous physical and mechanical characteristics, tire-derived materials either in the form of shredded, chip or crumb has been used as fill material for embankments (Humphrey 2008), as fill material behind retaining walls and abutments (Garcia et al. 2012; Hartman et al. 2013), as base isolation for buildings (Tsang 2008) and as lining in tunnel construction (Kim and Konagai 2001). Also, research on utilizing tire materials as part of the backfill behind the waterfront retaining wall was also conducted and successfully showed significant improvement in reducing horizontal displacement of the wall and seismic earth pressure that acts on the wall (Hazarika et al. 2003, 2006, 2008, 2010, 2012; Hazarika 2007, 2012).

In this study, the numerical analysis of the waterfront retaining wall reinforced with tire chips cushion was presented. The objective of this study is to evaluate the effectiveness of the reinforcement technique which installed as part of the retaining wall backfill, to sustain the impact of an earthquake. Since the experimental testing of this technique has been validated in Hazarika et al. (2003, 2006, 2008), the analysis in this paper was focused to highlight the improvement made by the reinforcement technique from the numerical point of view.

2 Methodology

2.1 *The Geometry*

In this study, a numerical model of waterfront retaining wall (quay wall) was developed using finite element software, PLAXIS 2D. The quay wall was rested on the rubble mound which is underlain by the seabed and the bedrock layer. The quay wall was functioned to retain the soil backfill. Two case studies were considered which the first one consists of only soil material as the backfill (Case 1) while in the

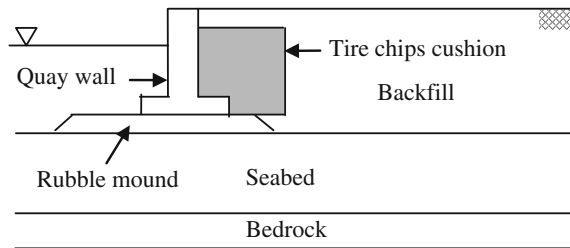


Fig. 1 Reinforced quay wall with tire chips cushion

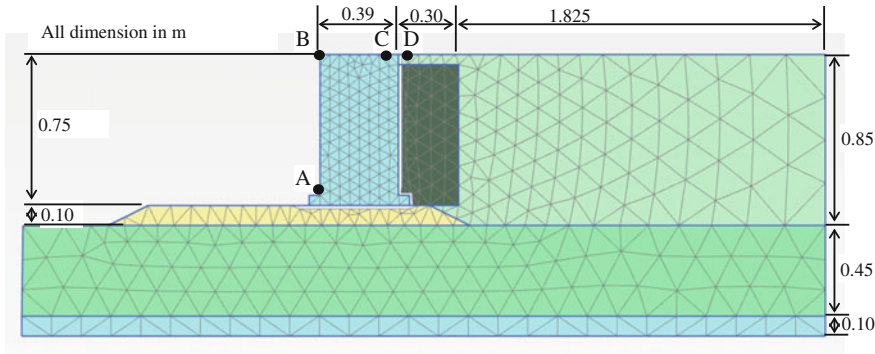


Fig. 2 Finite element mesh generated in the reinforced quay wall

latter case, cushion made of tire chips was installed as part of the backfill (Case 2) as shown in Fig. 1. The finite element mesh for the case of reinforced quay wall, generated from the software is shown in Fig. 2. Full fixities were applied at the bottom of the model to restrain movements in horizontal and vertical direction while on both sides of the model, only horizontal fixities were applied. Several points within the numerical model were selected as can be referred in Fig. 2. They are: Point A (1.50, 0.70), Point B (1.50, 1.40), Point C (1.86, 1.40), and Point D (2.00, 1.40). The dimension of the model was referred from the laboratory model developed in Hazarika et al. (2008).

2.2 Material Models and Parameters

In this study, the concrete quay wall (unit weight of 24 kN/m^3) was modeled using nonporous linear elastic model with the modulus of elasticity, $E = 30 \text{ MPa}$ and Poisson's ratio, $\nu = 0.2$. The bedrock in this study was modeled using nonporous Mohr–Coulomb model while the tire chip material was modeled using linear elastic

Table 1 Summary of material model and material parameters used in the study

| Element | Material model | Parameters |
|--------------------|------------------------------------|--|
| Concrete quay wall | Non porous linear elastic model | $\gamma = 24 \text{ kN/m}^3$, $E = 30 \text{ MPa}$, $\nu = 0.2$ |
| Bedrock | Non porous Mohr–Coulomb model | $\gamma = 21 \text{ kN/m}^3$, $E = 50 \text{ MPa}$, $\nu = 0.35$, $c = 1 \text{ kPa}$, $\phi = 39^\circ$ |
| Tire chips | Linear elastic | $\gamma = 6.6 \text{ kN/m}^3$, $E = 1.6 \text{ MPa}$, $\nu = 0.1$ |
| Rubble mound | Hardening soil model/UBCSAND model | As in Tables 2 and 3 |
| Seabed | Hardening soil model/UBCSAND model | As in Tables 2 and 3 |
| Backfill | Hardening soil model/UBCSAND model | As in Tables 2 and 3 |

Table 2 Material parameters as used in the Hardening Soil model to generate the initial stresses

| Parameters | Rubble mound | Seabed and backfill soil |
|-------------------------------------|-------------------|--------------------------|
| E_{50}^{ref} (kPa) | 36×10^3 | 24×10^3 |
| $E_{\text{oed}}^{\text{ref}}$ (kPa) | 36×10^3 | 24×10^3 |
| $E_{\text{ur}}^{\text{ref}}$ (kPa) | 108×10^3 | 72×10^3 |
| m | 0.51 | 0.58 |
| c_{ref} (kPa) | 1 | 1 |
| ϕ (°) | 35.5 | 33 |
| ψ (°) | 5.5 | 3 |

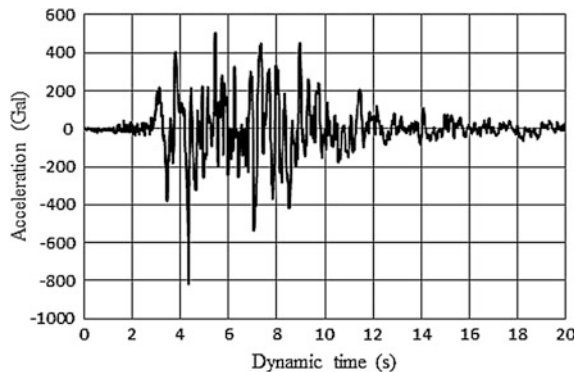
model. The rubble mound was modeled using the hardening soil model. For the soil backfill and the seabed layer, the hardening soil model also has been used during the drained analysis while the UBCSAND model offered in PLAXIS 2D were used to calculate the undrained dynamic response. Table 1 shows the summary of the material model used in the study while all the parameters involved during the drained and undrained analysis was tabulated in Tables 2 and 3 respectively.

2.3 Seismic Motion Input

Seismic motion was inputted to the model using prescribed displacement set at the bottom of the numerical model. The quay wall model was then subjected to the seismic excitation that was recorded in Port Island, Kobe, Japan during the 1995 Hyogo-ken Nanbu earthquake as shown in Fig. 3.

Table 3 Material parameters as used in the UBCSAND model

| Parameters | Rubble mound | Seabed | Backfill soil |
|---|--------------|--------|---------------|
| Unit weight, γ kN/m ³ | 17.95 | 14.73 | 13.6 |
| Elastic shear modulus number, k_G^e | 1176 | 1070 | 934 |
| Elastic bulk modulus number, k_B^e | 823 | 748 | 654 |
| Plastic shear modulus number, k_G^p | 1512 | 820 | 380 |
| Elastic shear modulus index, ne | 0.5 | 0.5 | 0.5 |
| Elastic bulk modulus index, me | 0.5 | 0.5 | 0.5 |
| Plastic shear modulus index, np | 0.5 | 0.5 | 0.5 |
| Peak friction angle, ϕ_p | 36 | 35 | 34 |
| Constant volume friction angle, ϕ_{cv} | 27 | 30 | 33 |
| Failure ratio, R_f | 0.9 | 0.9 | 0.9 |
| Tension cut off, σ_t (kPa) | 0 | 0 | 0 |
| Atmospheric pressure, P_A | 100 | 100 | 100 |
| Densification factor, f_{achard} | 1 | 1 | 1 |
| Corrected SPT value for soil, $(N_1)_{60}$ | — | — | — |
| Post liquefaction factor, fac_{post} | 0.2 | 0.2 | 0.2 |

Fig. 3 Earthquake record of the 1995 Hyogo-ken Nanbu earthquake

3 Results of Numerical Simulation

In this section, the results of numerical simulation were presented by comparing the performance indicators for the case of unreinforced quay wall and the case which the quay wall has been reinforced with cushion made of tire chips. Two indicators were selected and discussed in this paper in order to measure the effectiveness of the technique which are the wall displacement and the backfill subsidence.

3.1 Deformed Mesh

At the end of the seismic time, quay wall in both reinforced and unreinforced cases simulated were found shifted and tilted towards the seaside as shown in Figs. 4 and 5, respectively. The rubble mound in the unreinforced quay wall case has been pushed upward due to the movement of the quay wall. Subsequently, a relatively large amount of deformation also observed in the backfill area. However, in the reinforced quay wall case, improvement can be seen especially in front of the quay wall. The presence of cushion behind the quay wall also improved the deformation of the mesh in the area.

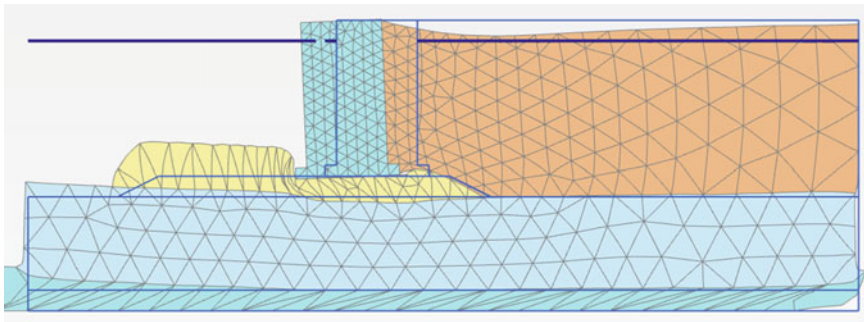


Fig. 4 Deformed mesh of the unreinforced quay wall

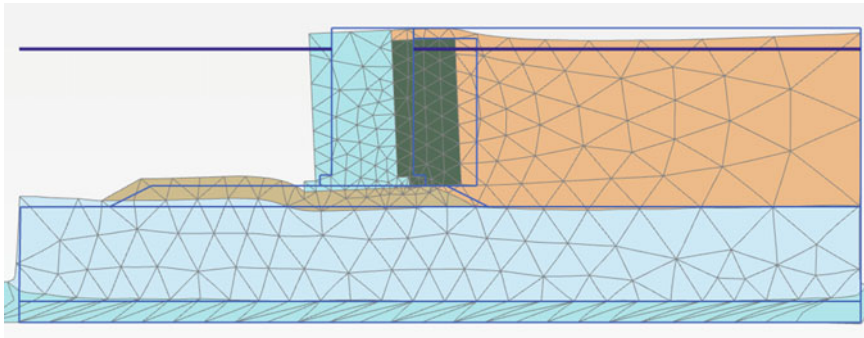


Fig. 5 Deformed mesh of the reinforced quay wall with tire chips cushion

3.2 Wall Displacement (Horizontal and Vertical Direction)

At the end of the simulation time, it was found that the quay wall reinforced with tire chips cushion experienced less displacement in horizontal as compared to the one without the cushion. The horizontal displacement measured throughout the simulated time for Point A and Point B was shown in Figs. 6 and 7 respectively. The displacement of the wall was observed towards the seaward side as shown by the negative sign in both figures. The horizontal displacement at the bottom point (Point A) was always larger compared to point at the top (Point B) in both cases. This indicates that the tiltation of the quay wall was towards the sea. The histories

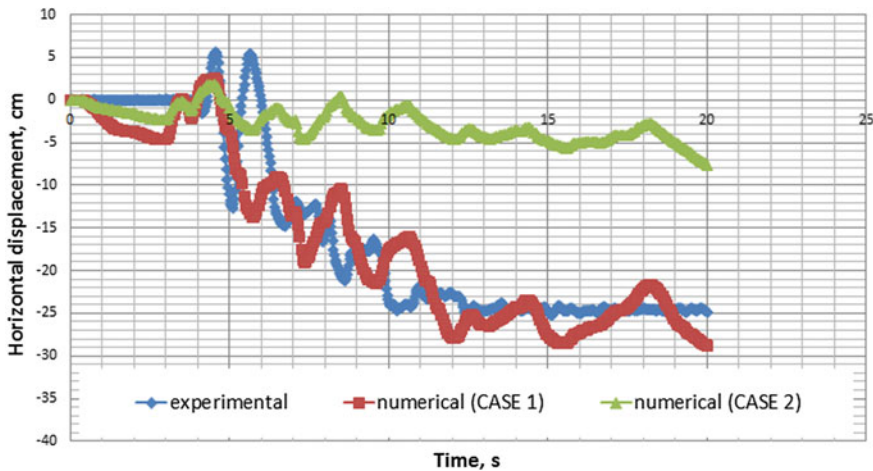


Fig. 6 Horizontal displacements at point A (1.50, 0.70)

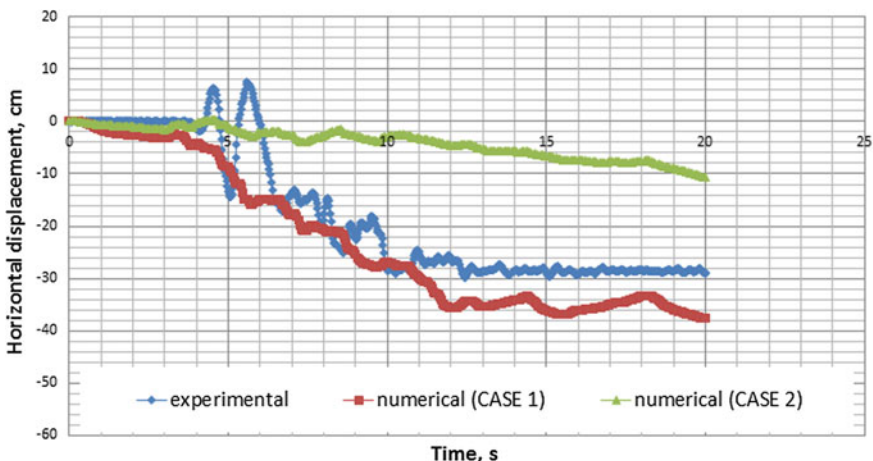


Fig. 7 Horizontal displacements at point B (1.50, 1.40)

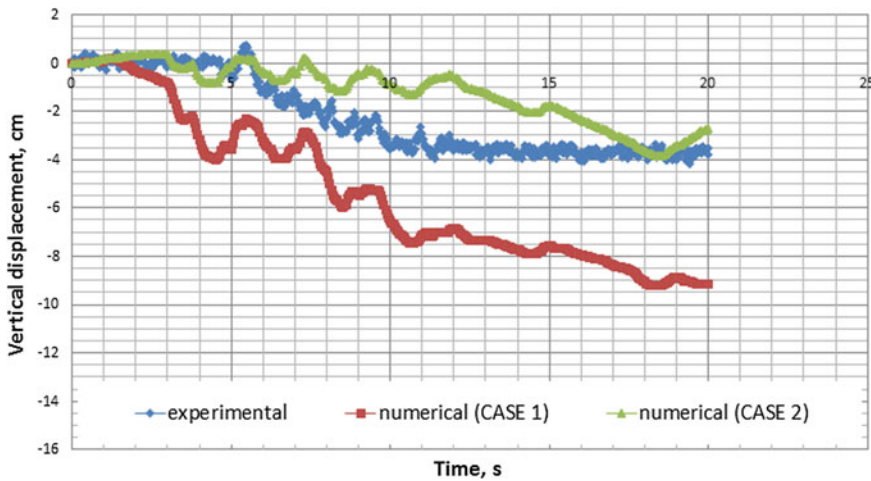


Fig. 8 Vertical displacements at point B (1.50, 1.40)

of horizontal displacement at Point A and Point B in case 1 (unreinforced quay wall) was found similar to those obtained through the laboratory test of conventional quay wall subjected to dynamic shaking as conducted in Hazarika et al. (2008). At the end of the simulation time, the unreinforced quay wall displaced about 29 and 38 cm at Point A and Point B respectively. With the presence of reinforcement made of tire chips, the amount of displacement was able to reduce to about 8 and 11 cm at the bottom and the top of the quay wall.

While for the vertical displacement of the wall, significant amount of settlement's reduction is shown by the unreinforced quay wall case as compared to the unreinforced case as shown in Figs. 8 and 9 respectively. Negative sign of the displacement indicates that the wall moves downward by the end of the simulated time. At the end of the earthquake, the top edge of the left and right of the quay wall experienced vertical displacement of 9 and 4.5 cm for case 1 (unreinforced quay wall). This amount, however, was able to be reduce to 3 and 1 cm respectively, with the installation of cushion made of tire chips behind the quay wall.

3.3 Backfill Subsidence

Figure 10 shows the settlement of backfill of Point D observed throughout the simulated time. Based on the analysis results of backfill, it was found that the amount of the settlement was significantly reduced in the area located near the quay wall. The settlement reduces from approximately 6 cm in the unreinforced case to less than 1 cm in the reinforced case. While for the area located far from the quay wall, the presence of the cushion did not have a significant impact since the amount of the backfill subsidence remains at the same with the one without the cushion.

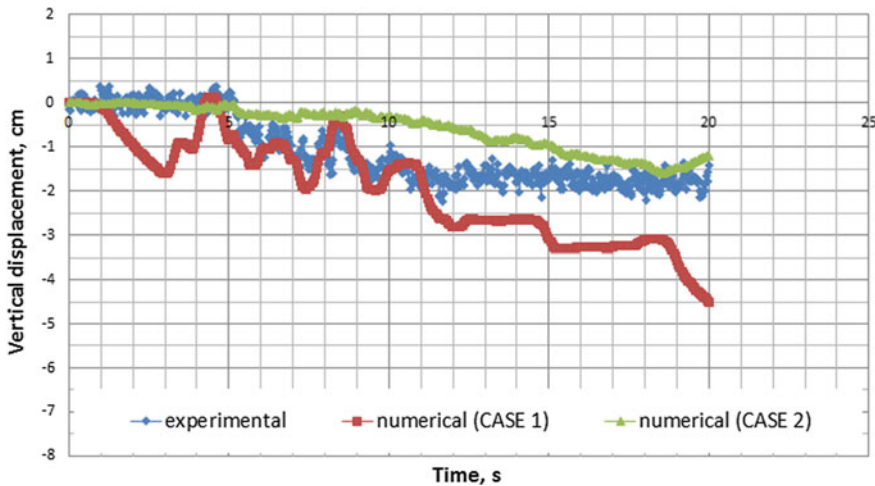


Fig. 9 Vertical displacements at point C (1.86, 1.40)

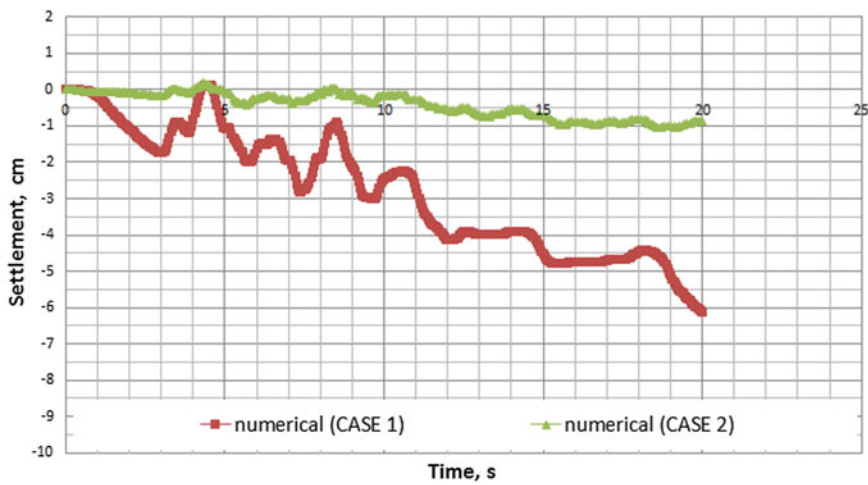


Fig. 10 Backfill subsidence at point D (1.90, 1.40)

4 Conclusions

In this paper, the preliminary study to investigate the effectiveness of the utilization of tire chips as a cushion behind the quay wall was presented. The results of this study reveal the advantages of the tire chips cushion in order to reduce the damage brought by an earthquake from the numerical point of view.

Generally, the quay wall reinforced with tire chips cushion was able to reduce the amount of displacement in both horizontal and vertical direction compared to the unreinforced quay wall. The presence of tire chips cushion also seems to be effective to reduce soil settlement only in the vicinity area of the cushion.

As mentioned beforehand, there are several aspects of this research, for example, the input parameters and analysis method that require some improvements and should be carefully examined so that better output can be obtained. Further study needs to be conducted in order to investigate the effectiveness of the technique in other parameters such as the earth pressure, pore water pressure generation, and ground acceleration. Finally, this study hopes to benefit in order to explain the failure mechanism of a quay wall which subjected to the earthquake forces.

References

Garcia M, Pando MA, Tempest B (2012) Tire derived aggregates as a sustainable recycled material for retaining wall backfills. In: International conference on sustainable design and construction. Missouri, pp 542–552

Hartman D, Ledezma M, Xiao M, Zoghi M (2013) Shake table test of MSE wall with tire derived aggregates (TDA) backfill. *Geo-Congress* 2013:1168–1177

Hazarika H (2007) SAFETY—An earthquake disaster mitigation measure considering cost-performance and environmental impact. In: Fourth international conference on urban earthquake engineering. Tokyo, pp 731–736

Hazarika H (2012) Earthquake resistant reinforcement of coastal structure using recycle material from waste tires. *Exp Mater Future* 12(4):34–41 (in Japanese)

Hazarika H, Okuzono S, Matsuo Y (2003) Seismic stability enhancement of rigid nonyielding structures. In: International offshore and polar engineering conference, pp 697–702

Hazarika H, Sugano T, Kikuchi Y, Yasuhara K, Murakami S, Takeichi H, Karmokar AK, Kishida T, Mitarai Y (2006) Model shaking table test on seismic performance of caisson quay wall reinforced with protective cushion. In: International offshore and polar engineering conference, pp 309–315

Hazarika H, Kohama E, Sugano T (2008) Underwater shake table tests on waterfront structures protected with tire chips cushion. *J Geotech Geoenvironmental Eng* 1706–1719

Hazarika H, Yasuhara K, Kikuchi Y, Karmokar AK, Mitarai Y (2010) Multifaceted potentials of tire-derived three dimensional geosynthetics in geotechnical applications and their evaluation. *J Geotext Geomembr* 28:303–315

Hazarika H, Yasuhara K, Kikuchi Y, Kishida T, Mitarai Y, Sugano T (2012) Novel earthquake resistant reinforcing technique (SAFETY) using recycled tire materials. *Geotech Eng Mag Japan Geotech Soc* 60(9):30–31 (in Japanese)

Humphrey DN (2008) Tire derived aggregate as lightweight fill for embankments and retaining walls. *Scrap Tire Derived Geomaterials Opportunities Challenges* 59–81

Inagaki H, Iai S, Sugahano T, Yamazaki H, Inatomi T (1996) Performance of caisson type quay walls at kobe port. *Spec Issue Soils Found* 119–136 (Japanese Geotechnical Society)

JATMA (2014) Tyre industry of Japan. <http://www.jatma.or.jp/english/media/>

Kim DS, Konagai K (2001) Key parameters governing the performance of soft tunnel coating for seismic isolation. *Earthq Eng Struct Dynam* 30(9):1333–1343

Tsang H (2008) Seismic isolation by rubber-soil mixtures for developing countries. *J Earthq Eng Struct Dyn* 37:283–303

Factors Controlling the Behavior of Piled Foundations Due to Cyclic Lateral Loading

**Mahmoud F. Awad-Allah, Noriyuki Yasufuku
and A.H. Abdel-Rahman**

Abstract The aim of this paper is essentially to investigate the influence of the following factors, namely slenderness of pile, loading frequency, and number of cycles on the behavior of pile foundations of wind turbines under lateral cyclic loading. Thus, an experimental study has been carried out using pile models founded into medium dense sandy soils, and two-way lateral cyclic loading displacement of several frequencies were applied on pile head. Experimental setup was explained in details, and results were presented in the form of cyclic load–displacement curves and normalized bending moment charts against the number of cycles. Besides, initial modulus of subgrade reaction and cyclic p–y curves were estimated. The results provide an insight into the key parameters controlling the performance of pile foundations under pure lateral cyclic loading conditions.

Keywords Cyclic loading · Deformation control test · Frequency · Lateral displacement · Slenderness of pile

1 Introduction

Coastal zones in Egypt enjoy high wind Energy potential. The Red Sea coast particularly at the Gulf of Suez is one of the highest windy areas of the world, with average wind speeds of around 12 m/s. In Egypt, the current objective is to expand in using the wind for generation of energy. Recently, large-scale wind farms at

M.F. Awad-Allah (✉)

Department of Civil Engineering, University of Kyushu, W2-1108-2,
744 Motooka, Nishi-ku, Fukuoka 819-0395, Japan
e-mail: h.mahmoud.099@s.kyushu-u.ac.jp

N. Yasufuku

Department of Civil Engineering, University of Kyushu, Nishi-ku, Japan

A.H. Abdel-Rahman

National Research Center, Cairo, Egypt

Zafarana (200 km south east of Cairo) in cooperation with Japan, Germany, Spain, and Denmark have been constructed. Pile foundations are mainly used to support wind turbines towers, and these types of structures are subjected to environmental dynamic loads (e.g., wind and waves). In some circumstances, lateral cyclic load can be the most critical loading case for a structure.

All cyclic loading sequences are characterized by four parameters, namely (1) the ultimate applied lateral load H_u , (2) the number of cycles N , (3) the frequency f (inverse of time period, $1/t$), and (4) maximum lateral displacement y_{\max} . Two-way cyclic loading can be considered as a simplified representation of dynamic loading without inertia nor damping. However, although alternating loading is symmetrical, the direction of the first loading remains in the pile memory (Rosquoet et al. 2007).

The consideration of cyclic effects when designing piles is generally deduced from the soil-pile interactions under applied static loads using Winkler model. In the case of a linear elastic response of the soil-pile system, the soil reaction $p(z)$, at a depth z , depends on the modulus of subgrade reaction K_h and lateral displacement $y(z)$. Reese and Matlock (Reese and Matlock 1956) suggest that K_h increases proportionally with z and coefficient of subgrade reaction n_h as follows:

$$K_h = n_h z \quad (1)$$

Long and Vanneste (1994) carried out field tests to investigate the factors affecting the cyclic behavior. These included soil density, pile type, installation method and, most importantly, the characteristics of the cyclic load. They proposed a method based on deterioration of static “p–y” curves, which is taken into account by reducing the static soil reaction modulus according to:

$$K_h = N^{-t} n_h z, \quad (2)$$

where N is number of cycles, and t is a degradation factor that depends on the pile installation method, the load characteristics (one or two-way loading), and on the relative density of sand.

Basically, p–y curves represent soil-pile interactions on the assumptions that the soil reaction (p) at all points of the pile is a nonlinear function of the lateral pile displacement. Different methods to determine the p–y curves can be found in the codes of practice such as [e.g., (API 1993; DNV 1977; PHRI 1980)]. However, only the American and Norwegian technical specifications consider existence of the cyclic effects for designing piles subjected to lateral loads by introducing a reduction factor A on the ultimate soil reaction p_u , as given by Eq. 3.

$$p = A p_u \tanh \left(\frac{K_h}{A p_u} y \right), \quad (3)$$

where A is a reduction factor to be considered for both monotonic loading ($A = 0.9$) and cyclic loading ($A = 3 - 0.8zB^{-1}$); and B is pile diameter.

However, although this reduction factor (A) considers that the cycles affect surface layers ($z/B \leq 2.625$), API (1993), DNV (1977) recommendations do not take into account the amplitude of the loading (i.e., neither H nor y), the slenderness of piles, the number of cycles (N), and the loading frequency (f).

From this earlier discussion, it is clear that the literatures and the practice of design of piled foundations subjected to lateral cyclic loading are still approximate, and they have ignored some key design parameters. Accordingly, it is essential to investigate the influence of pile slenderness, cyclic load frequency, and number of cycles on the performance of pile foundations. In order to examine the behavior of piled foundations under lateral cyclic loads, an extensive laboratory testing program has been carried out on a small scale pile model. Furthermore, parametric study has been conducted using the laboratory test results to evaluate the impact of those factors (i.e., L/B , N and f) on lateral pile capacity, bending moment of pile, and cyclic p-y curves.

2 Experimental Setup

2.1 Testing Apparatus

Figure 1 shows the laboratory test setup and the devices which are used for testing during current experimental course. Test facility consists of a testing tank, which has the following dimensions: 30 cm width, 60 cm length, and 60 cm depth, resting on steel foundation, and it is placed inside a loading steel frame constructed to support the loading actions during applying horizontal cyclic loading. Data logger and external control unit are used to record data and control the number of applied

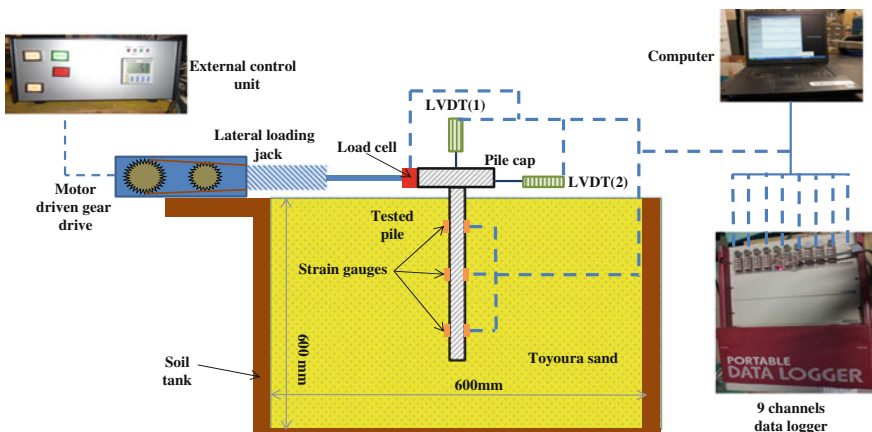


Fig. 1 Schematic of single pile model test setup

cycles during testing, respectively. Lateral cyclic loads are applied on the pile head at different rates (frequencies) by means of servo cylinder.

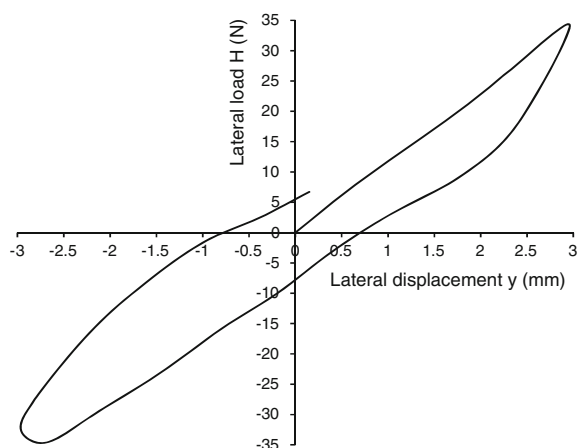
2.2 Loading Mechanism

During this laboratory test program, a symmetrical two-way cyclic lateral load is imposed horizontally on two opposite sides of pile head to provide horizontal displacement of 3 mm at pile as shown in Fig. 2. Input displacement cycle at pile head as follows: pile head is pushed forward laterally by 3 mm, and it is pulled back in opposite direction laterally by 6 mm, then it pushed back by 3 mm (i.e., set back to initial position). Cyclic horizontal displacement is applied for 50 cycles in all experiments. The objectives of conducting deformation control test rather than stress control test are that a wide range of load spectrum can be obtained, and accomplishment of ultimate lateral pile capacity at head displacement of 20 % pile diameter. Figure 3 illustrates sinusoidal harmonic lateral motion applied on pile model head during pile test. Cyclic lateral displacement is applied by frequencies ranging between 0.017 and 0.05 Hz.

2.3 Pile Model and Physical Modeling

Small scale pile models were manufactured from closed-end aluminum alloy 6061 tube of outer diameter of 15 mm and wall thickness of 1.5 mm. The Young's Modulus and yield stress of the used aluminum alloy are 70 GPa and 48.3 MPa,

Fig. 2 Symmetrical two-way lateral displacement and corresponding lateral load



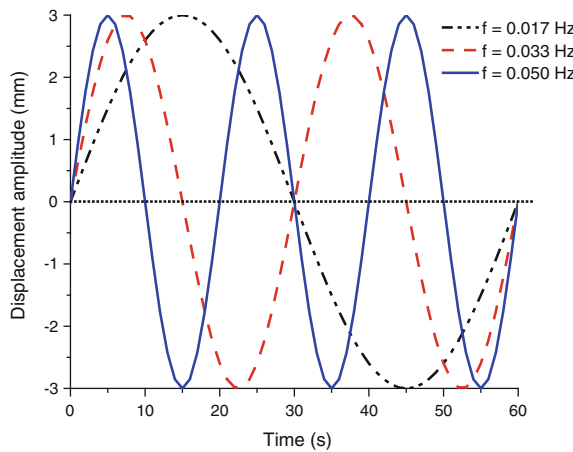


Fig. 3 Typical sinusoidal harmonic lateral motion pattern

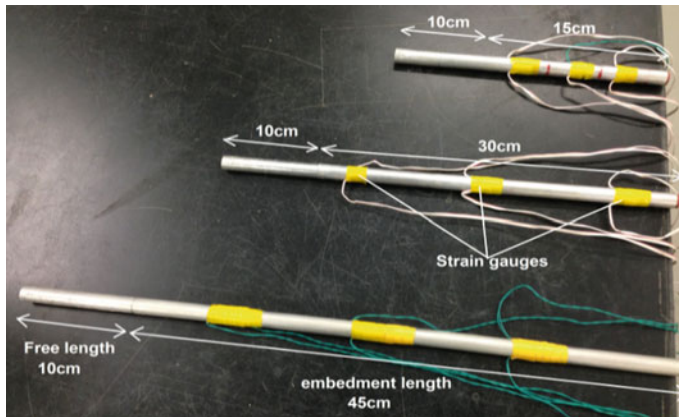


Fig. 4 Three slenderness ratios of aluminum pile models attached with strain gauges

respectively. Furthermore, three slenderness values (L/B) for model pile are selected, including 10, 20, and 30 as shown in Fig. 4. To ensure partial fixation condition between pile head and cap, piles were screwed into the holes provided in the pile cap to a depth of 40 mm. Moreover, to increase the pile wall friction angle, sand was added around the pile by adhesive material. Examples of derivation of scaling laws for general dynamic problems are proposed by Wood et al. (2002). Table 1 shows the relevant parameters for the prototype and the laboratory model.

Table 1 Equivalent values for the characteristics of prototype and experimental model

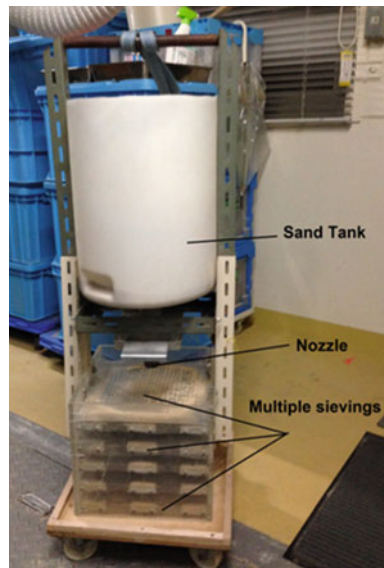
| Parameter | Model | Prototype |
|--|------------------------|-----------------------|
| Young's modulus of soil (E_s) | 10.40 MPa | 29.7 MPa |
| Shear modulus of soil (G) | 0.42 MPa | 1.20 MPa |
| Modulus of elasticity of pile material (E_p) | 70 GPa | 200 GPa |
| Pile embedded length (L) | 0.15, 0.30, and 0.45 m | 6.1, 12.2, and 18.3 m |
| Diameter of pile (B) | 15 mm | 610 mm |
| Load eccentricity (e) | 0.1 m | 4.07 m |
| Thickness of the pile wall (t_w) | 1.5 mm | 20 mm |

2.4 Preparation of Testing Ground (Soil)

Testing soil used in this laboratory work, is sub-angular, fine Toyoura sand, which is commonly used as testing soil in Japan, and its index properties are as follows: specific gravity (G_s) = 2.65; maximum dry density (ρ_{\max}) = 1.6 g/cm³; minimum dry density (ρ_{\min}) = 1.31 g/cm³; maximum void ratio (e_{\max}) = 0.98; minimum void ratio (e_{\min}) = 0.62; uniformity coefficient (U) = 1.4; coefficient of curvature (C) = 0.86; and effective diameter (D_{50}) = 0.18.

In order to conduct model tests in accuracy, testing ground has been prepared using especial compaction tool known as multiple sieving pluviation (MSP) method, which was developed by Miura and Toki (1982). Pluviation, or raining, is a method commonly used to prepare sand samples (Fig. 5).

Fig. 5 Testing soil placement method: multiple sieving pluviation apparatus



3 Test Procedures and Protocol

The following procedures have been adopted for conducting the laboratory tests. Testing tank is cleaned to make sure that it is free from any impurities or debris. Pile model is placed at the center of the testing tank by clamping it against the guide bar to avoid boundary effect; and meanwhile examination of its vertical alignment is performed. Then, sand is poured in carefully, slowly, and evenly layers of 10 cm of thickness using the previously described method Miura and Toki (1982). After reaching to the uppermost layer of sand, the guide beam is removed and the top surface is flattened.

Bending moment, horizontal load, and applied lateral displacement were measured and recorded during test performance.

4 Results and Discussion

4.1 Lateral Load–Displacement Response

A sample of results of cyclic lateral load–displacement tests for single piles of slenderness of (L/B) equal to 30, 20, and 10 are shown in Figs. 6, 7, and 8. From the obtained data, it was observed that pile lateral resistance increases with increasing loading frequency (f) and slenderness of pile. For short rigid pile ($L/B = 10$), it is clear that the lateral pile capacities reached to 21.6 and 16.3 N, at frequency equal to 0.05 and 0.017 Hz, respectively. On the other hand, for medium flexible piles ($L/B = 20$) the lateral pile capacities are 33.1 and 29.9 N, at frequency equal to 0.05 and 0.017 Hz, respectively, and for long flexible piles ($L/B = 30$) lateral pile capacities are 41.7 and 37.4 N, at frequency equal to 0.05 and 0.017 Hz, respectively.

Fig. 6 Hysteretic lateral load–displacement curves for single short piles of slenderness (L/B) equal to 10

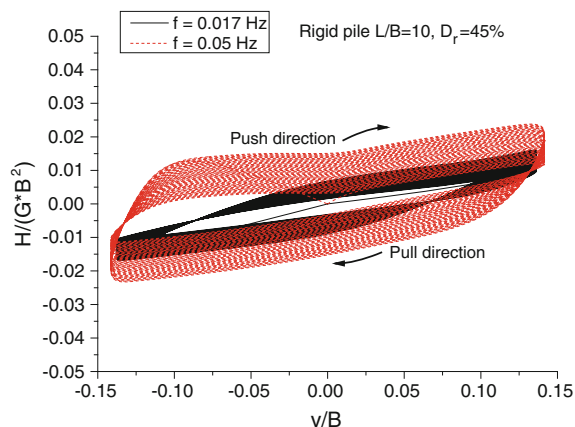


Fig. 7 Hysteretic lateral load–displacement curves for single short piles of slenderness (L/B) equal to 20

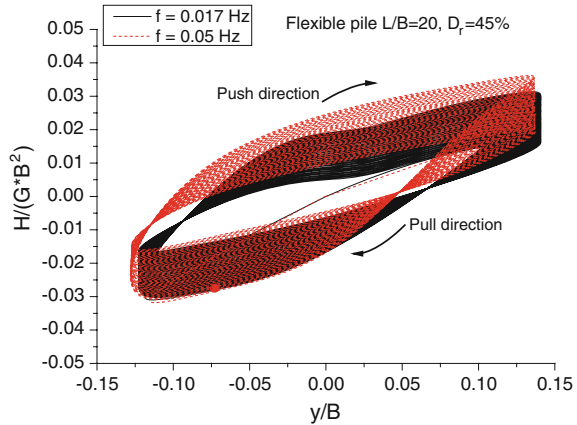
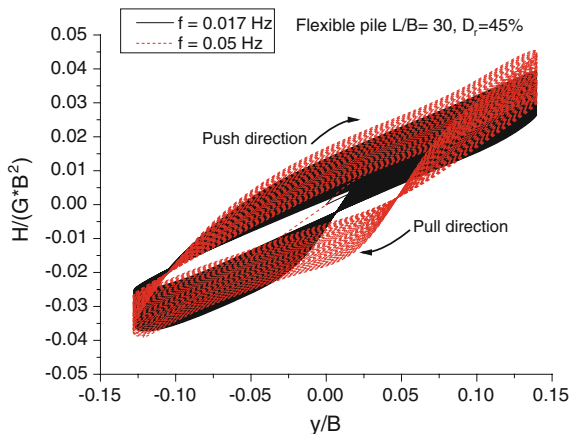


Fig. 8 Hysteretic lateral load–displacement curves for single short piles of slenderness (L/B) equal to 30



Likewise, number of cycles (N) have an impact of lateral pile capacity. Moreover, Fig. 9 depicts the change of maximum measured lateral pile capacity (H_{\max}) with number of cycles at different loading frequency. There is an evidence that pile lateral capacity increases continuously with increasing in number of cycles, which denotes that there is something related to soil-pile interaction has been changed during cyclic loading. The next section deals with this issue in details.

4.2 Secant Modulus of Subgrade Reaction (K_h)_S

To investigate the causes of increasing in lateral resistance of pile due to lateral cyclic loading, secant modulus values were estimated at lateral pile head displacement of 10 % d (i.e., 50 % of strain level) for certain numbers of loading cycles ($N = 0, 10, 30, 50$ cycle) from lateral load–displacement tests, as given in Eq. 4.

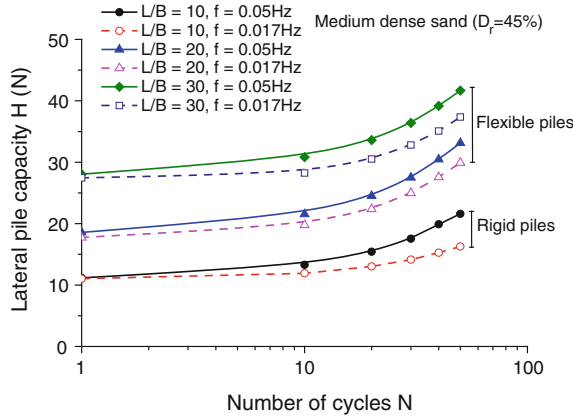


Fig. 9 Change of lateral pile capacity with number of cycles at different frequencies

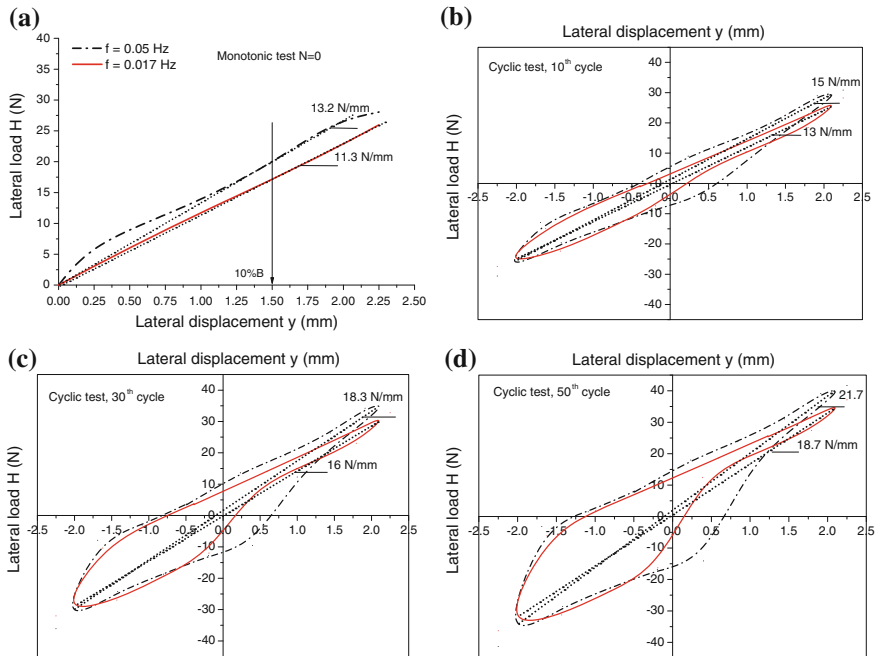


Fig. 10 Lateral load-displacement curves and change of lateral stiffness of pile with number of cycles for long flexible pile $L/B = 30$: **a** monotonic test, and **(b, c, and d)** cyclic test

$$(K_h)_s = \frac{\Delta H}{\Delta y * B} \quad (4)$$

Figure 10 shows the initial lateral stiffness ($\Delta H/\Delta y$) of pile at different loading frequencies (f) and number of cycles (N). Then, $(K_h)_i$ values were estimated by

dividing initial lateral stiffness over pile diameter. From Fig. 10, it can be noticed that, initial loading cycles (monotonic test, $N = 0$) generate the lowest values of $(K_h)_i$ than the succeeding cycles under the same strain level ($y/B = 10\%$). Increasing in $(K_h)_i$ with increase both of period time of loading ($t = 1/f$) and number of cycles (N) is an evidence that pile foundations constructed into dry sand undergo substantially time-dependent performance. This can be attributed to that repetitive occurrence of loading which leads to improvement of sand properties and reduction of void ratio. Moreover, the absence of ground water results in non-generation of pore water pressure in soil due to cyclic loading, subsequently soil particles come closer to each other causing packing of soil.

4.3 Maximum Bending Moment

From an engineering point of view, the maximum bending moment, in most cases, is considered as the key factor in regards of design of laterally loaded pile. Normalized bending moment (M_m/M_y), which is the ratio of measured bending moment to the yielding moment of pile material, was estimated for single and individual piles in group. Bending moment created due to applied lateral displacement is measured and calculated at various locations along the length of the instrumented pile model using Eq. 5.

$$M_m = \frac{E_m I_m \varepsilon}{r}, \quad (5)$$

where E_m = Young's modulus of the pile model material, I_m = moment of inertia of the pile model, ε = measured bending strain, and r = horizontal distance between strain gauge position (outer surface of the pile) and neutral axis.

Yielding moment (M_y) of the pile model is calculated using the following expression (σ_y = yield stress of pile material = 48.3 MPa):

$$M_y = \frac{\sigma_y I_m}{r} \quad (6)$$

Figure 11 illustrates the relationships between normalized bending moments and number of cycles for single piles constructed into medium dense sand ($D_r = 45\%$). Since the relationship (M_m/M_y) and (N) is nonlinear, a semi-log scale has been used. It can be noticed that the larger the value of slenderness ratio (L/B) of pile and the applied number of cycles (N) are, the higher the normalized bending moment (M_m/M_y) is, which means that the L/B and N control the mobilization of maximum bending moment. For short piles ($L/B = 10$), the values of (M_m/M_y) were much little than those values of piles of L/B equal to 20 and 30; a rapid increase in normalized bending moments occurred with increasing L/B over than value of 10, as shown in Fig. 12. This can be attributed to that short pile ($L/B = 10$) does not

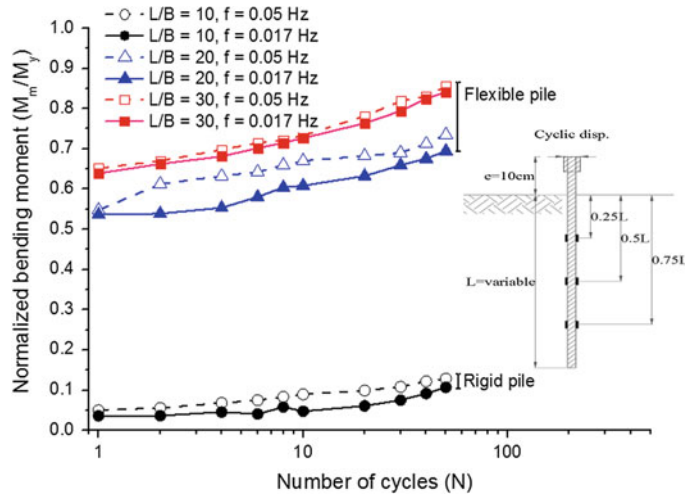


Fig. 11 Normalized bending moment versus number of cycles for single piles in medium dense sand

have enough embedment to anchor the toe against rotation; thus the applied load is controlled primarily by soil stiffness (i.e., soil fails before the pile reaches its flexural capacity). For long pile ($L/B = 20$ and 30), however, the toe is essentially fixed in the soil, and the applied load is controlled by flexural strength of the foundation because it will fail structurally before the soil fails.

4.4 Cyclic p-y Curve

Bending moments along the length of pile at discrete points previously calculated by Eq. 5 were analyzed using curve fitting involving a fifth order polynomial. Pile lateral displacement (y) and soil reaction (p) were determined by double integration (Eq. 7) and double derivation (Eq. 8) of moment curves along the pile shaft, respectively. The boundary conditions adopted to solve the equations are the measured pile head displacement and zero displacement at pile tip.

$$y(z) = \iint \frac{M(z)}{EI} dz^2 \quad (7)$$

$$p(z) = \frac{d^2 M(z)}{dz^2} \quad (8)$$

Figures 13 and 14 demonstrate the normalized cyclic p-y curves at two different soil layers of depths equal to $6B$ and $15B$ measured from ground surface,

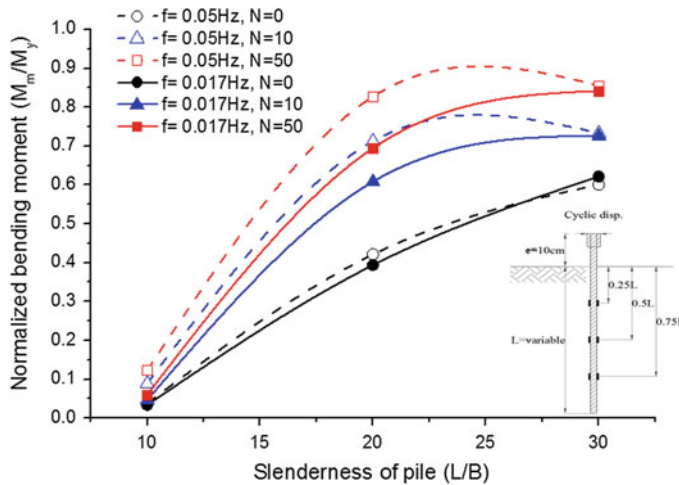


Fig. 12 Effect of length to diameter ratio of pile on the normalized bending moment

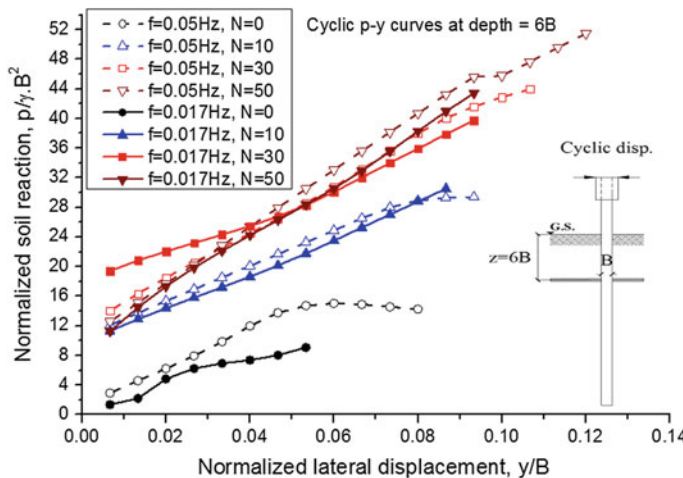


Fig. 13 Cyclic p-y curves at depth $6B$ for piles in medium dense sand ($D_r = 45\%$)

respectively. Figure 13 depicts that, at shallow depths from ground level ($z < 6B$), increasing of the number of cycles causes magnification of p-y curves. On the other hand, Fig. 14 shows that, at deeper depths ($z > 15B$) from ground surface, degradation of p-y curves has been observed due to increase of N .

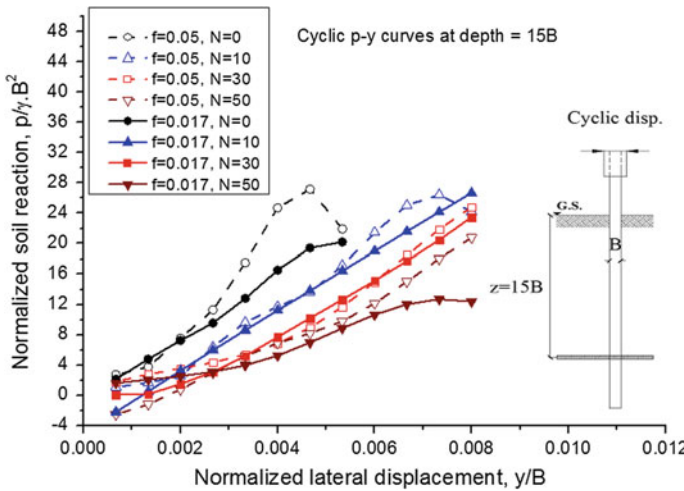


Fig. 14 Cyclic p-y curves at depth of 15B for piles in medium dense sand ($D_r = 45 \%$)

5 Summary and Conclusion

The chief goal of this work is basically to investigate the effect of the following factors on the behavior of piled foundations, namely number of cycles (N), loading frequencies (f), and slenderness of pile (L/d). Parametric study has been carried out to examine the influence of those factors on lateral pile capacity, bending moment of pile, and cyclic p-y curves. Conclusions of this study can be summarized as follows:

1. Single piles constructed into dry sandy soil and subjected to lateral cyclic push-pull loading revealed time-dependent behavior. Accumulated lateral pile capacity and bending moment have been increased with increasing the frequency of loading ($f = 1/t$), number of loading cycles (N), and slenderness of pile due to change of pile lateral stiffness (K_h) with time.
2. For soil layers at depths between 3B and 10B from the ground surface, magnification of cyclic p-y curves has been observed with number of loading cycles. On contrary, in deep layers at depths deeper than 10d from the ground surface, degradation of p-y curves occurs with increasing the numbers of loading cycles. As a result, from geotechnical point of view, the soil properties in those top (i.e. within $z < 10B$) layers govern the cyclic response of piles constructed in sandy soil formations.
3. Cyclic p-y curves do not only depend on soil properties, as given in the current design approach, but also on the number of loading cycles (N), loading frequencies (f), and the depth at which p-y curve is estimated. Accordingly, those factors have to be incorporated in the current design standards.

References

American Petroleum Institute (API) (1993) Designing and constructing fixed offshore platforms, RP2A-LRFD. Session G, Washington, D.C., pp 64–77

Det Norske Veritas (DNV) (1977) Rules for the design construction and inspection of offshore structures. Appendix F, Foundations, 5 p

Long J, Vanneste G (1994) Effects of cyclic lateral loads on piles in sand. *ASCE J Geotech Eng* 120(1):225–243

Miura S, Toki S (1982) A simple preparation method and its effect on static and dynamic deformation-strength properties of sand. *Soils Found* 22(1):61–77

Port and Harbor Research Institute (PHRI) (1980) Technical standards for port and harbor facilities in Japan. Office of ports and harbor, Ministry of Transportation, Japan, 317 p

Reese L, Matlock H (1956) Non-dimensional solution for laterally loaded in sand, Paper No. 2080. In: 6th annual offshore technical conference, vol 2. Houston, Texas

Rosquonet F, Thorel L, Garnier J et al (2007) Lateral cyclic loading of sand-installed piles. *Soils Found* 47(5):821–832

Wood D, Crewe A, Taylor C (2002) Shaking table testing of geotechnical models. *Inter J Phys Modell Geotech* 1:1–13

Centrifugal Model Loading Tests on Reinforced Soil Retaining Wall with Groundwater Permeation

Makoto Kobayashi, Kinya Miura and Takeharu Konami

Abstract The performance of reinforced soil retaining wall is remarkably deteriorated by the permeation of groundwater into the reinforced region through the backfill, not only in ordinary condition but also earthquake condition. In this study, three series of centrifugal loading tests were conducted on the models of multi-anchored reinforced soil retaining wall, and the behavior under the permeation of groundwater was observed. In the first series, the reinforcement and strength of the retaining wall were parametrically changed, in order to qualify the failure condition based on the factor of safety. As a result, in the process of groundwater permeation the stability can be evaluated reasonably by the decrease in safety factor for overall inner stability or integrity of reinforced region. In the second, the efficiency of the drainage equipment on the wall facing was changed in order to show the significance of the drainage in the stability of the retaining wall. In the final, the failure behavior was observed under a heavy rainfall regarding the analogy rule for seepage under centrifugal acceleration field. It was found that drainage equipment, which was placed on the back of wall facing panels, contributes to maintaining reinforcing effects even during permeation of groundwater as well as heavy rainfall. The capacity of the drainage equipment must be approximately designed for the intensity of possible rainfall and/or permeation of groundwater.

Keywords Soil reinforcement • Retaining wall • Centrifugal model test • Raining • Seepage force • Stability

M. Kobayashi (✉)

Toyota National College of Technology, Toyota 471-8525, Japan

e-mail: makotok@toyota-ct.ac.jp

K. Miura

Toyohashi University of Technology, Toyohashi, Japan

T. Konami

Okasan Livic Co. Ltd., Tokyo, Japan

1 Introduction

Soil reinforcement technology is utilized for constructing retaining wall consisted with vertical or steep wall facing, which makes it possible to construct fill embankment economically.

In accordance with the design of conventional soil structures, appropriate drainage facilities are needed to be arranged for preventing groundwater from permeating into backfill and reinforced region of reinforced soil retaining wall and maintaining the reinforcing effects; see Public Works Research Center (2002). Since the aged degradations of the drainage facilities are not yet evitable in current engineering practice, the reinforced soil retaining walls have occasionally failed due to the permeation of groundwater induced by heavy raining. In many of the retaining walls damaged during earthquakes, combined effect of earthquake shaking with groundwater permeation was recognized.

Perceptible effects of appropriate drainage of groundwater from reinforced region have been experimentally investigated, in retaining walls reinforced with geosyntheses or anchors; e.g., Hiro-oka et al. (2001), Hirakawa and Miyata (2010). The effects of rainfall on the stability of fill embankment are divided into two types of raining: short-term intensive rainfall and long-term rainfall. The characteristic formation and expansion of saturation region were observed in the fill embankment in the case of short-term rainfall.

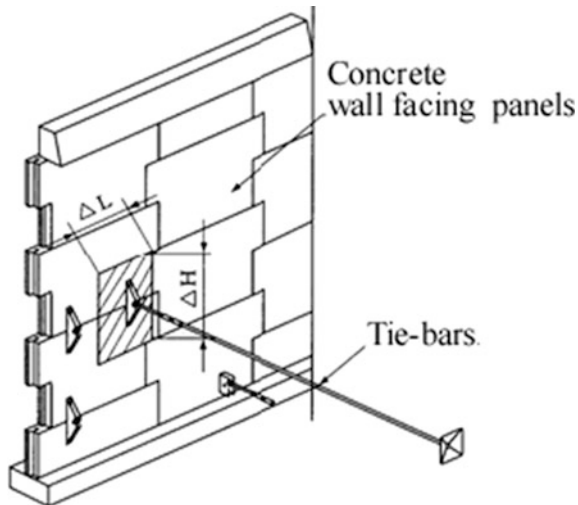
In this study, three series of centrifugal loading tests were conducted on the models of multi-anchored reinforced soil retaining wall, and the behavior under the permeation of groundwater was observed. In the first series, the reinforcement and strength of the retaining wall were parametrically changed, in order to estimate the failure condition based on the factor of safety. In the second, the efficiency of the drainage equipment on the wall facing was changed in order to show the significance of the drainage in the stability of the retaining wall. In the final, the failure behavior was observed under a heavy rainfall regarding the analogy rule for seepage under centrifugal acceleration field (see Butterfield 2000).

2 Reinforcing Mechanism

2.1 *Stability Condition*

Stability of reinforced soil retaining wall was evaluated from two aspects: internal stability and external stability. In the internal stability integrity of reinforced region is examined, and stability of reinforced region against sliding and overturning was examined as a rigid body. The integrity was evaluated on the equilibrium between the earth pressure on a wall facing panel and the pullout resistance of tie bars connected to the wall facing panels as shown in Fig. 1.

Fig. 1 Illustration of Multi-anchored reinforced concrete retaining wall



2.2 Evaluation of Stability

The pullout force T on a single tie bar is calculated as follows:

$$T = (P' \cos \delta + P_w) \times \Delta H \times \Delta L \quad (1)$$

where P' and P_w are effective earth pressure and water pressure, respectively. Pullout resistance of the tie bar is calculated based on the load bearing capacity formula originally proposed by Terzaghi; the formula was modified for square plate through numerical calculation by means of a slip line method under axisymmetrical condition (Miura et al. 1994)

$$\begin{aligned} Q_{pu} &= c \cdot N_c + q_p \cdot N_q - q_p \\ T_a &= (Q_{pu} \times A_p) / F_s \end{aligned} \quad (2)$$

where Q_u is ultimate load bearing capacity, N_c and N_q are bearing capacity coefficients, and q_p is effective confining stress surrounding an anchor plate. A_p is area of an anchor plate, and T_a is acceptable pullout force; factor of safety F_s is 3 under ordinary condition. For the internal stability $T \leq T_a$ is required for each tie bar.

In this study, the factor of safety for overall internal stability was evaluated using the summation for all the tie bars as follows;

$$F_{sa} = \sum T_a / \sum T \quad (3)$$

3 Model Tests

3.1 Soil Materials

Three soil materials were employed: Toyoura Sand (Japanese standard sand), Toyota Sand, and Drain Material. Toyota Sand is graded better than Toyoura Sand, as shown by the particle size accumulation curves in Fig. 2, and the physical properties are shown in Table 1.

3.2 Test Series

Three series of tests were conducted and performance of retaining wall was observed under a common centrifugal acceleration of 50g; therefore, the model scale was 1/50. The permeation of groundwater and deformation-failure behavior of the retaining wall was observed with a CCD-camera mounted on the model container and a monitor on a control room. The conditions for all the tests conducted are listed in Table 2.

3.2.1 TS Test Series

Model retaining walls without drainage equipment were constructed exclusively of Toyoura Sand, whose dry density was 1.49 or 1.56 g/cm³ and relative density was 55 or 75 %. Fundamental deformation behavior and failure condition were discussed comparatively between the four test cases with different backfill densities or anchor plate sizes.

Fig. 2 Grading of sand materials

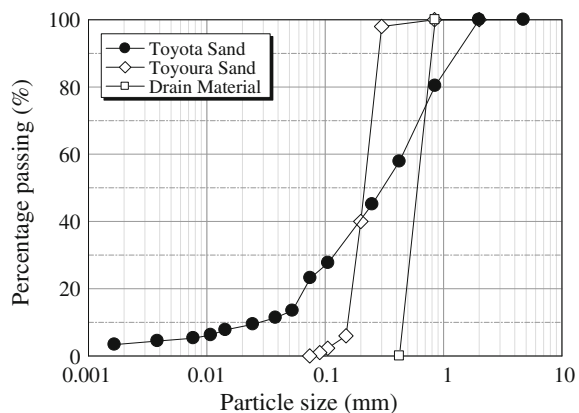


Fig. 3 Model retaining wall for centrifugal loading tests; **a** TS, **b** GS, **c** GR test series

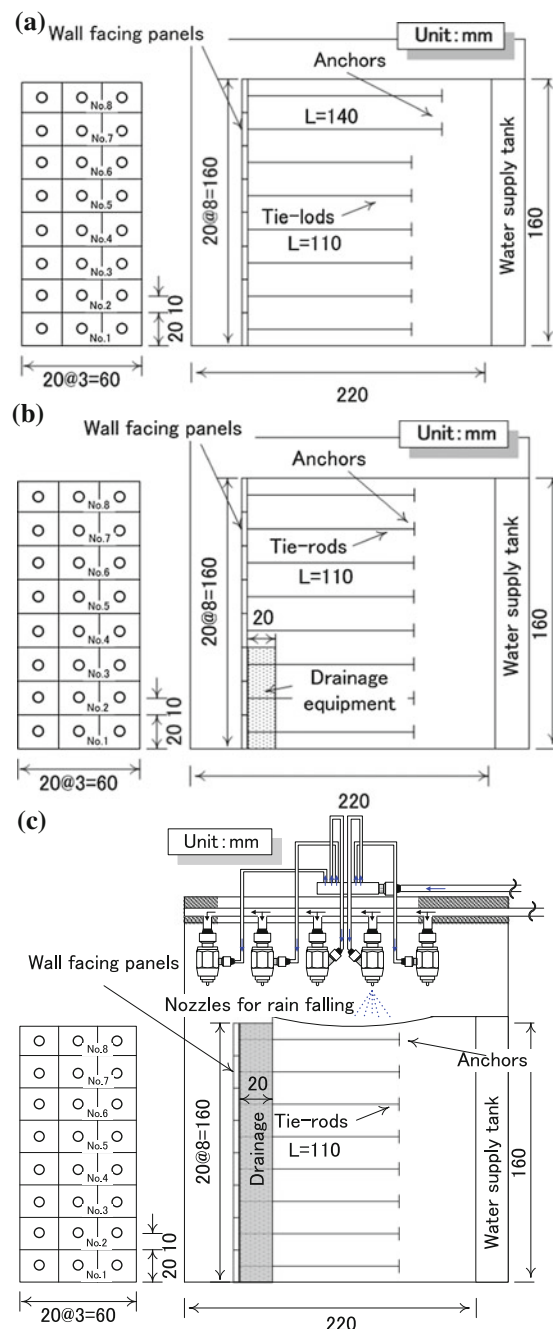


Table 1 Physical properties of Toyota Sand

| | |
|--|------|
| Density of soil particles (g/cm ³) | 2.60 |
| Maximum dry density (g/cm ³) | 1.88 |
| Optimum water content (%) | 12.0 |

Table 2 List of test condition

| Series | No. | Backfill | | Anchor plate (mm) | Drainage equipment | | Rainfall Intensity | Total vol. |
|--------|---------|--------------|----------------------------------|-------------------|--------------------|---------------------|---|------------|
| | | Sand | Dry density (g/cm ³) | | Model | Location, size (cm) | | |
| TS | D75A4 | Toyoura sand | 1.56, Dr = 75 % | 8 × 8 | None | | No rain fall Groundwater table was statically raised | |
| | D75A2 | | | 4 × 4 | | | | |
| | D55A4 | | 1.49, Dr = 55 % | 8 × 8 | | | | |
| | D55A2 | | | 4 × 4 | | | | |
| GS | G16 | Toyota sand | 1.50, Dc = 75 % | 6 × 6 | None | | No rain fall Groundwater table was statically raised | |
| | D4G12 | | | | l-small | Lower 4 | | |
| | D6G10 | | | | l-medium | Lower 6 | | |
| | D8G08 | | | | l-large | Lower 8 | | |
| | D16 | | | | Full | 16 | | |
| | G4D12 | | | | u-small | Upper 12 | | |
| | G6D10 | | | | u-medium | Upper 10 | | |
| GR | G16R100 | Toyota sand | 1.50, Dc = 75 % | 6 × 6 | None | | 100 | 500 |
| | D16R100 | | | | Full | 16 | 100 | 500 |

3.2.2 GS Test Series

Model retaining walls with or without drainage equipment were constructed with Toyota Sand, whose dry density was 1.50 g/cm³ and Degree of compaction was 70 %. The drainage equipment was placed behind the vertical wall facing panels with width of 1 cm; the position and size were parametrically changed as shown in Table 2. The drainage equipment was formed of Drain Sand, whose permeability coefficient was estimated to be 4.4×10^{-2} cm/s. The permeability coefficient of Toyota Sand was 5.0×10^{-4} cm/s. The effects of drainage equipment on the deformation and failure condition were discussed comparatively.

3.2.3 GR Test Series

Two model retaining walls with or without drainage equipment of full height were constructed in the same specification as that of GS test series. Deformation and failure process were observed under the same intensity of rainfall.

3.3 Members for Reinforcement

Model wall facing plate made of acryl resin is 10×10 mm in size and 4 mm in thickness. Model tie bar was made of steel wire ($\phi = 0.45$ mm; assumed deformed bar D22), and model anchor plates made of steel were prepared in different sizes as shown in Table 2; the one used in GS and GR test series is shown as an example in Photo 1.

3.4 Preparation of Model Retaining Walls and Test Schema

Model Retaining walls were prepared in the model container installed on a centrifugal loading apparatus. The formations and dimensions of the model retaining walls for each of the test series are shown in Fig. 3.

3.4.1 TS Test Series

Dried Toyoura Sand was pluviated to form each layer of 20 mm in thickness and tie bars and anchor plates were laid. Black lattice lines were drawn with black-colored sand on a side wall to visualize deformation behavior, see Photo 3. Water supply tank was placed on the back of the model retaining walls; a sheet of fine mesh was placed on the interface. The water level in the tank was controlled by supplying pure water through a swivel joint during the loading tests; the rate of water level rising was 4 cm/min.

3.4.2 GS and GR Test Series

Wet Toyota Sand with water content of 10 % was placed and compacted, to form each of the layers and tie bars and anchor plates were laid (Photo 2). White grid lines were drawn with kaolin powder. The drainage equipment was formed with dried Drain Material behind the wall facing panels. In GS test series water level of

Photo 1 Reinforcing member; tie rod and anchor plate

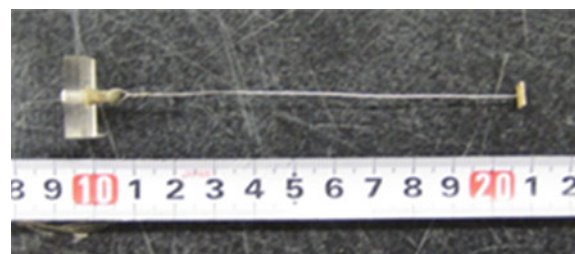


Photo 2 Overview of model retaining wall under construction

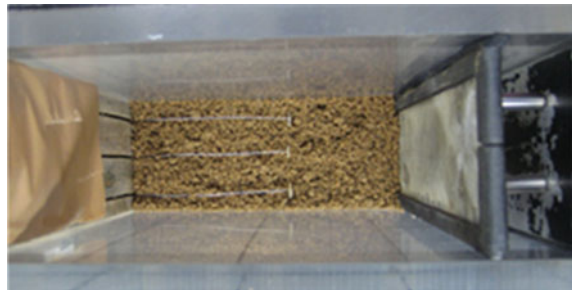
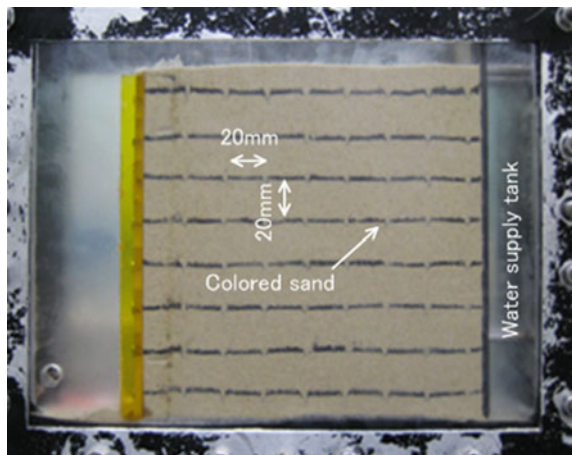


Photo 3 Side view of model retaining wall in TS test series



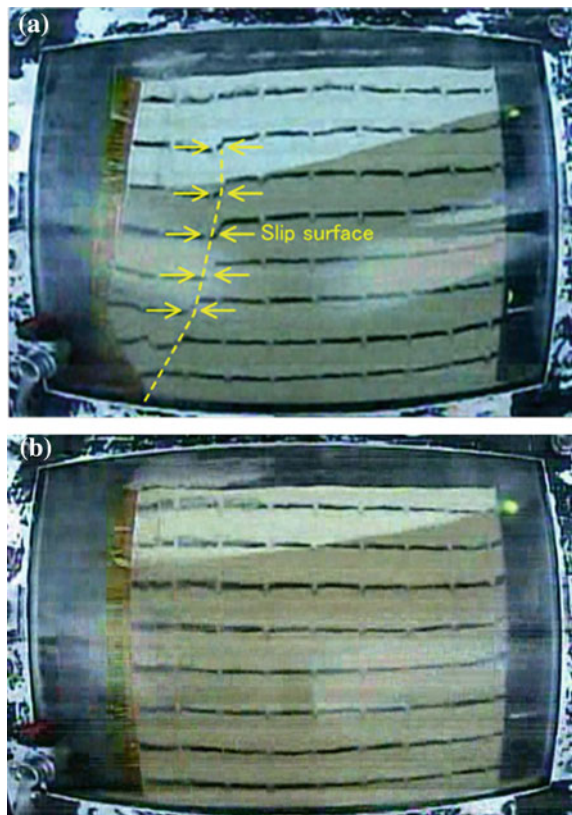
the water supply tank was controlled in the similar manner of TS test series; the rate of water level rising was 2 cm/min. In the case of GR test series only, the rain falling device comprised with water/air supplies and nozzles was mounted on the top of the model container. Instead of pure water a kind of cellulose solution was employed, whose viscous coefficient was 50 times higher than that of pure water to meet the modeling analogy rule.

4 Test Results and Discussion

4.1 Effect of Groundwater Permeation: TS Test Series

Model retaining walls without drainage equipment, which are different in relative density and anchor panel size, were subjected to groundwater permeation, and deformation behavior was observed to clarify fundamental deformation and failure characteristics.

Photo 4 Deformation of model retaining walls observed in TS test series; **a** D55A2, **b** D55A4



Deformed retaining walls at the final stage of loading tests of TS test series are shown in Photo 4; a sliding plane appeared clearly in D55A2 but not in D55A4. Total failure was observed only in the test cases D55A2 and D75A2 with smaller anchor plates. The lateral displacement of wall facing was less than a few percent in the test cases D55A4 and D75A4 with larger anchor plates.

Figure 4 shows the overall factor of safety F_s descending with an increase in groundwater level, where the factor of safety was calculated from the groundwater level at the installed anchor plates. In the test condition of TS test series, the anchor plate size has dominant effect compared with the relative density of retaining wall. Shown in Fig. 5 is the subsidence at the top of wall facing observed in the two test cases D55A2 and D75A2 with an increase in groundwater level; the sudden increase in the subsidence corresponded to the factor of safety becoming lower than unity; see Fig. 4.

Although factor of safety of individual tie rod was minimum at the bottom in the retaining wall subjected to groundwater permeation, the lateral displacement of wall facing was maximum at the level of bottom third tie rod due to the lateral resistance to wall facing from the foundation ground or soil container bottom.

Fig. 4 Reduction in factor of safety with an increase of groundwater level in TS test series

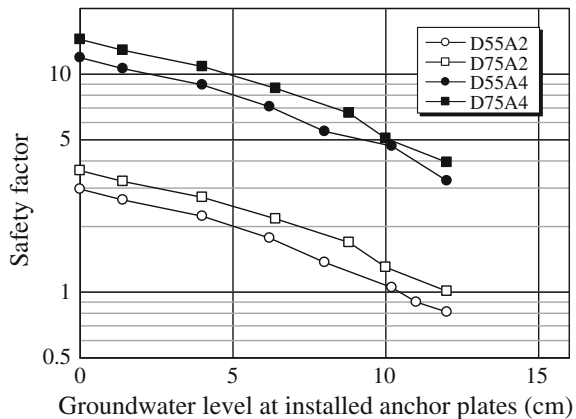
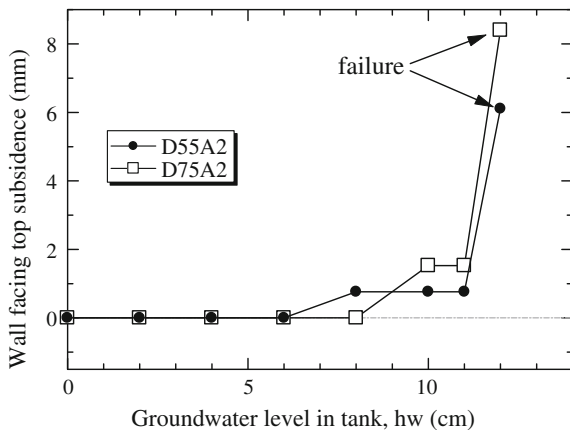


Fig. 5 Subsidence at the top of wall facing observed in TS test series



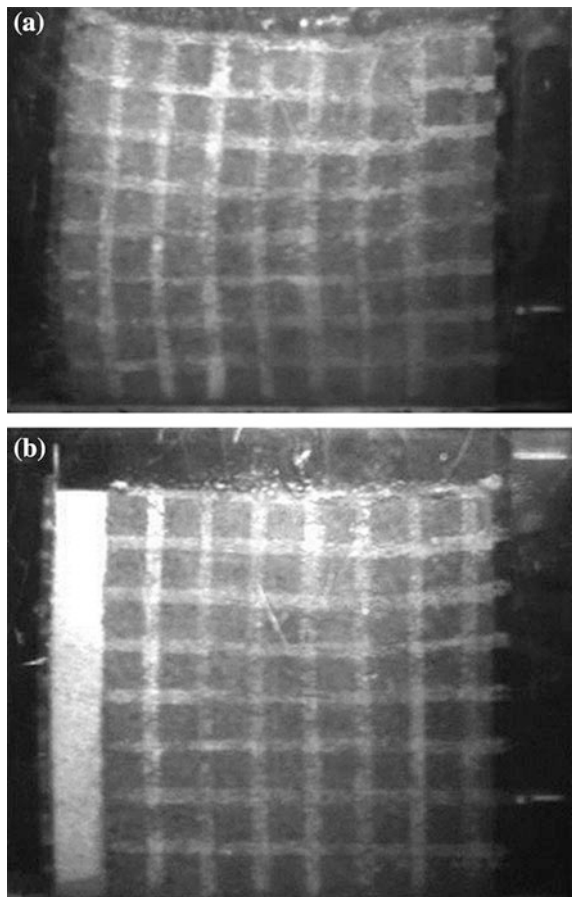
4.2 Effect of Drainage Equipment; GS Test Series

Model retaining walls with different drainage equipment in size and level were subjected to groundwater permeation, and deformation behavior was observed to examine the effects of the drainage equipment.

Shown in Photo 5 are deformed retaining walls at the final stage of loading tests of GS test series: G16 and D16 (with/without drainage equipment). Perceptive lateral displacement of wall facing and subsidence of top surface were observed in G16 (without drainage equipment) but not in D16. Even in G16, however, clear sliding plane was not recognized.

The above-mentioned contrast of the deformation behaviors shows simply the effect of drainage equipment. As shown in Photo 5, although the level of groundwater table was not so different at the position of anchor plates in both test cases D16 and G16, inside the drainage equipment the groundwater table level is

Photo 5 Deformation of model retaining walls observed in GS test series; **a** G16, **b** D16



lowered to less than 1 cm from bottom in D16. Thus, it seems that the degree of reduction in pullout resistance of anchor plate was not so different in spite of the drainage equipment, because the reduction is induced by the pore water pressure as a function of groundwater table level on the anchor plates. On the other hand, the pullout force on tie rod which is induced by earth pressure on wall facing panels would increase more in G16 than in D16 as a function of pore water pressure near the wall facing. Although it is primarily important to prevent groundwater from permeating into a reinforced region through a back fill body, drainage equipment placed behind wall facing panels even has effects on the suppression of deformation of retaining walls. Figure 6 shows the maximum lateral displacement of wall facing observed at middle of wall induced by groundwater permeation, for retaining walls with different drainage equipments in size and placement level. The behavior shows that the lower part of the drainage equipment is more important than the upper part; the maximum lateral displacement was smaller in D6G10 where drainage

Fig. 6 Maximum lateral displacement of wall facing observed in GS test series

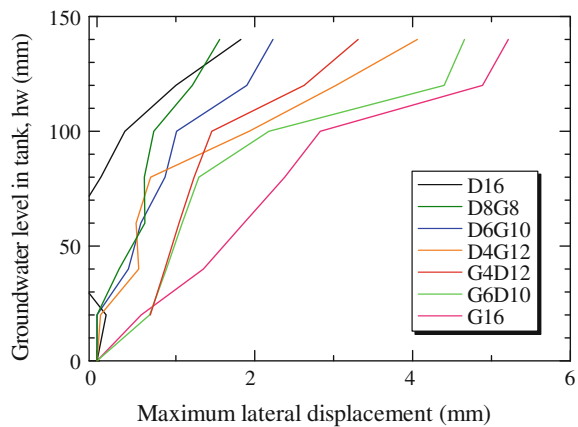
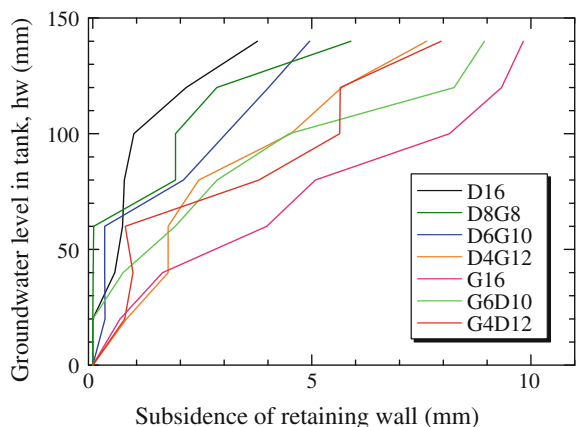


Fig. 7 Subsidence on the top of retaining wall-installed anchor plates



equipment was placed on lower part, than that in G6D10 where it was placed on upper part. Shown in Fig. 7 is the subsidence on the top of retaining wall installed anchor plates; the effects of drainage equipment are found also in this figure. As shown in Fig. 8, a linear relationship can be seen between the maximum lateral displacement and the subsidence in all the test cases conducted in GS test series.

4.3 Effect of Heavy Rainfall: GR Test Series

Model retaining walls with and without drainage equipment were subjected to heavy rainfall. Deformation behavior was observed and wet condition in the retaining walls was evaluated to examine the effects of the drainage equipment. The deformed retaining wall without drainage equipment in G16R100 is shown in Photo 6; the rainfall was equivalent to 100 mm/h in intensity for 5 h in prototype condition. The

Fig. 8 Relationships between lateral displacement of wall facing and subsidence on wall facing top in GS test series

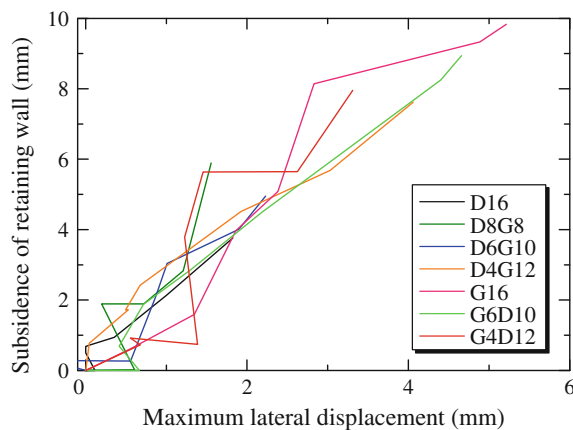
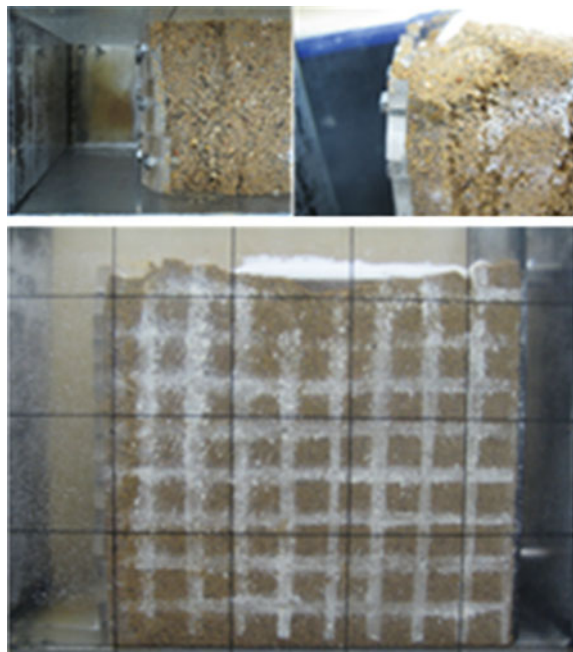
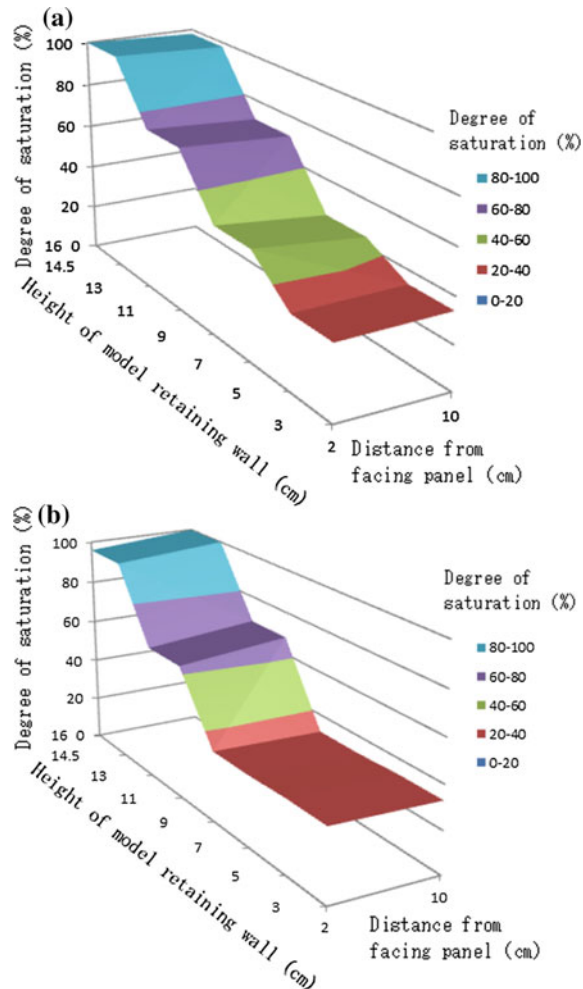


Photo 6 Deformation of model retaining wall without drainage equipment, G16R100 in GR test series



lateral displacements were larger in G16R100 than those in D16R100 due to the effects of the drainage facility. In this test series, the induced deformation was rather different from those in GS test series; the perceptive lateral displacement was found also on the upper part of the wall facing. After the tests, the distribution of saturation degree was evaluated through the measurement of water contents of samples collected from the model retaining walls; see Fig. 9. The effect of drainage equipment can be seen there; however, near the top surfaces the effect was limited, and the

Fig. 9 Distribution of saturation degree in GR test series; **a** G16R100, **b** D16R100



degree of saturation was increased and approached 100 % regardless of drainage equipment. Although it is primarily important to prevent rain water from permeating into reinforced region through top surface, placement of drainage equipment even along the wall facing was effective for the stability of retaining walls.

5 Conclusion

Three series of centrifugal loading tests on model reinforced soil retaining walls were conducted, and deformation-failure behavior was observed, the followings were found through the comparative examination of test results.

1. It was found that groundwater permeation harms the stability of reinforced soil retaining wall and importance of drainage equipment was clarified. An increase in pore water pressure increases earth pressure on wall facing, but reduces pullout resistance of anchor. As a result, the integrity of reinforced region is deteriorated, this mechanism sometimes leads to total failure of reinforced soil retaining walls.
2. It was found that drainage equipment, which was placed on the back of wall facing panels, contributes to maintaining reinforcing effects even during permeation of groundwater as well as heavy rainfall. The capacity of the drainage equipment must be approximately designed for the intensity of possible rainfall and/or permeation of groundwater.
3. In the process of groundwater permeation, the stability can be evaluated reasonably by the decrease in safety factor for overall inner stability or integrity of reinforced region.
4. In the case of groundwater permeation, the settlement of top surface as well as the lateral displacement of wall facing of barrel type were observed; the lateral displacement was maximum around the middle height. In the case of heavy rainfall, the lateral displacement became large also near the top surface level in retaining walls.

References

Butterfield R (2000) Scale-modeling of fluid flow in geotechnical centrifuge. *Soils Found* 40(6):39–45

Hirakawa D, Miyata Y (2010) Stabilization of fill structures by using geosynthetics during raining. *J Geosynthetics* 25:83–90

Hiro-oka A, Kobayashi M, Nagase H, Shimizu K, Fujiwara H (2001) Performance of geotextile reinforced embankment due to seepage flow. *Landmarks in earth reinforcement*. Balkema, pp 207–212

Public Works Research Center (2002) Design and construction manual of multi-anchored reinforced soil retaining wall

Miura K, Nomiyama H, Kusakabe O, Sakai T (1994) Model test on multi-anchored reinforced soil retaining wall and numerical calculation of pull-out resistance. In: 29th annual meeting on geotechnical engineering, pp 2445–2448

Horizontal Pressure on a Non-yielding Wall Due to Flexible and Rigid Strip Loading

Yung-Show Fang, Chia-Pei Lin and Cheng Liu

Abstract This paper studies lateral earth pressure on an unyielding wall due to flexible and rigid strip surcharge loads. Dry Ottawa sand was used as backfill material. The 1.5 m-high model retaining wall at National Chiao Tung University (NCTU) was used to investigate the horizontal earth pressure induced by flexible and rigid surcharge loads. The center lines of the strip footings were applied at 0.15, 0.30 and 0.60 m from the surface of the wall. Based on the experimental work, the following conclusions were made. As the strip loading approached the wall, the stress concentration zone under the footing moved closer to the unyielding wall, causing the horizontal stress increment $\Delta\sigma_h$ acting near the top of the wall to increase. The experimental R/H values were equal to or slightly greater than the R/H values calculated with the method of image (Mindlin 1936), where H is the wall height and R is the vertical distance between the increment loading resultant ΔP_h and wall base. The method proposed by NAVFAC DM-7.2 underestimated the point of application of the induced horizontal increment thrust. The test results of ΔP_h and R/H due to the application of flexible and rigid strip footings were quite similar.

Keywords Earth pressure · Flexible footing · Non-yielding wall · Rigid footing · Surcharge load

1 Introduction

Traditionally, civil engineers build retaining structures to resist the earth pressure. The retaining wall would support not only the horizontal pressure caused by the soil mass behind the wall, but also the pressure increase due to surcharge loads. Various

Y.-S. Fang (✉) · C.-P. Lin · C. Liu

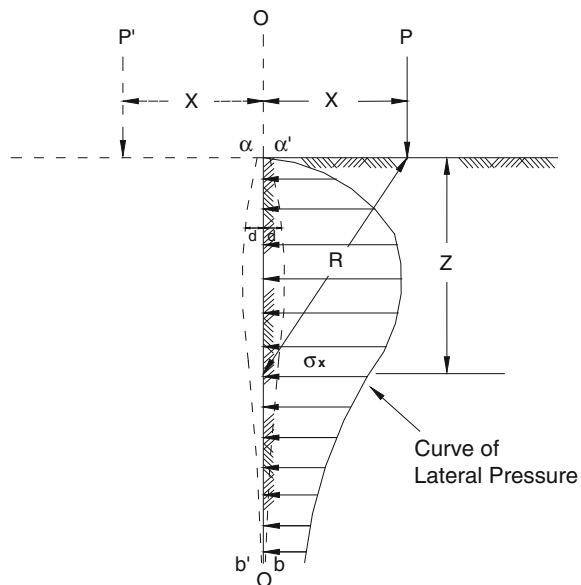
Department of Civil Engineering, National Chiao Tung University, Hsinchu, Taiwan
e-mail: ysfang@mail.nctu.edu.tw

types of loading may be applied on the surface of the backfill, such as a heavy roller, mechanical equipment, and passing vehicles. The various surcharge loads may cause different lateral pressure increment on the wall. The earth pressure distribution behind the wall has a great influence on the safety of the retaining structure. It influences not only the stress within the body, but also the structural safety. Therefore, the increment of lateral earth pressure due to surcharge loading on the retaining wall should be carefully considered.

The estimation of increment of lateral pressure on the wall due to various types of surcharge loads is based on the elastic solution. The application of elastic theory is limited to perfect elastic, homogeneous, and isotropic materials. Terzaghi (1954) proposed equations to estimate the horizontal stress due to a line load. The equations suggested by Terzaghi are widely adopted by design manuals, such as the U.S. Navy Facilities (NAVFAC) Design Manual DM-7.2 (1982).

Mindlin (1936) pointed out that, as the horizontal displacements at the rigid wall will be zero, the “method of image” may be invoked to predict the horizontal stress. The method of image was based upon the principle of superposition. As illustrated in Fig. 1, the stresses in an elastic solid due to a point load P imply horizontal deformations in the x -direction at the position of the wall. The horizontal deformation may be brought back to zero by the application of an imaginary point load P' , magnitude equal to P . However, by the principle of superposition, the horizontal stress σ_x on the wall will be doubled when P' is applied.

Fig. 1 Principle of the method of image (Mindlin 1936)



2 Surcharge Loading System

2.1 Reaction Frame

The NCTU non-yielding retaining wall facility (Chen and Fang, 2008) was used for all experiments in this study. To provide an adequate reaction for the surcharge load, a reaction frame was constructed around the soil bin, as shown in Fig. 2. The reaction frame consists of four parts: (1) columns; (2) fixed beams; (3) movable beam; and (4) lateral bracing. All of the columns and beams were made of I-section steel beams (Designation: W 6 × 20). Two 2.6 m-long fixed beams were connected to four fixed columns with steel bolts. The model wall shown in Fig. 2 was 1.5 m-wide, 1.6 m-high, 45 mm-thick and made of a solid steel plate. The model

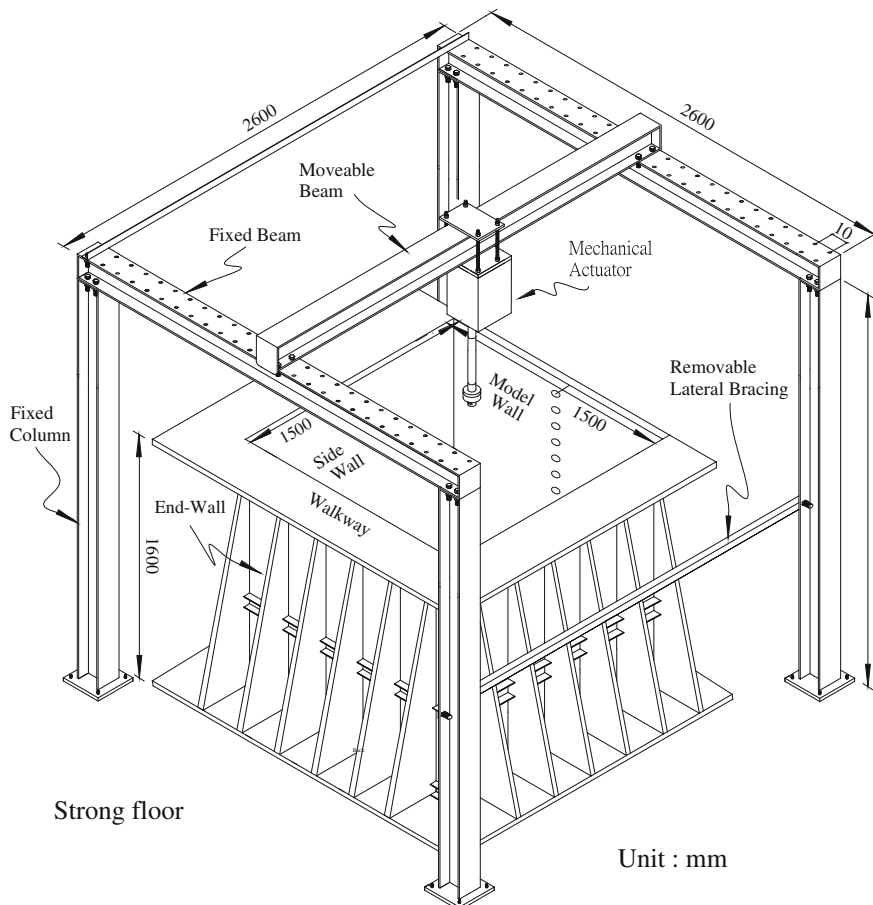


Fig. 2 Model wall and reaction frame

wall was actually the front side of the reinforced soil box. Fifteen transducers SPT1-SPT15 (Kyowa PGM-02 kg, capacity = 19.6 kN/m²) were arranged within the central zone of the model wall to measure the horizontal earth pressure σ_h acting on the model wall. For more information regarding the NCTU non-yielding retaining wall facility, the readers are referred to Chen and Fang (2008).

2.2 *Flexible Footing*

To transmit the vertical force from the actuator, a steel socket with semi-spherical fillister was welded on the lid as shown in Fig. 3a. The steel ball and socket were designed to ensure that only the vertical force was carried over to the footing. To provide a uniform strip pressure on the soil, an air cushion was sandwiched between the steel lid and soil, as shown in Fig. 3a.

2.3 *Rigid Footing*

In Fig. 3b, the footing plate was made with aluminum alloy to maintain the high stiffness of footing and to decrease the dead load of the footing. To provide a uniform loading on top of the rigid footing, an air cushion was sandwiched between the steel lid and footing. For measuring the settlement of the rigid footing, two displacement transducer stands on the steel lid were removed, so that the displacement transducers could be set on the stands of the rigid footing as shown in Fig. 3b.

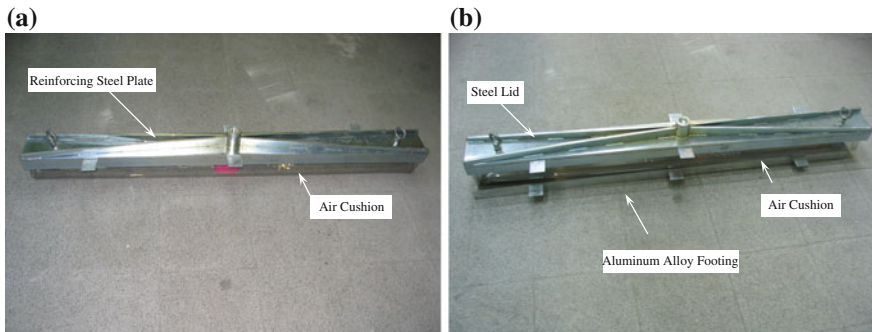


Fig. 3 **a** Flexible footing. **b** Rigid footing

3 Experimental Results

3.1 Earth Pressure at-Rest

Experimental results of the earth pressure at-rest were measured by soil pressure transducer (SPT) after the backfill was filled up to 1.5 m. The relative density achieved for the loose backfill was 35 %. The method of air-pluviation was adopted for all tests to prepare the backfill. As shown in Fig. 4, the experimental earth pressure at-rest for Tests 0518, 0526, 0609, and 0610 were compared with the Jaky (1944) solution for loose sand. In this figure, the Earth pressure distribution was approximately linear and in fairly good agreement with Jaky's equation. The point of application of the at-rest thrust would act at about third of the wall height $H/3$ above the base.

3.2 Ultimate Bearing Capacity of Loose Sand

To apply an appropriate surcharge intensity q on the surface of the backfill, it was necessary to determine the ultimate bearing capacity q_{ult} of the air-pluviated loose sand. As shown in Fig. 5, the surcharge loading system was used to establish the load-settlement relationship for the strip footing. A load cell (Kyowa LUK-A-5 KNSA1, capacity = 5 kN) was used to measure the vertical force transmitted to the footing.

Fig. 4 Earth pressure at-rest

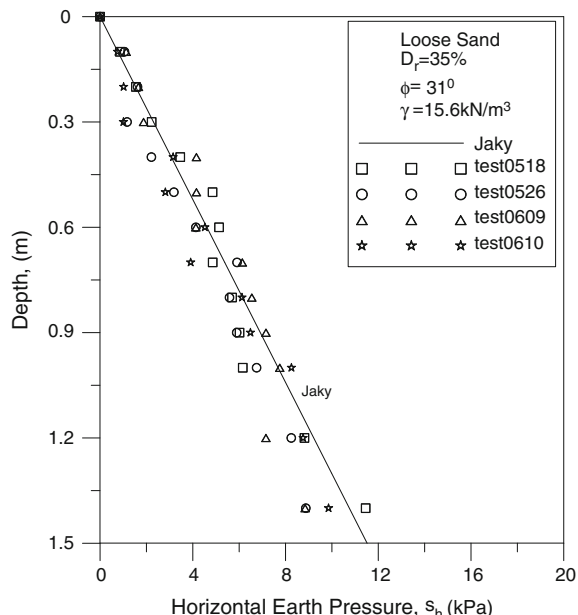
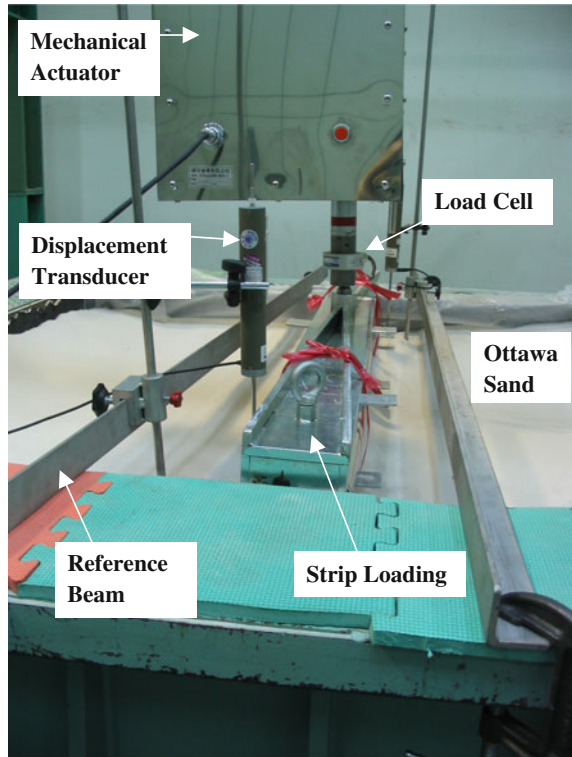


Fig. 5 Apparatus setup of ultimate bearing capacity test



The load-settlement relationships obtained were shown in Fig. 6. There was no obvious peak load measured during the loading process. Up to 2014, there is no reliable theory for estimating the ultimate bearing capacity of punching failure. Das (1994) reported that the ultimate bearing capacity q_{ult} of footing can be defined as the load corresponding to $S = 0.15B - 0.25B$, where S is settlement of the strip footing and B is the width of strip footing. From a conservative point of view, in Fig. 6, ($B = 100$ mm and $S = 15$ mm), $q_{ult} = 24.1$ kN/m² was selected as the ultimate bearing capacity for the strip footing on loose sand. Parameters used in this paper, such as H , R , X , q , m , n , $\Delta\sigma_h$, and ΔP_h , were illustrated in Fig. 7.

3.3 Lateral Pressure Due to Rigid Footing

3.3.1 Strip Load at $X = 0.1H$

Figure 8a showed the distribution of $\Delta\sigma_h$ due to a rigid strip load $q = 0.22q_{ult}$ applied on the surface of backfill. The test data were in fairly good agreement with that calculated with the method of image. In this figure, the DM 7.2 equation

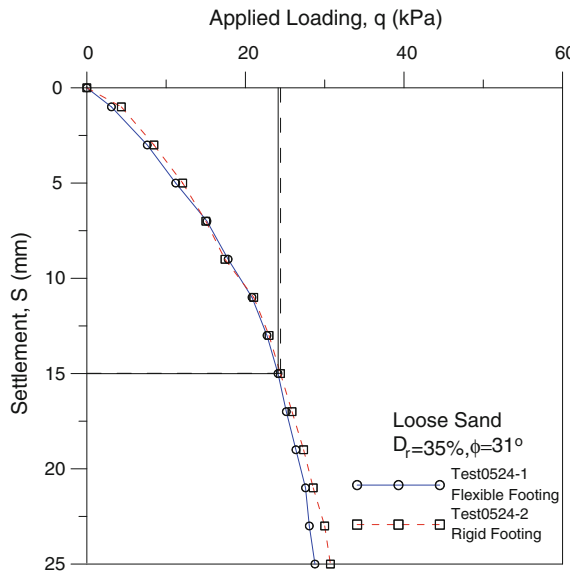


Fig. 6 Load-settlement relationships for strip footings on loose sand

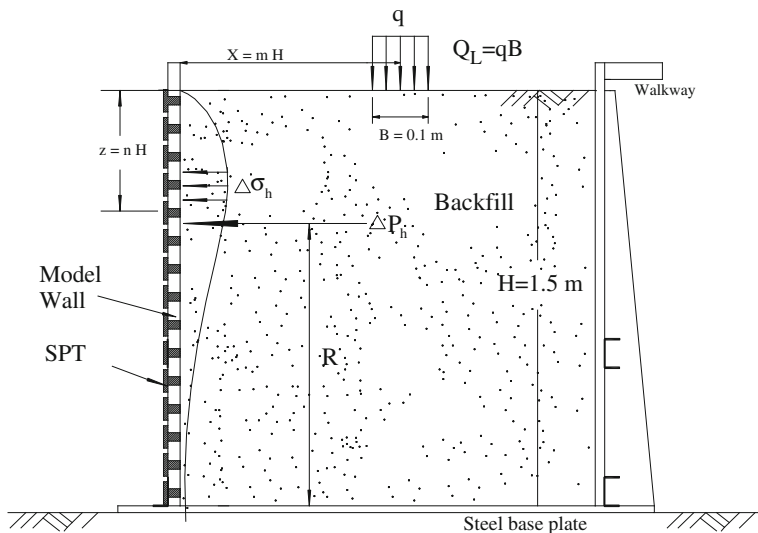


Fig. 7 Parameters discussed in paper

apparently underestimated the $\Delta\sigma_h$ at the upper 0.3 m of backfill, and it overestimated the $\Delta\sigma_h$ at lower 1.2 m of backfill. The similar observation could also be obtained for the $\Delta\sigma_h$ distribution shown in Fig. 8(b).

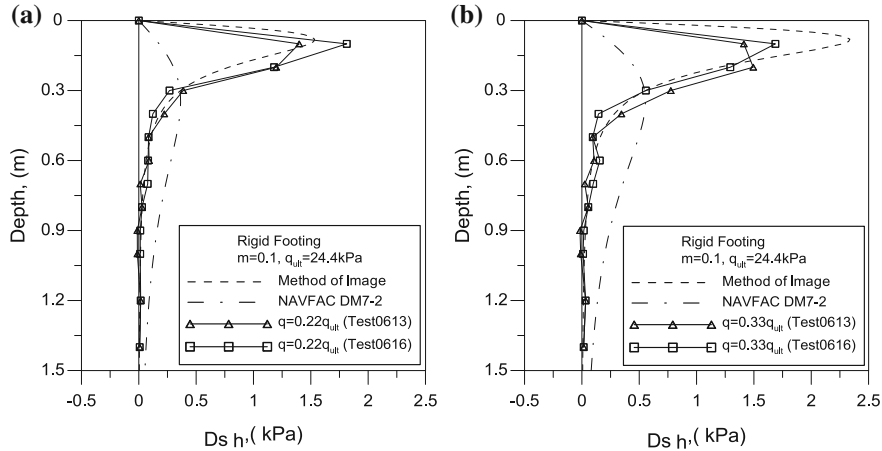


Fig. 8 Variation $\Delta\sigma_h$ with depth ($m = 0.1$)

3.3.2 Strip Load at $X = 0.2H$

The distribution of horizontal pressure increase $\Delta\sigma_h$ due to the application of a rigid surcharge $q = 0.22q_{ult}$ located at 0.30 m from the face of the wall ($m = 0.2$) was shown in Fig. 9a. It was found that the measured $\Delta\sigma_h$ was in fairly good agreement with that calculated with the method of image, but greater than that calculated with the DM 7.2 at upper 0.4 m of backfill. Figure 9b showed the $\Delta\sigma_h$ due to the application of surcharge $q = 0.33q_{ult}$. In the figure, the measured $\Delta\sigma_h$ at upper 0.5 m of backfill was slightly lower than that estimated with the method of image. However, the DM 7.2 method overestimated the $\Delta\sigma_h$ at lower 1.0 m of backfill.

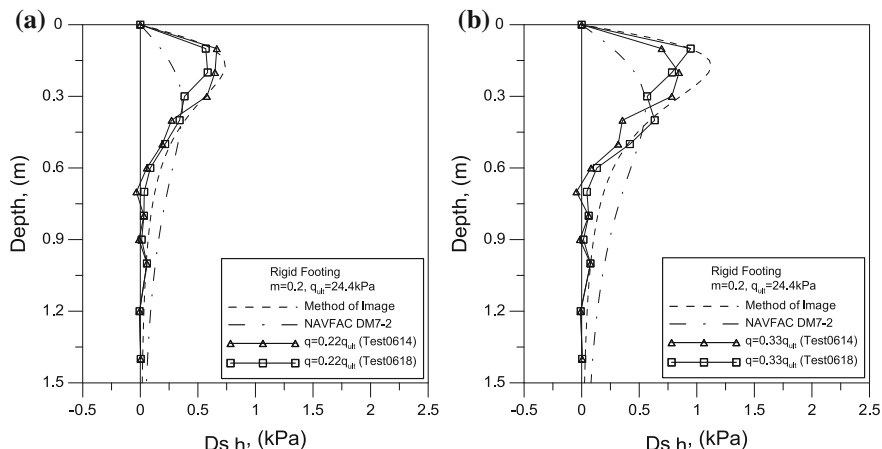


Fig. 9 Variation $\Delta\sigma_h$ with depth ($m = 0.2$)

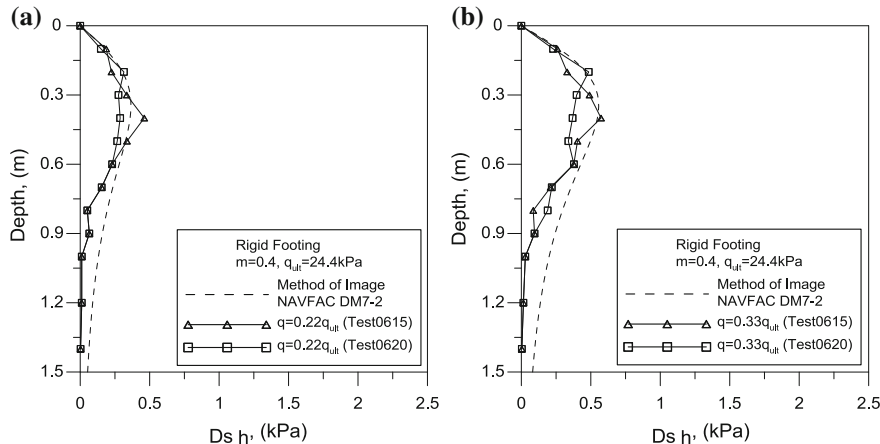


Fig. 10 Variation $\Delta\sigma_h$ with depth ($m = 0.4$)

3.3.3 Strip Load at $X = 0.4H$

Figure 10a showed the distribution of $\Delta\sigma_h$ due to the application of a rigid strip loading $q = 0.22q_{ult}$. At the depth less than 0.6 m, the experimental $\Delta\sigma_h$ values were in relatively good agreement with theoretical solution. At the depth greater than 0.6 m, the test results were obviously less than the theoretical solution. Similar observations could be obtained based on the test results shown in Fig. 10b.

3.4 Effect of Surcharge Location

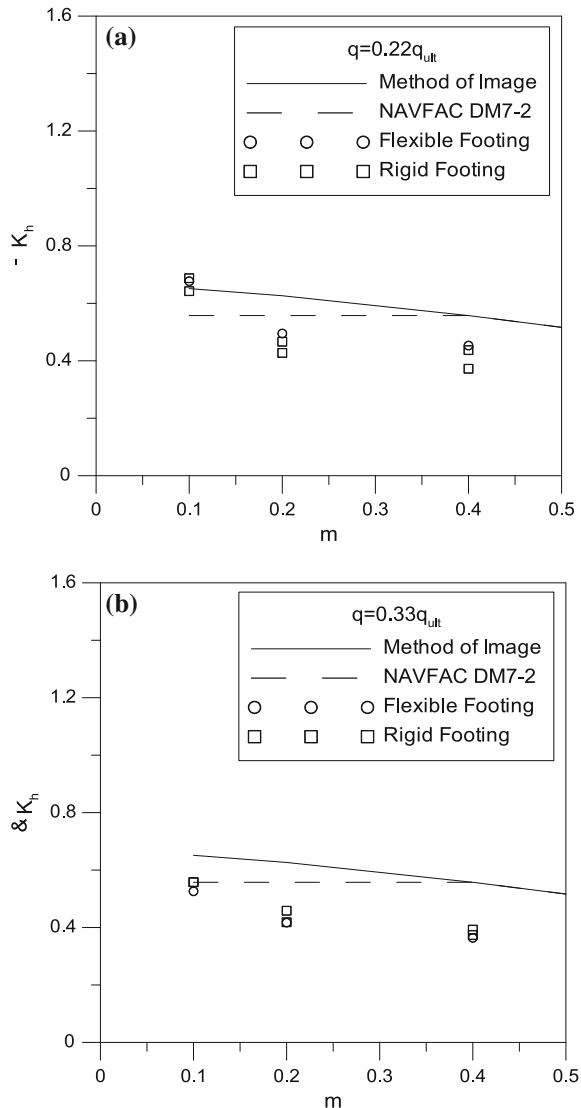
The variation of soil thrust coefficient ΔK_h (defined as $\Delta K_h = \Delta P_h / 0.5\gamma H^2$) as a function of location of surcharge for $q = 0.22q_{ult}$ and $q = 0.33q_{ult}$ was shown in Fig. 11a, b. It was found that

1. Both the experimental and theoretical ΔK_h increased with decreasing parameter m (the strip load approached the wall).
2. The test results of ΔK_h due to the application of flexible and rigid footings were quite similar.

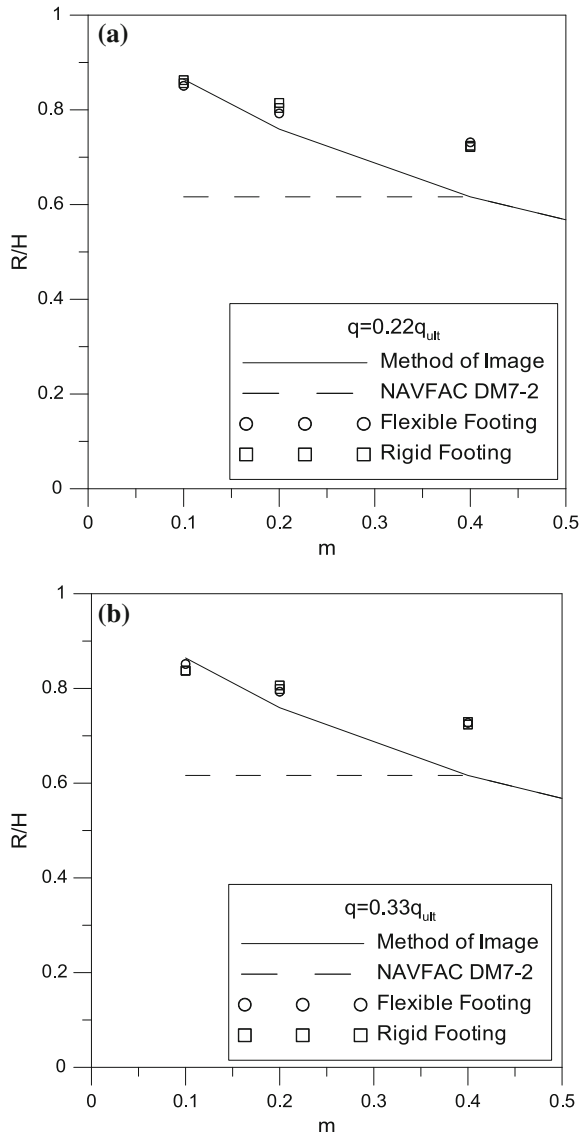
The variation of the point of application of the horizontal resultant ΔP_h as a function of surcharge location was shown in Fig. 12a, b. It was found that

1. Both the experimental and theoretical location (R/H) of ΔP_h increased with decreasing parameter m . As the strip load approached the wall, the stress concentration zone under the footing moved closer to the unyielding wall, causing the $\Delta\sigma_h$ acting near the top of the wall to increase.

Fig. 11 Normalized ΔK_h with parameter
 m a $q = 0.22q_{ult}$;
 b $q = 0.33q_{ult}$



2. The parameter R/H measured for $q = 0.22q_{ult}$ and $q = 0.33q_{ult}$ were almost identical. Typical R/H values ranged between 0.73 and 0.85.
3. The experimental R/H values were equal to or slightly greater than the R/H values calculated with the method of image. The DM-7.2 method underestimated the point of application of the induced force increment ΔP_h .

Fig. 12 Point of total thrust R/H with parameter**m a** $q = 0.22q_{ult}$;**b** $q = 0.33q_{ult}$ 

4 Conclusions

The measured earth pressure at-rest was in fairly good agreement with the Jaky solution. For the strip surcharge load applied quite close ($m = 0.1$) to the face of the wall, the $\Delta\sigma_h$ measured near the top of the wall was significantly greater than that estimated with the design manual DM-7.2. As the strip load approached the wall, the stress concentration zone under the footing moved closer to the unyielding wall,

causing the $\Delta\sigma_h$ acting near the top of the wall to increase. The experimental R/H values were equal to or slightly greater than the R/H values calculated with the method of image. The DM-7.2 method underestimated the point of application of the induced force increment ΔP_h . The test results of ΔK_h and R/H due to the application of flexible and rigid strip footings were quite similar.

References

Chen TJ, Fang YS (2008) Earth pressure due to vibratory compaction. *J Geotech Geoenvironmental Eng ASCE* 134(4):1–8

Das BM (1994) Principal of geotechnical engineering, 3rd edn. PWS Publishing Company, Boston

Jaky J (1944) The coefficient of earth pressure at rest. Budapest, Hungary, pp 355–358 (Journal for Society of Hungarian Architects and Engineers)

Mindlin, R. D. (1936) Discussion: pressure distribution on retaining walls. In: 1st ICSMFE, vol 3, pp 155–156

Terzaghi K (1954) Anchored bulkheads. *Transactions. ASCE*, vol 119, Paper No. 2720

US Navy (1982) Foundation and earth structures, NAVFAC design manual DM-7.2. Washington, D.C., pp 73–74

Part VI

Other Related Topics

Matric Suction and Shear Modulus of Unsaturated Compacted Lateritic Soil Subjected to Drying and Wetting

Horn-Da Lin, Cheng-Chun Wang and Johnson H.S. Kung

Abstract Compacted lateritic soils used widely in geotechnical engineering in Taiwan are usually under unsaturated condition. Nonetheless, their mechanical behavior is rarely studied. It may be due to complexities in the testing technique especially when comparing with saturated conditions. This study, therefore, attempts to investigate the effects of drying and wetting on the unsaturated compacted soil by self-developed moisture simulation apparatuses. A testing system is also developed to measure the matric suction and shear modulus by integrating bender element, pressure plate, and the filter paper technique. Soil specimens are compacted at different initial water contents including the optimum moisture content (OMC), OMC - 3 % (dry of optimum), and OMC + 3 % (wet of optimum). Then, soil specimens are subjected to different scenarios of drying–wetting paths before measuring the matric suction and shear modulus. The essence of the experimental processes of this study is described below. Conclusions of the test results are also summarized herewith.

Keywords Unsaturated soil · Matric suction · Soil-water characteristic curve · Shear modulus · Drying and wetting path

H.-D. Lin (✉) · C.-C. Wang

National Taiwan University of Science and Technology, Taipei, Taiwan
e-mail: hdlin@mail.ntust.edu.tw

C.-C. Wang
e-mail: wangnaslow@hotmail.com

J.H.S. Kung
Taiwan Professional Civil Engineers Association, New Taipei, Taiwan
e-mail: johnsonlive@yahoo.com.tw

1 Introduction

Residual lateritic soil, mostly in unsaturated condition, is commonly found in western tableland of Taiwan. Due to recent urbanization, lateritic soil has been used in geotechnical constructions such as embankments, dams, and highways. To evaluate the performance of these constructions, the soil properties especially soil stiffness and strength must be known. This paper intends to study the stiffness of the lateritic soil in terms of the shear modulus. This study adopts the bender element test since it provides a fast and simple mean to determine the shear wave velocity.

For an unsaturated soil, matric suction is an important index. The unsaturated lateritic soil is affected by the nature water cycle of wetting and drying due to seasonal rainfall. Drying can increase the matric suction, but it can also cause cracking and shrinkage when the water content is too low. On the other hand, wetting can decrease matric suction then result in soil bearing capacity decrease and shallow-type slope failure in the extreme condition. Therefore, it is worthwhile to study the influence of matric suction on the shear modulus upon drying and wetting. Former studies have showed that matric suction of unsaturated soils is closely related to shear modulus. In particular, by using filter paper method, Wang et al. (2010) showed that the matric suction increased due to drying path. In addition, Yang et al. (2008), Sawangsuriya et al. (2006) investigated the shear modulus of unsaturated soil under wetting path with bender element test and indicated that shear modulus decreased as matric suction decreased. Nevertheless, a comprehensive correlation between the shear modulus and the matric suction due to drying and wetting has not been investigated.

This paper presents a comprehensive experimental study on matric suction and shear modulus of unsaturated a compacted lateritic soil subjected to drying and wetting. In specific, the pressure plate test is used to measure the soil-water characteristic curve of the lateritic soil. Environmental simulation test is adopted to impose predetermined wetting and drying paths on soil samples. Soil specimens of three different initial compaction states are studied including the optimum moisture content (OMC), dry of optimum, and wet of optimum. When drying or wetting process is complete water contents are measured. Then, the bender element and filter paper method are utilized to measure the small-strain shear wave velocities and the matric suction, respectively. The essence of the experimental processes of this study is described below. Highlights of the test results are also discussed herewith.

2 Experimental Process

2.1 Soil Preparation

The lateritic soil is classified as CL according to Unified Soil Classification System. Its specific gravity, liquid limit, and plastic index are 2.69, 48.6, and 25 %,

respectively. The soil specimens were compacted by the Modified Proctor. Prior to the compaction, the soils were air-dried for several days and cleaned by removing large impurities such as roots and vegetation. The target moisture contents of the soil samples were optimum moisture content (OMC), OMC – 3 % (dry of optimum), and OMC + 3 % (wet of optimum). The corresponding dry densities were 1.69, 1.61, and 1.63 Mg/m³, respectively. The required amount of distilled water was sprayed on the air-dried soil and thoroughly mixed with the air-dried soil. The fully mixed soil was put into a plastic bag and stored in the humidity controlled room for about one day to ensure homogeneity. Soil specimens with 100 mm diameter and 120 mm height were compacted. After compaction, the soil specimens were trimmed to the desired size of 100 mm height and 50 mm diameter for the testing.

2.2 Environmental Simulation Test

The soil specimens were cured with different paths of drying or wetting by the apparatus shown in Fig. 1. The environmental simulation apparatus is shown in Fig. 1a. The apparatus contains three cube boxes. Each box has side dimension of 45 cm and was made of acrylic plates of 0.8 cm thick. Timer setting sprinklers installed on top are used to create a wetting apparatus that can simulate rainfall infiltration. The calibration test proves that the relative humidity in each box is indeed not affected by the change of relative humidity of outdoor. For drying simulation, a 60 W light bulb was installed beneath the ceiling of the box to simulate sunshine drying as shown in Fig. 1b. The drying room is a 48 cm cube box made of acrylic plate of 1 cm thick. The temperature in the box was controlled approximately at 37°. After the curing processes, the uniformity of the moisture content inside the soil specimen was carefully checked. Figure 2 shows that the

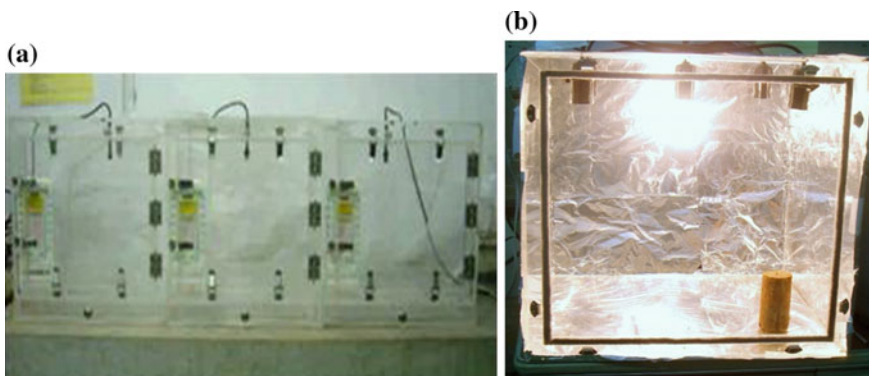
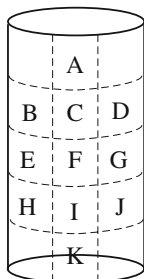


Fig. 1 Schematic diagram of environmental simulation apparatus. **a** Wetting apparatus. **b** Drying box



| Location | w(%) | $\Delta w(%)$ | Location | w(%) | $\Delta w(%)$ |
|----------|-------|---------------|----------|-------|---------------|
| A | 22.21 | 0.40 | G | 22.13 | 0.32 |
| B | 21.75 | -0.06 | H | 21.48 | -0.33 |
| C | 21.61 | -0.20 | I | 21.45 | -0.36 |
| D | 21.72 | -0.09 | J | 22.27 | 0.46 |
| E | 22.08 | 0.27 | K | 21.70 | -0.11 |
| F | 21.52 | -0.29 | Mean | 21.81 | - |

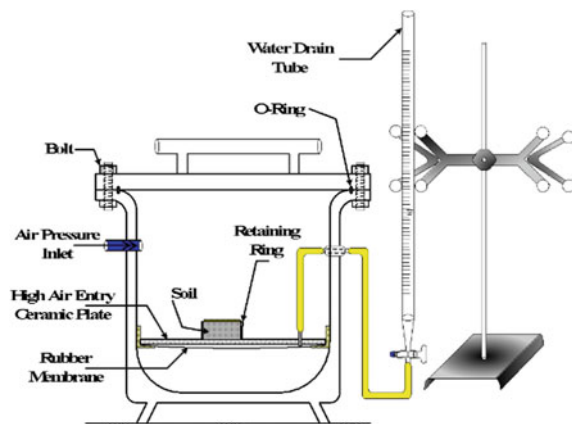
Fig. 2 Moisture content distribution of compacted soil sample after wetting

difference in moisture content after wetting, between the measured values and the mean value is less than 0.46 %. Extensive calibration tests have proven that the wetting and drying apparatuses can successfully impose desired wetting and drying paths onto the soil specimen with excellent moisture homogeneity (Wang et al. 2010; Yang et al. 2008).

2.3 Matric Suction Measurement (Pressure Plate Test and Filter Paper Test)

Pressure plate test in this study follows the ASTM D3152-72 standard (ASTM 2000). The specimen pre-saturated by oedometer was placed in the pressure chamber (5 or 15-bar) for testing. A schematic diagram of the pressure plate test was shown in Fig. 3. Afterwards, target air pressures were applied. For each stage of air pressure, if the difference in the specimen weight measured between two days was within 0.05 g the sample was deemed in equilibrium. The moisture content was

Fig. 3 Schematic diagram of pressure plate test apparatus



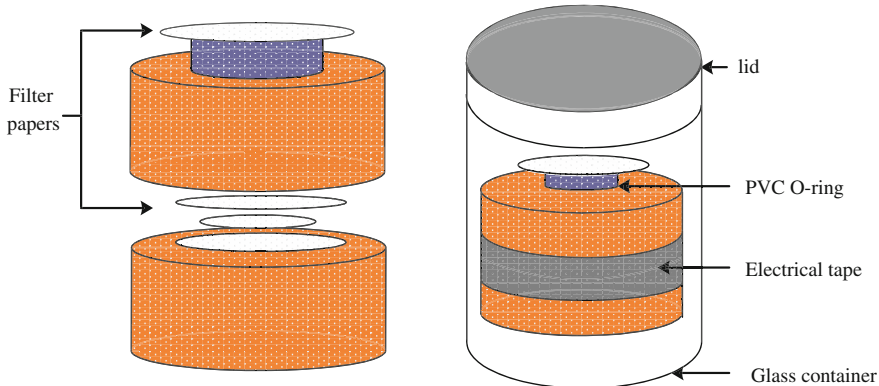


Fig. 4 Filter paper method for measuring soil suction

recorded. The soil-water characteristic curve (SWCC) can be constructed by correlating various stages of air pressure and moisture content values (ASTM 2000).

In this study, the filter paper method was also conducted according to ASTM D 5298-94 (2000), Wen (2007). Figure 4 illustrates the test setup for suction measurement. The soil specimens were cut into two layers. A stack of three filter papers was placed at the center of the two specimens. Then, the specimen was put into a glass container for about 7–10 days for equilibrium. The moisture content change of the central filter paper was measured by an electronic balance with 0.0001 g accuracy. It was then converted to equivalent matric suction values by the calibration curves (Yang et al. 2008).

2.4 Bender Element Test

When the moisture content of the soil specimen reached a preassigned state, the shear wave velocity was measured using the bender element. Particularly, the bender elements were placed in two ends of the specimens through striated notches, as shown in Fig. 5a. Its thickness, width and height are 1, 12, and 10 mm, respectively. One bender element functions as the shear wave transmitter and the other acts as the receiver. To facilitate the test under suction controlled condition, one of the bender elements needs to be installed into the triaxial base plate with high air entry disk, as shown in Fig. 5b. Figure 6 shows the integrated testing system of the bender element test. A sine pulse was generated by a EGC-3236A with 10 MHz and ± 10 V function generator. Signals were displayed on a high definition oscilloscope. The high definition oscilloscope is a Nicolet Type Pico ADC212/100 with a definition of 12 bit in each channel and a maximum sampling rate of 100 MS/s. The travel time of the shear wave was used to compute the shear wave velocity V_s . Finally, the shear modulus G_{\max} can be calculated according to equation: $G_{\max} = \rho V_s^2$.

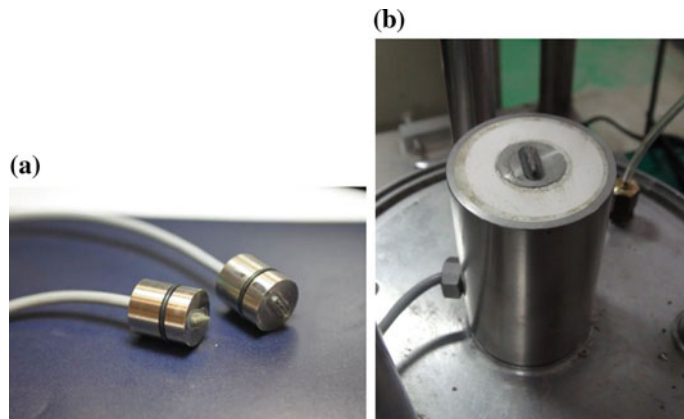


Fig. 5 Pictures of bender elements. **a** Bender element. **b** Bender element integrated with ceramic disk

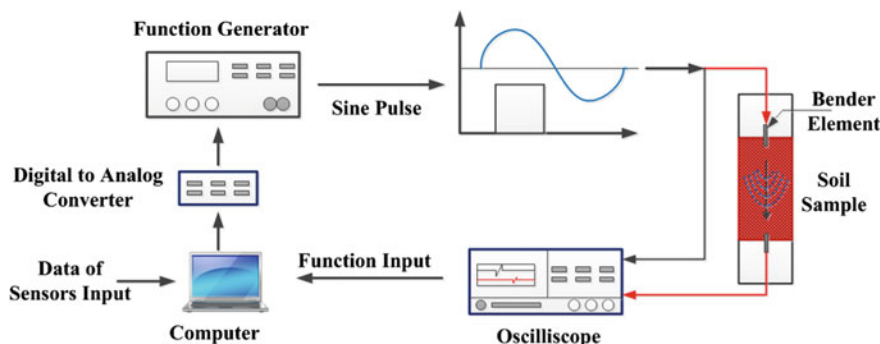
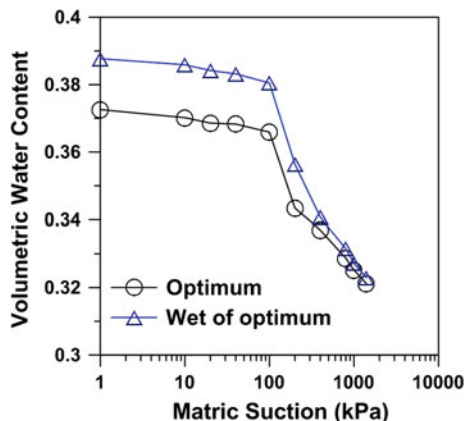


Fig. 6 Bender element testing system for measuring shear modulus

3 Test Result and Discussion

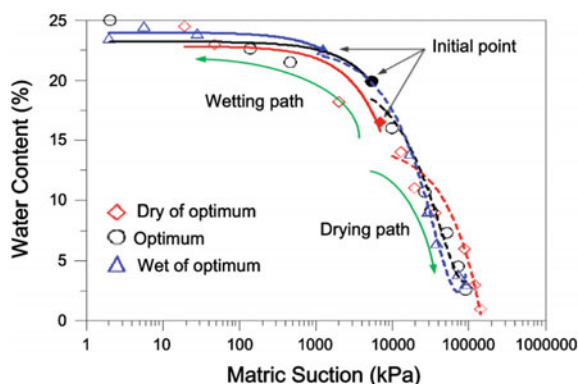
3.1 Unsaturated Soil Characteristic Curve

Figure 7 shows the SWCCs of two sets of soil samples with initial compaction water contents of OMC and OMC + 3 %. The water retention ability is better for optimum samples as expected. The test result indicated that the air entry value of the optimum soil specimen is slightly higher than that of the wet of optimum soil specimen. Besides, pore water dissipated easier when the air pressure increases for the wet of optimum soil specimen.

Fig. 7 SWCCs test results

3.2 Influence on Matric Suction Under Different Wetting and Drying Paths

All three sets of test results are plotted together in Fig. 8 to demonstrate the general trend of influence of the initial compaction state. The test results show that matric suction decreases and water content increases when soils are subjected to wetting. Matric suction decreases with increasing water content. The change in matric suction is much less significant upon wetting despite of the initial compaction condition. When wetting continues and reach the equilibrium water content all three sets of test results converge together. This implies that suction behavior is no longer influenced by the initial compaction state because soils are almost fully saturated under this circumstance. On the other hand, drying test results shows that the matric suction increases much more significantly and rapidly than that of wetting. The effect is the least for optimum samples as would be expected.

Fig. 8 Water content versus matric suction

3.3 Influence of Wetting and Drying on Shear Modulus and Matric Suction

Figure 9 shows the relationship between matric suction and shear modulus of unsaturated soil under drying and wetting paths. It is observed that the variation in the shear modulus is highly correlated to the change in the matric suction. For example, in the wetting path, the moisture content increases with reduction in the matric suction. As a result, shear modulus also decreases. On the other hand, in the drying path, the moisture content decreases quickly with sudden increase in the matric suction. This phenomenon leads to sudden increase in the shear modulus. Apparently, variations in both shear modulus and matric suction are more pronounced in the drying path than those in the wetting path.

A regression analysis is used to establish the correlation equations between shear modulus and matric suction, as shown in Table 1. The coefficient of determination (R^2) values range from 0.89 to 0.99. It indicates that the shear modulus and the matric suction are highly correlated. In other words, it is feasible to evaluate the shear modulus by means of the matric suction. Moreover, the regression analysis is conducted between the shear modulus and the water content. It is found that the

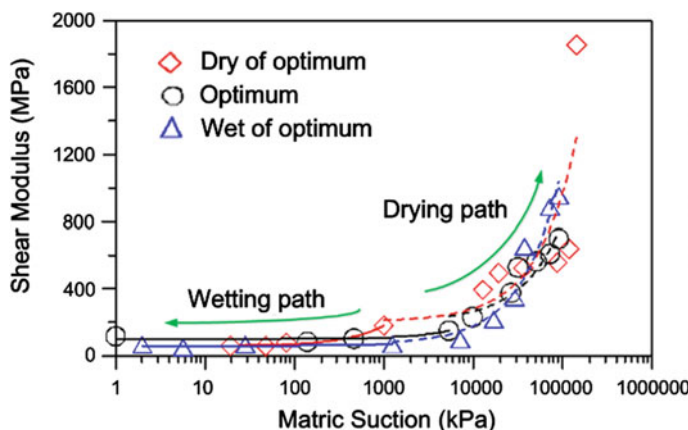


Fig. 9 Shear modulus versus matric suction

Table 1 Regression analysis results of matric suction and shear modulus

| Initial state | Drying path | | Wetting path | |
|----------------|-----------------------------------|-------|------------------------------------|-------|
| | Regression equation | R^2 | Regression equation | R^2 |
| Dry of optimum | $G_{\max} = 0.1192\psi + 60.3530$ | 0.98 | $G_{\max} = 0.0095\psi + 232.7399$ | 0.89 |
| OMC | $G_{\max} = 0.0113\psi + 90.2226$ | 0.94 | $G_{\max} = 0.0128\psi + 87.1897$ | 0.95 |
| Wet of optimum | $G_{\max} = 0.0102\psi + 57.6420$ | 0.97 | $G_{\max} = 0.0102\psi + 42.2416$ | 0.99 |

Note ψ = matric suction (kPa); G_{\max} = shear modulus (MPa)

shear modulus has higher correlation with the matric suction than the water content (Wang et al. 2010). Therefore, the matric suction is a good index to estimate the shear modulus in engineering applications.

4 Conclusions

In this study, the lateritic soil was tested to study the influence of the matric suction upon wetting and drying path. The environmental simulation apparatus filter paper method and bender element test were successfully integrated. The pressure plate test was also used to measure the SWCC curve. Soil samples were compacted at optimum moisture content, dry of optimum, and wet of optimum. They are then cured with different paths of drying or wetting using the environmental simulation apparatus. After wetting or drying, the specimens were tested to determine the shear wave velocity using the bender element, and then, the filter paper method was used to measure the matric suction.

The SWCC results show that the water retention ability is better for optimum samples as expected, and the air entry value is slightly higher than that of the wet of optimum samples. Test results also indicate that upon wetting soil's shear modulus and matric suction decrease as water content increases. On the other hand, the shear modulus and matric suction increase with water content decrease upon drying. Comparison of test results of drying and wetting indicate that the influence on matric suction and shear modulus is path dependent and more pronounced due to drying. The regression analysis showed that the coefficient of determination (R^2) between shear modulus and matric suction ranges from 0.89 to 0.99. The above findings suggest that the matric suction is a key index parameter when predicting the shear modulus of unsaturated lateritic soils.

Acknowledgments The research program was supported by Ministry of Science and Technology of Taiwan under grant number of NSC102-2221-E-011-103-MY2. This support is gratefully acknowledged.

References

- ASTM, Designation D3152-72 (2000) Standard test method for capillary-moisture relationships for fine-textured soils by pressure-membrane apparatus. In: Annual book of ASTM standard, vol 04, no 08. West Conshohocken, PA, pp 311–316
- ASTM, Designation D5298-94 (2000) Standard test method for measurement of soil potential (suction) using filter paper. In: Annual book of ASTM standard, vol 04, no 08. West Conshohocken, PA, pp 1082–1087
- Sawangsuriya A, Edil TB, Bosscher PJ, Wang X (2006) Small-strain stiffness behavior of unsaturated compacted subgrade. *Unsaturated Soils Geotech Spec Publ ASCE* 147:1121–1132

Wang CC, Kung JHS, Liao CY, Lin HD (2010) Experimental study on matric suction of unsaturated soil upon drying and wetting. In: Proceedings, 3rd international conference on problematic soils, CD-ROM. Adelaide, Australia, pp 345–352

Wen YC (2007) The influence of stress history and soil structure on the soil-water characteristics of compacted lateritic soils. Master Thesis, National Taiwan University of science and Technology

Yang SR, Lin HD, Kung JHS, Liao JR (2008) Shear wave velocity and suction of unsaturated soil using bender element and filter paper method. *J GeoEngineering* 3(2):67–74

A Constant-Head Well Permeameter Measurement of Saturated Hydraulic Conductivity in the Vadose Zone and the Capabilities of Carbon Dioxide Injection

Makoto Nishigaki and Sten-Magnus Mostek

Abstract The constant-head well permeameter (CHWP) method is a single-borehole infiltration test for in situ measurements of field-saturated hydraulic conductivity (K_{fs}) in the vadose zone. A measuring instrument was designed for the determination of K_{fs} at greater depths using a pipe-in-pipe overflow system with a submersible pump. The entrapment of air in the soil pore system inhibits truly saturated conditions during infiltration tests. A proven method to reduce the influence of entrapped air is the displacement of soil air with carbon dioxide. In this study, the designed CHWP was put to the test in a field experiment in a sandy soil. Injection of CO₂ was applied in 7 out of 11 tests for varying durations and flow rates in order to find an optimal combination. The experimental results show a considerable increase in K_{fs} by about a factor of 1.5 due to the application of CO₂. An average hydraulic conductivity of 1.6E-06 m/s was determined in tests without CO₂-injection, 2.4E-06 m/s in tests with sufficient CO₂-injection, and 2.8E-06 m/s in laboratory falling-head hydraulic conductivity tests. The optimal setting for the injection of CO₂ was duration of 1 h with a flow rate of 20 L/min.

Keywords Constant-head well permeameter · Entrapped air · Field-saturated hydraulic conductivity · Carbon dioxide

M. Nishigaki (✉) · S.-M. Mostek

Department of Environmental Design and Civil Engineering,
Okayama University, 3-1-1 Tsushima-naka, Okayama 700-8530, Japan
e-mail: n_makoto@cc.okayama-u.ac.jp

S.-M. Mostek
e-mail: sten-m.m@web.de

1 Introduction

Practical methods to determine the (field-)saturated hydraulic conductivity (K_{fs}) in the vadose zone are needed, especially for greater depths, in order to improve slope stability analysis in the event of heavy rainfall by taking seepage velocity and pore-water pressure distribution into account. Infiltrating rainfall as well as rising groundwater levels lead to an increase in pore-water pressure in the unsaturated soil. In consequence, the resisting forces cohesion and shear strength decrease. Commonly, slope stability analysis is based on the static equilibrium between the forces resisting movement and the forces driving movement. However, rainfall infiltration and seepage flow are transient processes. Possible mass wasting due to a loss of matric suction caused by high-intensity rainfall is described in detail by Fredlund et al. (1993). Fredlund's simulated data further show that the factor of safety decreases to a minimum at the end of a rainfall period, and afterwards slightly increases again until a steady state condition is reached. Another point of concern, especially for levees and for natural slopes close to groundwater level, is the moment when the wetting front reaches the phreatic zone. Seepage then causes the capillary fringe to drain and, in effect, raising the phreatic surface to an intermediate higher level. The resulting groundwater runoff increases the seepage force, further destabilizes the slope, or eventually triggers the failure even before a stable steady state condition is reached for the higher groundwater level. It is therefore considered important to take the seepage velocities under saturated and unsaturated conditions into account for slope stability analyses in order to improve risk management and disaster prevention for heavy rainfall events.

2 Theoretical Background

The method presented in this study is based upon a single-borehole percolation test referred to as (constant-head) well permeameter (U.S. Bureau of Reclamation 1990) or as shallow-well pump-in method (Boersma 1965). According to Phillip (Phillip 1985), the constant-head well permeameter (CHWP) is a technique that "...involves drilling a vertical borehole and determining the steady state discharge of water into the borehole, q , necessary to maintain the water in the hole at a prescribed level." A wide range of designs have been developed for the single-borehole permeameter test as well as various approaches to compute the saturated hydraulic conductivity (K_{sat}). Analytical solutions for different borehole designs were compared to results of numerical simulations by Reynolds (2013). In the present study, the solution of the Laplace's equation proposed by Glover (Zangar 1953) for steady state flow from an uncased borehole above the water table is applied

$$\psi = \frac{q}{2\pi k H^2} \left[H \sinh^{-1} \left(\frac{H}{a} \right) - \sqrt{a^2 + H^2} + a \right], \quad (1)$$

where ψ [L] is the pore pressure, q [$L^3 T^{-1}$] is the discharge, k [LT^{-1}] is the hydraulic conductivity, H [L] is the water level inside the borehole, and a [L] is the borehole radius, respectively. With H set sufficiently larger than a ($H/a \geq 10$) and ψ equal to H at the borehole bottom, Eq. (1) can be simplified to

$$k = \frac{q}{2\pi H^2} \left[\sinh^{-1} \left(\frac{H}{a} \right) - 1 \right] \quad (2)$$

Hereinafter, measured k is referred to as K_{fs} to clearly distinguish between theoretically full saturation and field saturation. The Glover solution is part of the standard methods proposed by the United States Bureau of Reclamation (U.S. Bureau of Reclamation 1990), as well as recommended in the Japanese Standards for Geotechnical and Geoenvironmental Investigation Methods (Japanese Geotechnical Society 2004), among others. However, a number of approximations are applied within: flow is confined in a saturated cylindrically shaped field, the free surface; flow occurs solely due to pressure from the source, the borehole; gravitational flow only adds a downward component; and the soil outside the free surface has no influence on the flow. Hence, the Glover solution neglects any form of flow due to capillarity. For that reason, a sorptivity coefficient α , or sorptive number, has been introduced by Philipp (1985) and Reynolds and Elrick (1985a, b) to adjust for capillary flow. However, Reynolds (2013) concluded for the Glover solution that it "... yield[s] accurate estimates of K_{fs} ($\leq 25\%$ error) when $H/a \geq 10$, $\alpha^* \geq 12 \text{ m}^{-1}$, $a \geq 10 \text{ cm}$ [...] and can therefore be used with reasonable confidence under those conditions." With the sorptive number $\alpha^* \geq 12 \text{ m}^{-1}$ is representing moderate capillarity as of loamy, medium grain size sandy soils.

3 Restrictions and Improvements

The theoretically required large volume of water as well as the long infiltration time to achieve steady, saturated conditions, are criteria restricting the viability of the USBR procedure. According to the USBR's specified Eq. (3), the volume is dependent on the borehole geometry, the ratio of H to a . With the aforementioned ratio of $H/a \geq 10$ and the specific yield (S) set to 0.35 for an unknown soil, Eq. (3) yields a minimum volume of water (V_{min}) of at least 60 L. The minimum time (t_{min}) is given with 6 h in the tests description, and up to days for very low permeable soils applying Eq. (5).

$$V_{\min} = 2.09 \cdot S \cdot H^3 \sqrt{\frac{2}{\sinh^{-1} H/a - 1}}^3 \quad (3)$$

$$V_{\max} = 2.05 \cdot V_{\min} \quad (4)$$

$$t_{\min} = \frac{V_{\min}}{q} \quad (5)$$

In an extensive field experiment Stephens and Neuman (1983) verified that the USBR's estimates for V_{\min} and V_{\max} are reasonable, though stable and highest infiltration rates were partially found at volumes exceeding V_{\max} . Further, Stephens utilized CO_2 to displace soil air in order to achieve a higher level of saturation. Compared to air, the injected CO_2 dissolves better and faster into the infiltrating water, thus, reducing the amount of entrapped air and resulting in higher K_{fs} -values due to an increased maximum saturation. In laboratory experiments with soil columns Christiansen et al. (1946) showed what Stephens and Neuman (1983) also approved in his field study: Pretreatment of the soil with CO_2 may reduce the required water and infiltration time as well as increase the measured hydraulic conductivity by a factor of about two to three.

Taking the findings of Stephens into account, the CHWP field experiment was conducted to put the practicability of the instrumental setup to the test and to compare the results of in situ measurements, with and without CO_2 -injection, to the results of a laboratory falling-head hydraulic conductivity tests.

4 Instrumental Setup and Measuring Procedure

The schematic design of the measuring instrument is shown in Fig. 1 and consists of the parts listed in Table 1.

The borehole and tubing dimensions used in this field test were chosen to match Japanese standard tubing diameters. The borehole depth and diameter were 1.9 m and 86 mm, respectively, with a screened height of 1 m. The inner tube had a diameter of 66 mm with vents at the height of 0.7 m.

The borehole was drilled to the desired depth using a core drill. A well screen with the outer tube was inserted to prevent the borehole from collapsing. The inner tube was prepared with vents to maintain the constant water level in the borehole at the designed height and the end of the inflow hose was fixed below the vents. The submersible pump with an attached water level meter was inserted into the inner tube and then placed inside the outer tube. The infiltration water was pumped from the supply tank on top of the scale to the constant-head reservoir, while excess water flowed back. From the constant-head tank, the water discharged into the borehole where it filled the void between the soil and the inner tube up to the height of the vents. Excess water flowed over into the inner tube, from where it was

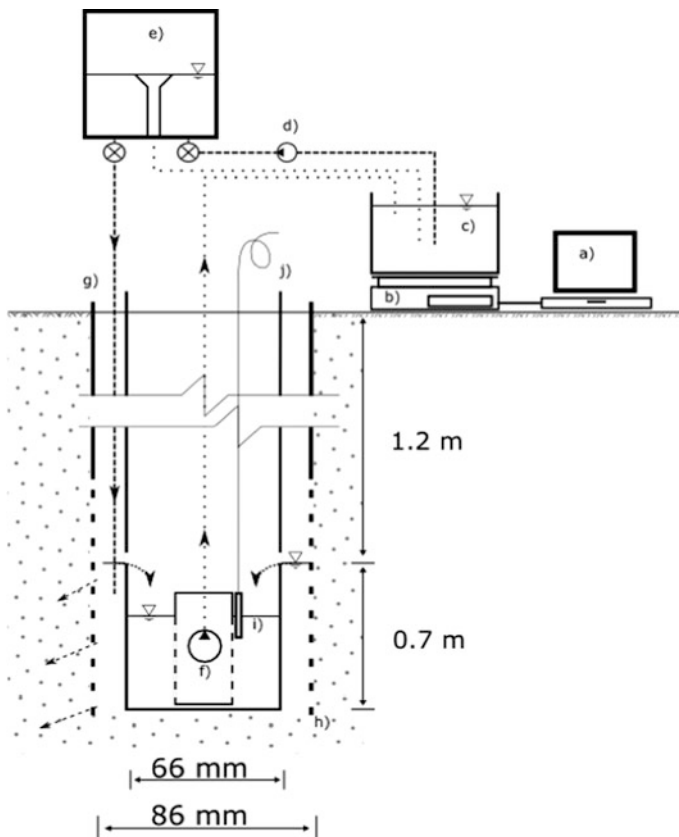


Fig. 1 Instrumental setup of the CHWP

Table 1 List of equipments

| | |
|-----------------------------------|---|
| (a) Computer | • Plastic hoses |
| (b) Electric scale | • Thermometer |
| (c) Water supply tank | • Automotive battery |
| (d) Hydraulic pump | • Ladder |
| (e) Constant-head water reservoir | • Engine-generator |
| (f) Submersible pump | For the pretreatment with CO ₂ : |
| (g) Outer tube | |
| (h) Well screen | • CO ₂ gas tank |
| (i) Water level meter | • Pressure regulator |
| (j) Inner tube | • Plastic cap |

pumped back up at the moment the water level reaches the water level meter. At first, fine, loose soil particles were washed out and for several times the pumped up water was discarded. As soon as the water became clear, the outflow hose was fixed to the inside of the supply tank. The inflow rate was regulated at the valve of the constant-head reservoir to maintain a slight overflow into the inner tube and lessen the pumping frequency. Over the course of a test, the water inflow had to be adjusted to the changing infiltration rate. A frequency of about five to ten minutes proved to be practical in terms of handling the manually operated pump as well as for the data analysis. The measurement was started and stopped with the inner tube filled up to the height of the water level meter. The weight of the supply tank was recorded by the scale in a one-second interval.

For the pretreatment with CO_2 the inner tube was removed, a plastic cap was fixed onto the outer tube and the borehole margin was sealed with plastic foil, duct tape, and weights in order to prevent gas leakage. The CO_2 was injected through the cap into the borehole at a constant pressure for the prescribed time and flow rate (Table 2).

Fifteen infiltration tests were conducted within five weeks in a sandy soil, the ancient fluvial deposits of the Asahi River in Okayama, Japan. Four test results had to be discarded because of clogging of the well screen as well as equipment failure, leaving eleven representative results. Seven of the tests were conducted with the injection of CO_2 for varying durations and flow rates, while the delivery pressure was kept constant at 100 kPa. K_{sat} was determined from four samples with falling-head hydraulic conductivity tests according to the Japanese Industrial Standard (JIS) A 1218 (Japanese Geotechnical Society 2009).

Table 2 Summary of test sequences and results

| Test | Infiltration time (h) | CO ₂ -injection | | | K_{fs} (m/s) |
|---|-----------------------|----------------------------|----------------|-------------------|-----------------------|
| | | Duration (h) | Pressure (kPa) | Flow rate (L/min) | |
| #01 | 3.5 | – | – | – | 1.49E–06 |
| #02 | 3.5 | – | – | – | 1.83E–06 |
| #03 | 3.5 | 1.0 | 100 | 10 | 1.76E–06 |
| #04 | 3.0 | 1.0 | 100 | 15 | 2.36E–06 |
| #05 | 3.0 | 1.0 | 100 | 20 | 2.49E–06 |
| #06 | 3.0 | 2.0 | 100 | 10 | 2.23E–06 |
| #07 | 3.5 | 2.0 | 100 | 20 | 2.30E–06 |
| #08 | 4.0 | – | – | – | 1.69E–06 |
| #09 | 4.5 | 0.5 | 100 | 10 | 1.33E–06 |
| #10 | 4.5 | 0.5 | 100 | 20 | 1.33E–06 |
| #11 | 4.5 | – | – | – | 1.32E–06 |
| Laboratory test – K_{sat} mean value | | | | | 2.83E–06 |

5 Data Analysis and Evaluation

The natural soil consisted of a medium to fine grained sand with a small fraction of silt (Fig. 2; Table 3). A layer of gravel and rubble covered the sand to a depth of 1 m.

The discharge into the borehole $q(t)$ was determined from the difference in weight of the supply tank after the water was pumped back up completely from the inner tube. $K_{fs}(t)$ was calculated using Eq. (2). The final K_{fs} -values are at best calculated from a portion of the $q(t)$ -series that shows a steady discharge rate. However, steady state conditions were not achieved in these short term measurements. Therefore, K_{fs} given in Table 2 was calculated from $q(t)$ at the end of each test.

Figure 3a shows the results of the tests without an injection of CO_2 . In the tests #1, #2, and #8, K_{fs} decreases in the first 1.5–2 h, and increases afterwards till the end of the infiltration test. It is believed, that the initial decrease in K_{fs} is mainly due to the decrease in capillary suction and the entrapment of soil air during the wetting process of the soil surrounding the borehole. The following increase in K_{fs} indicates the gradual dissolution and displacement of entrapped air. In Test #11, K_{fs} increases continuously from the beginning of test, presumably due to an initially higher moisture content. In these four tests, steady state infiltration was not achieved within the 3.5–4.5 h of water infiltration. Long term measurements could provide further information regarding the highest achievable K_{fs} and the necessary

Fig. 2 Particle size distribution

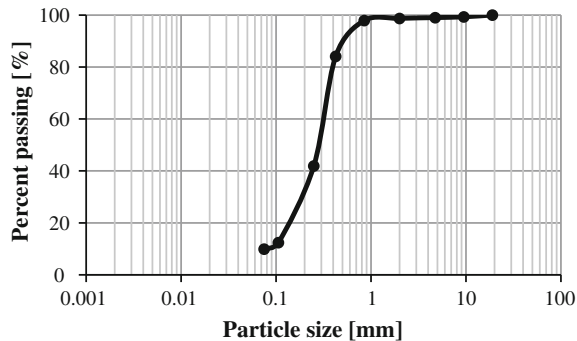


Table 3 Soil composition

| Soil parameter | |
|----------------|------------------------|
| Density | 1.44 g/cm ³ |
| Medium sand | 52 % |
| Fine sand | 34 % |
| Silt | 13 % |
| D_{50} | 0.25 mm |
| D_{20} | 0.13 mm |

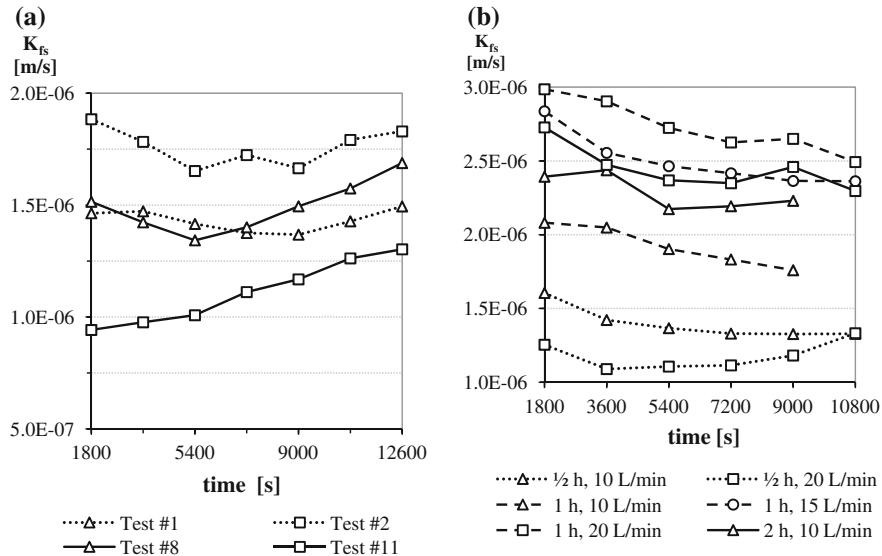


Fig. 3 Experimental results of the measurements **a** without CO_2 -injection, and **b** with CO_2 -injection for different durations and flow rates prior to the infiltration test

infiltration time for tests without the application of CO_2 and could be subject to future studies.

Figure 3b shows the results of the infiltration tests with an injection of CO_2 for the different durations and flow rates. It can be seen that an injection time of 30 min had no effect on the measured K_{fs} . The determined values are similar to the tests without CO_2 . The CO_2 -injection for 1 h with 10 L/min resulted in a slightly higher K_{fs} , nevertheless, not significantly higher than the results of Test #2 and Test #8 conducted without CO_2 . However, an injection for 1 h with 15 or 20 L/min as well as for 2 h with 10 and 20 L/min caused a significant increase in K_{fs} by about a factor of 1.5 compared to the average K_{fs} of tests without an injection of CO_2 .

In contrary to Fig. 3a, the results of the measurements with a CO_2 -injection for more than 30 min show a decrease in K_{fs} over the course of the measurement. The highest K_{fs} occurred at the beginning of the measurement, rather than at the end. Similar results were reported by Christiansen et al. (1946) and Stephens and Neuman (1983) for the use of CO_2 in laboratory experiments and in field experiments, respectively. Hence, indicating a successful displacement of air by CO_2 in those field tests. However, the CO_2 concentration and the moisture content in the soil surrounding the borehole were not monitored in this field experiment. Thus, the true extent of the soil air displacement, the influence of capillary suction, and the development of the wetted region remain unknown. The decline of K_{fs} near the end of the measurement might be influenced by capillary effects and entrapped air as the wetting front develops past the extent of the CO_2 treatment. Measurements of pressure head and soil moisture development during the infiltration tests with and

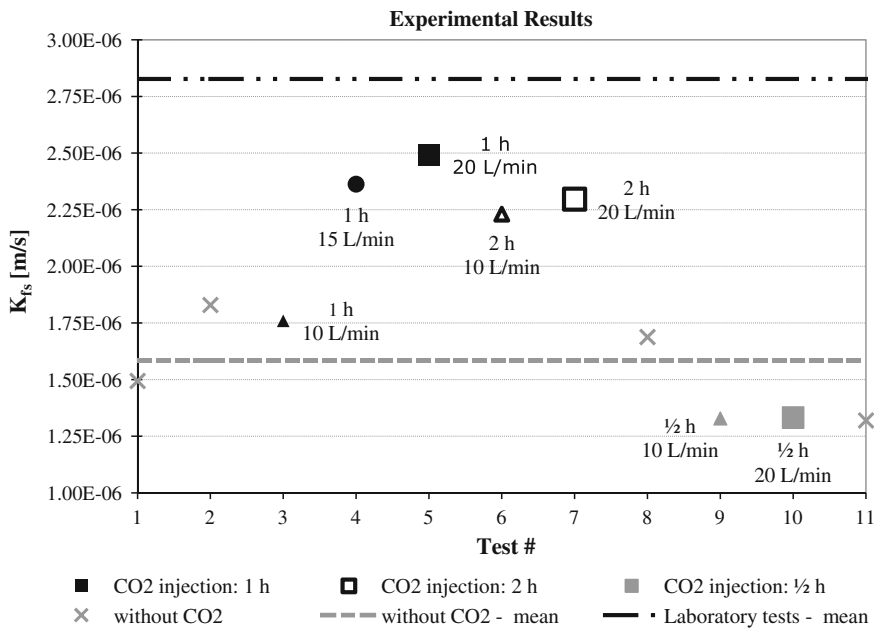


Fig. 4 Summary of the experimental results from the field tests and the laboratory tests

without CO₂ injection may provide further information on the infiltration process and could be another subject to future studies.

It needs to be mentioned that the K_{fs} -values given in Table 2 and Fig. 4 were not corrected for temperature changes and the corresponding changes in viscosity. Although the temperature of the infiltration water and the air temperature were recorded and showed strong diurnal variations depending on the weather conditions, continuous soil temperature measurements were not feasible in this small scale experiment. Since the measurements were conducted at a depth of 2 m and the total amount of infiltration water was only about 30 L in 4 h, soil temperature was considered as stable within the duration of a test as a first approximation. The laboratory saturated hydraulic conductivity is corrected to 15 °C, which resembles approximately the soil's temperature.

6 Conclusions and Prospects

The measuring instrument with a single electric scale and a submersible pump proved to be a practicable method for the in situ determination of K_{fs} in a depth of 2 m. The results of the field experiment (Fig. 4) show that measurements with this CHWP method underestimated K_{sat} . The injection of CO₂ proved to be a viable method to increase the field-saturated hydraulic conductivity closer to the

conductivity under saturated conditions. Injections for at least 1 h with 15–20 L/min were necessary in the silty, fine to medium sand. With an average of 1.58E–06 m/s for the tests without CO₂ (tests #1, #2, #8, #11) and 2.53E–06 m/s for the tests with sufficient CO₂ (tests #4, #5, #6, #7) the divergence from K_{sat} (2.83E–06 m/s) was reduced from 44 to 17 % due to the injection of CO₂.

Nevertheless, laboratory tests of the unsaturated hydraulic conductivity are considered necessary to estimate the degree of saturation achieved during the field tests. The effectiveness of the pretreatment with CO₂ needs to be examined for other kinds of soil, especially for consolidated and low permeability soils used in levee construction. In addition, the extent of the CO₂-injection of the saturated bulb around the borehole needs further experimental and numerical investigation to allow for a better understanding of the flow conditions and of the termination of each field test.

References

Boersma L (1965) Field measurement of hydraulic conductivity above a water table. In: Black CA (ed) Methods of soil analysis, part 1. American Society of Agronomy, Madison, pp 234–252

Christiansen JE, Fireman M, Allison LE (1946) Displacement of soil-air by CO₂ for permeability tests. *Soil Sci*

Fredlund DG, Rahardjo H (1993) Soil mechanics for unsaturated soils

Japanese Geotechnical Society (2004) Ground investigation: methods and descriptions. Japanese Geotechnical Society

Japanese Geotechnical Society (2009) Geomaterial testing: methods and descriptions

Philip JR (1985) Approximate analysis of the borehole permeameter in unsaturated soil. *Water Resour Res* 21(7):1025–1033

Reynolds WD (2013) An assessment of borehole infiltration analyses for measuring field-saturated hydraulic conductivity in the vadose zone. *Eng Geol* 159:119–130

Reynolds WD, Elrick DE (1985a) In situ measurement of field-saturated hydraulic conductivity, sorptivity, and the α -parameter using the Guelph permeameter. *Soil Sci* 140(4):292–302

Reynolds WD, Elrick DE (1985b) The constant head well permeameter: effect of unsaturated flow. *Soil Sci* 139(2):172–180

Stephens DB, Neuman SP (1983) In situ determination of hydraulic conductivity in the vadose zone using borehole infiltration tests

U.S. Bureau of Reclamation (1990) Performing field permeability testing by the well permeameter method, USBR 7300-89. In: Earth manual, part 2, 3rd edn. United States Department of the Interior, Bureau of Reclamation, Denver, pp 1227–1236

Zangar CN (1953) Theory and problems of water percolation, engineering. no 8. United States Department of the Interior, Bureau of Reclamation, Denver

Remediation of Volcanic Ash Soil in Related to Soil Erodibility Against the Heavy Rainfall

Rina Devnita, Ridha Hudaya, Rija Sudirja, Ade Setiawan, Mega F. Rosana and Hemanta Hazarika

Abstract Volcanic ash soil is a productive soil, but its P-retention has to be reduced to increase the available P. This research remedied the volcanic ash soil with steel slag and bokashi of husk to overcome the P-problem and to investigate their influence to soil physical aspects related to the soil erodibility. The treatments were arranged in randomized block designed in factorial pattern with two factors: steel slag and bokashi of husk, each consisted four levels: 0, 2.5, 5.0, and 7.5 % of soil weight (w/w), made the 4×4 or 16 combination treatments. The soil with each treatment was mixed thoroughly, filled into polybags, watered to the field capacity, closed tightly, incubated for four months, and sampled for chemical and physical analyses. The parameters were P-retention, available P, bulk density, organic carbon, permeability, and erodibility. Texture and structure was measured prior to the treatments to be calculated as erodibility factors. The results show that steel slag and bokashi of husk interact in increasing available P from 10.02 to 70.02 ppm. Steel slag and bokashi of husk do not interact in decreasing P-retention, decreasing bulk density and increasing permeability, but bokashi of husk individually shows the effect to such parameters. The soil erodibility is improved from 0.19 to 0.14. These results show that the remediation of volcanic ash soil to fix the P-status will also fix the soil erodibility against the heavy rainfall.

Keywords Steel slag • Bokashi of husk • Permeability • Organic carbon

R. Devnita (✉) · R. Hudaya · R. Sudirja · A. Setiawan
Department of Soil Science, Faculty of Agriculture, Padjadjaran University,
Jl. Raya Bandung-Sumedang km 21, Bandung 40600, Indonesia
e-mail: rina.devnita@unpad.ac.id; rinabursi@yahoo.com

M.F. Rosana
Faculty of Geology, Padjadjaran University, Bandung, Indonesia

H. Hazarika
Faculty of Engineering, Kyushu University, Fukuoka, Japan

1 Introduction

Volcanic ash soil can refer to soil that was derived from ash, tephras, or other pyroclastics materials (The Third Division of Soils 1973). Soil classification by United State Department of Agriculture classified this soil as Andisol (Soil Survey Staff 2014). The rapid weathering of pyroclastic materials serves the available nutrients for plants like calcium (Ca), potassium (K), magnesium (Mg), and others cations (Tan 1984). This contributes to its fertility, making this soil as one of the most productive soil in the world. The weathering product of ash materials also induces the distinctive soil physical characteristics like low bulk density (0.9 g cm^{-3} or lower), and lead to the another good soil characteristics like high total soil porosity, high permeability ($10^{-3}\text{--}10^{-4}\text{ cm s}^{-1}$), and high water holding capacity that can hold hygroscopic water of 35–36 %, capillary water of 21–27 %, gravitational water of 36–40 % (Bielders et al. 1990). These are the natural excellent and distinguish chemical and physical soil characteristics against the erosion.

Contrast to the distinguish some soil chemical and physical characteristics, volcanic ash soil has high phosphate (P) retention, contributes to the low P availability. Plants therefore have difficulty in absorbing P, one of the important macronutrient for plant (Nanzyo et al. 1993). This problem has to be overcome to reach the maximum capacity of this soil in serving food, fiber, and forage. Overcome the problem of P-retention to maintain the productivity of volcanic ash soils can be done by adding the silicate and organic matter. Steel slag and bokashi of husk can be used as silicate and organic matter in releasing the P-retention.

The main purpose of application steel slag and bokashi of husk is to remedy the soil chemical characteristics in reducing P-retention and increasing available P. The soil physical characteristics like bulk density, permeability, and aggregate stability should also gain attention as feared will aggravate them (Egashira 1983). Steel slag has a high-bulk density (1.7 g cm^{-3}) meanwhile volcanic ash soil has a low-bulk density ($\leq 0.9\text{ g cm}^{-3}$). Mixing steel slag with the soil was wonderer will increase the soil bulk density and lower the soil the permeability. There was not much research which considers the effect of chemical application to the soil physical characteristics. Whereas, those physical characteristics are the excellence hallmark of volcanic ash soil that must be protected due to allow the optimization of roots penetration, aerate condition, and the most important thing is the soil resistance against erosion or erodibility.

Soil erodibility was defined by McIntosh and Laffan (2005) as the inherent susceptibility of soil particles or aggregates to become detached or transported by erosive agents such as rainfall, runoff, throughflow, wind, or frost. The soil erodibility is calculated from parameters of soil permeability, texture, organic carbon content, and structure (Sing and Khera 2009). The application of steel slag and bokashi of husk will change the soil permeability and organic carbon content, and therefore is wondering will influence the soil erodibility against erosion.

This paper discusses the chemical (P-retention, available P, organic carbon) and physical properties (texture, structure, and permeability) of volcanic ash soil after

be treated with steel slag (as silicate) and bokashi (as organic matter), and their impact to the soil erodibility (K) against heavy rainfall.

2 Materials and Methods

The soil was collected from volcanic ash soil derived from Mt. Tangkuban Parahu in Lembang, West Java Indonesia. The experimental soil samples were acquired from several points in the location from the depth of 0–20 cm. Disturb soil samples were taken for measuring P-retention, available P, organic carbon, and texture. Undisturbed soil samples were taken with ring samples for measuring permeability. The soil was compositely mixed before be prepared for the treatments.

Randomized designed in factorial with two factors were used in the experimental polybags. The first factor was steel slag and the second factor was bokashi of husk with four levels: 0, 2.5, 5.0, and 7.5 % of soil on weight/weight (w/w) basis, respectively, and repeated twice. Soil used was 10 kg per polybag. Steel slag was crushed to the size of 200 mesh. Bokashi of husk were made by fermented the husk by the addition the microorganisms for 4 weeks. The combination of the treatments of this research is shown in Table 1, where s is stand for steel slag, and b is stand for bokashi of husk. The numeric of 0, 1, 2, and 3 represents the percentage of dosage treatments of 0, 2.5, 5.0, and 7.5 % of weight percentage (w/w) to the soil, respectively. The Duncan's new multiple range test was used for testing the mean differences.

The soils were mixed thoroughly with the treatments, filled in into the polybags of $60 \times 60 \times 60$ cm, watered to their field capacity and tightened well to prevent the evaporation. The soils with the treatments then be incubated for 4 months to have the expected reaction between the soils and the treatments. The soil analyses after treatments and incubation were P-retention (Blakemore et al. 1987), available P (Van Reeuwijk 1992), organic carbon (Walkley and Black 1934), permeability (Klute and Dirksen 1986), and structure (USDA 1983). The erodibility calculated following with the equation of erodibility by Wischmeier et al. (1971), Wischmeier and Smith (1978).

$$K = \frac{2.1M^{1.14}(10^{-4})(12 - \alpha) + 3.25(\beta - 2) + 2.5(\gamma - 3)}{100}, \quad (1)$$

where

M (% silt + % very fine sand) · (100-% clay),

α organic matter (%),

β structure code and

γ permeability rating.

Table 1 The combination treatments of steel slag and bokashi of husk

| Treatments | Steel slag (in weight percentage of soil) | | | | |
|---|---|-------------------------------|-------------------------------|-------------------------------|-------------------------------|
| | s ₀ | s ₁ | s ₂ | s ₃ | |
| Bokashi of husk (in weight percentage of soil) | b ₀ | s ₀ b ₀ | s ₁ b ₀ | s ₂ b ₀ | s ₃ b ₀ |
| | b ₁ | s ₀ b ₁ | s ₁ b ₁ | s ₂ b ₁ | s ₃ b ₁ |
| | b ₂ | s ₀ b ₂ | s ₁ b ₂ | s ₂ b ₂ | s ₃ b ₂ |
| | b ₃ | s ₀ b ₃ | s ₁ b ₃ | s ₂ b ₃ | s ₃ b ₃ |

3 Result and Discussions

3.1 Data of Soil, Steel Slag, and Bokashi of Husk Prior to the Treatmens

Based on the maps of soil, geology, topography, land use, climate, and administrative, the study area is volcanic ash soils developed from andesitic brownish sandy tuffs, very coarse hornblende crystals and red-weathered lahar, lapilli layers, and breccia of Mt. Dano and Mt. Tangkuban Parahu (Silitonga 2003), at the elevation of 8 %, at the coordinate point of 107°38'57.0" S-06°47'07.7" E, in district of Bandung Regency District, West Java Province, Indonesia.

Based on the laboratory analyses, the data of chemical and physical characteristics is presented in Table 2. This table informs that the organic carbon is less than 25 %, bulk density is less than 0.9 g cm⁻³, P-retention is more than 85 %, and Al + ½ Fe with ammonium oxalate is more than 2 %. These parameters inform that the soil fulfills the requirements of andic soil properties of volcanic ash soil (Soil Survey Staff 2014). The high P-retention (88.86 %) causes the low available P (9.41 ppm) Related to andesitic parent materials, the pH is acid (5.49). The texture is silty loam with granular to crumb structures, induce the medium permeability (3.36 cm h⁻¹) which is classed as 4 (USDA 1983). Erodibility following Wischmeier and Smith (1978) is 0.2.

The characteristics of steel slag and bokashi of husk is presented in Table 3. The steel slag used indicates that the content of silicate is high (12.5 %). During incubation period, the silicate was expected to release the anion to block the positive charge of Andisols and then release the P-retention to have the available Beck et al. (1999) inform that silicate can function as anion in releasing P-retention. The concentration of Ca was very high (42.00 %) which can function as lime to increase the pH and also help in releasing P-retention. Meanwhile the analyze of bokashi of husk indicated that the pH was high (7.47), expected in increasing soil pH. The C/N ratio was 17.95 indicated it can function as organic matter in serving the organic anion to block the positive charge of Andisol to release the P-retention.

Table 2 Physical and chemical characteristic of the soil

| No | Parameters | Unit | Value |
|----|--------------------------------------|--------------------|------------|
| 1 | Organic carbon | % | 4.43 |
| 2 | Bulk density | g cm ⁻³ | 0.95 |
| 3 | P-retention | % | 88.86 |
| 4 | Al + ½ Fe with acid ammonium oxalate | % | 5.00 |
| 5 | Available P | ppm | 9.41 |
| 6 | pH H ₂ O | — | 5.49 |
| 7 | Texture | — | Silty loam |
| | Silt | % | 60 |
| | Sand | % | 13 |
| | Very fine sand | % | 7 |
| | Clay (%) | % | 27 |
| 8 | Permeability | cm h ⁻¹ | 3.56 |
| | Permeability class | — | 4 |
| 9 | Erodibility (K) | — | 0.2 |

Table 3 Analyses of steel slag and bokashi of husk prior of treatments

| No. | Parameters | Unit | Value |
|------------------------|-------------------------------|-----------------------|-------|
| <i>Steel slag</i> | | | |
| 1 | SiO ₂ | % | 12.50 |
| 2 | CaO | % | 42.00 |
| 3 | MgO | % | 6.00 |
| 4 | P ₂ O ₅ | % | 0.50 |
| 5 | FeO | % | 0.81 |
| 6 | Water content | % | 1.00 |
| 7 | Bulk density | g cm ⁻³ | 1.70 |
| <i>Bokashi of husk</i> | | | |
| 1 | pH H ₂ O | — | 7.47 |
| 2 | CEC | cmol kg ⁻¹ | 50.01 |
| 3 | Organic carbon | % | 24.64 |
| 4 | Total nitrogen | % | 1.37 |
| 5 | C/N | — | 17.96 |
| 6 | Bulk density | g cm ⁻³ | 0.3 |

3.2 P-Retention and P Available

Steel slag and bokashi of husk do not interact in decreasing the P-retention but bokashi of husk individually decrease the P-retention from 92.33 % (without bokashi of husk) to 84.58 % (7.5 % bokashi of husk), as can be seen in Table 4.

Table 4 The individual influence of steel slag and bokashi of husk to P-retention (%)

| Steel slag | Dossage (%) | P-retention (%) | Bulk density (g cm ⁻³) | Permeability (cm h ⁻¹) | Organic carbon (%) | Erodibility |
|------------------------|-------------|-----------------|------------------------------------|------------------------------------|--------------------|-------------|
| s ₀ | 0 | 86.43 a | 86.43 a | 14.53 a | 12.69 a | 0.16 a |
| s ₁ | 2.5 | 87.10 a | 87.10 a | 15.44 a | 12.34 a | 0.16 a |
| s ₂ | 5 | 86.88 a | 86.88 a | 14.63 a | 12.52 a | 0.16 a |
| s ₃ | 7.5 | 87.88 a | 87.88 a | 12.30 a | 11.83 a | 0.16 a |
| <i>Bokashi of husk</i> | | | | | | |
| b ₀ | 0 | 92.33 b | 92.33 b | 3.66 a | 11.85 a | 0.19 b |
| b ₁ | 2.5 | 86.01 a | 86.01 a | 18.34 b | 11.94 a | 0.15 a |
| b ₂ | 5 | 85.31 a | 85.31 a | 16.72 b | 12.37 ab | 0.15 a |
| b ₃ | 7.5 | 84.58 a | 84.58 a | 18.18 b | 13.21 b | 0.14 a |

Note Same letters indicate no difference of the value between the treatments with Duncan multiple range test 5 %

Table 5 The interaction of steel slag and bokashi of husk to available P (ppm)

| Steel slag (%) | Bokashi of husk | | | |
|--------------------|--------------------|----------------------|--------------------|----------------------|
| | b ₀ 0 % | b ₁ 2.5 % | b ₂ 5 % | b ₃ 7.5 % |
| s ₀ 0 | 10.02 a (a) | 57.87 b (b) | 55.77 a (b) | 56.22 a (b) |
| s ₁ 2.5 | 34.24 b (a) | 43.21 a (b) | 65.51 b (c) | 70.02 b (c) |
| s ₂ 5 | 48.95 c (a) | 57.35 b (ab) | 60.53 ab (b) | 61.43 ab (b) |
| s ₃ 7.5 | 41.34 bc (a) | 54.34 b (b) | 58.18 ab (bc) | 65.24 ab (c) |

Note The letters in parentheses are read horizontally, the letters without parentheses are read vertically. Same letters indicate no difference of the value between the treatments with Duncan multiple range test 5 %

During the incubation period a certain amount of negative charge from bokashi of husk block the positive charge of volcanic ash soil make the P-retention decrease. Anion from organic material can release P and decrease the P-retention (Boniao 2000). In this research, the application of 2.5–7.5 % bokashi of husk reduced P-retention.

In other hand, steel slag and bokashi of husk interact in increasing the available as presented in Table 5. The available P increase from 10.02 % (without steel slag and bokashi of husk) to 34.24–70.02 % with the various combinations of steel slag and bokashi of husk. The increasing dosage of steel slag than bokashi of husk increases the available P. The highest available P (70.02 %) is obtained by the dosage of 2.5 % steel slag and 7.5 % bokashi of husk.

3.3 Bulk Density and Permeability

Steel slag and bokashi of husk do not interact in decreasing bulk density and increasing permeability, but bokashi of husk individually decreases bulk density to 0.47 g cm^{-3} (treatment of 7.5 % bokashi of husk) and increases the permeability to 18.34 cm h^{-1} as presented in Table 4. There is no effect of steel slag to bulk density means that steel slag do not increase it. The doubtfulness of the steel slag that has high bulk density (1.7 g cm^{-3}) much higher than soil bulk density (0.9 g cm^{-3}) will increase the bulk density of the media is therefore unproven. Perie and Quimet (2007), found the similar result with this research, where the increasing of organic matter will decrease the bulk density. Bouajila and Sanaa (2011) informed that the increase of organic matter will increase the permeability.

3.4 Organic Carbon

Steel slag and bokashi of husk do not interact in increasing organic carbon, but bokashi of husk individually increases it from 11.85 % (without bokashi of husk) to treatment of 7.5 % bokashi of husk and increases the permeability to 13.21 % (7.5 % bokashi of husk) as presented in Table 4. Increasing of bokashi of husk as organic matter logically will increase the organic carbon.

3.5 Erodibility

Soil erodibility is quite complex parameter that has to be determined by a various wide ranges of interlinked parameters, and be best obtained from direct measurements on runoff plots. However, many attempts have been made to relate the measurement of erodibility values with some soil parameters (Wischmeier et al. 1971; Wischmeier and Smith 1978). Following the equation of the erodibility by Wischmeier et al. (1971), the percentage of silt, very fine sand, clay, organic matter, structure, and permeability are involved in calculating of the erodibility. The percentage of the silt, very fine sand, and clay or particle size of these soils (with their treatments) has no difference since the particle size or texture will not change during the time of only several months. Therefore, erodibility in these treatments is only influenced by the organic carbon (%) and permeability value (classed from 1 to 7).

As the result, steel slag and bokashi of husk do not interact in improving the erodibility, but bokashi of husk individually improves it from 0.19 (without bokashi of husk) to 0.14 (treatment of 7.5 % bokashi of husk). The lower the erodibility value, the better the resistance of the soil against erosion, especially in facing the heavy rainfall.

4 Conclusions

Volcanic ash soil has good soil physical characteristics and a good value in erodibility which classified it as the soil with a high resistance against erosion in facing the heavy rainfall. Steel slag and bokashi of husk which is given to the soil for decreasing the P-retention and increasing the available P do not aggravate the soil erodibility, therefore those materials can be used to remediate the soil and keep maintaining the good soil physical aspects especially the soil erodibility.

References

Beck MS, Robarge WP, Buol SW (1999) Phosphorus retention and release of anions and organic carbon by two Andisols. *European J Soil Sci* 50:157–164

Bielders CLL, De Backer W, Delvaux B (1990) Particle density of volcanic soils as measured with a gas pycnometer. *Soil Sci Soc Am J* 54:822–826

Blakemore LC, Searle PL, Daly BK (1987) Methods for chemical analysis of soils. N. Z. Soil Bureau Sci Rep, vol 80. Soil Bureau, Lower Hutt, New Zealand, p 103

Boniao RD (2000) Amelioration of volcanic soils from Camiguin Island (southern Philippines) using natural amendments. Dissertation, University Putra Malaysia, p 250

Bouajila K, Sanaa M (2011) Effects of organic amendments on soil physico-chemical and biological properties. *J Matter Environ Sci* 2:485–490

Egashira K, Kaetsu Y, Takuma K (1983) Aggregate stability as an index of erodibility of ando soils. *Soil Sci Plant Nutr* 29:473–481

Klute A, Dirksen C (1986) Hydraulic conductivity and diffusivity, laboratory method. *Agron Monogram* 9:687–734

McIntosh PD, Laffan MD (2005) Soil erodibility and erosion hazard: extending these cornerstone soil conservation concepts to headwater streams in the forestry estate in Tasmania. *Forest Ecol Manag* 220:128–139

Nanzyo M, Shoji S, Dahlgren R (1993) Physical characteristics of volcanic ash soils. In: Shoji S, Nanzyo M, Dahlgren, R (eds) *Volcanic ash soil—genesis, properties and utilization. Developments in soil science*, vol 21. Elsevier, Amsterdam, pp 189–207

Perie C, Quimét R (2007) Organic carbon, organic matter and bulk density relationships in boreal forest soils. *Can J Soil Sci* 16:315–325

Silitonga PH (2003) Geological map of Bandung, west java, Indonesia. Department of Energy and Mineral Resources, Indonesia, p 1

Singh MJ, Khera KL (2009) Nomographic estimation and evaluation of soil erodibility under simulated and natural rainfall conditions. *Land Degr Devel* 20:471–480

Soil Survey Staf (2014) Keys to soil taxonomy 12th edn. Natural Resources Conservation Service, p 332

Tan KH (1984) Andosols. A Hutchinson Ross Benchmark Book, Van Nostrand, Reinhold Company, p 418

The Third Division of Soils (1973) Criteria for making soil series and a list of sol series. The first approximation. National Institute Agricultural Research, Japan

United State Department of Agriculture, USDA (1983) National soil survey handbook no 430. Washington, DC

Van Reeuwijk LP (1992) Procedure for soil analysis. ISRIC, Wageningen, The Netherlands 56 p

Walkley A, Black IA (1934) An examination of the method for determining organic carbon in soils: Effect of variations in digestion conditions and of inorganic soil constituents. *Soil Sci* 63:251–263

Wischmeier WH, Smith DD (1978) Predicting rainfall erosion losses—a guide to conservation planning. United States Department of Agriculture Agricultural Handbook, 537 US Government Printing Office, Washington, DC, USA

Wischmeier WH, Johnson CB, Cross BV (1971) A soil erodibility nomograph for farmland and construction sites. *J Soil Water Conserv* 5:189–193

Structural Pattern's Effects on the Tensile Properties of Hexagonal Wire Meshes (12 cm × 15 cm)

Chiwan Hsieh, Zhi-Yao Cai and In-Wei Liu

Abstract Three half-turn (Type A) and four half-turn (Type B) hexagonal wire mesh panels were used for tensile tests with and without one center-cut wire mesh panel. The panel opening was 120 by 150 mm. The test loadings were applied either parallel (in longitudinal direction) or perpendicular (in transverse direction) to the twist wire sections. The study results indicated that the ultimate tensile strength for Type A and hexagonal wire mesh panels without any cut loading in longitudinal or transverse direction were similar. However, the four half-turn hexagonal wire panels showed better tensile resistance after one wire broke at the panel center for both loadings either in longitudinal or in transverse condition. This implied that the presence of broken wires within the four half-turn hexagonal wire mesh showed slight influence on the panel's tensile strength. In general, the tensile strengths for the test conditions for loading in longitudinal direction were about double of those loading in transverse direction. In conclusion, four half-turn (Type A) hexagonal wire mesh is a better structural pattern than a three half-turn (Type B) hexagonal wire mesh for slope stability and river bank protection applications.

Keywords Hexagonal wire mesh · Gabion · River bank protection · Slope stabilization · Rockfall protection

1 Introduction

Metal wire mesh is commonly practiced for river bank protection, rockfall protection, and slope stabilization applications. Currently, the use of wire mesh for river bank protection and slope stabilization applications is more than 15 million square meters. Only the materials cost is more than 20 billion New Taiwan dollars. Currently, the replacement of wire mesh for these applications is too often. To develop a better mechanism to construct metal wire mesh is an important task. The

C. Hsieh (✉) · Z.-Y. Cai · I.-W. Liu

National Pingtung University of Science and Technology, Pingtung, Taiwan
e-mail: cwh@mail.npust.edu.tw

early age handmade fourth-twisted hexagonal wire meshes were observed to be more durable than those current machine made triple-twisted hexagonal wire meshes. Therefore, the objective of this study is to study a better structural pattern and connection mechanism to produce durable hexagonal wire mesh.

2 Test Materials and Test Method

Three half-turn (Type A) and four half-turn (Type B) twisted hexagonal wire mesh panels were tested to evaluate the difference in engineering behavior using tensile tests. The mesh was woven using a nominal diameter 4.0 mm galvanized steel wires with coating weight of 342 g/m^2 . The tensile strength of the steel wire is 430 N/mm^2 . 120 by 50 mm mesh opening was used to construct a near perfect hexagonal pattern wire for both types. ASTM A975 and A370 test methods were used in these tests. Wire mesh panel tensile tests loading either in longitudinal direction or in transverse direction with and without a center-cut wire were conducted.

The differences in weaving pattern between three half-turn (Type A) and four half-turn (Type B) twisted hexagonal wire meshes are shown in Fig. 1. As shown, top-down (vertical) and diagonal weaving patterns were observed for three half-turn and four half-turn wire meshes, respectively. The top-down or diagonal woven patterns were used for Type A and Type B wire mesh panels, respectively. Different engineering behaviors can be expected due to the differences in weaving

Fig. 1 Schematic view of wire weaving pattern for Type A and Type B wire meshes

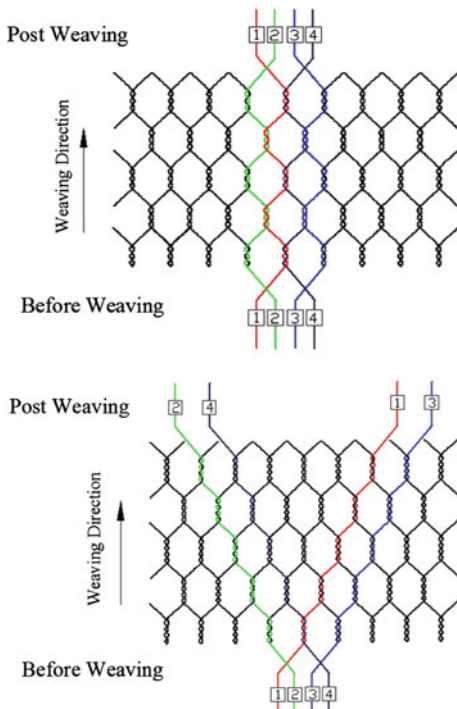


Fig. 2 Schematic view of the setup for tensile test



structure and loading direction of these two meshes. The tensile test sample setup is shown in Fig. 2. The tensile test panel dimension was 1000 by 533 mm.

3 Results and Conclusions

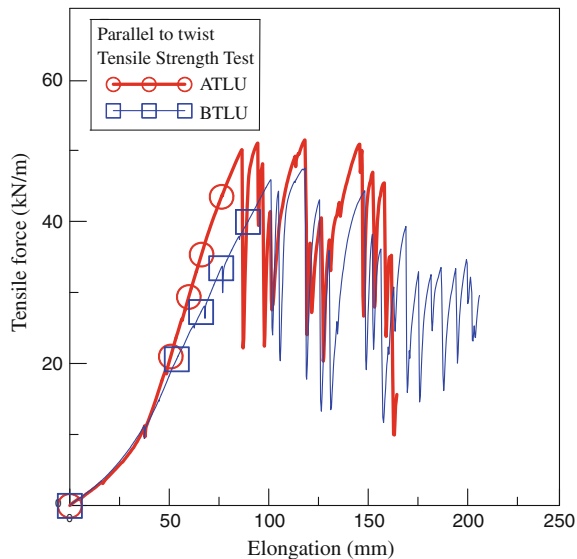
A series of wide width tensile tests were conducted according to the ASTM D975 test method. Tensile tests for Type A and Type B twisted hexagonal wire mesh panels loading either in longitudinal or in transverse direction with and without one center wire cut were conducted. A minimum of three tests were conducted for each test condition to prove the repeatability of the engineering behavior. A high degree of repeatability for the tensile tests for Type A and Type B twisted hexagonal wire mesh panels loading in longitudinal direction was achieved.

The research test results of the test conditions are discussed below. The material and test conditions are represented using four letters. The first letter indicated the test material, A for Type A wire mesh, or B for Type B mesh panel. Second letter T or P indicates the tensile test or punch test. Punch test is not discussed in this paper. The third letter of L or T represents the loading direction either in longitudinal or transverse direction. The fourth letter U or C indicates for uncut or cut center wire panel used in the test.

3.1 Tensile Tests Loading in Longitudinal Direction Without a Center-Cut Wire

The tensile test results loading in longitudinal direction for three half-turn (Type A) and four half-turn (Type B) hexagonal wire mesh panels without a center-cut wire are shown in Fig. 3. As shown, the tensile stress versus elongation curves can be divided into three stages. The initial tensile stress versus elongation curves for both mesh types are quite similar to each other. Based on observation, the elongations

Fig. 3 Typical tensile test results for Type A and Type B mesh panels loading in longitudinal direction without one cut wire



were contributed by both the straight and twisted wire sections of the hexagonal wire mesh for stage-1 and stage-2.

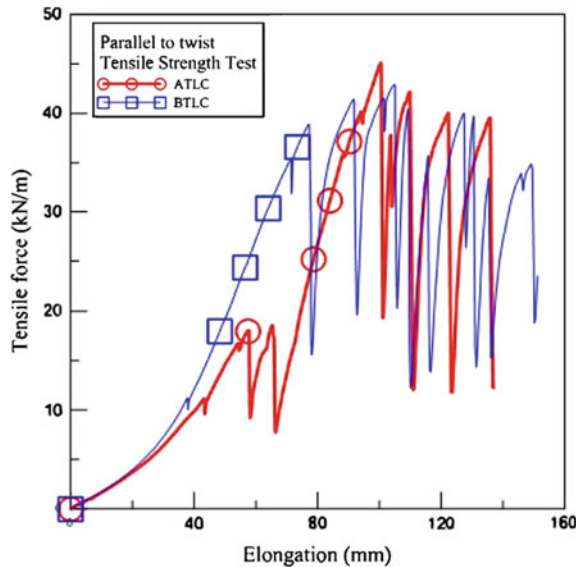
The first peak tensile stress occurred at elongation at 87 and 101 mm for Type A and Type B wire mesh, respectively. The first peak tensile stress for Type A wire mesh (50 kN/m) is slightly higher than that for Type B wire mesh (46 kN/m). After the tensile stress reached a peak and wire breakage, a drop in tensile stress associated with mesh elongation and steel wire de-twisting occurred near the broken wire. In general, one peak stress is associated with breaking one steel wire.

Several similar consecutive peak tensile forces were observed after the first peak tensile force occurred as the elongation continued for both wire mesh panels. The elongation after the first peak represented stage-3 elongation. A larger amount of elongation between each consecutive break was also observed for the Type A mesh test. This implied that Type A wire mesh elongated more and quicker than Type B wire mesh. The consecutive peak tensile forces for the Type B wire mesh panel decreased as the elongation increased. However, the elongation between each consecutive break was significantly less than that for Type A wire mesh. This implied that Type B wire mesh deformed less when subjected to tensile loads.

3.2 Tensile Test of Panel Loading in Longitudinal Direction with a Center-Cut Wire

In real-life situations, steel wires in a panel could be broken by stones or other objects during panel service life. Therefore, it is necessary to study the engineering behavior of steel wire mesh with a broken (cut) steel wire. A series of tensile tests

Fig. 4 Typical tensile test results for Type A and Type B mesh panels loading in longitudinal direction with one cut wire

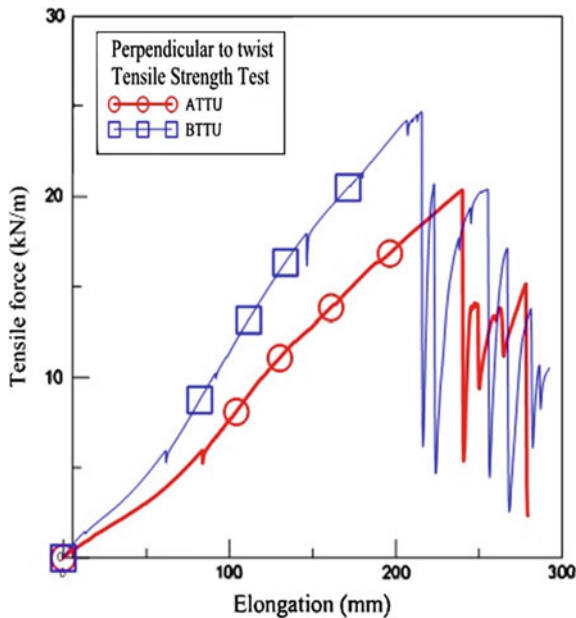


for Type A and Type B hexagonal wire mesh panels loading in longitudinal direction with one center wire cut was performed. The typical tensile stress versus elongation curves are shown in Fig. 4. Due to the presence of pre-cut wire, the first and second peak strengths were only about 18 kN/m and the peak elongations were about 60 mm for Type A wire mesh panel. Low loading resistance and steel wire de-twisting around the pre-cut wire were observed. On the other hand, the first and second peak tensile stresses for Type B mesh panel were around 40 kN/m. It is expected that to induce the failure of Type B required more tensile work energy to cause failure of pre-cut wire panel than that for Type A panel. As shown in the figure, the maximum tensile stresses for both wire mesh types were about 44 kN/m and quite similar to each other. The associated peak elongations were about 103 mm and also similar to each other.

3.3 Tensile Tests Loading in Transverse Direction Without a Center-Cut Wire

In addition to the tensile strength of mesh panel in longitudinal direction, the minimum tensile strength of hexagonal wire mesh loading in transverse direction is also an important material specification in the ASTM A975 standard specification. Therefore, a series of tensile test results loading in transverse direction for three half-turn (Type A) and four half-turn (Type B) hexagonal wire mesh panels without a center-cut wire was also conducted in the study.

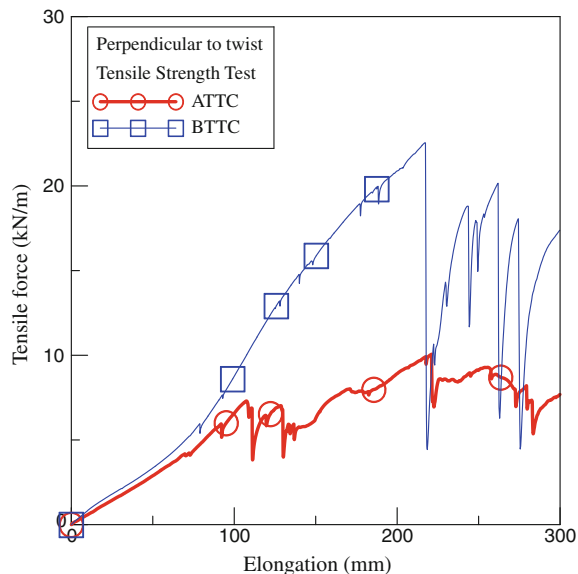
Fig. 5 Typical tensile test results for Type A and Type B mesh panels loading in transverse direction without one cut wire



The typical tensile test results loading in transverse direction for three half-turn (Type A) and four half-turn (Type B) hexagonal wire mesh panels without a center-cut wire are shown in Fig. 5. The tensile stress versus elongation curves can be divided into two stages. The initial tensile stress versus elongation curves (stage-1) for both mesh types are quite similar to each other. The tensile load was uniformly transferred through the panel steel wires and induced the necking in the central region of the panels. The peak tensile strength for the Type B panel (25 kN/m) is slightly higher than that for Type A panel (20 kN/m). However, the associated elongation at peak for Type B panel (215 mm) is also slightly less than that for Type A panel (240 mm).

Several similar consecutive peak tensile forces were observed after the first and highest peak tensile force occurred as the elongation continued for both wire mesh panels. Wire breakage normally occurred near two sides of the panels initially. The elongation after the first peak represented stage-2 elongation. A larger amount of elongation in conjunction of wire de-twisted around the broken wires between each consecutive break was also observed for the Type A mesh test. This implied that Type A wire mesh elongated more and quicker than Type B wire mesh. The consecutive peak tensile forces for the Type B wire mesh panel decreased as the elongation increased. However, the elongation between each consecutive break was significantly less than that for Type A wire mesh. This implied that Type B wire mesh deformed less when subjected to tensile loads.

Fig. 6 Typical tensile test results for Type A and Type B mesh panels loading in transverse direction with one cut wire



3.4 Tensile Test of Panel Loading in Transverse Direction with a Center-Cut Wire

A series of tensile tests for Type A and Type B hexagonal wire mesh panels loading in transverse direction with one center wire cut was also performed. The typical tensile stress versus elongation curves are shown in Fig. 6. Due to the presence of pre-cut wire, the first and second peak strength were only about 7 kN/m and the peak elongations were greater than 107 mm for Type A wire mesh panel. Low loading resistance and steel wire de-twisting around the pre-cut wire were observed. On the other hand, the first peak tensile stress for Type B mesh panel was 23 kN/m. The loading was uniformly distributed to all steel wires in the panel. The presence of pre-cut wire showed a minimum influence on the tensile test results. Consecutive wire breakages near the pre-cut wire were observed for Type B wire panel.

4 Conclusions

The average replacement time for wire mesh gabions for river bank protection and stabilization applications is about seven years in Taiwan. The annual material cost for this is more than 2 billion New Taiwan dollars. This study investigated the engineering behavior of three half-turn and four half-turn hexagonal wire meshes using tensile tests loading either in longitudinal direction or in transverse direction.

The results indicated that the ultimate tensile strength for three half-turn or four half-turn hexagonal wire mesh panels loading in longitudinal or transverse direction without cut wires were similar to each other. However, the four half-turn hexagonal wire panels showed better tensile after one wire was cut at the panel center to simulate mesh damage that could occur during typical field situations. This implies that the presence of broken wires within the four half-turn hexagonal wire mesh would have less effect on the panel tensile strength.

In general, the tensile strengths for the conditions for loading in longitudinal direction is about double in comparing with the conditions loading in transverse direction for both types wire mesh panels. The four half-turn hexagonal wire mesh is a more robust and durable weaving pattern than three half-turn hexagonal wire mesh. It is suggested that the place of wire mesh with twisted section is parallel to the loading direction. The results provide important technical information that, if implemented, could extend the design life and, thus, reduce the life cycle cost of wire gabion installations when used for river bank protection applications.

References

- ASTM A975-97 (1997) Double-twist hexagonal mesh gabions and revet mattresses (metallic-coated steel wire or metallic-coated steel wire with poly (vinyl chloride) (PVC) coating), Philadelphia, USA
- ASTM A370-97a (1997) Standard test methods and definitions for mechanical testing of steel products. Philadelphia, USA